Doctoral Thesis

DEVELOPMENT OF CONDITION-BASED TAMPING PROCESS IN RAILWAY ENGINEERING

Operating Phases and Motion Behavior, Ballast Condition Determination, Ballast fluidization

submitted in satisfaction of the requirements for the degree of
Doctor of Science in Civil Engineering
at TU Wien, Faculty of Civil Engineering

Dissertation

WEITERENTWICKLUNG DES ZUSTANDSABHÄNGIGEN GLEISSTOPFVERFAHRENS

Betriebsphasen und Bewegungsverhalten, Schotterzustandserkennung, Schotterfließen

ausgeführt zum Zwecke der Erlangung des akademischen Grades eines
Doktors der technischen Wissenschaften
eingereicht an der Technischen Universität Wien, Fakultät für Bauingenieurwesen
von

Dipl.-Ing. **Olja Barbir**

1. Gutachter & Betreuer: Univ.Prof. Dipl.-Ing. Dr.techn. **Dietmar Adam**
Betreuer: Assistant Prof. Dipl.-Ing. Dr.techn. **Johannes Pistrol**
Institut für Geotechnik
Technische Universität Wien
Karlsplatz 13/220-2, A-1040 Wien

2. Gutachter: Prof.Dr. **Janko Logar** univ.dipl.inž.grad.
Faculty of civil and geodetic engineering
University of Ljubljana
Jamova cesta 2, 1000 Ljubljana, Slovenia

3. Gutachter: Red.prof.dr.sc. **Željko Arbanas** dipl.ing.građ.
Faculty of Civil Engineering, Department of Geotechnics
University of Rijeka
Radmile Matejčić 3, 51000 Rijeka, Croatia

Wien, September 2022 _____

Die approbierte gedruckte Originalversion dieser Dissertation ist an der TU Wien Bibliothek verfügbar.
The approved original version of this doctoral thesis is available in print at TU Wien Bibliothek.

Die approbierte gedruckte Originalversion dieser Dissertation ist an der TU Wien Bibliothek verfügbar.
The approved original version of this doctoral thesis is available in print at TU Wien Bibliothek.

"bez tebe drveni konjići tužno stoje"

ovaj rad je, zajedno sa svime što jesam i što ću postići u životu,
inspiriran, motiviran i posvećen najboljem tati

zajedno s tvojim, stalo je i pola moga srca

volim te

Die approbierte gedruckte Originalversion dieser Dissertation ist an der TU Wien Bibliothek verfügbar.
The approved original version of this doctoral thesis is available in print at TU Wien Bibliothek.

Die approbierte gedruckte Originalversion dieser Dissertation ist an der TU Wien Bibliothek verfügbar.
The approved original version of this doctoral thesis is available in print at TU Wien Bibliothek.

Abstract

Maintenance of ballasted tracks becomes an increasingly demanding task with the continuous increase of railway traffic of both passengers and freight. Nowadays, most of track maintenance work is conducted using modern tamping machines. The process of lifting, leveling and non-synchronous, directional constant pressure tamping has been proven to provide optimal results in regard to continuous ballast compaction and restoration of initial track geometry.

Most desirable method of track maintenance, from an economic point of view, is condition - based predictive maintenance. This method dictates that decisive parameters should be adjusted to the encountered track condition. State-of-the-art tamping machines, however, operate with previously defined tamping parameter combination, whereby only a minority of parameters are adapted to the ballast bed condition.

Research conducted in the scope of this thesis investigates fundamentals of the tamping process and the soil mechanical component of ballast compaction. For this purpose, comprehensive investigation of the track tamping process during regular track maintenance in different ballast conditions is conducted, primarily focusing on the interaction between the tamping tine and the ballast matrix during ballast compaction. For the very first time, these two components are observed on a vibration cycle scale, and a new method of measuring and interpretation of their force-deformation relationship in form of a load-displacement diagram is developed. This presentation made it possible to determine tamping characteristics, such as reaction force and compaction energy, that result from a given set of tamping parameters. Comparison of tamping characteristics between tamping machine employment at different locations made it possible to clearly identify the ballast bed condition based on its interaction with the tamping tine. This observation represents the base for future development of condition-based tamping process in which the tamping parameters would be adapted to the ballast condition measured by the machine during tamping.

Irrefutable evidence of a periodic loss of contact between tamping tine and ballast matrix is presented based on contact points obtained from load-displacement diagrams. Existence of this contactless phase in each vibration cycle reduces ballast wear and has a positive influence on the compaction process. Soil dynamic behavior of track ballast during compaction was investigated and in-situ tests were conducted in order to enable a qualitative description of track ballast dynamic fluidization, a phenomenon that plays a decisive role in clean ballast compaction by both tamping unit and dynamic track stabilizer.

A numerical simulation of the tamping tine - ballast matrix interaction during com-

Die approbierte gedruckte Originalversion dieser Dissertation ist an der TU Wien Bibliothek verfügbar.
The approved original version of this doctoral thesis is available in print at TU Wien Bibliothek.
TU Bibliothek Your knowledge hub WIEN

paction was developed, providing the possibility to model continuous fouling of the track ballast by adjusting one single parameter - elastic stiffness of the ballast model. Model calibration was conducted using in-situ measurement results and it was utilized to carry out a comprehensive study of tamping parameters and their effect on the load-displacement curve and tamping characteristics.

Measurement system and analysis algorithm presented in this thesis provide the possibility to transform and upgrade the tamping unit from track maintenance into a *Smart tamping tool*, resulting in optimization of the tamping process and a prolongation of ballast life-cycle, while increasing the quality of the whole track system.

Die approbierte gedruckte Originalversion dieser Dissertation ist an der TU Wien Bibliothek verfügbar.
The approved original version of this doctoral thesis is available in print at TU Wien Bibliothek.
TU Bibliothek Your knowledge hub WIEN

Kurzfassung

Mit der kontinuierlichen Zunahme des Personen- und Güterverkehrs auf der Schiene wird die Instandhaltung von Schottergleisen zu einer immer anspruchsvolleren Aufgabe. Heutzutage wird ein Großteil der Gleisinstandhaltungsarbeiten mit modernen Stopfmaschinen durchgeführt. Das Verfahren des Hebens, Nivellierens und des Asynchron-Gleichdruck-Stopfens liefert nachweislich optimale Ergebnisse im Hinblick auf die kontinuierliche Schotterverdichtung und die Wiederherstellung der ursprünglichen Gleisgeometrie. Die aus wirtschaftlicher Sicht wünschenswerteste Methode der Gleisinstandhaltung ist zustandsorientiert, wobei die entscheidenden Parameter an den vorgefundenen Gleiszustand angepasst werden sollten. Moderne Stopfmaschinen arbeiten jedoch mit vorher definierter Stopfparameterkombination, wobei nur wenige Parameter an den Schotterbettzustand angepasst werden.

Die im Rahmen dieser Arbeit durchgeführten Untersuchungen befassen sich mit den Grundlagen des Stopfprozesses und den bodenmechanischen Aspekten der Schotterverdichtung. Dazu wurde eine umfassende Untersuchung des Stopfprozesses bei regelmäßiger Gleisinstandhaltung in unterschiedlichen Schotterzuständen durchgeführt, wobei vor allem die Wechselwirkung zwischen Stopfpickel und Schottermatrix bei der Schotterverdichtung im Vordergrund steht. Erstmals werden diese beiden Komponenten auf einer Schwingungszyklusskala betrachtet und eine neue Methode zur Messung und Interpretation ihrer Kraft-Verformungs-Beziehung in Form eines Arbeitsdiagramms entwickelt. Diese Darstellung ermöglicht es, Stopfkenngrößen wie Reaktionskraft und Verdichtungsenergie, die sich aus einem gegebenen Satz von Stopfparametern ergeben, zu bestimmen. Der Vergleich der Stopfkenngrößen zwischen Stopfmaschineneinsätzen an verschiedenen Standorten ermöglichte eine eindeutige Identifizierung des Schotterbettzustandes aufgrund seiner Wechselwirkung mit dem Stopfpickel. Diese Erkenntnis bildet die Grundlage für die künftige Entwicklung eines zustandsabhängigen Stopfverfahrens, bei dem die Stopfparameter an den von der Maschine während des Stopfens gemessenen Schotterzustand angepasst werden.

Der unwiderlegbare Beweis für einen periodischen Kontaktverlust zwischen Stopfpickel und Schottermatrix wird anhand der aus den Arbeitsdiagrammen gewonnenen Kontaktpunkte erbracht. Das Vorhandensein dieser kontaktlosen Phase in jedem Vibrationszyklus verringert den Schotterverschleiß und hat einen positiven Einfluss auf die Verdichtung. Bodendynamisches Verhalten des Gleisschotters während der Verdichtung wurde untersucht und In-situ-Versuche wurden durchgeführt, um eine qualitative Beschreibung der temporären dynamische Fluidisierung des Gleisschotterkorngerüstes zu ermöglichen, ein Phäno-

Die approbierte gedruckte Originalversion dieser Dissertation ist an der TU Wien Bibliothek verfügbar.
The approved original version of this doctoral thesis is available in print at TU Wien Bibliothek.
TU Bibliothek Your knowledge hub WIEN

men, das bei der Verdichtung von neuem Schotter durch Stopfaggregat und dynamischen Gleisstabilisator eine entscheidende Rolle spielt.

Es wurde eine numerische Simulation der Wechselwirkung zwischen Stopfpickel und Schottermatrix während der Verdichtung entwickelt, die es ermöglicht, die kontinuierliche Verschmutzung des Gleisschotters durch die Anpassung eines einzigen Parameters - der elastischen Steifigkeit des Schottermodells - zu modellieren. Die Kalibrierung des Modells wurde anhand von In-situ-Messergebnissen durchgeführt und für eine umfassende Untersuchung der Stopfparameter und ihrer Auswirkungen auf das Arbeitsdiagram und auf Stopfkenngrößen genutzt.

Das in dieser Arbeit vorgestellte Messsystem und der Analysealgorithmus bieten die Möglichkeit, das Stopfaggregat aus der Gleisinstandhaltungs- in ein intelligentes Stopfwerkzeug umzuwandeln und aufzurüsten, was zu einer Optimierung des Stopfprozesses und einer Verlängerung der Lebensdauer des Schotters führt, während die Qualität des gesamten Gleissystems erhöht wird.

Die approbierte gedruckte Originalversion dieser Dissertation ist an der TU Wien Bibliothek verfügbar.
The approved original version of this doctoral thesis is available in print at TU Wien Bibliothek.
TU Bibliothek Your knowledge hub WIEN

Acknowledgment

This thesis came into being during my employment at the Institute of Geotechnics, Research Unit Ground Engineering, Soil and Rock Mechanics of the TU Wien, in scope of the research project "Development of condition-based tamping process in railway engineering". I would like to express my deepest gratitude to Univ.Prof. Dipl.-Ing. Dr.techn. Dietmar Adam, not only for the continuous support, suggestions and supervision of this work, but also for giving me the opportunity to be a part of his team.

My gratitude goes out to Prof.Dr. Janko Logar for reviewing the thesis, for his support and for bringing a special kind of energy that made our institute a nicer place during his stay. Special thanks to Red.prof.dr.sc. Željko Arbanas for reviewing the thesis and for his inspiring lectures that sparked my interest in geotechnics.

I would like to extend my deepest appreciation to Priv.Doz. Dipl.-Ing. Dr.techn. Fritz Kopf - for all your support and patience, continuous encouragement and guidance, for all the fruitful discussions and for selflessly sharing your knowledge - thank you Fritz! To Assistant Prof. Dipl.-Ing. Dr.techn. Johannes Pistrol, for the guidance, support and priceless advice, for always finding time and for always understanding - thank you!

Without the support of Plasser & Theurer, Export von Bahnbaumaschinen, Gesellschaft m.b.H., this work would have been neither technically nor financially feasible. Special thanks to Dipl.-Ing. Dr.techn. Florian Auer for initiating this project and for his guidance and support. To the whole TAMP team - I am deeply grateful for the tireless efforts, for sitting in on all the meetings, for the feedback, cooperation and technical support. I would also like to extend my thanks to Dipl.-Ing. Dr. mont. Christian Koczwara, for his feedback and support during the last steps. Last but in no way least - to Dipl.-Ing. Bernhard Antony - thank you for supporting me when I needed it the most, thanks for your encouragement and for always pushing me forward. This endeavor would not have been possible without you.

A very special thanks goes out to my colleagues at the Institute of Geotechnics as well as to the laboratory staff. Thanks to Dipl.-Ing. Dr.techn. Adrian Kainrath, Dipl.-Ing. Viktoria Ostermann, Dipl.-Ing. Dr.techn. Cătălin Căpraru, Dipl.-Ing. Armin Steurer, Dipl.-Ing. Dr.techn. Stefan Blovsky, Dipl.-Ing. Gabrijela Kvasina, BSc and Dipl.-Ing. Joachim Wagner, BSc for always making me feel part of the team. I would like to offer my special thanks to Dipl.-Ing. Dr.techn. Péter Nagy, BSc, Dipl.-Ing. Mario Hager, BSc, Dipl.-Ing. Manuel Dafert, BSc and Dipl.-Ing. Adrian Brunner, BSc - thank you guys for making the past years much more enjoyable and for never letting me be thirsty. Many thanks to my IGB Girls, Dipl.-

Die approbierte gedruckte Originalversion dieser Dissertation ist an der TU Wien Bibliothek verfügbar.
The approved original version of this doctoral thesis is available in print at TU Wien Bibliothek.
TU Bibliothek Your knowledge hub WIEN

Ing. Marta Dimova and Julia Corinna Ickenroth, for your support, company and friendship. For their assistance and support in the laboratory I'm extremely grateful to Ing. Andreas Hausenberger, Gerhard Steinbauer, Michael Dürmoser and Alfred Nitz. For answering a million of my questions and always doing it with a smile on her face, thank you Gerda Bruckner-Pfleger! In addition, I would like to extend my sincere thanks to Ann-Christine Dziwok, Katharina Zak and Anna Zahradnik. Thank you all for everything!

Many thanks to Dipl.-Ing. Theresa Hofbauer, BSc, Dipl.-Ing. Robin Bayerhofer, BSc and Ing. Vojta Škara for their contribution to this thesis.

I am also thankful to Austrian Federal Railways (ÖBB) for their cooperation and for providing technical support during measurements on the tracks. For being patient and welcoming to both us and our measuring system, a special thanks goes out to Plasser & Theurer tamping machine operators.

♢

Najveća mi je sreća ovdje spomenuti ljude koji su me nesebično podržavali sve ove godine, iako znam da je to neprevodivo u riječi. Anja V., hvala za sve korake koje smo skupa prošle. Anja W., hvala što si uvijek tu, nesebično, stabilno i odlučno. Hvala ti za sve što si napravila, hvala što si bila tamo onaj dan da me zagrliš, to nikad neću zaboraviti. Vlasta, Enia, Dunja, Nina - hvala za sve. Mojoj dragoj Mami i Bratu, što me uvijek bezuvjetno podržavaju, hrabre i vole, hvala vam! Baka Bosi, svim nenavedenim prijateljima i obitelji - hvala!

Najveće hvala ide tebi, Bruno. Što si me podržavao, nasmijavao i trpio kroz sve ove godine, što si bio snažan i kad ja nisam. Što si prošao sa mnom kroz najgore trenutke, uvijek me čvrsto držeći za ruku. Hvala i za sav trud i vrijeme koje si sam uložio u ovaj rad, bez tebe on ne bi ni postojao.

Za kraj, Tata. Hvala ti. Za to što si me naučio kako gledati svijet, za tvoje veliko srce i najtoplije zagrljaje. Hvala ti što si uvijek bio tu, što si uvijek znao šta treba. Teško je zamisliti da nećeš biti tu da mi kažeš "Bravo mačak!", ali tako je valjda moralo biti. Hvala ti što sam imala najboljeg tatu. Nedostaješ nam, uvijek, isto kao i prvog dana.

Die approbierte gedruckte Originalversion dieser Dissertation ist an der TU Wien Bibliothek verfügbar.
The approved original version of this doctoral thesis is available in print at TU Wien Bibliothek.
TU Bibliothek Your knowledge hub WIEN

Contents

1 Introduction **1**

1.1 Background and problem statement 2

1.2 Objectives and research scope 3

2 Ballasted track **5**

2.1 Introduction 5

2.2 Ballast bed 7

2.2.1 Ballast behavior governing factors 8

2.2.2 Ballast aggregate parent rock compendium and strength 16

2.2.2.1 Geological deposits for track ballast production in Austria . 18

2.2.3 Technical requirements for railway ballast in Austria 19

2.2.3.1 Geometrical requirements 19

2.2.3.2 Chemical requirements 20

2.2.3.3 Physical requirements 20

2.2.3.4 Applicable standards 25

2.2.4 Resilient modulus 26

2.2.5 Ballast bed permanent strain 28

2.2.6 Ballast grain fracture strength 29

2.2.6.1 Tensile strength of a single particle 30

2.2.6.2 Particle embedded in a sample 31

2.2.6.3 Ultrasonic Pulse Velocity 32

2.3 Rails 33

2.4 Sleepers 34

2.5 Fastening systems 36

2.6 Subballast and subgrade 36

2.7 Stresses acting on the ballast bed 37

2.7.1 Stresses on the rail head 37

2.7.2 Ballast bed coefficient 40

2.7.3 Ballast pressure under the sleeper 41

2.7.4 Load dispersion in the ballast bed 42

2.7.5 Ballast shear strength 43

Die approbierte gedruckte Originalversion dieser Dissertation ist an der TU Wien Bibliothek verfügbar.
The approved original version of this doctoral thesis is available in print at TU Wien Bibliothek.

3 Ballast fouling **45**
3.1 Introduction . . . 45
3.1.1 Ballast hydraulic erosion . . . 46
3.2 Ballast fouling quantification . . . 47
3.2.1 Index of Particle Breakage (B_g) . . . 47
3.2.2 Fouling Index (FI) . . . 48
3.2.3 Percentage of Fouling (Percentage Passing) . . . 50
3.2.4 Percentage Void Contamination (PVC) . . . 50
3.2.5 Void Contaminant Index (VCI) . . . 51
3.2.6 Relative Ballast Fouling Ratio ($R_{b\text{-}f}$) . . . 52
3.2.7 Ballast Breakage Index (BBI) . . . 53
3.2.8 Ballast life prediction as a function of the ballast fouling quantification 54
3.2.9 Comparison of existing ballast fouling quantifications . . . 54
3.3 Ballast response and degradation assessment by laboratory testing . . . 56
3.3.1 Ballast behavior under monotonic loading . . . 56
3.3.1.1 Stress - strain behavior and particle breakage . . . 57
3.3.2 Ballast behavior under cyclic loading . . . 58
3.3.2.1 Large-scale triaxial testing apparatus with cylindrical chamber 58
3.3.2.2 Large-scale triaxial testing apparatus with prismoidal chamber 60
3.4 Effect of confining pressure on particle breakage . . . 61
3.5 Ballast condition assessment in-situ . . . 63
3.5.1 Ground penetrating radar . . . 63

4 Fundamental principles of track maintenance **65**
4.1 Introduction . . . 65
4.2 Deterioration of track geometry . . . 67
4.3 Track ballast compaction and compaction control . . . 70
4.4 Tamping process in railway engineering . . . 71
4.4.1 Principle of tamping machine operation . . . 71
4.4.2 Lifting and leveling . . . 74
4.4.3 Tamping parameters . . . 75
4.4.4 Tamping machines . . . 77
4.5 Design (overlift) tamping . . . 78
4.6 Stoneblowing . . . 79
4.7 Dynamic track stabilization . . . 81

5 Basic experimental research **85**
5.1 Introduction . . . 85
5.2 Initial approach and the scope of in-situ measurements . . . 85
5.2.1 Objectives . . . 86
5.2.2 Proposed measuring system . . . 86
5.2.3 Expected results . . . 88

Die approbierte gedruckte Originalversion dieser Dissertation ist an der TU Wien Bibliothek verfügbar.
The approved original version of this doctoral thesis is available in print at TU Wien Bibliothek.
TU Bibliothek Your knowledge hub WIEN

5.3 Initial in-situ measurements and results . . . 90
5.3.1 Instrumentation of the *Dynamic Tamping Express 09-4X* E^3 . . . 90
5.3.2 Total tine motion . . . 94
5.3.2.1 Relative tine motion - Integration of acceleration signals . . . 95
5.3.2.2 Absolute tine motion - Laser squeezing displacement measurement, validation and plausibility check . . . 97
5.3.3 Tamping process subdivision . . . 99
5.3.4 Variable tamping parameters . . . 105
5.4 Load-displacement curve and tamping characteristics . . . 106
5.4.1 Phases of a squeezing process . . . 109
5.4.2 Squeezing movement analysis - Operating phases . . . 111
5.5 Minimum required pulse duration . . . 112
5.6 Final observations . . . 113

6 Monitoring of tamping process during regular track maintenance 117
6.1 Introduction . . . 117
6.1.1 Objectives . . . 117
6.2 Locations of conducted measurements and ballast bed condition definition . 118
6.3 Measurement procedure and documentation . . . 120
6.3.1 Data analysis and documentation . . . 121
6.4 Tamping process evaluation . . . 122
6.4.1 Detection and identification of ballast condition . . . 123
6.5 Squeezing movement evaluation . . . 126
6.5.1 Load-displacement curve in different ballast bed conditions . . . 126
6.5.2 Statistical tamping characteristics analysis . . . 129
6.5.3 Statistical analysis - box plot diagrams . . . 133
6.5.3.1 Theory of box plots . . . 133
6.5.3.2 Application on the in-situ collected data . . . 134
6.5.3.3 Analysis of tamping characteristics in different ballast conditions . . . 136
6.5.4 Graphical analysis . . . 148
6.5.4.1 Waterfall diagrams . . . 148
6.5.4.2 Heat maps . . . 150
6.6 Ballast penetration evaluation . . . 152
6.6.1 Penetration resistance force - comparison between ballast conditions . 152
6.7 Squeezing velocity as a possible indicator of ballast bed condition . . . 155

7 Soil dynamic behavior of track ballast and experimental verification 157
7.1 Introduction . . . 157
7.2 In-situ measurement - Ballast fluidization . . . 159
7.2.1 Accelerations analysis . . . 160
7.2.2 Particle image velocimetry . . . 164

Die approbierte gedruckte Originalversion dieser Dissertation ist an der TU Wien Bibliothek verfügbar.
The approved original version of this doctoral thesis is available in print at TU Wien Bibliothek.
TU Bibliothek Your knowledge hub WIEN

7.2.2.1 Data analysis method . . . 164
7.2.2.2 Settings and parameters . . . 164
7.2.2.3 Results . . . 167
7.3 In-situ measurement - Tamping unit interaction with the track substructure . 172
7.3.1 Frequency triggering ballast fluidization under the sleeper . . . 173
7.4 Tensile strength of single ballast grains . . . 176
7.4.1 Introduction . . . 176
7.4.2 Motivation . . . 176
7.4.3 Experimental approach - single particle tests . . . 179
7.4.3.1 Uniaxial compression . . . 179
7.4.3.2 Ultrasonic Pulse Velocity tests . . . 184

8 Tamping unit - ballast matrix interaction Mechanical model 187
8.1 Introduction . . . 187
8.2 Model set-up . . . 188
8.3 Tamping unit model . . . 190
8.3.1 Friction element . . . 190
8.3.2 System geometry . . . 191
8.3.3 Tamping unit operating phases . . . 193
8.4 Ballast matrix model . . . 197
8.4.1 Cone model . . . 198
8.4.1.1 Static cone . . . 199
8.4.1.2 Dynamic cone . . . 200
8.4.1.3 Cone properties . . . 202
8.4.1.4 Ballast properties as elastic parameters of the cone model . . 203
8.4.2 Plastic spring . . . 206
8.4.3 Gap closing acceleration . . . 209
8.4.3.1 *Rankine*'s earth-pressure and the sliding block theory . . . 209
8.4.4 Ballast matrix operating phases . . . 211
8.4.4.1 B1 - Loading . . . 212
8.4.4.2 B2 - Unloading . . . 215
8.4.4.3 B3 - Withdraw / Loss of contact . . . 217
8.5 Energy consumption balance . . . 218
8.6 Load-displacement curve . . . 222
8.6.1 Influence of shear modulus and elastic spring stiffness on the load-displacement curve . . . 226
8.6.2 Modeling different ballast conditions . . . 228
8.6.3 Derivation of the *system response* stiffness from the load-displacement curve . . . 231
8.6.4 Mechanical model for ballast penetration . . . 234

Die approbierte gedruckte Originalversion dieser Dissertation ist an der TU Wien Bibliothek verfügbar.
The approved original version of this doctoral thesis is available in print at TU Wien Bibliothek.
TU Bibliothek Your knowledge hub WIEN

9 Result verification and study of tamping parameters **235**
9.1 Introduction 235
9.2 Results comparison 236
9.3 Impulse of force analysis as an indicator of ballast condition 239
9.4 Study of tamping parameters 242
9.4.1 Influence of squeezing velocity on tamping characteristics - Clean ballast 243
9.4.2 Influence of frequency on tamping characteristics - Clean ballast . . . 248
9.4.3 Influence of squeezing velocity on tamping characteristics - Fouled ballast 253
9.4.4 Influence of frequency on tamping characteristics - Fouled ballast . . . 258
9.5 Study of different ballast bed conditions 263
9.5.1 Influence of squeezing velocity on tamping characteristics 264
9.5.2 Influence of frequency on tamping characteristics 268
9.6 Identification of ballast condition 274

10 Summary, conclusions and outlook **277**

Glossary **283**

References **285**

List of Tables **295**

List of Figures **297**

List of abbreviations and symbols **309**

A Laboratory test results - fouled ballast **315**

Die approbierte gedruckte Originalversion dieser Dissertation ist an der TU Wien Bibliothek verfügbar.
The approved original version of this doctoral thesis is available in print at TU Wien Bibliothek.

Die approbierte gedruckte Originalversion dieser Dissertation ist an der TU Wien Bibliothek verfügbar.
The approved original version of this doctoral thesis is available in print at TU Wien Bibliothek.

Chapter 1

Introduction

Track tamping is the core maintenance activity in ballasted track and tamping machines are utilized to restore initial track geometry worldwide. Over the course of history, restoral of initial track geometry was developed empirically from a strenuous and with human error fraught manual operation to automatic lifting, leveling and tamping units that operate on a very high standard. The empirical approach was extended by a comprehensive research conducted by *Fischer* [59] in 1983, in scope of which the quality of conducted tamping operation was for the first time examined by means of direct measurement. The dependence of ballast matrix compaction and elevation to the desired position on the excitation frequency and amplitude was investigated. As a result, an optimal tamping unit excitation frequency of 35 Hz was selected in combination with a 4-5 mm amplitude. Condition of the ballast bed was not taken into consideration, given that the research was conducted only using clean ballast samples. Since then a certain stagnation in further development of the tamping process became apparent.

In the past, focus in regard to tamping unit further improvement was primarily on the implementation of newest developments in the field of mechanical engineering. Less attention was given to the soil mechanical component of ballast compaction. Ballast properties subjected to change during tamping tine - ballast matrix interaction were never investigated in detail. Research conducted in the scope of this thesis investigates fundamentals of the track tamping process as well as the mechanics of track ballast compaction and its soil mechanical (and dynamic) properties. On this grounds a base on which future developments and improvements of the tamping units can be built. Recording, interpretation and understanding of track ballast reaction to dynamic and quasi-static tamping tine movement imposed to the ballast matrix on the cycle level was the most important subject of the research. Based on conclusion drawn from this observations, track ballast condition should be made determinable by objective criteria based on its reaction to the loading imposed by the tamping tine, making the future development of a condition-based tamping process possible.

Die approbierte gedruckte Originalversion dieser Dissertation ist an der TU Wien Bibliothek verfügbar.
The approved original version of this doctoral thesis is available in print at TU Wien Bibliothek.
TU Bibliothek Your knowledge hub WIEN

1.1 Background and problem statement

Continuous compaction and a homogeneous ballast layer incorporate a successful track maintenance process and make a stable foundation for a durable track geometry after tamping. Different global tamping standards driven by local regulations and divergent boundary conditions define a wide spectrum of tamping parameters such as tamping time, squeezing pressure and number of insertions [35]. An incorrect setting of the tamping parameters leads to sub-optimal ballast bed compaction and shortens the interval between track maintenance activities. State-of-the-art tamping machines, one of which was utilized for in-situ measurements in the scope of this research project, operate with previously defined parameter combination whereby only a minority of parameters are adapted to the ballast bed condition. In addition, several tamping parameters such as squeezing pressure and the frequency modulation during ballast penetration are set empirically on the spot by the machine operator which significantly aggravates the comparison of conducted tamping work on different locations.

Ballast attrition or fouling as tamping after-effect is an important aspect to be considered in the process of tamping parameter optimization. Detainment of particle shape, size and angularity by minimizing the occurrence of ballast fouling and increasing the ballast bulk density only trough packing or rearranging the ballast particles in a matrix closer together is of high importance. Compaction of non-cohesive coarse-grained soils occurs primarily as a result of overcoming grain-to-grain friction. In practice, this is usually achieved by short-term dynamic effects, and the result of successful compaction can be seen in the increase of the bearing density and homogenization of the properties in the area under consideration [35].

Several frequently used dynamic compaction methods such as Dynamic roller compaction [105] or Deep Vibro compaction [95] provide the possibility of compaction progress measurement through Continuous Compaction Control by measuring either the acceleration, transmitted energy, loading stiffness or maximal contact force. None of these methods have been proven to be efficient or cost effective when applied to ballast tamping. Another possibility to conduct compaction control is by in-situ testing (dynamic probing or standard penetration tests) succeeding compaction. Available in-situ compaction control methods, however, require additional track closure and only provide a selective overview of the conducted work results. Another important aspect to consider is that compacted ballast is located lengthwise under the sleeper which significantly aggravates the employment of any existing compaction control mechanisms [35].

In the context of track ballast compaction, the aim is not to achieve the densest bedding, but rather to strive for the *optimum* compaction or bedding density. Definition of the stop criterion or the *optimum* compaction should be determined dependent on the ballast bed condition. In order to do so, the ballast bed condition has to be determined by the machine during tamping and an adjustment of tamping parameters to the respective ballast bed condition has to be conducted. This would also allow further automation of the tamping process.

Die approbierte gedruckte Originalversion dieser Dissertation ist an der TU Wien Bibliothek verfügbar.
The approved original version of this doctoral thesis is available in print at TU Wien Bibliothek.
TU Bibliothek Your knowledge hub WIEN

1.2 Objectives and research scope

As a necessary foundation for the development of condition-based tamping process, information about the track substructure and the ballast condition need to be determined and related to a customized parameter combination. For this purpose tamping tine interaction with the ballast matrix during tamping needs to be recorded and analyzed during track maintenance in different ballast conditions. The goal is to differentiate between ballast behavior and response dependent on various traffic loads and the degree of ballast bed fouling.

Following a thorough literature study in Chapters 2, 3 and 4, initial in-situ measurements conducted in the scope of this research project are presented, described and analyzed in Chapter 5. Tamping tine dynamic excitation overlapped by the movement initiated by opening of the hydraulic cylinder enables the ballast to fill the void under the sleeper and reach the desired elevation necessary to establish the correct track geometry. Tine oscillations during the squeezing movement trigger the re-position of the ballast grains in search of denser ballast matrix packing, thus providing a compacted ballast bed by increasing its bulk density. Every aspect of tamping tine movement plays an important role in determining the resulting quality of conducted tamping. One of the objectives of this research is to investigate the total tine motion behavior whereby putting a special emphasis on every single tine oscillation as a constituent part of the dynamic ballast compaction process. Single cycle or tine oscillation is presented in form of load-displacement curves that provided the basis for calculation of tamping characteristics. The characteristics result from the selected set of tamping parameters and the encountered ballast bed condition.

After a stable and reliable analysis algorithm is developed, a comprehensive amount of collected data from the conducted measurement is analyzed and interpreted in Chapter 6, in scope of which the monitoring of tamping process during regular track maintenance is described. A detailed statistical and graphical analysis is conducted and the results enabled singling out tamping characteristics that can be utilized for ballast condition determination in-situ.

Chapter 7 offers an insight into different additional experiments conducted in order to trigger and measure ballast fluidization during track tamping and dynamic track stabilization as well as the determination of single ballast grain tensile strength.

A mechanical model of the tamping tine interaction with the ballast matrix is described in Chapter 8. The model is calibrated using information assembled from the in-situ measurement and is developed as a tool to simulate different tamping parameter combinations and ballast bed conditions. Results of these simulations are presented in scope of a detailed parameter study in Chapter 9. A summary of the whole research, results, interpretations, conclusion and an outlook are given in Chapter 10.

Die approbierte gedruckte Originalversion dieser Dissertation ist an der TU Wien Bibliothek verfügbar.
The approved original version of this doctoral thesis is available in print at TU Wien Bibliothek.
TU Bibliothek Your knowledge hub WIEN

Die approbierte gedruckte Originalversion dieser Dissertation ist an der TU Wien Bibliothek verfügbar.
The approved original version of this doctoral thesis is available in print at TU Wien Bibliothek.

Chapter 2

Ballasted track

2.1 Introduction

The railway track has to provide a stable and efficient guided platform for the trains operating with different velocities and axle loads. Vertical and lateral alignments of the track must be maintained in order to assure safe train operation. In order to do so each component of the structure must perform its desired functions under various speeds, axle loads and operational conditions [76]. Notwithstanding modern technical developments, the ballasted track still holds an overwhelmingly dominant percentage of railway tracks worldwide. This traditional railway track form is composed of steel rails, railway fasteners and sleepers, which are embedded on a compacted ballast layer. The ballast bed lays on a sub-ballast layer that forms a transition layer to the subgrade (Figures 2.1 and 2.2). Ballasted track components are discussed in the following chapters. Progressive deterioration of ballast with increasing number of load cycles or traffic loading is one of the main disadvantages of the ballasted track in comparison with the slab track. Differential track settlements caused by heavy cyclic loading during track operation are primary caused by wearing off of the ballast aggregate, particle breakage and crushing of weak particles, causing an imperative need for regular maintenance in a ballasted track. According to *Esveld* [45] and *Indraratna et al.* [76] the following are the main advantages of a ballasted track:

- relatively low construction cost,
- relatively simple replacement of track components and correction of track geometry (maintenance),
- use of indigenous material,
- good drainage,
- elasticity and noise damping.

However, certain disadvantages of the ballasted track are becoming prominent in modern railway operation and can be summed up as follows [76]:

Die approbierte gedruckte Originalversion dieser Dissertation ist an der TU Wien Bibliothek verfügbar.
The approved original version of this doctoral thesis is available in print at TU Wien Bibliothek.

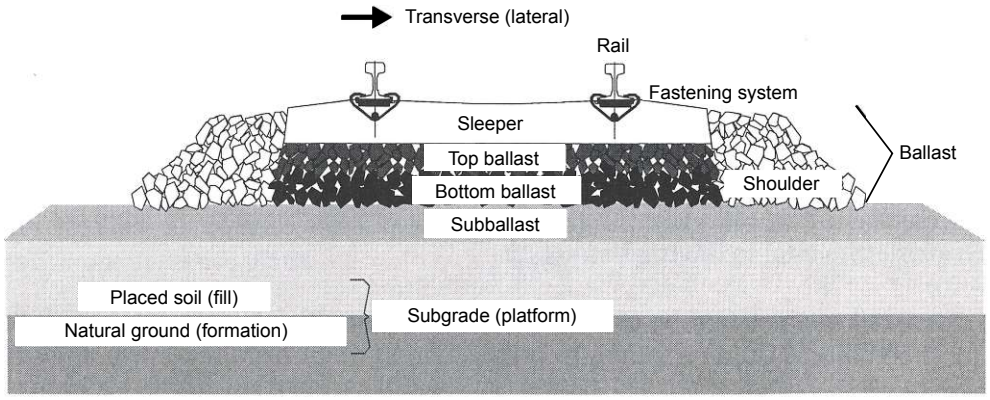

Figure 2.1: Principle of track structure: cross section (adapted from *Selig and Waters* [117])

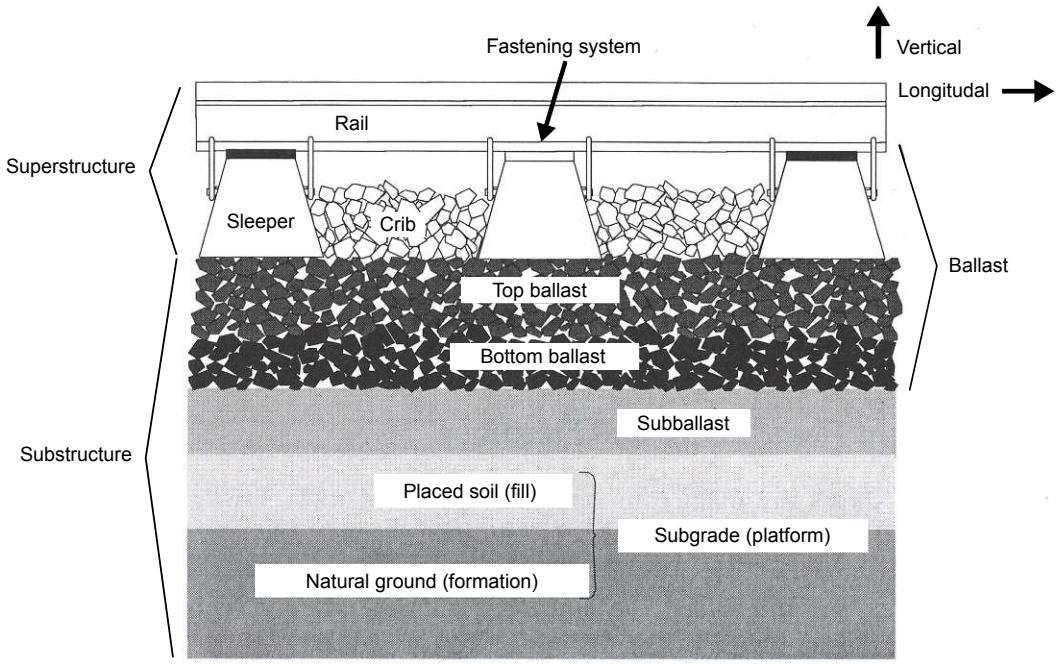

Figure 2.2: Principle of track structure: longitudinal section (adapted from *Selig and Waters* [117])

– degradation and fouling of ballast calling for frequent track maintenance and routine checks,

– reduction in permeability due to contamination caused by clogging of voids by crushed particles and infiltrated fines from the subgrade,

– pumping of subgrade clay- and silt-size particles (clay or mud pumping), to the top of ballast layer in areas with saturated and soft subgrade,

– relatively heavy and thick track structure requiring stronger structures for bridges and viaducts.

Chosen track type construction does not only depend on the train speed and expected

Die approbierte gedruckte Originalversion dieser Dissertation ist an der TU Wien Bibliothek verfügbar.
The approved original version of this doctoral thesis is available in print at TU Wien Bibliothek.

loads, but also on the type and amount of maintenance, local conditions and availability of the material, as well as on the required service life of the track.

2.2 Ballast bed

Consisting of a layer of coarse grained crushed granular material, the ballast bed can absorb considerable compressive, but no tensile stresses as a result of internal friction between the grains. According to *Selig and Waters* [117], ballast layer can be subdivided into four zones as shown in Figures 2.1 and 2.2:

- Bottom ballast - lower portion of supporting ballast layer not disturbed by tamping,
- Top ballast - upper portion of the supporting ballast exposed to tamping,
- Shoulder ballast - ballast zone between the end of the sleeper and the top of the sub-ballast layer,
- Crib / Sleeper bay ballast - ballast zones between the sleepers.

In combination with other track components, the ballast bed greatly influences the quality and durability of the track. Other than drainage and ventilation, ballast bed has a function of load distribution and load transfer to the subsoil as well as providing resistance against sleeper displacement in all directions - longitudinal, lateral and vertical, including uplift. Contamination of the ballast bed either by external or internal causes such as attrition or upwards penetration of fine particles from to lower layers (mud pumping) hinders water drainage which results in reduced shear resistance and enables possible freezing of the ballast bed. Uniformly graded, angular, crushed, dust and dirt free hard stones and rocks that are not prone to cementing are traditionally considered good ballast bed materials [45]. No universal agreement has been reached worldwide regarding exact properties and specifications for the ballast bed material such as abrasion resistance, size, shape, hardness and toughness, gradation and composition that would provide the best track performance for the given track section, in-situ conditions and traffic loads [117]. Lack of consensus on the optimal ballast material characteristics has lead to prioritizing the economical consideration during material selection such as availability and transport costs [117]. Properties of the ballast aggregates obtained by processing natural, manufactured or recycled crushed unbound aggregates for use in construction of the upper layer of railway track are specified to the European Standard with the EN 13450 [8], completed with a list of the source materials that have been considered and are within the scope of the European Standard that can be found in the EN 923-3 [18], Annex A - Nomenclature. Ballast behavior is governed by several factors, main being the bulk properties of the granular assembly i.e. ballast matrix as well as the characteristics of all constituting particles. Some of the criteria to describe the quality of ballast in these two categories are the size, shape, particle crushing strength, particle size distribution, density and void ratio, as well as the degree of saturation. Ballast response to

Die approbierte gedruckte Originalversion dieser Dissertation ist an der TU Wien Bibliothek verfügbar.
The approved original version of this doctoral thesis is available in print at TU Wien Bibliothek.
TU Bibliothek Your knowledge hub WIEN

loading such as current stress state and formed stress paths in the matrix together with susceptibility to fouling or particle degradation are the other two factor groups defining ballast behavior [76].

2.2.1 Ballast behavior governing factors

Ballast ability to perform its functions is not only governed by the particle characteristics, but also by the physical state of the ballast assembly or the ballast matrix (primarily by the structure and the void ratio), making the ballast behavior into an effect of many combined characteristics [117]. According to *Indraratna et al.* [76], behavior and mechanical response of ballast is determined by several factors that can be subdivided into four main groups:

1. Particle characteristics - properties of individual particles influence the behavior of the whole ballast matrix under static and dynamic loading as well as during track maintenance. Single particle size and shape as well as the particle surface roughness affect ballast mechanical behavior primarily by influencing the angle of shearing resistance or the internal friction angle, shearing strength and stability and ballast resilient modulus.

   The effect of ballast particle size that (typically in the range of 10-60 mm) was studied by several research groups, showing some contradictory results. *Marachi et al.* [91] report a decrease of internal friction angle with an increase of maximum particle size, supporting their claims by a series of experimental evidence. Similar results showing an increase in shear strength are presented by *Marsal* [92] that conducted high-pressure triaxial tests on rockfill dam material with a maximum size of 150 mm. *Indraratna et al.* [71] indicate that the peak internal friction angle decreases somewhat with an increase in grain size at low confining pressure (<300 kPa), while at high stress level (>400 kPa) the effect of particle size on internal friction angle is imperceptible [76]. Based on experimental evidence from monotonic triaxial test they also concluded that larger ballast has a Poisson´s ratio compared to smaller sized aggregates. In contrast, *Kolbuszewski and Frederick* [87] imply that the internal friction angle or its dilatory component increases with larger particle sizes. Considering available test results on particle characteristics, *Selig and Waters* [117] define an ideal ballast particle size to be in a range of 10-50 mm, with only a few particles beyond this range. Larger particles benefit track stabilization and smaller ones reduce the contact forces between single particles thereby minimizing particle breakage.

   Shape of ballast particles ensures interlocking between single ballast grains. The interlocking increases ballast shear strength and notably affects the load response behavior and field performance of the ballast bed. Several tests have been developed to determine particle shape aspects that are known to influence the mechanical behavior of the ballast [117]:

   – Flakiness or flatness - defined by a flakiness index as the percent by weight of flaky or flat particles in a sample. According to the British Standard [16], a flaky

Die approbierte gedruckte Originalversion dieser Dissertation ist an der TU Wien Bibliothek verfügbar.
The approved original version of this doctoral thesis is available in print at TU Wien Bibliothek.
TU Bibliothek Your knowledge hub WIEN

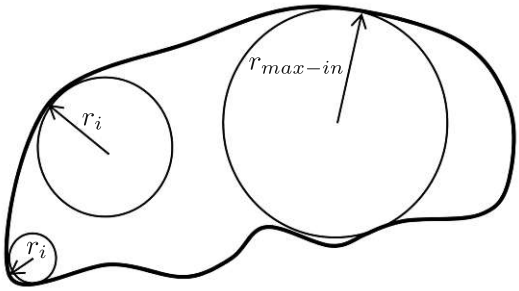

Figure 2.3: Definition of roundness, adapted from *Sun* [123]

particle is one in which the ratio of thickness to width is less than 0.6, whereas the U.S. Army Corps of Engineers [132] defines a flat particle as one with thickness to width ratio of less than 1/3.

– Elongation - defined as the percentage by weight of the elongated particles in a sample [117]. Elongated particles have a length to width ratio of more than 1.8 according to the British Standard [16], or greater than 3, as defined by the U.S. Standards [132].

– Sphericity S_p - a measure of how much the shape of a particle differs from a sphere [117]. Sphericity S_p is defined as:

$$S_p = \frac{(\frac{6V}{\pi})^{\frac{1}{3}}}{L} \tag{2.1}$$

where V is the particle volume and L the diameter of the smallest sphere that would circumscribe the particle. A prefect sphere has a sphericity of 1. Sphericity of a granular material sample is the average of the sphericities of all particles in a representative sample [117].

– Angularity or roundness R - the measure of sharpness of the edges and corners of a particle [118]. First definition of roundness was given by *Wadell* [135] for 2D analysis of granular material. The radius of each corner in the outline is measured, averaged, and then divided by the radius of the maximum inscribed circle. Surface angularity R is calculated as:

$$R = \frac{\sum_{i=1}^{n} r_i}{r_{max-in}} \tag{2.2}$$

where r_i is the radius of each corner in the particle outline and r_{max-in} is the radius of the maximum inscribed circle (Figure 2.3) [123]. Projected image of particles is used to obtain the measurements. Particles in a sample are grouped according to their angularity, with categories ranging from angular to well-rounded.

– Shape factor S_f - defined using every particle in a sample as:

Die approbierte gedruckte Originalversion dieser Dissertation ist an der TU Wien Bibliothek verfügbar.
The approved original version of this doctoral thesis is available in print at TU Wien Bibliothek.

$$S_f = \frac{\sum L_i}{\sum T_i} \tag{2.3}$$

where L_i presents the longest and T_i the shortest dimension of the particle i [117].

– Fractured particles F_P - developed by the Canadian Pacific Railroad, the percent fractured particles test divides a representative ballast sample into individual particle sizes and examines them for fractured faces[1]. A particle is considered fractured, if it has three or more fractured faces. The percent of fractured particles in a sample F_p is calculated as follows [117]:

$$F_P = \frac{W_p}{W_T} \tag{2.4}$$

where W_p is the combined weight of fractured particles and W_T the total weight of the sample.

– Particle index test - developed by *Huang* [68] in order to meet the demand for a single value representing the shape, angularity and surface texture of ballast particles. Single-sized aggregate is rodded in a rhombohedral mold and the void ratio is compared to the void ratio of uniform spheres in order to determine the particle index [117].

Several researchers have found that the angularity of the particles affects the internal friction angle of a ballast sample (Figure 2.4a)[133] and its shear strength (Figure 2.4b) [67]. According to *Chrismer* [44], the shearing resistance increases with further dilation that is needed for particle movement as the grain angularity increases.

Surface roughness or particle surface texture can be defined as a deviation in the direction of the normal vector of a real surface from its ideal shape. It determines the frictional characteristics of a fractured ballast particle grain and is considered to be a key influence on the strength and stability of the ballast bed. Crushed or fractured particles are preferred as ballast matrix structural components. Mechanical properties of fractured particles ensure optimal ballast performance and assume that freshly exposed particle surfaces comprise a higher roughness compared to previously exposed surfaces which have been smoothed by mechanical attrition or weathering [117].

Parent rock and particle crushing strength, as well as the resistance to weathering and attrition as technical requirements defined by European standards are discussed in detail in Chapters 2.2.2 and 2.2.3.

2. Particle degradation - when exposed to stresses higher than normal geotechnical ranges, granular materials exhibit considerable particle breakage and degradation which influence its mechanical behavior to a great extent. Various factors like the loading amplitude and frequency, grain angularity and density but above all the strength of

[1] Freshly exposed rock surface with a maximum dimension of at least 1/3 of the maximum particle dimension [117]

Die approbierte gedruckte Originalversion dieser Dissertation ist an der TU Wien Bibliothek verfügbar.
The approved original version of this doctoral thesis is available in print at TU Wien Bibliothek.
TU Bibliothek Your knowledge hub WIEN

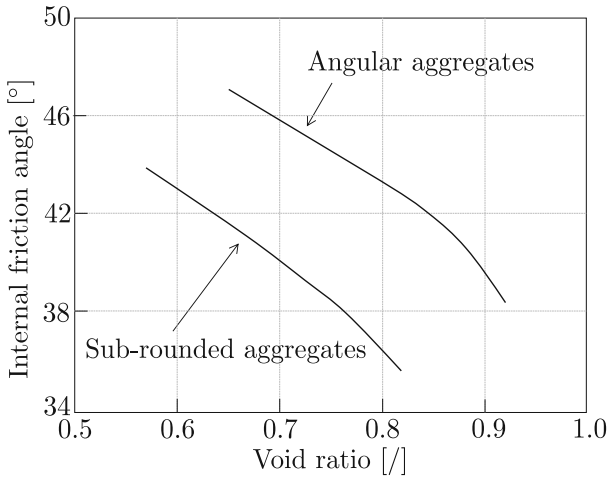

(a) Influence of particle shape on the ballast internal friction angle (adapted from [133])

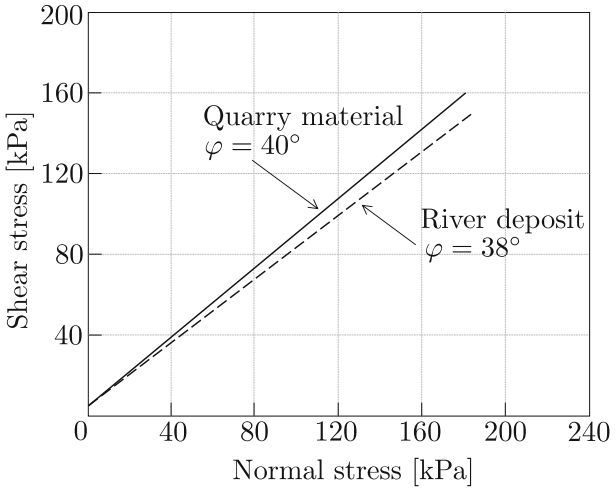

(b) Influence of particle shape on the ballast shear strength (adapted from[67])

Figure 2.4: Influence of particle shape on the ballast mechanical properties [117]

Die approbierte gedruckte Originalversion dieser Dissertation ist an der TU Wien Bibliothek verfügbar.
The approved original version of this doctoral thesis is available in print at TU Wien Bibliothek.

ballast matrix constituent particles affect the level and form of ballast degradation. Various empirical indices or parameters as well as methods for quantifying particle breakage and ballast fouling are discussed in Chapter 3.

3. Ballast matrix or aggregate characteristics - characteristics of the whole ballast assembly that govern ballast bed behavior are described in the following section.

   Particle size distribution or gradation - determined by washing and mechanical sieving of a ballast sample. Sample gradation is usually represented as a plot with percent by weight passing a given sieve as the vertical axis and a log of particle size as the horizontal axis. A gradation curve can be described as uniformly-graded, broadly-graded or gap-graded, depending on the coefficient of uniformity C_u and the coefficient of curvature C_c:

$$C_u = \frac{d_{60}}{d_{10}} \tag{2.5a}$$

$$C_c = \frac{{d_{30}}^2}{d_{10} \cdot d_{60}} \tag{2.5b}$$

   where d_{10} is the grain diameter corresponding to 10%, d_{30} corresponding to 30% and d_{60} corresponding to 60% passing by weight. New ballast is considered to be uniformly-graded, while fouled ballast is typically gap-graded, having a relatively small amount of particles in a given size range within the total range of sizes in a sample. Repeated load triaxial tests were conducted by several researchers on ballast samples with different gradation in order to determine the influence of a ballast sample particle size distribution. *Roenfeld* [116] conducted the test on two limestone ballast samples with a narrow range of particle size ($C_u = 1.4$) and with a broader grading ($C_u = 4.1$), concluding that the cumulative plastic strain of the uniform sample was almost double in comparison to the broadly-graded. Particle degradation for the uniformly-graded sample was four to five times greater than the degradation of the broadly-graded ballast [117]. Triaxial test by *Marachi et al.* [91] showed an increase in strength as the particle size decreases. *Marsal* [92] came to the same conclusion testing rockfill dam material. His tests displayed an increase of the shear strength as the gradation became broader for the same top size, despite the decrease of the mean particle size. Repeated load triaxial tests on crushed dolomite were also conducted be *Thom and Brown* [130], keeping maximum particle size a constant and varying the gradation from broadly-graded to uniformly-graded in several steps giving each grading curve an exponent n, with a higher n value presenting greater uniformity (Figure 2.5) [117]. They also compared three different compaction efforts with different sample gradations n. As expected, elastic shear stiffness and the sample permeability increase and the density and internal friction angle of the sample decrease as the value of n increases (Figure 2.5(b)-(e)). No significant influence of the sample gradation in uncompacted condition on the internal friction angle could be observed (Figure 2.5(d)) [117]. It is an established understanding that a uniformly-graded ballast has larger void volume in comparison

Die approbierte gedruckte Originalversion dieser Dissertation ist an der TU Wien Bibliothek verfügbar.
The approved original version of this doctoral thesis is available in print at TU Wien Bibliothek.
TU Bibliothek Your knowledge hub WIEN

to a broadly-graded sample, causing a higher stiffness and stability of the latter, but also a higher permeability of the uniformly-graded sample. Chosen optimum ballast gradation as a coarse, free draining medium should, therefore, be between uniformly-graded and broadly-graded, providing sufficient drainage capacity as well as shear strength and resilient modulus [117].

Void ratio or density - mechanical characteristics of the ballast bed are highly dependable on the volume of voids in a representative sample compared to the volume of solids (void ratio). Aggregates with a lower initial void ratio or higher initial density show higher shear strength and stability. They have also been proven to generate smaller settlements than aggregates with a higher initial void ratio and lower initial density that are prone to high plastic strains [117]. *Indraratna et al.* [76] concluded that the critical stage of ballast life is immediately after track construction or maintenance when ballast is in its loosest state (i.e. highest void ratio). In addition, increasing ballast bulk density, either by further compaction or by using broadly-graded aggregates, improves its stability [76].

Degree of saturation - ballast mechanical properties are also affected by an increased degree of saturation. Water influences track settlement and particle breakage. Clay pumping from the subgrade under cyclic traffic loading is one of the major causes of ballast contamination. Water between the particles can lead to an increase of contact forces and cause particle breakage [117]. *Indraratna et al.* [76] concluded that ballast saturation increased settlement by about 40% in comparison to dry ballast bed.

4. Loading characteristics - apart from various properties of ballast material itself, external loading characteristics have an important influence on the deformation and degradation of the ballast bed.

   Load history influences the deformation behavior of ballast as a work-hardening plastic material. One of the most comprehensive researches looking into the effects of the magnitude of the applied stresses and stress history on resulting permanent deformation was conducted by *Diyaljee* [50]. His research shows that a previous stress history of more than 50% of the currently applied cyclic deviator stress significantly decreases the plastic strain accumulation in ballast.

   Confining pressure was found to influence not only the deformational behavior of the ballast, but also ballast internal friction angle and particle breakage considerably. Angle of internal friction decreases with the increase in confining pressure, a phenomenon that can be explained by the fact that high values of apparent friction angle at low confining pressures are related to low contact forces well below grain crushing strength and the ability of aggregates to dilate at low stress levels [76]. Apart from the confining pressure, the current stress state in soil mechanics is usually defined by two stress invariants: the mean effective normal stress p', and the deviator stress q, has a significant role in defining plastic deformation of ballast and other granular materials. Triaxial compression test performed by *Poorooshasb et al.* [107] have shown a high slope

Die approbierte gedruckte Originalversion dieser Dissertation ist an der TU Wien Bibliothek verfügbar.
The approved original version of this doctoral thesis is available in print at TU Wien Bibliothek.
TU Bibliothek Your knowledge hub WIEN

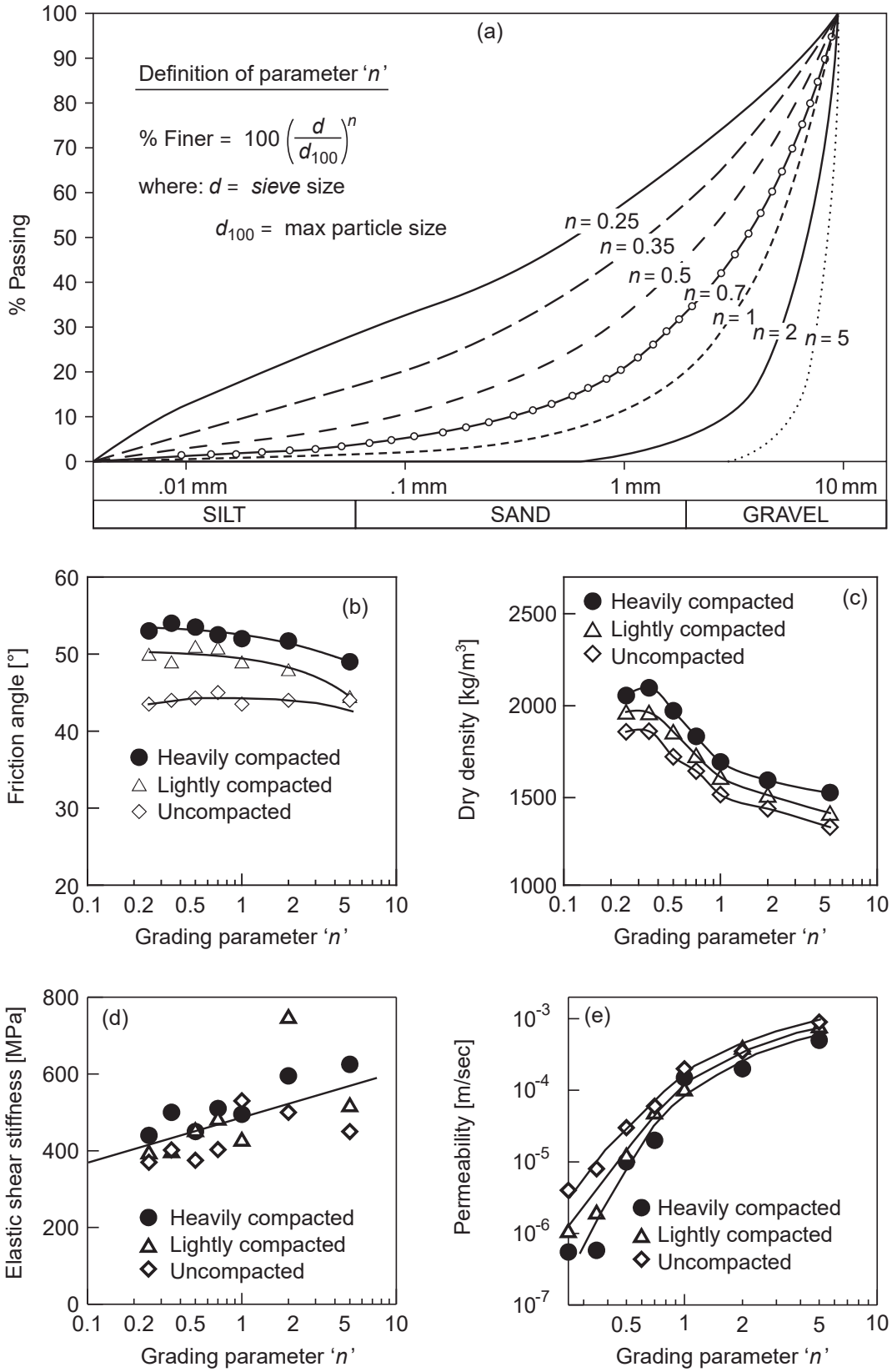

Figure 2.5: Particle size distribution of crushed dolomite ballast samples with different gradation parameter n (a), and the influence of sample gradation on: friction angle (b), density (c), elastic shear stiffness (d) and permeability (e) (*Thom and Brown* [130] and *Indraratna et al.* [76])

Die approbierte gedruckte Originalversion dieser Dissertation ist an der TU Wien Bibliothek verfügbar.
The approved original version of this doctoral thesis is available in print at TU Wien Bibliothek.

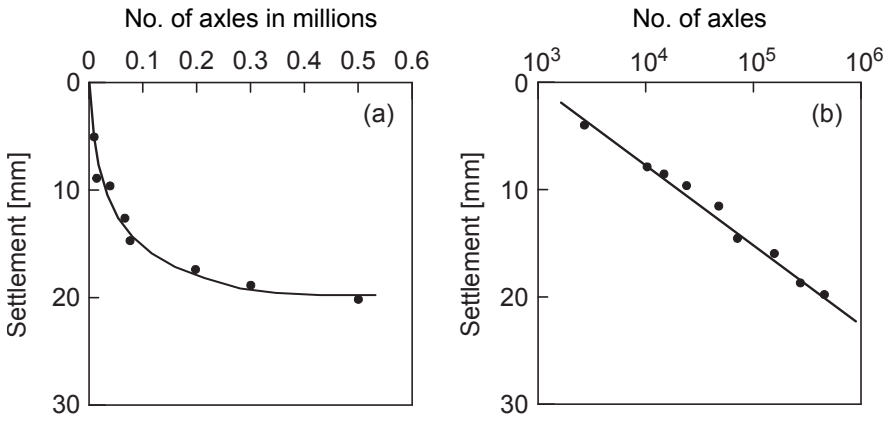

Figure 2.6: Track settlement after tamping: a) in plain scale, b) in semi-logarithmic scale (adapted from *Shenton* [120] and *Indraratna et al.* [76])

of the plastic strain in a stress state close to failure, demonstrating that the plastic shear strain increment is much higher than the plastic volumetric strain increment.

Number of load cycles is recognized as one of the most influential factors regarding accumulation of ballast plastic deformation. It is clear that the ballast bed settlement is going to increase with the increase of load cycles, but the number of cycles also defines the rate of this increase. As can be seen in Figure 2.6, based on his research, *Shenton* [120] concluded that the settlement following track tamping increases with a decreasing rate with the increasing number of axles and has shown that track settlement can be estimated by a linear relation when using a semi-logarithmic scale to present the number load cycles (Figure 2.6), which has been confirmed by other researchers [76]. However, this is only valid up to a certain number of axles ($\approx 10^6$) after which this would lead to a significant underestimation of track settlements.

Several researches ([76], [120]) have shown that the frequency of external loading of the ballast bed does not influence the deformation behavior of ballast significantly. Train speed of up to about 150 km/h is likewise proven to have an insignificant influence on the dynamic vertical stress and track settlement. However, *Kempfert and Hu* [85] have proven by several in-situ conducted measurements that the influence of train speed significantly increases starting at 150 km/h and reaching its maximum at 300 km/h and staying at a constant rate up to 400 km/h. Amplitude of cyclic loading also plays an important role in ballast deformation. An increase of load amplitude has been proven to cause an increase in the permanent strain in the first load cycle. *Indraratna et al.* [76] report that an increase in load amplitude beyond the maximum past stress level increased settlement immediately, apart from increasing the final (long term) cumulative strain.

Die approbierte gedruckte Originalversion dieser Dissertation ist an der TU Wien Bibliothek verfügbar.
The approved original version of this doctoral thesis is available in print at TU Wien Bibliothek.
TU Bibliothek Your knowledge hub WIEN

2.2.2 Ballast aggregate parent rock compendium and strength

As stated in the EN 13450 [8], an important factor in the selection of the material for the ballast bed is the parent rock source. The strength depending on the parent rock defines both tensile and compressive behavior of the ballast matrix as well as its gradation and indirectly the settlement and lateral deformation of the track. Suitable parent rocks can be classified into three major divisions, according to their origin: igneous, metamorphic and sedimentary, with several subdivisions based on their texture and composition (Figure 2.7). The EN 923-3 [18] defines the major parental rock sources as follows:

1. Igneous rocks: formed through the cooling and solidification of magma or lava either at the Earth's surface (extrusive) or below (intrusive). The latter can be divided into two classes, plutonic and hypabyssal. Plutonic rocks are formed at depth in large bodies and typically have a coarse crystalline texture, with crystals clearly visible to the naked eye. Hypabyssal rocks are formed in smaller bodies near the Earth's surface and have a fine crystalline texture. Extrusive or volcanic rocks are formed from lavas and pyroclastics at the Earth's surface and have a very fine or glassy texture [18].

2. Sedimentary rocks: formed at the Earth's surface by the accumulation or precipitation of the products of weathering (mechanical or chemical) and erosion of existing rocks. They can also be formed by the accumulation of organic debris. Such accumulated material can remain unconsolidated or it can be lithified into rock [18]. Sedimentary rocks are usually layered. There are two major groupings of sedimentary rocks: clastic, formed by weathering processes which break down rocks into finer particles by exposure to sun, snow, wind, ice, and water, and non-clastic, sedimentary rocks that are formed from chemical reactions, mainly in the ocean. Clastic sedimentary rocks are named according to the grain size of the sediment particles and non-clastic according to the mineral present.

3. Metamorphic rocks: formed from pre-existing igneous or sedimentary rocks that have undergone a change in mineral composition, texture, orientation of minerals and structure by the action of heat (temperatures greater than 150 to 200°C) and/or pressure (100 MPa or more) in the Earth's crust which has caused mineralogical and structural transformations. Metamorphic rocks frequently have anisotropic texture [18][117].

Parent rock strength is likely the most significant factor that directly governs ballast degradation. Indirectly, it influences settlement and lateral deformation of the track [136]. Parent rock contributes to both compressive and tensile strength [76]. Regardless of its origin, rock chosen for the ballast production should demonstrate good breaking behavior as well as resistance to weathering and low crack formation. The rock should also be free of loam, earth and fine particles and hold an acceptable level of toughness, hardness and low cleavability [88].

Die approbierte gedruckte Originalversion dieser Dissertation ist an der TU Wien Bibliothek verfügbar.
The approved original version of this doctoral thesis is available in print at TU Wien Bibliothek.
TU Bibliothek Your knowledge hub WIEN

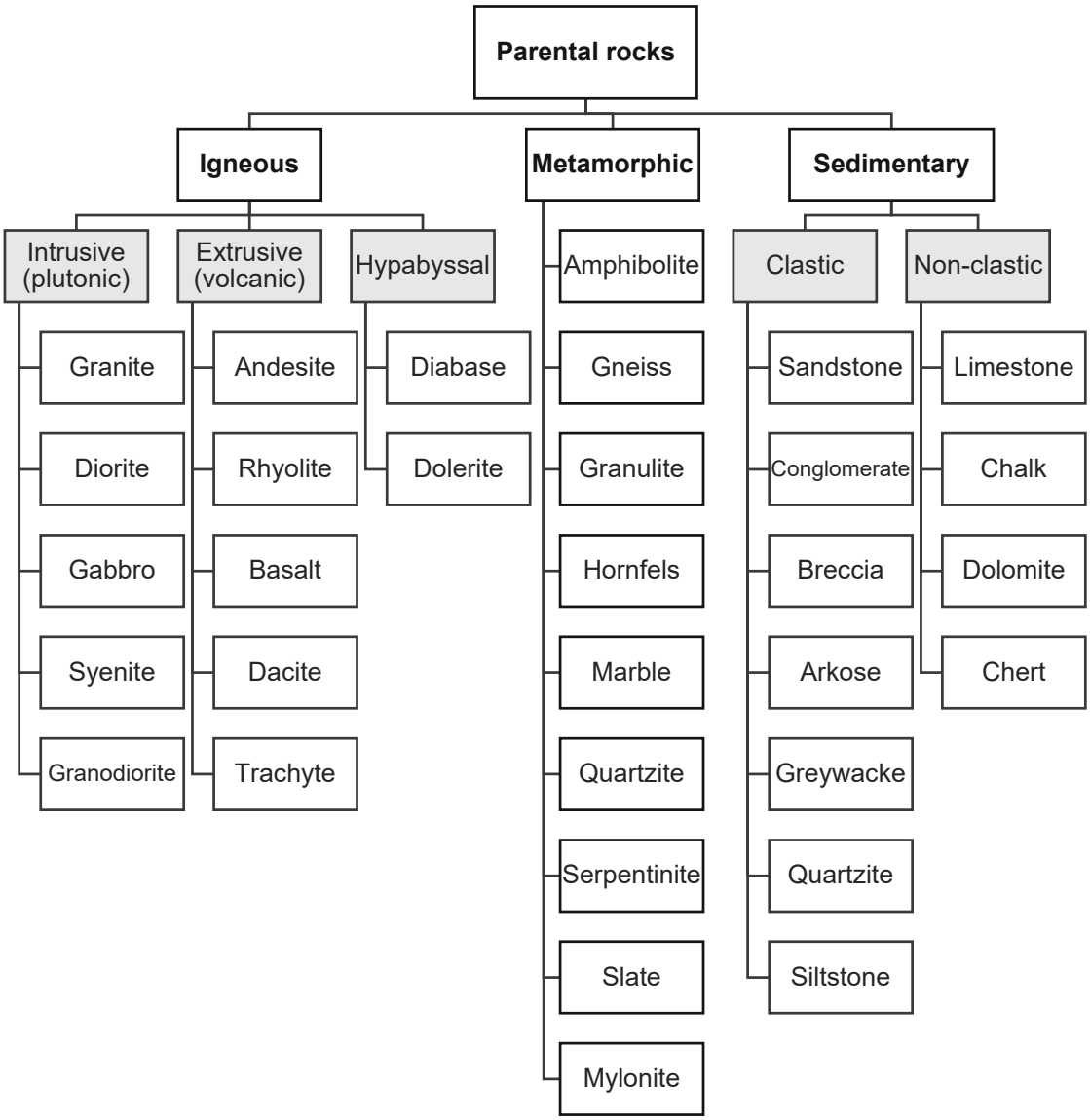

Figure 2.7: Parent rock classification for ballast aggregate selection

Die approbierte gedruckte Originalversion dieser Dissertation ist an der TU Wien Bibliothek verfügbar.
The approved original version of this doctoral thesis is available in print at TU Wien Bibliothek.

2.2.2.1 Geological deposits for track ballast production in Austria

As priorly stated, one of the main advantages of the ballasted track is the opportunity to use indigenous material, thus reducing transportation and altogether track construction cost. Available rock quarries in Austria provide following materials for track ballast production, with quantities of different railway ballast rock types during one year shown in Figure 2.8:

- Basalt - basic, mafic[2], extrusive igneous rock (Figure 2.7), consisting primarily of a mixture of iron and magnesium silicates with olivine and pyroxene and calcium-rich feldspar [88]. Constituting more than 90% of all volcanic rock on Earth, basalt is normally dark grey to black and consists of a fine-grained elementary material. According to *Kuttelwascher and Zuzic* [88], in Austria basalts only occur in the east and south-east (Burgenland, Styria and Carinthia).

- Diabase - mafic, hypabyssal or subvolcanic rock, generated as a result of metamorphosis (transformation processes under the influence of pressure and temperature) of basalts [88]. Diabase is dense to medium-grained with a fine but visible structure. Only few diabase deposits in Austria fulfil the suitability criteria for track ballast (e.g. northern Grauwacken zone and Bleiberg Hochtal) [88].

- Dolomite (Limestone) - sedimentary carbonate rock that contains a high percentage of the mineral dolomite, $CaMg(CO_3)_2$. Northern Limestone Alps stretch from Vorarlberg to Lower Austria and consist mainly of limestone or dolomite, rocks only partially suitable for ballast production [88].

- Dunite - igneous intrusive rock of ultramafic[3] arrangement, with coarse-grained or phaneritic[4] surface and typical greenish colour found in the middle Austro-Alpine Grundgebirgsdecke of Styria[86][88].

- Granite - intrusive, igneous coarse grained rock with between 20% and 60% of quartz and at least 35% of the total feldspar by volume, formed from the very slow cooling of the magma which provided sufficient time for the crystal to grow large enough to be seen with an unaided eye. Content of feldspar determines the high colour variability of granite rocks with the colour spectrum ranging from light grey to bluish, reddish and orange to yellow[88]. Yellow granite typically shows poorer technical performance in comparison to the grey. Large deposits of granite from which track ballast in Austria is produced lay in the Bohemian Massif, north of the Danube [86][88].

- Granite porphyry - igneous, phaneritic rock consisting of large-grained crystals such as feldspar or quartz, dispersed in fine-grained to dense basic mass. Austrian granite porphyry deposits come from the transition zone between the Bohemian Massif and the Molasse zone [88].

[2] iron-rich
[3] portions of rocks with over 90% dark minerals of the magmatic rocks
[4] rock whose micro-structure is made up of crystals large enough to be distinguished with the unaided eye

Die approbierte gedruckte Originalversion dieser Dissertation ist an der TU Wien Bibliothek verfügbar.
The approved original version of this doctoral thesis is available in print at TU Wien Bibliothek.
TU Bibliothek Your knowledge hub WIEN

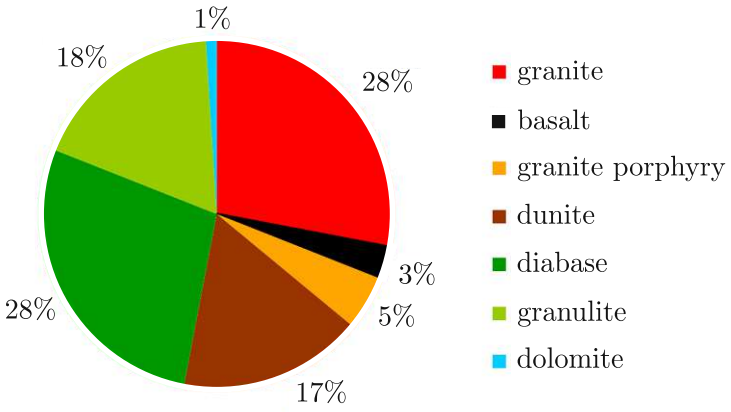

Figure 2.8: Delivery quantities of different railway ballast rock types during the year 2008 according to the Austrian Federal Railways (ÖBB) [97]

– Granulite - metamorphic rock formed under high-temperature and moderate-pressure, consisting of quartz, feldspar and ferromagnesian minerals. High resistance to wear and compressive strength makes granulite rocks suitable for track ballast production. Granulite deposits occur in the Moldanubicum of the Bohemian Massif in the north of Austria (Waldviertel) [88].

2.2.3 Technical requirements for railway ballast in Austria

Track ballast is defined as a granular material of natural, manufactured or recycled origin used in track construction where 100% of the surface of the particles can be described as totally crushed used in the construction of the upper layer of railway track, with sizes e.g. 22/40 mm, 31.5/50 mm or 31.5/63 mm [8]. Austrian Federal Railways [98] drew up a testing system determining exact characteristics and a criteria of suitability for the new track ballast, divided into geometrical, chemical and physical requirements.

2.2.3.1 Geometrical requirements

Geometrical requirements defined by the Austrian Federal Railways [98] encompass the definition of particle size, shape, distribution and fine particle content. Particle size distribution of a ballast sample is determined by washing and mechanical sieving using procedures defined in the EN 933-1 [19] and EN 933-2 [20]. Generally speaking, a properly selected ballast grain size distribution enables a fitting load dispersion, drainage and load transfer [88]. Uniformly or close-grained aggregates with a narrow range of particle sizes have a positive effect on the drainage and elastic properties of the ballast bed. New ballast is usually considered to fit this category. It is important to state that the ballast shearing resistance also decreases with increasingly narrower grading, which has a negative influence on the ballast bed load transfer properties [88]. Austrian Federal Railways distinguish between new railway ballast of granulation K1 (Figure 2.9a) or Category 1, similar to the category $G_{CRB}B$

Die approbierte gedruckte Originalversion dieser Dissertation ist an der TU Wien Bibliothek verfügbar.
The approved original version of this doctoral thesis is available in print at TU Wien Bibliothek.

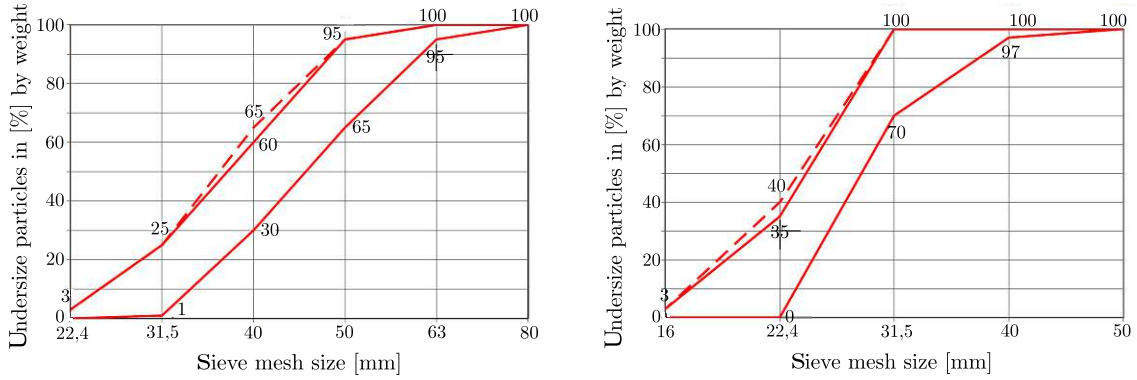

(a) Grain size distribution curve Category 1/K1 (b) Grain size distribution curve Category 2/K2

Figure 2.9: Grain size distribution curves of railway ballast. Solid lines indicate the lower and upper limits; the dashed line delineates the tolerance limit [97]

defined by the EN 13450 [8] and ballast granulation K2 (Figure 2.9b) or Category 2, used in track areas where the workers have to have access to the track on a regular basis [88].

Particle shape also has an important influence on the ballast bed stability, as it influences the interlocking of ballast grains. The particle shape is determined according to EN 933-4 [22] and defined by the particle shape index, calculated as the mass of particles with a ratio of particle length to thickness more than 3, expressed as a percentage of the total dry mass of particles tested.

2.2.3.2 Chemical requirements

Chemical analysis determines the type and proportion of ballast bed constitutive elements as wall as ballast chemical balance when exposed to weather, water, stress, different railroad materials (steel, wood, etc.). If the ballast has unsuitable chemical composition it may lead to development of corrosion on the track, chemical particle breakdown or other unwanted consequences. For example, trace elements such as sulphur in coal are highly likely to increase the acidity of any moisture trapped within the ballast. This acidity will cause solution weathering of the aggregate, particularly limestone [112]. Chemical requirements also guarantee the ecological compliance of the parent rock material. They are based on the national regulations concerning recycling and waste dumping [88]. In Austria, these are primarily the Waste Management Act, Federal Waste Management Plan and Landfill Ordinance [88]. Ballast bed chemical requirements can be related to the environmental pollution expected at a certain location.

2.2.3.3 Physical requirements

– Durability and Impact-attrition strength (Los Angeles test) - Los-Angeles Abrasion test (LAA) was originally developed to determine the toughness and abrasion of aggregates for asphalt concrete and other road surface material. LAA test is used to test durability and strength properties of ballast, as well as the impact-attrition strength by

Die approbierte gedruckte Originalversion dieser Dissertation ist an der TU Wien Bibliothek verfügbar.
The approved original version of this doctoral thesis is available in print at TU Wien Bibliothek.
TU Bibliothek Your knowledge hub WIEN

creating dynamic impact environment in the laboratory, with results based on an inter-laboratory comparison in 28 labs with three aggregate types. The evaluation method is based on a determination of the mass loss rate named LAA loss or Los Angeles coefficient LA_{RB} given by Equation 2.6 in compliance with EN 13450 [8] and EN 1097-2:2018, Annex 2 - Determination of resistance to fragmentation of aggregates for railway ballast [2]. LA_{RB} coefficient is a vital indicator of the relative quality of aggregates and provides a reliable evaluation of ballast behavior. The test measures the degradation of a coarse aggregate sample that is placed in a rotating drum with 12 spherical steel balls, each with a diameter of between 45 mm and 49 mm and a weight between 400 g and 445 g, resulting in a total weight of 5210 ± 90 g. As the drum rotates the aggregate degrades by abrasion and impact with other aggregate particles and the steel spheres (Figure 2.10). Once the test is complete, the calculated mass of aggregate that has broken apart to smaller sizes and retained on a 1.6 mm sieve is determined and expressed as a percentage of the total mass of aggregate.

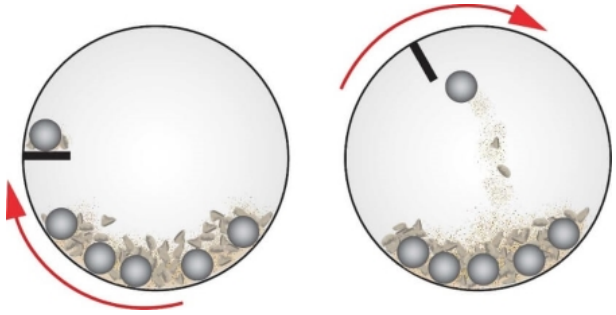

Figure 2.10: Los Angeles testing drum - test kinematics and impact [127]

$$LA_{RB} = 1 - \frac{m_2}{m_1} \tag{2.6}$$

where m_1 is the initial dry mass of the test portion and m_2 the dry mass retained on the 1.6 mm sieve after fragmentation, both in grams. Lower Los Angeles coefficient values indicate aggregate that is tougher and more resistant to abrasion. Only rock with Los Angeles coefficients of maximum 22% in weight are utilized as track ballast in Austria [88]. Categories for maximum values of Los Angeles coefficient LA_{RB} according to EN 13450 [8] are shown in Table 2.1. Regarding different track ballast rocks in Austria, typical LA_{RB} values of are shown in Figure 2.11.

Die approbierte gedruckte Originalversion dieser Dissertation ist an der TU Wien Bibliothek verfügbar.
The approved original version of this doctoral thesis is available in print at TU Wien Bibliothek.

Table 2.1: Categories for maximum values of LA_{RB} as a result of the LAA Test defined by EN 13450 [8]

Los Angeles coefficient [%]	Category LA_{RB}
≤ 12	LA_{RB} 12
≤ 14	LA_{RB} 14
≤ 16	LA_{RB} 16
≤ 20	LA_{RB} 20
≤ 22	LA_{RB} 22
≤ 24	LA_{RB} 24
> 24	LA_{RB} Declared
No requirement	LA_{RB} NR

– Impact strength (impact fragmentation value) - Resistance to fragmentation of railway ballast is determined by the impact test method [88] in compliance with EN 13450 [8] and EN 1097-2:2018, Annex 2 - Determination of resistance to fragmentation of aggregates for railway ballast [2]. Ballast test sample of at least 10 kg and size fraction 31.5 mm to 40 mm is placed in a steel mortar (170 mm inside diameter) and after washing and drying stressed by twenty impacts of a 50 kg drop hammer, falling from a predefined height of 420 mm. Samples of the same material with the weight difference between the samples lower than 1% from the nominal mass are prepared and used in three identical successive tests. The amount of fragmentation caused by the twenty impacts is measured by sieving in accordance with EN 933-1 [20] on the 8 mm sieves [2]. If the total mass of the first test specimen after sieving differs from the original mass by more than 0.5%, the impact test is carried out on a further test specimen. The impact fragmentation value is calculated according to Equation 2.7:

$$SZ_{RB} = \frac{M_1}{M} \tag{2.7}$$

where M_1 is the mass passing the 8 mm sieve and M the mass of the test specimen before testing. The lower the impact fragmentation value, the more resistant the rock is to impact stresses. Only rock with impact fragmentation values of maximum 22% in weight are utilized as track ballast in Austria [88]. Categories for maximum values of SZ_{RB} according to EN 13450 [8] are shown in Table 2.2. Regarding different track ballast rocks in Austria, typical SZ_{RB} values of are shown in Figure 2.11.

Die approbierte gedruckte Originalversion dieser Dissertation ist an der TU Wien Bibliothek verfügbar.
The approved original version of this doctoral thesis is available in print at TU Wien Bibliothek.
TU Bibliothek Your knowledge hub WIEN

Table 2.2: Categories for maximum values of resistance to impact SZ_{RB} as a result of impact test method defined by EN 13450 [8]

Impact value [%]	Category SZ_{RB}
≤ 14	SZ_{RB} 14
≤ 18	SZ_{RB} 18
≤ 20	SZ_{RB} 20
≤ 22	SZ_{RB} 22
> 22	SZ_{RB} Declared
No requirement	SZ_{RB} NR

– Resistance to wear (Micro-Deval coefficient $M_{DE,RB}$) - Deval Attrition Test according to BS812 (British Standards Institution) [16] is a test for determining the resistance to abrasion. The test method was included in Austrian Railways' engineering specification for railway ballast up to the 1960s but was then eventually replaced by the Micro-Deval test (Österreichisches Normungsinstitut (2004b) and Österreichisches Normungsinstitut (2004a)) [32]. The resistance to wear is determined in compliance with EN 13450 [8] and EN 1097-1:2011, Annex 1 - Determination of the resistance to wear (micro-Deval) for railway ballast [1]. Two ballast test samples of at least 25 kg and size fraction 31.5/40 mm and 50/40 mm are prepared according to the EN 933-1 [19], washed and dried. Each fraction is additionally subdivided in two fractions both 5000 $\pm$ 50 g in weight. Each of the obtained samples is mixed together with the other fraction, forming two samples of 10000 $\pm$ 100 g in weight. Samples are placed in a drum (20 cm diameter), filled with 2.0 $\pm$ 0.05 l of water and stressed with 100 revolutions per minute until 14000 $\pm$ 10 revolutions are completed. The Micro-Deval coefficient is calculated according to the following equation [1]:

$$M_{DE,RB} = \frac{m_A - m_B}{m_A} \tag{2.8}$$

where m_B is the mass of material retained on the 1.6 mm sieve, and m_A the original sample weight, both expressed in grams.

Typical $M_{DE}RB$ values of different track ballast stones in Austria can be seen in Figure 2.11.

Die approbierte gedruckte Originalversion dieser Dissertation ist an der TU Wien Bibliothek verfügbar.
The approved original version of this doctoral thesis is available in print at TU Wien Bibliothek.

Table 2.3: Categories for maximum values of resistance to wear M_{DERB} as a result of Micro-Deval test defined by EN 13450 [8]

Micro-Deval coefficient [%]	Category M_{DERB}
≤ 5	M_{DERB} 5
≤ 7	M_{DERB} 7
≤ 9	M_{DERB} 9
≤ 11	M_{DERB} 11
≤ 13	M_{DERB} 13
≤ 15	M_{DERB} 15
> 15	M_{DERB} Declared
No requirement	M_{DERB} NR

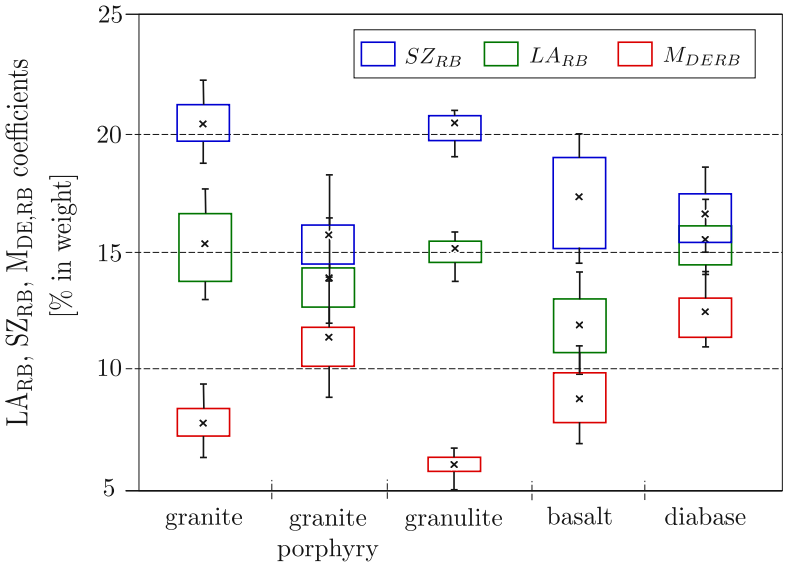

Figure 2.11: Overview and comparison of mean values and scattering[5]of coefficients for different ballast rock types (adapted from [88])

– Resistance to weathering - Track ballast grains must be resistant to weathering. Weathering is defined as the process of stone disintegration due to physical, chemical or biogenous influences and their combinations [88]. Several methods of evaluation are used to determine the resistance to weathering - visual inspection in the deposit and from broken material, petrographic examination and a number of laboratory tests such as determination of water absorption and resistance to freezing and thawing [88].

– Gross density[6] - defined as the density of the raw stone as a ratio of mass (determined by weighing the specimen in water-saturated and surface-dried and then again in

[5]definition of parameters for the statistical analysis is given in Chapter 6.5.3.1

[6]in contrast to gross density, the bulk density describes the ratio of mass to volume of an unconsolidated, dry stone granulation and the vibration density the density of a heap of material that is achieved by vibration [88]

Die approbierte gedruckte Originalversion dieser Dissertation ist an der TU Wien Bibliothek verfügbar.
The approved original version of this doctoral thesis is available in print at TU Wien Bibliothek.
TU Bibliothek Your knowledge hub WIEN

oven-dried conditions) to volume (contains all voids and cavities specific to the rock), gross density is determined in accordance with EN 1097-6 [3]. Exact values for the gross density are not given by standards, but in general high gross densities are required for track ballast [88]. Gross density of track ballast amounts to approximately 1.3 - 1.5 t/m^2 [88].

2.2.3.4 Applicable standards

Technical conditions of delivery for track ballast determined by the Austrian Federal Railways in 2007 [98] define the ÖNORM EN 13450: Aggregates for railway ballast [8] and the ÖNORM B3133: Railway ballast - Rules for the implementation of ÖNORM EN 13450 [15] as fundamental requirements for new railway ballast specifications. The following standards, in whole or in part, are normatively referenced in the ÖNORM EN 13450 [8] and ÖNORM B3133 [15] documents and are indispensable for their application:

- EN 932-1,: Tests for general properties of aggregates - Part 1: Methods for sampling [17]
- EN 932-3: Tests for general properties of aggregates - Part 3: Procedure and terminology for simplified petrographic description [18]
- EN 933-1, Tests for geometrical properties of aggregates - Part 1: Determination of particle size distribution - Sieving method [19]
- EN 933-2, Tests for geometrical properties of aggregates - Part 2: Determination of particle size distribution - Test sieves, nominal size of apertures [20]
- EN 933-3, Tests for geometrical properties of aggregates - Part 3: Determination of particle shape - Flakiness index [21]
- EN 933-4, Tests for geometrical properties of aggregates - Part 4: Determination of particle shape - Shape index [22]
- EN 933-5, Tests for geometrical properties of aggregates - Part 5: Determination of percentage of crushed and broken surfaces in coarse aggregate particles [23]
- EN 1097-1, Tests for mechanical and physical properties of aggregates - Part 1: Determination of the resistance to wear (micro-Deval) [1]
- EN 1097-2, Tests for mechanical and physical properties of aggregates - Part 2: Methods for the determination of resistance to fragmentation [2]
- EN 1097-6, Tests for mechanical and physical properties of aggregates - Part 6: Determination of particle density and water absorption [3]
- EN 1367-1, Tests for thermal and weathering properties of aggregates - Part 1: Determination of resistance to freezing and thawing [9]

Die approbierte gedruckte Originalversion dieser Dissertation ist an der TU Wien Bibliothek verfügbar.
The approved original version of this doctoral thesis is available in print at TU Wien Bibliothek.
TU Bibliothek Your knowledge hub WIEN

- EN 1367-2, Tests for thermal and weathering properties of aggregates - Part 2: Magnesium sulphate test [10]
- EN 1367-3, Tests for thermal and weathering properties of aggregates - Part 3 : Boiling test for "Sonnenbrand basalt" [11]
- EN 1367-6, Tests for thermal and weathering properties of aggregates - Part 6: Determination of resistance to freezing and thawing in the presence of salt (NaCl) [12]
- EN 12880, Characterization of sludges - Determination of dry residue and water content [5]
- EN 13346, Characterization of sludges - Determination of trace elements and phosphorus - Aqua regia extraction methods [7]
- EN 12407, Natural stones - Petrographic examination [4]
- B 3123, Testing of natural stones - Resistance to weathering [14]

2.2.4 Resilient modulus

Behavior of ballast under cyclic loading conditions is non-linear and stress-state dependent with strain developing rapidly during the first loading and being only partially recovered after unloading [79]. Every following loading cycle contributes another increment of plastic strain and the magnitude of plastic strain increment decreases with the number of cycles. The difference between the maximum strain under peak load and the permanent strain after unloading for each cycle is the *resilient* or *recoverable strain* [117]. Material resilient modulus, denoted either M_R or E_r dependent on the author, is defined as the ratio of repeatedly applied deviator stress to the recoverable axial strain during unloading whereas the amount of resilient strain generally decreases with number of cycles (Equation 2.9, Figure 2.12). Resilient modulus significantly increases with the increase of confining pressure and bulk stress (sum of principal stresses) and its magnitude is highly stress-state dependent. The magnitude of repeated deviator stress however, has a significantly lower influence on the resilient response of unbound granular materials [79].

$$M_R = \frac{\Delta q}{\varepsilon_r} \tag{2.9}$$

where q is the deviator stress equal to $\sigma_1' - \sigma_3'$, Δq the difference between q_{max} and q_{min}, and ε_r the recoverable (resilient) axial strain during triaxial unloading.

Alternatively, the resilient modulus can be determined as a function of the stress state and soil characteristics [79]:

$$M_R = K_1 \cdot \theta'^{K_2} \tag{2.10}$$

where K_1 and K_2 are soil constants determined from laboratory tests and θ' the bulk effective stress in the loaded phase calculated as the sum of the three principal effective

Die approbierte gedruckte Originalversion dieser Dissertation ist an der TU Wien Bibliothek verfügbar.
The approved original version of this doctoral thesis is available in print at TU Wien Bibliothek.
TU Bibliothek Your knowledge hub WIEN

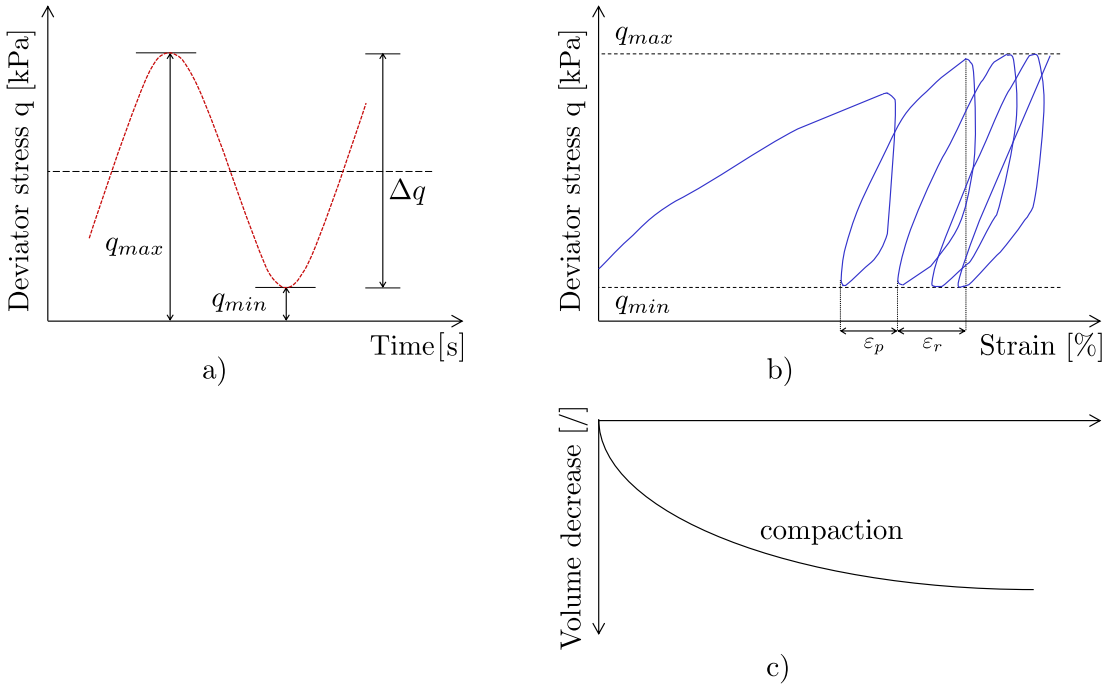

Figure 2.12: Ballast behavior under cyclic loading: a) showing the maximum and minimum deviator stress; b) representation of strains under cyclic load application (ε_p - plastic strain, ε_r - resilient or recoverable strain); c) decrease of volume representing ballast compaction (adapted from [117] and [79])

stresses at maximum loading [79]:

$$\theta' = \sigma'_1 + \sigma'_2 + \sigma'_3 \tag{2.11}$$

A more general understanding of railway ballast resilient behavior is gained from cyclic loading test conducted by *Stewart* [122], who calculated the ballast resilient modulus during partial unloading and shear stress reversal, the latter consisting of first applying an axial compressive stress followed by unloading to an extensional stress and reloading to isotropic conditions. As can be seen in Figure 2.13, even if the peak stress remains constant, the resilient modulus decreases when changing from partial to full unloading or to stress reversal.

Brown and Selig [40] developed an accurate model for ballast resilient modulus prediction using the resilient bulk modulus B and the shear modulus G as a function of deviator stress and the mean normal effective stress. Selection of these parameters allowed them to relate to both volumetric and shear strain, as well as a calculation of ballast Poisson's ratio v and Young's modulus E.

Janardhanam and Desai [81] have proven that the ballast particle size does not influence the volumetric strain, but it has an important influence on the resilient modulus. They have shown that the resilient modulus increased with the mean grain size independent on the stress level (Figure 2.14).

Several research studies have been carried out in order to determine the influence of the resilient modulus of railway ballast on numerous ballast parameters such as stress his-

Die approbierte gedruckte Originalversion dieser Dissertation ist an der TU Wien Bibliothek verfügbar.
The approved original version of this doctoral thesis is available in print at TU Wien Bibliothek.

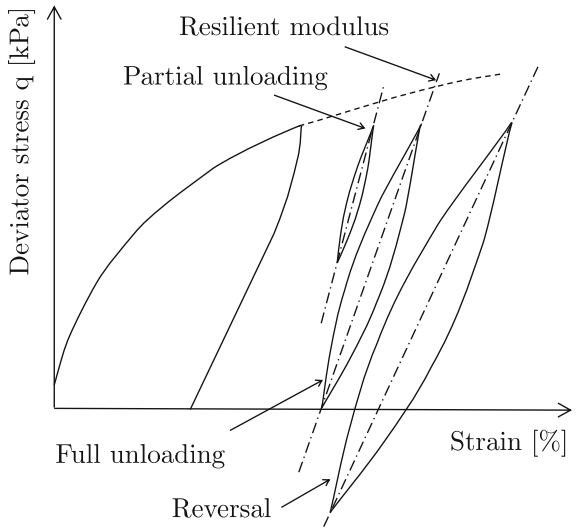

Figure 2.13: Resilient modulus under partial unloading and stress reversal conditions (adapted from [117])

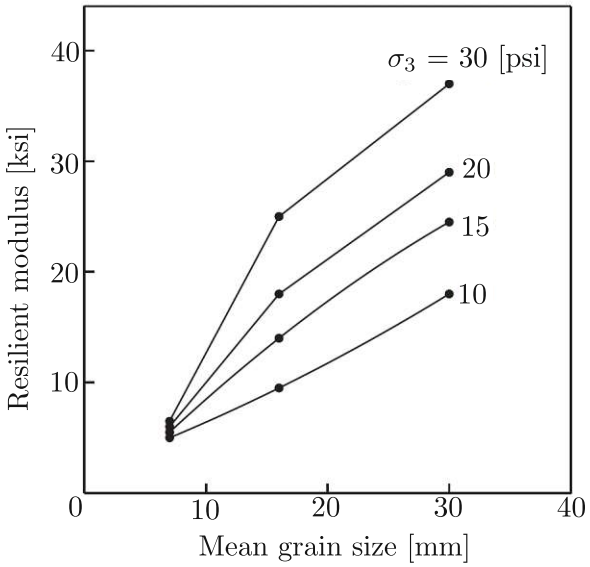

Figure 2.14: Effect of grain size on ballast resilient modulus (ksi = 6.894 MPa, psi = 6.894 kPa) (adapted from [81])

tory, number of loading cycles, density, grading, fines content, maximum grain size, aggregate type, particle shape and moisture content [79]. Main utilization for the resilient modulus is the determination of cyclic densification or compaction of granular aggregates (Figure 2.12, c).

2.2.5 Ballast bed permanent strain

Soils accumulate plastic strain under repeated loading due to progressive volume change and progressive shear strain or distortion. Progressive volume change under repeated wheel

Die approbierte gedruckte Originalversion dieser Dissertation ist an der TU Wien Bibliothek verfügbar.
The approved original version of this doctoral thesis is available in print at TU Wien Bibliothek.

loading occurs due to particle rearranging to a more dense packing and due to particle breakage with smaller particles moving into the voids between the larger particles. Particle breakage is not only caused by particle contact forces induced by wheel loading but also from cyclic freezing and thawing, chemical breakdown and different environmental factors. Progressive shear strain under repeated loading occurs due to the fact that the vertical stress acting on the ballast layer is greater than the horizontal stress. Shear strain implies horizontal spreading and particle rearrangement, lead by a reduction in ballast layer height and track settlements. Shear deformations can be prevented to a certain level by confinement from the cribs and shoulders and from friction at the sleeper and underlying layer interfaces. Depending on the initial density state, the amount of permanent strain from each of the two sources is a function of the cyclic stress path [117].

The development of permanent, cumulative plastic deformation of the ballast bed is a function of both the confining pressure and the cyclic deviator stress. *Selig and Waters* [117] report that, as expected, the increase of rate of strain accumulation increases with the stress ratio[7]. Furthermore, initial sample compaction influence the magnitude of plastic strain, given that ballast samples with lower initial density exhibit significantly higher plastic strains in a given number of cycles that samples with higher initial density.

The Office for Research and Experiments (ORE) [113] investigated the influence of repetitive loads on the ballast bed behavior and primarily on the permanent strain. Based on conducted repeated load triaxial test and in-situ tests on two different ballast samples and various densities, following equation was proven to demonstrate the influence of sample porosity and stress state on the ballast bed plastic strain:

$$\varepsilon_N = 0.082(100n - 38.2) \cdot (\sigma_1 - \sigma_3)^2 \cdot (1 + 0.2 \log N) \tag{2.12}$$

where ε_N is the permanent strain after N loading cycles, n is the initial porosity of the sample, $\sigma_1 - \sigma_3$ the deviator stress and N the number of repeated loading cycles.

Based on the Equation 2.12, it can be concluded that the development of the permanent ballast bed deformation reduces considerably as the number of cycles increases. Moreover, the permanent deformation was proven to be influenced by the initial compaction of the sample and it is determined mainly by the largest load applied [117].

2.2.6 Ballast grain fracture strength

Crushing strength of individual particles or their resistance to fracture significantly influences particle degradation. Particle prone to grain splitting and to breakage of sharp corners under loading can be described using a low value of particle resistance to fracture. Grain geometry, parent rock and loading characteristics such as loading point and loading direction together with the void ratio for embedded particles define the particle crushing strength [76].

According to *Festag and Katzenbach* [84], grain crushing can be divided into the following

[7] ratio of deviator stress to confining pressure

Die approbierte gedruckte Originalversion dieser Dissertation ist an der TU Wien Bibliothek verfügbar.
The approved original version of this doctoral thesis is available in print at TU Wien Bibliothek.

two categories:

- particle breakage (fracture) - high stress levels dissect the grain into parts of approximately same dimensions
- grain abrasion - independent of the stress level, very small particles detach from the grain surface. In track ballast, grain abrasion results from particles slipping or rolling over each other during shear deformation

2.2.6.1 Tensile strength of a single particle

Fracture in rock grains is initiated by tensile failure and the fracture strength can be measured indirectly by diametral compression between flat plates (Figure 2.15) [136]. The characteristic tensile stress σ is obtained from a simple test in which a diametral compressive force F is applied to the particle of diameter d under. Result is given by Equation 2.13 [76].

$$\sigma = \frac{F_c}{d^2} \tag{2.13}$$

Equation 2.13 is consistent with the definition for the tensile strength of concrete in the Brazilian or Splitting Tensile Strength Test test, conducted in rock mechanics to indirectly determine the tensile strength of rocks. The Brazilian Test is conducted on a disc (cylindrical) specimen placed in a cell where it is compressed diametrically and split by induced tensile stress [90]. Using Equation 2.13, characteristic particle tensile strength σ_f can be calculated:

$$\sigma_f = \frac{F_f}{d^2} \tag{2.14}$$

where the subscript f denotes failure.

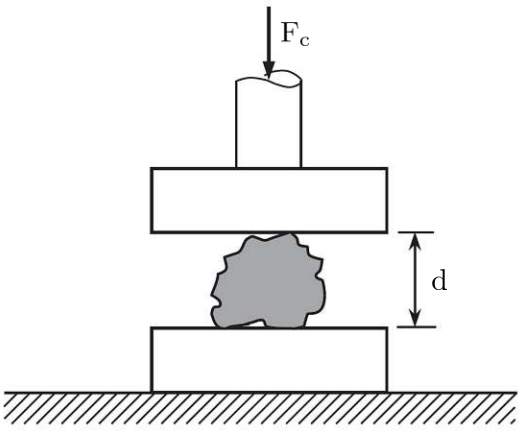

Figure 2.15: Schematic presentation of ballast grain fracture test (adapted from [76])

Indraratna and Salim [75] performed a series of single particle crushing tests in order to determine the characteristic tensile strength of fresh and recycled ballast samples. As can be seen in Figure 2.16, fresh ballast comprises higher tensile strength in comparison to the recycled samples, especially when testing smaller grains. This can be explained by microcracks that are contained in recycled ballast grains as a consequence of millions of load

Die approbierte gedruckte Originalversion dieser Dissertation ist an der TU Wien Bibliothek verfügbar.
The approved original version of this doctoral thesis is available in print at TU Wien Bibliothek.
TU Bibliothek Your knowledge hub WIEN

cycles the grains were exposed to in the past, making them more prone to crushing. This research shows that recycled ballast grains have about 35% lower tensile strength than the fresh ballast samples, whereby the strength of both samples decreases with increasing grain size, showing that small particles are more resistant to crushing [75].

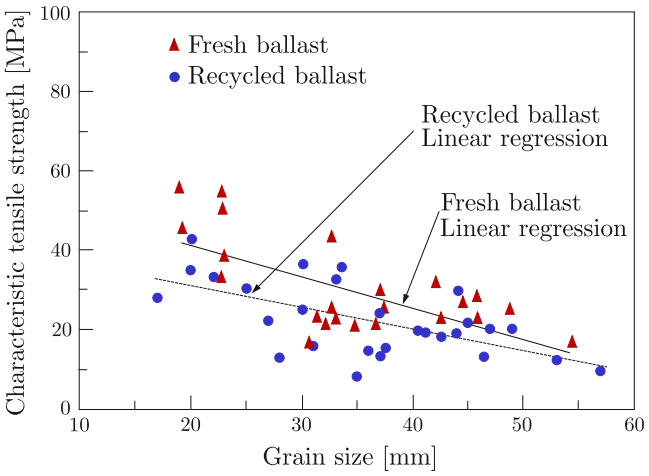

Figure 2.16: Characteristic tensile strength determined by single particle crushing tests (modified from [75])

2.2.6.2 Particle embedded in a sample

A different approach to defining the fracture strength of a single particle was presented by *Nakata et al.* [96], who examined the yielding characteristics of a single particle in a ballast matrix undergoing uniaxial and triaxial loading of different sand samples. Under the presumption that a unit cubic volume of the sample contains N particles, the number of particles per unit cross sectional area can be calculated as $(N^{1/3})^2$. Average volume of the single particle V_{sp} in the matrix is calculated as:

$$V_{sp} = \frac{\pi \cdot d^3}{6} \tag{2.15}$$

where d is the mean particle diameter. In order to obtain the force acting on a single ballast particle, volume of solids on a unit volume is calculated as:

$$V_s = \frac{1}{1+e} \tag{2.16}$$

where e is the ballast sample void ratio. Substituting Equations 2.15 and 2.16 to 2.13 yields to an expression for the force on a single particle F_{sp} embedded in a soil matrix [96]:

$$F_{sp} = \sigma \cdot d^2 \cdot \left(\sqrt[3]{\frac{(1+e)\cdot\pi}{6}} \right)^2 \tag{2.17}$$

proving that the acting force on a particle embedded in a sample is undependable on the particle size but rather depends on the matrix void ratio.

Die approbierte gedruckte Originalversion dieser Dissertation ist an der TU Wien Bibliothek verfügbar.
The approved original version of this doctoral thesis is available in print at TU Wien Bibliothek.

2.2.6.3 Ultrasonic Pulse Velocity

An non-destructive, significantly faster and less elaborate alternative method to determine the uniaxial compressive strength of ballast particles is the Ultrasonic Pulse Velocity (UPV) test (Figure 2.17). General application of the UPV is determination of concrete and natural rocks quality by measuring the velocity of an ultrasonic pulse passing through a rock or concrete sample. The UPV test is carried out using a high-energy pulse-receiver on the driving side and a two-channel digital storage oscilloscope on the receiving side [42]. Results can be expressed by the following equation for single grains:

$$v_{UPV} = \frac{b_{UPV}}{t} \tag{2.18}$$

where b is the length/width of the sample, t the travel time and v_p the travel velocity of the P-wave through the rock sample. High strength granite should exhibit high values of velocity. Several researchers have proven high level of correlation between the uniaxial compression strength of a single particle and the UPV results by testing different parent rock samples (marble, granite and dolerite [55] and different sandstones [42]). *Eze* [55] compared the UPV test results with uniaxial compressive strength test conducted on the same samples and discovered a very high level of correlation for Marble and Dolerite samples (correlation coefficient 0.97 and 0.98, respectively) and somewhat lower for granite samples (correlation coefficient 0.67). *Vasconcelos et al.* [134] used UPV tests to predict the strength and elastic properties of granitic stones and determine the relationships between the longitudinal ultrasonic wave velocity and tensile and compressive strength. They observed a reasonable nonlinear correlation between the tensile strength and ultrasonic velocity (correlation coefficient 0.89) proving that ultrasonic velocity can provide a reliable preliminary prediction of the tensile strength. The research also showed that the compressive strength can only be roughly estimated by the linear function with a correlation coefficient of 0.72.

Figure 2.17: Ultrasonic Pulse Velocity test on a single ballast grain

Die approbierte gedruckte Originalversion dieser Dissertation ist an der TU Wien Bibliothek verfügbar.
The approved original version of this doctoral thesis is available in print at TU Wien Bibliothek.

2.3 Rails

Rails are constitutive members of the ballasted track (Figures 2.1 and 2.2) with a primary function of supporting the train wheels and guiding them in a lateral direction, as well as transferring any vertical wheel and horizontal transverse forces on the rail head without excessive deformation between two sleepers, equally spaced along the length of the track [76]. Along with a smooth ruining surface, rails distribute breaking and accelerating forces by means of adhesion [45] and serve as an electrical and signal conductor on an electrified line. Defects in the rail surface can cause disturbances of the traffic movement in terms of large dynamic loads that can be unfavorable for the track structure. The cross sectional shape of a railway rail, perpendicular to its length and asymmetric about a horizontal axis is the rail profile. Some of the existing rail profiles used around the world can be seen in Figure 2.18. The flat-bottom rail or the Vignole rail is the standard profile used in conventional track derived from the I-profile with the upper flange converted to form a rail head [45]. The flat-bottom rail can be divided into three in cross-section (Figure 2.18): the rail head, ensuring good contact with the wheel, rail web, enabling adequate stiffness against bending and buckling and the rail foot, providing the stability of the rail profile and load distribution to the sleeper.

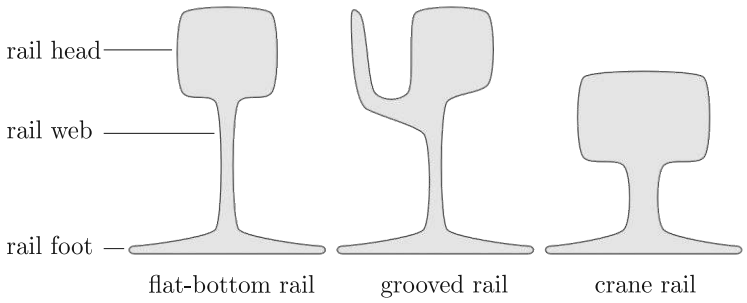

Figure 2.18: Rail profile types

Sections of steel rail lengths must be connected in a way that the geometrical deviations are small enough to limit dynamic effects, either by bolted joints or by welding. Bolted rails, most commonly used in curves or on secondary lines, are connected with drilled plates called *fishplates* and are considered to be one of the major locations of maintenance problems [136]. Track running surface discontinuity resulting from this kind of joint type can cause vibrations and additional dynamic loads which had been known to cause accelerated joint failure [76]. Due to the fact that joints are generally considered to increase track deterioration and create a need for more frequent track maintenance, in most important passenger and commonly used high speed lines the joints are eliminated entirely by the use of continuous welded rail (CWR). This method enables improved riding quality and extends rail life, thus causing significant savings by reducing maintenance cost and reducing wear on rolling stock and the damage made to the track substructure [117]. According to *Selig and Waters* [117] some of the disadvantages of CWR are higher initial cost of welding, transporting and laying longer tracks, difficulties in changing worn and defective rails and sleepers

Die approbierte gedruckte Originalversion dieser Dissertation ist an der TU Wien Bibliothek verfügbar.
The approved original version of this doctoral thesis is available in print at TU Wien Bibliothek.
TU Bibliothek Your knowledge hub WIEN

and breakage of rail or track buckling due to temperature induced stress changes.

(a) Fishplated joint (b) Welded joint

Figure 2.19: Implemented rail joints [138]

2.4 Sleepers

Sleepers or ties (Figures 2.1 and 2.2) build the basis of a rail fastening system and provide a resilient, flat and even platform for holding the rails assuring the designed rail gauge [76]. Some of the most important sleeper functions and requirements are [117],[76]:

- to receive and sustain track loads and distribute them as uniformly as possible over the supporting ballast layer at an acceptable pressure level,
- preserving track inclination and adequate electrical insulation between the rails,
- provide resistance to mechanical influences and weathering,
- to restrain all rail movement (longitudinal, lateral and vertical) by anchoring the superstructure to the ballast bed.

Sleeper stability is ensured by proper ballast packing, only supporting the sleeper in the areas beneath the rails. Sleeper rotation as a result of the vertical loads must be disabled in order to avoid any changes in rail inclination and gauge. Furthermore, the ends and sides of sleepers must be fully embedded in the ballast in order to ensure ballast resistance in longitudinal and lateral directions [76].

Most frequently used materials in sleeper production are timber (wood), concrete, steel and recently even recycled plastic (Figure 2.20). Timber sleepers, prismatic in shape, 15 cm high and 25 cm wide, have a length of 2.60 - 2.70 m (excluding switch and crossing sleepers) and weigh about 100 kg, meaning that they can be replaced by hand. They are still in use in older tracks worldwide, but due to environmental concerns as well as their higher rate of degradation (service life of between 20 years for pine-wood and 40 to 60 years for oak), they are mostly replaced by concrete sleepers. Speed of mass production and higher strength make concrete sleepers most popular and frequently used sleeper type. Much heavier than

Die approbierte gedruckte Originalversion dieser Dissertation ist an der TU Wien Bibliothek verfügbar.
The approved original version of this doctoral thesis is available in print at TU Wien Bibliothek.
TU Bibliothek Your knowledge hub WIEN

the timber ones (200 - 300 kg), concrete sleepers show good resistance to movement and are very useful in connection with stability of CWR tracks. Concrete provides numerous possibilities in design, manufacture and construction. Some of the disadvantages are lower elasticity in comparison to timber sleepers, susceptibility to corrugations and poor quality welds and up to 25% higher dynamic loads and stresses transferred to the ballast bed [45]. Concrete sleepers can also provide an overall stiffer track that enhances fuel consumption. Steel sleepers are rarely used due to the high production and installation price as well as some insulation problems, despite some significant advantages such as long service life and great dimensional accuracy. According to *Indraratna et al.* [76], a number of companies in the recent years have turned to manufacturing sleepers out of recycled plastic materials. This new material still assures proper damping of impact load as well as sound absorption and lateral track stability, while providing an environmental friendly alternative to timber sleepers that can be used in harsh climatic conditions.

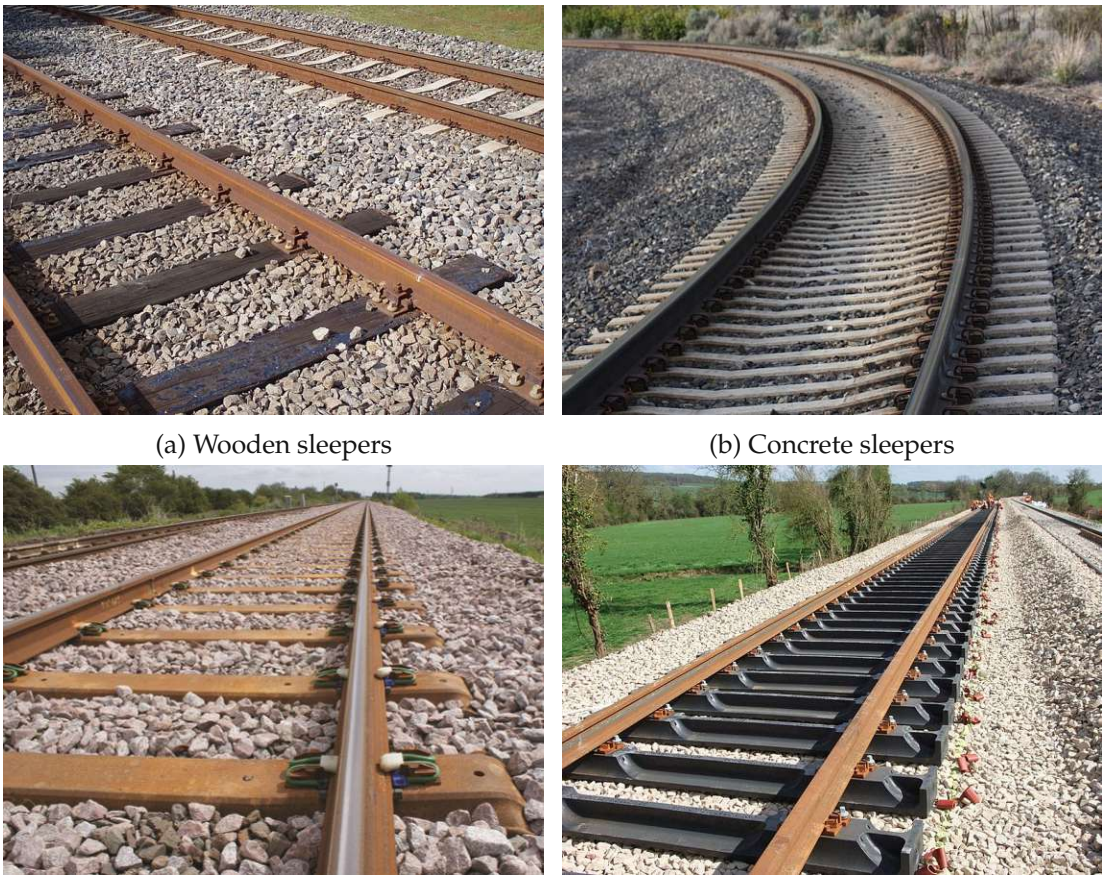

(a) Wooden sleepers (b) Concrete sleepers

(c) Steel sleepers (d) Recycled plastic sleepers

Figure 2.20: Different sleeper materials [137]

Die approbierte gedruckte Originalversion dieser Dissertation ist an der TU Wien Bibliothek verfügbar.
The approved original version of this doctoral thesis is available in print at TU Wien Bibliothek.

2.5 Fastening systems

All components forming the structural connection between the sleeper and rails with a great variety in use worldwide are described as fastening systems or fastenings. Their primary function is to fasten the rails to the sleeper, thus preventing vertical, lateral and longitudinal movement by elastically absorbing forces inflicted by wheel loads and temperature changes in the rails. In addition, fastening systems should damp vibrations and impacts caused by traffic as much as possible and retain the track gauge and rail inclination within certain limits. Fastening systems consist of coach screws used to hold the baseplate to the sleeper, clip bolts, rigid sleeper clips and spring washers and nuts [76].

The choice of the fastening system depends on the sleeper type, properties and geometry of the rail section. For example, in case of steel and concrete sleepers the fastenings also need to provide electrical insulation between the rails and the sleepers. Pads are also required between the rail seat and the concrete sleeper in order to provide damping of wheel induced vibrations and prevent or reduce rail/sleeper attrition at contact [117]. Wooden sleepers require steel plates under the rails to distribute the force over the wood surface, providing suitable bearing pressure and protection from mechanical wear.

Fastening systems can be subdivided into direct fastenings, where the rail and the baseplate are fixed to the sleeper using the same fasteners, and indirect fastenings, where the rail is connected with the baseplate by other fastening than those used to fasten the baseplate to the sleeper [45].

According to *Auer* [29] special consideration is given to the fastening systems in track curves where the resultant of acting vertical and lateral forces causes a bending or overturning moment that can lead to a tilting of the rail. Direct rail fastening is used to prevent excessive lift-off cause by the bending moment.

2.6 Subballast and subgrade

Subballast (Figures 2.1 and 2.2) is the layer of aggregates placed between the ballast layer and the subgrade, usually made of broadly graded materials such as well-graded crushed rock or sandy gravel mixture in order to assure proper drainage and filtering functions. Some of the subballast functions are provided by asphalt concrete layers, geosynthetic materials (geotextiles), cement, lime or asphalt stabilized soils. According to *Selig and Waters* [117], main functions of the subballast layer are to extend the subgrade frost protection and reduce the traffic induced stress at the bottom of the ballast layer. Additionally, it prevents the migration of subgrade particles into the ballast and the interpenetration of subgrade and ballast as well as subgrade attrition which leads to slurry formation and mud-pumping in the presence of water.

Subgrade is the ground formation of naturally deposited soils of artificially placed fill material on which the rail track structure is built (Figures 2.1 and 2.2). Existing, naturally deposited soils should be used whenever possible for economical reasons, provided that the soil is resistant to failure modes such as subgrade attrition, frost heave and thaw softening,

Die approbierte gedruckte Originalversion dieser Dissertation ist an der TU Wien Bibliothek verfügbar.
The approved original version of this doctoral thesis is available in print at TU Wien Bibliothek.
TU Bibliothek Your knowledge hub WIEN

significant volume change induced by moisture changes, progressive shear failure from repeated wheel loading, consolidation and excessive progressive settlements [117]. Instability or failure of the subgrade results in unacceptable deformations of the track and deviations from the desired track geometry, regardless of the quality of ballast and subballast layers. Should soft soils be utilized as subgrade layer, they should be stabilized by ground improvement techniques such as vibratory compaction, installation of vertical drains, lime-cement columns or deep cement grouting [76].

Main subgrade function is to provide a stable foundation for the overlaying subballast and ballast layers and the track structure altogether, as well as to contribute to the superstructure support resiliency.

2.7 Stresses acting on the ballast bed

Understanding the type and magnitude of stresses acting on the track substructure is the key element in an effort of proper track design. Forces imposed on the track structure are classified as mechanical, dynamical and thermal. A combination of the three transferred through the track superstructure to the substructure determines the dynamic loads that must be supported by the substructure. Forces acting on the superstructure can be subdivided as follows [117]:

- Vertical forces, perpendicular to the rails: vertical wheels and uplift forces,
- Lateral forces, parallel to the sleeper axis: lateral wheel and buckling reaction forces,
- Longitudinal forces, parallel to the rails: thermal induced rail deformation, rail wave action, breaking forces from the locomotive and the cars and locomotive traction force including acceleration forces.

2.7.1 Stresses on the rail head

The contact pressure between the rail and the wheel is an important aspect in the study of plastic flow and fatigue life of the rail head, as well as in calculation of pressures that are transmitted to the substructure. Initial contact between a wheel and rail is determined by the geometric features of the two bodies, but the final contact area is also determined by how much they deform under the applied forces. The general theory of localized contact between elastic bodies with simple local curvatures was formulated by *Heinrich Hertz* in 1895 [66]. According to his theory, the contact area A between two curved elastic bodies like the wheel and rail head is ellipsoidal (shown in Figure 2.21). The governing equation of the contact ellipse with major and minor axes a_e and b_e is given by the Equation 2.19:

$$\frac{x^2}{{a_e}^2} + \frac{y^2}{{b_e}^2} = 1 \tag{2.19}$$

The dimension of the contact ellipse can be determined by the acting normal force F on the contact area. The a_e/b_e ratio depends on the curvature of the wheel and rail profiles [45].

Die approbierte gedruckte Originalversion dieser Dissertation ist an der TU Wien Bibliothek verfügbar.
The approved original version of this doctoral thesis is available in print at TU Wien Bibliothek.
TU Bibliothek Your knowledge hub WIEN

Contact stress distribution p_{mean} is semi-ellipsoidal (Equation 2.20) with the highest contact pressure p_{max} occurring in the center, i.e. at the first point of contact (Equation 2.21) [45].

$$p_{mean} = p_{max} \cdot \left(1 - \frac{x^2}{{a_e}^2} - \frac{y^2}{{b_e}^2}\right)^{-\frac{1}{2}} \tag{2.20}$$

$$p_{max} = \frac{3}{2} \cdot \frac{F_N}{\pi a_e b_e} \tag{2.21}$$

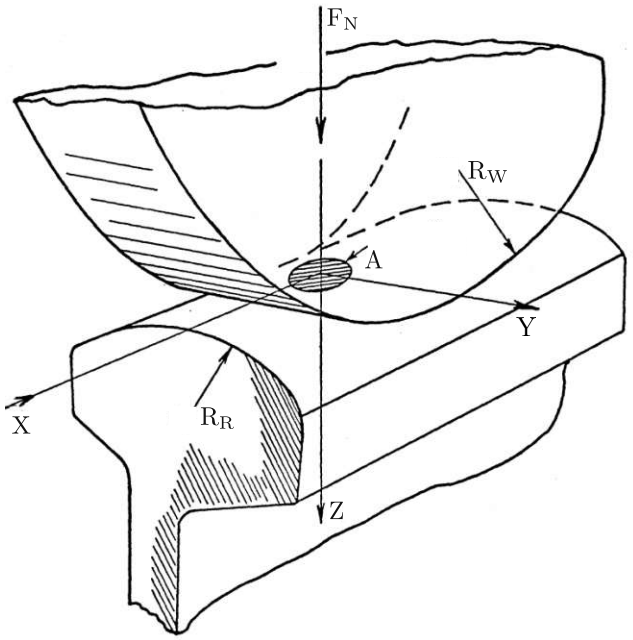

Figure 2.21: Wheel-rail contact according to the *Hertzian* theory (modified from [82])

A simplification of the original approach based on the *Hertz* theory was proposed by *Eisenmann* [53], who developed a calculation of the wheel-rail contact based on the consideration that a simplified two-dimensional calculation was proven to be accurate for wheel diameters between 60 and 120 cm. His analysis is based on a cylinder representing the wheel (radius R_W) on a plane substituting the rail (radius $R_R = \infty$).

Half-length of the wheel-rail contact area b_e is taken as a constant of 6 mm [53], while the half-width of the contact area can be expressed as [66]:

$$a_e = \sqrt{R d_p} \tag{2.22}$$

where R presents the radius of both bodies in contact that can be calculated using the general expression for a cylinder on a plane [105]:

$$\frac{1}{R} = \frac{1}{R_W} + \frac{1}{R_R} \tag{2.23}$$

Given that the rail radius R_R is assumed to be infinitely large, the Equation 2.23 yields to $R = R_w$. In Equation 2.22 d_p denotes the displacement due to rail-wheel contact caused

Die approbierte gedruckte Originalversion dieser Dissertation ist an der TU Wien Bibliothek verfügbar.
The approved original version of this doctoral thesis is available in print at TU Wien Bibliothek.
TU Bibliothek Your knowledge hub WIEN

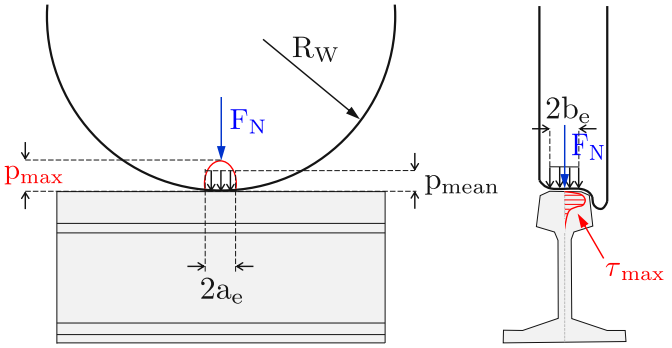

Figure 2.22: Contact distribution between wheel and rail according to *Eisenmann* (modified from [45])

by the wheel loads transferred to the rail head that exceed the yield limit of the contacting material, i.e. the rail. The resulting plastic deformation jointed with the wear process acts to flatten out the contact area [104]. Therefore, based on *Hertz's* theory, *Eisenmann* [53] suggested the following formula for the calculation of mean rolling contact stress p_{mean} where the acting force F_N is distributed over the rectangular area:

$$p_{mean} = \frac{F_N}{2a_e \cdot 2b_e} \tag{2.24}$$

The contact length $2a_e$ is calculated as:

$$2a_e = \frac{4}{\sqrt{\pi}} \cdot \sqrt{\frac{F_N \cdot R_W}{2b_e \cdot E^*}} \tag{2.25}$$

The contact stress distribution becomes semi-elliptical as can be seen in Figure 2.22. Equivalent system stiffness E^* can be expressed as [108]:

$$\frac{1}{E^*} = \frac{1}{2}\left(\frac{1-\nu_W^2}{E_W} + \frac{1-\nu_R^2}{E_R}\right) \tag{2.26}$$

where E_W and E_R represent the moduli of elasticity, ν_W and ν_R *Poisson's* ratios of the wheel and rail, respectively. Given that the stiffness of the wheel is higher than the stiffness of the rail, an additional simplification is made with $E_R = \infty$, making the equivalent system stiffness equal to [108]:

$$E^* = \frac{E_W}{2(1-\nu_W^2)} \tag{2.27}$$

The mean stress acting on the rail head can now be calculated as:

$$p_{mean} = \sqrt{\frac{\pi}{32}} \cdot \sqrt{\frac{E^* \cdot F_N}{R_W \cdot b_e}} \tag{2.28}$$

Lastly, the mean stress acting on the rail head can be expressed by taking the equivalent system stiffness E^* into account and substituting Equation 2.27 in 2.28:

Die approbierte gedruckte Originalversion dieser Dissertation ist an der TU Wien Bibliothek verfügbar.
The approved original version of this doctoral thesis is available in print at TU Wien Bibliothek.

$$p_{mean} = \sqrt{\frac{\pi}{64}} \cdot \sqrt{\frac{E_W \cdot F_N}{(1-\nu_w^2) \cdot R_W \cdot b_e}} \tag{2.29}$$

where $E = 210\,kN/mm^2$, $\nu_W = 0.3$ and $b_e = 6\,mm$, which yields into:

$$p_{mean} = 43.5 \cdot \sqrt{\frac{F_N}{R_w}} \tag{2.30}$$

Stress state in the rail head can be determined using the *Boussinesq* half space theory, given that it has been experimentally proven that the theory of elasticity does not apply [45].

Maximum shear stress in the rail head that occurs across the rail (Figure 2.22) is dependent on the wheel radius and dependent but not proportional to the magnitude of the normal principal stress:

$$\tau_{max} = C \cdot p_{mean} = 13.05 \cdot \sqrt{\frac{F_N}{R_w}} \tag{2.31}$$

C is a factor between 0.31 and 0.33, approximated with 0.3 for maximum shear stress [88]. This simplified calculation model is applicable for maximum shear stresses that occur 4-7 mm beneath the rail head.

2.7.2 Ballast bed coefficient

Stress acting on the ballast is expressed as ballast pressure, resulting the sleeper load in relation to the effective supporting surface of the sleeper in contact to the ballast [88]. Traffic loads, acting as the greatest loads in the ballast bed are primary quasi-static and dynamic vertical loads. Discontinuities in the track (e.g. switch points, joint gaps) or on the vehicle (e.g. flat spots) produce localized, dynamic force peaks [88].

Zimmermann's [142] method is used to evaluate the stresses acting on the track components and produces reliable results for the purposes of measuring and track design. The method describes the rails as bearers on an elastic foundation. The ballast bed coefficient, i.e. modulus C_b, describes the relationship between the surface pressure of the supporting point and the depression or the elasticity of the ballast bed and the subsoil. It can be expressed as [88]:

$$C_b = \frac{p_b}{z} \tag{2.32}$$

where C_b is the ballast bed coefficient (Table 2.4), p_b the surface pressure between the sleeper and ballast and z the elastic depression of the rail that can be determined by depression measurements or rail foot tensions [88].

Die approbierte gedruckte Originalversion dieser Dissertation ist an der TU Wien Bibliothek verfügbar.
The approved original version of this doctoral thesis is available in print at TU Wien Bibliothek.
TU Bibliothek Your knowledge hub WIEN

Table 2.4: Ballast bed modulus for different subsoils [86]

Type of subsoil	Ballast bed coefficient C_b [MN/m^3]
concrete floor (bridges, tunnels)	≥ 300
very good subsoil	≥ 150
good subsoil (gravel)	≥ 100
poor subsoil (cohesive soils)	≥ 50
very poor subsoil (organic soils)	< 50

2.7.3 Ballast pressure under the sleeper

Sleepers, contrary to the rails, may not be considered as beams of infinite length. Stability in ballast bed is ensured by supporting the sleepers only under the rails, distributing the vertical contact force evenly over the contact surface. Calculation of the pressure on the ballast bed is based on *Zimmermann's* [142] theory converting cross-sleeper support surface into equal surface longitudinal sleepers (Figure 2.23).

The elastic depression z of the rail is obtained as [86]:

$$z = \frac{F_w}{2b_s \cdot C_b \cdot l_s} \cdot \eta \tag{2.33}$$

where F_w is the acting effective wheel force [86], b_s the width and l_s the fictive sleeper length based on the assumed longitudinal beam/sleeper. *Zimmermann*'s influencing factor η takes into consideration the influence of several axles of a vehicle and can be set to 1 for a single load acting in the center of the sleeper [86]. The fictive sleeper length l_s is obtained as:

$$l_s = \sqrt[4]{\frac{4 \cdot EI}{C_b \cdot b_s}} \tag{2.34}$$

where E stands for the modulus of elasticity of the rail steel (210 kN/mm^2) and I for the rails moment of inertia. Width of the assumed longitudinal beam b_s is calculated using following equations referring to Figure 2.23:

$$A = A_1 = A_s \tag{2.35a}$$

$$A_1 = 2o_s \cdot b_1 \tag{2.35b}$$

$$A_s = b_s \cdot a_s \tag{2.35c}$$

a representing the sleeper spacing equal to a_s and o_s the sleeper overhang.

$$b_s = \frac{A_s}{a_s} = \frac{2o_s \cdot b_1}{a_s} \tag{2.36}$$

Ballast pressure under the sleeper p can now be calculated by including Equations 2.33, 2.34 and 2.36 into 2.32:

Die approbierte gedruckte Originalversion dieser Dissertation ist an der TU Wien Bibliothek verfügbar.
The approved original version of this doctoral thesis is available in print at TU Wien Bibliothek.

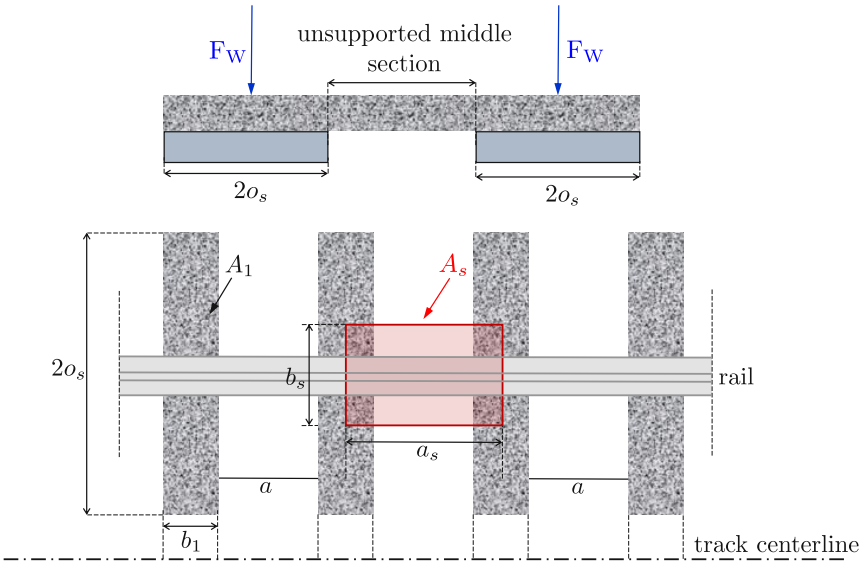

Figure 2.23: Conversion of the cross-sleeper track in a theoretical longitudinal sleeper track (s - track gauge) [86]

$$p = C_b \cdot z = \frac{F_w}{2b_s \cdot l_s} = \frac{F_w \cdot a_s}{2A_s} \cdot \sqrt[4]{\frac{C_b \cdot A_s}{4 \cdot EI \cdot a_s}} = \frac{F}{2A} \cdot \sqrt[4]{\frac{C_b \cdot a^3 \cdot A}{4 \cdot EI}} \tag{2.37}$$

It can be seen from Equation 2.37 that a heavier rail profile decreases stresses acting on the ballast layer, as well as an increase of the sleeper-rail contact surface and a decrease of sleeper spacing. The relation between vertical stress and track geometry deterioration is assumed to be calculated as [45]:

$$\text{Decrease in track geometry quality} = (\text{increase in stress on ballast bed})^m \tag{2.38}$$

in which m equals 3 to 4, meaning that a 10% higher stress on the ballast bed leads to a 1.2 to 1.5 times faster reduction in track geometry quality and a proportional increase in maintenance [45].

2.7.4 Load dispersion in the ballast bed

Even distribution of traffic loads over the substructure and/or subsoil without exceeding its load-bearing capacity is achieved by properly sizing the ballast bed [88]. Initial track settlements are necessary to transfer and distribute the wheel load over several sleepers and activate the underlying resistance force of the ballast bed so that the traffic loads can be dispersed uniformly into the subsoil. Load transfer occurs through force paths randomly formed in the ballast bed (Figure 2.24).

In order to optimally use the bearing capacity of the ballast layer and the underlying soil, as well as to achieve an even distribution of pressure on the formation, it is necessary to carefully select the depth of the ballast layer [88]:

Die approbierte gedruckte Originalversion dieser Dissertation ist an der TU Wien Bibliothek verfügbar.
The approved original version of this doctoral thesis is available in print at TU Wien Bibliothek.

$$h_b = \frac{a_s}{2 \cdot tan\lambda} \tag{2.39}$$

Whereby h_b is the ballast bed depth under the sleeper, a_s the sleeper spacing and λ the load dispersion angle [88].

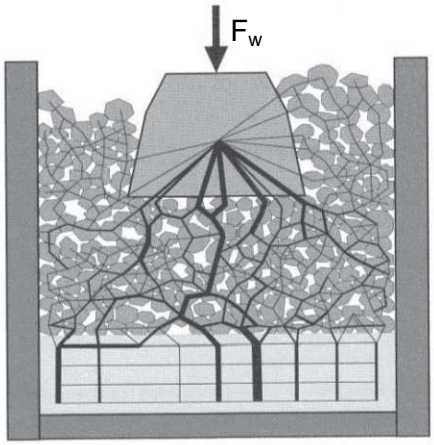

Figure 2.24: Individual force paths in the ballast bed (modified from [26])

2.7.5 Ballast shear strength

Apart from the vertical and horizontal principal stresses σ_x and σ_z, ballast bed is also subjected to shear stresses. Bearing capacity of the ballast bed depends mainly on the shear strength, defined by the internal friction angle φ, cohesion c and the effective normal stress σ acting perpendicular to a slip surface [88]. Internal friction angle depends on the grain size distribution as well as on the shape, roughness and edge stability of the ballast grains. Many of these parameters are influenced by stone processing but defined by rock properties and mineralogy [88]. Ballast shear strength can be determined using a large shear apparatus. *Fischer* [60] reports about laboratory tests on different ballast qualities, showing that the shearing strength of fouled ballast is significantly lower in comparisons with new ballast (similar results can be seen in Figure 2.4a). When wet, fine particles in large quantities reduce the ballast internal friction angle and lower the shearing strength. This results influences the load transfer properties and causes stress peaks that lead to (uneven) settlements [88].

Die approbierte gedruckte Originalversion dieser Dissertation ist an der TU Wien Bibliothek verfügbar.
The approved original version of this doctoral thesis is available in print at TU Wien Bibliothek.

Die approbierte gedruckte Originalversion dieser Dissertation ist an der TU Wien Bibliothek verfügbar.
The approved original version of this doctoral thesis is available in print at TU Wien Bibliothek.

Chapter 3

Ballast fouling

3.1 Introduction

Ballast fouling is one of the primary causes of degradation of the subsurface support structure in railways. It weakens resistance to the vertical (including uplift), lateral and longitudinal forces applied by the sleepers, and reduces resilient modulus and energy absorption capacity. The proportion of fine particles (<0.5 mm) and finest grain (<0.063 mm) is usually limited to a maximum of 1.0M% because fine particles in larger quantities can hinder the drainage and also reduce the shearing strength of the ballast bed [88]. With a rate of increase depending on the circumstances (traffic loads, ballast quality), the amount of fouling material will increase with time. According to *Selig and Waters* [117] and *Panjamani* [103], sources of ballast fouling can be divided into the following categories:

- breakdown of ballast particles due to mechanical traffic loading forces, ballast degradation during construction (handling at quarry, during transportation and from dumping) and rail-road maintenance, changes in temperature and chemical weathering,
- infiltration from the surface (coal or iron ore from the railcars, dust, dirt, plant life decay),
- sleeper (tie) wear,
- infiltration from the underlying gravel layer (subballast),
- subgrade infiltration (traction of the formation soil, soft clays and silts).

Selig and Waters [117] report that ballast breakdown causes approximately 76% of ballast fouling in North America, 13% is generated by infiltration from the subballast, 7% by infiltration from the ballast surface, 3% comes from subgrade intrusion, and 1% is due to sleeper wear. Studies on fouling of rail-road ballast in Germany and Austria state infiltration from the surface and the effect of subgrade infiltration as main sources of finer components in the ballast matrix. Generally speaking a combination of ballast fouling sources should be expected at each individual location, with the most influential groups depending on specific site conditions. *Huang et al.* [69] developed a three-phase system to determine the stability

Die approbierte gedruckte Originalversion dieser Dissertation ist an der TU Wien Bibliothek verfügbar.
The approved original version of this doctoral thesis is available in print at TU Wien Bibliothek.
TU Bibliothek Your knowledge hub WIEN

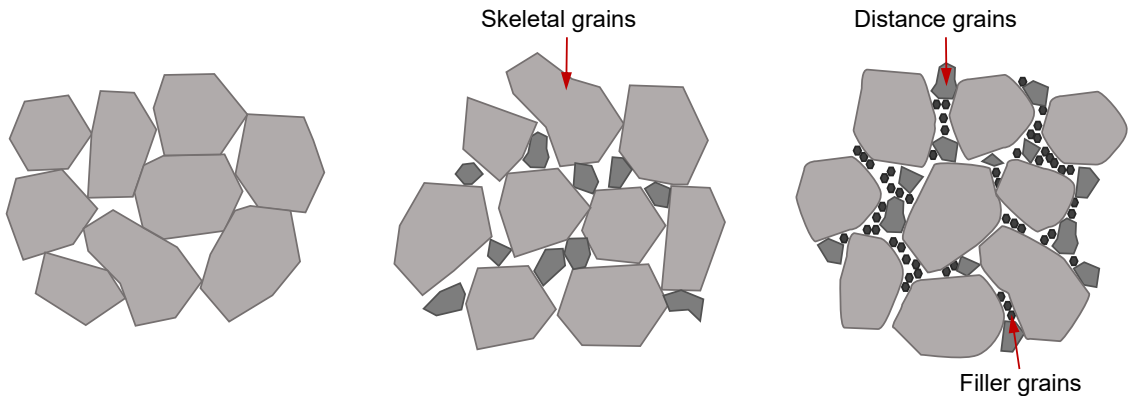

(a) Phase 1: clean ballast (b) Phase 2: partially fouled ballast (c) Phase 3: heavily fouled ballast

Figure 3.1: Critical ballast fouling phases (adapted from [69] and [86])

of the fouled ballast layer. Three phases (Figure 3.1) can be identified in dependence on fine materials filling the void space:

a) Phase 1 - clean or very slightly fouled ballast sample with almost all grains establishing contact with each other (Figure 3.1a),

b) Phase 2 - voids in between grains filled with enough fine particles to significantly reduce the strength, grain-to-grain contact still maintained (Figure 3.1b),

c) Phase 3 - excessive amount of fine particles, grain-to-grain contacts are mostly eliminated, single grain movement is constrained only by the fine particles filling the matrix or voids between the particles (Figure 3.1c).

Huang et al. [69] also state that the ballast condition in Phase 3 should be defined as the end of the ballast service life, needing immediate ballast replacement action. They indicate that the three-phase system should be utilized to differentiate between fouling sources at different phases and used to describe ballast strength and the influence on track stability. The importance of finding a distinct definition of the transition between the first two phases is emphasized, as it also indicates the trigger for maintenance activities, such as ballast cleaning.

3.1.1 Ballast hydraulic erosion

A somewhat uncommon but particularly sever ballast and sleeper degradation problem is the hydraulic erosion that is observed mostly near welds. *Selig and Waters* [117] report of severe limestone abrasion to fine powder forming a slurry when mixed with water, eroding the concrete sleepers and ballast and forming voids under the sleepers (Figure 3.2). High hydraulic gradient in the liquid slurry beneath the sleeper is believed to cause the sleeper and most of the ballast attrition - under the influence of traffic loading the sleeper is driven downwards, raising the high fluid pressure within the slurry formed beneath the sleeper

Die approbierte gedruckte Originalversion dieser Dissertation ist an der TU Wien Bibliothek verfügbar.
The approved original version of this doctoral thesis is available in print at TU Wien Bibliothek.
TU Bibliothek Your knowledge hub WIEN

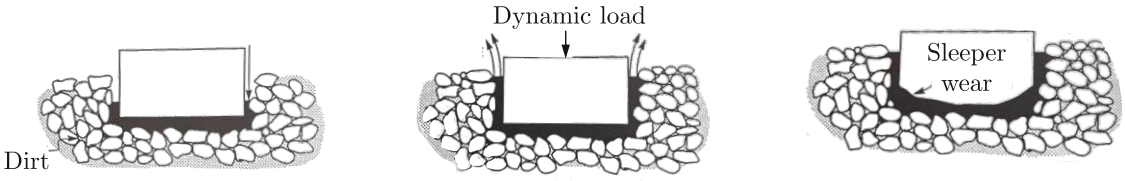

(a) Ponded water in the voids beneath the sleeper (b) Water and fine dirt particles pumped out under pressure (c) Sleeper wear due to hydraulic erosion

Figure 3.2: Hydraulic action on ballast and sleepers [117]

that dissipates by jetting or pumping sideways and upwards around the sleeper. Higher traffic speed causes higher water pressure, meaning that the increasing speed increases the erosion [117]. The pumping action described displaces ballast particles from around the sleeper and reduces the track lateral displacement resistance.

3.2 Ballast fouling quantification

Quantification of ballast fouling is a unique problem in geotechnical engineering. Detailed classification scheme is available for most of the geotechnical materials but only a limited classification is available for two dissimilar materials combination, which is a case for most of the ballast fouling. Fouled ballast is characterized by a large variation in particle size, particle shape and specific weight of the material. Existing ballast fouling quantifications that have been proposed as *level of ballast fouling* determination factors are summarized and reviewed in this section. All of the described quantifications are empirical indices with a greater value indicating a greater degree of fouling for all of the presented methods, suggesting a reduction in track performance. Given ballast fouling quantifications should be used to determine and classify ballast performance for given traffic loads, speed and track geometry and as such provide an advantage in defining the optimum time for ballast bed cleaning or renewal [34].

3.2.1 Index of Particle Breakage (B_g)

As one of the pioneers in developing methods and indices for quantifying ballast breakage, *Marsal* [92] proposed the use of an Index of Particle Breakage B_g. During large-scale triaxial test conducted on rockfill materials, he noticed a significant amount of particle breakage that resulted in noticeable changes in the particle size distribution of the tested samples after loading [92]. Based on the sieve analysis conducted on samples prior to and after loading *Marsal* [92] calculated the difference in percentage retained on each sieve size and developed the following equation:

$$\Delta W_k = W_{ki} - W_{kf} \tag{3.1}$$

W_{ki} is the percentage retained in sieve size k before (initial) and W_{fi} the percentage retained on the same sieve size after the test (final). Due to particle breakage, the value of ΔW_k

Die approbierte gedruckte Originalversion dieser Dissertation ist an der TU Wien Bibliothek verfügbar.
The approved original version of this doctoral thesis is available in print at TU Wien Bibliothek.
TU Bibliothek Your knowledge hub WIEN

for some sieves is positive and for some negative, whereas the sum of all positive values of ΔW_k must be equal to the sum of all negative values [76]. Index of Particle Breakage B_g is defined as the sum of all positive values of ΔW_k, in percentage:

$$B_g = \sum(\Delta W_k > 0) \tag{3.2}$$

The lower limit of ΔW_k is 0, meaning no particle breakage occurred. The upper (theoretical) limit of ΔW_k is 100%, indicating that all particles were broken to sizes below the smallest sieve size [76]. A disadvantage of this ballast fouling quantification is the dependence of the B_g index on the sieve sizes used, meaning that only B_g values calculated using the same sized sieve sets can be compared with each other.

3.2.2 Fouling Index (FI)

Selig and Waters [117] emphasize the importance of silt and clay-sized (<0.075 mm) fouling particles by proposing a quantification of the fouled ballast for North American railways in terms of the Fouling Index (FI):

$$FI = P_{0.075} + P_{4.75} \tag{3.3a}$$

$$FI = P_{200} + P_4 \tag{3.3b}$$

where $P_{0.075}$ or P_{200} are percentages of ballast particles passing the 0.075 mm or the number 200 sieve, and the $P_{4.75}$ or P_4 passing the 4.75 mm or the number 4 sieve, respectively. Size distribution curves showing ballast conditions with Fouling Index from clean to highly fouled are shown in Figure 3.3. Considering the fact that North American railway system uses finer ballast gradation (D_{min}= 4.76 mm, D_{max}= 51 mm), the Equation 3.3 was modified by *Ionescu* [80], applied to Australian track conditions (D_{min}= 13.2 mm) and is now widely used in academic research:

$$FI = P_{0.075} + P_{13.2} \tag{3.4}$$

The revised approach should be additionally modified for European conditions where the undersized grain portion of D_{min} < 22.4 mm is set to a maximum 5% in sample weight. For this reason a more unified Fouling Index was proposed by *Ionescu* [80], based on the grain diameter ratio:

$$FI_D = \frac{D_{90}}{D_{10}} \tag{3.5}$$

Both D_{90} and D_{10} corresponding to 90% and 10% passing by weight respectively can be obtained from the particle size distribution curve of the fouled ballast supplied directly from the track making it unnecessary to know the gradation of the clean ballast. Additionally, a high D_{90} to D_{10} ratio describes a wide-graded material indicating a lack of drainage capability and a loss of resilience of the ballast bed, as was proven by a series of permeability tests performed on ballast samples stating that good ballast drainage is assured with a coefficient of permeability k_f greater than 10^{-5} m/s [80][111]. A classification criteria based on the Equations 3.3, 3.4 and 3.5 is presented in Table 3.1.

Die approbierte gedruckte Originalversion dieser Dissertation ist an der TU Wien Bibliothek verfügbar.
The approved original version of this doctoral thesis is available in print at TU Wien Bibliothek.
TU Bibliothek Your knowledge hub WIEN

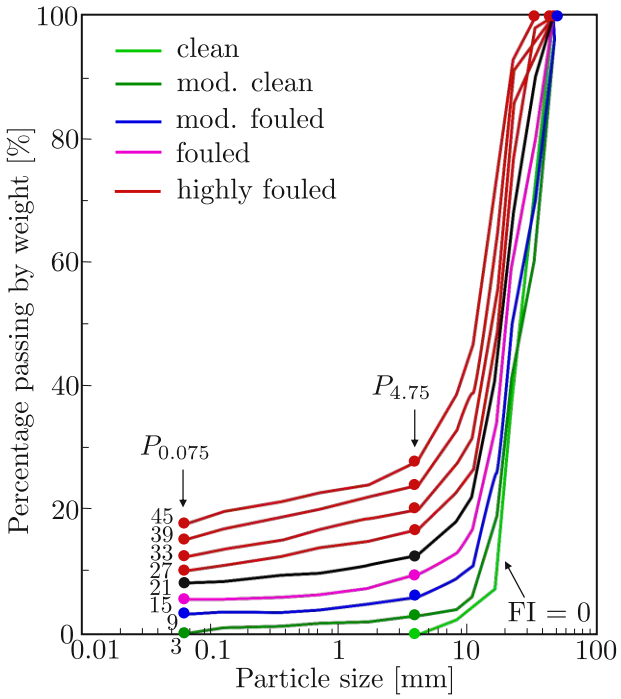

Figure 3.3: Size distribution curves showing ballast conditions with Fouling Index FI from clean to highly fouled given by Equation 3.3a, adapted from [117]

Table 3.1: Fouled ballast classification based on the Fouling Index FI [80]

Fouling Index FI			Classification
$FI = P_{0.075} + P_{4.75}$	$FI = P_{0.075} + P_{13.2}$	$FI_D = D_{90}/D_{10}$	
< 1	< 2	< 2.1 and $P_{13.2} \geq 1.5\%$	clean
1 to < 10	2 to < 10	2.1 to < 4	mod. clean
10 to < 20	20 to < 40	4 to < 9.5	mod. fouled
20 to < 40	20 to < 40	9.5 to < 40	fouled
$\geq$ 40	$\geq$ 45	$\geq$ 40, $P_{13.2} \geq 40\%$, $P_{0.075} \geq 5\%$	highly fouled

Two additional criteria ($P_{0.075}$ and $P_{13.2}$) are added to highly fouled ballast classification (Table 3.1) in order to avoid an overestimation or underestimation of the Fouling Index calculation based on Equation 3.5. Since the content of fines (< 0.075 mm) is limited to 5 %, this limit was adopted as a classification criterion. Limit $P_{13.2}$ ensures that the ballast is cleaned, even if $P_{0.075} < 5\%$ so as to guarantee the required ballast resiliency and good track performance [80]. The deformational behavior of the track ballast is highly influenced by changes in the contact points between fouled ballast particles. However, fouling material of the same mass but different specific gravity[1] would occupy different volumes in the ballast matrix. Relative volume of voids filled with fouling material are proportional to contact points of fouled ballast particles. The influence of volume of different fouling materials in the ballast matrix was studied by *Ebrahimi et al.* [52] and a volumetric Fouling Index was

[1]Dimensionless unit that defines the ratio of density of a substance to the density of water

Die approbierte gedruckte Originalversion dieser Dissertation ist an der TU Wien Bibliothek verfügbar.
The approved original version of this doctoral thesis is available in print at TU Wien Bibliothek.

proposed:

$$FI_{Volumetric} = FI \cdot \frac{G_{S0}}{G_S} \tag{3.6}$$

where G_{S0} is the reference specific gravity (the G_S of mineral fouling), G_S is the specific gravity of the given fouling material, and FI the Fouling Index from Equation 3.4. Volumetric FI is used to define the state and nature of fouling from different sources and its control of plastic deformations [52].

3.2.3 Percentage of Fouling (Percentage Passing)

Percentage of Fouling is defined as a ratio of the dry weight of material passing a 9.5 mm sieve to the dry weight of the total sample developed by *Selig and Waters* [117]. It is an index related to FI, also calculating the ballast fouling based on mass calculation in the sieve analysis. As stated before, the Percentage Passing is also highly dependable on the selection of the correct grain-size threshold to define the "fouling material" for local conditions that differ significantly (material passing 22.4 mm sieve for Europe, 4.75 mm for the US and 0.075 mm for South Korea). This ballast fouling quantification criteria also does not give information regarding fouling material properties. The plasticity, composition, specific weight and the origin of the fouling material affect especially the permeability of the ballast layer. Ballast fouled with sand-sized particles will probably retain better permeability, strength, and compressibility properties than ballast fouled with plastic fine-grained particles even though they have similar values of Percent Passing a particular grain-size diameter (*Stark et al.* [121]). Ballast condition classification based on the Percentage of Fouling Index is presented in Table 3.2.

Table 3.2: Fouled ballast classification based on the Percentage of Fouling (Percentage Passing), adapted from [76]

Percentage of Fouling (%)	Classification
< 2	clean
2 to < 9.5	moderately clean
9.5 to < 17.5	moderately fouled
17.5 to < 34	fouled
≥ 34	highly fouled

3.2.4 Percentage Void Contamination (PVC)

Percentage Void Contamination index was presented by *Feldman und Nissen* [56] and is defined as the ratio of volume of voids in the ballast sample to the volume of contaminates of fouling material present in the ballast. It expresses fouling as a percentage of volume instead of a percentage of sample weight. PVC defines the fouling material as particles passing the 9.5 mm (3/8 inch) sieve by volume not weight. According to *Stark et al.* [121], the development of PVC was prompted by inadequate predictions made using Percent Passing and the

Die approbierte gedruckte Originalversion dieser Dissertation ist an der TU Wien Bibliothek verfügbar.
The approved original version of this doctoral thesis is available in print at TU Wien Bibliothek.
TU Bibliothek Your knowledge hub WIEN

Fouling Index for ballast fouled with coal ash. The divergence in results arises from the specific gravity of coal ash (∼1.28) being about one-half of most rock or soil particles (∼2.76). For this reason the volume of coal ash in the fouled ballast will be twice as big as that of most rock or soil particles for the same value of Percent Passing because it is based on weight not volume [121]. Percentage Void Contamination index is expressed as:

$$PVC = \frac{V_2}{V_1} \cdot 100 \tag{3.7}$$

where V_1 is the void volume between re-compacted clean ballast particles (> 9.5 mm) for a given density and V_2 is the total volume of fouling material (particles passing the 9.5 mm sieve) that fills V_1. For example if V_1 is one-half of V_2, one-half of the voids are filled with fouling material (< 9.5 mm). V_1 represents the void volume of the whole ballast layer, given that the samples for the PVC tests are taken from the total depth of the ballast bed [56]. Ballast conditions based on the Percentage Void Contamination are defined by *Feldman und Nissen* and are presented in Table 3.3. The main shortcoming of the PVC index lays in the fact that the usage of bulk volume in the calculation of PVC does not take the gradation of the fouling particles into account. *Indraratna* [77] reports that the PVC index may overestimate the fouling level in case the fouling material is composed of coarse particles (4.75 - 9.5 mm). In this case the permeability of the ballast bed would not have been significantly reduced, as would be implied by the PVC index.

Table 3.3: Fouled ballast classification based on the Percentage Void Contamination, adapted from [76]

PVC (%)	Classification
0 - 20	clean
20 - 29	moderately fouled
> 30	fouled

3.2.5 Void Contaminant Index (VCI)

Void Contaminant Index (VCI) was proposed by *Tennakoon et al.* [125], capturing the role of different fouling materials as a modification to the PVC, using void ratio, specific gravity and dry mass of the fouling and clean ballast material to calculate the volume. By substituting the relevant soil parameters, Equation 3.7 can be re-written as:

$$VCI = \frac{1 + e_f}{e_b} \cdot \frac{G_{sb}}{G_{sf}} \cdot \frac{M_f}{M_b} \cdot 100 \tag{3.8}$$

where e_b is the void ratio of clean ballast and e_f of the fouling material. G_{sb} and M_b stand for specific gravity and dry mass of the clean ballast. G_{sf} and M_f represent the specific gravity and dry mass of the fouling material, respectively. For example, VCI = 20% indicates that 20% of the total ballast voids is occupied by the fouling material. VCI is more sensitive to the changes of the fouling type and extent, apart from being more realistic as it is the only

Die approbierte gedruckte Originalversion dieser Dissertation ist an der TU Wien Bibliothek verfügbar.
The approved original version of this doctoral thesis is available in print at TU Wien Bibliothek.
TU Bibliothek Your knowledge hub WIEN

fouling characterization method that incorporates the specific gravity of the fouling material [125]. *Tennakoon et al.* also report that the effect of fouling on ballast bed permeability depends on the type of fouling materials. For example, coal and sand fouling may not decrease the overall permeability of the track significantly, while clay fouling can decrease the track drainage more dramatically.

3.2.6 Relative Ballast Fouling Ratio ($R_{b\text{-}f}$)

Indraratna et al. [77] proposed the Relative Ballast Fouling Ratio as a new ballast fouling quantification method by comparing Percentage passing and Percentage Void Contamination. $R_{b\text{-}f}$ is a ratio of the dry weight of fouling particles passing the 9.5 mm sieve to the dry weight of the ballast sample (particle being retained on a 9.5 mm sieve) [77]. Relative Ballast Fouling Ratio is defined as (parameters detain the notation from VCI, and subscripts f and b represent the fouling materials and ballast, respectively):

$$R_{b-f} = \frac{M_f\left(\frac{G_{b-f}}{G_{sf}}\right)}{M_b} \cdot 100\% \tag{3.9}$$

Only the dry mass and the specific gravities need to be determined in order to calculate the Relative Ballast Fouling Ratio. According to *Indraratna et al.* [77], this method should greatly speed up the measurements compared to the PVC method. $R_{b\text{-}f}$ is the ratio between the solid volumes of the fouling and ballast particles and the magnitude of $R_{b\text{-}f}$ can therefore, in comparison with FI, better represent the degree of fouling by various materials of different specific gravities. Ballast condition classification based on the Relative Ballast Fouling Ratio is presented in Table 3.4. Fouled ballast classification based on the Relative Ballast Fouling Ratio $R_{b\text{-}f}$ can be seen in Figure 3.4.

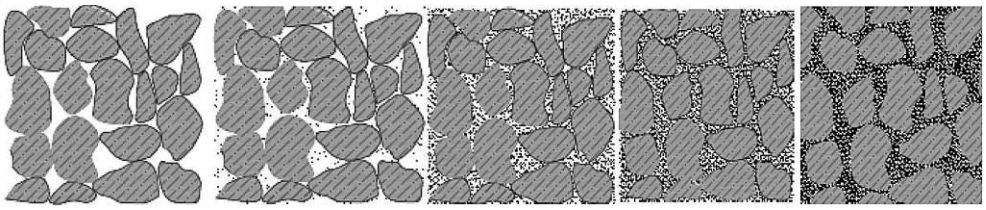

Clean	Moderately clean	Moderately fouled	Fouled	Highly fouled
<2%	2% to <10%	10% to <20%	20% to <50%	≥ 50%

Figure 3.4: Ballast fouling phases, classification by Relative Ballast Fouling Index (adapted from [49])

Die approbierte gedruckte Originalversion dieser Dissertation ist an der TU Wien Bibliothek verfügbar.
The approved original version of this doctoral thesis is available in print at TU Wien Bibliothek.

Table 3.4: Fouled ballast classification based on the Relative Ballast Fouling Ratio (adapted from [76])

$R_{b\text{-}f}$ (%)	Classification
< 2	clean
2 to < 10	moderately clean
10 to < 20	moderately fouled
20 to < 50	fouled
≥ 50	highly fouled

3.2.7 Ballast Breakage Index (BBI)

One of the most commonly used ballast fouling quantifications is the Ballast Breakage Index, proposed specifically for qualification of railway ballast by *Indraratna et al.* [74]. *BBI* quantifies the change in the particle size distribution prior to and after sample testing [136], i.e. ballast fouling and is determined using Equation 3.10:

$$BBI = \frac{A}{A+B} \tag{3.10}$$

where the parameters A and B are defined in Figure 3.5.

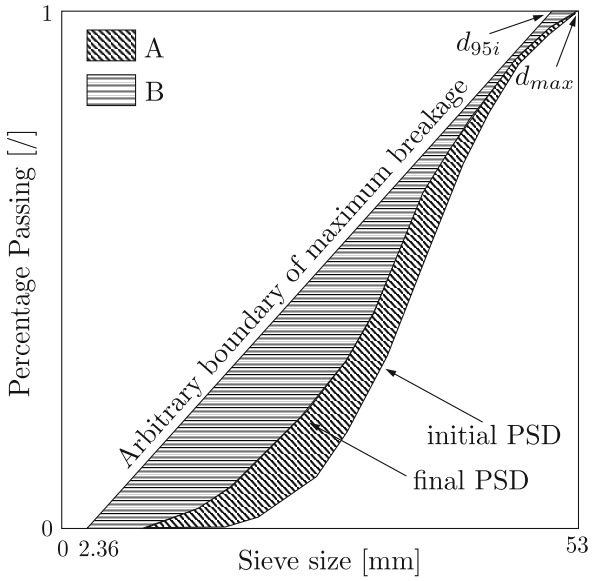

Figure 3.5: Ballast Breakage Index determination [77]

With increasing number of breakages, the particle size distribution (PSD) curve is shifted to the smaller particles size part of the PSD, and the area between this new line and the original particle size distribution is defined as the breakage zone [106]. According to *Indraratna et al.* [74], ballast breakage potential is defined as the area between the original PSD and a reference line connecting the point between the intersection of d_{95} of the largest sieve size and the minimum particle size of 2.36 mm, as can be seen in Figure 3.5. The area A between the initial and final particle size distribution curve yields a greater BBI value that has a lower

Die approbierte gedruckte Originalversion dieser Dissertation ist an der TU Wien Bibliothek verfügbar.
The approved original version of this doctoral thesis is available in print at TU Wien Bibliothek.
TU Bibliothek Your knowledge hub WIEN

limit of 0 (no breakage) and an upper limit of 1.

3.2.8 Ballast life prediction as a function of the ballast fouling quantification

A method of estimating the needed ballast-cleaning cycles for a given track section or rail corridor is presented by *Feldman and Nissen* [56] and extended by *Ionescu* [80] and *Indraratna et al.* [77] for the ballast fouling quantification factors described in the preceding chapters. This method calls for a thorough monitoring of ballast fouling by sample collection at 2 km sections in order to determine the classification of the fouled ballast bed. Once the classification is determined, the rate of ballast bed fouling (Fouling Rate FR) can be calculated for the monitored track section using the average values (AV) for either of the fouled ballast quantifications (Fouling Index, Percentage Void Contamination or Relative Ballast Fouling Ratio) divided by the Ballast Life (BL) since the last undercutting of the track section as follows:

$$FR = \frac{FI_{AV}}{BL} \tag{3.11a}$$

$$FR = \frac{PVC_{AV}}{BL} \tag{3.11b}$$

$$FR = \frac{R_{b-fAV}}{BL} \tag{3.11c}$$

Now the Allowable Ballast Life BL_{ALL} can be calculated (in years) as a function of the prescribed allowable ballast fouling quantification or the fouling limit for highly fouled ballast (FI_{ALL}, PVC_{ALL} or $R_{b\text{-}fALL}$) and the rate of fouling for the track section in question:

$$BL_{ALL} = \frac{FI_{AV}}{FR} \tag{3.12a}$$

$$BL_{ALL} = \frac{PVC_{AV}}{FR} \tag{3.12b}$$

$$BL_{ALL} = \frac{R_{b-fAV}}{FR} \tag{3.12c}$$

Obtained BL_{ALL} can be incorporated in track maintenance schedules as a quantitative index, in addition to standard track inspections. The described test programme should be be performed in six-year cycles for freight lines and three-year cycles for lines subjected to fouling from train spillage [76],[80] in order to establish possible occurring changes in the rate of ballast bed fouling.

3.2.9 Comparison of existing ballast fouling quantifications

A review of existing ballast fouling quantifications reveals a lack of consensus on grain-size diameter as well as a lack of better fouling parameter definition (gradation of the fouling particles) used to define fouled ballast. When comparing the Fouling Index to the Percentage Void Contamination it can be seen that FI cannot differentiate between types of foul-

Die approbierte gedruckte Originalversion dieser Dissertation ist an der TU Wien Bibliothek verfügbar.
The approved original version of this doctoral thesis is available in print at TU Wien Bibliothek.
TU Bibliothek Your knowledge hub WIEN

ing material, although the difference in specific gravity of different fouling materials have a great influence on fouled ballast behavior. The PVC method of fouled ballast quantification takes the total volume of fouling particles into consideration and does not provide the possibility to express the influence of the gradation of the fouling material, causing an overestimation of the extent of fouling for coarse fouling materials that do not reduce the drainage capacity of the ballast matrix significantly. Comparison of Percentage of Fouling and Relative Ballast Fouling Ratio to the Fouling Index is presented in Figure 3.6.

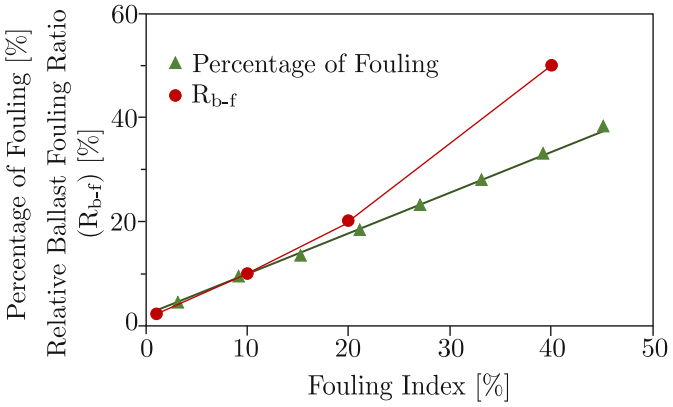

Figure 3.6: Comparison of Percentage of Fouling and Relative Ballast Fouling Ratio to the Fouling Index, adapted from [77]

According to *Indraratna et al.* [77] the Relative Ballast Fouling Ratio reflects the influence of both the specific gravity and gradation of the fouling material. Only the mass of ballast and contaminates and the specific gravity of the fouling material are needed to calculate $R_{b\text{-}f}$, making its determination quick, realistic and more attractive to track engineers. Several railway track lines in Australia were used to conduct an in-situ comparison between Percentage Void Contamination, Percentage of Fouling and the Relative Ballast Fouling Ratio (Table 3.5, Figure 2.9). The main source of ballast fouling particles on the observed lines are coal fines, it is possible to calculate the $R_{b\text{-}f}$ based on the specific gravities of coal (1.05 to 1.4) and ballast (2.5 to 2.8), assuming a specific gravity ratio of ballast to fouling material to be 2.4. Table 3.5 shows that the categories of fouling based on PVC and Percentage of Fouling are quite different, while categories of fouling obtained from the PVC and $R_{b\text{-}f}$ are more consistent [77].

An application of any of the existing ballast fouling quantification methods described in this chapter requires in-situ ballast sampling and additional laboratory testings. Given that in-situ sampling requires additional track closure (reduces track availability) and the laboratory tests increase the costs, the determination of ballast condition is considered to be a time-consuming and challenging task [35].

Die approbierte gedruckte Originalversion dieser Dissertation ist an der TU Wien Bibliothek verfügbar.
The approved original version of this doctoral thesis is available in print at TU Wien Bibliothek.

Table 3.5: Comparison between PVC, Percentage of Fouling and Relative Ballast Fouling Ratio $R_{b\text{-}f}$ [77]. For example, a value of 10 would characterize a clean ballast according to PVC, moderately fouled according to Percentage of Fouling and moderately clean according to $R_{b\text{-}f}$

PVC		Percentage of Fouling		$R_{b\text{-}f}$	
Value	Category	Value	Category	Value	Category
32.78	Fouled	7.9	Moderately clean	21	Fouled
27.68	Moderately fouled	5.9	Moderately clean	15	Moderately fouled
35.69	Fouled	8.1	Moderately clean	21	Fouled
11.63	Clean	3	Moderately clean	7	Moderately clean
31	Fouled	6.2	Moderately clean	16	Moderately fouled

3.3 Ballast response and degradation assessment by laboratory testing

The most important role of the ballast bed is to withstand both axial and lateral forces. The effective axial stresses (σ_1') are generated by static and dynamic axial train loads and the effective lateral stresses (σ_3') present the restraint provided by the sleepers and the shoulders and crib ballast [71]. An in-situ measurement of the lateral and axial forces acting on the ballast bed is a complex, costly and time-consuming task that requires temporarily traffic restrictions on the tested sections. In order to prevent the negative economic aspects and create a controlled testing environment, state-of-the-art laboratory testing methods are utilized to investigate and describe fresh, fouled to various FI levels and recycled ballast behavior and its deformation, strength and degradation under monotonic and cyclic loading. Apart from large-scale triaxial tests and impact testing to investigate the progressive degradation of fresh ballast, several laboratory tests described in the Chapter 2.2.3 are used to generate fouled ballast by means of laboratory induced ballast degradation, such as the Los Angeles abrasion test, mill abrasion test, Deval abrasion test, and micro-Deval abrasion test.

3.3.1 Ballast behavior under monotonic loading

Due to the fact that conventional triaxial test cells can accommodate samples of 38 - 100 mm, and the fresh ballast grains measure 63 mm, laboratory testing of ballast behavior is usually conducted in large-scale cylindrical triaxial apparatus as consolidated drained shearing tests. Large-scale triaxial apparatuses for testing ballast have been designed and built at several institutes (in detail in [110] and [73]) over the last two decades, providing in-situ similar conditions and more realistic information on the stress-strain and degradation behavior of the ballast sample. Large scale triaxial apparatus usually accommodates a ballast sample 300 mm in diameter and 600 mm in high. An alternative to large-scale triaxial test is to either scale down the ballast grains or to fabricate a larger testing ring [136]. However, a reduction in particle sizes for testing in smaller equipment is considered to reduce the

Die approbierte gedruckte Originalversion dieser Dissertation ist an der TU Wien Bibliothek verfügbar.
The approved original version of this doctoral thesis is available in print at TU Wien Bibliothek.
TU Bibliothek Your knowledge hub WIEN

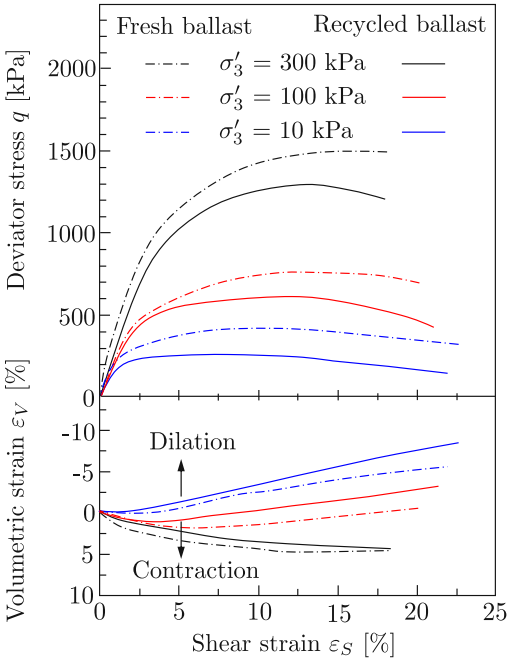

Figure 3.7: Stress-strain and volumetric behavior of fresh and recycled ballast under monotonic loading (adapted from [76])

internal angle of friction of the ballast matrix as well as the angularity of the particles and therefore influence the volumetric changes during the shearing process [73].

3.3.1.1 Stress - strain behavior and particle breakage

Results of test conducted by *Indraratna et al.* [78] at three confining pressure levels (10, 100 and 300 kPa) that can be seen in Figure 3.7 clearly show that the shear behavior of the tested samples cannot be described as linear. At lower confining pressure levels a dilation of the samples is observed, presented with a negative volumetric strain ε_V, while as confining stresses greater that ≈100 kPa cause a sample contraction ($\varepsilon_V > 0$). Peak deviator stress in triaxial tests presents sample failure, and for the tests conducted the failure is only recognizable for low confining pressures, followed by a post-peak strain softening associated to volume increase [76]. Higher angularity and the grain corners breaking can be recognized in higher deviator stresses (σ'_1 - σ'_3) for fresh ballast in comparison with the recycled ballast samples that are expected due to finer particles accumulated around fine ballast grains, lowering the friction angle and shear strength.

All of the samples for the tests described were recovered at the end of each test, then dried and sieved, and changes in particle size were recorded. Sieve analysis results are expressed by the method proposed by *Marsal* [92] (Chapter 3.2.1) that allows even the smallest changes in the particle size distribution on every sieve to be seen. As expected, particle breakage increases with the confining pressure, with lager particles less resistant to breakage. As can be seen in Figure 3.8, particle breakage is more prominent in recycled ballast samples at all sieve sizes, showing that the previous loading caused micro-cracks in the grains and has made them more vulnerable to breakage and degradation [76].

Die approbierte gedruckte Originalversion dieser Dissertation ist an der TU Wien Bibliothek verfügbar.
The approved original version of this doctoral thesis is available in print at TU Wien Bibliothek.
TU Bibliothek Your knowledge hub WIEN

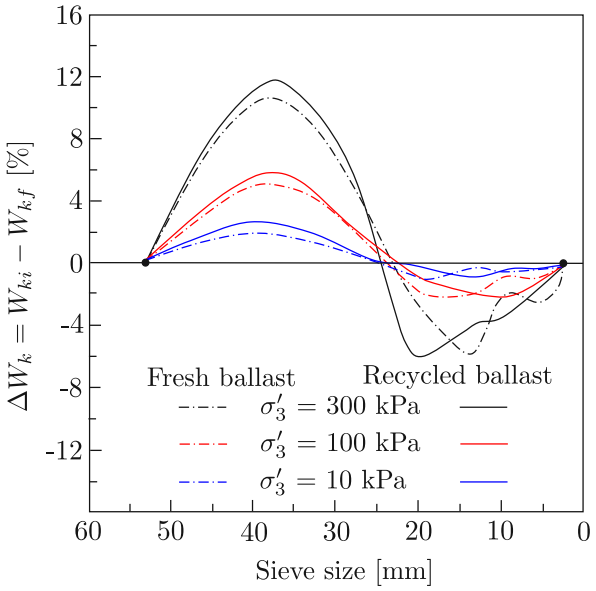

Figure 3.8: Particle breakage, comparison of fresh and recycled ballast (adapted from [76])

3.3.2 Ballast behavior under cyclic loading

Exposing the ballast bed to in-situ similar loading conditions during laboratory experiments calls for ballast samples testing under dynamic loads. Loads simulating the passing trains and the stresses transferred to the ballast bed are achieved in cyclic (dynamic) large-scale triaxial testing apparatus with either cylindrical [94], [110] or prismoidal triaxial chamber simulating a small section of the track [76].

3.3.2.1 Large-scale triaxial testing apparatus with cylindrical chamber

Moaveni et al. [94] and *Qian et al.* [110] conducted several testing series on ballast specimens that meet the American Railway Engineering and Maintenance-of-Way Association (AREMA) No. 24 gradation requirements [54] (Figure 3.9).

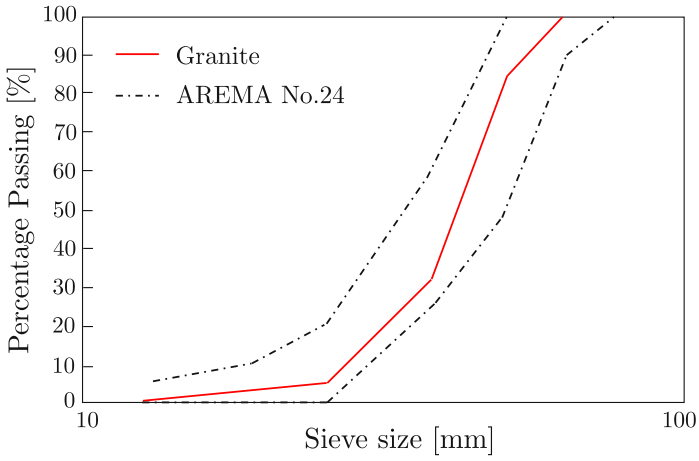

Figure 3.9: Gradation properties of granite ballast material (adapted from [109])

Die approbierte gedruckte Originalversion dieser Dissertation ist an der TU Wien Bibliothek verfügbar.
The approved original version of this doctoral thesis is available in print at TU Wien Bibliothek.

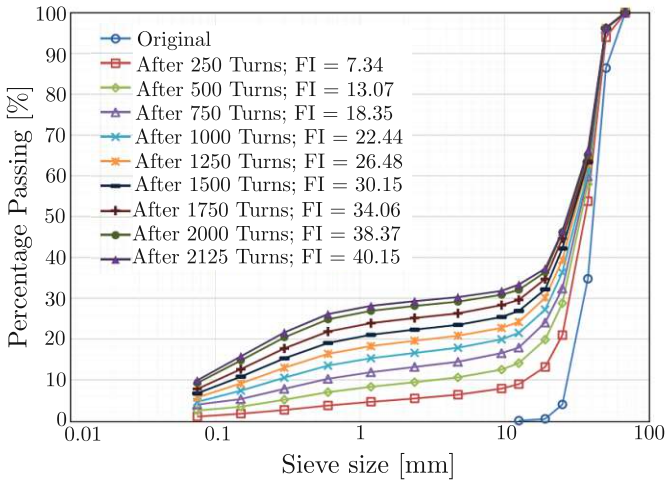

Figure 3.10: Gradations of granite ballast changing with LA abrasion drum turns (adapted from [109])

Researchers recognized the need to investigate both ballast particle size and shape properties at different fouling conditions which typically change according to the service tonnage of the track in the field in order to improve the understanding of ballast performance associated with its usage and life-cycle degradation due to particle abrasion and breakage. Therefore, prior to large-scale triaxial test, they conducted a series of LA abrasion tests in order to continuously break down each ballast sample until the desired maximal value of FI was reached. LA abrasion tests served as a simulation of the in-situ ballast fouling process by accelerating ballast degradation under well-controlled laboratory conditions. LA test results revealed quite important linkages between ballast fouling and degradation trends. Figure 3.10 shows the gradation curves obtained from the sieve analysis test results of the granite specimen after the total 2,125 turns of the LA abrasion drum until the FI values for highly fouled ballast was reached. Figure 3.10 also presents FI values calculated for each gradation curve. With the number of turns increasing in the LA abrasion test, the ballast specimen changed gradually from uniformly graded to more well graded. This change is also indicated by the increasing FI values with a decreasing rate.

After the desired level of ballast fouling has been reached, the effect of ballast degradation on permanent deformation behavior of the ballast matrix is tested. The samples were prepared by compacting the ballast and following the gradation requirements as indicated in Figure 3.10. Samples are then loaded with realistic field train loading dynamic pulse with 0.4-second load duration and 0.6 second rest period between two pulses was selected. The peak deviator stress applied on the specimen was 165 kPa and the confining pressure was 55 kPa [110].

Results of the large-scale triaxial test are presented in Figure 3.11, showing the permanent deformation of new and degraded ballast cylindrical specimens, with the highest permanent axial strain achieved on the degraded ballast sample (FI = 40, nearly all the voids were filled with fines) [110]. The difference between the degraded ballast and the degraded sample without fines is fouling fine material (particles smaller than 9.5 mm) generated dur-

Die approbierte gedruckte Originalversion dieser Dissertation ist an der TU Wien Bibliothek verfügbar.
The approved original version of this doctoral thesis is available in print at TU Wien Bibliothek.
TU Bibliothek Your knowledge hub WIEN

ing LA abrasion test due to the ballast degradation. These fine materials not only filled the voids but in fact caused loss of contact between large particles in the heavily fouled ballast aggregate skeleton, resulting in a reduction in the friction angle and shear strength.

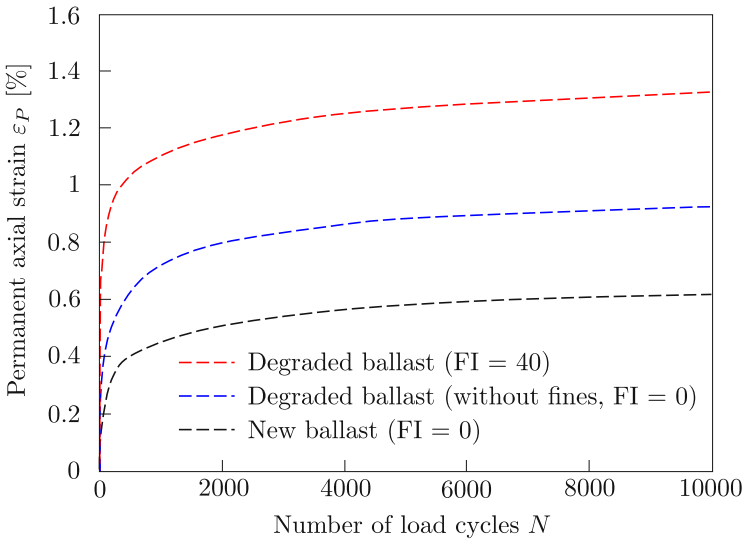

Figure 3.11: Repeated load triaxial test results for permanent deformation accumulation [110]

3.3.2.2 Large-scale triaxial testing apparatus with prismoidal chamber

Indraratna et al. [72], [71], [76] conducted their experiments in a prismoidal triaxial chamber that accommodates samples 800 mm long and 600 mm wide and high. The test is designed in a way that the ballast sample can deform laterally under pressure, since that best describes the confinement by the shoulder and crib ballast in-situ - it is not sufficient to prevent lateral movement. Ten cyclic triaxial tests on both fresh and recycled ballast were conducted, 50% of the samples were tested dry and the rest were tested wet in order to determinate the effect of sample saturation. Results are plotted in a semi-logarithmic scale (Figure 3.12) and show linear trend lines of the settlement data indicating a semi-logarithmic cyclic load - settlement relationship [76]:

$$S = a_c + b_c \cdot \ln N \tag{3.13}$$

where S is the ballast settlement, N the number of load cycles and a_c and b_c two empirical constants depending on ballast characteristics.

Figure 3.12 shows the lowest settlement in fresh dry ballast, which can be attributed to better particle interlocking and to a high angularity. Settlement in recycled ballast is higher due to a lower friction angle - a behavior that is even better recognizable in wet conditions given that the presence of water leads to further friction angle reduction [76].

Prior and subsequently to the large-scale triaxial test, the method proposed by *Marsal* [92] (Chapter 3.2.1) was once again used to determine the degree of particle breakage. The analysis showed that recycled ballast suffered more particle breakage in comparison to the fresh

Die approbierte gedruckte Originalversion dieser Dissertation ist an der TU Wien Bibliothek verfügbar.
The approved original version of this doctoral thesis is available in print at TU Wien Bibliothek.
TU Bibliothek Your knowledge hub WIEN

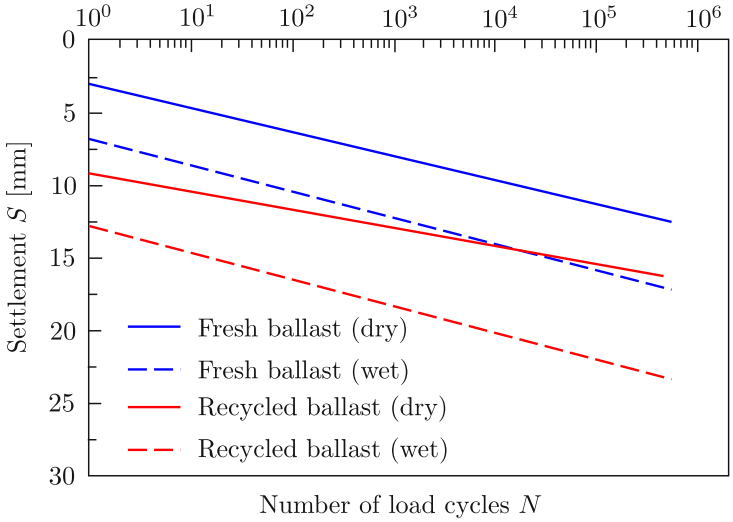

Figure 3.12: Settlement of fresh and recycled ballast under cyclic loading (25 ton/axle, 15 Hz), modified from [76]

ballast samples in both wet and dry conditions with large particles being more vulnerable to particle breakage due to lower tensile strength [71]. *Indraratna et al.* [76] concluded that the particle breakage in recycled ballast is approximately 95-97% higher than in fresh ballast and that the saturation increases ballast degradation for about 8%.

3.4 Effect of confining pressure on particle breakage

Strength and deformation behavior of all soils is greatly influenced by the confining pressure (σ_3'). Even though the only lateral constraint acting on the track structure is the frictional resistance of the load bearing ballast and shoulder ballast, the influence of σ_3' should not be overlooked in the track design. Effects of the confining pressure on the volumetric and shear strain have been a topic of many researchers [72], [76] and some of the result are shown and discussed in Chapter 3.3. According to *Indraratna et al.* [72], the effects of σ_3' on particle breakage can be subdivided into two zones (Figure 3.13):

- (Dilatant) Unstable degradation zone - ballast samples exposed to low confinement (<15 kPa) under cyclic loading deform rapidly and undergo relatively large axial strains due to lateral expansion and volumetric dilation. The unstable degradation, i.e. high level of particle breakage is caused by high axial strains and small particle-to-particle contact areas [76].

- (Compressive) Stable degradation zone - ballast samples exposed to high confinement (>60 kPa) show a low lever of axial strain and a noticeable increase in particle-to-particle contact area i.e. inter-particle contact stress due to suppressed particle movement. *Indraratna et al.* [76] state that ballast particles under these stress conditions fail not only at the beginning of loading when the axial strain reaches the highest value,

Die approbierte gedruckte Originalversion dieser Dissertation ist an der TU Wien Bibliothek verfügbar.
The approved original version of this doctoral thesis is available in print at TU Wien Bibliothek.
TU Bibliothek Your knowledge hub WIEN

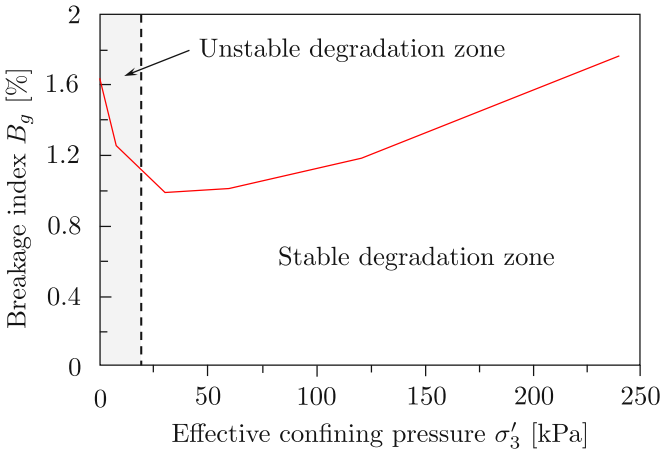

Figure 3.13: Zones of effect of confining pressure on ballast particle breakage [76]

but also due to fatigue at higher load cycles. The compressive zone is also characterized by an increase of M_R (Chapter 2.2.4) due to the restriction of internal particle sliding and rolling.

As the lateral stresses increase from low levels up to ≈45-60 kPa, the axial strain decreases and the volumetric strain changes from dilation to contraction. Exact ranges of the confining pressures at which this change occurs are defined by the applied stress magnitude [79]. This zone is referred to as Optimum degradation zone [72] characterized by optimum internal contact stress distribution resulting in reduced stress concentration and tensile stresses resulting in a decrease in extent of particle breakage.

Estimated in-situ lateral stresses in track are ≈10-12 kPa, clearly falling into the unstable degradation zone. Increasing the lateral pressure by introducing intermittent lateral restrains or winged sleepers would reduce particle breakage and improve track performance and dynamic resilience [76].

Die approbierte gedruckte Originalversion dieser Dissertation ist an der TU Wien Bibliothek verfügbar.
The approved original version of this doctoral thesis is available in print at TU Wien Bibliothek.

3.5 Ballast condition assessment in-situ

Determination of ballast bed condition is crucial for planning and prediction of track maintenance and renewal works as well as for quality control during construction. Condition of the ballasted bed is usually inspected by visual inspection and trial pits that can, due to economical and practical reasons, only be excavated at sections where higher levels of ballast fouling is expected. A more detailed and consequential method without traffic interference (track closure) is required to obtain and monitor the consequences of ballast fouling on the track condition.

3.5.1 Ground penetrating radar

In addition to visual inspection and trial pits, a non-destructive high-speed geophysical track condition monitoring technique - Ground penetration radar (GPR) can be used to observe and measure the ballast condition in-situ. GPR is based on electromagnetic pulses (frequency range 10 MHz to 2.6 GHz) that are reflected at interfaces between materials of dissimilar dielectric permittivity. It operates by transmitting short electromagnetic waves into the subsurface. Due to the contrast of dielectric permittivity, a portion of the signal energy will be reflected back and the remaining energy will be transmitted through the interface. The reflected energy is recorded and displayed.

Data obtained from GPR testing is the time domain waveform (in newer research extended by frequency and spectral domain [61]) representing the electromagnetic energy transmitted from the antenna and reflected off subsurface back to the antenna [124]. The emitted signal enables an assessment of ballast and substructure condition, moisture content and can even help detect voids and foreign objects. The difference between different ballast conditions can primarily be noticed due to the moisture trapped in the fouled sections that has a significant influence on the texture of the GPR result.

The quality of raw data obtained from GPR employment is predominantly dependent on the following factors [39]:

- data collection parameters that control the waveform emitted into the ground (wave velocity, wavelength, relationship between frequency and depth and between frequency and resolution),
- characteristics of the materials through which the electromagnetic wave propagates (electrical conductivity, permeability, permittivity),
- quality and accuracy of data analysis.

First GPR based investigations were conducted using ground-coupled antennas operating with frequencies below 500 MHz, advancing to 1 GHz center-frequency air-launched antennas that provide high(er) resolution images of the ballast structure in the last years. Next important development was the usage of 2 GHz center-frequency horn antennas, introduced in 2005, which had shown a significant increase in data quality. In regard to data

Die approbierte gedruckte Originalversion dieser Dissertation ist an der TU Wien Bibliothek verfügbar.
The approved original version of this doctoral thesis is available in print at TU Wien Bibliothek.
TU Bibliothek Your knowledge hub WIEN

processing, the 2 GHz horn data from ballast contain waveforms from void space scattering that overlap and interfere with increasing time [115]. GPR signal frequency determines the inspection depth and recorded data resolution - lower frequency signals can penetrate deeper into the track substructure, but results in a lower resolution, meaning that the signal is less sensitive to changes in the track substructure. On the other hand, higher signal frequency provides better resolution but has a reduced penetration depth. .

Existing algorithms for GPR data acquisition and processing can be used to interpret GPR signals in order to determine the following track substructure condition and performance parameters [89]:

- ballast and subballast layer thickness
- degree and depth of ballast fouling
- water trapped in ballast and/or subballast
- presence of ballast pockets (fluctuation of deformed subgrade surface along and across the track)

Even if the GPR is a non-destructive method, it still requires an additional machine employment during which a significant amount of data is collected, analysis of which is rather time-consuming. As stated before, quality and accuracy of data analysis is of crucial importance. Currently, the common strategy is to record and store the data, which are accessed punctually and/or in the event of any sever problems with the track structure or to estimate the percentage ballast fouling [61]. In order to improve this system and obtain a more accurate assessment of the track quality, many studies recommend GPR inspections to be be performed at least twice a year: during dry and during wet season. In addition, inspections should be carried out in the same month in consecutive years for a more precise comparison between measurements [61]. This method would help identify only the changes in the GPR signal that are related to changes in the track structure and provide overall assessment of the condition of the line.

Die approbierte gedruckte Originalversion dieser Dissertation ist an der TU Wien Bibliothek verfügbar.
The approved original version of this doctoral thesis is available in print at TU Wien Bibliothek.
TU Bibliothek Your knowledge hub WIEN

Chapter 4

Fundamental principles of track maintenance

4.1 Introduction

Both vertical and lateral track deformations under cyclic (traffic) loading cause deviations from the design track geometry, invariably calling for maintenance after track construction. Maintenance of ballasted tracks becomes an increasingly demanding task with the continuous increase of railway traffic of both passengers and freight. Up until 1945, track geometry maintenance was manual labor, associated with tremendous efforts and armies of engaged workers. First purely mechanical mechanism to carry out track tamping was put into use in 1933. Existing shortcomings of the first design were eliminated by development of the first hydraulic tamping machine in 1953 by *Franz Plasser* and *Josef Theurer*, an advancement that started the mechanization and automation of track maintenance that is still ongoing today [33].

Preferred method of preventive maintenance is condition-based predictive maintenance. The expected deterioration rate should be determined for a specific track section based on long-term measurements and used to determine the point in time at which a specific maintenance measure is needed [27].

The term track maintenance implies the total process of maintenance and renewal (Figure 4.1). Effective and timely use of available resources and maintenance measures significantly improves riding quality and safety levels and at the same time minimizes maintenance costs.

Die approbierte gedruckte Originalversion dieser Dissertation ist an der TU Wien Bibliothek verfügbar.
The approved original version of this doctoral thesis is available in print at TU Wien Bibliothek.

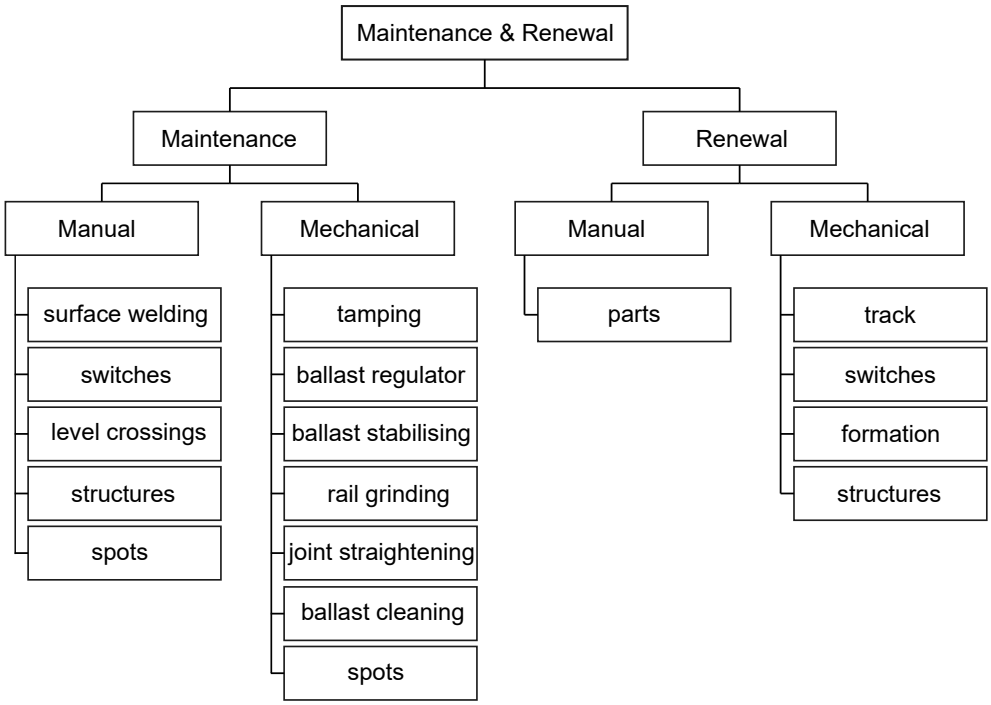

Figure 4.1: Schematic survey of maintenance and renewal methods [45]

Broadly speaking, track maintenance can be divided into:

- rail geometry
- track geometry
- track structures
- ballast bed
- level crossings
- miscellaneous

Esveld [45] and *Auer* [27] provide a complete overview of all track maintenance and renewal methods (manual and mechanical) that are scheduled on basis of control data from measuring systems, visual observation and financial-economic aspects, bearing local condition in mind. In the scope of this thesis only mechanical maintenance methods related to track ballast are considered, with a special emphasis on tamping and stabilization process:

- track tamping
- dynamic track stabilization
- (ballast distribution and regulation)
- (ballast cleaning)
- (ballast renewal)

Die approbierte gedruckte Originalversion dieser Dissertation ist an der TU Wien Bibliothek verfügbar.
The approved original version of this doctoral thesis is available in print at TU Wien Bibliothek.
TU Bibliothek Your knowledge hub WIEN

4.2 Deterioration of track geometry

All track components are subject to deterioration either through forces exerted on the track components (Chapter 2.7) or/and wear and contamination. Deterioration of track geometry is determined as the deviation from design values of principal track geometry parameters given by EN 13848-1:20191 [13]:

- track gauge (Figure 4.2a) - defined as the smallest distance between lines perpendicular to the running surface intersecting each rail head profile at the gauge face contact point in a range from 0 to z_p below the running surface. According to EN 13848-1:20191 z_p is equal to 14 mm[1] [13].
- longitudinal level (Figure 4.2b) - defined the deviation in z-direction (vertical) of running table levels on any rail from the smoothed vertical position, i.e. reference line [13].
- super-elevation or cross level (Figure 4.2c) - the difference in height of the adjacent running tables computed from the angle between the running surface and a horizontal reference plane. It is expressed as the height of the vertical leg of the right-angled triangle having a hypotenuse that relates to the nominal track gauge plus the width of the rail head rounded to the nearest 10 mm [13].
- alignment (Figure 4.2d) - the deviation y_p in y-direction (axis parallel to the running surface) of the position of the gauge face contact point on any rail from the smoothed lateral position (reference line) [13].
- twist - the algebraic difference between two cross levels divided by a defined distance, typically expressed as mm/m [13].

Objective of maintenance is to lower the track geometry deterioration rate and preserve service life of the track. Understanding track geometry deterioration decisively influences the planning and optimization of track maintenance and renewal works and consequently reduces related cost. The first step in maintaining track geometry is to determine the geometrical condition using a proven track measuring and recording car. Deviations from nominal values of all of the listed track geometry parameters can be rectified by employing a lifting, leveling and tamping machine [140].

[1] In Austria the so-called "standard gauge" of 1435 mm is used, representing the nominal size of z_p

Die approbierte gedruckte Originalversion dieser Dissertation ist an der TU Wien Bibliothek verfügbar.
The approved original version of this doctoral thesis is available in print at TU Wien Bibliothek.

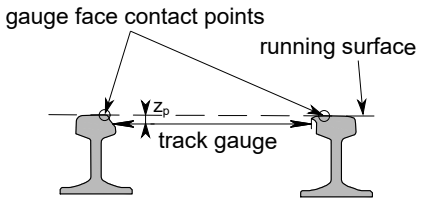

(a) Track gauge for worn rail[a]

[a] z_p denotes the limit of range below the running surface within which the gauge is measured

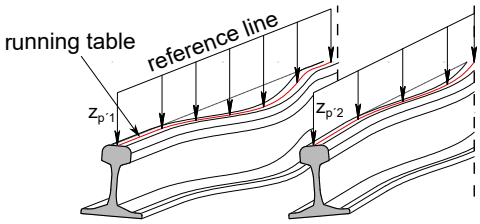

(b) Longitudinal level[a]

[a] $z_{p'1}$ and $z_{p'2}$ denote the deviation in the direction of consecutive running table levels on left and right hand rail, respectively

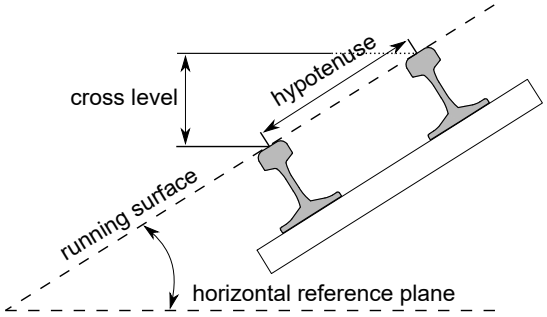

(c) Cross level

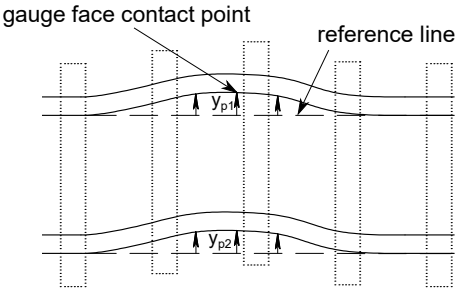

(d) Alignment[a]

[a] $y_{p'1}$ and $y_{p'2}$ denote the distance between the gauge face contact point and a reference line on left and right hand rail, respectively

Figure 4.2: Definition of principal track geometry parameters according to the EN 13848-1:20191 [13] (adapted from [47]). Coordinate system: x - track direction, y - sleeper direction, z - vertical

Die approbierte gedruckte Originalversion dieser Dissertation ist an der TU Wien Bibliothek verfügbar.
The approved original version of this doctoral thesis is available in print at TU Wien Bibliothek.

Where the geometry meets a set threshold, maintenance is required (Figure 4.3).

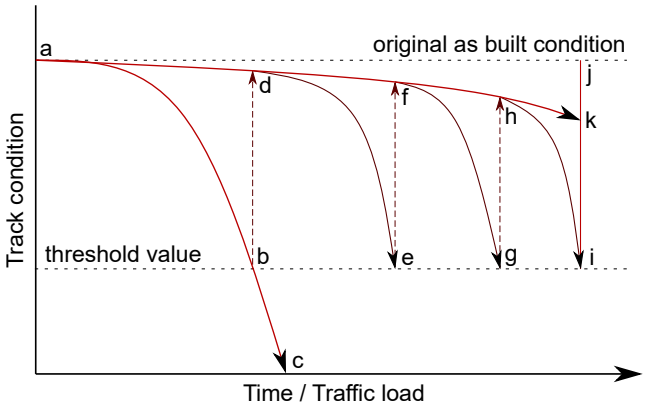

Figure 4.3: Theoretical track condition deterioration curve (adapted from [140])

Original (design) track geometry *(a)* deteriorates over time due to traffic loads and would in the absence of maintenance intervention follow the deterioration curve *(a)-(c)*. Due to an increase in track roughness resulting from dynamic loads the track deterioration will accelerate over time and, if the deterioration is left unattended, reduce the track functionality until it no longer exceeds the set threshold value *(b)*. Maintenance work is conducted before the threshold value has been reached, improving the track condition and reducing the deterioration from *(b)* to *(d)* in order to extend the track service life. The track condition is only improved to the point *(d)* and not back to the original as built condition due to wear of the track components. Track deterioration will continue succeeding maintenance following the curve *(d)-(e)* until the threshold value is met again, calling for a second employment of the track tamping machine. Maintenance output brings the track to point *(f)*, given that, as before, the condition achieved after previous maintenance cannot be regained. As the deterioration - maintenance process continues, the interval between two maintenance measures that can be observed as the distance between points *(b)-(e)* and *(d)-(g)*, decreases exponentially. This process will continue until the period between required maintenance input becomes uneconomically short after which a complete track renewal, replacement of sleepers, rails, fastening or ballast replacement/cleaning will be required, bringing the track condition back to the original condition in point *(j)*. As can be seen in Figure 4.3, the track service life is significantly extended (from *(a)-(c)* to *(a)-(k)*) as a consequence of regular and timely track maintenance [140].

Die approbierte gedruckte Originalversion dieser Dissertation ist an der TU Wien Bibliothek verfügbar.
The approved original version of this doctoral thesis is available in print at TU Wien Bibliothek.

4.3 Track ballast compaction and compaction control

Compaction is the volume reduction of soils by means of mechanical manipulation which implies reduction in air void through particle rearrangement [118]. Water content remains the same, consequently increasing the degree of saturation with a purpose of gaining desired soil properties [118]:

- increasing strength
- reducing compressibility
- minimizing volume change potential
- decreasing permeability
- reducing frost susceptibility
- controlling resiliency properties

Different ballast materials poses different particle physical and chemical properties such as abrasion resistance, absorption and shape, many of which are currently utilized to quantify and categorize ballast properties. Laboratory tests and standards used to quantify these properties in Austria are described in Chapter 2, but regarding compaction work of the ballast bed, only geometrical and no geotechnical requirements or material properties are specified. The strength and compressibility characteristics of ballast are directly related to its relative degree of compaction within the track structure [118]. Determination of the relative degree of ballast (or other coarse-grained soils with little cohesion) compaction using existing methods used in geotechnical engineering has been proven to only have limited application. In addition, no quantitative ballast compaction definitions are given by any standards and measurement of the degree of ballast compaction is rarely done [118].

Relative degree of ballast compaction can be determined by either laboratory compaction, vibratory densification or by in-situ testing. Field, i.e. in-situ compaction is conducted by rollers, plate vibrators and tampers, depending on the intended function of the compacted material. Independent of the intended function, vibratory or dynamic compaction has been proven to as the most effective method for compacting granular materials, therewith also for compacting track ballast. Success of conducted compaction depends on a wide spectrum of parameters such as frequency, amplitude, surcharge, test conditions and soil properties, which additionally aggravates its measurement.

Material properties that are improved as a result of compaction such as strength, compressibility, resiliency, wave velocity and density could theoretically be used as criteria to define the effectiveness of compaction [118]. In the context of track ballast tamping, i.e. compaction, development of a method to determine relative degree of ballast compaction is additionally complicated due to the fact that ballast compaction is concentrated in certain areas (under the sleepers) during tamping machine deployment. Direct measurement of compaction success by additional machine deployment in order to determinate any of the

Die approbierte gedruckte Originalversion dieser Dissertation ist an der TU Wien Bibliothek verfügbar.
The approved original version of this doctoral thesis is available in print at TU Wien Bibliothek.
TU Bibliothek Your knowledge hub WIEN

above listed material properties would, therefore, significantly increase maintenance cost and duration. There are, however, two basic approaches to ballast compaction measurement [118][47]:

- measuring the compaction itself - dry density, strength or stiffness tests or the evaluation of ballast structure change prior to and after compaction [118].
- measuring the effect of ballast compaction - track geometric configuration and track stability changes due to ballast compaction, such as: track settlement, vertical stiffness of the overall structure, lateral and longitudinal sleeper resistance (horizontal stiffness), track modulus and track geometry [118].

Track ballast dry density can be determined using radiometric methods, whereby the insertion of the measuring rods is delicate and often leads to falsified results since even a small change in dry density has a relatively large effect on ballast mechanical properties. A very accurate measurement method with low scatter would be required n order to assess the success of ballast compaction with this parameter. Various static and dynamic methods like Falling Weight Deflectometer or Light Dynamic Penetrometer (PANDA) are used to determine vertical track stiffness but most of them only allow a selective stiffness assessment. For all of the above stated reasons, development of a machine-integrated ballast compaction control system would mark a big advancement in the field of track tamping.

4.4 Tamping process in railway engineering

The main maintenance activity used on ballasted tracks it track tamping, a maintenance method utilized worldwide. At present, track tamping is based on modern tamping machines that have been developed to carry a wide range of advanced functions such as dynamic track stabilization, leveling, lining and 4-sleeper-tamping [45].

4.4.1 Principle of tamping machine operation

Desired result of the tamping process, extended by lifting and lining, is to restore the track geometry that is as close as possible to the original (design) condition. To be able to recover the original track position in the vertical direction, the track must be lifted so that a void is created under the sleeper. In order to do so, the lifting unit is set in motion prior to tamping. Simultaneously, the track is positioned laterally by the leveling unit. An example of a continuous action tamping machine[2] with an incorporated dynamic track stabilizer can be seen in Figure 4.4.

Plasser & Theurer tamping machines operate following the non-synchronous constant pressure tamping principle (Figure 4.5). Two factors are decisive in non-synchronous constant pressure tamping principle - all tamping tines work with the same pressure and ballast under the sleepers is compacted with the aid of dynamic movement (oscillation) of the

[2]tamping machine moves at constant speed with only the tamping unit relocating from sleeper to sleeper providing a higher output of up to 2.2 km/h

Die approbierte gedruckte Originalversion dieser Dissertation ist an der TU Wien Bibliothek verfügbar.
The approved original version of this doctoral thesis is available in print at TU Wien Bibliothek.
TU Bibliothek Your knowledge hub WIEN

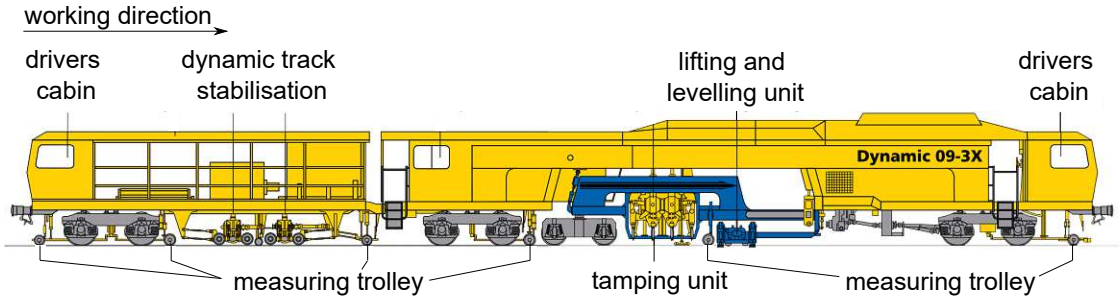

Figure 4.4: Tamping machine *Dynamic 09-3X* (©*Plasser & Theurer*)

tamping tines that vibrate with the ideal frequency of 35 Hz. Each individual tamping arm with its tamping tines continues its squeezing motion towards the sleeper until the intended degree of compaction is achieved. This directional, linear vibration combined with the non-synchronous tine movement produces a homogeneously compacted ballast bed. In contrast to other tamping methods (overview given by *Bayerhofer* in [38]), non-synchronous constant pressure tamping principle has proven to have significant advantages in terms of track stability.

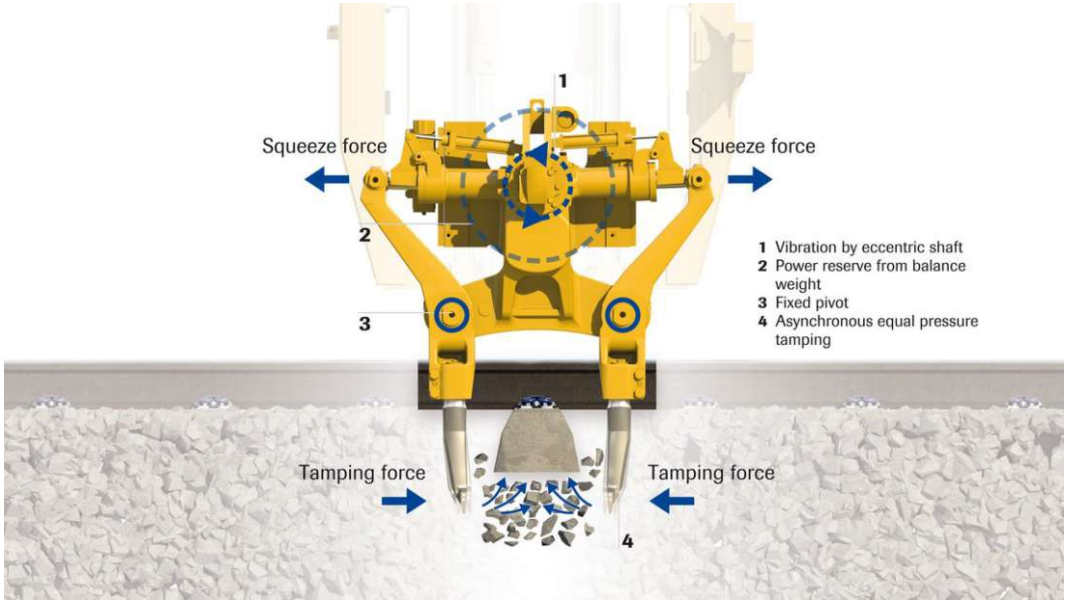

Figure 4.5: Tamping unit lowered into work position (©*Plasser & Theurer*)

State-of-the-art tamping machines provide the possibility to conduct continuous action tamping of several sleepers at once, which significantly increases the machine production capability. Tamping machines with single, double, triple (Figure 4.6) and quadruple (Figure 5.1) tamping units are available on the market.

Die approbierte gedruckte Originalversion dieser Dissertation ist an der TU Wien Bibliothek verfügbar.
The approved original version of this doctoral thesis is available in print at TU Wien Bibliothek.
TU Bibliothek Your knowledge hub WIEN

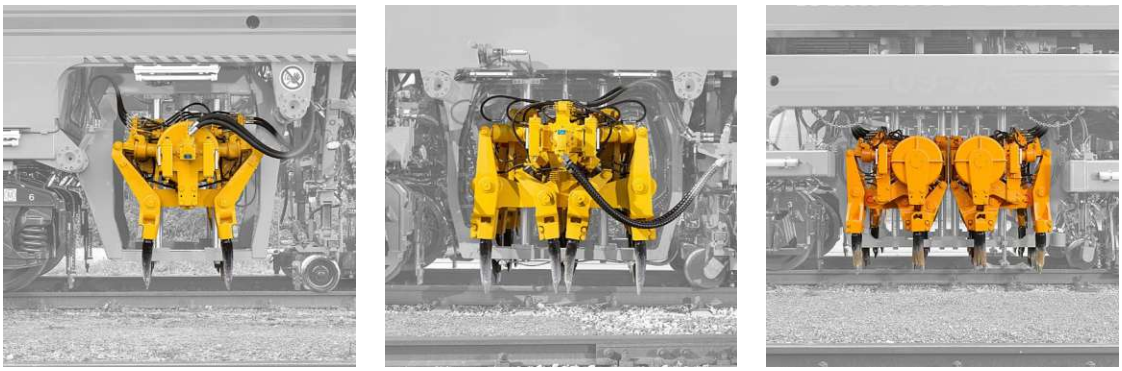

(a) Single-sleeper (b) Duomatic (two-sleeper) (c) Three-sleeper

Figure 4.6: Tamping units [131]

The four-sleeper tamping machine *Dynamic Tamping Express 09-4X E*^{3} is equipped with 64 tamping tines altogether, 16 tines per sleeper (Figure 5.5). Greatest stresses during tamping are extended on the tamping tines, given that they are the machine component that interacts with the ballast during compaction. Newly developed shape of the tamping tine (Figure 4.7) significantly lessens stress by making the tine shaft considerably slimmer, which reduces the resistance during ballast penetration. In addition, the underside of the tine plate is built with a 5° slope to facilitate ballast penetration. The optimized tine shape also results in reduction of wear forces and extends the tine service life to about 700,000 tamping cycles [31].

Figure 4.7: Low-wear tamping tine in optimized shape (©*Plasser & Theurer*)

Detailed information about the tamping process subdivision and compaction procedure as well as about the absolute and relative tamping tine motion is given in the scope of experimental approach description in Chapter 5.

Die approbierte gedruckte Originalversion dieser Dissertation ist an der TU Wien Bibliothek verfügbar.
The approved original version of this doctoral thesis is available in print at TU Wien Bibliothek.

4.4.2 Lifting and leveling

Before tamping is conducted, the track it lifted up to the level determined by previous measurements and simultaneously positioned laterally. The lifting and leveling units (Figure 4.4) are mounted in front of the tamping unit, between the boogies. Dependent on the machine type, a subdivision can be made between lifting and leveling units for universal tamping machines (Figure 4.8b) and for those for plain track tamping (Figure 4.8a). Lifting and leveling units of universal tamping machines are equipped with lifting hooks that grip the rails under the rail head to allow lifting in restricted space conditions in turnouts, roller clamps for plain track tamping and one or two flange rollers that transfer the lateral force to the track for horizontal alignment [140]. Plain track tamping machine lifting and leveling units are equipped with double roller clamps for high speed lifting on the open line and two flanged rollers for lateral force transfer. During the forward motion between the tamping cycles, the pressure on the lifting and leveling units is switched off so that the rollers move along easily. As soon as the track is positioned correctly, the tamping process begins.

(a) Roll lifting clamps and double-flange lining rollers of a plane tamping machine

(b) Roller lifting clamps with lifting hooks and lining rollers for universal use in turnouts

Figure 4.8: Lifting and levelling units [131]

The fully automatic measuring system determines the relative difference in the vertical and horizontal positions of the track at a center measuring trolley (Figure 4.4) serving as a recording point between the front and back measuring trolleys. This system of track leveling and lining is known as the compensation method. Relative vertical alignment is established by steel cords above each rail extended from the rear to the front measuring trolleys, with a reference steel cord extended along track center [140]. Lifting and leveling units lift the track to a uniform height removing any vertical deviations in the process and simultaneously align the track to correct horizontal defects. Research has shown that a minimum lift of 20 mm or more dependent on ballast grain size is necessary to ensure residual lift after tamping [140].

Die approbierte gedruckte Originalversion dieser Dissertation ist an der TU Wien Bibliothek verfügbar.
The approved original version of this doctoral thesis is available in print at TU Wien Bibliothek.
TU Bibliothek Your knowledge hub WIEN

4.4.3 Tamping parameters

Quality of conducted track tamping primarily depends on the selected set of tamping parameters that influence the durability and reliability of track maintenance. Decisive parameters, standard used values and the effect of parameter variation can be summed up as follows:

Excitation frequency and amplitude

Only squeezing the ballast into the desired position under the sleeper by a quasi-static movement would require a very high force level and would not provide even compaction, given that the ballast grains would not be able to re-arrange in relation to each other. In a comprehensive research conducted by *Fischer* [59] in 1983, different levels of tine oscillation frequency were investigated in order to determine the optimum tamping frequency needed to trigger ballast grain rearrangement or ballast fluidization under the sleeper into a denser ballast matrix.

According to *Fischer* [59], the ideal oscillation frequency of the tamping tine plates amounts to 30 to 35 Hz. At this frequency range the best compaction effect in combination with the desired ballast elevation can be achieved (Figure 4.9). Excitation frequency of 35 Hz allows for an build-up of uplift force resulting in an elevation of the ballast matrix. Frequency levels of 40 Hz and higher trigger uncontrollable ballast movement away from the tamping tines, thus lowering the ballast body.

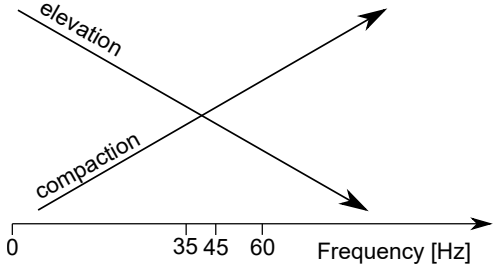

Figure 4.9: Ballast compaction and elevation in dependence on excitation frequency (adapted from [59])

Selection of a suitable vibration amplitude has a positive influence on the compaction quality. Figure 4.10 shows results of settlement measurements in which the vibration amplitude was varied.

It can be stated that tine oscillation with a higher amplitude results in higher degree of ballast bed compaction. This is observable on slower progression of track settlement. State-of-the-art *Plasser & Theurer* tamping units operate with an oscillation amplitude of 4 to 5 mm, based on the research conducted by *Fischer* [59].

Squeezing pressure, velocity and duration

Squeezing force per unit effective area of squeezing piston gives the squeezing, i.e. tamping pressure. With non-synchronous constant pressure tamping principle the tamping opera-

Die approbierte gedruckte Originalversion dieser Dissertation ist an der TU Wien Bibliothek verfügbar.
The approved original version of this doctoral thesis is available in print at TU Wien Bibliothek.
TU Bibliothek Your knowledge hub WIEN

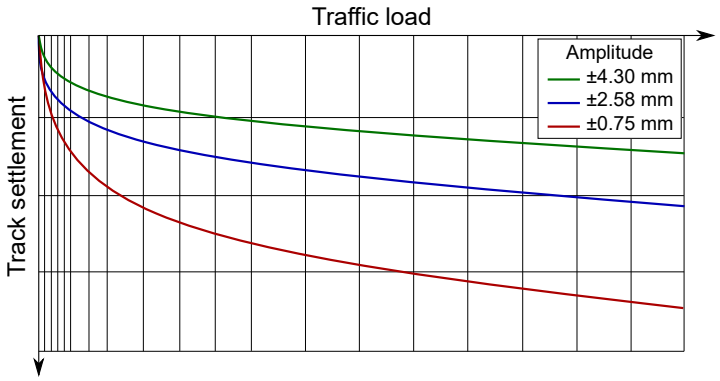

Figure 4.10: Track settlement in dependence on vibration amplitude [31]

tion is terminated when the set squeezing force is reached for a pair of tamping tines. Correct selection of the tamping pressure value enables the transmission of vibratory impact force to the ballast front which results in ballast compaction. Squeezing pressure is kept constant during the tamping process on one sleeper (for single tamping units), and the velocity of the tamping tine movement is determined by the ballast resistance. Squeezing velocity has a direct influence on the minimal required pulse duration (in detail in Chapter 5.5), and according to *Fischer* [59], higher squeezing velocity values result in longer contact duration between the tamping tine and the ballast, which prolongs the time available for the transfer of kinetic energy needed for ballast grain re-arrangement [140]. The squeezing duration should be between 0.8 and 1.2 seconds in total, depending on local conditions, in order to achieve a good tamping result.

Penetration depth

The tine penetration or tamping depth has a significant effect on the compaction of ballast under the sleeper. For effective packing of the ballast right below the sleeper bottom edge, the void between top edge of the tamping tine plate closed position and bottom edge of the sleeper needs to be adjusted depending upon the type of sleeper to impart compacting energy at correct location [119]. If the set depth is too small, tamping tine presses the ballast grains against the sleeper or comes into contact with the sleeper itself. In this case no compaction but rather damage to the sleeper and tamping tine takes place. Too great depth results in compacting an area well below sleeper bottom with uneven and incomplete compaction, thus creating loose ballast pockets right under the sleeper [31]. The EN 13231-1:2013 [6] recommends the gap between top edge of the tamping tine plate and bottom edge of sleeper to be 13-30 mm.

Lifting values

Next very important prerequisite for a uniform ballast compaction is the track uplift preceding the tamping operation. Track lifting is conducted hydraulically by the lifting and leveling unit (Chapter 4.4.2) and the procedure for determining the lifting values depends on the target track geometry. A predetermined lifting value has to be reached not only to

Die approbierte gedruckte Originalversion dieser Dissertation ist an der TU Wien Bibliothek verfügbar.
The approved original version of this doctoral thesis is available in print at TU Wien Bibliothek.
TU Bibliothek Your knowledge hub WIEN

ensure the vertical track alignment but also to provide the necessary space for ballast grains to re-arrange into a denser ballast matrix. According to *Seling and Waters* [117], the minimum lifting value of 20 mm is necessary to ensure residual track lift after traffic loads. If a lift of more than 10 mm over the minimum is required, single tamping process should be replaced by a double in order to uniformly distribute the area of impact of the tamping tines, resulting in uniformly compacted load-bearing ballast structure [31].

4.4.4 Tamping machines

Many different ballast tamping machines are available to satisfy every possible tamping requirement, ranging from low-cost low-production machines tamping one sleeper at the time to high production tamping machines using the continuous action tamping principle and tamping up to four sleepers at once. Each of these machines have specialized components which identify the machine specific function [140]:

- plain (line) track tamping machine (example in Figure 4.11a) - designed for high production tamping on open track of busy lines where the maximum number of sleepers must be tamped in short available maintenance windows. Production capability of such machines has improved tremendously over the years - from tamping less than 4 sleepers per minute to tamping approximately 70 sleepers per minute nowadays

- universal tamping machine (example in Figure 4.11b) - in limited spaces and close to obstructions such as in turnouts, switch blades and crossings, tamping machines with the possibility to tilt each individual tine sideways are used. Universal tamping machine are equally applicable for plain track tamping a tamping rate similar to that of other single sleeper tamping machines

- spot tamping machine (example in Figure 4.11c) - spot tamping over short distances is a costly activity due to low production achieved. Utilization of spot tamping machines is, however, necessary in exceptional situation such as for failed formations or severe rail surface defects

- lightweight tamping machine (example in Figure 4.11d) - practical for their size, given that some tamping requirements are too remote or unpractical to be tamped with a line or universal tamping machines. Lightweight tamping machine cannot, however, lift, level and align the tracks

Die approbierte gedruckte Originalversion dieser Dissertation ist an der TU Wien Bibliothek verfügbar.
The approved original version of this doctoral thesis is available in print at TU Wien Bibliothek.
TU Bibliothek Your knowledge hub WIEN

(a) Dynamic Tamping Express 09-4X E[3]

(b) Unimat 08-475/4S

(c) Unimat Combi 08-275

(d) Minima 2

Figure 4.11: Tamping machines (©*Plasser & Theurer*)

4.5 Design (overlift) tamping

Key motivation behind the development of design overlift tamping approach was the observation that the track "memorizes" the geometry it hat deteriorated to prior to the tamping operation [45]. In addition, during regular tamping the subsequent geometry deterioration is not taken into consideration and the resulting improved geometry is usually a straight line. Following initial substantial deformation, the changes to track geometry stabilize and the resulting geometry never tends towards a straight line.

Examples of track geometry resulting from conventional in comparison to design overlift tamping can be seen in Figure 4.12. Track kilometer is plotted on the x axis and following deviations from the desired track geometry on the y axis:

- Track position prior to maintenance (green line)
- Nominal track position (red line)
- Theoretical resulting track position after mechanized maintenance train[3] (MDZ) employment (blue line)
- Actual track situation after MDZ employment (gray line)

[3]Mechanized maintenance train consists of the levelling, lining and tamping machine, ballast regulator and dynamic track stabilizer

Die approbierte gedruckte Originalversion dieser Dissertation ist an der TU Wien Bibliothek verfügbar.
The approved original version of this doctoral thesis is available in print at TU Wien Bibliothek.
TU Bibliothek Your knowledge hub WIEN

- Track situation 1 month after MDZ employment (black line)

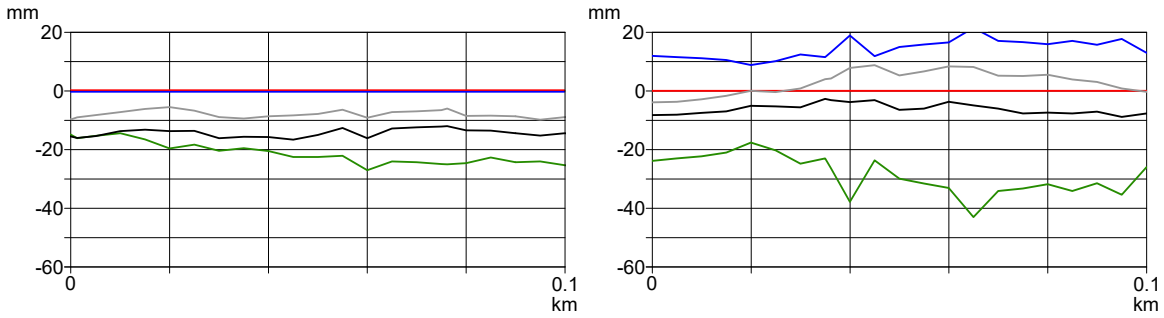

(a) Conventional tamping (b) Design tamping (50% overlift)

Figure 4.12: Comparison of conventional and design overlift tamping methods and the influence of "track memory" (modified from [28])

In conventional tamping presented in Figure 4.12a, the deteriorated track geometry presented by he green line should be brought back to the desired position by employment of the mechanized maintenance train (red and blue line). However, by using the dynamic track stabilization (DTS), initial settlements are already inflicted and the actual track position corresponds to the grey line. A month after MDZ employment (black line), the track returns to the original error variation due to traffic loads. This behavior is known as "memory of the track". This phenomenon can be explained by the fact that no additional ballast is added during tamping and as a result correspondingly large settlements occur on the spots where higher lifting values have been used.

In comparison, result of design tamping with 50% overlift can be seen in Figure 4.12b. Lifting values 50% greater than those that would bring that track back into its nominal position are used, following the idea to overlift the track in places where severe settlement have been observed in the past (blue line). Following DTS employment, the track level is brought closer to the nominal level (grey line). The subsequent traffic loads (black line) contribute to a further improvement and not to deterioration as with conventional tamping. This combined application achieves a more permanent and sustainable track position.

4.6 Stoneblowing

Stoneblowing system developed by the British Railways as the stone blowing machine PBI 84 (Figure 4.13b) is conducted by a self-contained railway track maintenance machine that lifts and the sleepers and "blows" a predetermined amount of small single sized ballast stones into the void beneath the sleeper, thus reinstalling the railway track to its desired line and level. This mechanized alternative to the process that was primary conducted manually by hand shovel packing (Figure 4.13a) is know as *pneumatic ballast injection* [76].

According to *Selig and Waters* [117], the stoneblowing process can be subdivided into following stages (Figure 4.14):

Die approbierte gedruckte Originalversion dieser Dissertation ist an der TU Wien Bibliothek verfügbar.
The approved original version of this doctoral thesis is available in print at TU Wien Bibliothek.
TU Bibliothek Your knowledge hub WIEN

(a) Handheld stoneblower [100] (b) Stoneblowing machine PBI 84 [45]

Figure 4.13: Different stoneblowing principles

1. Measuring the track geometry. Sleeper rests in the ballast prior to adjustment. A precise calculation of the track lifting values is conducted for each sleeper to restore it to the acceptable geometry.

2. The sleeper is raised to create a void into which the stone can be blown. The stoneblowing tubes are driven down alongside the sleeper.

3. Stoneblowing, i.e. blowing the measured quantity of stone (track ballast) by compressed air into the void is conducted. The quantity is determined bases on desired track geometry that should be achieved when ballast is compacted by subsequent traffic.

4. Stoneblowing tubes are removed and the sleeper is lowered onto the surface of the blown stone.

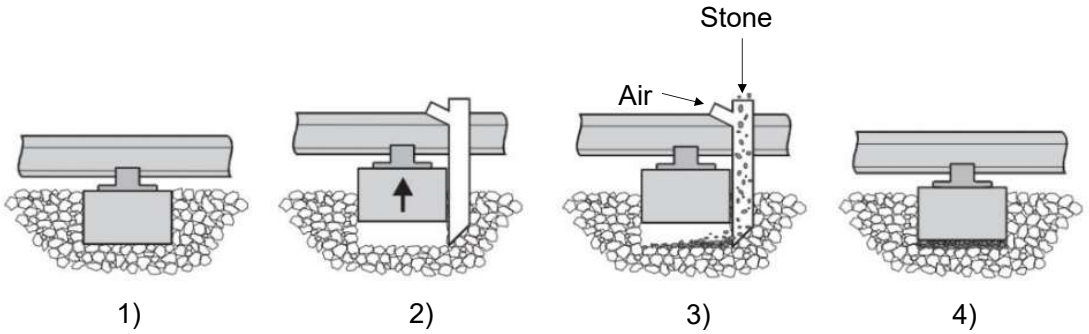

Figure 4.14: Schematic presentation of the stoneblowing principle [76]

An important consideration is that the stone used in the stoneblowing process has to be of the highest possible quality since it is positioned at the point of maximum stress, at the ballast - sleeper interface. The nominal particle size of the ballast grains used for stoneblowing is predefined with approximately 14-20 mm and is thereby one of the most important sources of objection to the principle of stone blowing given that relatively small grains sized are inserted to the ballast matrix. The small size of the stones provides a greater number of contact point between the ballast bed and the sleeper, thus lowering the contact stress and

Die approbierte gedruckte Originalversion dieser Dissertation ist an der TU Wien Bibliothek verfügbar.
The approved original version of this doctoral thesis is available in print at TU Wien Bibliothek.
TU Bibliothek Your knowledge hub WIEN

the probability of particle attrition. The ballast particle size used for stoneblowing should not influence the ballast bed drainage possibilities. Only stones with a high mechanical strength and a low attrition values should be used [45].

4.7 Dynamic track stabilization

Natural track stabilization induced by successive passages of regular traffic trains at lower speed which is equivalent to applying cyclic vertical loads to the sleepers for a given time. This long-lasting stabilization process is progressively replaced by faster operations which do not disturb the regular train traffic, most popular of which is the dynamic stabilization [57]. Following the leveling, lifting and tamping unit, dynamic track stabilizer (DTS) (Figure 4.4) is employed as an indispensable part of track maintenance process of many railway infrastructure operators. The first prototype of the Dynamic Track Stabilizer (DGS 42 N, Figure 4.15) was constructed by *Plasser & Theurer* in 1974. The DTS was initially designed as an independent track maintenance machine but in the meantime it has also been integrated into lifting, leveling and tamping machines such as the *Dynamic Tamping Express 09-4X* E^3.

Figure 4.15: First production version - DTS 42 N [114]

Track resistance to lateral displacement is increased after tamping by additional DTS compaction in order to prevent track buckling and speed restrictions. Moving continuously across the track and inducing horizontal vibrations crosswise to the track axis in combination with static vertical pressure (Figure 4.16), DTS is used to assure that unavoidable initial settlements which follow maintenance actions are accurately anticipated.

Artificial settling process induced by the DTS is uniform and friction-free and the ballast grains are rearranged closer together with more surface contact, resulting with lower specific pressure stresses during load transmission. The result is a track position of higher vertical and horizontal stability [62]. Dynamic track stabilization produces a homogeneous compaction (Figure 4.17b) of the entire ballast bed ensuring that the cavities in the sleeper bay are reduced (Figure 4.17a), resulting in improved anchoring of the track skeleton in the ballast bed [30].

Die approbierte gedruckte Originalversion dieser Dissertation ist an der TU Wien Bibliothek verfügbar.
The approved original version of this doctoral thesis is available in print at TU Wien Bibliothek.
TU Bibliothek Your knowledge hub WIEN

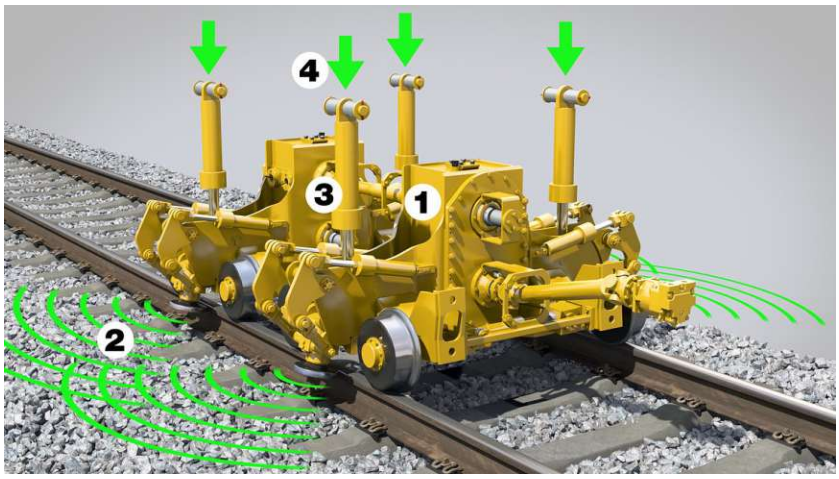

Figure 4.16: The principle of Dynamic Track Stabilization: (1) variable unbalance, (2) induced horizontal vibrations, (3) hydraulic cylinder, (4) vertical load [51]

Increasing the resistance to lateral track displacement is one of the most important goals of dynamic track stabilization. According to *Auer and Antony* [30], if dynamic track stabilization is performed after track tamping it increases the lateral track displacement resistance by up to 80% in comparison to a fully consolidated track, which corresponds to the traffic loading of 100,000 load tonnes. Given that the lateral track displacement resistance depends strongly on the ballast compaction state, the development of a DTS continuous compaction monitoring system is in development [47].

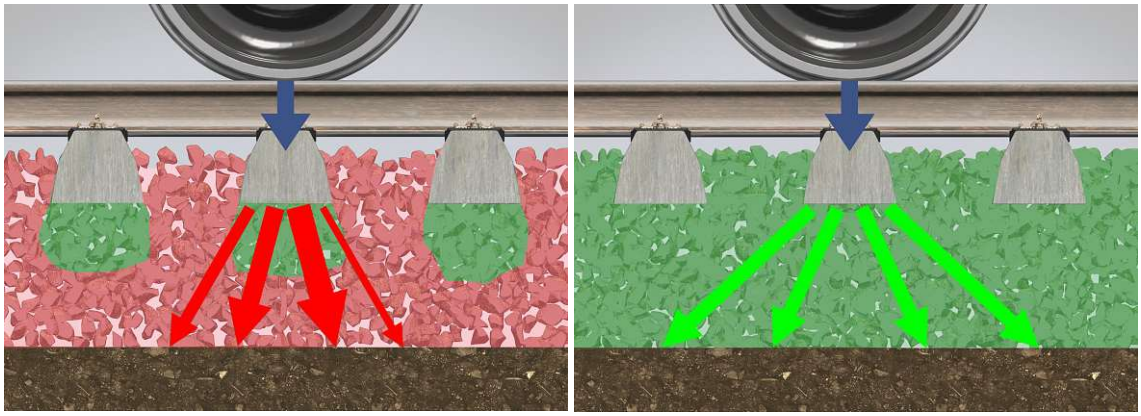

(a) After tamping: ballast underneath the sleepers has been compacted, vertical load not distributed uniformly

(b) After stabilizing: ballast rearranged into a homogeneous structure, vertical load distributed optimally

Figure 4.17: Ballast bed compaction - effect of tamping and dynamic track stabilization [51]

The DTS modus operandi is based on two independent main components:

- unbalance exciters (dynamic stabilization units) - two counter-rotating unbalances, arranged directly above one another and rotated 180° from one another in the starting position. Due to this arrangement, generated forces generated cancel each other out in the vertical direction and add up in the horizontal direction [47].

Die approbierte gedruckte Originalversion dieser Dissertation ist an der TU Wien Bibliothek verfügbar.
The approved original version of this doctoral thesis is available in print at TU Wien Bibliothek.
TU Bibliothek Your knowledge hub WIEN

- vertical loading cylinders - two for each stabilizing unit, applying vertical load to the rails, sleepers and ballast.

Contact between the rails and DTS is achieved by loading cylinders and by pressure rollers in conjunction with hydraulic expansion axles.

Operation of the DTS is influenced by following parameters (range of values for the *Dynamic Tamping Express 09-4X* E^3 DTS given in brackets) [128]:

1. vibration frequency (0-42 Hz) - corresponds to the frequency range in which ballast fluidization occurs and the ballast grains start to rearrange in search of a denser bedding, prescribed to between 30 and 35 Hz by the ÖBB.

2. impact force - frequency dependent impact force F_{dyn} can be determined from the given eccentric mass m, eccentricity r (between 0% and 100%) and the vibration frequency f:

$$F_{dyn} = m \cdot r \cdot (2\pi f)^2 \tag{4.1}$$

   Impact force affects the track settlement the most, making it possible to produce even smoother transitions at the start and end of a work site. New developments in the field have made it possible for the impact force to be adapted to the prevailing conditions without changing the vibration frequency. [30]

3. vertical load (max. 356 kN) - higher load on the ballast bed leads to a more intensive redistribution of the ballast and to a better compaction. ÖBB has specified a contact pressure of 60 to 75 bar which corresponds to a contact force of 229 or 277 kN.

4. working speed (0.2 km/h and 2.5 km/h) - plays subordinate role in the effectiveness of track stabilization. Despite varying working speed of the machine, the ballast bed is settled in a constant manner and homogenized uniformly

In addition to providing homogeneous ballast bed structure and preventing track buckling, the usage of DTS extends the maintenance intervals, prolongs the durability of accurate track geometry, raises the track quality reserve, lowers the cost of track maintenance and increases travel safety.

Die approbierte gedruckte Originalversion dieser Dissertation ist an der TU Wien Bibliothek verfügbar.
The approved original version of this doctoral thesis is available in print at TU Wien Bibliothek.
TU Bibliothek Your knowledge hub WIEN

Die approbierte gedruckte Originalversion dieser Dissertation ist an der TU Wien Bibliothek verfügbar.
The approved original version of this doctoral thesis is available in print at TU Wien Bibliothek.

Chapter 5

Basic experimental research

5.1 Introduction

Geotechnical aspects connected to track ballast condition and behavior are considered to be the most costly part of the track maintenance process. Even though the tamping machines have been proven to provide a quick and efficient improvement and reduction of deviations from the design track geometry, their effectiveness could be additionally optimized by determining the optimum point in time to conduct track maintenance and defining the necessary tamping parameter combination for the given ballast bed condition. This approach would also ensure durability of the track geometry after tamping. As a necessary foundation for the development of condition-based tamping process, information about the track substructure and the ballast condition need to be determined and related to a customized parameter combination. For this purpose tamping tine interaction with the ballast matrix during tamping needs to be recorded and analyzed during every track maintenance process in order to differentiate between ballast behavior dependent on various traffic loads and the degree of ballast bed fouling.

Preliminary considerations, development of the basic measuring system as well as the scope and principles of the conducted initial in-situ measurements and data analysis are presented in this chapter. An exact definition of the terminology used in the following chapters can be found in the Glossary.

5.2 Initial approach and the scope of in-situ measurements

General research objective is the optimization of existing tamping process and utilization of the tamping unit as not only a ballast compaction but also a ballast bed condition measuring tool. This is primarily conducted by performing several in-situ measurements in order to gain an insight into ballast behavior during track tamping and its response to compaction. The main focus point was set on the interaction between the tamping tine(s) and the ballast matrix underneath the sleepers during tamping.

Die approbierte gedruckte Originalversion dieser Dissertation ist an der TU Wien Bibliothek verfügbar.
The approved original version of this doctoral thesis is available in print at TU Wien Bibliothek.
TU Bibliothek Your knowledge hub WIEN

Figure 5.1: Tamping machine *Dynamic Tamping Express 09-4X E*^{3} (©*Plasser & Theurer*)

5.2.1 Objectives

Expected results are defined as guiding principles for the development of the measuring system to be used in order to record the tine - ballast matrix interaction during regular track maintenance performed by the *Plasser & Theurer*[1] high- performance four-sleeper tamping machine *Dynamic Tamping Express 09-4X E*^{3} (Figure 5.1) and can be summed up as follows:

- total tine movement as a combination of an absolute (due to the extension in the hydraulic cylinder) and relative (due to dynamic excitation) movement
- reaction and penetration resistance forces exerted by the tamping tine
- ballast matrix response to the tamping tine movement
- load-displacement curves presenting the interaction of the tamping tine and ballast matrix in form of reaction (tamping) force - tamping tine oscillation diagrams.

5.2.2 Proposed measuring system

A measuring system required to obtain all the necessary data to evaluate the tamping tine - ballast matrix interaction during a tamping process is proposed in cooperation with Fritz Kopf[2] and can be seen in Figure 5.2:

1. Total tamping tine movement measurement:
   (a) absolute tine motion - squeezing displacement induced by the extension in the hydraulic cylinder is proposed to be measured from the frame of the machine by either a laser rangefinder or a string potentiometer (Figure 5.2b, green) in order to minimize measuring errors induced by dynamic motion effects.
   (b) relative tine motion - double integration of the signals recorded by two biaxial accelerometers (Figure 5.2b, blue) of which the first should be located right above the tamping tine and the second as close as possible to the center of tamping arm

[1] Plasser & Theurer, Export von Bahnbaumaschinen, Gesellschaft m.b.H.
[2] FCP Fritsch, Chiari & Partner ZT GmbH

Die approbierte gedruckte Originalversion dieser Dissertation ist an der TU Wien Bibliothek verfügbar.
The approved original version of this doctoral thesis is available in print at TU Wien Bibliothek.
TU Bibliothek Your knowledge hub WIEN

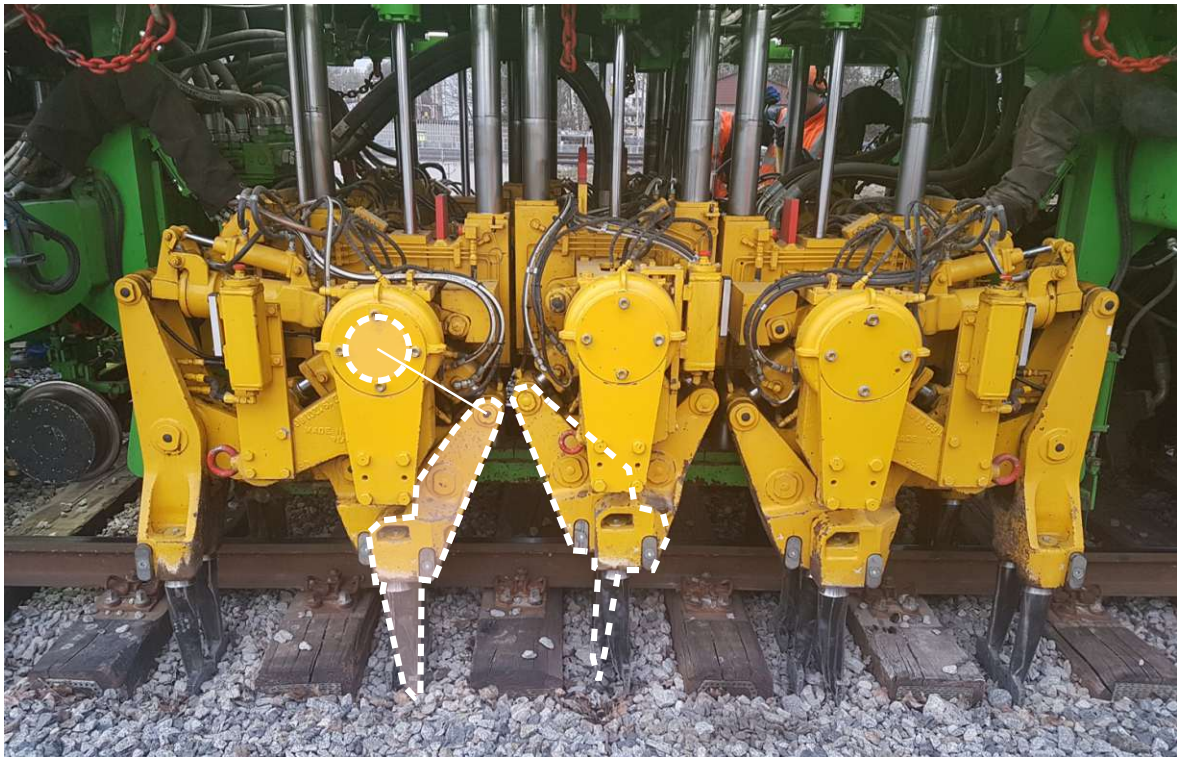

(a) Tamping unit of the *Dynamic Tamping Express 09-4X E*^{3} with one highlighted tamping arm

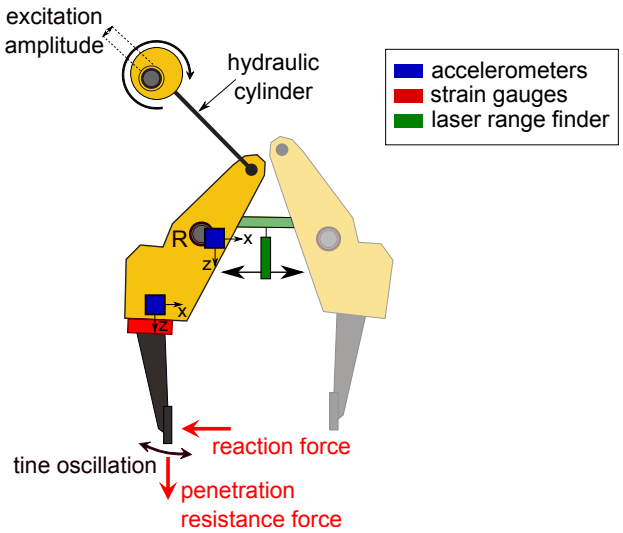

(b) Exact position of the proposed measuring units on one of the tamping arms of the *Dynamic Tamping Express 09-4X E*^{3}: strain gauges (red), accelerometers (blue), squeezing distance measurement from the machine frame (green)

Figure 5.2: Tamping unit and the proposed sensor positions

Die approbierte gedruckte Originalversion dieser Dissertation ist an der TU Wien Bibliothek verfügbar.
The approved original version of this doctoral thesis is available in print at TU Wien Bibliothek.
TU Bibliothek Your knowledge hub WIEN

rotation (presumed with the point R, Figure 5.2b). An output data rate of min. 500 Hz and the measurement range of ±30g is proposed in order to capture all the dynamic effects of the relative tine motion with the excitation frequency varying between 25 and 48 Hz.

2. Half-bridge strain gauges (Figure 5.2b, red) are proposed to be installed to a position at the top of the tamping tines in order to record the momentum exerted by both the penetration resistance and reaction forces at the tamping tine plate.

In addition to the sensors listed above, the exact vertical position of the tamping unit and the hydraulic cylinder pressures that are a part of routing measurement during track tamping shall be recorded.

5.2.3 Expected results

State of the art *Plasser & Theurer* track tamping machines operate with a frequency of 35 Hz during the squeezing movement which was proven to be the optimum approach for clean ballast conditions by *Fischer* [59]. Taking an average squeezing movement duration of 1 s, the tine completes 35 oscillations with an amplitude of 4-5 mm. Every tamping tine oscillation can be singled out of the process and presented as a load-displacement curve, i.e. resistance force-oscillation displacement diagram.

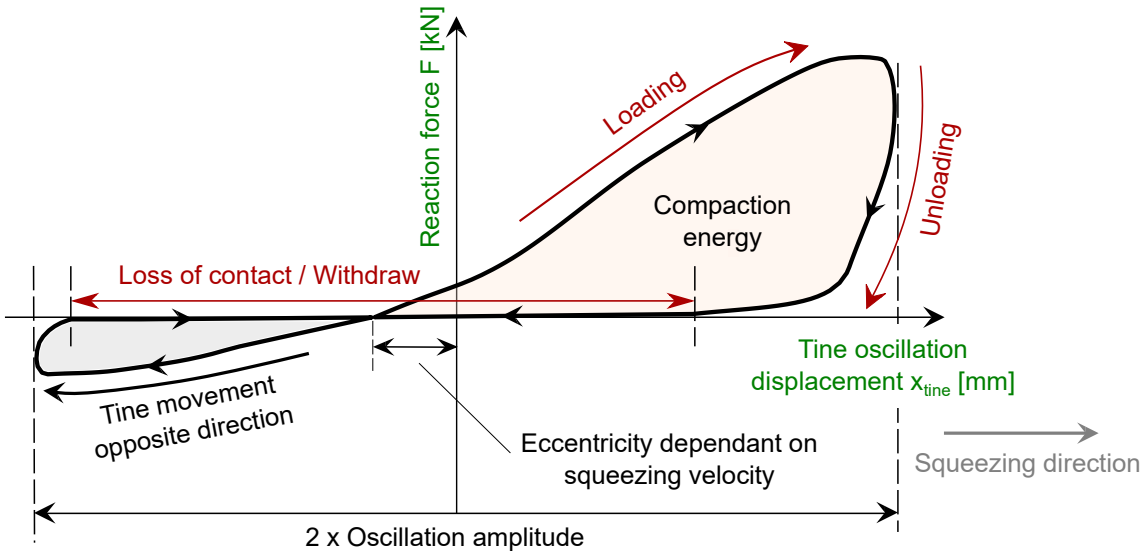

Figure 5.3: Expected simplified load – displacement curve showing a single tamping tine oscillation

A simplified expected form of a single load-displacement curve can be seen in Figure 5.3, showing one tamping tine oscillation backwards and forwards with a total oscillation of two times the amplitude (4-5 mm) on the x and the reaction or tamping force on the y axis. The two measurement signals needed for this visualization of a single cycle (see Glossary) are the reaction force measured by the strain gauges and the tine oscillation displacement as a result of the double integration of the measured accelerations, both recorded during tine

Die approbierte gedruckte Originalversion dieser Dissertation ist an der TU Wien Bibliothek verfügbar.
The approved original version of this doctoral thesis is available in print at TU Wien Bibliothek.
TU Bibliothek Your knowledge hub WIEN

motion in and opposite to squeezing direction, parallel to the rails. Progress of these two characteristics during one cycle is expected to provide information about several additional tamping characteristics that will depict not only the tine motion during tamping, but also the soil, i.e. ballast matrix reaction to this motion during compaction.

One single cycle can be additionally subdivided into three constituent phases (Figure 5.3):

1. Loading - Contact phase - tamping tine in contact with the ballast matrix, evident by the values of the reaction force F higher than zero. Tamping tine moves *in* the squeezing direction enforcing the ballast matrix deformation and causing an increase in the measured reaction force (= reaction force in the ballast matrix). Inclination of the load-displacement curve during loading is expected to provide information about the loading response of the ballast matrix as a reaction to the exerted deformations. End of the loading phase is determined by the maximum reaction force F_{max} (Figure 5.4).

2. Unloading - Contact phase - tamping tine in contact with the ballast matrix, decrease of the measured reaction force F is apparent, force stays in the positive domain ($F > 0$). Similar to the loading phase, the curve inclination will again serve as an indicator of the unloading response of the ballast matrix as a reaction to the exerted deformations.

3. Loss of contact / Withdraw - Non-contact phase - reaction force F equals (or is similar) to zero. During this phase, the tamping tine moves in the direction opposite to squeezing until it reaches its maximum elongation (amplitude). It is expected that the tine hindquarter will come in contact with the ballast on the opposite side of the tamping plate which will result in negative reaction forces measured by the strain gauges (grey area visible in Figure 5.3). This however does not contribute ballast compaction under the sleeper. After reaching its maximum elongation, the tine starts its movement in the squeezing direction once again. As soon as an increase in the reaction force is visible, a new loading phase begins.

The bright red area in Figure 5.3 enclosed by the load-displacement curve during both contact phases (loading and unloading) is used for the calculation of the energy transferred to the ballast matrix during one cycle:

$$E_{contact} = \int_{start\ loading}^{end\ unloading} F(x)dx \tag{5.1}$$

Comparable to the lightweight falling deflectometer, the displacement (distance traveled) by the tamping tine in the loading phase ($\Delta x_{Loading}$) will be significantly greater than the displacement in the unloading phase ($\Delta x_{Unloading}$) (Figure 5.4) due to the proportion of permanent (plastic) deformation. Given that the reaction force increase/decrease in both contact phases remains the same (ΔF reaches from 0 to F_{max} and vice-versa), the unloading response calculated as the ratio of the reaction force to the displacement ($\Delta F/\Delta x$) will be much higher that the matrix response of the loading phase.

Die approbierte gedruckte Originalversion dieser Dissertation ist an der TU Wien Bibliothek verfügbar.
The approved original version of this doctoral thesis is available in print at TU Wien Bibliothek.
TU Bibliothek Your knowledge hub WIEN

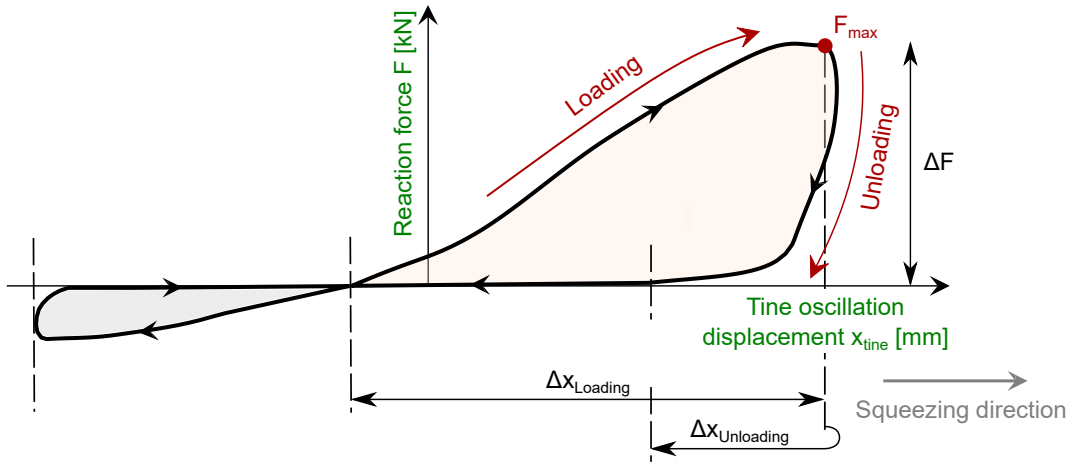

Figure 5.4: Expected simplified load – displacement curve showing a single tamping tine oscillation and the simplified approach to ballast matrix response calculation during the both contact phases

This approach will provide the possibility to observe the compaction progress and ballast response to every single tamping tine impact during the tamping process directly under the sleeper.

5.3 Initial in-situ measurements and results

In spring 2016 first in-situ measurements conducted during regular track maintenance by a *Plasser & Theurer* high-performance four-sleeper tamping machine *Dynamic Tamping Express 09-4X* E^3 were recorded at the following two locations in Austria:

– 2016-05-30 Eisenstadt

– 2016-10-11 Tullnerbach Westbahn

In-situ measurements were conducted using a measuring system developed for the purpose of this research project (described in detail in Chapter 5.3.1). Apart for these additional sensors, routinely stored data such as the GPS location, lowering position of the tamping unit, squeezing pressure and other machine-related information was collected yielding to 60 measurement channels per location. Analysis and interpretation of the executed measurements are conducted using *FAMOS Professional 7.1*, data analysis software that provides a full range of analysis functions needed developed by *imc Test & Measurement GmbH*. Detailed description of the measuring system used, scope of the conducted measurements as well as the first results and interpretations are presented in the following chapters.

5.3.1 Instrumentation of the *Dynamic Tamping Express 09-4X* E^3

Tamping unit of the *Dynamic Tamping Express 09-4X* E^3 track tamping machine (Figure 5.5a) was equipped with a set of purposefully placed sensors (Figure 5.6) in order to obtain the data required to describe the interaction between the tamping tines and the ballast matrix

Die approbierte gedruckte Originalversion dieser Dissertation ist an der TU Wien Bibliothek verfügbar.
The approved original version of this doctoral thesis is available in print at TU Wien Bibliothek.
TU Bibliothek Your knowledge hub WIEN

and its compaction underneath the sleepers. Four tamping tines of the *Dynamic Tamping Express 09-4X E*^{3} were equipped altogether (№ 59, 60, 63 and 64 - Figure 5.5b), and the first successful in-situ measurement took place on the 30th of May 2016. All measurement data analyzed and presented in this thesis are obtained from tamping unit 3, tamping tine 64 (outward, far left, highlighted in Figure 5.5a).

With some deviations from the proposed measuring system and sensor locations, the following sensors are installed:

- Strain Gauges (Figure 5.7a) – measuring the ballast penetration resistance (direction z) and reaction forces (direction x) are applied at the connection between the tamping tine and the tamping unit arm. Measured forces are converted into the reaction and ballast penetration resistance forces applied by the tamping tine to the ballast matrix. Full-bridge strain gauges produced by the company *PJM – Railway Systems Solutions* with a 6-wire configuration are installed externally and then protected by metal cladding.

- Accelerometers (Figure 5.7b) – measuring the accelerations in the directions axial and tangential to the axis connecting the sensor position and the center of rotation (local coordinate system, axes u and v). Through double integration (Chapter 5.3.2.1) of the acceleration signals the tamping tine oscillation at the tine plate (relative tine movement) is obtained. 50g *PJM* acceleration sensors are used, delivering a voltage signal of $\pm$ 4V.

- Squeezing Displacement Measurement (Figure 5.7c) – measuring the squeezing displacement, i.e. the change of length of the hydraulic cylinder whilst opening/closing. The value is recalculated with a unit geometry dependent factor obtained from a conducted calibration in order to get the tine plate absolute movement that occurs during the squeezing process (Chapter 5.3.2.2). The displacement is measured by a laser range finder (μ-Epsilon, type ILD1302). Due to its position on the tamping arm and not on the frame of the machine the results are highly affected by dynamic motion effects.

- Pressure Measurement – measuring the pressure in the hydraulic cylinders. No additional sensors are applied since the squeezing pressure is measured and recorded as a part of the standard routine during tamping by the volume flow transmitters (type EVS 3106-A-0300-000) produced by the company *Hydac*.

Apart from the listed sensors and measuring channels, the lowering position of the tamping unit and the lowering pedal signal are additionally utilized for the tamping process subdivision (in detail in Chapter 5.3.3).

Die approbierte gedruckte Originalversion dieser Dissertation ist an der TU Wien Bibliothek verfügbar.
The approved original version of this doctoral thesis is available in print at TU Wien Bibliothek.
TU Bibliothek Your knowledge hub WIEN

(a) Tamping unit with highlighted tamping tine Nº 64

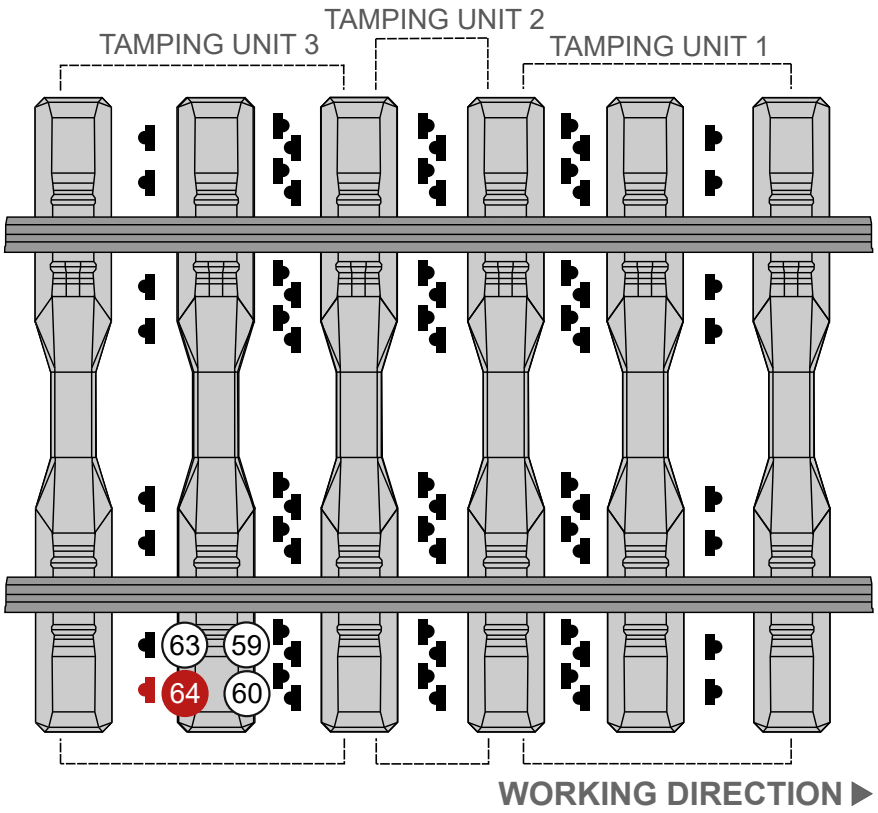

(b) Tamping tines array with highlighted tines equipped with sensors (© *Plasser & Theurer*)

Figure 5.5: Tamping unit and tine array of the *Dynamic Tamping Express 09-4X E*^{3} track tamping machine

Die approbierte gedruckte Originalversion dieser Dissertation ist an der TU Wien Bibliothek verfügbar.
The approved original version of this doctoral thesis is available in print at TU Wien Bibliothek.
TU Bibliothek Your knowledge hub WIEN

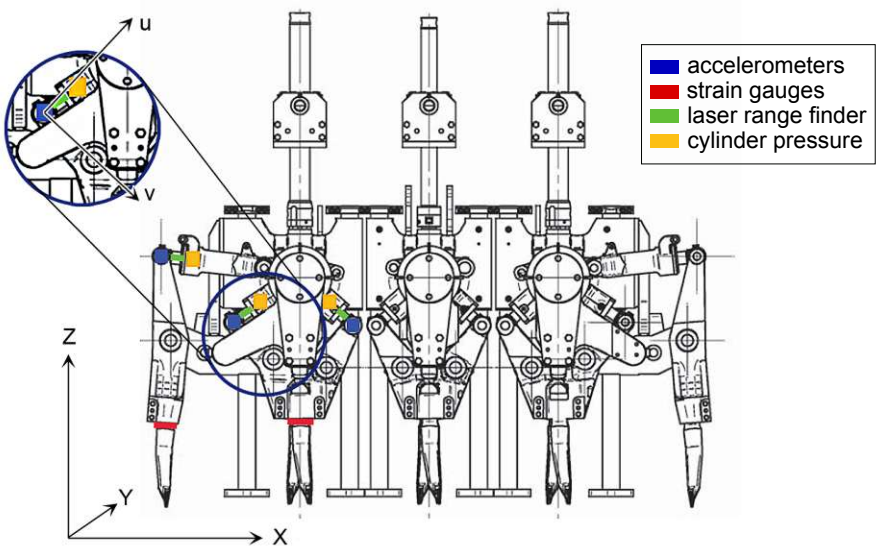

Figure 5.6: Exact position of the applied sensors on the tamping unit of *Dynamic Tamping Express 09-4X E*^{3}: strain gauges (red), accelerometers (blue), squeezing distance measurement (green), pressure measurement (yellow) (©*Plasser & Theurer*)

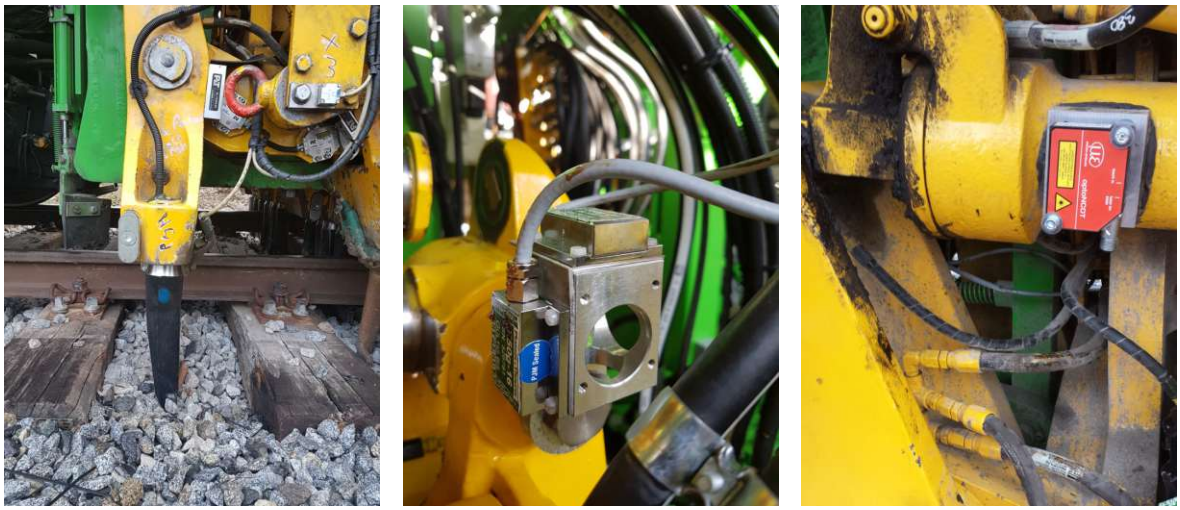

(a) Tamping tine № 64 with applied strain gauge

(b) Tamping arm with applied accelerometer

(c) Tamping arm with applied laser range finder

Figure 5.7: Tamping unit 3 - applied sensors

Die approbierte gedruckte Originalversion dieser Dissertation ist an der TU Wien Bibliothek verfügbar.
The approved original version of this doctoral thesis is available in print at TU Wien Bibliothek.

5.3.2 Total tine motion

Total motion of the tamping tines during track tamping incorporates the *absolute tine movement* (Chapter 5.3.2.2) driven by the squeezing velocity and the *relative tine movement* (Chapter 5.3.2.1) that is dependent on the excitation frequency and amplitude. Without dynamic excitation, the lowering of tamping unit alone would not be sufficient for the tamping tines to penetrate the ballast and reach the necessary position under the sleeper. If the dynamic excitation was only utilized to facilitate the ballast bed penetration but not to perform the squeezing movement, the usual tamping force would not suffice to overcome the passive earth pressure and rearrange the ballast grains to fill the void under the sleeper. On the other hand, increasing the excitation frequency would accelerate the process, but could also lead to ballast bed loosening by dilatation (in detail in Chapter 7). The squeezing motion of the tamping tines in the direction of the sleeper is therefore initiated by the opening of the hydraulic cylinder (absolute tine movement) and supported by the tine oscillations (relative tine movement). Total tine motion dependent on the squeezing velocity is presented in Figure 5.8, showing several consecutive cycles during a squeezing movement, each of which can be presented in the form of a load-displacement diagram showing all three constituent phases (loading-unloading-withdraw) as well as points of contact beginning and end for each cycle (presented in blue and discussed further in Chapter 5.4).

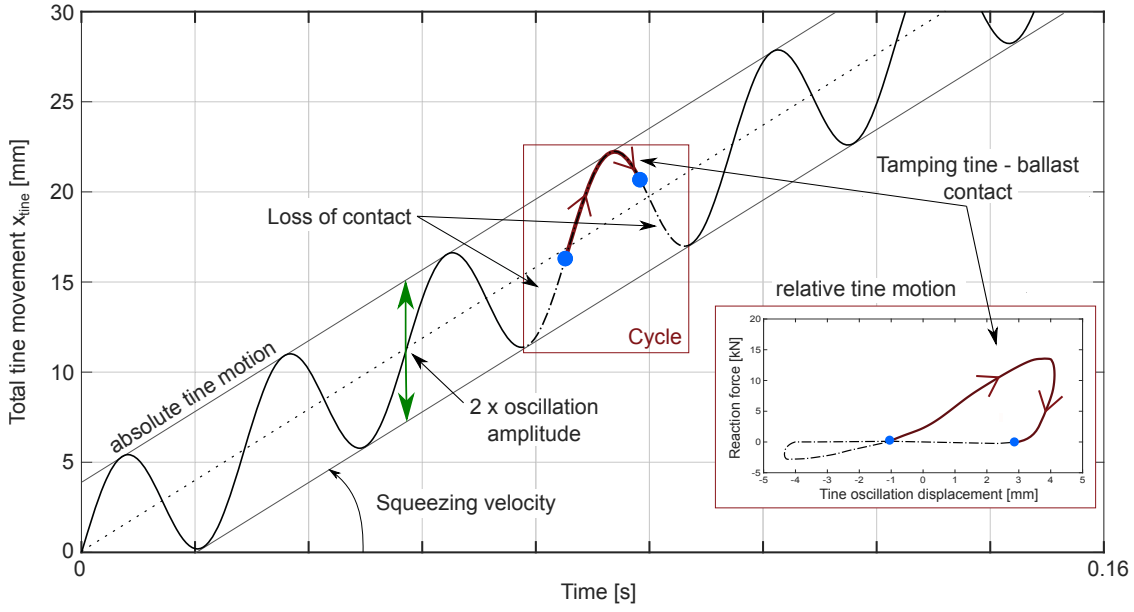

Figure 5.8: Total tamping tine motion and the influence of squeezing velocity

Periodic tine impacts on the track ballast cause a temporary (visco-)fluidization of the grain structure by reducing the inter-particle friction and encouraging the ballast grains to search for positions to form a denser bedding. The temporary fluidization leads to a locally reduced friction angle and shear strength of the ballast bed, which reduces the ballast resistance to compaction.

Die approbierte gedruckte Originalversion dieser Dissertation ist an der TU Wien Bibliothek verfügbar.
The approved original version of this doctoral thesis is available in print at TU Wien Bibliothek.
TU Bibliothek Your knowledge hub WIEN

5.3.2.1 Relative tine motion - Integration of acceleration signals

During regular track tamping the *Dynamic Tamping Express 09-4X E*^{3} tamping machine operates with an excitation frequency of 35 Hz and an excitation amplitude of 2-2.5 mm. An insight into every single tine oscillation is gained through double integration of the accelerometers to obtain the tine oscillation and plotted against the reaction force in the form of a load-displacement curve.

The integration is conducted using *FAMOS Professional 7.1* fairly simple, effective algorithm where the sum of all sampling values of the data set is calculated up to (but not including) the current point and then multiplied by the sampling rate. Prior to performing every step of integration an offset compensation is conducted in order to nullify the integration constant and meet the boundary condition $y_{(t=0)} = 0$. This is done by firstly smoothing the data set over a smoothing width of 0.15 s (giving approximately a moving mean value function) and subsequently subtracting this new data set from each individual measured value (Figure 5.9). This shifts the curve to the zero point and results in correct tamping tine oscillation displacement calculation. Gained results are multiplied with the ratio of lever arms of the attached accelerometer obtained from the tamping unit geometry and equal to 75/32 in order to obtain the velocity and displacement at the tine plate center.

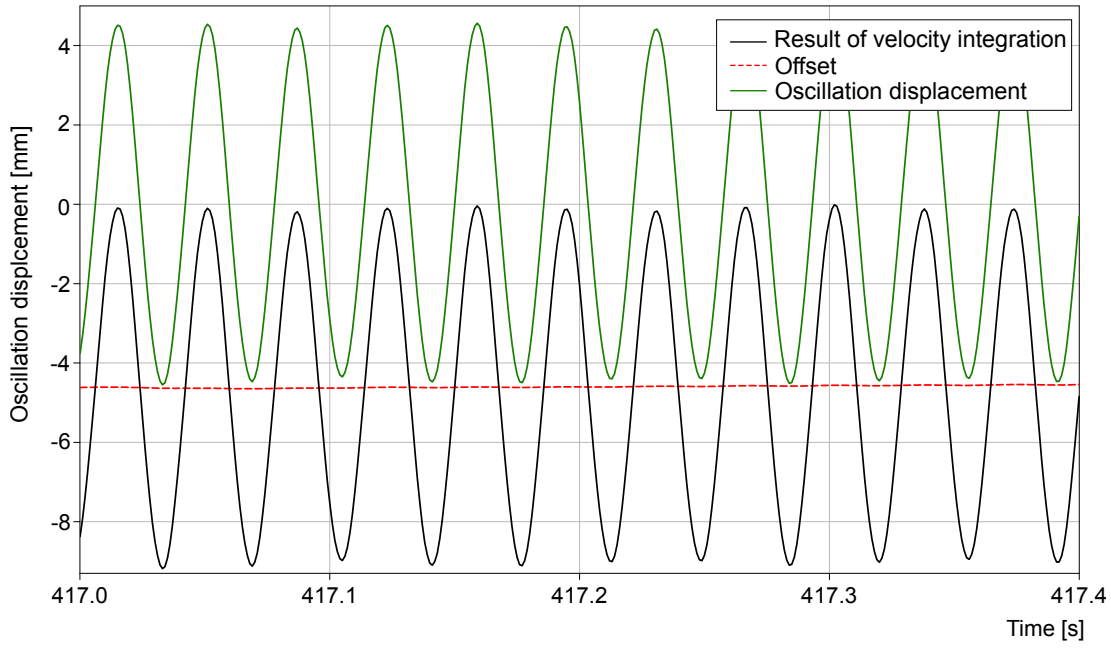

Figure 5.9: Result of integration of oscillation velocity (black) to oscillation displacement (green) and the calculated moving mean value function (red) for offset removal. Data set segment shows the tamping tine oscillation in the air prior to ballast penetration

Results of the conducted integration of measured tine accelerations to oscillation velocity and displacement of the tine plate are shown for a data segment in Figure 5.10. As can be seen, the integration process itself causes a distinct data smoothing and noise removal, giving a close to harmonic tine oscillation with the amplitude of 4-5 mm.

Die approbierte gedruckte Originalversion dieser Dissertation ist an der TU Wien Bibliothek verfügbar.
The approved original version of this doctoral thesis is available in print at TU Wien Bibliothek.
TU Bibliothek Your knowledge hub WIEN

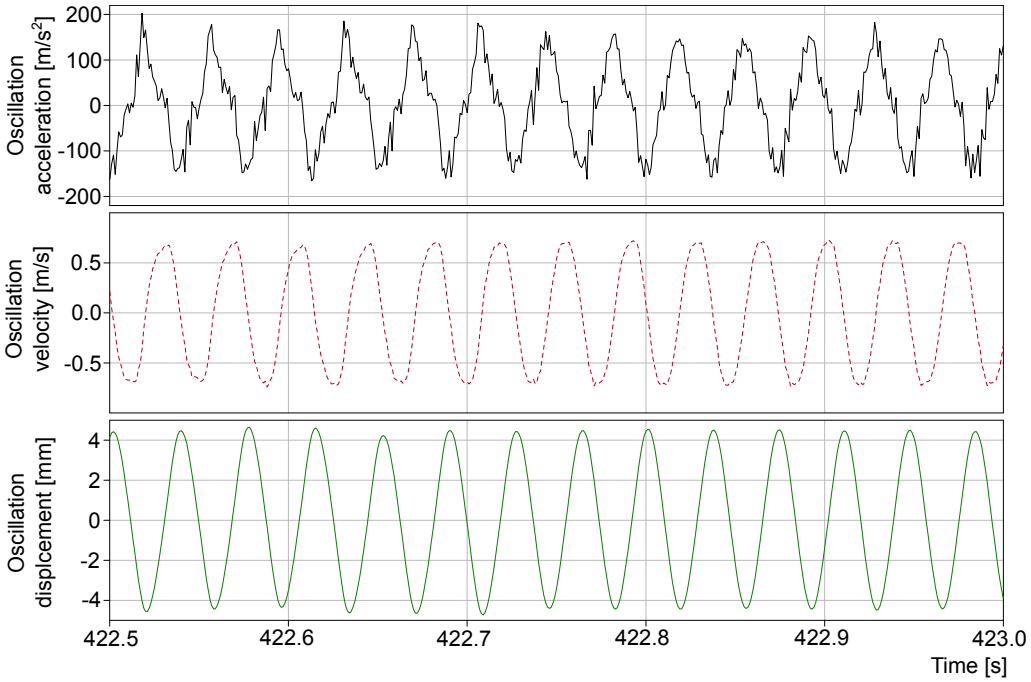

Figure 5.10: Tine oscillation velocity and displacement as a result of the double integration of the measured accelerometers. Data set segment shows the tamping tine oscillation in the air prior to ballast penetration

Same data set over the duration of 0.1 s can be seen in Figure 5.11 with highlighted one cycle i.e. one tine oscillation. Maximum acceleration correlates with the maximum tine elongation prior to the change of tine movement direction at which point the oscillation velocity is equal to 0. Accordingly, the maximum oscillation velocity is reached as the tine reaches the zero position (tine acceleration and displacement equal to 0).

Die approbierte gedruckte Originalversion dieser Dissertation ist an der TU Wien Bibliothek verfügbar.
The approved original version of this doctoral thesis is available in print at TU Wien Bibliothek.

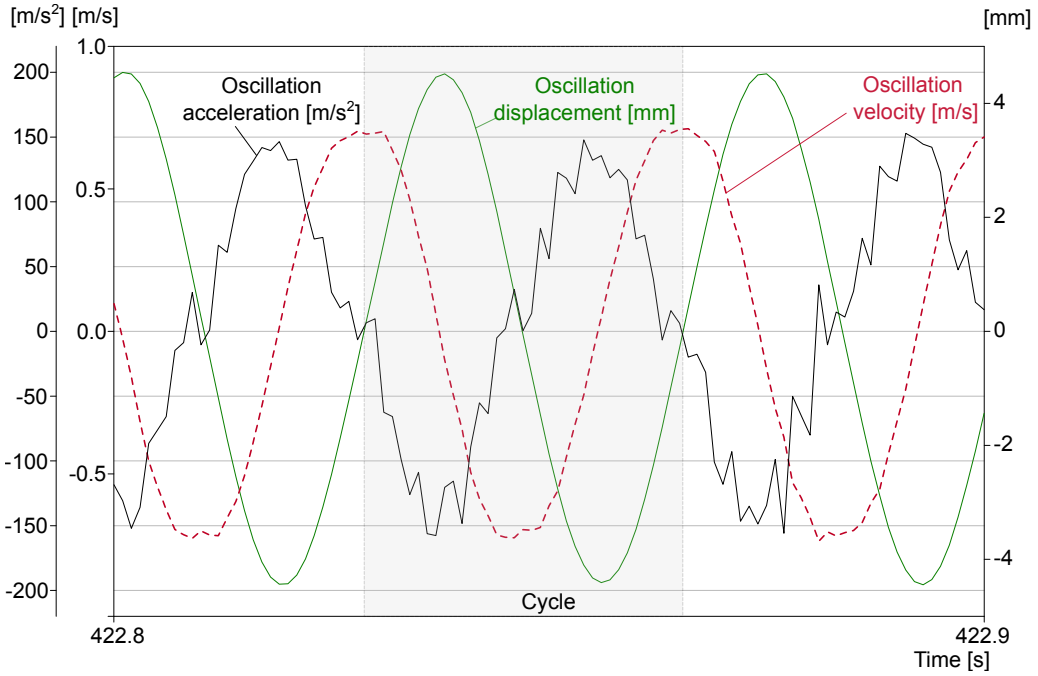

Figure 5.11: Tine oscillation velocity and displacement as a result of the double integration of the measured accelerometers over 0.1 seconds with highlighted one cycle. Data set segment shows the tamping tine oscillation in the air prior to ballast penetration

5.3.2.2 Absolute tine motion - Laser squeezing displacement measurement, validation and plausibility check

During initial measurements, absolute tamping tine motion or the squeezing displacement is obtained from the laser range finder applied to the upper part of the tamping arm (Figure 5.6, green). Plausibility check of the sensor was conducted after sensor output instalment by moving the tine manually and measuring the tine plate distance from the selected fixed point on the tamping unit and plotting the values against the data given by the laser range finder for the same tine motion (dynamic excitation turned off). Results can be seen in Figure 5.12, high level of correlation confirming the plausibility of the values measured by the laser range finder. This additional measurement validation also provided the possibility to calculate the ratio of lever arms for laser measurements (attached laser - tamping tine) that amounts to 75/40.

The conducted validation, however, only takes into consideration higher values than those that can be measured during the squeezing motion and considerably higher values than the relative tine motion that is also expected to be measured by this sensor.

A plausibility check is performed by looking into the tine oscillations measured by the laser in order to confirm the magnitude of influence of the dynamic tine motion on the laser measurements. Figure 5.13 shows the measuring signal of the laser mounted to the upper part of the tamping arm converted with the lever ratio 75/40 to the corresponding movement of the tamping tine plate. Given the position of the laser sensor, expected results should show the extensions/shortenings in the squeezing cylinder. If the squeezing cylinder

Die approbierte gedruckte Originalversion dieser Dissertation ist an der TU Wien Bibliothek verfügbar.
The approved original version of this doctoral thesis is available in print at TU Wien Bibliothek.
TU Bibliothek Your knowledge hub WIEN

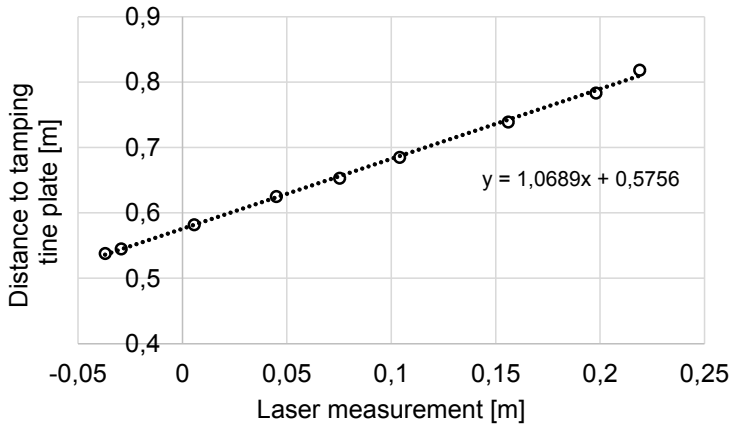

Figure 5.12: Validation of the laser range finder measurements

acts as a rigid rod ($v_{squeezing} = 0$), the tamping tine plate should oscillate with an amplitude of 3.75 mm given the excitation amplitude of 2 mm and the lever arm 75/40. Therefrom as much as 1.4 mm should be lost during the tine motion in the air (prior to ballast penetration) due to the cylinder movement. Furthermore, it appears that the dynamic movement in the squeezing cylinder is greatest in the air and decreases when the tine is in contact with the ballast, which is also plausible.

These results indicate an inaccuracy of the performed squeezing displacement measurement that most likely arises from high dynamic loads that cannot be steadily measured by the employed sensor. This dynamic loss factor causing the inaccuracies in the laser measurements can most likely be significantly reduced or avoided by positioning the laser on frame of the track tamping machine.

Nevertheless, the data recorded by the laser was utilized for the calculation of the squeezing velocity during the squeezing movement. As can be seen in Figure 5.13, the steady motion (only the extensions/shortenings in the squeezing cylinder, with no regard to the tine oscillation) is not greatly influenced by the tine oscillation, even if they are not correctly measured by the laser sensor. Therefore the inclination of the stationary motion line during the squeezing movement can be used for the calculation of the squeezing velocity. In addition, Figure 5.13 displays another built-in feature of the *Dynamic Tamping Express 09-4X E*^{3} - the stone cropper ("*Steindlzwicker*"), presenting the short opening of the squeezing cylinder after the squeezing process is completed in order to clean the tamping tine from any possibly remaining ballast grains.

Die approbierte gedruckte Originalversion dieser Dissertation ist an der TU Wien Bibliothek verfügbar.
The approved original version of this doctoral thesis is available in print at TU Wien Bibliothek.
TU Bibliothek Your knowledge hub WIEN

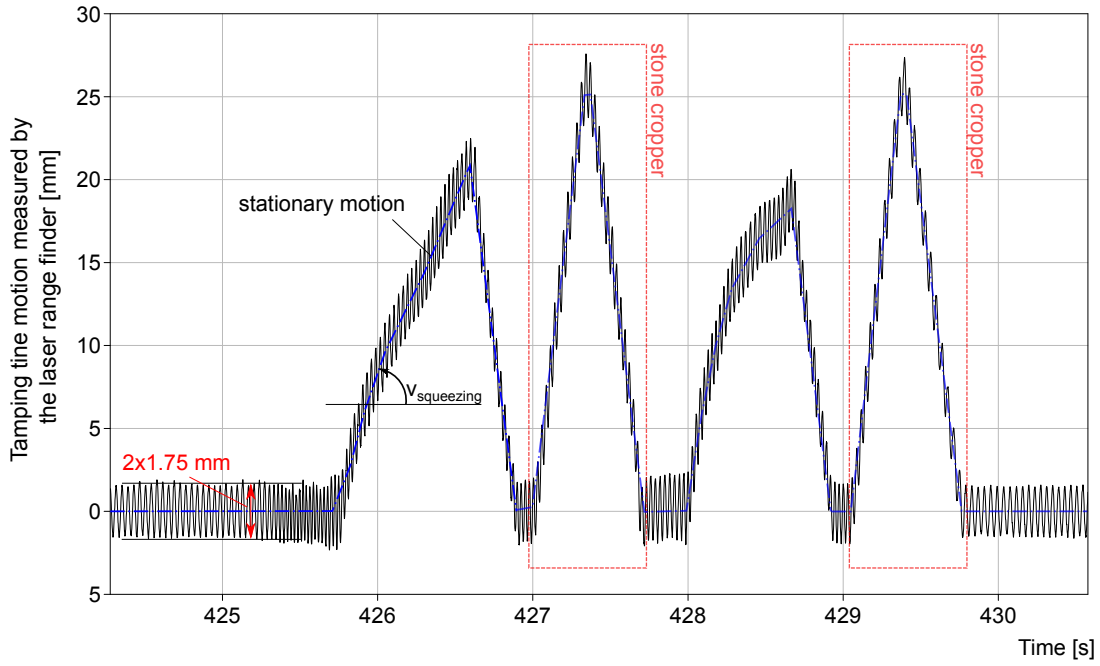

Figure 5.13: Plausibility check of the laser range finder measurements

5.3.3 Tamping process subdivision

Primary goal of the conducted in-situ measurements was to observe the interaction between the tamping tine and the ballast matrix during ballast compaction underneath the sleeper. The lowering pedal signal given by the machine operator to initiate the downward motion of the tamping unit is used to record start and end time of every tamping process (Figure 5.16). Depending on the number of squeezing processes conducted on a single sleeper (single, double or triple tamping), the tamping process is furthermore separated into single squeezing processes. In the interest of filtering out the part of the squeezing process containing ballast compaction, following subdivision is made:

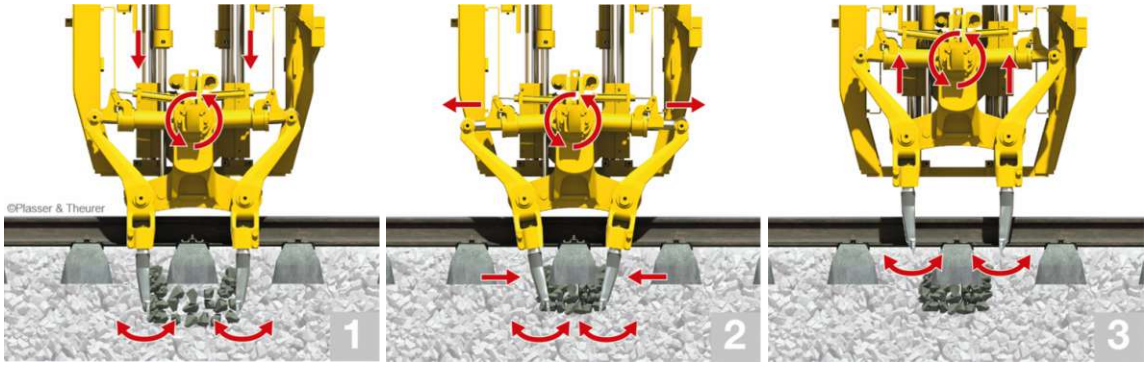

(a) Ballast penetration (b) Squeezing movement (c) Lifting the tamping unit

Figure 5.14: Tamping process subdivision (©*Plasser & Theurer*)

Die approbierte gedruckte Originalversion dieser Dissertation ist an der TU Wien Bibliothek verfügbar.
The approved original version of this doctoral thesis is available in print at TU Wien Bibliothek.

(1) Ballast penetration (Figure 5.14a)
Tamping tines penetrate the ballast on the left and right hand side of the sleeper, but the squeezing movement has not yet begun. This phase is characterized by a higher frequency (approximately 45-48 Hz) that aides ballast penetration and by a minor lateral displacement. Ballast penetration begins with exceeding the unit lowering position trigger (Figure 5.17), which is set to a constant value of 100 mm beneath the neutral position of the tamping unit.

(2) Squeezing movement (Figure 5.14b)
Tamping tines have reached the nominal depth of 13-30 mm below the bottom of the sleeper and begin the lateral squeezing movement directed towards the sleeper as the squeezing cylinder pressure exceeds the trigger value set to 50 bar. The movement is initiated by the opening of the hydraulic cylinder. Squeezing movement is the part of every squeezing process in which ballast compaction with a frequency of 35 Hz and tine oscillation amplitude of 4-5 mm takes place. Additional control of the start and end times defining the squeezing movement is possible by comparisons with the squeezing displacement measured by a laser range finder (Figure 5.17).

(3) Lifting the tamping unit (Figure 5.14c)
Simultaneously opening and pulling the tamping tines out of the ballast. The phase is characterized by the closing of hydraulic cylinder and loss of contact between the tamping tines and the ballast. It is initiated by a rapid decrease of the cylinder pressure that no longer exceeds the set trigger value of 50 bar (Figure 5.17).

As soon as the lowering position trigger value is no longer exceeded, the tamping unit is either relocated to the next sleeper or returned to the neutral position before the following squeezing process on the same sleeper begins. This phase is characterized by a complete loss of contact between the tines and the ballast (no forces measured by the strain gauges), and by a lower, noise reduction frequency of approximately 28 Hz.

Overview of the tamping and squeezing process subdivision can be seen in Figure 5.15. A color code is assigned to each component part in order to simplify component comparison between chapters of this thesis.

Die approbierte gedruckte Originalversion dieser Dissertation ist an der TU Wien Bibliothek verfügbar.
The approved original version of this doctoral thesis is available in print at TU Wien Bibliothek.
TU Bibliothek Your knowledge hub WIEN

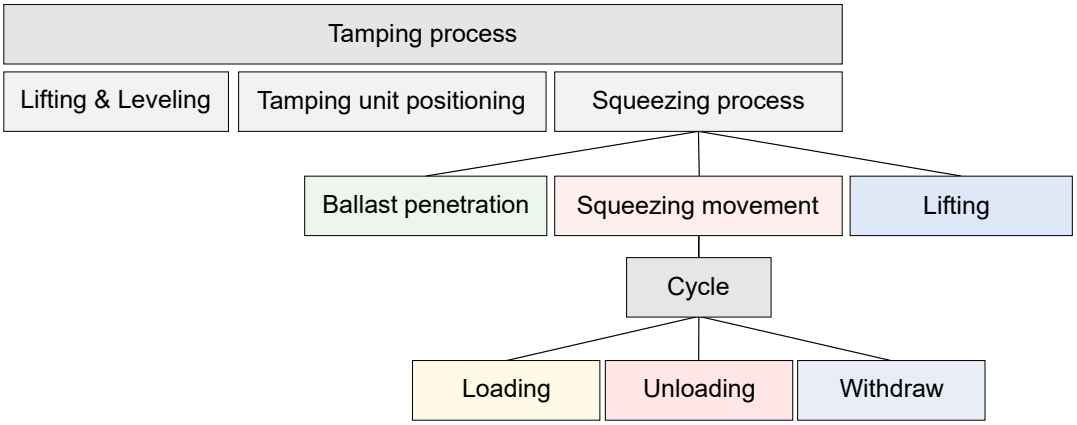

Figure 5.15: Overview of the tamping and squeezing process subdivision and component parts color code

Same exemplary time interval that can be seen in Figures 5.16 and 5.17 is presented in Figure 5.18a, showing raw measurement data, triggering signals and values recorded by the sensors during double tamping process conducted on one sleeper. In the course of ballast penetration (green), the reaction force alternates between positive and negative values as the tamping tine encounters ballast resistance on both sides. During squeezing movement (red) the reaction force is primarily positive, given that the tamping tine oscillation is overlapped by the absolute tine motion. Figure 5.18b shows calculated data for the same exemplary time interval, including the amplitude derived from the oscillation displacement, excitation frequency as well as the energy calculated as the area within the load-displacement curve of every cycle.

Die approbierte gedruckte Originalversion dieser Dissertation ist an der TU Wien Bibliothek verfügbar.
The approved original version of this doctoral thesis is available in print at TU Wien Bibliothek.

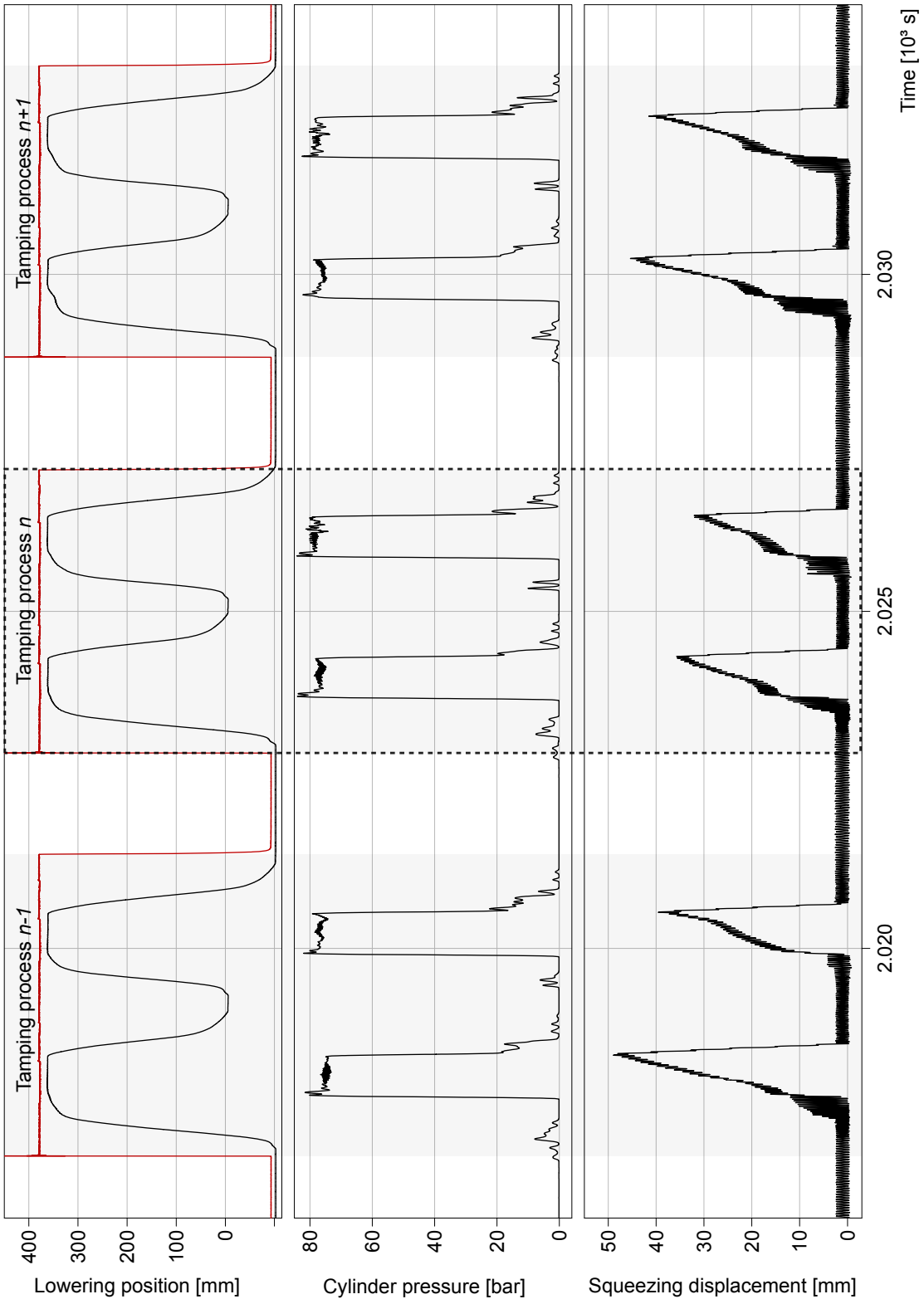

Figure 5.16: Three consecutive tamping processes and signals used for the tamping process subdivision. Start and end time of a single process are obtained from the lowering pedal signal given by the machine operator, presented by a red line

Die approbierte gedruckte Originalversion dieser Dissertation ist an der TU Wien Bibliothek verfügbar.
The approved original version of this doctoral thesis is available in print at TU Wien Bibliothek.

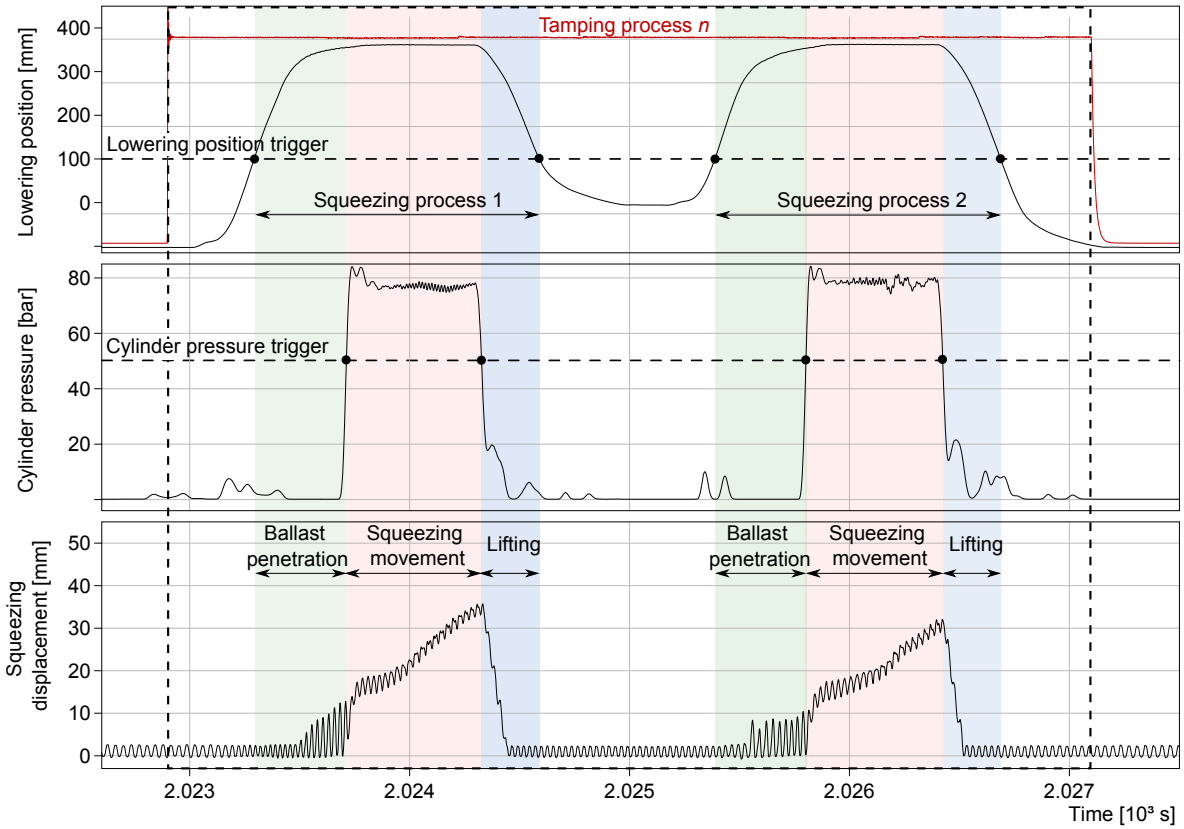

Figure 5.17: Subdivision of a double tamping process performed on one sleeper - ballast penetration (green), squeezing movement (red) and lifting the tamping unit (blue)

Die approbierte gedruckte Originalversion dieser Dissertation ist an der TU Wien Bibliothek verfügbar.
The approved original version of this doctoral thesis is available in print at TU Wien Bibliothek.

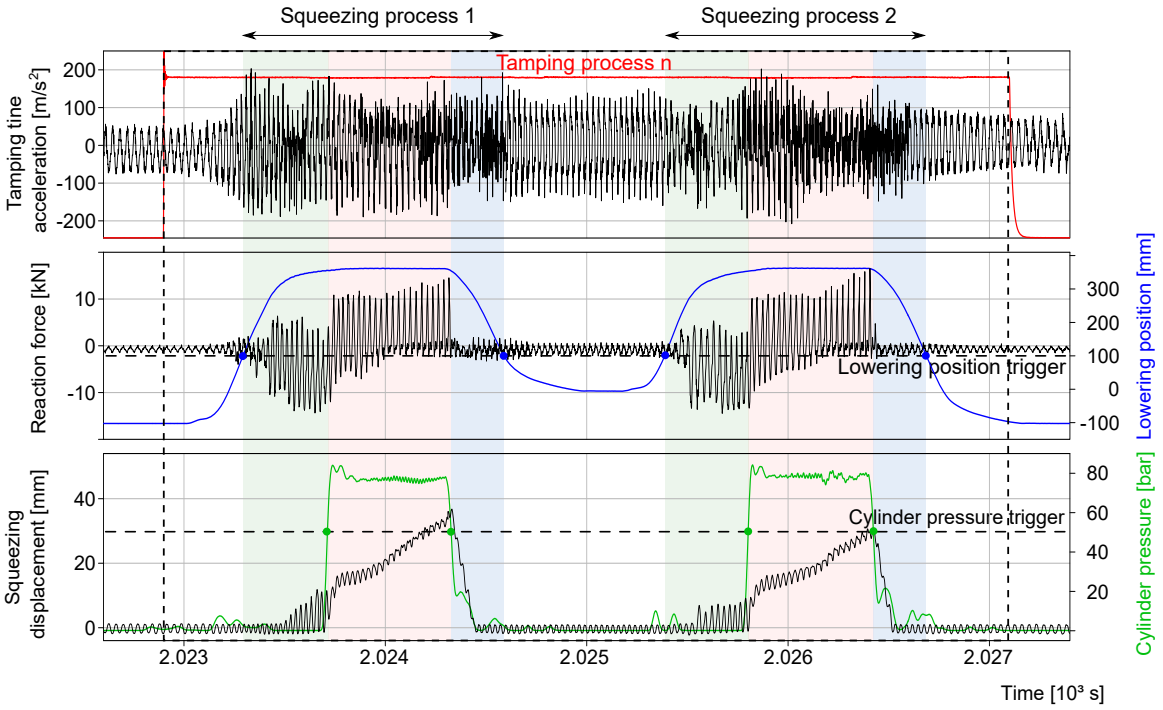

(a) Raw measurement data showing accelerations, reaction force, squeezing displacement and the triggers for tamping process subdivision

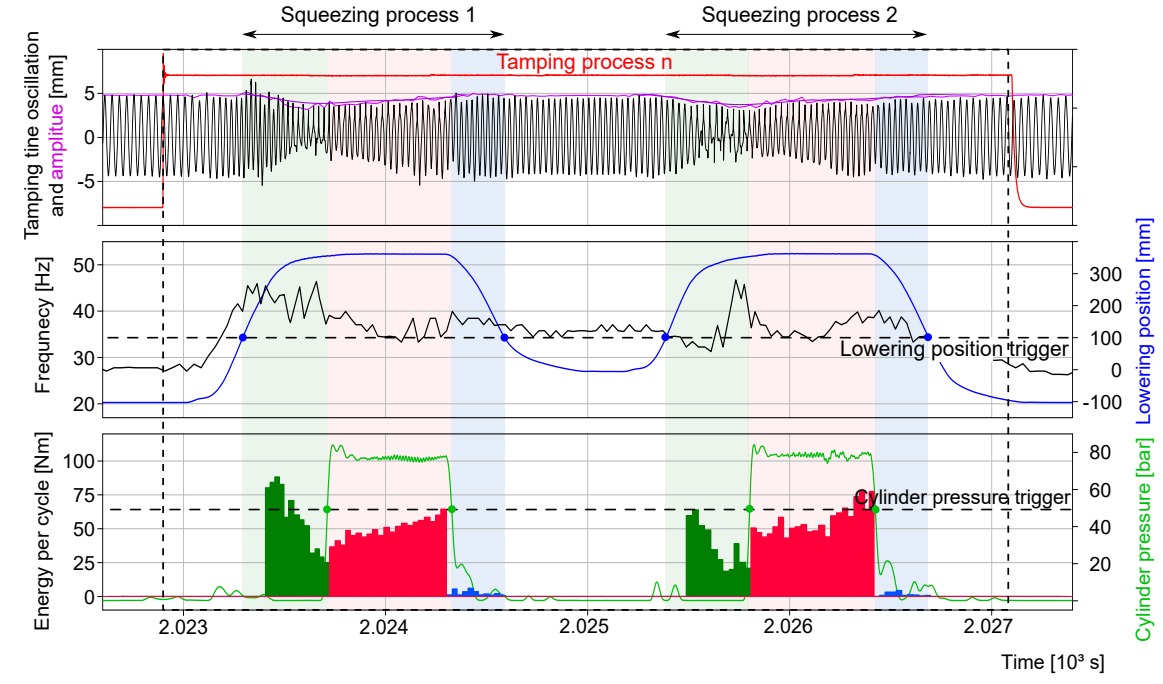

(b) Calculated data showing tine oscillation, amplitude (raw and smooth), frequency, energy per cycle and the triggers for tamping process subdivision

Figure 5.18: Subdivision of a double tamping process performed on one sleeper - ballast penetration (green), squeezing movement (red) and lifting the tamping unit (blue)

Die approbierte gedruckte Originalversion dieser Dissertation ist an der TU Wien Bibliothek verfügbar.
The approved original version of this doctoral thesis is available in print at TU Wien Bibliothek.
TU Bibliothek Your knowledge hub WIEN

5.3.4 Variable tamping parameters

Track maintenance conducted during this research project was in no way adapted or altered from the regular routine. Performance of the the four-sleeper tamping machine utilized for the measurements is automatized to a very high level, assuring constant tamping parameters during the whole maintenance process:

- Tamping frequency with needed modulation (Chapter 4.4.3)
- Tamping tine oscillation amplitude 4-5 mm (selected based on the research conducted by *Fischer* [59])

The non-automatized tamping parameters [65] are selected by the machine operator in order to improve the resulting track quality and the working performance of the machine, giving him the opportunity to react to each particular track situation. Parameter selection is based on track geometry deviations, ballast condition, in some cases sleeper type and prior lifting values

- Number of squeezing processes per tamping process (number of insertions - single, double or triple tamping process)
- Cylinder pressure
- Squeezing time (between 0.8 and 1.2 s)
- Lifting values (correction values)
- Tamping depth (13-30 mm)

Selecting ideal tamping parameters influences the resulting track quality significantly, meaning that an inexperienced operator runs the risk of delivering inconsistent quality [64]. The influence of "human factor" can be reduced by developing a system that automatically selects parameters based on the specific track and ballast condition and optimizes the resulting quality and overall track stability.

Die approbierte gedruckte Originalversion dieser Dissertation ist an der TU Wien Bibliothek verfügbar.
The approved original version of this doctoral thesis is available in print at TU Wien Bibliothek.
TU Bibliothek Your knowledge hub WIEN

5.4 Load-displacement curve and tamping characteristics

State of the art *Plasser & Theurer* track tamping machines operate with a frequency of 35 Hz during the squeezing movement which was proven to be the optimum approach for clean ballast conditions by *Fischer* [59]. Taking an average squeezing movement duration of 1 s, the tine completes 35 oscillations with an amplitude of 4-5 mm. Every tamping tine oscillation is singled out of the process, analyzed and presented as a load-displacement curve i.e. reaction force-oscillation displacement diagram. This approach provides, for the first time, the possibility to observe the compaction progress and ballast matrix response to every single tamping tine impact during the tamping process directly under the sleeper.

Data presented as load-displacement curves is obtained from two recording channels – acceleration in the u direction and the reaction force measured by the strain gauge in the direction x (Figure 5.6). The tamping tine oscillation amplitude is calculated by double integration of the acquired acceleration and portrayed against the reaction force. This presentation provides a possibility to calculate and/or extract the listed tamping characteristics crucial for the data evaluation:

1. Reaction force progression and the maximum reaction force per cycle - course of the reaction force measured by the strain gauges and calibrated to the tamping tine plate clearly indicates the beginning and end of tine contact to the ballast matrix and the two contact phases (loading and unloading) in between ($F > 0$), as well as the contactless phase ($F = 0$) where the tine reaches back (movement opposite to the squeezing direction) before it starts a new cycle [35]. The rate of reaction force increase gives information about the ballast matrix response to the tamping tine motion and consequently about the ballast bed condition. During each cycle, the tamping tine first moves towards the ballast, i.e. in the squeezing direction reaching the maximum reaction force at the same time as or followed by the maximum tine elongation. As the process continues within one squeezing movement an increase of the maximum reaction force with each cycle is expected as the ballast compaction progresses. Reaction force measured in every cycle (= ballast reaction force) is taken as an indicator for the switch condition (trigger F_{max}) between the two contact operating phases (Chapter 5.4.2), as well as the indicator to mark the beginning of the loading phase ($F \neq 0$).

2. Tine oscillation displacement and maximum elongation (amplitude) - movement of the tamping tine (x_{tine}) and its exact position in regard to the ballast matrix (in contact or contactless) can be observed in every load-displacement curve. Previous research conducted by *Fischer* [59] has proven that the optimum amplitude for clean ballast compaction is between 4 and 5 mm. Tine oscillation displacement provides information about the exact position of the tine during contact beginning and end, thus giving information about the pulse duration, i.e. the duration of tamping tine-ballast matrix contact during one cycle. Pulse duration has to be kept between certain limits in order for the energy to be successfully transferred between the tine and the ballast matrix (Chapter 5.5).

Die approbierte gedruckte Originalversion dieser Dissertation ist an der TU Wien Bibliothek verfügbar.
The approved original version of this doctoral thesis is available in print at TU Wien Bibliothek.
TU Bibliothek Your knowledge hub WIEN

3. Compaction energy transferred - calculated from every cycle as the area within the load-displacement curve during tine movement in the squeezing direction (red area, Figure 5.19). Depending on the ballast bed condition the squeezing time and number of squeezing processes conducted on a sleeper varies. Compaction energy is divided by the squeezing time, resulting in a standardized power parameter showing the energy transferred or converted per unit time [J/s] in order to compare measurement results from different locations. Since the amplitude of tine oscillation is kept constant, with the progress of squeezing movement the needed energy to exert the amplitude increases as the degree of compaction or the density index increases. Ideally, the squeezing movement should be carried out as long as an increase of energy between two cycles is observed, assuring at the same time that the reaction force applied does not contribute to fouling of the ballast matrix.

4. Ballast matrix response during tine movement in the squeezing direction (loading response) - ballast matrix response or resistance to compaction during the loading phase is calculated from the inclination of the middle 45% of the load-displacement curve in regard to the y axis or the reaction force F (in detail in Chapter 5.4.1). It is obtained from the ratio of reaction force F to the tine position x_{tine} and has the unit N/m. The ballast matrix loading response does not only provide valuable information about the stiffness of the ballast bed in the direction of the tamping tine motion, but also about both geometrical and material damping from curvature of the diagram in the loading phase. Higher values of the loading response would indicate a higher ballast matrix resistance to compaction.

5. Ballast matrix response during tine movement and against the squeezing direction (unloading response) - similar to the loading response, ballast matrix response during the unloading phase is calculated from the inclination of the middle 45% of the load-displacement curve with regard to the y axis (in detail in Chapter 5.4.1). Positive values of the unloading response indicate that the beginning of tamping tine movement opposite to the squeezing direction approximately corresponds to the maximum measured reaction force, whereas a negative value indicates a significant tamping tine movement in the squeezing direction even after the maximum reaction force has been reached.

6. Beginning of contact - intersection or contact point between the tamping tine and the ballast matrix marked by the sudden increase in the reaction force. The point of contact beginning is expressed in mm as the position of the tamping tine and it shows the moment the tine reaches the ballast. Influenced by many factors (primarily by the squeezing velocity), the contact being point controls the eccentricity of the load-displacement curve around the y axis and the length of tamping tine - ballast matrix contact.

7. Loss of contact - intersection or contact point between the tamping tine and the ballast matrix marked by the drop of reaction force to zero. The point of loss of contact is

Die approbierte gedruckte Originalversion dieser Dissertation ist an der TU Wien Bibliothek verfügbar.
The approved original version of this doctoral thesis is available in print at TU Wien Bibliothek.
TU Bibliothek Your knowledge hub WIEN

the second parameter (next to beginning of contact) needed for the contact duration calculation. It marks the moment (expressed in mm as the position of the tamping tine) where the tine looses contact to the soil and begins its motion in the direction opposite of the squeezing motion.

Additionally, the (total) inclination of the load – displacement curve (Figure 5.20) provides information about the influence of inertial forces on the tamping tines movement and their effect on the consumed energy (in detail in Chapter 5.4.1). A simplified form of the load – displacement curve showing all seven tamping characteristics can be seen in Figure 5.19.

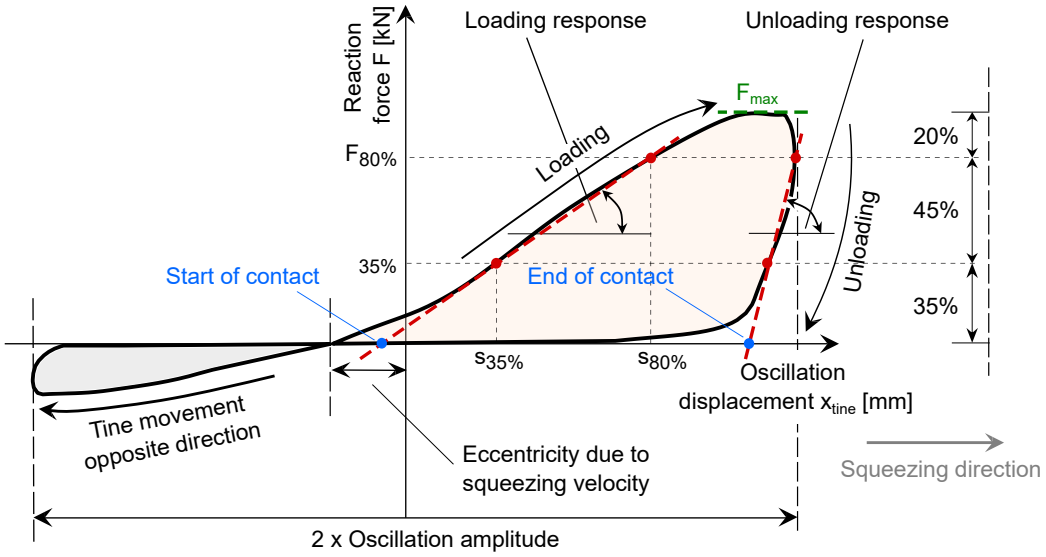

Figure 5.19: Simplified load – displacement curve showing a single tamping tine oscillation and the seven obtained tamping characteristics

Die approbierte gedruckte Originalversion dieser Dissertation ist an der TU Wien Bibliothek verfügbar.
The approved original version of this doctoral thesis is available in print at TU Wien Bibliothek.

5.4.1 Phases of a squeezing process

Phases of a squeezing process can be distinguished based on typical forms of the load-displacement curve (Figure 5.20). During ballast penetration (Figure 5.20a), the tines are vertically lowered into the ballast and the only tine movement is the oscillation with a higher frequency of about 45 Hz that is set in order to facilitate the tine movement and decrease ballast resistance during penetration. The squeezing cylinder remains closed. Typical elliptical shape of the diagram that is observed during ballast penetration is attributed to the asymmetrical shape of the tine (Chapter 4.4.1) and shows a high level of energy consumption needed to execute the ballast penetration.

The load-displacement curve of the tine-ballast matrix interaction during the squeezing movement (Figure 5.20b) is of high importance for attaining the seven tamping characteristics listed in Chapter 5.4. Once the tamping tine has reached the nominal depth underneath the sleeper, movement of the squeezing cylinder is activated and the typical "butterfly" shape of the load-displacement curve can be seen. During the loading phase the reaction force increases until it reaches its maximum and drops steeply during the unloading phase before the contact is lost again. The squeezing movement phase is the part of every squeezing, i.e. tamping process where the ballast compaction and rearrangement takes place and will therefore be the main field of interest during the analysis of the in-situ collected data.

Lifting part of the squeezing process is conducted simultaneously with the opening of the tamping tines, i.e. closing of the squeezing cylinder and has an average duration of approximately five cycles. During this phase, the tines are pulled out of the ballast bed. Similar load-displacement curves are measured during tamping tine oscillation in the air between two squeezing processes, i.e. prior to ballast penetration (Figure 5.20c). The green line in Figure 5.20c presents the total inclination of the load-displacement curve, giving information about the inertial forces acting on the tamping tine. Similar to the inclination of the base line that can be seen in Figure 5.20b, load-displacement curve during lifting or during tine oscillation in the air confirms that the inertial forces are present and have not been compensated. The enclosed area has a very small surface because virtually no energy is transferred from the tamping tine to the ballast matrix. In this 'powerless' phase the measured force acting on the tamping tine is not zero but contains the mass inertia forces, which is why the load-displacement curve runs on the inclined straight green line.

During the tine movement in the air the squeezing velocity is set to zero, and the work required to break the motion of the tamping tine is transmitted via the linkage to the crankshaft and stored in the flywheel mass of the crankshaft, where it is used again to accelerate the tine in the other direction. Due to the small amplitude, the change in angle of the connecting rod is negligible and at each tine position the same force acts once to break and once to accelerate the tine by the same amount. Thus the working diagram is "self-compensating", if the ballast matrix response (obtained from the curve inclination) is related to the slightly inclined load-displacement curve. The same thing applies to the calculation of the area enclosed by the curve giving the compaction energy of every cycle.

Die approbierte gedruckte Originalversion dieser Dissertation ist an der TU Wien Bibliothek verfügbar.
The approved original version of this doctoral thesis is available in print at TU Wien Bibliothek.
TU Bibliothek Your knowledge hub WIEN

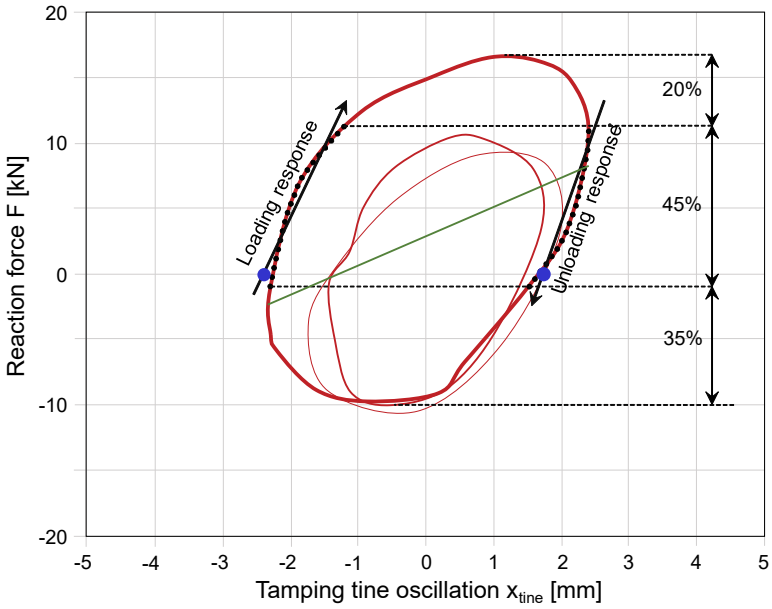

(a) Example of the load-displacement curve during ballast penetration

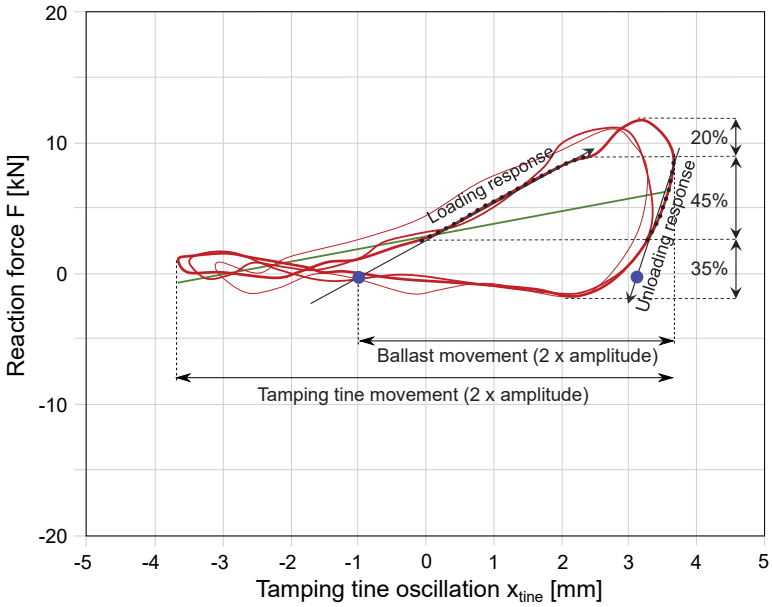

(b) Example of the load-displacement curve during the squeezing movement

Die approbierte gedruckte Originalversion dieser Dissertation ist an der TU Wien Bibliothek verfügbar.
The approved original version of this doctoral thesis is available in print at TU Wien Bibliothek.

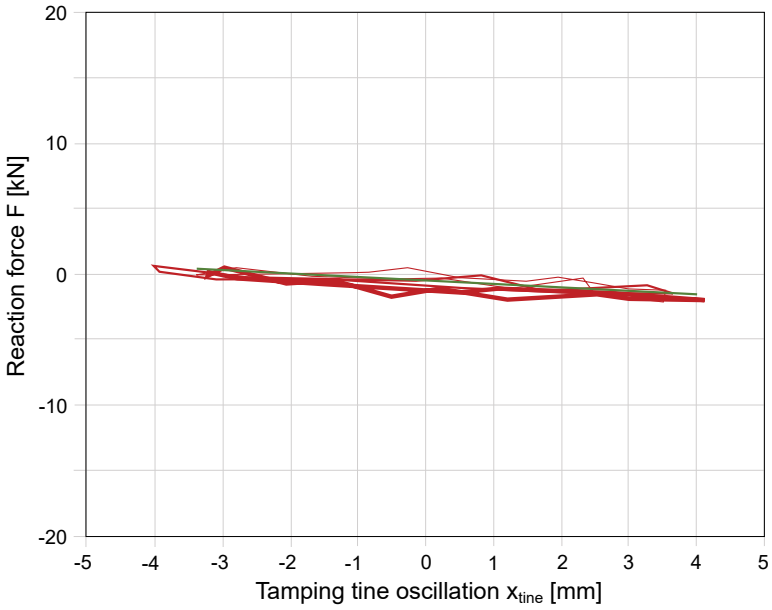

(c) Example of the load-displacement curve during the lifting phase / tamping tine oscillation in the air

Figure 5.20: Examples of the load-displacement curves during different phases of a squeezing process. Three consecutive cycles and the total inclination (green line) of the thickest curve are displayed

5.4.2 Squeezing movement analysis - Operating phases

During one tine oscillation or cycle in the course of the squeezing movement, three phases can be identified (Figure 5.19):

Loading

Starting from a neutral, vertical position, the tine moves towards the ballast, i.e. in the squeezing direction until maximum reaction force is reached, compacting the ballast under the sleeper. As the process continues, an increase of the reaction force with each cycle is expected. Loading response is calculated from the linear approximation of the inclination of the load-displacement curve during this oscillation phase. The inclination of the middle 45% of the curve "height" dependent on the reaction force (all measured values between $F_{35\%}$ and $F_{80\%}$, Figure 5.19) is taken into consideration in order to obtain purposeful values of the loading response from every form of the load-displacement curve. This approach allows a reliable calculation of the response values, consciously avoiding the curve inclination immediately upon start of contact and prior to the turning point of the tine, where most of the outliers, i.e. values that do not belong to the actual course of the curve can be observed. Loading response of the ballast matrix cannot be closely identified to the ballast matrix stiffness, as the curve inclination is also highly influenced by both internal and external damping properties of the ballast matrix. Even though this parameter does not have a real correlation to the ballast stiffness alone, an increase in the loading response during the

Die approbierte gedruckte Originalversion dieser Dissertation ist an der TU Wien Bibliothek verfügbar.
The approved original version of this doctoral thesis is available in print at TU Wien Bibliothek.
TU Bibliothek Your knowledge hub WIEN

squeezing movement can still be considered to be a positive indicator of ballast compaction. Should a decrease in ballast response during loading occur, this could indicate a possible ballast movement away from the tamping tines, i.e. ballast "fluidization", specifically noticeable at higher frequency levels. Furthermore, the intersection point between the linear approximation of the curve inclination and the x axis marks the start of the tamping tine-ballast matrix contact (Figure 5.19 - Start of contact).

Unloading
Tamping tine movement after the maximum reaction force is reached and prior to loss of contact to the ballast matrix is described as the unloading phase of the oscillation. Start of the unloading part of every cycle is defined by a decrease of the measured reaction force and not by change of tine movement direction even though the point of maximum tine elongation and the maximum force usually approximately slot together. This approach is selected due to the fact that, dependent on the ballast condition, the tine can continue its motion in the squeezing direction even after the maximum force has been reached, even to the level that the tine loses contact to the ballast matrix just as the movement in the opposite direction begins. Examples of such load-displacement curves can be seen in Figure 6.4a. The ballast matrix response during unloading is once again calculated from the linear approximation of the curve inclination during unloading, taking only the middle 45% of the load-displacement curve in regard to the y axis dependent on the reaction force (Figure 5.19). Point denoting the end of contact is obtained from the intersection point between the linear approximation of the curve inclination and the x axis (Figure 5.19 - End of contact).

Withdraw
Phase enveloping the tine movement without contact to the ballast matrix. Staring immediately upon end of contact at the end of the unloading phase, the tine reaches back with a maximum elongation/amplitude of $-$4-5 mm and starts its movement in the squeezing direction again. As soon as the contact between the two components during tine movement in the squeezing direction is reinitialized, loading part of the next cycle begins. Depending on the ballast condition and response, the tine can form contact with the ballast with the opposite side of the tamping tine (gray area in Figure 5.19). Continuous contact or a direct switch between loading and unloading phases without loss of contact occurring is also possible but was not observed in-situ.

5.5 Minimum required pulse duration

The eccentricity of the curve regarding the y axis is attributed to the squeezing velocity as well as to the tine shape, where the negative share of the curve would decrease with the increase of velocity, given a constant frequency. However, the squeezing velocity has to be kept between certain limits for the tamping tine to remain in loading contact with the ballast for the time required for the energy to be transferred to the ballast matrix [59]. This minimum required impulse duration t_i is also affected by the amplitude (Figure 5.21) where

Die approbierte gedruckte Originalversion dieser Dissertation ist an der TU Wien Bibliothek verfügbar.
The approved original version of this doctoral thesis is available in print at TU Wien Bibliothek.
TU Bibliothek Your knowledge hub WIEN

with a greater amplitude ($a_2 > a_1$) and a constant frequency and squeezing velocity $v_{squeezing}$ the impulse duration decreases ($t_{i(2)} > t_{i(1)}$). Independent of the amplitude changes, the loading contact length s_i remains unchanged ($s_{i(1)} = s_{i(2)}$) with constant frequency f and can be calculated as [59]:

$$s_i = \frac{v_{squeezing}}{f} \tag{5.2}$$

Pulse duration decreases with increasing frequency. According to *Fischer* [59], the pulse duration for optimum clean ballast compaction should be between 2 and 4 ms for a squeezing velocity of 18 mm/s. As the ballast matrix compaction progresses the pulse duration decreases. As soon as the lower limit for the pulse duration is undershot, the desired rearrangement of the ballast grains is no longer possible, despite potential increase of the reaction force. Increasing the pulse duration prolongs the loading contact duration thus increasing the transferred energy within the cycle, but an increase beyond the upper limit has also been proven to accelerate the process of ballast fouling [59].

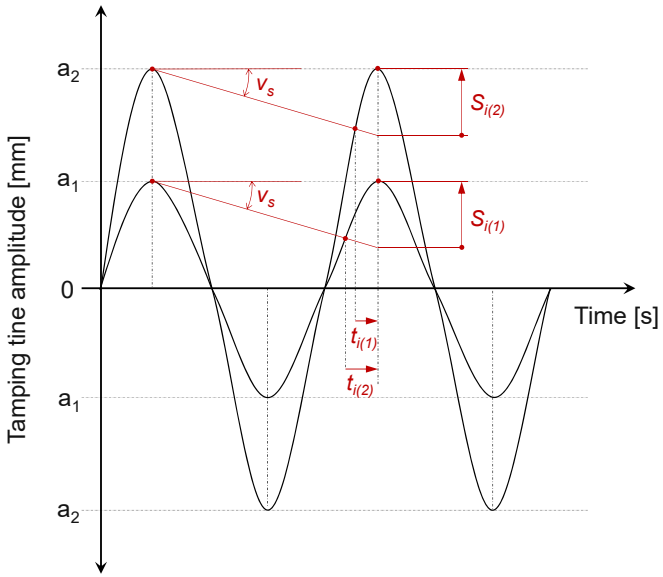

Figure 5.21: Influence of amplitude on the pulse duration [59]

5.6 Final observations

Following the basic experimental research conducted and described in this chapter, a more detailed fundamental research with the possibility to vary several tamping parameters would have been meaningful. Several tests performed at either location on a secondary track with one parameter variation at the time would allow for a detailed parameter study that would provide the necessary missing information:

- identification of influence of squeezing velocity and cylinder pressure on the load-displacement curve and selected tamping characteristics

Die approbierte gedruckte Originalversion dieser Dissertation ist an der TU Wien Bibliothek verfügbar.
The approved original version of this doctoral thesis is available in print at TU Wien Bibliothek.
TU Bibliothek Your knowledge hub WIEN

- difference between multiple and single tamping processes and comparison of selected tamping characteristics between the squeezing processes. Investigation into tamping characteristics when conducting multiple tamping process in moderately fouled and fouled ballast conditions (given that only single tamping process is usually conducted in moderately fouled and fouled conditions)

- detailed investigation of the ballast penetration resistance force and comparison between the squeezing processes as well as between single and multiple tamping processes. Investigation into the exact position (depth) of the tamping tine in the ballast matrix and possible conclusions about the ballast bed conditions

- comparison of the tamping characteristics between locations with different ballast bed conditions outside of regular track maintenance (secondary track) with unchanged tamping parameters such as squeezing pressure, squeezing duration etc. between locations

- investigation of "out of the limits" tamping parameters such as unrealistic high frequency or cylinder pressure levels - observing the influence of different frequency, amplitude and squeezing velocity levels on the tamping characteristics.

Apart from the aspects listed above, additional tests conducted solely for the purpose of investigating the influence of a certain parameter combination on the selected tamping characteristics would provide a possibility to conduct tests in order to compensate the following influences of the machine properties on the load-displacement curves:

- Mass inertia - correct measurement of the squeezing displacement would render the possibility to compensate the inertial forces acting on the tamping tines during operation and exclude their influence on the result gained from the in-situ measurements. The influence can best be seen in Figure 5.20c and is explained in detail in Chapter 5.4.1.

- Tine elasticity - the premise that the tamping tine rotates around the fixed bearing R as the center of rotation is only partially correct. Likewise, the tamping tine is considered to be a infinitely rigid body and its deflection during contact with the ballast matrix (Figure 5.22) has not been taken into consideration. This influence of the tine elasticity on its motion behavior and foremost on the oscillation amplitude should be considered and determined by additional tests.

Investigation of the influence of different tamping parameters was not possible during the monitoring of tamping process in the course of regular track maintenance described in Chapter 6 due to a high number of tamping parameters that were changed between locations.

Die approbierte gedruckte Originalversion dieser Dissertation ist an der TU Wien Bibliothek verfügbar.
The approved original version of this doctoral thesis is available in print at TU Wien Bibliothek.
TU Bibliothek Your knowledge hub WIEN

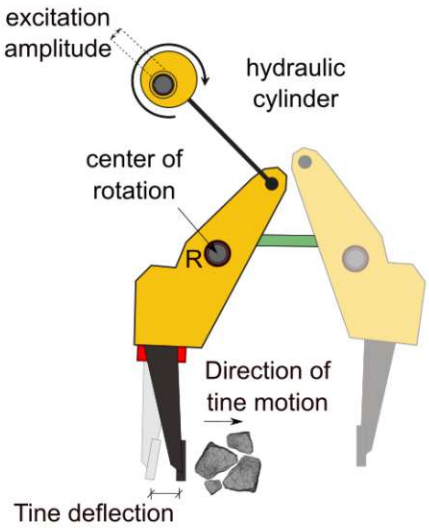

Figure 5.22: Display of the tamping tine deflection and its influence on the tine motion behavior

Die approbierte gedruckte Originalversion dieser Dissertation ist an der TU Wien Bibliothek verfügbar.
The approved original version of this doctoral thesis is available in print at TU Wien Bibliothek.

Die approbierte gedruckte Originalversion dieser Dissertation ist an der TU Wien Bibliothek verfügbar.
The approved original version of this doctoral thesis is available in print at TU Wien Bibliothek.

Chapter 6

Monitoring of tamping process during regular track maintenance

6.1 Introduction

Following the basic experimental research described in Chapter 5, installed sensors and measuring equipment recorded data of over two years of track tamping during regular maintenance and following track reconstruction whereby the process of track tamping was in no way adapted or altered for the purpose of this research project. Measurement data collected was analyzed employing the algorithm presented in the previous chapter using *FAMOS Professional 7.1*. Information about the ballast bed condition for some locations was firstly obtained from the Austrian Federal Railways (*ÖBB*) or rather from the deployment plan of the *Dynamic Tamping Express 09-4X* E^3. The deployment plan provided data about last track maintenance and track reconstruction that are used as a base for ballast bed condition definition. Condition of the ballast bed at remaining locations was firstly defined based on the results of prior conducted track maintenance and reconstruction that are presented in this chapter and subsequently correlated to the data provided by the *ÖBB*, proving the correctness of the ballast bed definition algorithm (in detail in Chapter 6.2).

Ballast aggregate parent rock and source, weather conditions during machine operation, sleeper type, particle size distribution, ballast matrix particle shape and the source of potential ballast fouling were not taken into consideration during data analysis and result interpretation. Only the squeezing movement as a constituent part of every squeezing process was evaluated with the exception of the penetration resistance force that was measured during the ballast penetration phase.

6.1.1 Objectives

Primary objective of the conducted in-situ measurements is to gain an insight into ballast matrix behavior during regular track tamping and into its response to compaction. In addition to the goals defined during the basic experimental research, additional research interests and expected results were defined for the monitoring of tamping process during regular

Die approbierte gedruckte Originalversion dieser Dissertation ist an der TU Wien Bibliothek verfügbar.
The approved original version of this doctoral thesis is available in print at TU Wien Bibliothek.
TU Bibliothek Your knowledge hub WIEN

track maintenance:

- tamping tine oscillation in every cycle during the squeezing movement and the changes of measured tamping characteristics between cycles
- insight into duration of contact between the tamping tine and ballast matrix
- influence of squeezing velocity and squeezing displacement (absolute tine movement) on the ballast matrix behavior
- influence of squeezing pressure on the ballast matrix behavior
- compaction energy, ballast matrix responses during loading and unloading and their influence on the shape of the load-displacement curve
- detection and identification of ballast bed condition
- differences in tamping characteristics and ballast matrix response in different ballast conditions
- possible optimization of the tamping parameters for the given ballast bed condition
- determination of parameters relevant for successful ballast compaction and durability of the track geometry after tamping
- determination of the optimum ballast bed compaction
- detection and interpretation of possible ballast fluidization during the squeezing movement

6.2 Locations of conducted measurements and ballast bed condition definition

Extensive amount of data was attained during standard tamping machine employment on altogether 12 locations (Figure 6.1, Table 6.1) of the Austrian Federal Railways (*ÖBB*) main network with different tamping parameter settings and ballast conditions. Single and double squeezing processes on more than 10.000 sleepers are evaluated and the evaluation results are presented in the following chapters.

Regarding ballast bed condition classification, two borderline cases are encountered on majority of locations. In correlation with the Fouling index FI_D definition (Table 3.1, Chapter 3.2.2), ballast bed condition is defined as follows:

- Track reconstruction - tamping of newly constructed lines to avoid temporary speed restrictions that are normally imposed after reconstruction in order to allow initial settlements to take place. Ballast bed can be described as *clean*, characterized by high specific gravity, bigger particle size, higher particle angularity, rough surface and a high void ratio.

Die approbierte gedruckte Originalversion dieser Dissertation ist an der TU Wien Bibliothek verfügbar.
The approved original version of this doctoral thesis is available in print at TU Wien Bibliothek.
TU Bibliothek Your knowledge hub WIEN

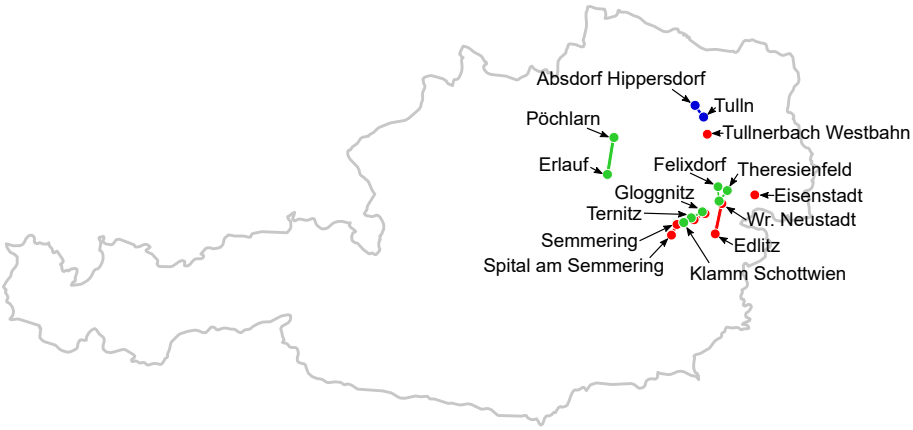

Figure 6.1: Locations of recorded track maintenance conducted by the *Dynamic Tamping Express 09-4X* E^3 in Austria. Locations with *clean* ballast conditions are presented in green, *moderately clean* in blue and *fouled* conditions in red color

– Track 6 weeks after reconstruction - ballast bed has experienced initial consolidation and fouling in form of low level particle abrasion and attrition, causing minor changes of the particle size distribution. Ballast bed condition is described as *moderaltey clean*.

– Track maintenance - ballast bed compaction during regular track maintenance in order to minimize the deterioration of track geometry and improve track stability. Ballast bed can be described as *fouled*, characterized by smaller particle sizes, excessive amount of fine particles filling the voids, lower angularity, higher bulk density and higher degree of compaction. Strong frictional contact between ballast particles is reduced and replaced by weaker frictional contact between the ballast and/or fouling particles.

Classification of *moderately clean* and *fouled* ballast described is not based on conducted particle size distribution and particle shape analysis, but rather on information provided by the *ÖBB* based on traffic loads and frequency of conducted track maintenance. This ballast bed condition definition is later on supported by specific tamping characteristics obtained from the statistical analysis and additionally confirmed by visual in-situ interpretation.

Ballast condition determination stated in Table 6.1 is a result of a "blind tasting" - the analysis algorithm described in Chapter 5 and further developed and construed in this chapter was given measurement data of initially unknown origin. Results, i.e. values of decisive tamping characteristics are compared to the definition of ballast bed condition given in Chapter 6.5 and an effort was made to determine the ballast bed condition based on these values. The hit rate after correlation with ballast condition data provided by the *ÖBB* was 100%, and it was not only possible to distinguish between *fouled* and *clean* ballast, but also to clearly identify intermediate grades (in detail in following chapters).

Die approbierte gedruckte Originalversion dieser Dissertation ist an der TU Wien Bibliothek verfügbar.
The approved original version of this doctoral thesis is available in print at TU Wien Bibliothek.
TU Bibliothek Your knowledge hub WIEN

Table 6.1: Ballast bed condition and locations of conducted measurements

Condition	Location / Route
track reconstruction *clean ballast*	Felixdorf - Wiener Neustadt Theresienfeld - Wiener Neustadt Gloggnitz - Ternitz Klamm Schottwien Pöchlarn - Erlauf
tamping conducted 6 weeks after track reconstruction *moderately clean ballast*	Tulln - Absdorf Hippersdorf
track maintenance *fouled ballast*	Ternitz-Gloggnitz Eisenstadt Wiener Neustadt - Edlitz Wiener Neustadt Semmering - Spital am Semmering Tullnerbach Westbahn

6.3 Measurement procedure and documentation

The substantial amount of recorded signals and information about the tracks at each measurement location were documented in a protocol and can be divided into following three groups:

1. Route information
   (a) track
   (b) kilometer
   (c) traffic load pear year
   (d) line speed
   (e) curve radius
   (f) rail profile
2. Signals obtained from additionally applied sensors (Chapter 5.3.1)
   (a) penetration resistance force at the tine plate
   (b) reaction force at the tine plate
   (c) squeezing displacement
   (d) acceleration at the tine plate (local coordinate system, Figure 5.6)
3. Signals and information recorded routinely during track maintenance
   (a) lowering position of the tamping unit

Die approbierte gedruckte Originalversion dieser Dissertation ist an der TU Wien Bibliothek verfügbar.
The approved original version of this doctoral thesis is available in print at TU Wien Bibliothek.
TU Bibliothek Your knowledge hub WIEN

(b) cylinder pressure / squeezing pressure

(c) lowering pedal - signal given by the machine operator in order to initiate the tamping process

(d) number of squeezing processes on every sleeper

(e) lifting values

(f) date and time

(g) GPS signal (longitude, latitude, height)

For the purpose of this research project, this list is additionally extended by the data obtained from the *ÖBB-Infrastruktur AG* and the Institute of Railway Engineering and Transport Economy at TU Graz such as sleeper type, rail installation year, sleeper installation year, rail steel grade and information about installations (stations, bridges, turnouts, railway crossings, tunnels).

6.3.1 Data analysis and documentation

A stable and reliable algorithm for data analysis, graphical and statistical evaluation is developed, allowing an overview of every measurement as a whole (locations listed in Table 6.1) but also separately storing needed information about every tamping and constitutive squeezing process, as well as about every single conducted tine oscillation, i.e. cycle. Given the considerable volume of collected data, emphasis is put on transparency and efficiency of data analysis and storing. Following system of evaluation and recording was developed for every conducted measurement:

– Statistical analysis of tamping characteristics:

1. Spreadsheets with average values of all 13 selected characteristics (Table 6.2) for the entire length of each route
2. Box plot diagram analysis (Chapter 6.5.3) of selected tamping characteristics:
   (a) maximum reaction force per cycle
   (b) energy per cycle
   (c) loading response
   (d) contact point beginning (start of contact)
   (e) cylinder pressure
   (f) maximum penetration resistance force

– Graphical analysis of the squeezing movement as a whole:

1. Tamping characteristics during every tamping process, including: tamping process subdivision triggers, energy per cycle, energy per squeezing process, tamping tine oscillation, oscillation frequency, reaction force and squeezing displacement (Figure 6.2)

Die approbierte gedruckte Originalversion dieser Dissertation ist an der TU Wien Bibliothek verfügbar.
The approved original version of this doctoral thesis is available in print at TU Wien Bibliothek.
TU Bibliothek Your knowledge hub WIEN

2. Load-displacement curves for every cycle during all three phases of the tamping process.
3. Waterfall diagrams of every squeezing movement (Figure 6.24)
4. Heat maps of every squeezing movement (Figure 6.25)

– Detailed overview and description of every tamping process in form of *Microsoft Excel* spreadsheet

1. General information (date, time, GPS coordinates, number of squeezing processes)
2. Route information (route, track, kilometer, traffic load per year, line speed, curve radius, sleeper type, rail profile)
3. Lifting and lining values
4. Tamping process direct information (squeezing cylinder pressure, squeezing velocity, motor flow rate and energy consumption)
5. Tamping process calculated characteristics (energy consumption per cycle and per squeezing process phase, loading and unloading response per cycle, squeezing time)

Every dataset is stored under a corresponding name consisting of the measurement location, tamping process number, date, time and kilometer, enabling a quick insight into all stored tamping process information, as well as a correlation with the conducted statistical and graphical analysis.

6.4 Tamping process evaluation

Prior to tamping, the track is aligned and lifted to a predefined position. The void created under the sleepers as the track is lifted is predetermined by the extent of track deterioration given by lifting values. Given that ballast penetration is conducted with a higher frequency in comparison to the squeezing movement (Chapter 5.3.3), the rearrangement of ballast particles due to the reduction of the interlocking friction between the grains is facilitated. However, given the fact that the grains are only rearranged around the tines and not under the sleepers this does not significantly improve track stability and has no influence on the improvement of track geometry. For the reasons stated above, main focus of the measuring data analysis was on the squeezing movement.

In the scope of this research project data describing approximately 10.000 tamping processes are analyzed and subdivided according to track maintenance locations (Table 6.1). Obtained results are compared based on selected tamping characteristics listed in Table 6.2. In addition to characteristics analysis, load-displacement curves for every phase of a squeezing process are plotted together with an overview containing the tamping process subdivision and triggering signals, energy, reaction force and excitation frequency (Figure 6.2). Moreover, waterfall diagrams (Chapter 6.5.4.1) containing consecutive load-displacement curves during the squeezing movement and heat maps (Chapter 6.5.4.2) showing the progress

Die approbierte gedruckte Originalversion dieser Dissertation ist an der TU Wien Bibliothek verfügbar.
The approved original version of this doctoral thesis is available in print at TU Wien Bibliothek.
TU Bibliothek Your knowledge hub WIEN

of reaction force, contact points and the tine displacement are plotted, providing detailed graphical and statistical analysis of the collected data.

6.4.1 Detection and identification of ballast condition

Over time, ballast bed void ratio and permeability decrease as the voids are filled by smaller particles that are either the result of particle breakdown due to mechanical traffic loading forces or come from external sources (Chapter 3). Single ballast grains forming the ballast bed experience change in shape, angularity and surface structure which causes a significant decrease of ballast bed internal friction angle, shear strength and overall stability. As mentioned before, the data provided by the *ÖBB* based on traffic loads and frequency of conducted track maintenance and the deployment plan of the *Dynamic Tamping Express 09-4X E^3 Plasser & Theurer* track tamping machine were used to confirm conclusions regarding the ballast bed condition ("blind tasting", Chapter 6.2). During analysis of measurement data collected in the course of regular track maintenance in 2016 and 2017 it was proven that the load-displacement curve, or rather the tamping characteristics obtained from it, can be used as a reliable indicator of different ballast bed conditions. The form of the curve as well as four selected tamping characteristics showed a 100% accordance to the data provided by the *ÖBB* and the deployment plan of the *Dynamic Tamping Express 09-4X E^3* track tamping machine.

Typical representatives for *clean*, *moderately clean* and *fouled* ballast bed are selected among the locations presented in Table 6.1 and were subjected to a detailed analysis. Analysis results are discussed in the following chapters. Following locations are selected:

- Track reconstruction (*clean* ballast) - *Theresienfeld - Wiener Neustadt* (tamping process on 930 sleepers analyzed)
- Tamping was performed 6 weeks after track reconstruction (*moderately* clean ballast) - *Tulln - Absdorf Hippersdorf* (tamping process on 757 sleepers analyzed)
- Track maintenance (*fouled* ballast) - *Ternitz-Gloggnitz* (tamping process on 392 sleepers analyzed)

It is standard practice in track tamping to adjust the number of squeezing processes per tamping process to the track conditions and geometry. In *clean* ballast conditions (tamping following track reconstruction) the optimum results in all measurements analyzed for this thesis are achieved by a double squeezing process (duration 2·0.6 s) due to the fact that the ballast grains lay in a loose position and have not yet experienced any consolidation or settlements. Ballast matrix elevation under the sleeper in *fouled* ballast bed or hard bedding is conducted by a single tamping process with a duration of 0.8-1.2 s.

Die approbierte gedruckte Originalversion dieser Dissertation ist an der TU Wien Bibliothek verfügbar.
The approved original version of this doctoral thesis is available in print at TU Wien Bibliothek.
TU Bibliothek Your knowledge hub WIEN

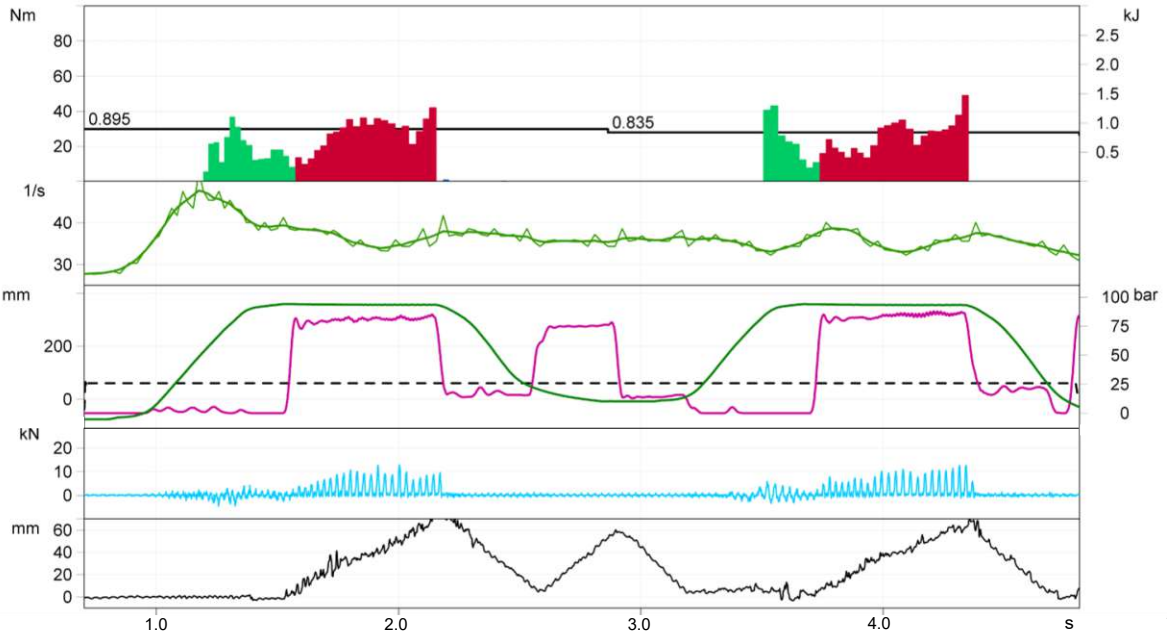

(a) Tamping process overview - *clean* ballast, double tamping process

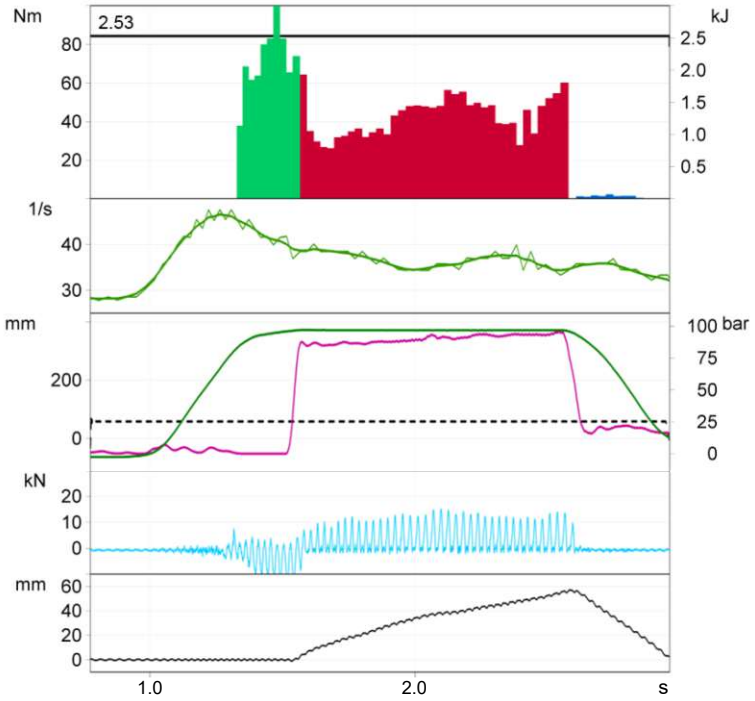

(b) Tamping process overview - *moderately clean* ballast, single tamping process

Die approbierte gedruckte Originalversion dieser Dissertation ist an der TU Wien Bibliothek verfügbar.
The approved original version of this doctoral thesis is available in print at TU Wien Bibliothek.

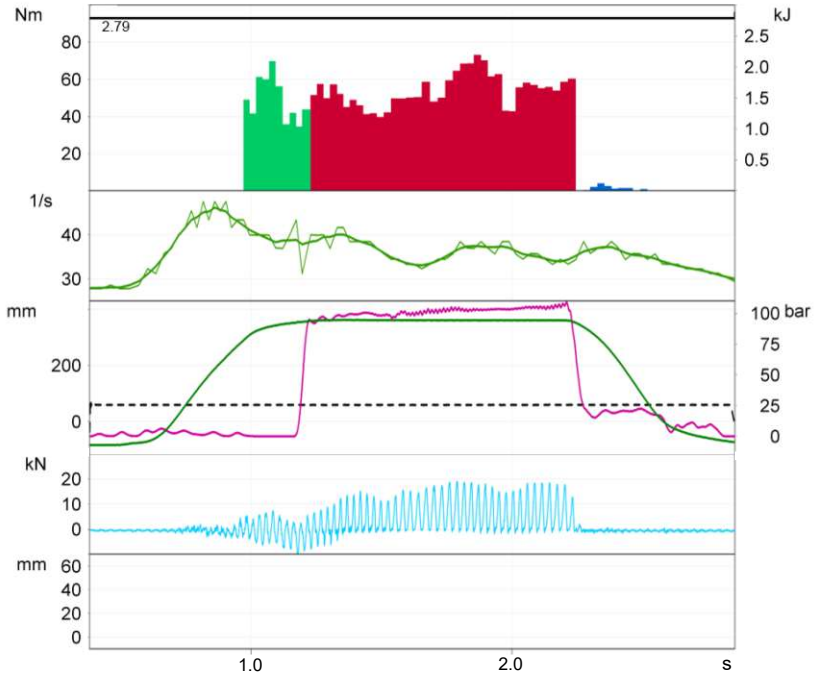

(c) Tamping process overview - *fouled* ballast, single tamping process[a]

[a] squeezing displacement not shown due to a sensor malfunction

Figure 6.2: Examples of tamping process in overview. Presented are the consumed energy per cycle (subdivided into phases: ballast penetration - green, squeezing movement - red, lifting - blue) [Nm] and per tamping process [kJ], frequency (raw and smooth) [Hz], lowering position of the tamping unit [mm] (green line), pressure in the hydraulic cylinder [bar] (pink line), position of the lowering pedal (dashed line) and the reaction force [kN], respectively, for all three measured ballast bed conditions

Die approbierte gedruckte Originalversion dieser Dissertation ist an der TU Wien Bibliothek verfügbar.
The approved original version of this doctoral thesis is available in print at TU Wien Bibliothek.

6.5 Squeezing movement evaluation

As mentioned before, main focus of interest during data analysis is given to the squeezing movement, being the part of the squeezing process in which the rearrangement and elevation of ballast grains as well as a ballast matrix compaction under the sleeper takes place. Squeezing movement is initiated as the tines complete ballast penetration and the top of the tamping tine plate reaches the predetermined depth (13-30 mm) under the sleeper bottom edge [64]. Tamping tines execute an absolute closing movement towards the sleeper and a relative one by tine oscillation. Ballast matrix grains are pushed up to fill the void under the sleeper providing desired track elevation by the absolute movement of the tamping tines and at the same time rearranged into a uniformly compacted matrix that provides the desired track stability by the relative tine movement (oscillation). Energy transmitted to the ballast matrix during the squeezing movement is utilized for ballast compaction by setting the ballast grains into a *visco-fluid* motion (in detail in Chapter 7). Detailed data analysis with a special emphasis on the tamping characteristics of the squeezing movement recorded during track maintenance in three different track conditions is presented in the following chapters.

6.5.1 Load-displacement curve in different ballast bed conditions

Following a successful tamping process subdivision (Chapter 5.3.3), the squeezing movement was additionally subdivided into its integral components - cycles. Every cycle of tamping tine oscillation is presented in a form of a load-displacement curve and utilized for the calculation of tamping characteristics (Chapter 5.4). As the described process of ballast fouling progresses, ballast matrix behavior and response during contact to the tamping tine change, resulting in different shapes of the load-displacement curves in dependence on ballast condition.

Characteristic load-displacement curves for all three measured ballast bed conditions (Chapter 6.4.1) are plotted in Figure 6.4 and for a direct comparison in Figure 6.3. Clear distinction between individual ballast bed conditions and the influence of ballast fouling process on the shape of the load-displacement curve as well as on the tamping characteristics selected and are discussed in Chapter 6.5.2. Apart from the changes caused by earliest effects of ballast fouling, differences between *clean* and *moderately clean* ballast are additionally emphasized by initial settlements and consolidation due to traffic loads. *Fouled* ballast bed forms a hard bedding with higher relative density as well as higher bedding modulus value. As the fouling process progresses, significantly higher force is needed to implement the tine relative motion which results in significantly higher compaction energy required. Fouling progress has also been proven to influence the response of ballast matrix during both loading and unloading stages of the cycle. The differences can be detected in curve inclination in Figure 6.4 - loading response increases as the fouling progresses resulting in significantly higher values in *fouled* ballast conditions confirming the increase of effective ballast bed stiffness.

Die approbierte gedruckte Originalversion dieser Dissertation ist an der TU Wien Bibliothek verfügbar.
The approved original version of this doctoral thesis is available in print at TU Wien Bibliothek.
TU Bibliothek Your knowledge hub WIEN

Apart from the reaction force, energy and loading response values, several other conclusions can be drawn from the typical load-displacement curve representatives for different ballast conditions plotted in Figure 6.4. Shape of the load-displacement curve in the unloading phase defines the unloading response value. It can be seen in Figure 6.4 that with the progress of ballast fouling the reaction force increases, the "belly shape" form in the unloading phase progressively changes its sign i.e. inclination as the point of contact loss simultaneously shifts to the left. In *fouled* ballast the tine movement in the direction opposite to squeezing begins almost immediately after the maximum reaction force has been reached. In comparison, in *clean* ballast the tine motion in the squeezing direction continues after the maximum reaction force is reached and the loss of contact occurs simultaneously with tine motion direction change. It should once more be stated that the position of the both contact points is determined as the intersection of the loading and unloading response lines with the x axis, meaning that the points can theoretically also be positioned outside the tine maximum elongation. Following this approach, the contact points would have the highest (absolute) value for *clean* ballast conditions, which can be seen in Figure 6.5.

Amplitude of the tamping tine is kept constant at 4-5 mm independent of the ballast condition. These exact values cannot always be achieved during contact to the ballast matrix. Figure 6.3 shows a reduction in the maximum tine elongation with advancement of ballast fouling.

Significant differences in tamping characteristics are confirmed by a detailed statistical analysis and presented in the next chapter.

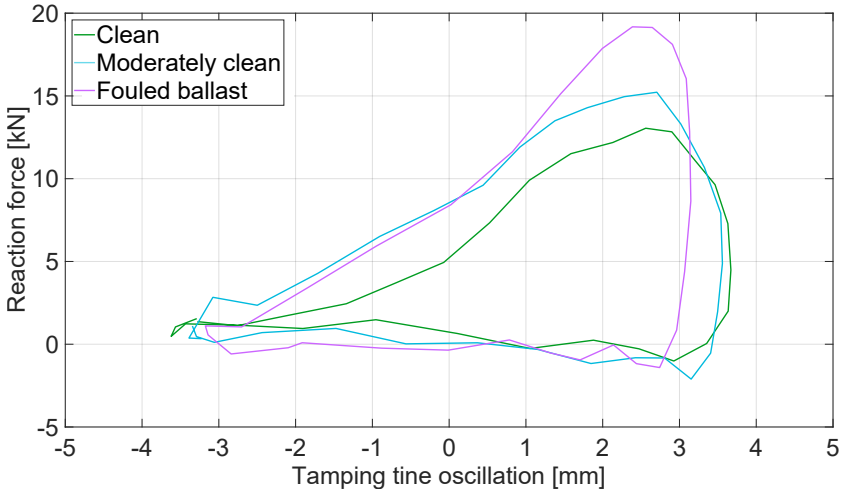

Figure 6.3: Comparison of characteristic load-displacement curves for three different ballast bed conditions

Die approbierte gedruckte Originalversion dieser Dissertation ist an der TU Wien Bibliothek verfügbar.
The approved original version of this doctoral thesis is available in print at TU Wien Bibliothek.

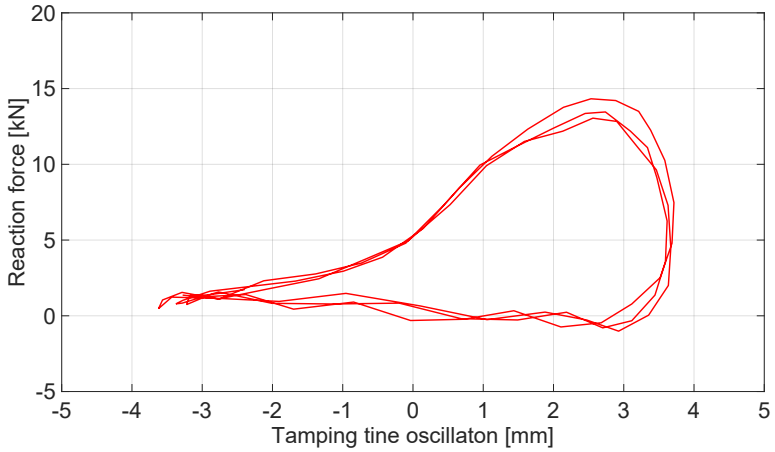

(a) Three consecutive load-displacement curves during *clean* ballast bed compaction

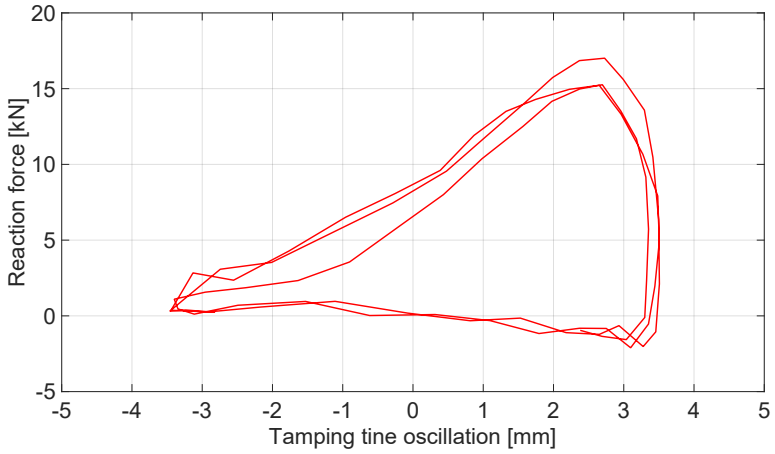

(b) Three consecutive load-displacement curves during *moderately clean* ballast bed compaction

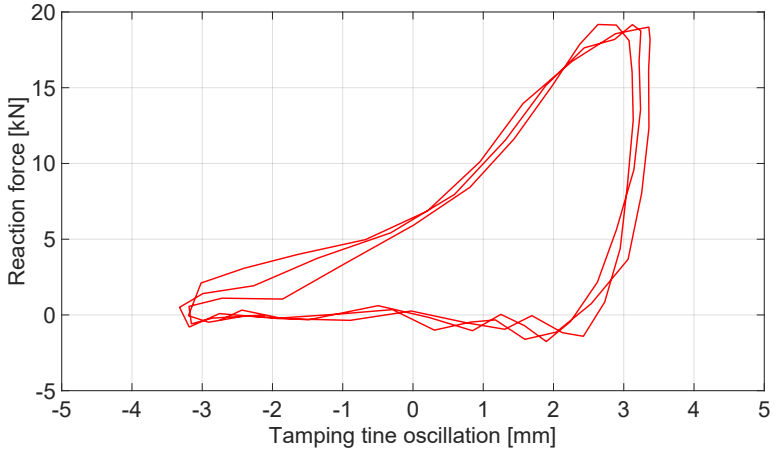

(c) Three consecutive load-displacement curves during *fouled* ballast bed compaction

Figure 6.4: Characteristic load-displacement curves for three different ballast conditions

Die approbierte gedruckte Originalversion dieser Dissertation ist an der TU Wien Bibliothek verfügbar.
The approved original version of this doctoral thesis is available in print at TU Wien Bibliothek.

6.5.2 Statistical tamping characteristics analysis

Detailed study on eleven tamping characteristics listed in Table 6.2 is conducted for every measurement, giving decisive values for all first and/or second squeezing movements of a tamping process conducted on a sleeper. All of the listed characteristics (except for the penetration resistance force) are obtained from load-displacement curves as described in Chapter 5.4.

Table 6.2: Calculated and analyzed tamping characteristics

Tamping characteristic	Unit
Maximum reaction force per cycle	[kN]
Compaction energy per cycle	[J]
Transferred energy per SM per unit time	[J/s]
Duration of the squeezing movement	[s]
Squeezing velocity	[mm/s]
Ballast matrix response during loading	[MN/m]
Ballast matrix response during unloading	[MN/m]
Total inclination of the load-displacement curve	[MN/m]
Start of contact (1^{st} contact point)	[mm]
End of contact (2^{nd} contact point)	[mm]
Penetration resistance force[1]	[kN]

[1] only characteristic measured during ballast penetration phase

Average values of the eleven tamping characteristics measured in all three ballast bed conditions can be seen in Table 6.3 and in Figure 6.5. Some of the listed characteristics are a direct result of the parameter setting selected by the machine operator - the non-synchronous constant pressure tamping principle of the *Dynamic Tamping Express 09-4X E*[3] tamping machine dictates that once the required squeezing force is reached, i.e. the ballast resistance to compaction increases to the set tamping pressure value, movement of the corresponding tamping tine pair stops squeezing automatically. Desired result of the conducted statistical analysis is to recognize tamping characteristic(s) that can be used as reliable ballast condition indicator(s) and should as such be mainly dependent on the ballast bed resistance to the imposed tamping tine movement and not only on the selected tamping parameters. Maximum reaction as well as the penetration force are both expected to increase with the progress of ballast fouling independent of the tamping parameters, which was confirmed by the analysis (Figure 6.5). Same can be said for the loading and unloading response of the ballast matrix and the calculated energy. Motion of the tamping tine that can be interpreted from the tine-ballast contact points indicates a decrease in absolute contact duration value as the ballast bed resistance, indicated by the fouling level, increases. This observation should, however, be additionally inspected under constant squeezing pressure conditions.

In the next step, all of the in-situ collected data from location listed in Table 6.1 were analyzed and the effort was made to correlate tamping characteristics between different

Die approbierte gedruckte Originalversion dieser Dissertation ist an der TU Wien Bibliothek verfügbar.
The approved original version of this doctoral thesis is available in print at TU Wien Bibliothek.
TU Bibliothek Your knowledge hub WIEN

ballast bed conditions and tamping parameters settings in order to single out ones that can be used to describe the ballast condition, even if the tamping parameters are altered.

Table 6.3: Tamping characteristics measured in different ballast conditions

Tamping characteristic	Unit	Clean ballast	Mod. clean ballast	Fouled ballast
Max. reaction force	[kN]	11.28 / 12.28	14.95	19.78
Energy per cycle	[J]	21.24 / 23.77	35.60	52.06
Energy per SM / time	[J/s]	858.17 / 1050.37	1365.23	1978.51
SM duration	[s]	0.65 / 0.64	1.06	1.04
Squeezing velocity	[mm/s]	99.89 / 78.55	61.68	x[1]
Loading response	[MN/m]	0.85 / 1.23	1.84	2.15
Unloading response	[MN/m]	-11.29 / -13.64	-18.50	16.82
Total inclination	[MN/m]	0.07 / 0.19	0.42	1.11
Start of contact	[mm]	-5.51 / -4.21	-3.89	-3.34
End of contact	[mm]	3.65 / 3.35	2.61	2.35
Max. penetration force	[kN]	11.47 / 12.02	13.05	15.72

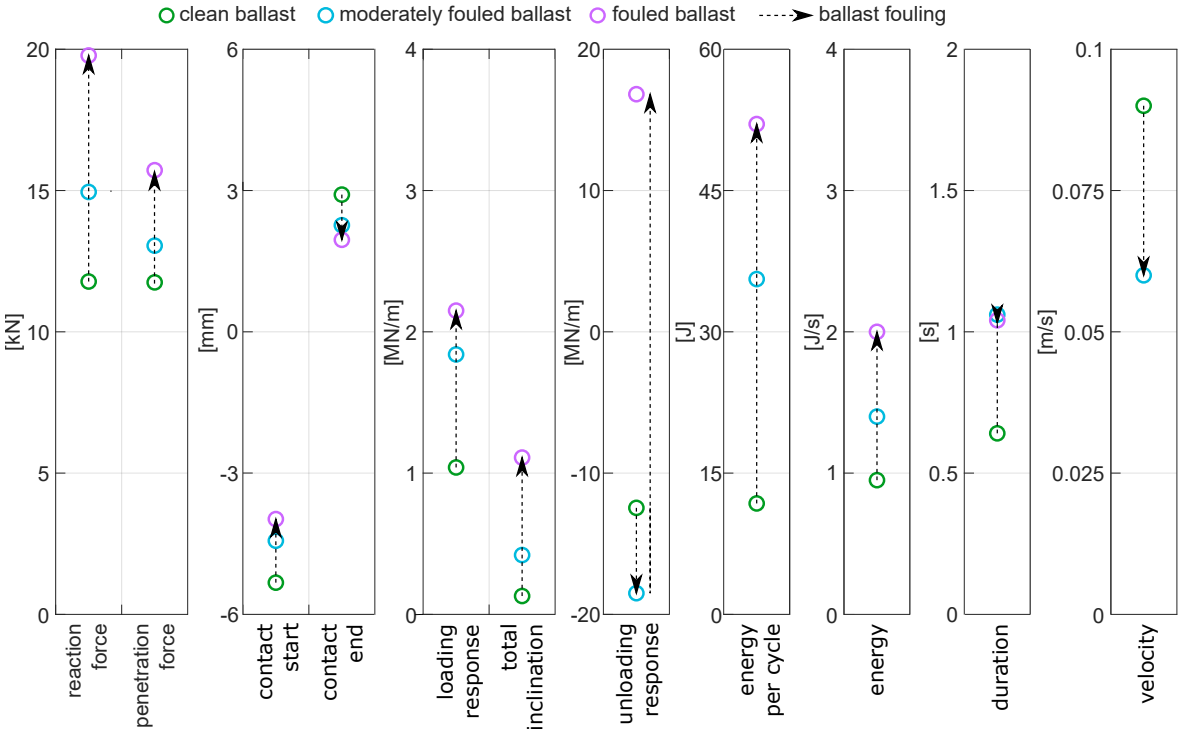

Figure 6.5: Overview of all tamping characteristics presented in Table 6.3 and comparison between ballast conditions

[1] malfunctioning sensor

Die approbierte gedruckte Originalversion dieser Dissertation ist an der TU Wien Bibliothek verfügbar.
The approved original version of this doctoral thesis is available in print at TU Wien Bibliothek.

Following statistical analysis of the selected tamping characteristics recorded at all analyzed locations listed in Table 6.1, it has been proven that the condition of the ballast bed can be interpreted from a back analysis based on the following four characteristics:

- Maximum reaction force per cycle - values significantly increase with the progress of ballast fouling process. Highest values are measured during *fouled* ballast compaction.
- Energy per squeezing movement - reaction force has a direct influence on the total transferred compaction energy during a squeezing movement that approximately doubles in value, if comparing *fouled* and *clean* ballast conditions.
- Loading and unloading response - different values of ballast matrix response to compaction dependent on the ballast condition is additionally confirmed by the shape of the load-displacement diagrams, showing changes in ballast behavior and movement during and between cycles. Highest values of the loading response are measured during *fouled* ballast compaction. The unloading response governs the shape of the curves in the unloading phase and changes from a negative to a positive value as the fouling of the ballast bed progresses.

Ranges of characteristic values for the four tamping characteristics in clean and fouled ballast conditions are listed in Table 6.5.

Table 6.4: Characteristic values for the four tamping characteristics in both reference ballast conditions. Values for the *clean* ballast are presented for the first and second squeezing movement respectively

Tamping characteristic	Unit	Value	
		Clean ballast	Fouled ballast
Maximum reaction force per cycle	[kN]	11.28 / 12.28	19.78
Energy per SM per unit time	[kJ/s]	0.86 / 1.05	2.0
Loading response	[MN/m]	0.85 / 1.23	2.15
Unloading response	[MN/m]	-11.29 / -13.64	16.82

Table 6.5: Ranges of characteristic values for the four tamping characteristics in both ballast conditions for all analyzed locations

Tamping characteristic	Unit	Value range	
		Clean ballast	Fouled ballast
Maximum reaction force per cycle	[kN]	9.0 – 13.0	15.0 – 20.0
Energy per SM per unit time	[kJ/s]	0.85 – 1.2	1.6 – 2.1
Loading response	[MN/m]	0.85 – 1.9	2.0 – 2.8
Unloading response	[MN/m]	-16.0 – -10.0	11.0 – 18.0

Four selected taping characteristics of the measurements preformed at the location *Tulln - Absdorf Hippersdorf* in *moderately clean* ballast conditions show a level of divergence in comparison to other *clean* ballast locations, and indicate the initial progress of the ballast fouling

Die approbierte gedruckte Originalversion dieser Dissertation ist an der TU Wien Bibliothek verfügbar.
The approved original version of this doctoral thesis is available in print at TU Wien Bibliothek.
TU Bibliothek Your knowledge hub WIEN

process (Table 6.6). Collected data can be used as an additional confirmation of the characteristic values for the two edge cases, i.e. of changes in characteristic values with the progress of ballast fouling.

Table 6.6: Characteristic values of the selected tamping characteristics. Track tamping conducted 6 weeks after track reconstruction

Tamping characteristic	Unit	Value
Maximum reaction force per cycle	[kN]	14.95
Energy per SM per unit time	[kJ/s]	1.36
Loading response	[MN/m]	1.84
Unloading response	[MN/m]	-18.50

The outlined values, presented in an overview in Figure 6.6, are not only used to clearly indicate ballast bed condition at every location, but can also be utilized in the development of a *ballast condition sensor*, where the level of ballast bed fouling is recognized by the tamping machine and the tamping parameters are modified accordingly. This would provide the possibility to perform track maintenance with the highest level of efficiency and reduce intervals between two maintenance measures by keeping the track within the tolerance ranges for track design as long as possible.

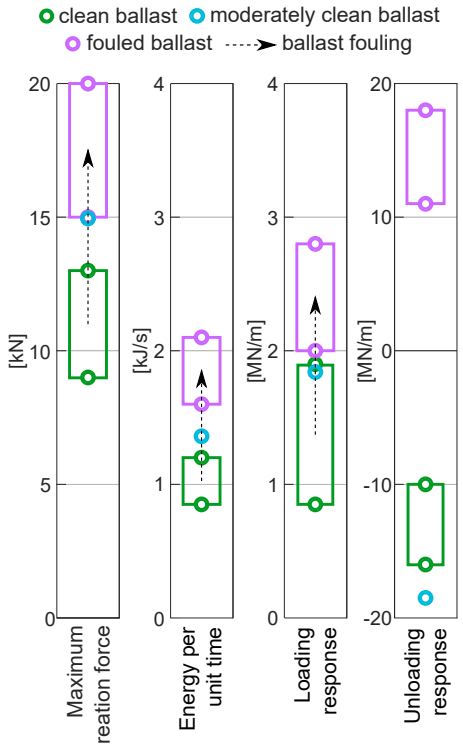

Figure 6.6: Ranges of values for the four tamping characteristics and comparison between ballast conditions for all analyzed locations

Die approbierte gedruckte Originalversion dieser Dissertation ist an der TU Wien Bibliothek verfügbar.
The approved original version of this doctoral thesis is available in print at TU Wien Bibliothek.

6.5.3 Statistical analysis - box plot diagrams

6.5.3.1 Theory of box plots

Succeeding an entire data set analysis results are also plotted in form of box plot (also called box-and-whisker plot) diagrams. Box plots are mainly used in descriptive statistics as a method for graphically displaying groups of numerical data through their quartiles which divide the given data set into fourths, where the median[2] and quartiles divide a row of values into four groups of equal size. They are particularly useful for comparing distributions between data groups, in this case in-situ collected data from various locations (Table 6.1).

Box plot diagram, as can be seen in Figure 6.7 [58], displays:

1. Full range of variation within the dataset (difference between the lowest value and the highest value)
2. Likely range of variation called the *interquartile range* or IQR, ranging between the first quartile Q_1 and the third quartile Q_3, presented by a rectangular *box*
3. Median, presenting the second or middle quartile Q_2, separating the higher half of a data sample from the lower half
4. Whiskers, showing the upper and lower adjacent values of the dataset, extending from Q_1 and Q_3 in the direction of the dataset maximum and minimum before fences. Depending on the selected approach, whiskers can be extended and can replace the fences, as was done in the dataset analysis that follow in Chapter 6.5.3.3
5. Fence, upper and lower fences are defined in order to identify possible outliners using the IQR and equations $Q_3 + 1.5 \cdot IQG$ for the upper and $Q_1 - 1.5 \cdot IQG$ for the lower fence, thus fixing the fence value at $1.5 \cdot IQR$ above and below the box, respectively
6. Outliners are defined as values beyond the fences and usually display an error in the collected data, numerically distant from the rest of the data. In the calculation made for the dataset analysis shown in the next chapters, outliners are defined as all values that are located outside the whiskers and are not presented in the diagrams.
7. Average value, calculated as arithmetic mean of the dataset without outliners, presented with a x symbol. The trend of average values between the boxes in a single box plot diagram is presented by a thick black line.

Distribution of the analyzed dataset defines the form of the diagram, resulting in a symmetric or an asymmetric box plot, as can be seen in Figure 6.8. For a dataset with a normal distribution the values generate a box plot with symmetric shape, the position of the line identifying the median is in the middle of the box and the whiskers have the same size in length. An asymmetric distribution would generate a box plot with a median line moved

[2]Middle value in a row of data in ascending order, commonly used as a measure of central tendency of a set of observations. The median divides the data in two, 50% of the values is lower than the median and 50% higher than the median.

Die approbierte gedruckte Originalversion dieser Dissertation ist an der TU Wien Bibliothek verfügbar.
The approved original version of this doctoral thesis is available in print at TU Wien Bibliothek.
TU Bibliothek Your knowledge hub WIEN

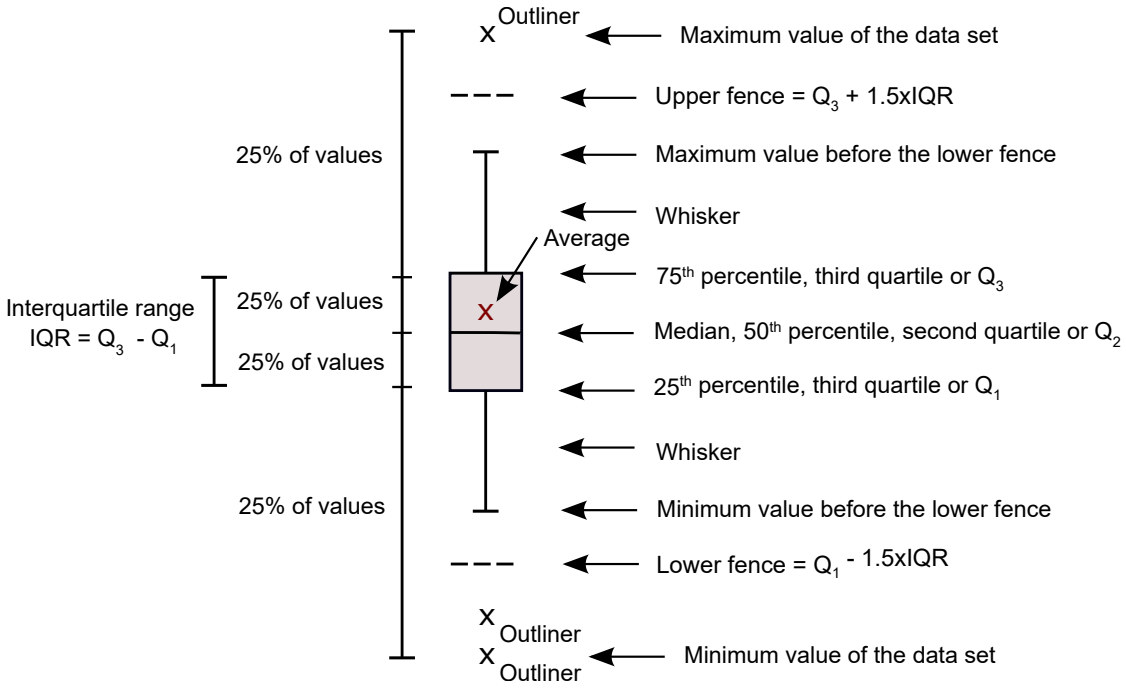

Figure 6.7: Comparison of characteristic load-displacement curves for different ballast conditions, adapted from [58]

from the box center and with whiskers of different lengths, revealing the data is skewed in the direction of the longer whisker. Negative or left skewed distribution creates a box plot with median moved to the right and the right-hand whisker is shorter than the left-hand whisker. Positive or right skewed distribution creates a box plot with median generally moved to the left and the left-hand whisker is shorter than the right-hand whisker [58].

6.5.3.2 Application on the in-situ collected data

Box plot diagrams are selected to display selected tamping characteristics in a context of a cycle (single tine oscillation) for every sleeper on a location with x axis showing the cycle number and y axis the selected tamping characteristic. Boxes represent values between the lower and upper quartiles (25^{th} and 75^{th} percentile) and whiskers values within 1.5 of the interquartile range. Outliners outside this range are rarely observed and are not taken into consideration for the statistical analysis. For example, first box in a diagram displaying the maximum reaction force per cycle comprises of maximum force values measured in the first cycle of the squeezing movement on each sleeper for a given location. Even when taking the considerable scattering into consideration, this method provides a very efficient overview of selected tamping characteristics.

This kind of statistical data evaluation provides the possibility to observe the distribution of quantitative values for the whole location observed, with the premise that both ballast bed condition and the variable tamping parameters set by the machine operator remain constant during track maintenance on one location. Box plot statistical analysis is conducted on the

Die approbierte gedruckte Originalversion dieser Dissertation ist an der TU Wien Bibliothek verfügbar.
The approved original version of this doctoral thesis is available in print at TU Wien Bibliothek.

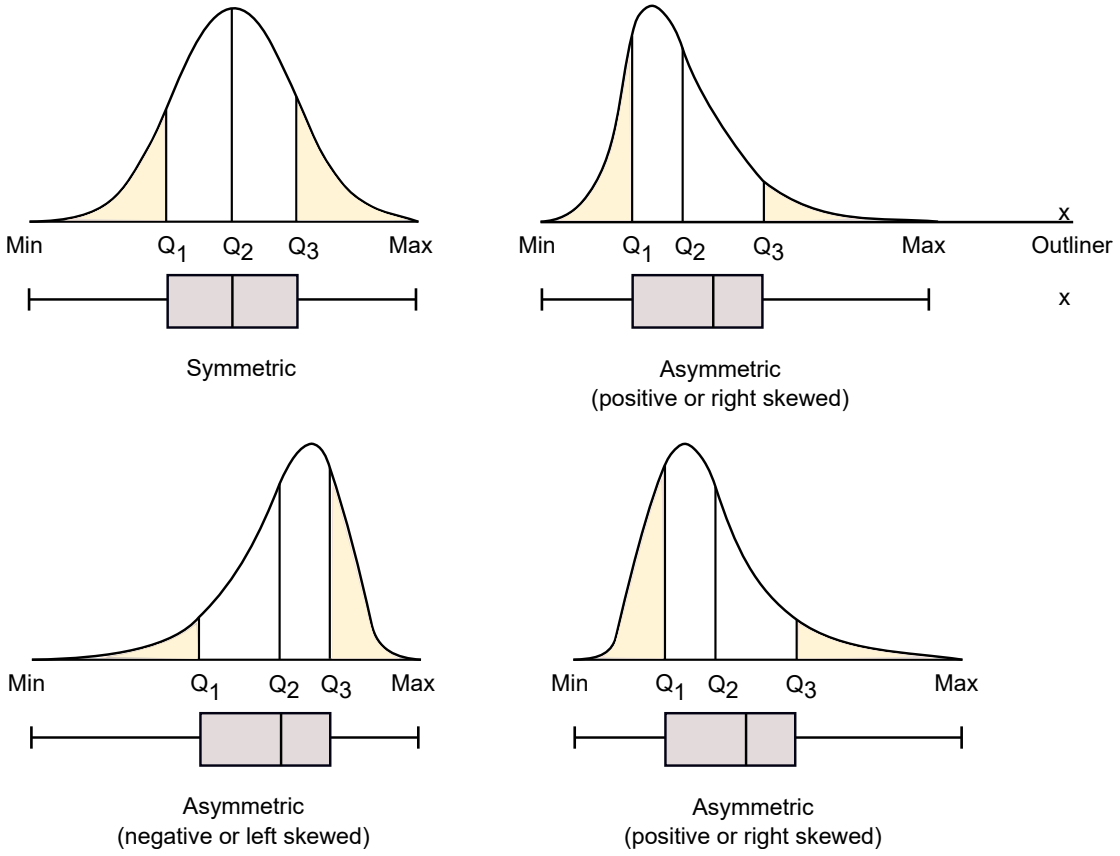

Figure 6.8: Symmetric and asymmetric dataset distributions and the corresponding box plots, adapted from [58]

following characteristics:

- maximum reaction force per cycle
- energy per cycle
- loading response of the ballast matrix
- start of contact (1st contact point)
- cylinder pressure
- maximum penetration resistance force per cycle (during ballast penetration)

Results of track tamping conducted in *clean* ballast displaying a double tamping process can be seen in Figures 6.9 to 6.13, followed by the same tamping characteristics plotted for *moderately clean* and *fouled* ballast condition as single tamping processes, respectively. Box plot analysis is conducted for the three representative locations selected and described in Chapter 6.4.1.

In an ideal case, the first three of the selected tamping characteristics should increase during ballast compaction. With ballast grains rearrangement into a matrix with higher

Die approbierte gedruckte Originalversion dieser Dissertation ist an der TU Wien Bibliothek verfügbar.
The approved original version of this doctoral thesis is available in print at TU Wien Bibliothek.

relative density the matrix resistance to further compaction should increase. Force required to exert the same amplitude increases, increasing the compaction energy and the matrix loading response. Special attention must be given to the fact that the goal of a successful ballast compaction underneath the sleeper is to achieve *optimum* compaction and increase the ballast bed shear strength without causing changes in the particle size distribution, grain angularity or surface structure. In other words, the compaction energy implemented by the tamping tines should only be utilized to rearrange the grains which make up the ballast matrix, without initiating/accelerating the ballast fouling process.

6.5.3.3 Analysis of tamping characteristics in different ballast conditions

Statistical data evaluation of track data collected during track tamping conducted with the *Dynamic Tamping Express 09-4X E^3 Plasser & Theurer* tamping machine is processed in form of box plot diagrams with average values per cycle presented by a black line. Typical representatives are once again selected among the locations where the measurements were conducted (Chapter 6.4.1).

- Track reconstruction (*clean* ballast) - *Theresienfeld - Wiener Neustadt* (tamping process on 930 sleepers analyzed)
- Tamping was performed 6 weeks after track reconstruction (*moderately clean* ballast) - *Tulln - Absdorf Hippersdorf* (tamping process on 757 sleepers analyzed)
- Track maintenance (*fouled* ballast) - *Ternitz-Gloggnitz* (tamping process on 392 sleepers analyzed)

In following chapters, results of the box plot analysis are presented and interpreted for all three ballast conditions and six tamping characteristics (Chapter 6.5.3.2), respectively. A double tamping process is analyzed for *clean* and a single one for *moderately clean* and *fouled* ballast bed conditions.

Die approbierte gedruckte Originalversion dieser Dissertation ist an der TU Wien Bibliothek verfügbar.
The approved original version of this doctoral thesis is available in print at TU Wien Bibliothek.
TU Bibliothek Your knowledge hub WIEN

Clean ballast

As stated before, track tamping in *clean* ballast conditions at all analyzed locations is conducted as a double tamping process with a single process duration of about 0.6 s or approximately 22 cycles (given a 35 Hz excitation frequency). All of the tamping characteristics are analyzed for both squeezing movements and their progress throughout the whole tamping process is evaluated and interpreted.

Maximum reaction force per cycle increases by a small increment with every cycle until it reaches an almost constant value towards the end of the second squeezing movement, beginning approximately at cycle No.17. Flattening of the average value curve (Figure 6.9) potentially indicates that the optimum relative ballast compaction has been reached for the given tamping parameter combination. Average measured value of the maximum reaction force per first cycle of the first squeezing movement is $\approx$ 2.5 kN and it increases to $\approx$ 9.0 kN towards the end of the first squeezing movement (Figure 6.9a). Nevertheless, first cycle of the second squeezing movement shows an average force of only $\approx$ 3.0 kN, meaning that the ballast matrix resistance to compaction changes significantly between the two squeezing processes, i.e. squeezing movements. Value in the last cycle remains almost the same as in the last cycle of first squeezing movement (approximately 10 kN, Figure 6.9b). Same phenomena can be observed when comparing values of the 1st and 2nd squeezing movement for energy per cycle (Figure 6.10) and ballast matrix loading response (Figure 6.11). An explanation for this behavior must be found in the ballast penetration phase. Even if the higher frequency of up to 45 Hz used to aid the tamping tines movement downwards during ballast penetration is only activated prior to the first squeezing movement, the ballast matrix is still loosened around the tines during penetration prior to the second squeezing movement, but not additionally compacted since the tines only move downwards, and the motion is not overlapped by the squeezing movement of the tines around the sleeper. The last third of the second squeezing movement, however, shows an increase in the total maximum reaction force per cycle of about 20% in comparisons to the end of the first squeezing movement, which still indicates an increase in the relative ballast matrix density.

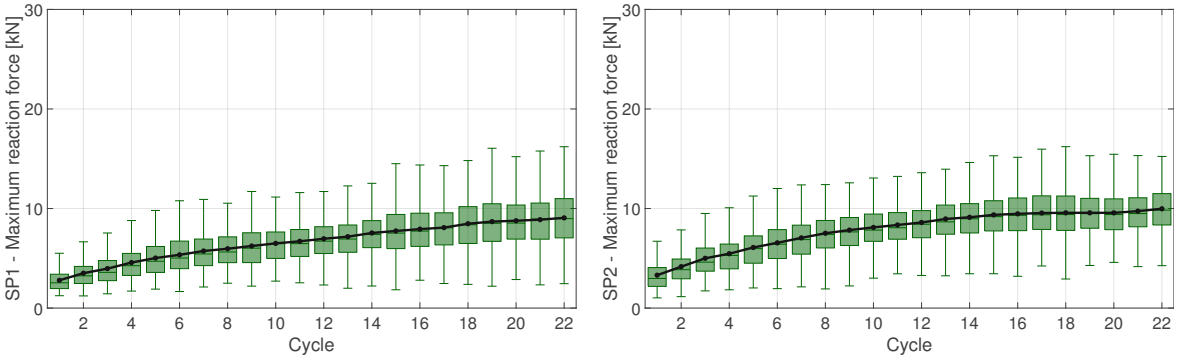

(a) Max. reaction force - First SM (b) Max. reaction force - Second SM

Figure 6.9: Maximum reaction force per cycle of two consecutive squeezing movements (SM) of a double tamping process conducted in *clean* ballast bed conditions

Energy per cycle (Figure 6.10) increases with a constant rate in the course of both squeez-

Die approbierte gedruckte Originalversion dieser Dissertation ist an der TU Wien Bibliothek verfügbar.
The approved original version of this doctoral thesis is available in print at TU Wien Bibliothek.

ing movements. This increase can most likely be correlated with a similar increase of the cylinder pressure plotted in Figure 6.13. An important consideration is that an additional increase of energy per cycle does not necessarily indicate further ballast matrix compaction since it is difficult to ascertain that the consumed energy is entirely utilized for ballast matrix compaction. This observation is confirmed by the loading response of the ballast matrix where a stable increase is observed in both squeezing movements until a typical peak in value during the 2nd squeezing movement is reached (Figure 6.11), most likely occurring as the void under the sleeper is filled and the ballast vertical movement upwards obviated by the sleeper. Similar peaks in the loading response of the ballast matrix are observed at all location where track tamping is performed after track reconstruction, i.e. in *clean* ballast conditions.

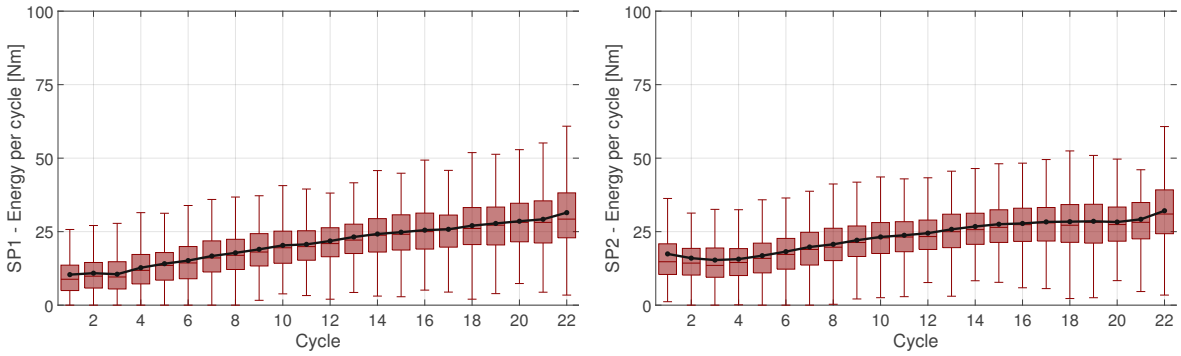

(a) Energy per cycle - First SM (b) Energy per cycle - Second SM

Figure 6.10: Energy per cycle of two consecutive squeezing movements (SM) of a double tamping process conducted in *clean* ballast bed conditions

As discussed in Chapter 5.3.2, the cyclic impact load transmitted to the ballast matrix by the tines initiates a temporary reduction of the ballast bed shear strength by reducing the inter-particle friction which aides the ballast grains rearrangement while they are being pushed to fill the void under the sleeper by the quasi-static closing movement. However, the peak and a sudden decrease of the ballast matrix loading response could also indicate the movement of ballast grains away from the tines towards the sleeper head and/or sleeper bay. Given that the appearance of the peak in loading response coincides with the flattening of the maximum force per cycle, it can be said that tamping beyond this point does not advance the process of ballast matrix compaction. It can, however, be argued that the ballast movement under and along the sleeper toward the sleeper bay contributes the homogenization of the ballast distribution along the entire sleeper length.

Die approbierte gedruckte Originalversion dieser Dissertation ist an der TU Wien Bibliothek verfügbar.
The approved original version of this doctoral thesis is available in print at TU Wien Bibliothek.

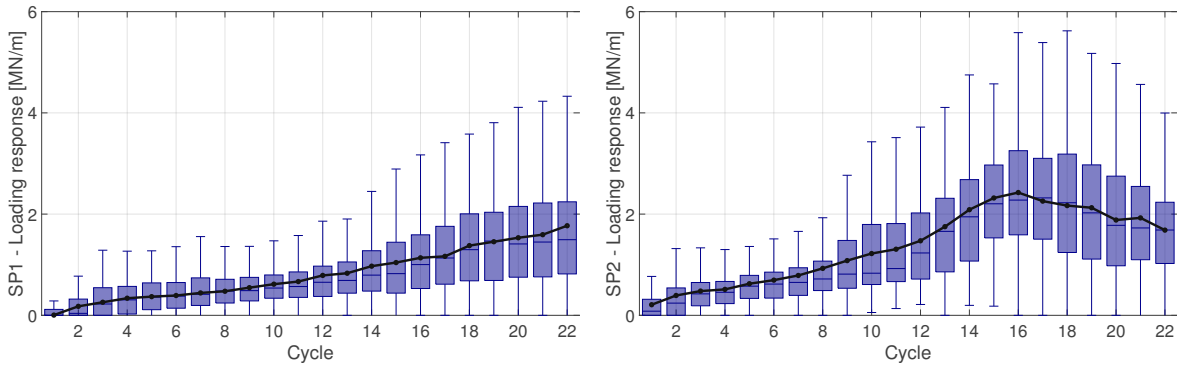

(a) Loading response - First SM (b) Loading response - Second SM

Figure 6.11: Loading response of the ballast matrix per cycle of two consecutive squeezing movements (SM) of a double tamping process conducted in *clean* ballast bed conditions

As mentioned earlier in Chapter 5.4, the position of the first contact point is calculated as the intersection point between the linear approximation of the curve inclination in the loading phase and the x axis. In other words, if the curve slope is minor, this intersection point could be beyond the limits of the tamping tine movement presented by the load-displacement curve. Nevertheless, not the exact values but rather the progress of the first contact point throughout the cycles is used as a relevant confirmation of a correct loading response calculation. Typical peak in the loading response that can be seen in Figure 6.11 showing a local increase during the second squeezing movement is validated by a peak in the box plot diagram displaying the beginning of contact during the second squeezing movement (Figure 6.12), showing higher contact point values. In addition, the start of contact is also used for comparison between different ballast bed conditions, showing a distinct increase in values with the progress of ballast fouling (Table 6.3), confirming the differences in *clean* ballast behavior in comparison to the *fouled* one once more.

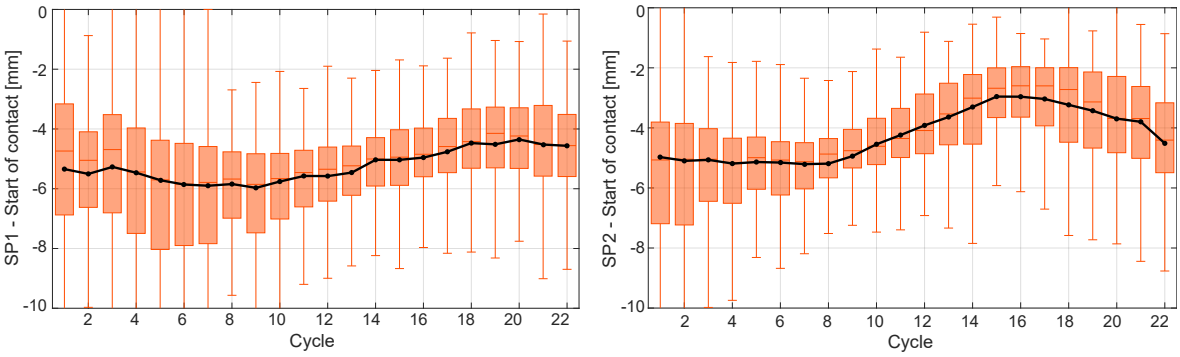

(a) Start of contact - First SM (b) Start of contact - Second SM

Figure 6.12: Start of contact in every cycle of two consecutive squeezing movements (SM) of a double tamping process conducted in *clean* ballast bed conditions

Cylinder pressure plotted in Figure 6.13 presents the average value per cycle as well as the value course for all 930 sleepers analyzed.

Die approbierte gedruckte Originalversion dieser Dissertation ist an der TU Wien Bibliothek verfügbar.
The approved original version of this doctoral thesis is available in print at TU Wien Bibliothek.

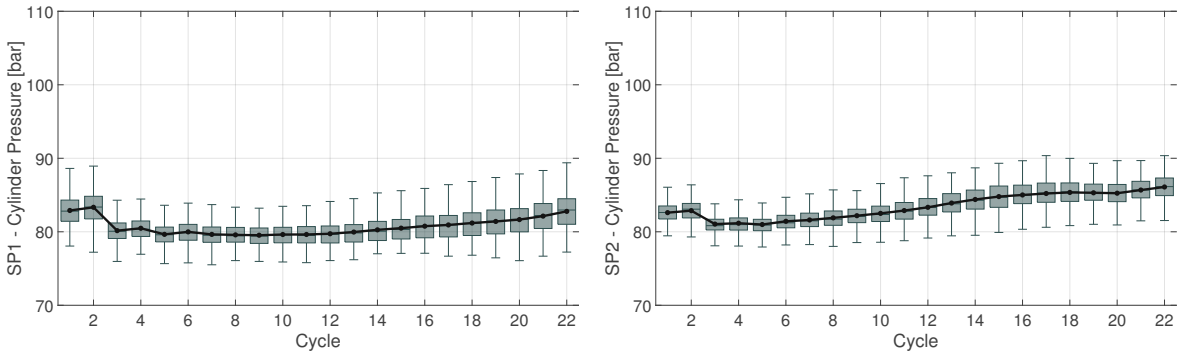

(a) Cylinder pressure - First SM (b) Cylinder pressure - Second SM

Figure 6.13: Cylinder pressure in every cycle of two consecutive squeezing movements (SM) of a double tamping process conducted in *clean* ballast bed conditions

Generally speaking, there is no possibility to manually vary the cylinder pressured during the squeezing movement. The pressure is set to a constant value, in this particular case to approximately 85-87 bar, and it increases continuously with every cycle until the set value is reached, which corresponds approximately to the 16^{th} cycle of the second squeezing movement. The increase of cylinder pressure in *clean* ballast between the minimum and maximum value amounts to less than 5%, and is not expected to have a substantial influence on the tamping characteristics.

Die approbierte gedruckte Originalversion dieser Dissertation ist an der TU Wien Bibliothek verfügbar.
The approved original version of this doctoral thesis is available in print at TU Wien Bibliothek.
TU Bibliothek Your knowledge hub WIEN

Moderately clean ballast

Track tamping was conducted six weeks after track reconstruction on the track section between Tulln - Absdorf Hippersdorf, spanning over 757 sleepers. As stated before, based on result of conducted measurement analysis, this ballast bed condition is defined as *moderately clean* following the Fouled index definition (Chapter 3.2.2). Tamping was conducted as a single squeezing process with a duration of 36 cycles or approximately 1 s. Box plot analysis of the tamping characteristics yielded results as discussed in the following.

Significant increase of the reaction force average value between the first and the last cycle can be observed in Figure 6.14, showing a single tamping process in *moderately clean* ballast conditions. Flattening of the average value curve, similar to the one observed in *clean* ballast evaluation can be noticed after approximately 22 cycles and it correlates with the flattening of the average energy per cycle curve (Figure 6.15). The reaction force increases by an average of 8 kN between the first and last cycle, accompanied by simultaneous increase of energy per cycle average value by 14 Nm. The increase of both values is, however, quite negligible after approximately 22 cycles. A stagnation of both the reaction force and energy value could possibly indicate that the optimum tamping result can be reached with a shorter squeezing process. In order to extend this theory into a proven fact, several other influences like the lifting values, squeezing velocity and the cylinder pressure set by the machine operator have to be taken into consideration.

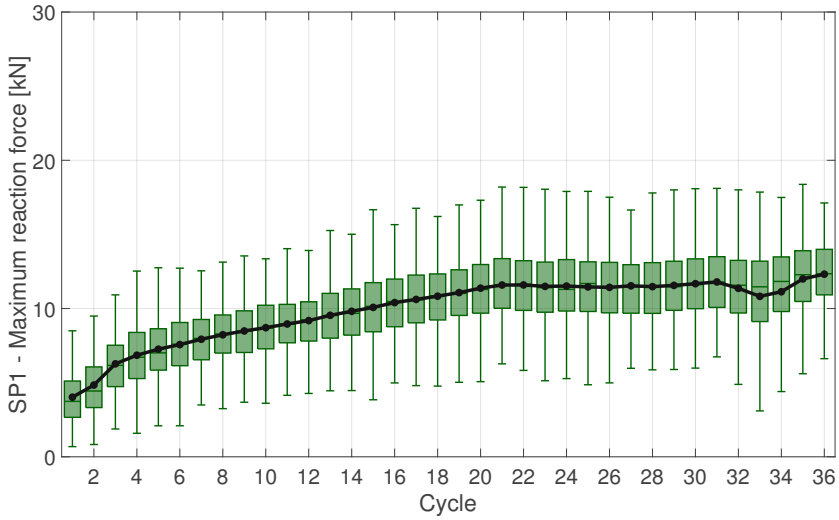

Figure 6.14: Maximum reaction force per cycle during one squeezing movement of a single tamping process conducted on one sleeper in *moderately clean* ballast conditions

Die approbierte gedruckte Originalversion dieser Dissertation ist an der TU Wien Bibliothek verfügbar.
The approved original version of this doctoral thesis is available in print at TU Wien Bibliothek.

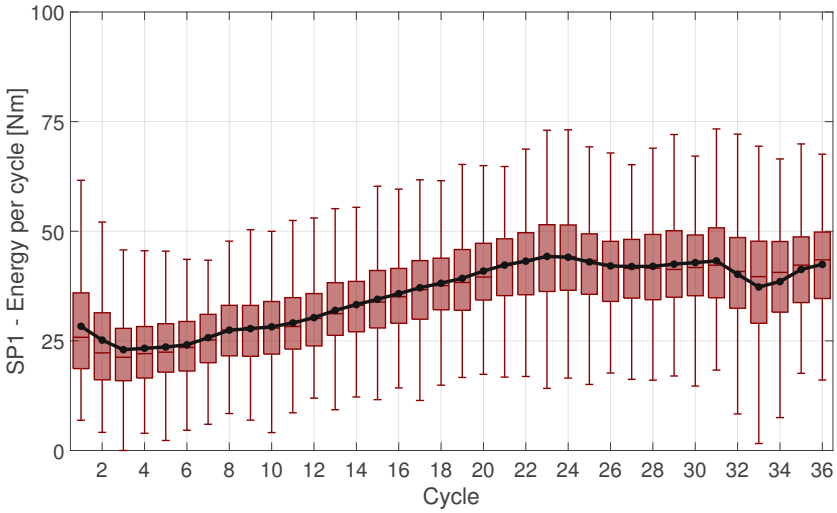

Figure 6.15: Energy per cycle during one squeezing movement of a single tamping process conducted on one sleeper in *moderately clean* ballast conditions

At the same time, ballast matrix loading response increases up to the 22nd cycle and starts the decrease slightly afterwards. Although less obvious, this peak in value is correlated to the similar loading response peak measured in *clean* ballast (Figure 6.11). It can be concluded that the emphasis of the peak decreases as the ballast fouling process progresses. This behavior will be additionally confirmed by an almost complete absence of it in *fouled* ballast conditions (Figure 6.21), confirming the loading response as a reliable indicator of ballast bed condition. Even if the comparison between *clean* and *moderately clean* ballast response to compaction is not entirely straightforward due to the fact that a single tamping process is compared to a double one, significant changes can be observed not only in the course of characteristic value development during the squeezing movement, but also in significantly higher values of the first three observed characteristics (Tables 6.4 and 6.6).

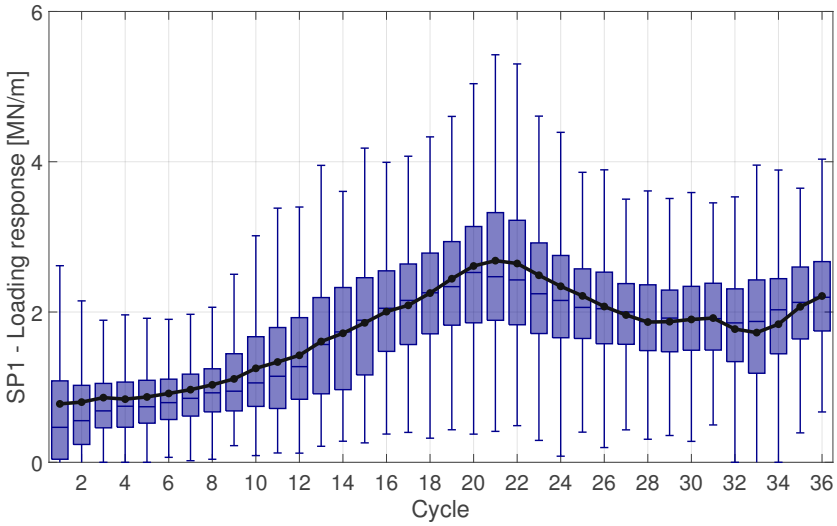

Figure 6.16: Loading response of the ballast matrix per cycle during one squeezing movement of a single tamping process conducted on one sleeper in *moderately clean* ballast conditions

Die approbierte gedruckte Originalversion dieser Dissertation ist an der TU Wien Bibliothek verfügbar.
The approved original version of this doctoral thesis is available in print at TU Wien Bibliothek.
TU Bibliothek Your knowledge hub WIEN

Points marking the beginning of contact between the ballast matrix and tamping tine in form of a box plot diagram can be seen in Figure 6.17. The values vary insignificantly throughout the squeezing movement, but as stated before, a meaningful gain can be observed in comparison to the *clean* ballast bed condition, with an increase from -5.51 mm and -4.21 mm for the both squeezing movements in *clean* to -3.89 mm in *moderately clean* ballast (Table 6.3). As stated before, position of the first contact point is calculated as the intersection point between the linear approximation of the curve inclination in the loading phase and the x axis meaning that the points can lay beyond the limits of the tamping tine movement presented by the load-displacement curve. This can once again be correlated to the increase of the loading pressure of the ballast matrix which is in fact expected to increase with the progress of the ballast fouling progress.

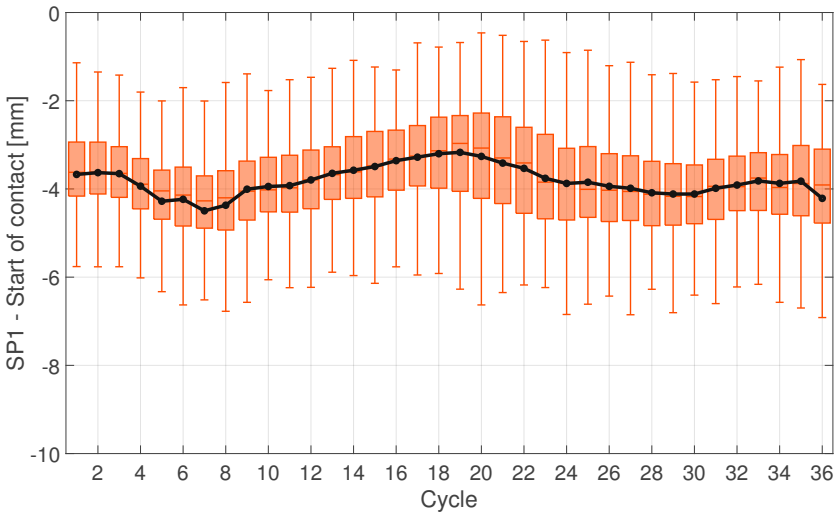

Figure 6.17: Start of contact in every cycle during one squeezing movement of a single tamping process conducted on one sleeper in *moderately clean* ballast conditions

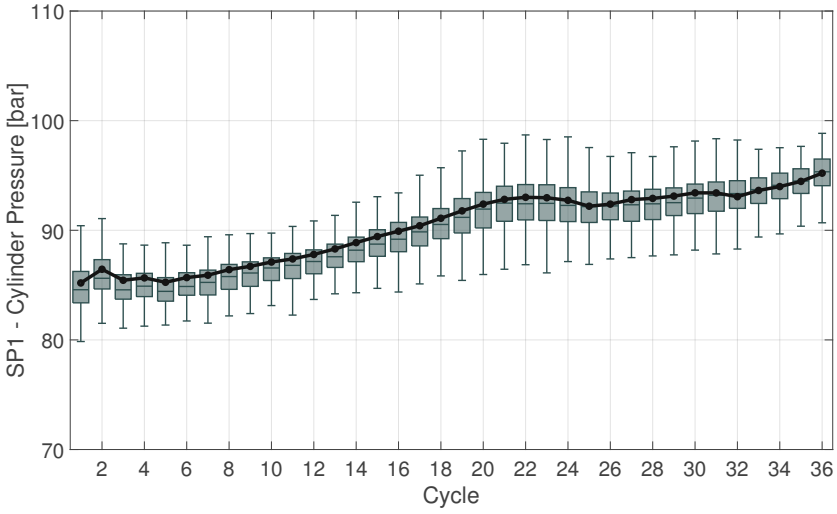

Figure 6.18: Cylinder pressure in every cycle during one squeezing movement of a single tamping process conducted on one sleeper in *moderately clean* ballast conditions

Die approbierte gedruckte Originalversion dieser Dissertation ist an der TU Wien Bibliothek verfügbar.
The approved original version of this doctoral thesis is available in print at TU Wien Bibliothek.
TU Bibliothek Your knowledge hub WIEN

Figure 6.18 shows the increase of cylinder pressure from approximately 85 bar in the first to 95 bar (target value) in the last cycle. The increase is continuous up to the 22nd cycle, after which the rate of increase decreases. The difference in cylinder pressure in *moderately clean* ballast between the minimum and maximum value amounts to approximately 11%, which is a significant enhancement (even relatively speaking) in comparison to the values measured in *clean* ballast conditions.

Fouled ballast

Single tamping process on 392 sleepers in *fouled* ballast conditions on the track section between Ternitz and Gloggnitz is conducted with a duration of 36 cycles or approximately 1 s. Detailed analysis of selected tamping characteristics follows.

Significant increase of the maximum reaction force per cycle is only noticeable before the 8th cycle, remaining constant until the last cycle (Figure 6.19). The values differentiate from the first two observed ballast bed conditions, as the force is significantly higher, reaching up to 16 kN in average for this location and up to almost 20 kN in average for all locations (Table 6.3). Higher force values are attributed to the more "complex" structure of the *fouled* ballast matrix that composes not only of skeletal but also of a high level of filler and distance ballast grains (Figure 3.1). Apart from the grain size, the process of ballast fouling generates changes to the grain shape and angularity as the roundness of the particle increases. Generally speaking, a *fouled* ballast matrix can also be characterized by a lower void ratio (or higher density) and a higher degree of saturation in comparison to the *clean* ballast matrix. All of these properties make the *fouled* ballast matrix more resistant to grain restructuring and further compaction. Constant values of the reaction force after approximately cycle number 8 can also lead to the conclusion that not ballast matrix compaction but rather the re-installment of the desired track geometry is the main goal of track tamping in *fouled* conditions.

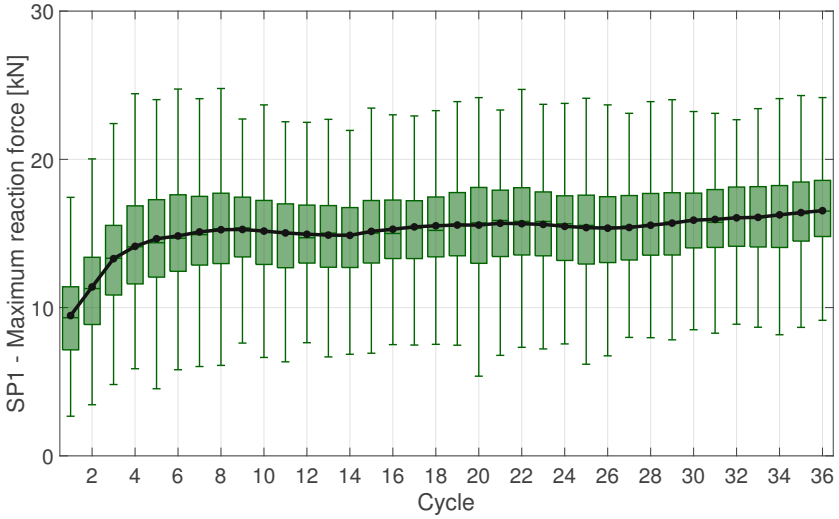

Figure 6.19: Maximum reaction force per cycle during one squeezing movement of a single tamping process conducted on one sleeper in *fouled* ballast conditions

Decrease of energy per cycle over the squeezing movement can be observed in Fig-

Die approbierte gedruckte Originalversion dieser Dissertation ist an der TU Wien Bibliothek verfügbar.
The approved original version of this doctoral thesis is available in print at TU Wien Bibliothek.
TU Bibliothek Your knowledge hub WIEN

ure 6.20. However, besides the fact that the values only differ slightly between the first and the last cycle (about 15%), the high dispersion of the collected data also makes it difficult to draw conclusions based on this tamping characteristic alone. Energy per cycle values, however, correlate with the condition of the ballast matrix and are significantly higher (Table 6.3) in comparison with the *clean* and *moderately clean* ballast bed condition.

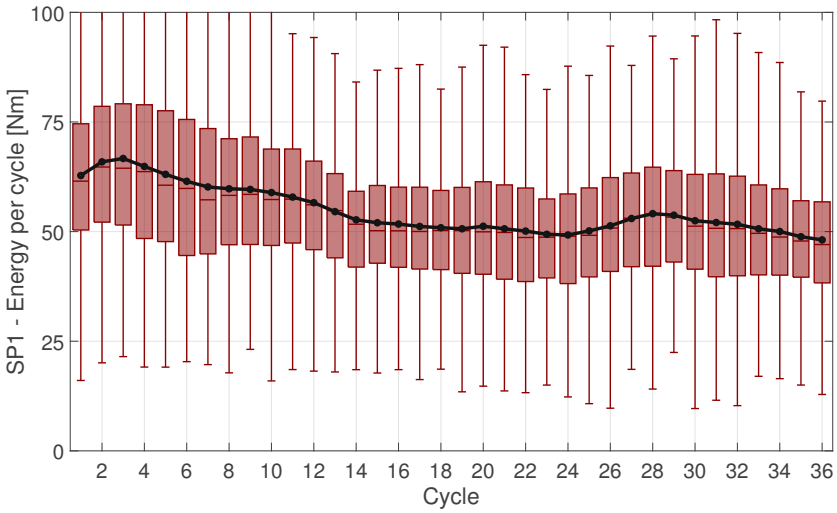

Figure 6.20: Energy per cycle during one squeezing movement of a single tamping process conducted on one sleeper in *fouled* ballast conditions

Similar to the energy per cycle presentation in Figure 6.20, Figure 6.21 shows the ballast matrix loading response and also displays a high dispersion level of measured data. Values of the loading response are considerably higher in comparison to the other ballast conditions, showing values of up to 2.15 MN/m in average (Table 6.3), and 2.7 MN/m for this location. A peak similar to the one in *clean* ballast condition is also present here but less prominent. If technical, machine-related influences can be excluded as possible triggers for the appearing peaks, this behavior measured on the contact between the ballast matrix and the tine would indicate that at approximately 2/3 of the squeezing movement the void under the sleeper is filled and the grains start their motion in the direction parallel to the sleeper. This hypothesis, however, needs to be further examined and cross-referenced with the lifting values.

Die approbierte gedruckte Originalversion dieser Dissertation ist an der TU Wien Bibliothek verfügbar.
The approved original version of this doctoral thesis is available in print at TU Wien Bibliothek.
TU Bibliothek Your knowledge hub WIEN

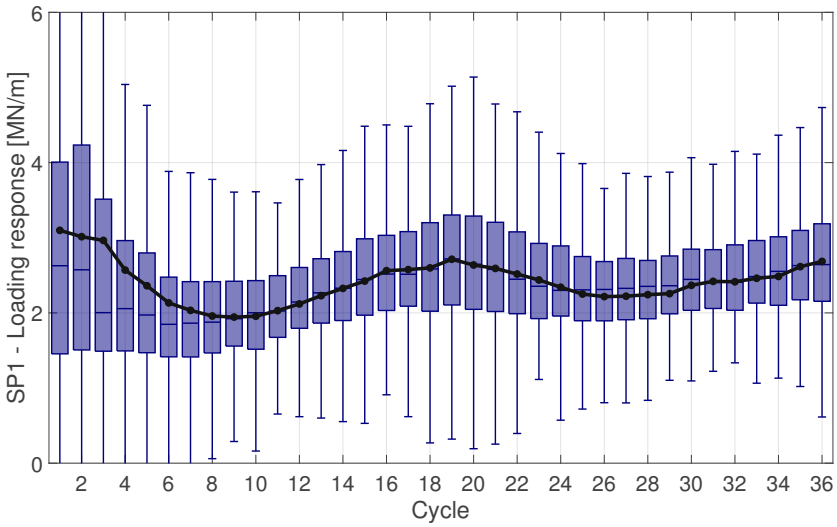

Figure 6.21: Loading response of the ballast matrix per cycle during one squeezing movement of a single tamping process conducted on one sleeper in *fouled* ballast conditions

Regarding the first contact point between the tine and ballast matrix, values vary somewhat during the first third of the process and remain constant afterwards. The values are approximately -3.34 mm in average. Constant values of the first contact point position indicated that there is no ballast movement following the tamping tine in the contactless phase. In combination with the decrease of maximum elongation, it can be concluded that the share of elastic deformation decreases with the progress of ballast fouling.

Measured value of cylinder pressure increases from approximately 92 bar in the first to the set value of 105 bar in the last cycle, giving an increase of approximately 15%. Ballast tamping is in general conducted with higher pressure values in *fouled* ballast conditions to match the expected higher resistance to compaction.

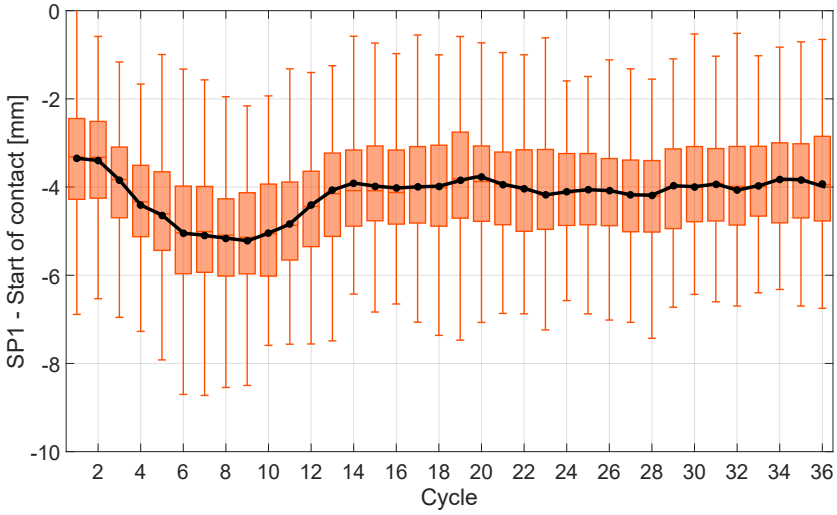

Figure 6.22: Start of contact in every cycle during one squeezing movement of a single tamping process conducted on one sleeper in *fouled* ballast conditions

Die approbierte gedruckte Originalversion dieser Dissertation ist an der TU Wien Bibliothek verfügbar.
The approved original version of this doctoral thesis is available in print at TU Wien Bibliothek.
TU Bibliothek Your knowledge hub WIEN

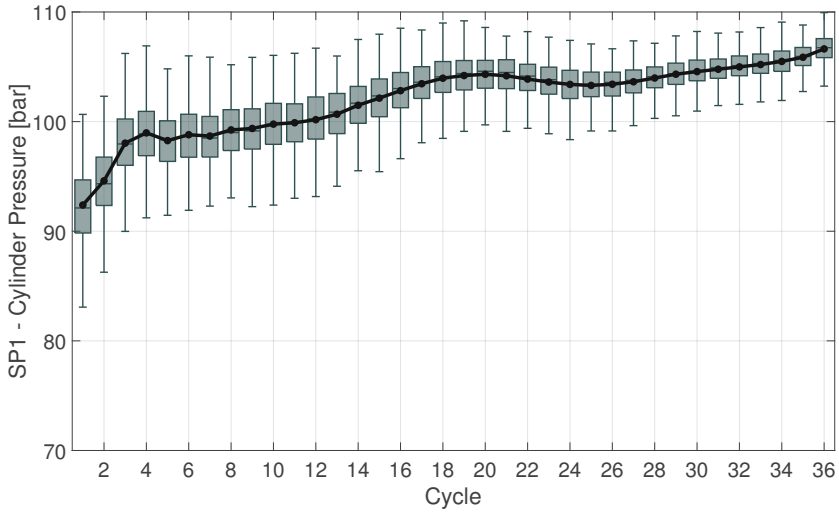

Figure 6.23: Cylinder pressure in every cycle during one squeezing movement of a single tamping process conducted on one sleeper in *fouled* ballast conditions

Fluidization as described in *clean* ballast is not possible in *fouled* ballast conditions due to a higher proportion of cohesive material in a *fouled* ballast matrix, meaning that the ballast grains can be rearranged by force but there is no compaction. On the contrary, loosening is theoretically possible (Chapter 7.1). Showing little to no changes in analyzed tamping characteristics, the results indicate that hard bedding created by *fouled* ballast already has a significantly higher bulk density due to the finer particles filling the voids, meaning that *fouled* ballast compaction cannot be significantly induced by track tamping, but the ballast can be used to fill the void under the sleeper and provide the necessary track elevation.

Die approbierte gedruckte Originalversion dieser Dissertation ist an der TU Wien Bibliothek verfügbar.
The approved original version of this doctoral thesis is available in print at TU Wien Bibliothek.

6.5.4 Graphical analysis

Depending on the squeezing time, every squeezing movement, preformed with a 35 Hz excitation frequency consists of a certain number of cycles, i.e. load-displacement curves. Statistical analysis presented in the last chapter provides information about the whole track section that is analyzed, but only one value at the time. With the following graphical analysis an effort is made to provide a complete overview of all tamping parameters and load-displacement diagrams during one squeezing movement. Examples plotted in Figures 6.24 and 6.25 cannot represent the whole measurement in given ballast condition, but they still grant the possibility to have a 3D and a color scheme model of one squeezing movement. Representative illustrations that show typical values of tamping characteristics for the given ballast condition are selected. The two presentations are complementary in the sense that the tamping characteristics that are not presented or not observable in one are given in the other.

6.5.4.1 Waterfall diagrams

Waterfall diagram is composed for the entire squeezing movement as an overview of ballast compaction progress. The diagram shows the tamping tine oscillation x_{tine} on the x, reaction force F on the y and the cycle number on the z (spatial) axis. Every load–displacement curve is plotted stacked behind the previous one. Typical examples for every ballast condition analyzed are plotted in Figure 6.24. Even without consulting the statistical analysis, differences in certain tamping characteristics are obvious. The reaction force shows significantly higher values in *fouled* (Figure 6.24c) compared to the *clean* ballast condition (Figure 6.24a). Even if the exact value cannot be read from the diagram, it is quite easily interpretable from the area within the load-displacement curve that the energy also increases with the progress of ballast fouling. A significant increase of the load-displacement curve inclination in the loading phase between Figures 6.24a and 6.24c is also observable. The most emphasized difference, however, can be seen in the shape of load-displacement curves in the unloading phase. As was already confirmed with the statistical analysis, tamping in *clean* ballast conditions results in negative unloading response values that are visible as "belly shaped" diagram forms in the unloading phase. It is difficult to draw conclusions about the tamping tine amplitude of the position of the first contact point from this 3D presentation. It is, however, quite obvious that the position of the second contact point (loss of contact) shifts to the left as the process of ballast fouling progresses, causing the before mentioned change on sign in the unloading response from negative in *clean* to positive in *fouled* ballast condition.

Die approbierte gedruckte Originalversion dieser Dissertation ist an der TU Wien Bibliothek verfügbar.
The approved original version of this doctoral thesis is available in print at TU Wien Bibliothek.

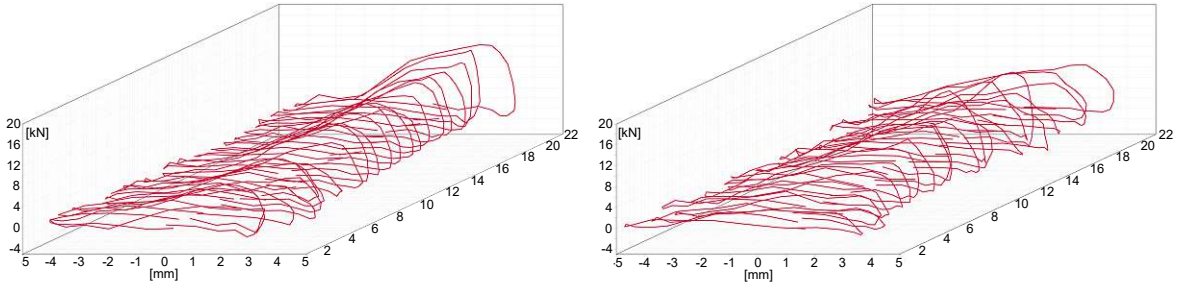

(a) Squeezing movement overview - waterfall diagram of *clean* ballast (1st and 2nd squeezing movement)

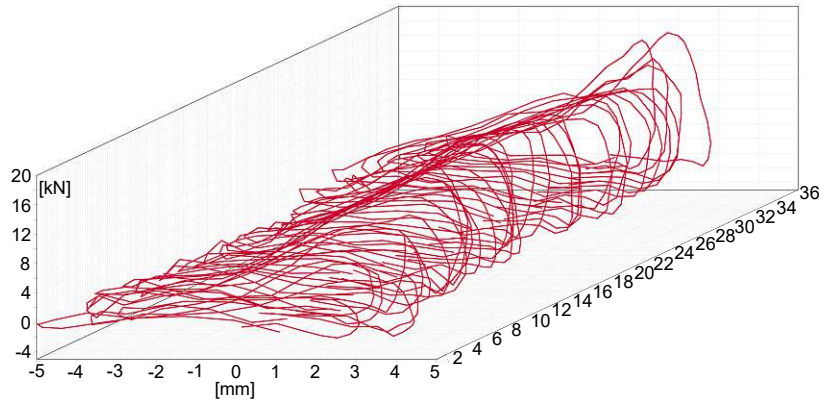

(b) Squeezing movement overview - waterfall diagram of *moderately clean* ballast

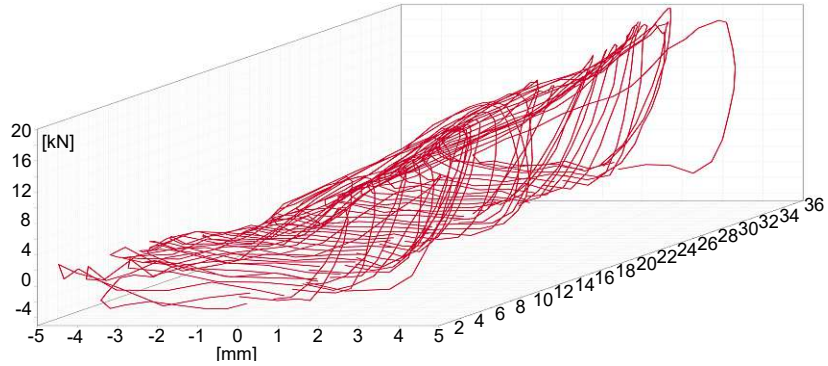

(c) Squeezing movement overview - waterfall diagram of *fouled* ballast

Figure 6.24: Squeezing movement, waterfall diagrams – showing selected stacked consecutive load–displacement curves in different ballast conditions

Die approbierte gedruckte Originalversion dieser Dissertation ist an der TU Wien Bibliothek verfügbar.
The approved original version of this doctoral thesis is available in print at TU Wien Bibliothek.

6.5.4.2 Heat maps

In addition to waterfall diagrams, heat maps of the above presented examples are presented. A heat map is a graphical representation of data in which the individual values contained in a matrix are represented as colors. Figure 6.25 shows a top view of the waterfall diagram, where the reaction force F is presented in a color scale, the full tamping tine displacement x_{tine} is plotted on the x, and the cycle number on the y axis. The contour lines (i.e. isolines) connect areas of the same particular value, in this case area with the same reaction force values. Both contact points marking beginning and end of contact are plotted on the heat maps additionally. As stated before, the position of each point is calculated as the intersection point of the loading, i.e. unloading response line with the x axis, which partially leads to unrealistic results of contact where contact points are positioned outside the tine maximum elongation in both directions.

The most noticeable difference between the sub-figures of Figure 6.25 is the color representing the reaction force. Prevailing lighter colors in Figure 6.25a indicate maximum reaction force values of about 12 kN. The colors darken in Figure 6.25b as the maximum reaction force increases to about 15 kN and continues to increase in Figure 6.25c up to the force reaches approximately 20 kN. No statement can be made about the energy per cycle, as the area of the load-displacement diagram is not plotted in this presentation. Before mentioned isolines provide a very practical and quick insight in both response values - given that the lines connect areas of the same particular value, the closer the lines are to one another, the steeper the inclination of the curve in the loading or unloading phase. An important fact to state, however, is that this is only valid for negative values of the unloading response since the positive inclination cannot be observed in this top view presentation given that the second contact point is located more to the left than the maximum tine elongation in the squeezing direction. An enhancement of load-displacement curve steepness in the loading phase (i.e. loading response) can be noted between Figures 6.25a, 6.25b and 6.25, indicated by a decrease of distance between the contour lines.

Die approbierte gedruckte Originalversion dieser Dissertation ist an der TU Wien Bibliothek verfügbar.
The approved original version of this doctoral thesis is available in print at TU Wien Bibliothek.
TU Bibliothek Your knowledge hub WIEN

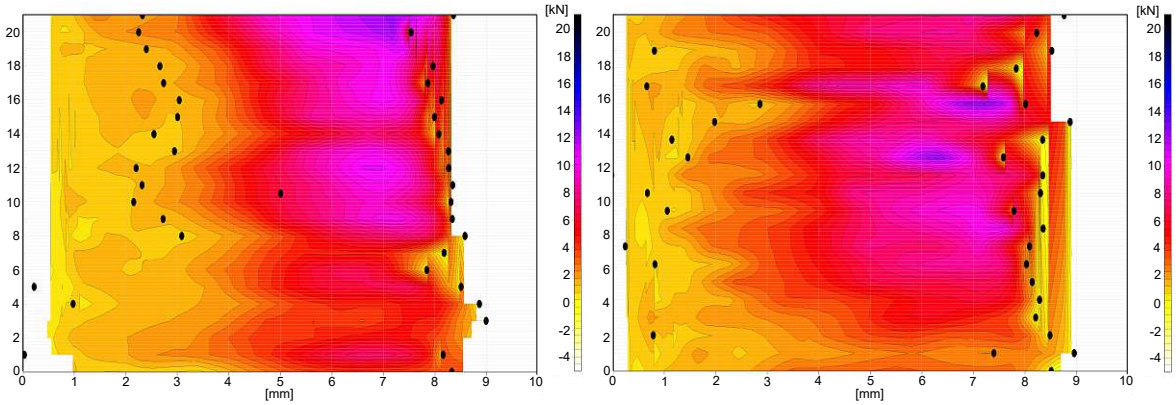

(a) Squeezing movement overview - heat map of *clean* ballast (1st and 2nd squeezing movement)

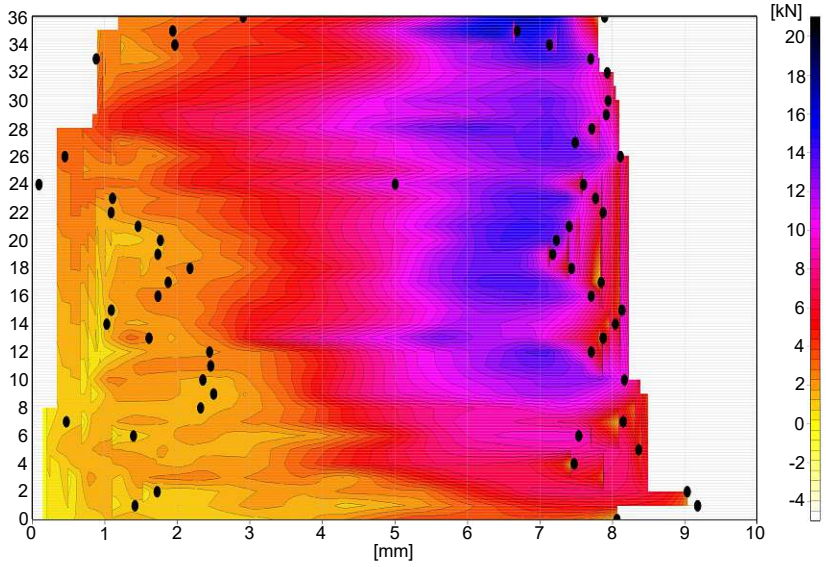

(b) Squeezing movement overview - heat map of *moderately clean* ballast

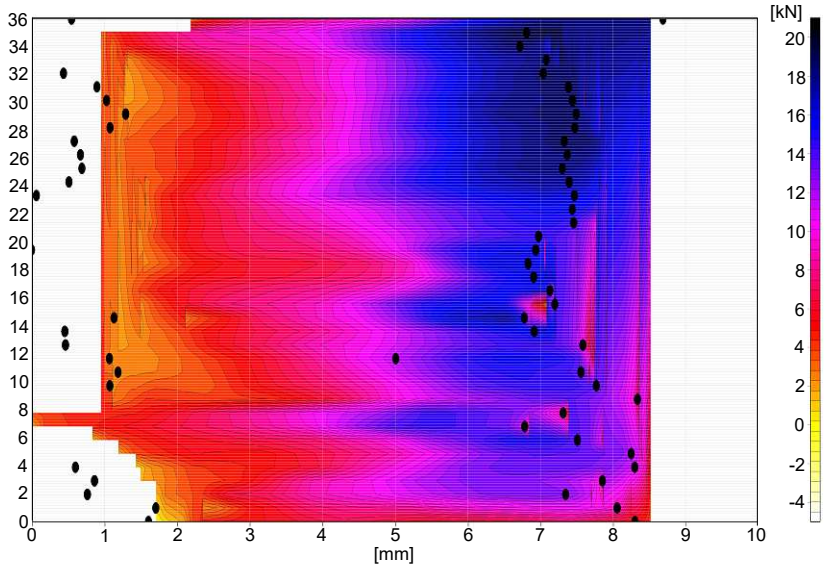

(c) Squeezing movement overview - heat map of *fouled* ballast

Figure 6.25: Squeezing movement, heat maps – showing selected stacked consecutive load–displacement curves in different ballast conditions

Die approbierte gedruckte Originalversion dieser Dissertation ist an der TU Wien Bibliothek verfügbar.
The approved original version of this doctoral thesis is available in print at TU Wien Bibliothek.

6.6 Ballast penetration evaluation

In addition to tamping characteristics analyzed during the squeezing movement, penetration resistance force measured by strain gauges during the process of ballast penetration is analyzed. As stated before, ballast penetration beginning is triggered as soon as the unit is lowered in the predefined position and the tines reach the ballast. End of ballast penetration is indicated by a steep increase in cylinder pressure that triggers the beginning of a squeezing movement. During ballast penetration, the tamping tines are lowered into the ballast bed until they reach the desired positions under the sleeper. In the course of penetrating the ballast, the frequency modulation described in Chapter 4.4 is used, aiding the process by a higher excitation frequency. An increase of frequency reduces the cycle duration, thus influencing the penetration resistance force. Nevertheless, this does not prevent comparison of penetration resistance force between different ballast conditions analyzed in previous chapters. An important fact to state is that the sleeper type does not change between the three analyzed measurements and the duration of the penetration process only varies insignificantly.

Statistical box plot analysis showing the values of penetration resistance force for each cycle of different ballast conditions for the whole track section analyzed is shown in Figures 6.26, 6.27 and 6.29.

6.6.1 Penetration resistance force - comparison between ballast conditions

Table 6.3 shows an increase of average penetration resistance force value with the progress of ballast fouling. Figure 6.26 shows the course of values as well as the average value for each cycle during ballast penetration of a double tamping process in clean ballast condition. Quite stable and reliable force values neither change significantly between the first and the last cycle, nor between the two squeezing movements. The average value of penetration resistance force in both squeezing processes is about 7 kN, with a slight increase in the second squeezing process. Table 6.3 shows the average maximum force value of 11.47 kN for the first and 12.02 kN for the second squeezing movement.

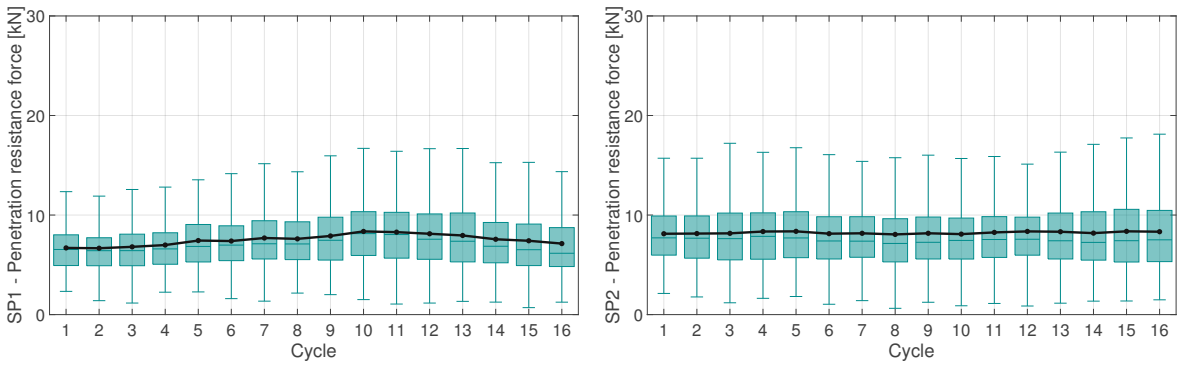

(a) Penetration resistance force - First SM (b) Penetration resistance force - Second SM

Figure 6.26: Penetration resistance force during every cycle of two consecutive ballast penetrations of a double tamping process conducted on one sleeper in *clean* ballast conditions

Die approbierte gedruckte Originalversion dieser Dissertation ist an der TU Wien Bibliothek verfügbar.
The approved original version of this doctoral thesis is available in print at TU Wien Bibliothek.
TU Bibliothek Your knowledge hub WIEN

Figure 6.27 displays similar force progression with no visible changes to the value between the first and the last cycle. Sightly higher average value of approximately 9.0 kN can be seen and correlated to the average maximum force value of 13.05 kN given in Table 6.3. It can be seen that even after only 6 weeks, a noticeable difference in the force needed for the tamping tines to penetrate the ballast matrix is present.

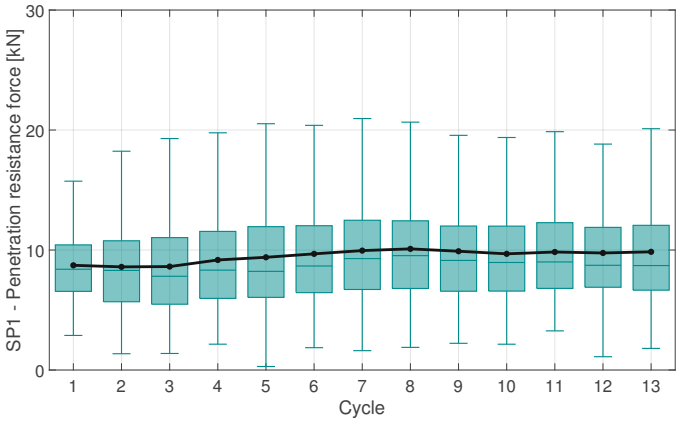

Figure 6.27: Penetration resistance force during every cycle of a single tamping process conducted on one sleeper in *moderately clean* ballast conditions

Another interesting observation can be made when looking into maximum penetration resistance force during every cycle of *fouled* ballast penetration. The force values are not only much higher in average, increasing up to 12.0 kN, and up to 15.72 kN for the average maximum, but a stable rate of increase can also be noticed between the cycles. As mentioned before, the matrix of a *fouled* ballast bed contains a high number of finer grains that fill the existing voids.

(a) Sleeper bay surface (b) Sleeper bay, bottom edge of the sleeper (c) Sleeper bay, upper edge of the subgrade

Figure 6.28: *Fouled* ballast bed depth profile

When exposed to dynamic loading, the fine particles tend to move downwards through the voids in the ballast matrix. As the process of ballast fouling progresses, the ballast matrix

Die approbierte gedruckte Originalversion dieser Dissertation ist an der TU Wien Bibliothek verfügbar.
The approved original version of this doctoral thesis is available in print at TU Wien Bibliothek.
TU Bibliothek Your knowledge hub WIEN

profile changes with depth - close to the surface the void ratio is higher as the matrix is mostly built of skeletal grains (Figure 3.1). With depth, the ratio of distance and filler grains increases and decreases the void ratio. In other words, the ballast matrix density increases with depth. The x axis of Figure 6.29 does not only give information about the cycle number but also about the current position or the depth of the tamping tine in the ballast bed. As the tine penetrates deeper, the percentage of finer particles increases and a higher force is necessary to continue the tine motion.

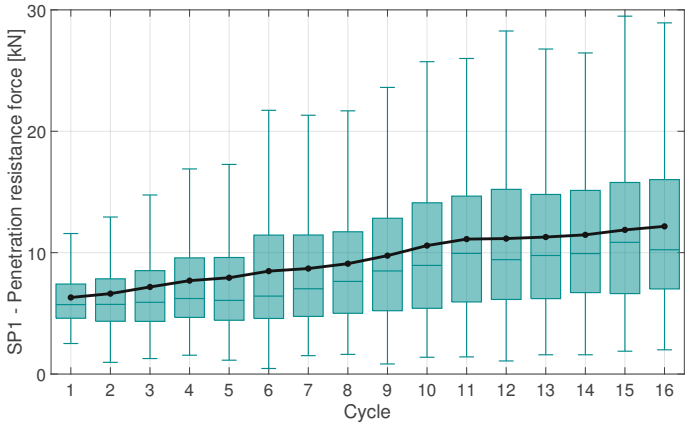

Figure 6.29: Penetration resistance force during every cycle of a single tamping process conducted on one sleeper in *fouled* ballast conditions

Die approbierte gedruckte Originalversion dieser Dissertation ist an der TU Wien Bibliothek verfügbar.
The approved original version of this doctoral thesis is available in print at TU Wien Bibliothek.

6.7 Squeezing velocity as a possible indicator of ballast bed condition

In the scope of in-situ measurements conducted during 2016 and 2017, the squeezing displacement was measured by means of a laser range-finder (in detail in Chapter 5.3.1). Unfortunately, this approach supplied results only for a limited number of measurements, given that the position of the sensor was not optimal and the high dynamic loads influenced the measurement quality. In later measurement campaigns, this sensor was replaced by a highly reliable angle decoder, showing the exact absolute position of the tine at any given moment.

Squeezing velocity is calculated for all the measurements with available data, using the following principle:

$$v_{squeezing} = \frac{\text{squeezing displacement}}{\text{duration of squeezing movement}} \tag{6.1}$$

The squeezing displacement used for the calculation is the maximum tamping tine stationary motion between the start and end of each squeezing movement (Figure 6.30). By dividing this tine displacement over the duration of the squeezing movement, the squeezing velocity is obtained. Calculated values are then compared to the maximum force per cycle values measured by the strain gauges for all of the locations listed in Table 6.3 from which the squeezing displacement values were obtained prior to sensor malfunction.

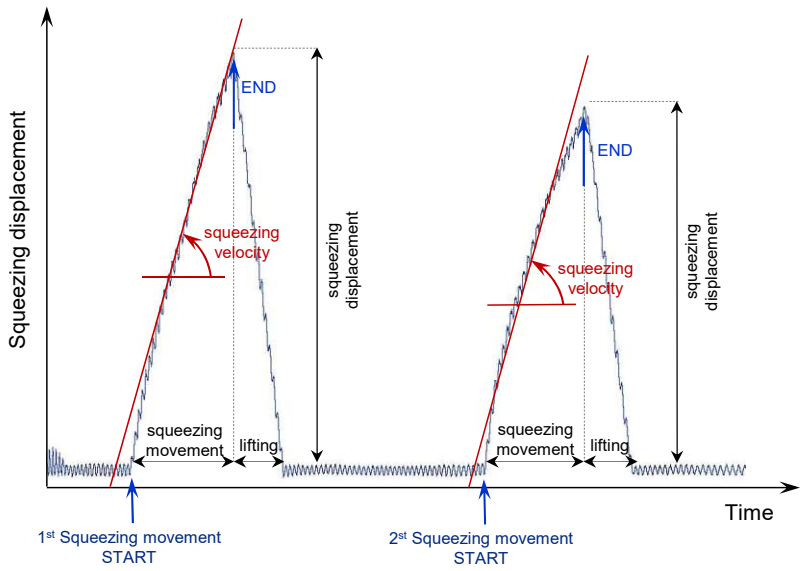

Figure 6.30: Calculation of squeezing velocity in a double squeezing process from the displacement measurement

Result of this comparison can be seen in Figure 6.31. Squeezing velocity for eight locations altogether is plotted together with the squeezing duration and the maximum reaction force per cycle as an average value for each location. Value ranges for the maximum reaction force per cycle are defined using the ranges from the in-situ measurement presented in Tables 6.5 and 6.6. Following a similar approach, measured squeezing velocity of 60 mm/s

Die approbierte gedruckte Originalversion dieser Dissertation ist an der TU Wien Bibliothek verfügbar.
The approved original version of this doctoral thesis is available in print at TU Wien Bibliothek.

measured in *moderately clean* ballast is taken as the reference limit value between the *clean* and *fouled* ballast conditions. Figure 6.30 shows that all squeezing velocity values higher than the selected reference value represent tamping in *clean* ballast conditions, whereas the values lower than the reference tamping are in *fouled* ballast conditions.

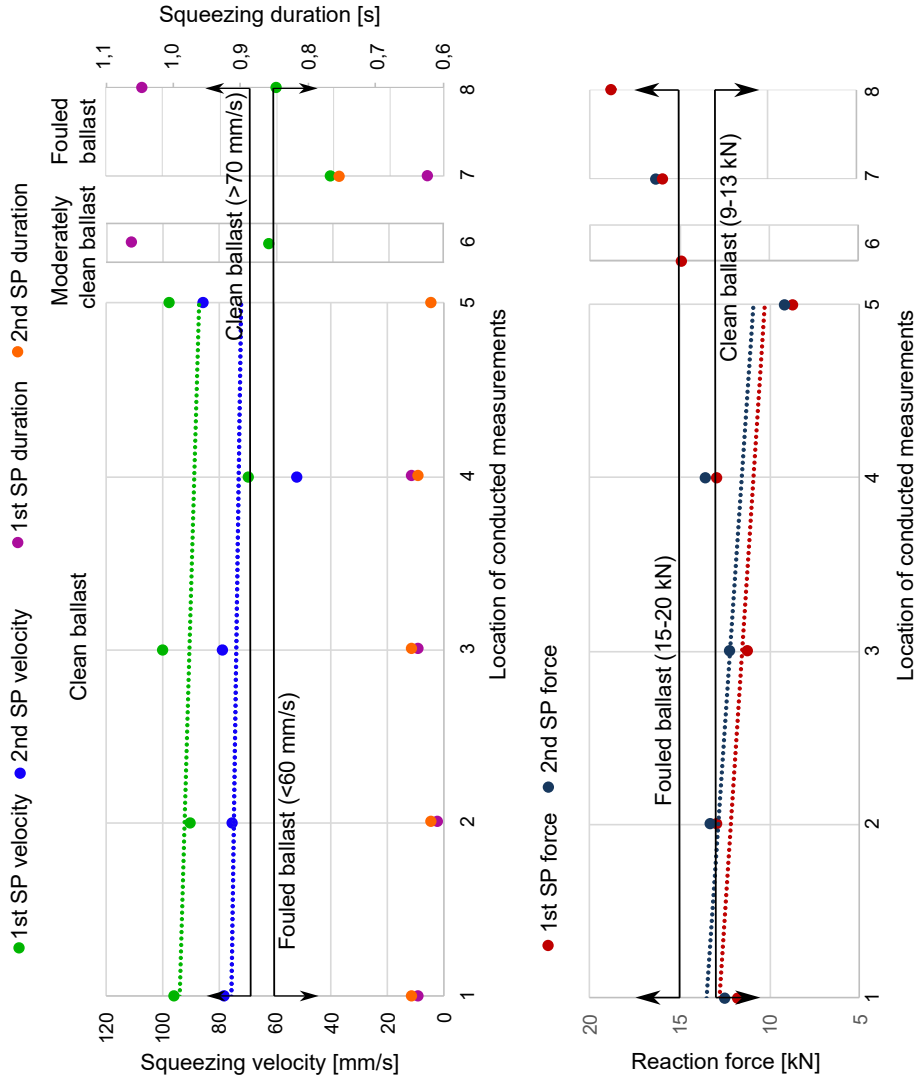

Figure 6.31: Comparison of squeezing velocity and maximum reaction force per cycle in different ballast conditions

Die approbierte gedruckte Originalversion dieser Dissertation ist an der TU Wien Bibliothek verfügbar.
The approved original version of this doctoral thesis is available in print at TU Wien Bibliothek.

Chapter 7

Soil dynamic behavior of track ballast and experimental verification

7.1 Introduction

Frequency modulation used during track tamping (Chapter 5) ensures ballast matrix compaction and rearrangement of ballast grains in a way that the desired track elevation is achieved. *Fischer* [59] conducted a detailed study about the influence of tamping frequency and amplitude on the compaction and stabilization of the ballast bed. An ideal tamping frequency of 35 Hz is suggested in order to accomplish both the aspired track elevation and the needed ballast compaction for a sufficient load-bearing capacity. Tamping with lower frequencies (< 25 Hz) provides the possibility of ballast bed elevation but results in insufficient load-bearing capacity. Higher frequencies (> 50 Hz) have been proven to lead to a stable ballast bed with a high load-bearing capacity, however the elevation of the ballast bed is not possible due to the fact that the ballast grains move away from the tamping tines in a manner that can be described as ballast fluidization.

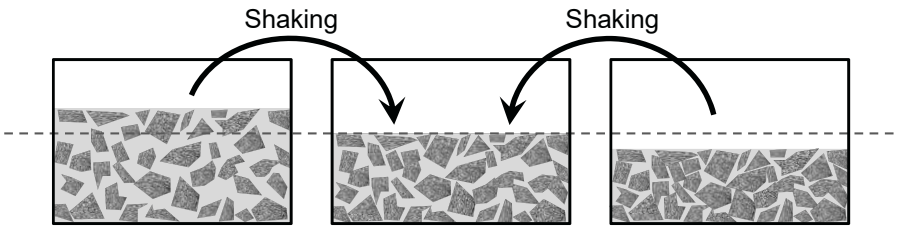

Figure 7.1: Loosely bedded ballast sample moves to a denser bedding due to ballast fluidization (contraction). Extremely dense ballast sample goes into a somewhat looser bedding when subjected to fluidization (dilatancy)

This (visco-)fluidization of the ballast grains during dynamic excitation can also be observed during regular track tamping with a frequency of 35 Hz and is necessary for a successful ballast bed compaction. When triggered, the grain fluidization forces single ballast grains into a denser bedding. During this process, contact points between single grains are almost non-existent, the angle of internal friction is greatly reduced as well as are the stresses

Die approbierte gedruckte Originalversion dieser Dissertation ist an der TU Wien Bibliothek verfügbar.
The approved original version of this doctoral thesis is available in print at TU Wien Bibliothek.
TU Bibliothek Your knowledge hub WIEN

acting on the ballast bed. A mechanism similar to the „*slip-stick*“ is activated, and the ballast grains rotate and turn searching for a dense(r) bedding. An important aspect is that the goal of successful ballast compaction is to achieve not the *maximum* but rather the *optimum* ballast bed compaction.

Loosely bedded ballast sample tends to change to a denser bedding due to ballast fluidization (or when put on a shaking table), while an extremely dense ballast sample goes into a somewhat looser bedding (Figure 7.1). In soil dynamics these two opposite phenomena can be described as contraction and dilatancy.

If the lateral ballast movement under and along the sleeper is constrained by either the "*Vorkopfverdichter*" in-situ or the constraints during laboratory testing [59], the resulting effect of the described movement would be a stable and compacted ballast bed. Given that the lateral displacement of the ballast grains during routine track maintenance cannot be controlled, higher tamping frequency would result in an even lower ballast bed position than prior to track tamping. As the grains become wedged in the grain structure, their mobility is no longer ensured and the dilatation is prevented (Figure 7.2).

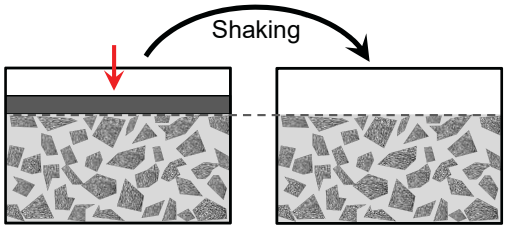

Figure 7.2: Excess pressure (hydrostatic pressure on the grain structure) significantly reduces or prevents ballast fluidization entirely

During ballast fluidization there is no continuous contact in the grain structure. The transmission of impacts and waves is therefore strongly limited. If the fluidization is completed or prevented (e.g. by excess pressure), the propagation of vibrations is largely unhindered. Wave transmission through the ballast bed during fluidization through a loose bedding is much slower than through a dense bedding following the fluidization.

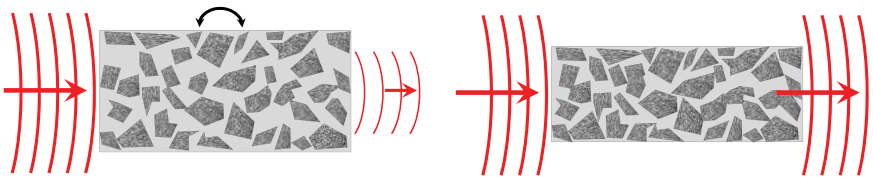

Figure 7.3: Wave transmission in ballast bed, during fluidization through a loose bedding (left) and following the fluidization through a dense bedding (right)

In order to validate some of these statements, additional experiments were carried out. Results are discussed in the following chapters.

Die approbierte gedruckte Originalversion dieser Dissertation ist an der TU Wien Bibliothek verfügbar.
The approved original version of this doctoral thesis is available in print at TU Wien Bibliothek.
TU Bibliothek Your knowledge hub WIEN

7.2 In-situ measurement - Ballast fluidization

During the in-situ conducted measurement in the scope of this research project, ballast matrix response during loading was plotted using the approach described in Chapter 6.5.3. Possible ballast fluidization is observed in the second squeezing process during tamping in all locations where track reconstruction was conducted (example in Figure 6.11b). Loading response of the ballast matrix increases during the first squeezing movement as the compaction progresses. Similar behavior is observed in the first part of the second squeezing movement after which a significant peak forms between the 15th and 19th cycle, depending on the squeezing movement duration, i.e. on the total number of cycles. Loading response of the matrix continuously decreases during remaining cycles.

An improvised in-situ experiment was conducted in December 2017 on a secondary track near Linz railway station in order to determine the triggering parameters and capture possible ballast fluidization. Granite ballast grains with a grain-size distribution Category 1 (Figure 2.9a) were arranged in an approximately 1 m wide and 0.50 m high ballast pile directly next to one of the sleepers (Figure 7.4).

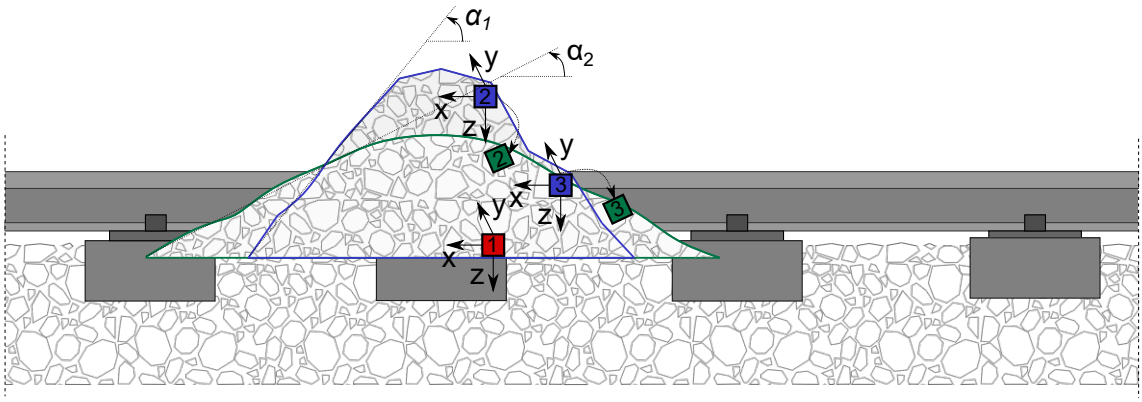

Figure 7.4: Ballast fluidization testing in-situ

Three accelerometers were built into the pile - at the bottom, middle and at the top in order measure the near field response, i.e. in order to move and rotate together with the ballast grains as the tamping machine *Dynamic Tamping Express 09-4X* E^3 was set into operation on the sleepers close to the pile. Ballast fluidization was observed through the loss of shear strength and changes in slope inclination α. An additional accelerometer was placed 12 m away from the pile to measure the vibration effects on the the surrounding area (far field). Expected results of this in-situ test measured during deployment of both the tamping unit and the dynamic track stabilizer are:

- accelerations leading to ballast fluidization
- detection of ballast fluidization based on additional frequencies due to moving grains and tilting of the built-in sensors
- intensity of ballast fluidization, temporary reduction or loss of shear strength, changes of pile slope and width

Die approbierte gedruckte Originalversion dieser Dissertation ist an der TU Wien Bibliothek verfügbar.
The approved original version of this doctoral thesis is available in print at TU Wien Bibliothek.

Approximate dimensions of the two piles prior to and after the tamping and dynamic track stabilization can be taken from the Table 7.1.

Table 7.1: Approximate pile dimensions prior to and after the test

		width [m]	height [m]	α [°]
Test 1	initial	1.0	0.50	45.0
	residual	1.25	0.20	17.7
Test 2	initial	1.0	0.50	45.0
	residual	1.30	0.20	17.1

7.2.1 Accelerations analysis

Employment of the tamping unit and the DTS and their influence on the single grain displacements in the ballast pile were observed through measured accelerations. Absolute values of acceleration measured in all three directions (x, y and z) for every of the four installed sensors was calculated using the following equation:

$$a_{abs} = \sqrt{a_x^2 + a_y^2 + a_z^2} \tag{7.1}$$

As can be seen in Figure 7.6, the three sensors located in the pile of fine-grained granite measured absolute accelerations of up to $3g$, while the values measured by the accelerometer in the far field were negligibly small. The exact position, i.e. orientation of the sensors during the test, is obtained from the detected static activities or constant accelerometer signals (Figure 7.6), determining the angle between the accelerometer axis and the gravity vector. Significant differences can be observed between tamping unit and DTS employment, given that the latter induces ten times higher accelerations measured in the ballast pile, even if the difference in the excitation frequency is relatively small (35 Hz compared to 33 Hz). Figure 7.6 also shows changes of the ballast pile shape and inclination induced by the dynamic motion of the two components. Highest values of "peaks" that can be seen during both tamping and dynamic stabilization occur as the tamping unit, i.e. DTS is located directly behind the ballast pile. The peak is preceded by an increasing unbalance or tilting of the sensors that is triggered by ballast fluidization.

Greatest motion was detected by the second accelerometer located in the middle of the pile (Figure 7.7), capturing ballast fluidization by excessive rotation and displacement during track tamping (35 Hz, highlighted in red) and even more distinctly during dynamic stabilization (33 Hz). Figure 7.7 also shows that in the context of this improvised approach, the uncontrollable motion of the ballast particles does not only occur while ballast under a certain sleeper is undergoing compaction, but increases as the tamping unit approaches the monitored sleeper.

The individual ballast grains in the grain structure (at least 4 contact points) move and rotate in interaction to find a denser bedding. The entire ballast pile spreads slowly and becomes smaller in height (inner movement of the grain structure). Larger grains are "ejected"

Die approbierte gedruckte Originalversion dieser Dissertation ist an der TU Wien Bibliothek verfügbar.
The approved original version of this doctoral thesis is available in print at TU Wien Bibliothek.
TU Bibliothek Your knowledge hub WIEN

by the grain structure on the slope and roll down (outer movement of individual grains).

In addition to the analysis presented in Figure 7.6, accelerations in y direction (direction of the sleeper, perpendicular to the rails) obtained from all four sensors during both tamping and dynamic track stabilization are converted to a representation in the frequency domain by the Fast Fourier Transformation (FFT). The predominant frequency can be observed in Figure 7.5 and it roughly to the excitation frequency of the DTS (approximately 33 Hz).

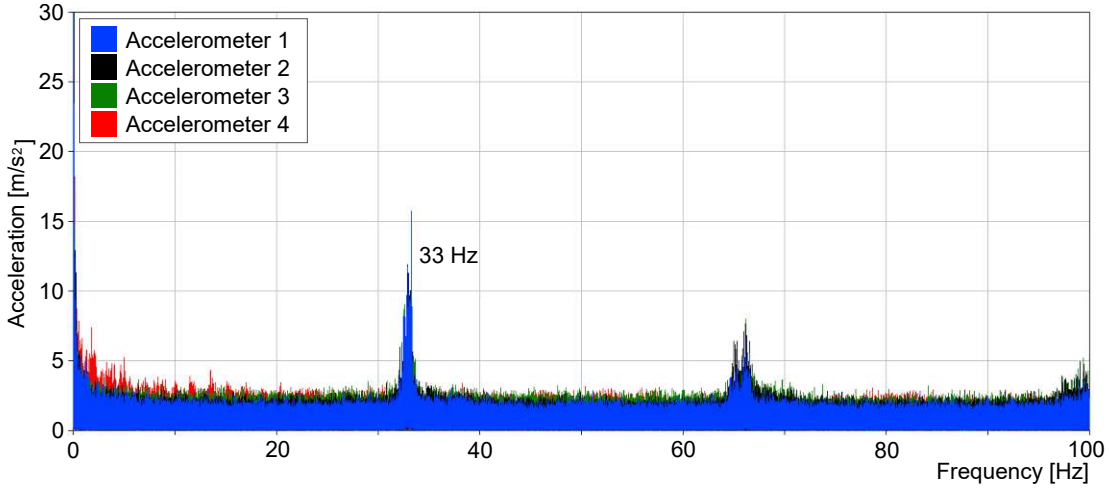

Figure 7.5: *Fast Fourier Transformation* of the accelerations measured by all four sensors in y direction

Die approbierte gedruckte Originalversion dieser Dissertation ist an der TU Wien Bibliothek verfügbar.
The approved original version of this doctoral thesis is available in print at TU Wien Bibliothek.

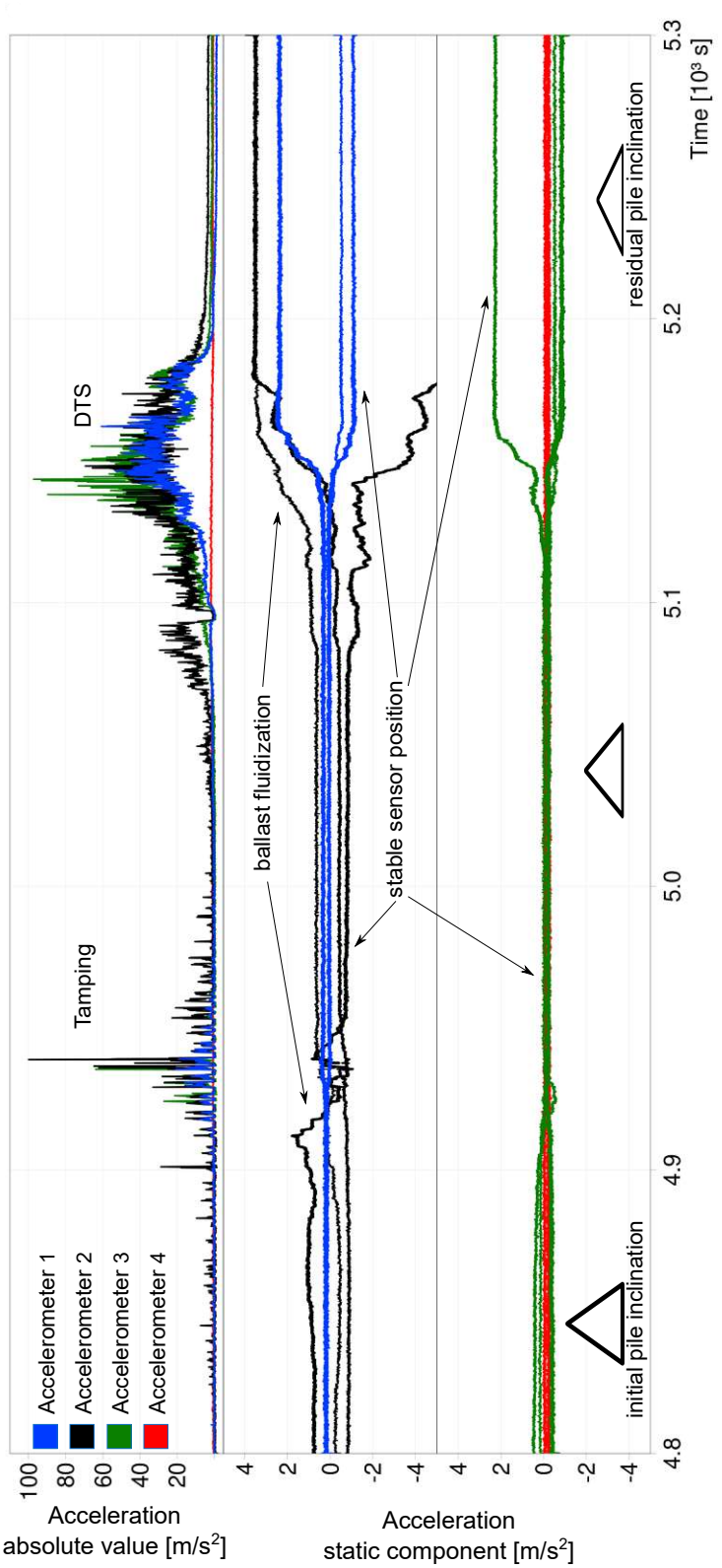

Figure 7.6: Absolute and static acceleration measured by all four accelerometers

Die approbierte gedruckte Originalversion dieser Dissertation ist an der TU Wien Bibliothek verfügbar.
The approved original version of this doctoral thesis is available in print at TU Wien Bibliothek.

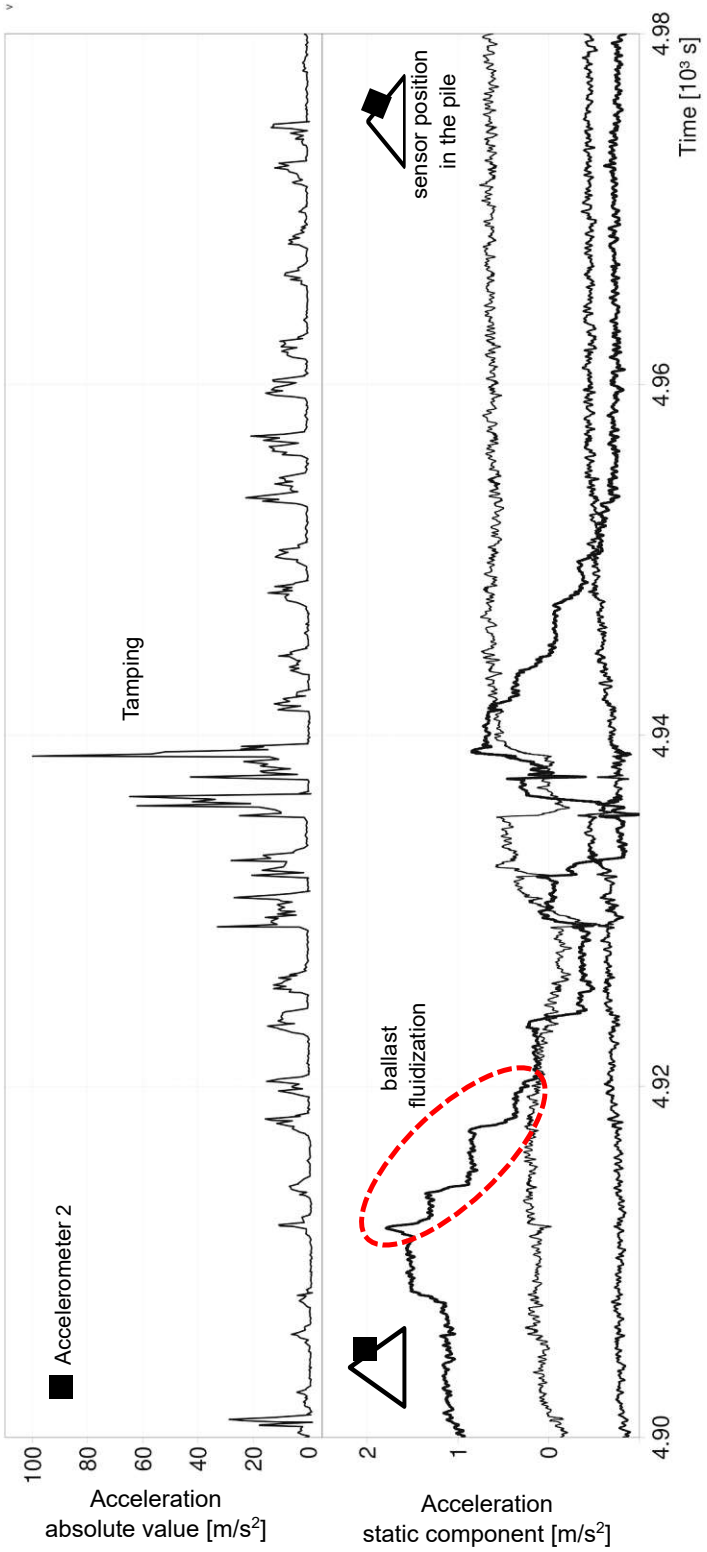

Figure 7.7: Detail showing measurement results of accelerometer 2

Die approbierte gedruckte Originalversion dieser Dissertation ist an der TU Wien Bibliothek verfügbar.
The approved original version of this doctoral thesis is available in print at TU Wien Bibliothek.

7.2.2 Particle image velocimetry

In addition to analysis of data collected by the built-in accelerometers (Chapter 7.2.1), video recording of the in-situ measurement of ballast fluidization is analyzed using the Particle Image Velocimetry (PIV), an effective optical technique for measuring surface particle movement, i.e. surface displacements of solids or fluids. The method is based on calculation of single grain velocities between successive digital images with constant time between frames. In addition to the velocity, the method was used to monitor the rotation, velocity magnitude and direction of ballast grain movement in the ballast pile. An open-source PIV software *PIVLab* (v.2.54) [129] running from *MATLAB R2021a* command line is used for the analysis.

7.2.2.1 Data analysis method

PIV data analysis method was successfully applied to granular materials in dynamic centrifuge testing [93], [37], scaled slope models [83] and many others. Key features of this method are the non-intrusive, direct velocity measurement of the whole field (high number of single grains), meaning that it allows an observation of displacements and strain fields on the scale of grains and the spatial and temporal resolution, meaning that a quantification of velocity across the whole image is possible and the quality of analysis can be significantly influenced by the number of recorded frames per second. Decreasing the time between frames would lead to an improvement of the result reliability. Basic principle of any Particle Image Velocimetry software is to divide every image extracted from the video into a large number of square regions, each with a unique combination of color or gray-scale values that represents the amount of light reflected from the recorded region. Differences in light intensity are used by PIV system to create a gray-scale pattern. The gray level range can be between 0 (black) and 255 (white) for an 8-bit image [37]. Every region in the frame M_t is given a set of coordinates (u_t and v_t). In the next image/frame M_{t+dt}, a search for coordinates u_{t+dt} and v_{t+dt} is conducted within a specified distance set by the interrogation area. Correlation between pixels in each search region and the original region is computed. Calculating the correlation value at each position results in a correlation function over the search area. Location at which the highest correlation is found gives the new location of the region, and the vector joining the two locations r_t is then calculated (Figure 7.8) [93].

7.2.2.2 Settings and parameters

PIV analysis is conducted using a high-speed (60 frames per second) and high-resolution ($1920 \cdot 1080$ Pixels) video recorded by the *GoPro* camera installed on a vibration decoupled rubber tripod that was used to record the tests described in Chapter 7.2. Sixty images per second are extracted from the video (Figure 7.10) and analyzed following the principle described in Chapter 7.2.2.1. Prior to image analysis, following parameters and settings are defined:

- Regions of interest and masks: region of every image within which vectors will be computed. Masks are areas of the region of interest which are not analyzed. Figure 7.9

Die approbierte gedruckte Originalversion dieser Dissertation ist an der TU Wien Bibliothek verfügbar.
The approved original version of this doctoral thesis is available in print at TU Wien Bibliothek.
TU Bibliothek Your knowledge hub WIEN

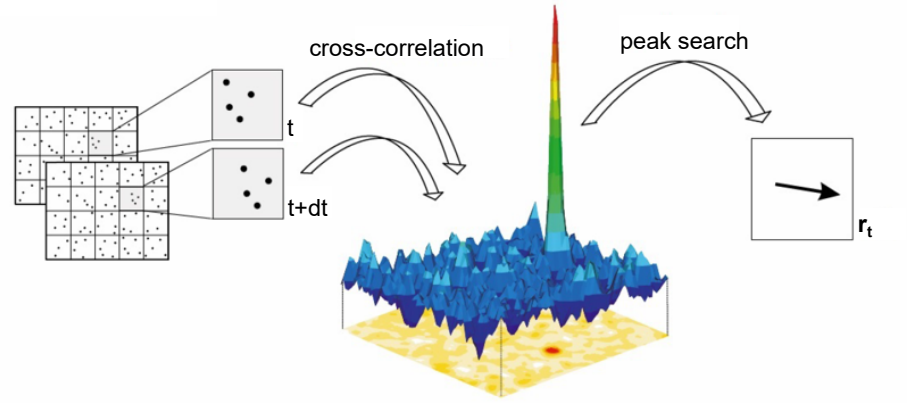

Figure 7.8: Description of PIV vector calculation [37]

shows the mask as the red area of the image. Setting the mask increases the processing time significantly. Figure 7.9a also shows the biggest set interrogation area (red square) dependent on the average analyzed particle size. This interrogation area is additionally subdivided into quarters to refine the analysis.

- Fast Fourier Transform window deformation: Velocity vectors are calculated using image processing algorithms. The algorithm used in *PIVlab* is the cross correlation through Fast Fourier Transform technique with linear window deformation interpolation [93].

- Image pre-processing: the contrast of all single images is increased by Contrast Limited Adaptive Histogram Equalisation (CLAHE) image processing technique, facilitating the following analysis (Figure 7.9b).

- Distance calibration: The length unit of the vectors is converted from pixels to meters by specifying a fixed distance in the image (Figure 7.9a) using the measuring tapes. An important aspect to state is that due to the fish-eye effect, the recording is distorted and the set distance will vary slightly from its real value.

- Vector validation: outliners, i.e. resulting velocity vectors that vary more than seven standard deviations from the average are excluded and replaced with interpolated vectors.

In the next step, a calculation of velocity magnitude using the following equation is conducted:

$$r_t = \sqrt{u_t^2 + v_t^2} \tag{7.2}$$

where u is the horizontal component of the velocity vector, defined with a negative sign in the direction of the tamping machine movement. Vertical component v defines movement downwards with a positive sign (Figure 7.9a). Calculation of the resulting velocity vector of ballast movement is possible for any desired profile/plane of the pile.

Die approbierte gedruckte Originalversion dieser Dissertation ist an der TU Wien Bibliothek verfügbar.
The approved original version of this doctoral thesis is available in print at TU Wien Bibliothek.

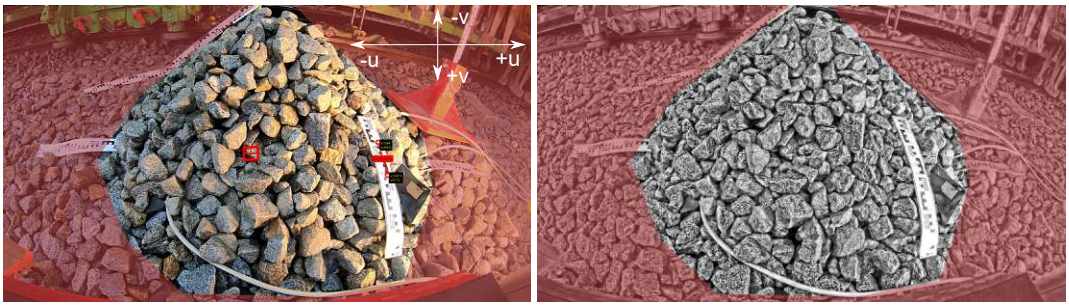

(a) Mask, interrogation area and calibration (b) *CLAHE* image pre-processing

Figure 7.9: PIV analysis - Settings and parameters

(a) Initial stage (b) Lifting and levelling unit

(c) Tamping unit approaching (d) Tamping unit passed

(e) DTS approaching (f) Final stage

Figure 7.10: Examples of single images extracted from the video recording used for the PIV analysis

Die approbierte gedruckte Originalversion dieser Dissertation ist an der TU Wien Bibliothek verfügbar.
The approved original version of this doctoral thesis is available in print at TU Wien Bibliothek.
TU Bibliothek Your knowledge hub WIEN

7.2.2.3 Results

An analysis following the method described in the previous chapter is conducted in two parts:

- Tamping unit - 3500 frames are extracted from the video recording of the tamping unit conducting track tamping on five sleepers altogether, including the sleeper located directly behind the ballast pile.
- Dynamic track stabilizer - 4500 frames are extracted from the video recording of the DTS operation on the same sleepers

Velocities in both v (vertical) and u (horizontal) directions (Figure 7.11) as well as the velocity magnitude (Figure 7.12) are calculated between single frames and a resulting frame showing average velocity values for the whole tamping and DTS process is created. Outliners showing extreme velocity values should be exempt from consideration as they present single ballast grain from the top of the pile falling downwards due to the accelerations and are not decisive for the ballast fluidization observation. An important point to state is that all of the velocity magnitude values calculated using the PIV method described should be interpreted with caution due to the fact that the (spatial) motion of ballast grains towards the camera cannot be taken into consideration in the analysis. Only a relative comparison of values results from the tamping unit and DTS utilization is possible.

Tamping

Histograms showing average velocities in both directions can be seen in Figure 7.11. Values significantly higher than the average show single grain motion on the surface of the pile, i.e. grains rolling down from the pile top and should not be taken into consideration regarding ballast fluidization.

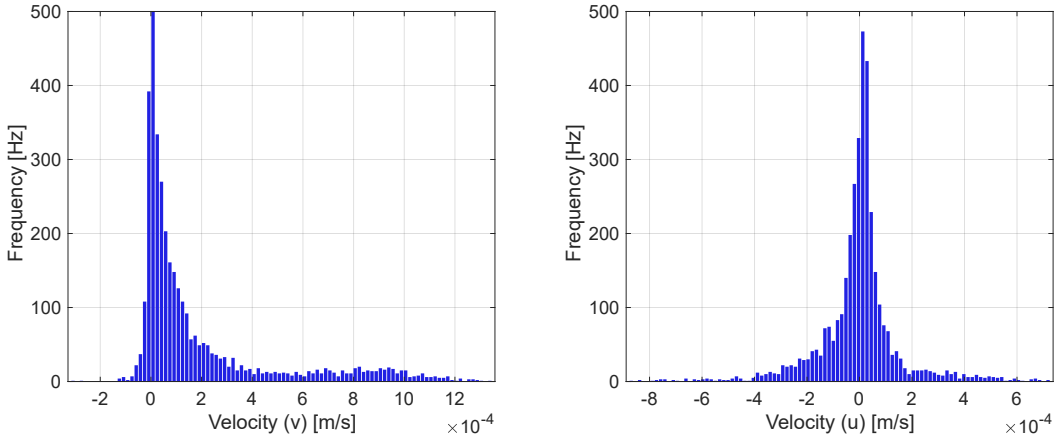

(a) Average vertical single grain velocities (b) Average horizontal single grain velocities

Figure 7.11: Histograms showing average single grain velocities in both directions during tamping unit employment

Die approbierte gedruckte Originalversion dieser Dissertation ist an der TU Wien Bibliothek verfügbar.
The approved original version of this doctoral thesis is available in print at TU Wien Bibliothek.

In addition to grain velocities in both vertical and horizontal direction the velocity magnitude is calculated and plotted in Figure 7.12. A general observation can be made that the motion velocity of single ballast grains triggered by the tamping unit employment is in average lower than $2 \cdot 10^{-4}$ m/s].

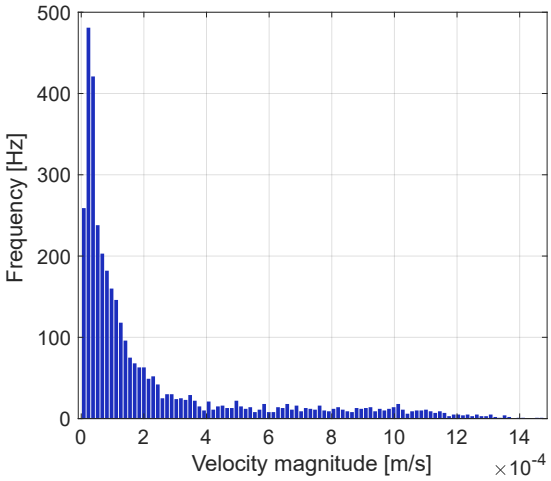

Figure 7.12: Histograms showing velocity magnitudes recorded during tamping unit employment

Analysis does not only show the movement of the ballast grains, but also the tine oscillations and the tamping machine passing by. Lowering the tamping tines towards the ballast bed can be easily noticed in both resulting velocity fields (Figure 7.13, vertical component v defines movement downwards with a positive sign) and are not taken into consideration during result interpretation.

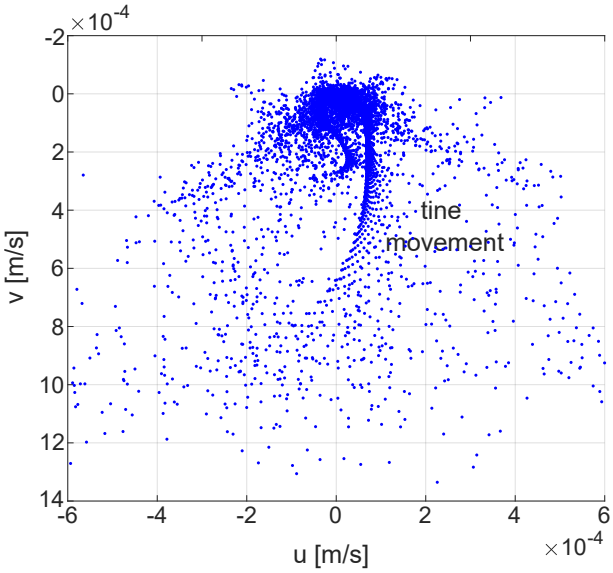

Figure 7.13: Velocity field resulting from tamping unit employment

Die approbierte gedruckte Originalversion dieser Dissertation ist an der TU Wien Bibliothek verfügbar.
The approved original version of this doctoral thesis is available in print at TU Wien Bibliothek.

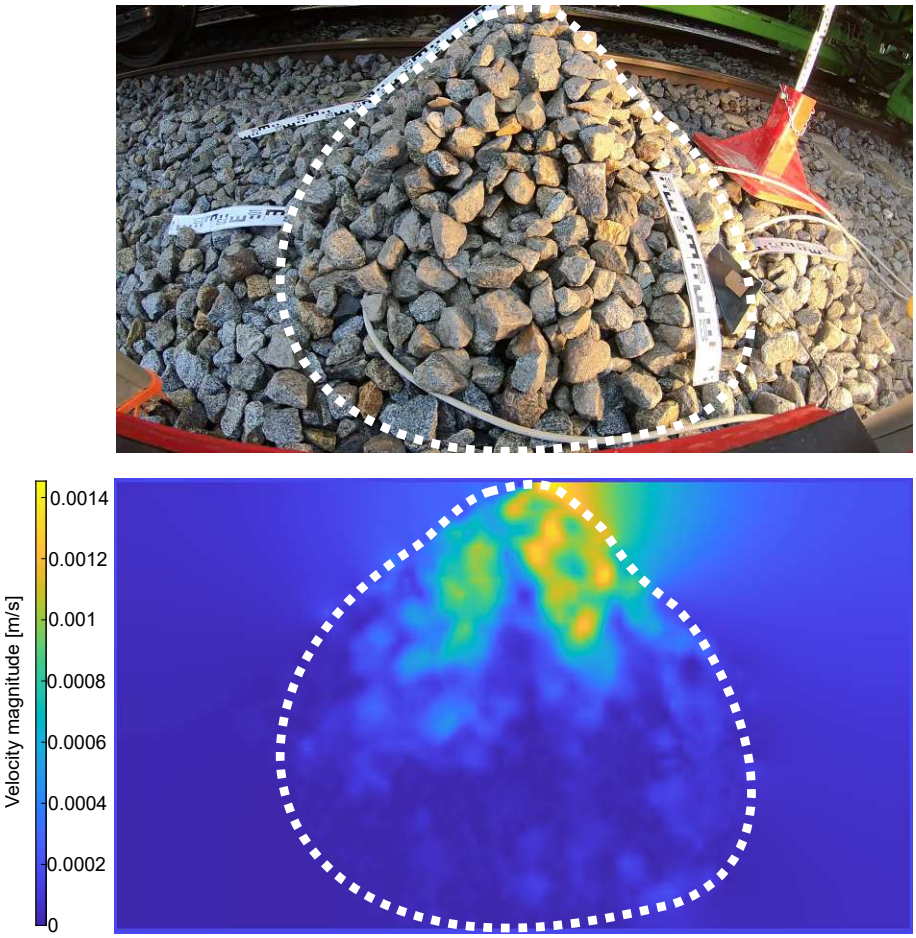

Figure 7.14: Heat map showing velocity magnitudes of the highlighted area recorded during the tamping process

Heat map of the frame of average values can be seen in Figure 7.14. Highest values can be observed on the top of the pile and present the machine movement but also single grains on the pile surface. The average velocity of single grains decreases towards the bottom of the pile and correlates in values with Figure 7.12 as it is also in average lower than $2 \cdot 10^{-4}$ [m/s].

Dynamic track stabilizer

PIV analysis using same process parameters is conducted for the frames resulting from the video recording of the DTS employment. As can be seen in Figure 7.15 average horizontal movements u are between -1 m/s and 1 m/s for DTS employment. Vertical movements v occur with velocities between -0.5 m/s and 1 m/s. Higher velocities in the horizontal direction are easily explained by ballast grains rearrangement in the lowest stable position.

Ten times higher velocities are initiated by the dynamic track stabilizer in comparison to the tamping unit. The difference can be noted when comparing the histogram plotted in Figures 7.11 and 7.15, as well as when comparing Figure 7.12 to Figure 7.16. Significant increase of velocity is caused primarily by different excitation frequency and operating principle of the DTS but also by a longer DTS-track contact duration.

Die approbierte gedruckte Originalversion dieser Dissertation ist an der TU Wien Bibliothek verfügbar.
The approved original version of this doctoral thesis is available in print at TU Wien Bibliothek.
TU Bibliothek Your knowledge hub WIEN

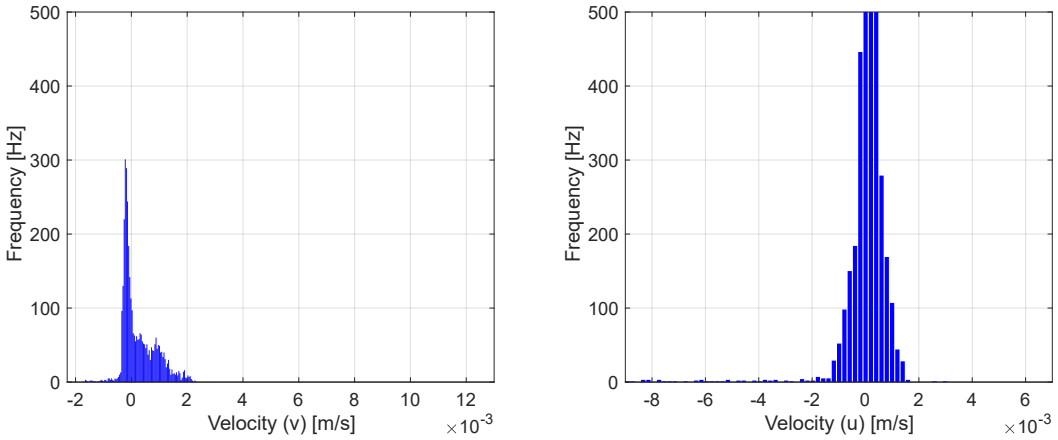

(a) Average vertical single grain velocities (b) Average horizontal single grain velocities

Figure 7.15: Histograms showing average single grain velocities in both directions during DTS employment

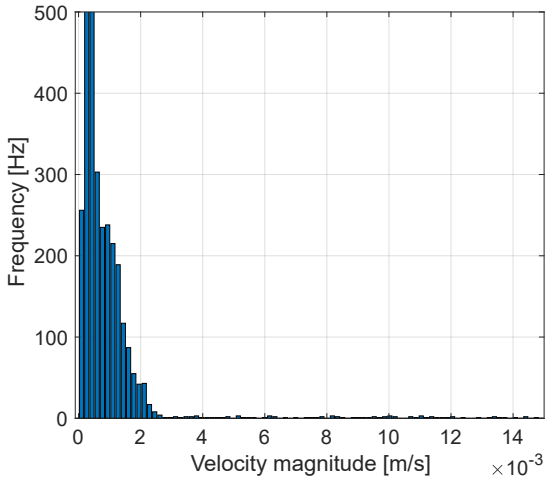

Figure 7.16: Histograms showing velocity magnitudes recorded during during DTS employment

Machine movement on the track can be easily observed in Figure 7.17 and is, once more, not relevant for the analysis of ballast fluidization. However, movement of ballast grains downwards can also be observed, with average velocity between -0.5 m/s and 1 m/s.

Figure 7.18 shows the heat map velocity magnitudes recorded during the DTS employment. Given that the scaling is the same as in Figure 7.14, the significant increase of single grain velocity can be observed.

Die approbierte gedruckte Originalversion dieser Dissertation ist an der TU Wien Bibliothek verfügbar.
The approved original version of this doctoral thesis is available in print at TU Wien Bibliothek.

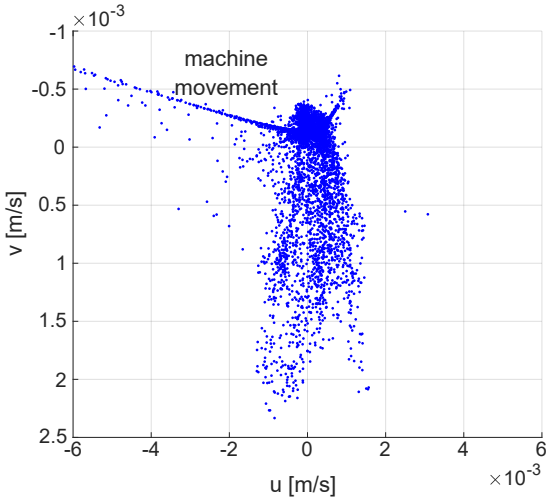

Figure 7.17: Velocity field resulting from DTS employment

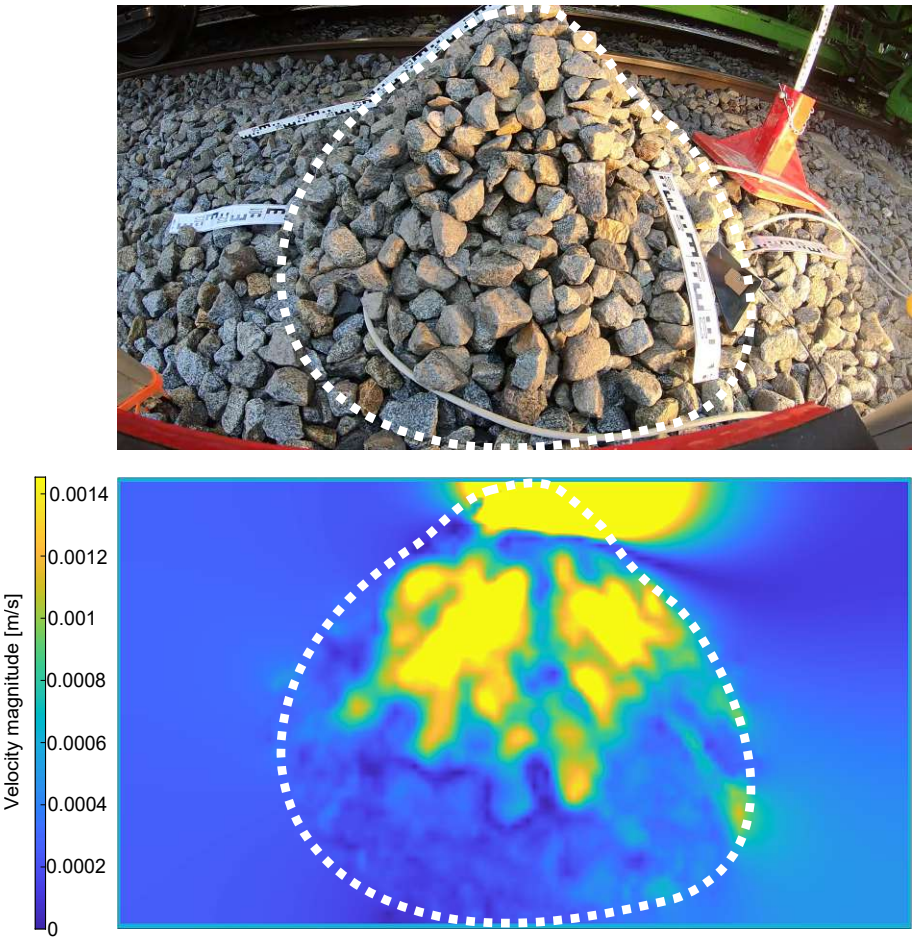

Figure 7.18: Heat map showing velocity magnitudes of the highlighted area recorded during DTS employment

Should deformations that occur in the soil under cyclic or dynamic loading be much larger than expected, this process can be described as flowing of soil or soil fluidization. Unlike soil liquefaction, the described process can also take place in non water-saturated

Die approbierte gedruckte Originalversion dieser Dissertation ist an der TU Wien Bibliothek verfügbar.
The approved original version of this doctoral thesis is available in print at TU Wien Bibliothek.

and non-cohesive soils without excess pore water pressures. In the context of the two conducted tests discussed in this chapter, the transmission of accelerations that occurs, allows individual ballast grains also to move *out* of their dense bedding and disables the transfer or shear stresses. If ballast fluidization occurs as described, track ballast under the sleepers will not undergo the desired compaction as due to a lack of grain-on-grain friction, the compaction energy cannot be transmitted to the ballast matrix. Even though the conducted tests present an improvised approach to capture and measure ballast fluidization during tamping and dynamical stabilization due to the fact that the pile is located next to and not directly under the sleeper, valuable conclusions about movement of single grains under dynamic loading can still be drawn.

7.3 In-situ measurement - Tamping unit interaction with the track substructure

In the scope of an on site measurement conducted at location Retz-Unternalb in Austria (Line 1124C, kilometre 79,346) between June and September 2020, the following measurement system was installed in order to observe and interpret the interaction of the *Plasser & Theurer Unimat 09-4x4/4S* universal tamping machine and dynamic track stabilizer (DTS) with the track (sub)structure:

- Pressure cells - at ballast and subballast bottom edge (P_o and P_u, Figure 7.19)
- 3D acceleration sensors - on two sleepers (presented in blue and orange, Figure 7.19), at ballast and subballast bottom edge (presented in black, Figure 7.19), in the surrounding area (presented in red, Figure 7.19)
- 6D acceleration sensors - on DTS (presented in blue, Figure 7.19)
- Inductive sensors for unbalance position (phase) - on DTS (presented in light blue, Figure 7.19)

Exact position of the sensors can be seen in Figure 7.19 and is described in detail in [48]. Following the sensor installation, track maintenance was conducted at this location by the *Unimat 09-4x4/4S* tamping unit and DTS. Prior to the employment of the tamping machine the track was renewed by a *Plasser & Theurer Unimat AHM 800R* and *RUS 1000S* track renewal formation rehabilitation machine. Clean ballast bed measured 45 cm in height and 3.35-3.40 m in width, measured from the track axis.

Die approbierte gedruckte Originalversion dieser Dissertation ist an der TU Wien Bibliothek verfügbar.
The approved original version of this doctoral thesis is available in print at TU Wien Bibliothek.
TU Bibliothek Your knowledge hub WIEN

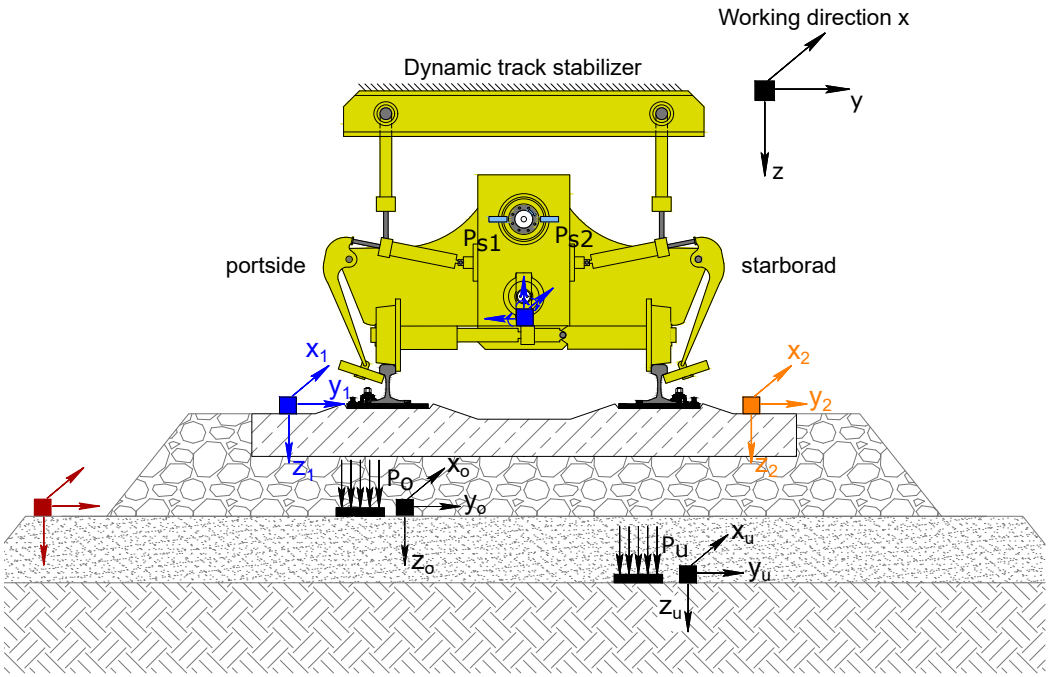

Figure 7.19: Exact position of the sensors on the Unimat 09-4x4/4S DTS and in the track (adapted from [48])

7.3.1 Frequency triggering ballast fluidization under the sleeper

The data measured by acceleration and pressure sensors built under the sleeper on the upper edge of the ballast bed (Figure 7.19, accelerations x_o, y_o and z_o, pressure P_o) are analyzed in order to investigate the influence of tamping tine induced motion on the ballast bed at the intersection point between the sleeper and the rail. Analysis results for both adjacent squeezing processes of a double tamping process are plotted in Figure 7.20.

Acceleration measured during both squeezing movements (highlighted red in Figure 7.20) are converted to a representation in the frequency domain by the Fast Fourier Transformation (FFT). Results of the FFT analysis can be seen in Figure 7.21.

Universal tamping machine *Unimat 09-4x4/4S* conducts the squeezing motion with a frequency of approximately 35 Hz. Since only the two adjacent squeezing movements are analyzed, this frequency is expected to prevail as can be seen in Figure 7.5. However, as can be seen from Figure 7.21, the almost double frequency level of about 70 Hz occurs most frequently in the FFT analysis. This can be attributed to the tamping tine dynamic motion during one cycle. As can been seen in the tamping tine array of the *Dynamic Tamping Express 09-4X* E^3 tamping machine (Figure 7.22), during one cycle, i.e. one tine oscillation, the tamping positioned on the opposite sides of the rails move in opposite directions. The same tine movement occurs during tamping with the *Unimat 09-4x4/4S* universal tamping machine. This non-synchronous tine movement leads to overlapping of the excitation frequency at the sleeper-rail intersection. The ballast matrix compaction directly on the contact to the tamping tine is conducted with the set excitation frequency of 35 Hz, but the frequency level increases with distance from tine and reaches the double value directly under the sleeper

Die approbierte gedruckte Originalversion dieser Dissertation ist an der TU Wien Bibliothek verfügbar.
The approved original version of this doctoral thesis is available in print at TU Wien Bibliothek.
TU Bibliothek Your knowledge hub WIEN

and rail intersection point. This higher frequency level significantly influences and aides the occurrence of ballast fluidization that has been proven to have a positive effect on the ballast grain rearrangement and compaction of the ballast matrix.

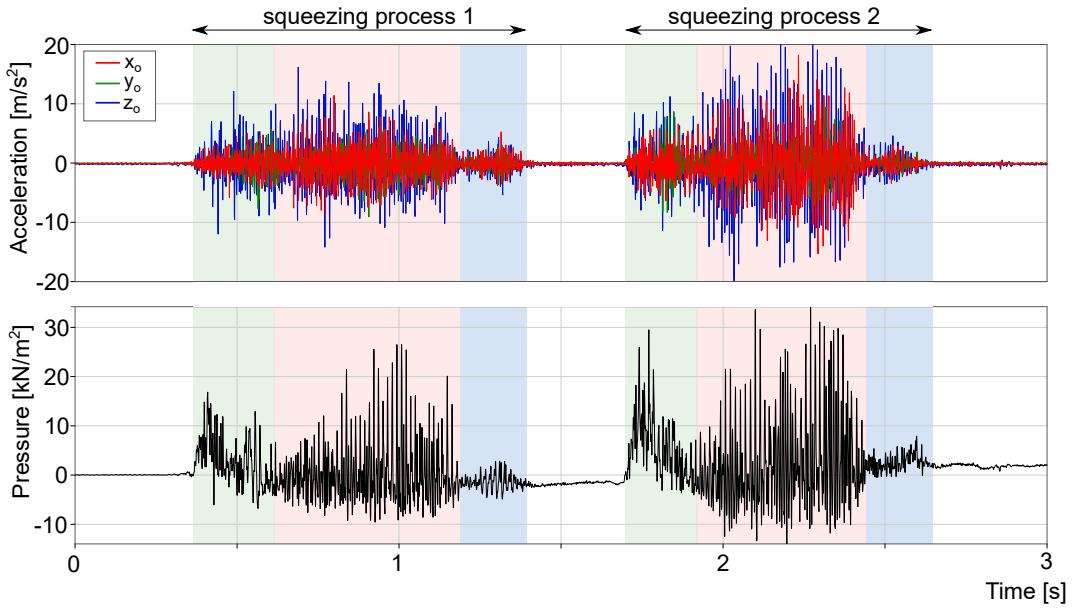

Figure 7.20: Accelerations in all three directions (x_o, y_o and z_o) and the pressure P_o, measured under the sleeper at the bottom edge of the ballast bed. Squeezing process subdivision color code: ballast penetration (green), squeezing movement (red), lifting (blue)

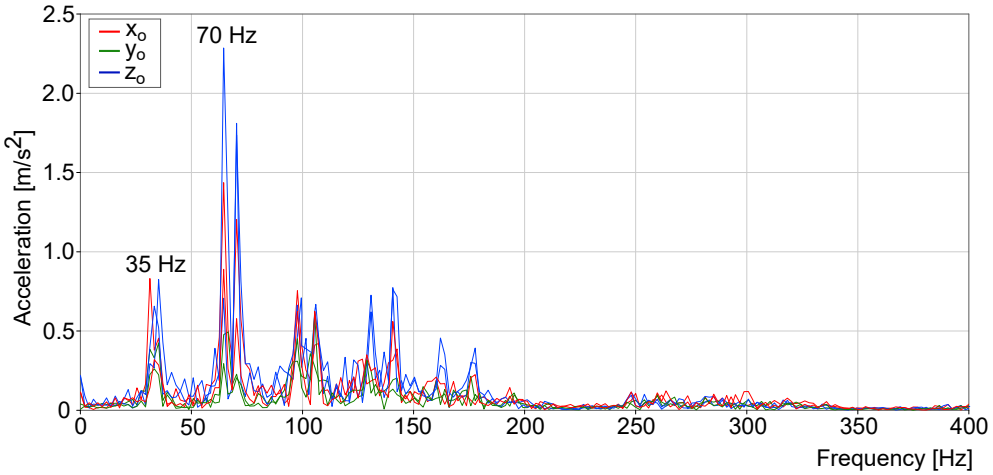

Figure 7.21: *Fast Fourier Transformation* of the accelerations plotted in Figure 7.20 for both squeezing processes

Die approbierte gedruckte Originalversion dieser Dissertation ist an der TU Wien Bibliothek verfügbar.
The approved original version of this doctoral thesis is available in print at TU Wien Bibliothek.

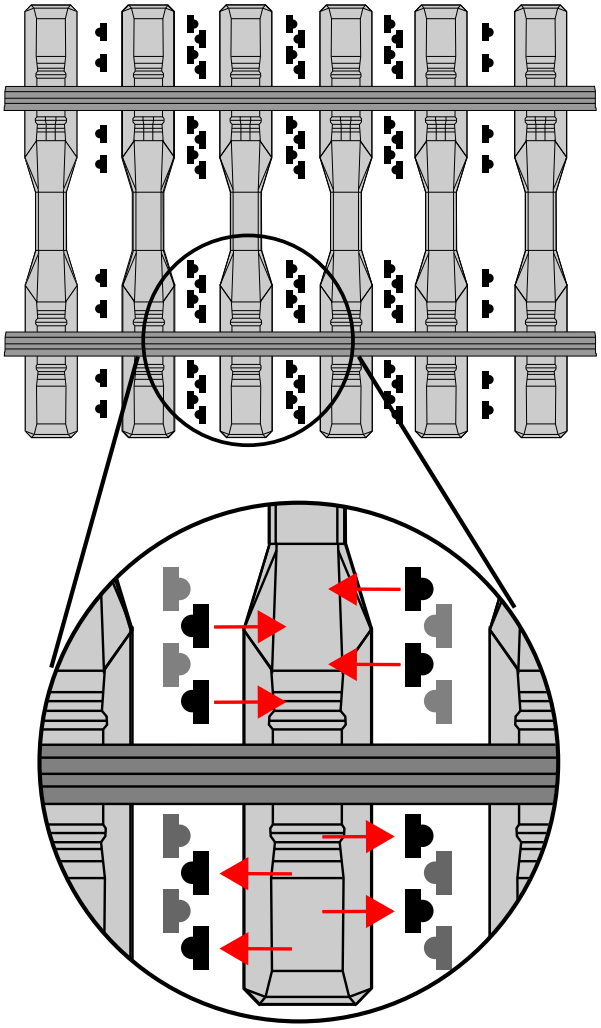

Figure 7.22: Tamping tine array of the Tamping machine *Dynamic Tamping Express 09-4X E*^{3}, showing the dynamic motion direction of single tamping tines in a cycle context

Die approbierte gedruckte Originalversion dieser Dissertation ist an der TU Wien Bibliothek verfügbar.
The approved original version of this doctoral thesis is available in print at TU Wien Bibliothek.

7.4 Tensile strength of single ballast grains

7.4.1 Introduction

Most frequently used dynamic compaction methods such as dynamic roller compaction [105] or deep vibro compaction [95] provide the possibility of compaction progress measurement through either Continuous Compaction Control (*CCC*) by measuring the acceleration, transmitted energy, loading stiffness or maximum contact force, or by in-situ testing (dynamic probing or standard penetration tests) succeeding compaction. Additional possibility of compaction control is given by dynamic load plate tests after roller pass. None of the sampling methods have been proven to be efficient or cost effective when applied to ballast tamping, mostly due to the following facts:

- Taking undisturbed ballast samples from under the sleeper is a very challenging task.
- Dynamic load plate tests are unsuitable since they cannot be conducted without establishing direct contact between the plate and the soil that is to be tested.

7.4.2 Motivation

Ballast attrition or fouling as tamping after-effect is an important aspect to be considered when optimizing the tamping parameters such as number of insertions, duration of the squeezing process and maximum reaction forces exerted onto the ballast during tamping. Another distinctive feature to be considered in the context of ballast compaction is the importance of detainment of particle shape, size and angularity by minimizing the occurrence of ballast fouling and increasing the ballast bulk density only through packing or rearranging the ballast particles in a matrix closer together causing a reduction in the volume of air. As mentioned before, there are still no reliable methods of compaction progress determination during ballast tamping, mostly due to the fact that the compacted ballast is located lengthwise under the sleeper which significantly aggravates the employment of any existing compaction control mechanisms [35]. In-situ measurements conducted in the scope of this research project enabled an insight into the tamping tine - ballast matrix interaction during track tamping for the very first time, providing the possibility of reaction force measurements, calculation of the ballast matrix response during loading and unloading and the computation of compaction energy. However, in order to prevent or minimize ballast fouling in form of particle chipping or attrition, the determination of stop criterion for optimal compaction should not only be dependent on the changes of (yet to be determined) tamping characteristics between two cycles. Maximum loads should also be limited according to ballast characteristics in order to prevent the acceleration of ballast fouling.

During monitoring of tamping process in regular track maintenance (Chapter 6), maximum reaction forces exerted to the ballast matrix measured at the tine plate amounted to about 20 kN during the squeezing movement and approximately as much (in absolute value) during ballast penetration. During both of these phases, the ballast grains are set into motion by the dynamic tine impulse as they strive to move away from the tine and thereby

Die approbierte gedruckte Originalversion dieser Dissertation ist an der TU Wien Bibliothek verfügbar.
The approved original version of this doctoral thesis is available in print at TU Wien Bibliothek.
TU Bibliothek Your knowledge hub WIEN

allow the tines to be lowered into the ballast bed (during ballast penetration) and form a denser bedding (during the squeezing movement). However, during the lifting phase (simultaneously opening the tamping tines and pulling the unit out of the ballast) high forces are not expected, especially not after the lifting phase is finished. Nevertheless, as can be seen in the example shown in Figure 7.23, forces as high as 13 kN (in absolute value) have been measured in and following the lifting phase in several locations during regular track maintenance.

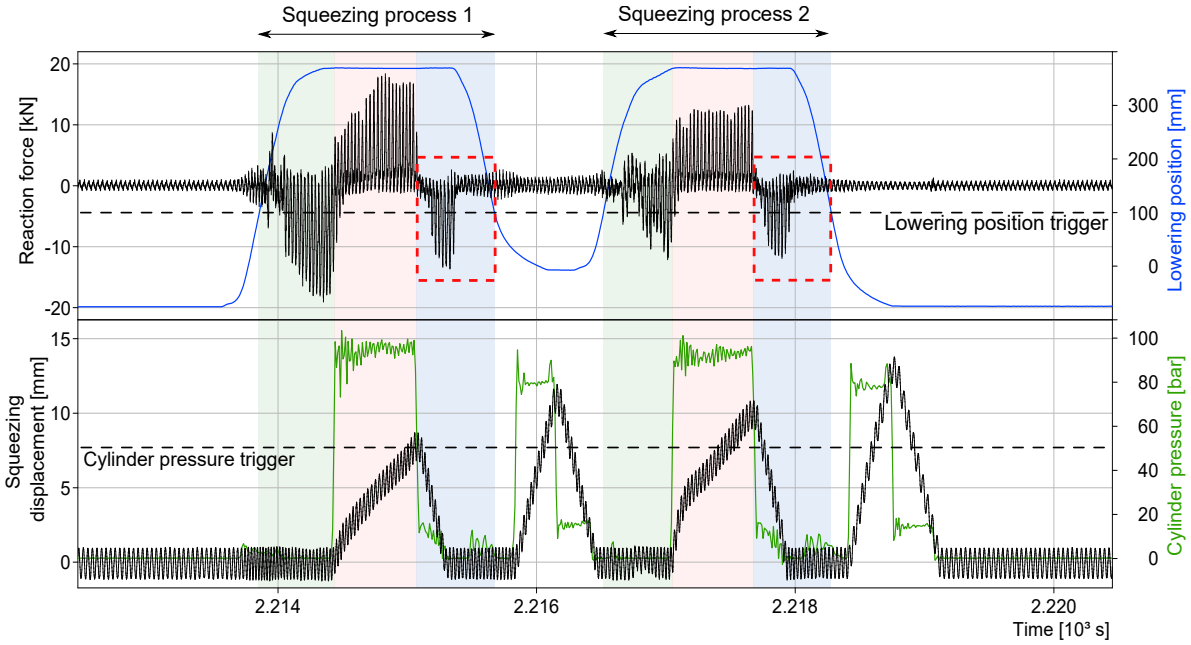

Figure 7.23: Example of a double tamping process with high reaction forces (framed in a red rectangle) measured during the lifting phase of both squeezing processes. Squeezing process component parts color code: ballast penetration (green), squeezing movement (red), lifting (blue)

A possible and plausible explanation behind the high reaction forces in question can be found in a single ballast grain getting "trapped" between two opposite positioned tamping tines while they open and perform a motion in the opposite direction to the squeezing movement (Figure 7.24). The prevailing negative sign also indicates that the force is measured on the back side of the tamping tine, arising the question if the "entrapment" of the single grain under the influence of such high forces could trigger particle chipping or attrition, thus changing its size and shape and contributing to the process of ballast bed fouling.

Die approbierte gedruckte Originalversion dieser Dissertation ist an der TU Wien Bibliothek verfügbar.
The approved original version of this doctoral thesis is available in print at TU Wien Bibliothek.

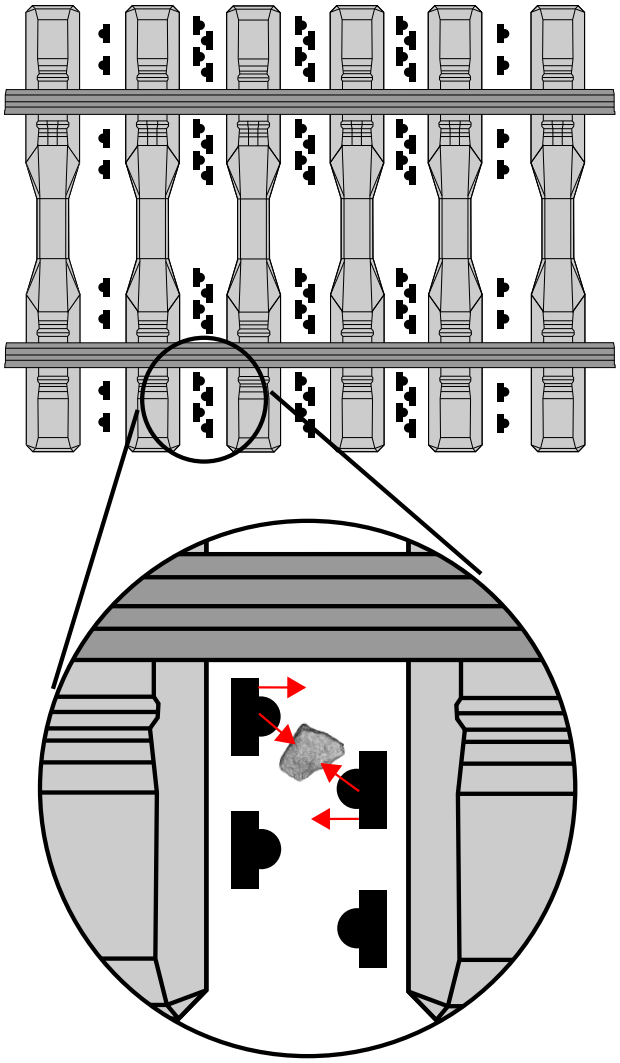

Figure 7.24: Tamping tine array of the Tamping machine *Dynamic Tamping Express 09-4X E*^{3}, showing the position of a single "trapped" ballast grain

Die approbierte gedruckte Originalversion dieser Dissertation ist an der TU Wien Bibliothek verfügbar.
The approved original version of this doctoral thesis is available in print at TU Wien Bibliothek.

7.4.3 Experimental approach - single particle tests

7.4.3.1 Uniaxial compression

Several ballast grain fracture tests (Chapter 2.2.6.1) were conducted in the Soil Mechanics Laboratory at TU Wien using the apparatus for uniaxial compression in order to determine the particle tensile strength and observe grain abrasion, attrition and particle breakage. For this purpose a single grain of size d is compressed diametrically by a force F between two rigid plates (Figures 2.15 and 7.25). Compression force and the vertical strain are measured and the tensile strength σ_f of a single grain is defined as the force at failure F_f divided by the square of the grain diameter, determined as the distance between two plates at failure (Equation 2.13). Prior the the compression tests each ballast particle is set in its most stable position and the upper plate is set in downward motion until it comes in contact with the ballast particle. Compression test were conducted subsequently with a constant displacement rate of 0.2% of the grain height per minute (quasi-static conditions) until particle breakage occurred (Figure 7.27). The relationship between single particle and ballast matrix crushing behavior still remains to be determined, but the importance of single particle behavior under compressive load is of special importance for determination of track tamping influence on the ballast matrix and the caused changes in the ballast particle size distribution. Average force and tensile stress action on a particle embedded in a sample can be calculated using the approach described in Chapter 2.2.6.2.

Figure 7.25: Single grain compression test on three grains of fine-grained granite

Results of several conducted tests can be seen in Table 7.2 as well as in Figures 7.26 and 7.28. Equation 2.13 is used for tensile strength calculation. Although a significantly higher number of tests would be necessary to obtain plausible and statistically comprehensible results, approximate values of single particle tensile strength and vertical force that generates particle attrition can be derived from the conducted experiments.

Die approbierte gedruckte Originalversion dieser Dissertation ist an der TU Wien Bibliothek verfügbar.
The approved original version of this doctoral thesis is available in print at TU Wien Bibliothek.
TU Bibliothek Your knowledge hub WIEN

Table 7.2: Results of tensile strength tests conducted on eight ballast grains

Sample No.	Particle diameter[1][cm]	Force [kN]	Tensile strength [MPa]
1	6.21	17.51	4.56
2	5.19	15.45	5.71
3	4.01	23.55	14.72
4	3.50	15.15	12.37
5	3.21	15.10	14.75
6	4.92	32.18	13.40
7	3.40	16.60	14.36
8	4.48	19.19	9.48

[1] defined as the distance between two plates at failure

Dependent on how stable the initial positioning of the particle on the plate is, the force-displacement diagrams (Figure 7.28) consist of two or three phases [70]. In case that a stable initial positioning is not possible due to particle shape, smaller peaks resulting from rotation and slippage caused by unstable contact to the plate are visible in the first phase on the conducted compression test (Figure 7.28a). Some particle abrasion is also expected in this phase. Following full contact establishment between the particle and the plate, the second phase begins, characterized by a stable increase of vertical force and displacement. Significant peaks seen in this phase result from particle chipping or attrition that is visible during test execution. Attrition of ballast particles causes significant changes in particle shape and angularity that leads to ballast fouling and weakens ballast bed resistance to vertical and lateral displacement. Third phase is characterized by the particle failure at which point the tensile strength σ_f is determined. Breakage is followed by a sharp drop of force (Figure 7.28) at which moment tested particles are split in two parts (Figure 7.27). Effect of particle size on tensile strength is discussed in Chapter 2.2.6.1 and presented in Figure 2.16. Ballast particles subjected to single grain compression tests have confirmed higher values of tensile strength with decreasing grain size and can be seen in Figure 7.26.

The *Weibull* distribution [43] function has been theoretically and experimentally verified to give a good approximation of the grain crushing strength [70][141]. The function defines the survival probability P_s of a single particle size d under diametric compression as:

$$P_s(d) = \exp\left[-\left(\frac{d}{d_0}\right)^3 \cdot \left(\frac{\sigma}{\sigma_0}\right)^m\right] \tag{7.3}$$

where m is the *Weibull* modulus, a dimensionless parameter of the *Weibull* distribution which is used to describe variability in measured material strength, increasing with decreasing modulus. Grain size d_0 is the reference size and σ_0 the characteristic stress for a grain of size d_0, under the assumption that 37% of the tested grains "survive" [70].

Die approbierte gedruckte Originalversion dieser Dissertation ist an der TU Wien Bibliothek verfügbar.
The approved original version of this doctoral thesis is available in print at TU Wien Bibliothek.
TU Bibliothek Your knowledge hub WIEN

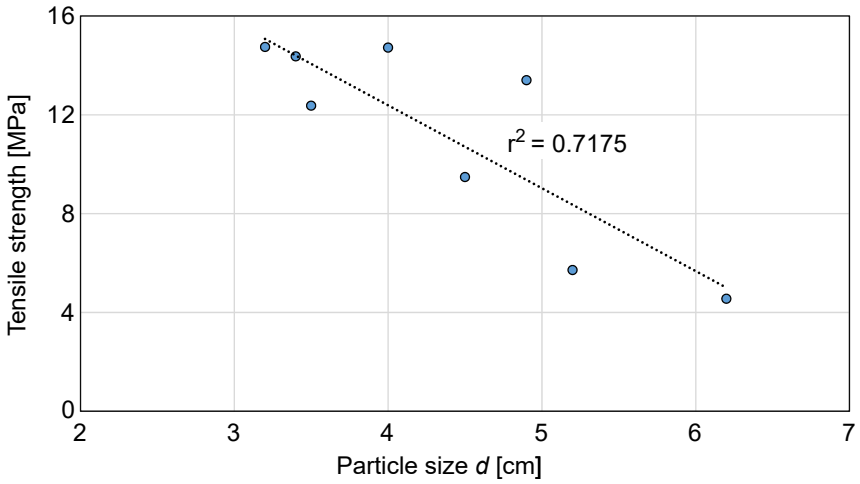

Figure 7.26: Effect of particle size (d is defined as the distance between two plates at failure) on single particle tensile strength

Figure 7.27: Ballast particle breakage as a result of conducted compression tests

According to *Haung et al.* [70], the survival probability P_s can be calculated for every particle in the testing series using the following equation:

$$P_s(d) = 1 - \frac{i}{1+N} \tag{7.4}$$

Die approbierte gedruckte Originalversion dieser Dissertation ist an der TU Wien Bibliothek verfügbar.
The approved original version of this doctoral thesis is available in print at TU Wien Bibliothek.

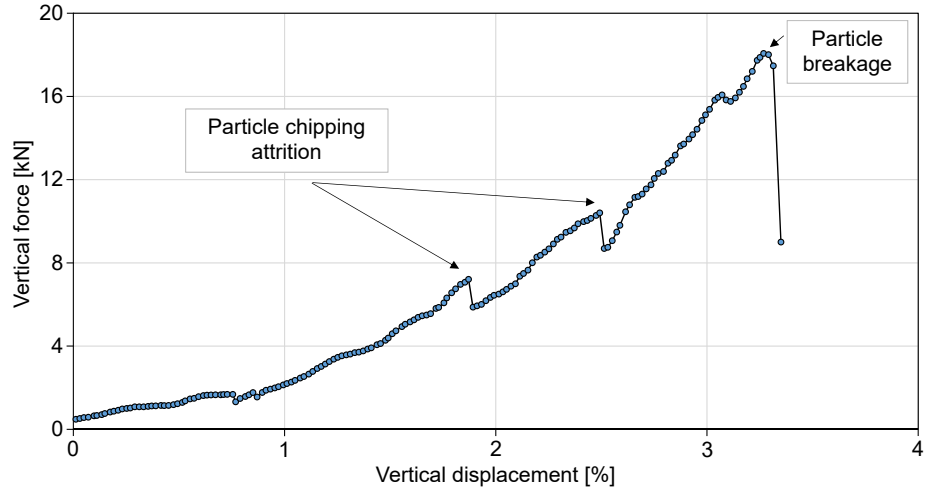

(a) Stable initial position of the ballast particle, local peaks due to chapping and attrition visible

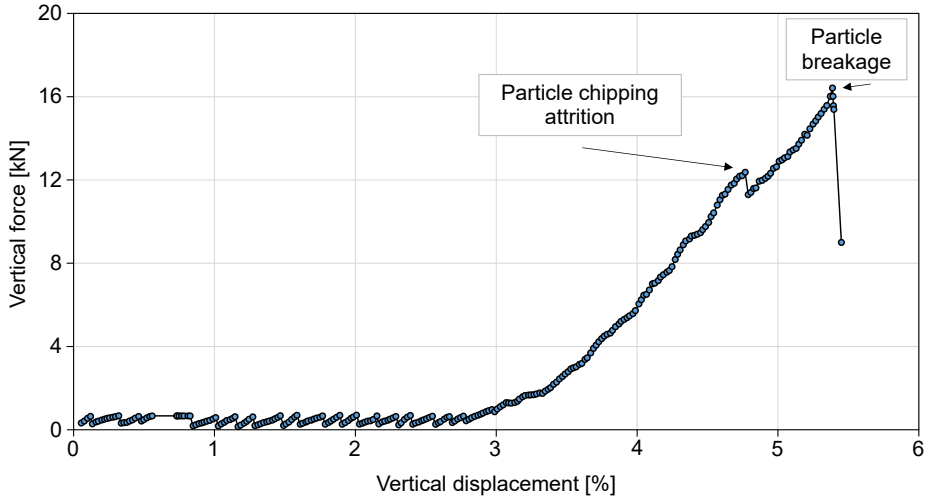

(b) Smaller peaks due to rotation and slippage caused by unstable contact to the plate visible in the first phase

Figure 7.28: Examples of single grain compression test on two particles

where N is the total number of grains and i the rank of the grain arranged in ascending order. Alternatively, the survival probability P_s can be expressed as the ratio of number of particles that survive crushing at stresses greater than the mean single particle crushing strength divided over the total number of particles tested. By substituting $d = d_0$ in Equation 7.3, the following equation is obtained [70]:

$$\ln\left(\ln\left(\frac{1}{P_s}\right)\right) = m\ln\left(\sigma\right) - m\ln\left(\sigma_0\right) \tag{7.5}$$

Crushing stress in logarithmic form $\ln(\sigma)$ is plotted against $\ln(\ln(1/P_s))$ in order to determine the *Weibull* modulus or the variability in the particle tensile strength for the specimens tested. The slope of the linear approximation is used to obtain the modulus m (Figure 7.29). Somewhat lower coefficient of determination R^2 in comparison to the existing

Die approbierte gedruckte Originalversion dieser Dissertation ist an der TU Wien Bibliothek verfügbar.
The approved original version of this doctoral thesis is available in print at TU Wien Bibliothek.

studies by *Haung et al.* [70] and *Zaidan and Al Ani* [141] can be attributed to the significantly lower number of conducted tests. Nevertheless it validates the usage of *Weibull* distribution when predicting the probability of particle survival under compression. Very low value of the modulus m indicates a very high variability in the crushing strength. Such values are characteristic for inhomogeneous, anisotropic materials with existing micro-cracks. In the context of track ballast it can be stated that the conducted tests have confirmed the dependence of the grain size on the single grain tensile strength, as well as that even the force as low as ≈7 kN can cause particle attrition and initiate changes in the particle size distribution of the ballast bed.

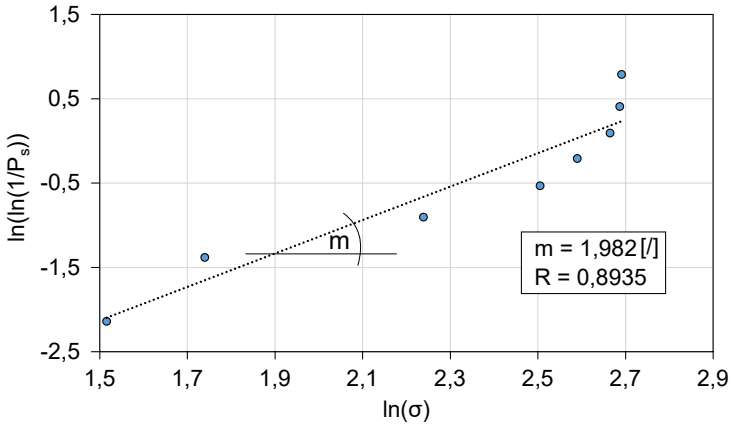

Figure 7.29: Determination of the *Weibull* modulus

Using the obtained *Weibull* modulus the survival probability curve for the tested samples is plotted using second degree polynomial best fit curve (Figure 7.30). The characteristic tensile stress where 37% of the particles do not undergo splitting is σ_0 = 13.7 MPa [70].

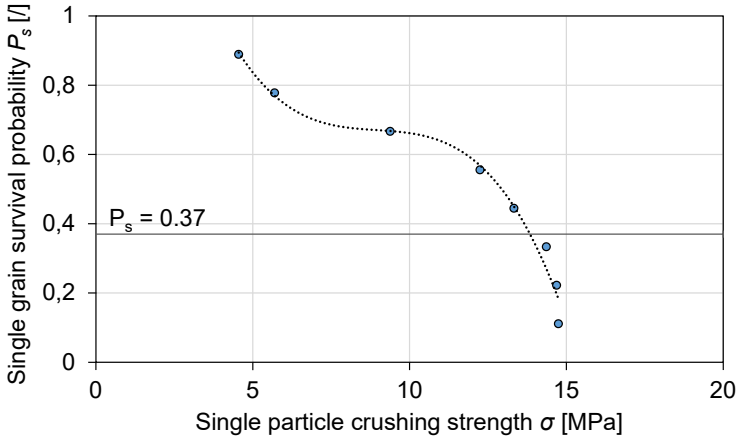

Figure 7.30: Single particle crushing strength of fine-graded granite samples and the survival probability curve

Die approbierte gedruckte Originalversion dieser Dissertation ist an der TU Wien Bibliothek verfügbar.
The approved original version of this doctoral thesis is available in print at TU Wien Bibliothek.

7.4.3.2 Ultrasonic Pulse Velocity tests

Prior to the uniaxial compression tests the tested particles were subjected to an Ultrasonic Pulse Velocity test (Chapter 2.2.6.3). Although usually used to determine the quality and homogeneity of concrete and natural rock samples with predefined dimensions, an alternative approach was used in the scope of this research, and the UPV tests were used to determine the mechanical properties of granite ballast grains and its tensile strength.

A single grain is placed between a high-energy pulse-receiver on the driving side and a 2-channel digital storage oscilloscope on the receiving side (Figure 2.17) and the travel velocity of the P-wave through the rock sample is determined using Equation 2.18, dependent on the grain width and measured time. Results of pulse velocity calculation are presented in Table 7.3.

In the next step, UPV test results are compared to those obtained by *Vasconcelos et al.* [134] following a much more extensive series of tests presented in Figure 7.31. As stated before in Chapter 2.2.6.3, their research confirmed a fairly strong nonlinear correlation between tensile strength and ultrasonic velocity based on tests conducted on cubic granite samples (Figure 7.31), showing that the UPV test can be used as preliminary evaluation of the fracture behavior of granite. Using the nonlinear correlation that arose from this comprehensive study, the tensile strength σ_f of a single ballast grain can be calculated from the pulse velocity UPV with the following equation:

$$\sigma_f = 0.701e^{0.00052 \cdot UPV} \tag{7.6}$$

Calculation of the tensile strength of ballast grains tested in scope of the research described in this thesis using Equation 7.6 resulted in values that are presented in Table 7.3 as well as in Figure 7.31. It can be seen that the measured values of pulse velocity are outside the value framework of the research conducted by *Vasconcelos et al.* [134]. However, Figure 7.32 shows a quite high correlation between values of single ballast grain tensile strength obtained from the two different test approaches.

Table 7.3: Results of UPV tests conducted on eight ballast grains

Sample No.	Sample width [cm]	Pulse velocity [m/s]	Tensile strength [MPa]
1	3.12	4887	8.89
2	5.59	5053	9.68
3	5.69	5274	10.88
4	6.70	5182	10.37
5	4.66	5350	11.32
6	4.16	5381	11.51
7	5.29	5062	9.74
8	6.55	5112	9.99

Die approbierte gedruckte Originalversion dieser Dissertation ist an der TU Wien Bibliothek verfügbar.
The approved original version of this doctoral thesis is available in print at TU Wien Bibliothek.
TU Bibliothek Your knowledge hub WIEN

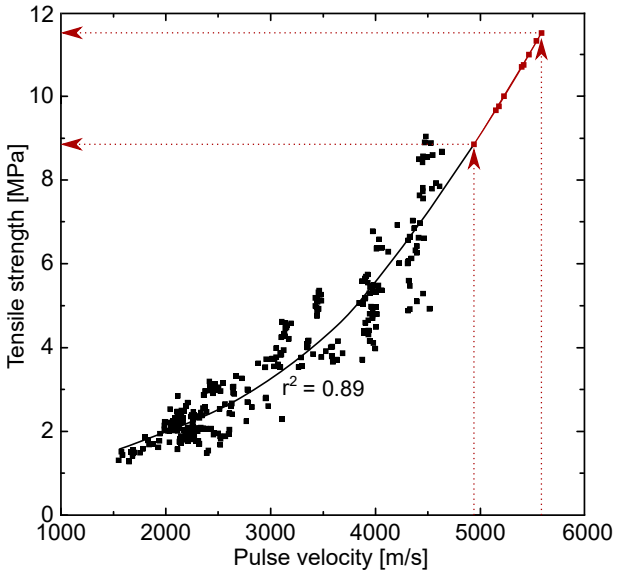

Figure 7.31: Relation between UPV and granite tensile strength (extended from [134])

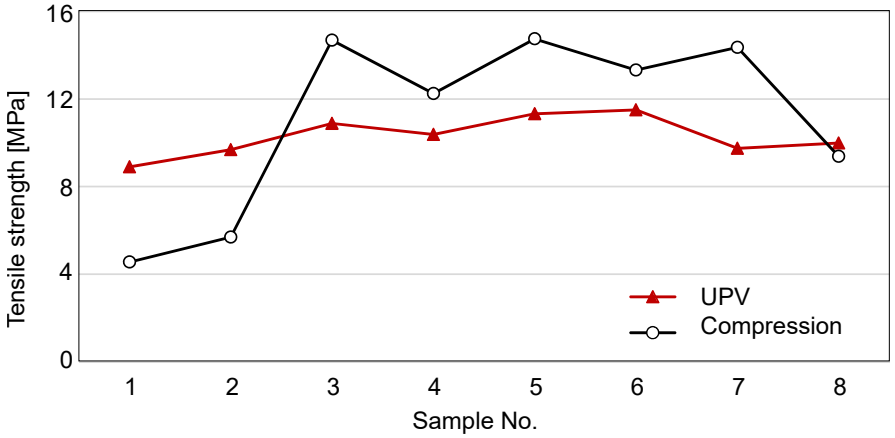

Figure 7.32: Comparison of tensile strength values from UPV and compression tests on single ballast grains

Die approbierte gedruckte Originalversion dieser Dissertation ist an der TU Wien Bibliothek verfügbar.
The approved original version of this doctoral thesis is available in print at TU Wien Bibliothek.

Die approbierte gedruckte Originalversion dieser Dissertation ist an der TU Wien Bibliothek verfügbar.
The approved original version of this doctoral thesis is available in print at TU Wien Bibliothek.

Chapter 8

Tamping unit - ballast matrix interaction Mechanical model

8.1 Introduction

Based on an extensive research conducted using clean ballast by *Fischer* [59] in 1983, state-of-the-art *Plasser & Theurer* track tamping machines operate with the parameter combination that has been proven to grant an optimum combination of ballast bed compaction trough the tine oscillatory motion and elevation to the predefined position by the tine squeezing movement. Measurements conducted during regular track maintenance, analyzed and discussed in Chapter 6, have shown significant differences in ballast response to compaction dependent on the ballast bed condition. Apart from the ballast bed condition, several other parameters influence the quality of the conducted ballast compaction, i.e. track geometry correction significantly. Although parameters such as squeezing duration, cylinder pressure and lifting values are usually kept constant during tamping on the same route, variations of these parameters hinder the comparison of conducted track tamping between different locations.

A semi-analytical mechanical model of the tamping tine - ballast matrix interaction during the squeezing movement is developed in order to investigate the influence of ballast bed condition on the quality and durability of the conducted track tamping. The model can simulate total tine motion - relative motion that is governed by the dynamic excitation and the absolute motion, governed by the squeezing velocity [35]. Tamping unit is modeled as a system of rods with a dynamic excitation overlapped by a hydraulic cylinder movement modeled by a variable rod length. The whole system rotates around the bearing M (Figure 8.1). The soil, i.e. the ballast matrix in contact with the tamping tine is modeled by a semi-infinite truncated cone for vertical translation (Cone model according to *Wolf* [139], Chapter 8.4.1) extended by a plastic spring (Chapter 8.4.2) [36] [35]. Special attention is given to the tamping tine - ballast matrix model contact conditions, providing the possi-

Die approbierte gedruckte Originalversion dieser Dissertation ist an der TU Wien Bibliothek verfügbar.
The approved original version of this doctoral thesis is available in print at TU Wien Bibliothek.
TU Bibliothek Your knowledge hub WIEN

bility to simulate both continuous contact and the loss of contact between the two model parts. In addition, ballast movement during loss of contact is taken into consideration by implementing the gap closing acceleration (Chapter 8.4.3). Primary objective of the semi-analytical approach is the simulation of three ballast conditions (Chapter 6.2) based on the conducted statistical analysis of the tamping parameters listed in Chapter 6.5.3 as well as on the load-displacement curves measured in-situ. Following the development of a stable algorithm that is able to simulate the ballast bed conditions encountered in-situ, the model is used to conduct parameter studies in order to determine the influence of selected tamping parameters and parameter combinations on the quality of performed track tamping and that are, in further consequence, going to be adapted to the ballast condition.

8.2 Model set-up

Mechanical model described in this chapter consists of two parts – tamping unit and the ballast matrix (soil) model, focusing especially on the interaction between the two parts and on tamping tine - ballast matrix contact conditions. The calculations are done using *Matlab R2020a* and notations and symbols used for the model geometry, input machine parameters as well as time dependent state variables and phase-descriptive notations are listed and described in Table 8.1. The calculation of all state variables is time dependent, based on the selected sampling rate and time step. A vector is calculated for each state variable, portraying their development throughout the squeezing movement modeled. The simulation time of 1 second is selected based on the state-of-the-art tamping machine characteristics, working with a squeezing time ranging from 0.8 to 1.2 seconds.

Table 8.1: Mechanical model parameters, notations and symbols

Notation	Unit	Description
f	[Hz]	excitation frequency
e	[m]	amplitude of excitation
ω	[rad/s]	angular frequency
I_M	[kgm^2]	tamping arm moment of inertia around bearing M
$v_{squeezing}$	[m/s]	constant squeezing velocity of the hydraulic cylinder
a_{gc}	[m/s^2]	gap closing acceleration
v_{gc}	[m/s]	gap closing velocity
t	[s]	simulation time/squeezing time
Δt	[s]	time step
Tamping unit		
l_1	[m]	distance bearing-soil contact M-T
l_2	[m]	distance upper-bearing M-B
l_3	[m]	distance excitation-bearing M-E
a, b	[m]	half length and width of tamping tine-area
α_4	[rad]	angle between l_2 and l_3 when the tamping tine is in vertical position

Die approbierte gedruckte Originalversion dieser Dissertation ist an der TU Wien Bibliothek verfügbar.
The approved original version of this doctoral thesis is available in print at TU Wien Bibliothek.
TU Bibliothek Your knowledge hub WIEN

l_4	[m]	distance excitation-bearing B-E
$\dot{l}_4$	[m/s]	velocity or rate of change of the length l_4
$\ddot{l}_4$	[m/s^2]	acceleration or rate of change of $\dot{l}_4$
l_{4p}	[m]	compensation of the change in length l_4 (T1 to T2)
h_4	[m]	distance l_4 – M (lever)
P	[N]	force in the tamping unit
P_{max}	[N]	maximum allowed force in the tamping unit (per tine)
β	[rad]	angle of rotation (around M)
$\dot{\beta}$	[rad/s]	angular velocity
$\ddot{\beta}$	[rad/s^2]	angular acceleration
x_{tine}	[rad]	tamping tine displacement in T
$\dot{x}_{tine}$	[rad/s]	tamping tine velocity
$\ddot{x}_{tine}$	[rad/s^2]	tamping tine acceleration
T1/T2	[/]	tamping unit operating phases
Soil/Ballast parameters		
ν	[/]	ballast *Poisson's* ratio
ρ	[kg/m^3]	ballast density
G_d	[N/m^2]	ballast dynamic shear modulus
Soil model/Ballast matrix		
x_e	[rad]	deformation of the *Kelvin-Voigt* model
$\dot{x}_e$	[rad/s]	rate of increase of deformation in the *Kelvin-Voigt* model
x_p	[rad]	cumulative predeformation in the plastic spring
$\Delta x, \Delta \dot{x}$	[rad], [rad/s]	single time step values of observed state variables
$x_{ballast}$	[rad]	ballast matrix position in T
$\dot{x}_{ballast}$	[rad/s]	ballast matrix velocity
$\ddot{x}_{ballast}$	[rad/s^2]	ballast matrix acceleration
F	[N]	force in the ballast matrix
F_{ke}	[N]	force in the elastic spring (ballast matrix)
F_{ce}	[N]	damping force (ballast matrix)
F_p	[N]	preload force in the ballast model when switching from unloading to loading
k_p	[N/m]	plastic spring rate/stiffness
k_e	[N/m]	elastic spring rate/stiffness *Kelvin-Voigt* model
c_e	[Ns/m]	dashpot coefficient *Kelvin-Voigt* model
B1/B2/B3	[/]	ballast matrix operating phases

Die approbierte gedruckte Originalversion dieser Dissertation ist an der TU Wien Bibliothek verfügbar.
The approved original version of this doctoral thesis is available in print at TU Wien Bibliothek.
TU Bibliothek Your knowledge hub WIEN

8.3 Tamping unit model

The tamping unit model was developed for tine number 64 (Figure 5.5b, outward, far left), and is based on the exact geometry, moment of inertia and position of the tine selected. Input system geometry (tine measurements, rod lengths and angles) can easily be altered and adapted to other tamping units or tines. The unit is modeled as a system with two bearings (E and M, Figure 8.1) connected by rods l_1, l_2 and l_4. The dynamic excitation induced by eccentric unbalance rotation of the bearing E with a 2 mm amplitude was replaced by a pulsating changing length of the rod l_4. This simplification is based on a calculation of the maximum error between two reversal points of the oscillation path of 0.25% of the rod length referred to a 4 mm oscillation displacement. The dynamic excitation is overlapped by a hydraulic cylinder opening during the squeezing movement modeled as an elongation of the rod l_4 (Figure 8.1). The variable length of the rod l_4 represents the opening/closing of the hydraulic cylinder during the squeezing movement i.e. during ballast compaction. The tamping unit model is additionally extended by a friction element, incorporated into the upper part of the tamping arm (Figure 8.1) [36]. The friction element represents an existing valve on the tamping unit, triggered by exceeding the maximum allowed pressure exerted on the tine during ballast compaction, preventing possible tamping tine and/or sleeper damage. In the event of reaching the maximum pressure value, the valve is activated, allowing a certain amount of oil to be released from the hydraulic cylinder, thus reducing the exerted pressure.

Maximum tine elongation during rotation around the bearing M is approximately 4-5 mm and the vertical component of this rotation is overlapped by a significantly greater squeezing motion defined by the squeezing velocity. For these reasons, a simplification is made to reduce the rotatory dynamic tine motion to a horizontal translatory motion with an amplitude of 4-5 mm (Table 8.2) [36].

8.3.1 Friction element

For the purpose of the mechanical model, the existing valve on the tamping unit is presented by a friction element that is activated when the maximum force in the tamping unit is reached, causing the element to open and allow the rod l_4 to slide, thus reducing its total length, modeling a decrease of cylinder pressure [36]. If the maximum force has not been reached, the friction element grips on the rod, and the length of the rod l_4 is defined by the current position of the hydraulic cylinder and the dynamic excitation. The friction element modus operandi defines the two operating phases of the tamping unit model [36]:

- T1 - Friction element closed (grip) - displacement controlled motion
- T2 - Friction element opened (sliding) - force controlled motion

The operating phases are described in detail in Chapter 8.3.3. The purpose of the valve is to control the maximum pressure exerted on the squeezing cylinder by the tamping tine, hindering possible damages to the tamping unit or the cylinder that could occur if the tamping

Die approbierte gedruckte Originalversion dieser Dissertation ist an der TU Wien Bibliothek verfügbar.
The approved original version of this doctoral thesis is available in print at TU Wien Bibliothek.
TU Bibliothek Your knowledge hub WIEN

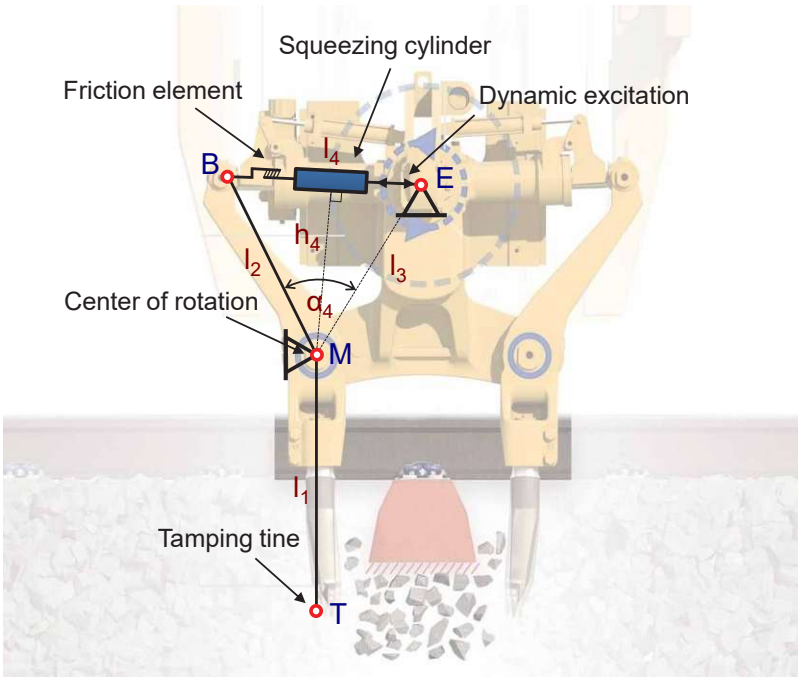

Figure 8.1: Mechanical model of the tamping unit lowered into work position

tine does not reach the intended penetration depth and encounters the sleeper during the squeezing movement.

8.3.2 System geometry

Rod lengths l_1, l_2, length l_3, as well as the angle α_4 (Figure 8.1) are constant input parameters taken from Table 8.2, dependent on the position and the geometry of the tine modeled. The position of the first fixed bearing is marked by the point E, also marking the center of the eccentric rotation replaced by a pulsating rod length. The initial length $l_{4(0)}$ of the rod l_4 is calculated by means of the cosine theorem and it is dependent on the lengths l_3 and l_2, as well as on the angle α_4 (Figure 8.2):

$$l_{4(0)} = \sqrt{l_2^2 + l_3^2 - 2 \cdot l_2 \cdot l_3 \cdot \cos(\alpha_4)} \tag{8.1}$$

As stated before, the rotatory eccentric motion of the dynamic excitation is replaced by a pulsating rod length. The dynamic excitation can be described by the following equation, dependent on the amplitude of excitation e, calculation time and frequency f:

$$\Delta l_4 = e \cdot \sin(\omega t) \tag{8.2}$$

where ω represents the angular frequency of the excitation and is given by the following equation:

$$\omega = 2 f \pi \tag{8.3}$$

Die approbierte gedruckte Originalversion dieser Dissertation ist an der TU Wien Bibliothek verfügbar.
The approved original version of this doctoral thesis is available in print at TU Wien Bibliothek.

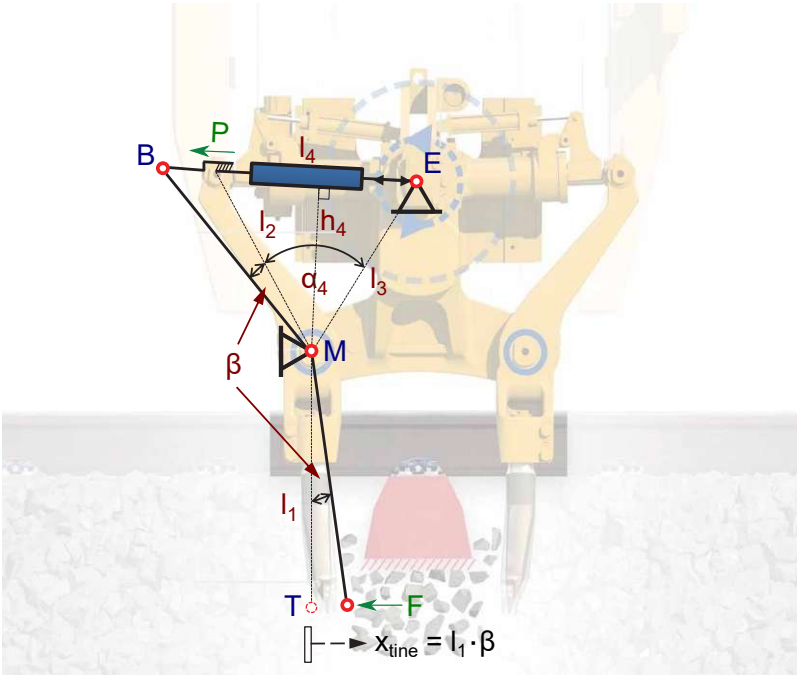

Figure 8.2: Mechanical model of the tamping unit during squeezing movement [36]

Based on previous research by *Fischer* [59], the state-of-the-art tamping machines used for this research operate with a constant frequency of $f = 35$ Hz during the squeezing movement. The length of the rod l_4 is likewise dependent on the elongation of the hydraulic cylinder that occurs with a constant velocity $v_{squeezing}$ during the squeezing movement. In other words, the total length of the rod l_4 at any given time can be calculated as:

$$l_4 = l_{4p} + v_{squuezing} \cdot t + e \cdot \sin(\omega t) \tag{8.4}$$

Table 8.2: Tamping unit geometry and constant input parameters

Parameter	**Value**
Excitation frequency	$f = 35\text{Hz}$
Excitation amplitude	$e = 0,002\text{m}$
Moment of inertia around the bearing M	$I_M = 7,32\text{kgm}^2$
Distance bearing-soil contact M-T	$l_1 = 0,744\text{m}$
Distance upper-bearing M-B	$l_2 = 0,4005\text{m}$
Distance excitation-bearing M-E	$l_3 = 0,6785\text{m}$
Angle between l_2 and l_3	$\alpha_4 = 1,288\text{rad}$
Half length and width of tamping tine-area	$a = 0,085\text{m}$, $b = 0,05\text{m}$

where the length l_{4p} describes the compensation of the rod elongation due to the friction element when switching from force controlled to displacement controlled motion, described in detail in Chapter 8.3.3. During the squeezing movement, the hydraulic cylinder elongates with a constant velocity, causing the tamping arm to rotate around the bearing M. The angle

Die approbierte gedruckte Originalversion dieser Dissertation ist an der TU Wien Bibliothek verfügbar.
The approved original version of this doctoral thesis is available in print at TU Wien Bibliothek.
TU Bibliothek Your knowledge hub WIEN

of rotation during the squeezing movement is labeled β (Figure 8.2) and can be calculated in dependence on the current length of the rod l_4 using the following equation:

$$\beta = \arccos\left(\frac{l_2^2 + l_3^2 - l_4^2}{2 \cdot l_2 \cdot l_3}\right) - \alpha_4 \tag{8.5}$$

8.3.3 Tamping unit operating phases

Depending on the machine parameters, the value of the maximum force P_{max} needs to be set as an input parameter for the model. Supposing that the maximum force has not been reached, the friction element grips on the rod l_4, causing no additional changes in the rod length. This operating phase of the tamping unit is identified as an inactive phase of the friction element, denoted with T1. During the inactive phase T1, the motion of the unit is displacement-controlled. The length of the rod l_4 is solely dependent on the dynamic excitation and the squeezing velocity of the hydraulic cylinder and can be calculated using Equation 8.4. With the first two derivatives of the length l_4 the velocity and acceleration of the elongation can be calculated:

$$\dot{l}_4 = v_{squeezing} + e \cdot \cos(\omega t) \cdot \omega \tag{8.6}$$

$$\ddot{l}_4 = -e \cdot \sin(\omega t) \cdot \omega^2 \tag{8.7}$$

As stated before, the elongation of the rod l_4 causes the tamping arm to rotate around the bearing M, bringing the tamping tine in contact with the ballast matrix. This deviation from the initial unit position can be best described with the angle β that forms between the current and the initial position of the rod l_2 and l_1 (Figure 8.2). Angle β, as well as the angular velocity $\dot{\beta}$ and the angular acceleration $\ddot{\beta}$ as the first and second derivative of β (Figure 8.3), are dependent on the current length of l_4 and can be calculated with Equation 8.5, resulting in following set of equations:

$$\dot{\beta} = \frac{l_4 \cdot \dot{l}_4}{l_2 \cdot l_3} \cdot \frac{1}{\sqrt{1 - \frac{l_2^2 + l_3^2 - l_4^2}{4 \cdot l_2^2 \cdot l_3^2}}} \tag{8.8}$$

$$\ddot{\beta} = \frac{\dot{l}_4^2 + l_4 \cdot \ddot{l}_4}{l_2 \cdot l_3} \cdot \frac{1}{\sqrt{1 - \frac{l_2^2 + l_3^2 - l_4^2}{4 \cdot l_2^2 \cdot l_3^2}}} - \frac{l_4^2 \cdot \dot{l}_4^2 \cdot (l_2^2 + l_3^2 - l_4^2)}{2 \cdot l_2^3 \cdot l_3^3} \cdot \frac{1}{\left(1 - \frac{(l_2^2 + l_3^2 - l_4^2)^2}{4 \cdot l_2^2 \cdot l_3^2}\right)^{\frac{2}{3}}} \tag{8.9}$$

Additionally, the current length of the lever h_4 can be calculated:

$$h_4 = \frac{l_2 \cdot l_3}{l_4} \cdot \sin(\alpha_4 + \beta) \tag{8.10}$$

Die approbierte gedruckte Originalversion dieser Dissertation ist an der TU Wien Bibliothek verfügbar.
The approved original version of this doctoral thesis is available in print at TU Wien Bibliothek.
TU Bibliothek Your knowledge hub WIEN

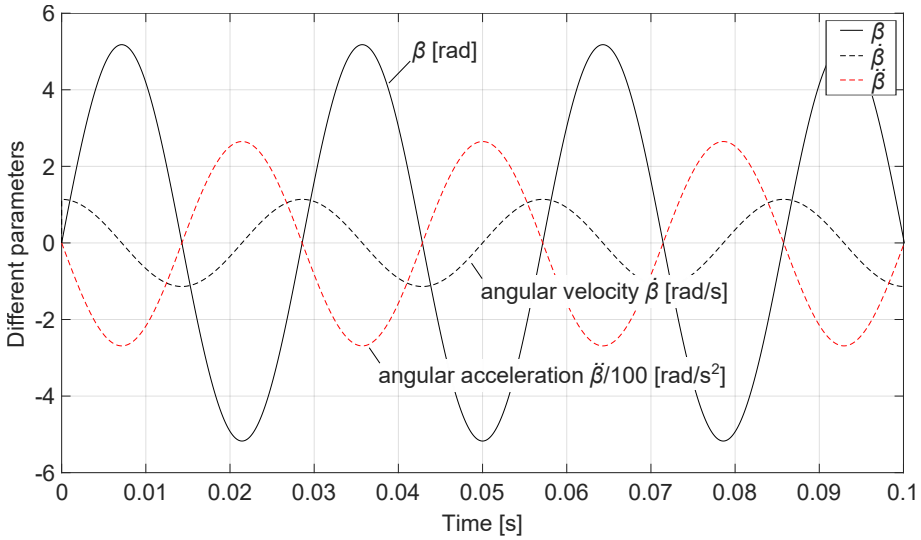

Figure 8.3: Angle of rotation β around the bearing M, angular velocity $\dot{\beta}$ and angular acceleration $\ddot{\beta}$ during 3.5 cycles, $f = 35$ Hz, $v_{squeezing} = 0$ m/s

Finally, the displacement of the tamping tine from the vertical position, as well as the tine velocity and acceleration can be calculated in dependence of the angle β (Figure 8.4):

$$x_{tine} \rightarrow f(\beta) \tag{8.11a}$$

$$x_{tine} = l_1 \cdot \beta \tag{8.11b}$$

$$\dot{x}_{tine} = l_1 \cdot \dot{\beta} \tag{8.11c}$$

$$\ddot{x}_{tine} = l_1 \cdot \ddot{\beta} \tag{8.11d}$$

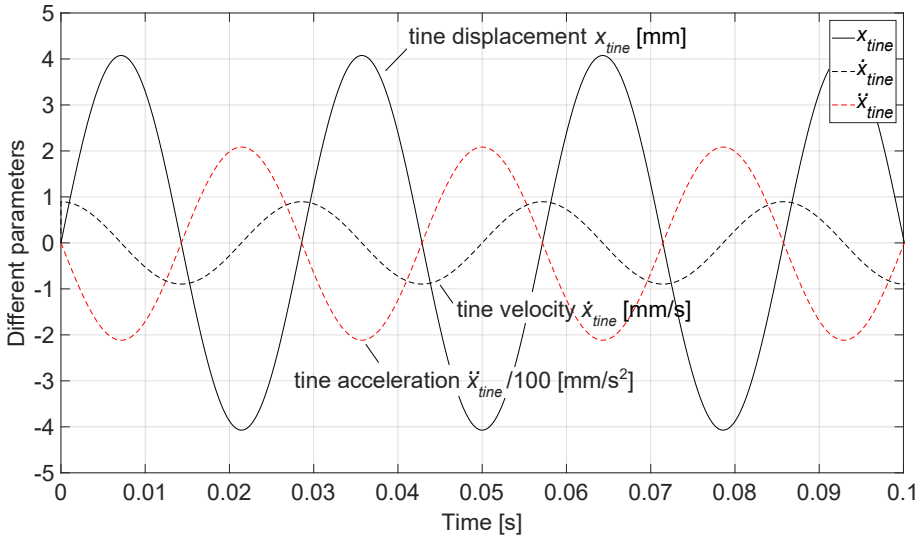

Figure 8.4: Tamping tine oscillation x_{tine}, velocity $\dot{x}_{tine}$ and acceleration $\ddot{x}_{tine}$ during 3.5 cycles, $f = 35$ Hz, $v_{squeezing} = 0$ m/s

During ballast compaction the tine displacement from the vertical position x_{tine} is em-

Die approbierte gedruckte Originalversion dieser Dissertation ist an der TU Wien Bibliothek verfügbar.
The approved original version of this doctoral thesis is available in print at TU Wien Bibliothek.

bossed into the soil model, causing a deformation of the ballast matrix and simultaneously generating a force F on contact to the ballast matrix that is transmitted back to the tamping unit as an input for the next cycle [34]. Once the contact force F is calculated (in detail in Chapter 8.4), using the principle of angular momentum and taking into consideration the current position of the tamping unit trough β and h_4, as well as the moment of inertia of the system, the force P in the tamping unit is obtained[36]. As long as the maximum force in the tamping unit P_{max} is not reached, the condition to remain in phase T1 is fulfilled:

$$P = \frac{F \cdot l_1 + \ddot{\beta} \cdot I_M}{h_4} \leq P_{max} \tag{8.12}$$

Stiffness of the ballast matrix is expected to increase as the compaction with a constant oscillation amplitude progresses, thus increasing the matrix resistance to further compaction and causing both the calculated contact force F and the force P in tamping unit to increase. The maximum force P_{max} in the tamping unit has to be predefined dependent on the machine parameters. Once this force is reached, the friction element is opened, allowing the rod l_4 to slide, virtually reducing its length and the pressure on the hydraulic cylinder. This active state of the friction element defines the second phase of tamping unit operation, denoted with T2. During this active phase, the motion of the unit is force-controlled, and the force in the unit is kept at the constant value of P_{max} (Figure 8.5). Once again, by means of the angular momentum principle, the angular acceleration $\ddot{\beta}$ is calculated, dependent on P_{max}:

$$\ddot{\beta} = \frac{P_{max} \cdot h_4 - F \cdot l_1}{I_M} \tag{8.13}$$

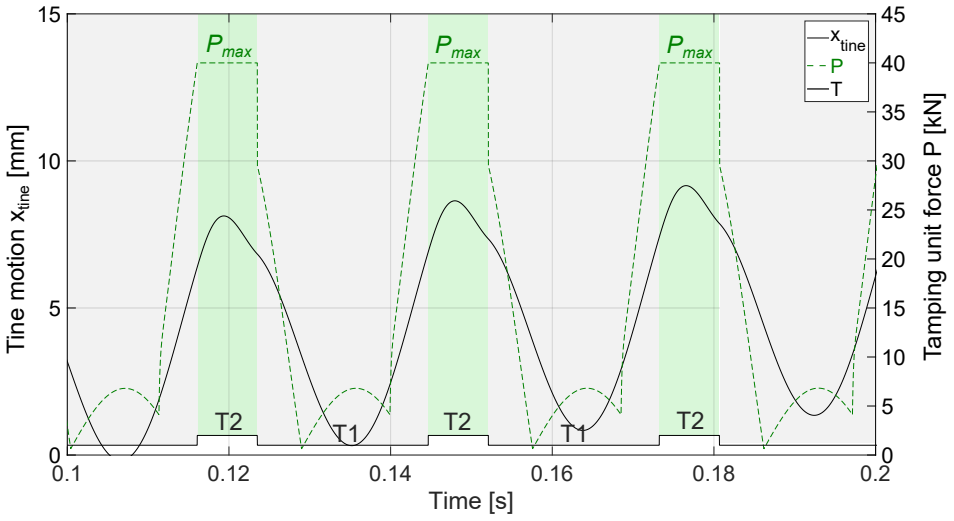

Figure 8.5: Tamping tine oscillation x_{tine} during both tamping unit operating phases T1 and T2, f = 35 Hz, $v_{squeezing}$ = 0.05 m/s

This approach assures a correct consideration of the force-controlled unit motion. As stated before, the calculation of all the state variables is time dependent, based on the selected time step. In other words, once the angular acceleration is calculated, the angular

Die approbierte gedruckte Originalversion dieser Dissertation ist an der TU Wien Bibliothek verfügbar.
The approved original version of this doctoral thesis is available in print at TU Wien Bibliothek.
TU Bibliothek Your knowledge hub WIEN

velocity and the angle β can be obtained using the following equations and the time vector of the two variables:

$$\dot{\beta} = \dot{\beta}_{(i-1)} + \ddot{\beta} \cdot \Delta t \qquad (i = 1,2,3,...\,length(t)) \tag{8.14}$$

$$\beta = \beta_{(i-1)} + \dot{\beta} \cdot \Delta t \qquad (i = 1,2,3,...\,length(t)) \tag{8.15}$$

Once the exact current position of the unit has been determined, the displacement of the tamping tine, as well as the tine velocity and acceleration can be calculated, once again using the Equations 8.11b, 8.11c and 8.11d, and used for the calculation of the soil model force F. As shown in Equation 8.13, a calculation of the lever h_4 is necessary to determine the angular acceleration in every following cycle. In order to be able to do so, the correct current length of the rod l_4, dependent on β, has to be calculated:

$$l_4 = \sqrt{l_2^2 + l_3^2 - 2 \cdot l_2 \cdot l_3 \cdot \cos(\alpha_4 + \beta)} \tag{8.16}$$

The length of the lever h_4 is then computed from:

$$h_4 = \frac{l_2 \cdot l_3}{l_4} \cdot \sin(\alpha_4 + \beta) \tag{8.17}$$

However, if only one cycle is observed, one can easily conclude that the force in the unit is going to increase during the loading part of the cycle, where the tine movement is directed towards the ballast matrix, and decrease during unloading, where the tine reaches back before starting a new cycle, moving in the opposite direction. During the backwards movement of the tine, the pressure on the cylinder is going to decrease until the moment in which the maximum force is no longer exceeded, and a switch to phase T1 is necessary. Since the active phase of the friction element T2 describes a force-controlled motion of the tamping unit with a constant maximum force P_{max}, the velocity or the rate of change of length l_4 is selected as a reliable indicator and as a condition to switch in-between the two operating phases of the unit. As stated before, during the active phase (during sliding) the friction element reduces the length of the rod l_4, thus reducing the pressure on the cylinder. However, the model only allows the active phase during loading, i.e. during ballast compaction, since much higher pressures are expected in this part of every cycle. In other words, the friction element does not provide a possibility to contribute to the elongation of the rod. During the active phase of the process, the rate of change of length l_4 is determined as:

$$\dot{l}_4 = \frac{l_2 \cdot l_3 \cdot \dot{\beta} \cdot \sin(\alpha_4 + \beta)}{\sqrt{l_2^2 + l_3^2 - 2 \cdot l_2 \cdot l_3 \cdot \cos(\alpha_4 + \beta)}} \tag{8.18}$$

In the event that $\dot{l}_4$ exceeds the sum of cylinder opening velocity and dynamic excitation velocity, indicating that the friction element would slide in the opposite direction, a phase switch is required:

$$\dot{l}_4 \geq v_{squeezing} + e \cdot \cos(\omega t) \cdot \omega \tag{8.19}$$

Die approbierte gedruckte Originalversion dieser Dissertation ist an der TU Wien Bibliothek verfügbar.
The approved original version of this doctoral thesis is available in print at TU Wien Bibliothek.
TU Bibliothek Your knowledge hub WIEN

Immediately before the friction element closes, the condition given by the Equation 8.19 is already fulfilled, and a compensation of the rod elongation due to the friction element is required before Equation 8.1 is used to calculate the rod length for the next cycle:

$$l_{4p} = l_4 - [v_{squeezing} \cdot t + e \cdot \sin(\omega t)] \tag{8.20}$$

During the phase T1, the friction element remains closed, thus keeping l_{4p} at a constant value.

8.4 Ballast matrix model

Squeezing movement of the tamping tine towards the sleeper is initiated by the dynamic excitation overlapped by the elongation of the hydraulic cylinder in the tamping arm, both modeled as a change of length of rod l_4. As soon as the rotation around M begins, the tamping tine (point T, Figure 8.2) comes in contact with the ballast matrix, implementing the 4-5 mm oscillation amplitude. Soil i.e. ballast matrix model reaction to the tamping tine motion is modeled by a *Kelvin-Voigt* model consisting of a purely elastic spring with a stiffness k_e and a purely viscous damper with a coefficient c_e connected in parallel based on the Cone model theory according to *Wolf* [139], described in detail in Chapter 8.4.1 [36]. The model is extended by a plastic spring with a stiffness k_p, modeling the plastic deformation of the ballast matrix, i.e. its compaction under the sleeper (Chapter 8.4.2). The model described adapts the theory of the *Zener* or *Standard solid model* in the *Kelvin* representation [101], used to describe both the creep and stress relaxation behaviors of a viscoelastic material. Furthermore, in case of a loss of contact a gap will appear between the tamping tine and the ballast matrix model [36]. Following either the sliding block or the *Rankine's* earth-pressure theory [126], the ballast grains are going to strive to fill this void, causing the tine to come in contact with the ballast matrix sooner in the following cycle. Influence of the ballast grains movement during the loss of contact is calculated as a so called "gap closing acceleration", explained in detail in Chapter 8.4.3 [36]. The three components of the soil, i.e. ballast model can be seen in Figure 8.6.

Mechanical model described depicts the interaction between the center of the tamping tine plate and the ballast matrix in the most straightforward possible way that assures the possibility to simulate all essential phenomena of this interaction observed in-situ, including plastic deformations and material damping that both occur during compaction [36]. The system's degree of freedom is the position of the tamping tine x_{tine}, i.e. the position $x_{ballast}$ in case of lost of contact. During the tamping unit operating phase T2, where the tine motion is force-controlled, the degree of freedom is given by the current length of the rod l_4 that determines the force in the tamping unit and the exact positioning of the tine [36]. The tamping tine position is defined by the angle of rotation β around M. As stated before, a simplification is made by reducing the rotatory dynamic tine motion to a translatory motion, therefore transforming all ballast matrix model deformations into horizontal ones.

Several authors have made an effort to develop mechanical models to simulate the in-

Die approbierte gedruckte Originalversion dieser Dissertation ist an der TU Wien Bibliothek verfügbar.
The approved original version of this doctoral thesis is available in print at TU Wien Bibliothek.
TU Bibliothek Your knowledge hub WIEN

teraction between different compaction devices and the compacted soil. *Adam* [24] investigated soil compaction by vibratory rollers, using a similar approach to model the contact zone between the roller drum and the elastic part of the soil using the Cone model for vertical translation separately for cohesive and non-cohesive soils. A semi-analytical approach to modeling the dynamic drum-soil interaction is developed by *Pistrol* [105] to identify a relation between the soil stiffness and the motion behavior of the drum during compaction with oscillation rollers using Cone models for horizontal and vertical translation.

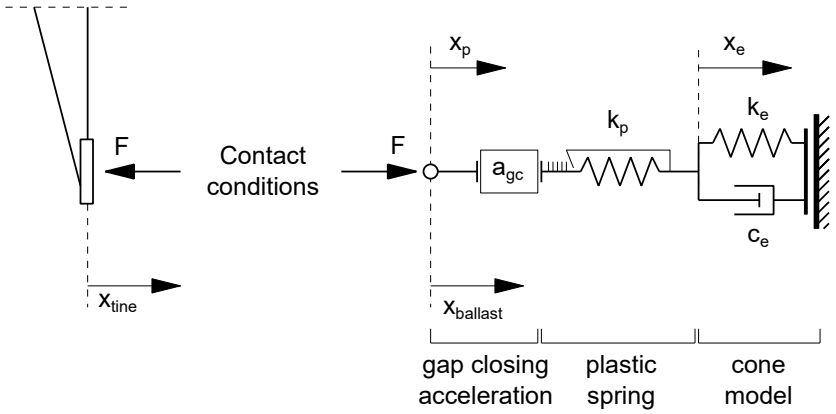

Figure 8.6: Ballast matrix model with its three components

8.4.1 Cone model

Simple physical models have been proven to be able to determine e.g. the interaction force-displacement relationship of foundations and a seismic input motion or the interaction of the oscillatory roller drum and the soil during dynamic compaction, offering simplicity in application as well as in the physics and in mathematical solutions. The Cone models according to *Wolf* [139] are used to determine the dynamic interaction of a massless circular foundation with a radius r_0 and a surface area A_0 embedded in a homogeneous half-space during either translational or rotatory motion. The part of the soil affected by the interaction is modeled by a truncated cone, whereby a corresponding model should be defined for each degree of freedom. The model assumes the propagation of wave to be cone-like through the soil and similar to one dimensional wave propagation in a rod. Basic model assumption is a linear-elastic soil behavior when seismically induced, meaning that the soil remains linearly elastic with hysteretic material damping during dynamic excitation [139]. The main simplification is based on the approach to neglect the part of the half-space (far field) which only insignificantly influences the deformations and forces in a certain part of the space (near field), meaning that the motion behavior in the cone does not simulate the processes but the reaction of the half-space to the surface on the truncated cone. Simulating the soil affected by the tine motion with a cone model allows simplification of an exact and complex three-dimensional wave pattern of a half-space with body and surface waves and three different wave velocities (c_p, c_s, c_r) with an approximate simple one-dimensional wave propagation governed by one constant dilatation-wave velocity of the cone [139].

Die approbierte gedruckte Originalversion dieser Dissertation ist an der TU Wien Bibliothek verfügbar.
The approved original version of this doctoral thesis is available in print at TU Wien Bibliothek.
TU Bibliothek Your knowledge hub WIEN

The interaction of the tamping tine and the ballast matrix is simulated using the Cone model with a translational degree of freedom [36]. Area A_0 is calculated as the tine plate area ($= 2a \cdot 2b$). The semi-infinite truncated cone for vertical translation is rotated in 90° in order to determine the interaction force-displacement relationship in the tamping tine motion direction. The resulting cone can be described as a semi-infinite rod with a conical shape and a circular cross section. Opening angle of the cone, expressed by the ratio x_0/r_0, can be determined by equating the static-stiffness coefficient of the truncated semi-infinite cone K to that of the rectangular disk on a isotropic elastic half-space K_R [139].

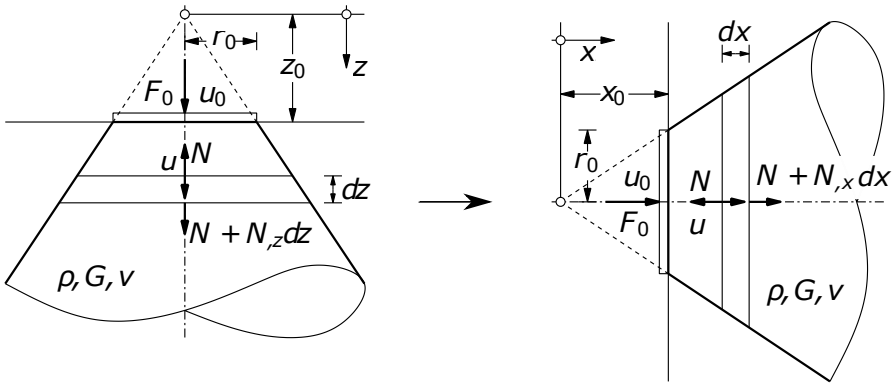

Figure 8.7: Disk on surface of half-space with truncated semi-infinite cone for vertical translation rotated in 90° to model the ballast matrix-tamping tine interaction in the tamping tine movement direction x (adapted from [105] and [139])

8.4.1.1 Static cone

The displacement of the dilatational waves that propagate along the cone axis with the wave velocity c_p are depicted by u and the normal force acting along the same axis with N (Figure 8.7). The area at depth x can be expressed as:

$$A_x = \frac{x^2}{x_0^2} \cdot A_0 \tag{8.21}$$

For translatory tine motion the rectangular load application area A_0 is converted into a circle of equal area with a radius r_0:

$$r_0 = \sqrt{\frac{4a \cdot b}{\pi}} \tag{8.22}$$

The dynamic equilibrium equation of an infinitesimal element can be expressed as [139]:

$$-N + N + N_{,x}dx = 0 \tag{8.23}$$

where $N_{,x}dx$ denotes the partial derivative of N with respect to x [105]. The force-displacement relationship can be expressed using the dilatational wave (P-wave, compressional or longitudinal) velocity:

Die approbierte gedruckte Originalversion dieser Dissertation ist an der TU Wien Bibliothek verfügbar.
The approved original version of this doctoral thesis is available in print at TU Wien Bibliothek.

$$c_p = \sqrt{\frac{E_s}{\rho}} = \sqrt{\frac{2G}{\rho}\frac{1-v}{1-2v}} \tag{8.24}$$

$$N = E_s A_x u_{,x} \tag{8.25}$$

with the constrained modulus E_s, mass density ρ and the *Poisson's* ratio v [139]. Substituting Equations 8.25 and 8.21 into 8.23, the following second-order differential equation in the time domain is obtained:

$$u_{,xx} + \frac{2}{x}u_{,x} = 0 \tag{8.26}$$

that can be solved by enforcing the boundary conditions $u(x = x_0)$ and $u(x = \infty)$ and written as:

$$u = \frac{x_0}{x}u_0 \tag{8.27}$$

with:

$$F_0 = -N(x = x_0) = -E_s A_0 u_{0,x} \tag{8.28}$$

Substituting the derivative calculated from Equation 8.27 yields to:

$$F_0 = \frac{E_s A_0}{x_0}u_0 \tag{8.29}$$

The static-stiffness coefficient can now be defined using either the constrained modulus E_s or the velocity of the dilatational wave as [139]:

$$K = \frac{E_s A_0}{x_0} \tag{8.30a}$$

$$K = \frac{\rho c_p^2 A_0}{x_0} \tag{8.30b}$$

8.4.1.2 Dynamic cone

If a dynamic load, such as the one implemented by the tamping tine, is applied to the disk it would lead to a wave originating at the disc and propagating away from the source with the cross-section area increasing in the direction of the wave propagation [139] [105]. Inertial loads are also taken into consideration and the Equation 8.24 can be extended as follows in order to describe dynamic interaction between the tine and the ballast matrix:

$$-N + N + N_{,x}dx = \rho A_0 dx\ddot{u} \tag{8.31}$$

Substituting the force-displacement relationship given by the Equation 8.25 once more leads to the following equation of motion in the time domain [139]:

Die approbierte gedruckte Originalversion dieser Dissertation ist an der TU Wien Bibliothek verfügbar.
The approved original version of this doctoral thesis is available in print at TU Wien Bibliothek.

$$u_{,xx} + \frac{2}{x}u - \frac{1}{c_p^2}\ddot{u} = 0 \tag{8.32}$$

This equation can be rewritten in form of a one-dimensional wave equation as a function of xu:

$$(xu)_{,xx} - \frac{(\ddot{xu})}{c_p^2} = 0 \tag{8.33}$$

Enforcing the same boundary conditions as used for the Equation 8.27, the solution for a prediscribed disc displacement u is given by *Wolf* [139]:

$$u = \frac{x_0}{x^2}u_0\left(t - \frac{x - x_0}{c_p}\right) \tag{8.34}$$

Substituting the force-displacement relationship given by the Equation 8.25 for $x = x_0$ the equation yields to:

$$F_0 = \frac{\rho c_p^2 A_0}{x_0}u_0 + \rho c_p A_0 \dot{u}_0 \tag{8.35}$$

or in general form:

$$F_0 = K\,u_0 + C\,\dot{u}_0 \tag{8.36}$$

In this interaction force-displacement relationship K and C are constant coefficients of the spring and the dashpot [139]:

$$K = \frac{\rho c_p^2 A_0}{x_0} \tag{8.37a}$$

$$C = \rho c_p A_0 \tag{8.37b}$$

An ordinary spring and a dashpot connected in a parallel forming a lumped-parameter model can be described using the spring stiffness and dashpot coefficient defined in Equation 8.37, whereby the dashpot coefficient C takes into consideration the energy of the wave radiating towards infinity (radiation or geometric damping the same as that of a semi-infinite prismatic bar) [139]. Except for the static loads ($\omega = 0$), the Cone model also yields exact results for the high frequency limit ($\omega = \infty$), in which case the spring force K can be neglected as it is much smaller than the corresponding dashpot force C. Given that the opening angle of the cone is calculated by matching the stiffness coefficients K and K_R, a doubly-asymptotic approximation results for the cone, providing exact results for both zero and high frequency limit dominated by the radiation dashpot C [139].

Die approbierte gedruckte Originalversion dieser Dissertation ist an der TU Wien Bibliothek verfügbar.
The approved original version of this doctoral thesis is available in print at TU Wien Bibliothek.
TU Bibliothek Your knowledge hub WIEN

8.4.1.3 Cone properties

If the ballast matrix is considered a medium constituting of mass particles connected by springs, the tamping tine motion on a mass particle would be transmitted to the adjacent mass particle via the connecting spring parallel to the direction of the P-wave propagation (dilatational-wave velocity given by the Equation 8.24) and similar to wave propagation in a simple prismatic bar [139]. Should the particle motion be perpendicular to the wave propagation direction it would result in shear strain and stresses from shear-waves. Since the tamping tine primarily inflicts displacements that propagate along the cone axis, only the P-waves, dominant in energy transport, are taken into consideration. This is, however, only valid for $v \leq 1/3$, which is equivalent to compressible (granular, non-cohesive) soils. In fine grained, water-retaining, incompressible cohesive soils ($1/3 \leq v \leq 1/2$), the velocity of P-wave propagation increases strongly and strives towards infinity. For this reason, instead of the dilatation wave *Wolf* [139] proposed the the use of double shear-wave velocity, trapped mass Δm and a trapped moment of inertia assigned to the disc. Given that the semi-analytical model described is meant to simulate the interaction of the tine and railway ballast, only the compressible soil solution will be considered. Apart for body (dilatational and shear) the exact three-dimensional wave pattern of a half-space also takes the surface (*Rayleigh*) waves into consideration, which is not possible with the Cone model. However, even if the surface waves are considered to transport a significant proportion of energy, it is once again important to differentiate between their influence in far and near field. In low frequency range the surface waves have very little to no influence in the near field described by the cone model, whereas at high frequencies they are generally negligible [24].

As mentioned before, opening angle of the cone, expressed by the ratio x_0/r_0, can be determined by equating the static-stiffness coefficient of the truncated semi-infinite cone K to that of the rectangular disk on a isotropic elastic half-space K_R [139]. According to *Pais and Kausel* [102], the static-stiffness of an embedded rectangular foundation for vertical displacement can be calculated from the following equation:

$$K_R = \frac{G\, b_0}{1-v}\left[3.1\left(\frac{a_0}{b_0}\right)^{0.75} + 1.6\right] \tag{8.38}$$

Matching the static-stiffness coefficients by equating Equations 8.37a and 8.38 and using the following expression to relate the constrained modulus E_s to the shear modulus G:

$$E_s = \frac{1-v}{1-2v}\,2G \tag{8.39}$$

gives the hight x_0 of the cone peak for compressible soils for a displacement parallel to the cone axis:

$$x_0 = 8a_0\frac{(1-v)^2}{1-2v}\left[3.1\left(\frac{a_0}{b_0}\right)^{0.75} + 1.6\right]^{-1} \tag{8.40}$$

Opening angle of the cone (x_0/r_0) is therefore dependent not only on the *Poisson's* ratio but also on the aspect ratio of the rectangular surface area (a_0/b_0). It reaches a maximum

Die approbierte gedruckte Originalversion dieser Dissertation ist an der TU Wien Bibliothek verfügbar.
The approved original version of this doctoral thesis is available in print at TU Wien Bibliothek.
TU Bibliothek Your knowledge hub WIEN

value at $v = 1/3$ and decreases with an increase of a_0 to b_0 ratio [24].

The equation of motion in the time domain for the displacement u_0 in a general form reads [139]:

$$\Delta m\, \ddot{u}_0(t) + C\, \dot{u}_0(t) + K\, u_0(t) = F_0(t) \tag{8.41}$$

For compressible soils ($v \leq 1/3$) the stiffness of a *Hooke*an elastic spring $K = k_v$ is given by the Equation 8.38, and the viscous *Newton*ian dashpot coefficient $C = c_v$ is calculated by substituting Equation 8.24 into Equation 8.37b:

$$k_v = \frac{G\, b_0}{1 - v} \left[3.1 \left(\frac{a_0}{b_0} \right)^{0.75} + 1.6 \right] \tag{8.42a}$$

$$c_v = 4 \sqrt{2\rho\, G \frac{1 - v}{1 - 2v}}\, a_0 b_0 \tag{8.42b}$$

Given that the spring stiffness k_v and dashpot coefficient c_v simulate the ballast matrix model *elastic* response to the displacement implemented by the tamping tine, they will hereinafter be referred to as k_e and c_e. As stated before, according to *Wolf* [139], the trapped mass Δm can be neglected ($\Delta m = 0$) when simulating compressible soils, giving the final form of the equation of motion in the time domain:

$$4 \sqrt{2\rho\, G \frac{1 - v}{1 - 2v}}\, a_0 b_0\, \dot{u}_0(t) + \frac{G\, b_0}{1 - v} \left[3.1 \left(\frac{a_0}{b_0} \right)^{0.75} + 1.6 \right] u_0(t) = F_0(t) \tag{8.43}$$

8.4.1.4 Ballast properties as elastic parameters of the cone model

The cone presented by a *Kelvin-Voigt* model (*Newton*ian dashpot and *Hooke*an elastic spring connected in parallel) proposed by *Wolf* [139] and used in the semi-analytical modeling simulates he homogeneous half-space disregarding material damping with the elastic soil properties based on the following parameters:

Bulk density ρ

In contrast to smaller-grained bulk material such as fine gravel or sand, the exact density of railway ballast is more difficult to determine. Random particle positioning in a unit volume has a greater influence on the material density due to irregular grain shapes. The railway bulk density, expressed as the dry weight of soil per unit volume of soil, is defined in dependence on the specific gravity and the parent rock. Density used for the calculation of the Cone model parameter c_e is 1900 kg/m^3, selected in accordance with the ÖNORM EN 13450 [8].

***Poisson's* ratio** v

Poisson's ratio v is the measure of material compressibility perpendicular to applied stress, or the ratio of latitudinal to longitudinal strain. It is used to define the dominant seismic wave for the transport of energy. If velocities of both P and S-waves are known, *Poisson's*

Die approbierte gedruckte Originalversion dieser Dissertation ist an der TU Wien Bibliothek verfügbar.
The approved original version of this doctoral thesis is available in print at TU Wien Bibliothek.
TU Bibliothek Your knowledge hub WIEN

ratio can be determined exactly by applying the theory of elasticity [24]:

$$v = \frac{c_p^2 - 2c_s^2}{2(c_p^2 - c_s^2)} \tag{8.44}$$

Alternatively, the static *Poisson's* ratio can be determined in dependence on the soil type and water content. *Poisson's* ratio applied for the calculation of the Cone model parameters k_e and c_e is 0.3, selected for elastic, compressible soils (gravel and sand $v = 0.25 - 0.35$).

Shear modulus G_d

As can be seen from Equations 8.42a and 8.42b, the dynamic shear modulus affects both the elastic spring stiffness (linearly) and the dashpot coefficient (with a power of 1/2), greatly influencing the soil reaction defined by the Cone model. Value of the dynamic shear modulus G_d as the ratio of shear stress to the shear strain under dynamic loading conditions can be determined in-situ by measuring shear wave velocity c_s using the following equation [25]:

$$c_s = \sqrt{\frac{G_d}{\rho}} \tag{8.45}$$

Apart from the in-situ measurement by cross-hole tests, down-hole tests, suspension logging etc., and resonant column test performed in the laboratory there is no universally accepted theoretical method of dynamic shear modulus determination, mostly due to the non-linear soil behavior that is greatly influenced by changes in the particle size distribution, particle shape and particle packing within the soil matrix [24]. Several researchers have put an effort into comparison of dynamic and static shear modulus ([41][63]), showing that simply using the static modulus leads to great underestimation of soil properties, especially in fine-grained soils. Ratio of the static shear modulus G to the dynamic modulus G_d increases with the increase of the shear strain.

Ballast shearing behavior is greatly influenced by the changes in the particle size distribution that occur as a consequence of ballast fouling by different materials (Chapter 3) [35]. Dependent on the aggregate parent rock, the dynamic shear modulus obtained from the in-situ measurements varies from 29 - 34 MPa for clean ballast, corresponding to a density range of 1.58 - 1.64 t/m^3. Shear modulus of ballast fouled by clayey sand varies from 28 to 40 MPa (Figure 8.8), and the one of ballast fouled by coal from 17 do 40 MPa [76].

At lower fouling levels the shear modulus of fouled ballast, together with the shear wave velocity, increase until a maximum value is reached. The highest shear modulus and shear wave velocity determine the *optimum fouling point OFP* after which the shear stiffness decreases. For ballast fouled by clayey sand, the *OFP* is between 13 and 17% fouling, defined by the Percentage of fouling (Figure 8.8). After the *OFP* is reached, the ballast bed shear stiffness is still higher than in clean ballast conditions meaning that the track is sufficiently resistant [76].

Die approbierte gedruckte Originalversion dieser Dissertation ist an der TU Wien Bibliothek verfügbar.
The approved original version of this doctoral thesis is available in print at TU Wien Bibliothek.
TU Bibliothek Your knowledge hub WIEN

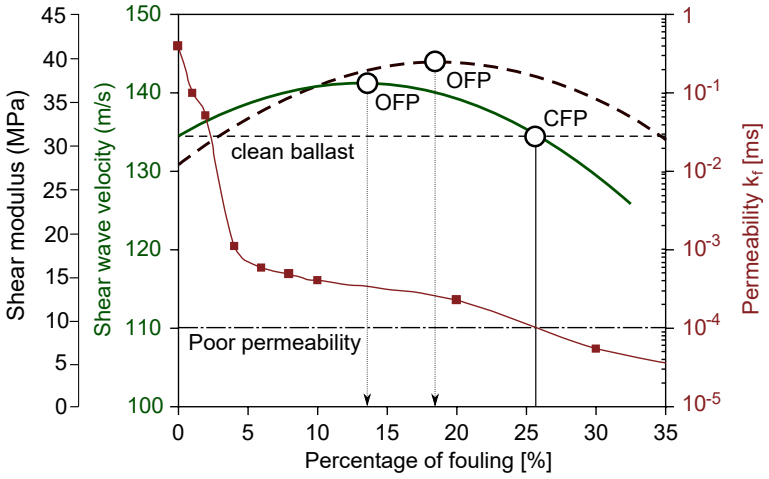

Figure 8.8: Variation of shear modulus and shear wave velocity of clayey sand fouled ballast with Percentage of fouling (modified from [76])

The fouling process continues until the *critical fouling point CFP* is reached, defined by the track drainage conditions [35]. Ballast permeability of 10^{-4} m/s is considered to be the limit value after which track drainage conditions become unsuitable [117]. Critical Percentage of fouling for ballast contaminated by clayey sand is about 26%, as can be seen in Figure 8.8 [76].

The dynamic shear modulus G_d used for the calculation of the Cone model parameters k_e and c_e is varied between 10 and 50 MPa, resulting in different ballast matrix model reactions that can be seen in Chapter 8.6. Influence of the shear modulus on the elastic spring stiffness (Eq. 8.42a) and dashpot coefficient (Eq. 8.42b) of the Cone model can be seen in Figure 8.9.

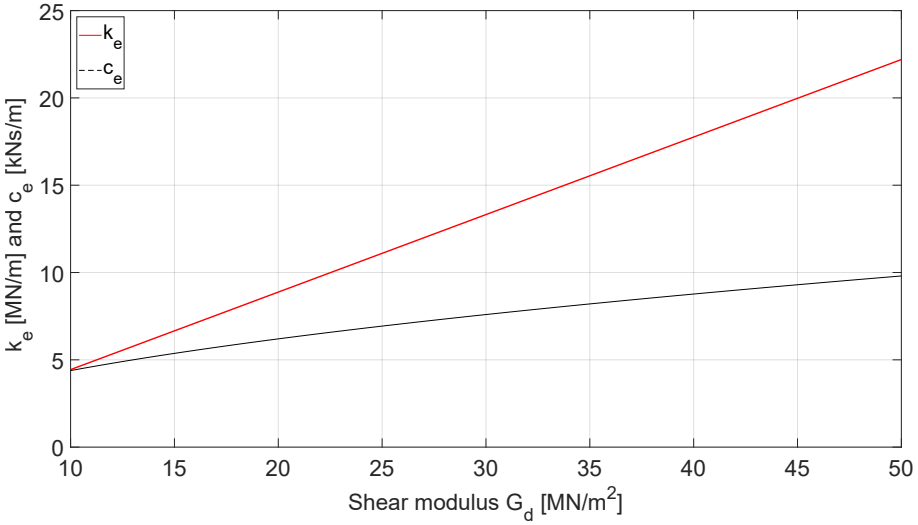

Figure 8.9: Stiffness of the elastic spring k_e [MN/m] and the dashpot coefficient c_e [kNs/m] in dependence of the shear modulus

Die approbierte gedruckte Originalversion dieser Dissertation ist an der TU Wien Bibliothek verfügbar.
The approved original version of this doctoral thesis is available in print at TU Wien Bibliothek.

8.4.2 Plastic spring

The deformation of the ballast matrix model $x_{ballast}$ during both contact phases (loading and unloading) is equal to the tamping tine displacement x_{tine} from the neutral position [35]. The total deformation consist of the elastic component presented by the Cone model, and the residual (plastic) deformation of the ballast matrix presented by a spring with a stiffness k_p that is compacted during the loading and remains "locked" during the unloading phase[36]. In every following cycle the plastic spring is replaced by a new one and is utilized to simulate ballast compaction under the sleeper. This residual deformation of the ballast matrix is also detected in the results of the in-situ conducted measurements (Chapter 6.5.4) and can be interpreted from the contact points between the tamping tine and the ballast. First contact points (beginning of contact) during one squeezing process are plotted as a constituent part of the heat map graphical analysis, showing that even after the influence of the squeezing velocity is compensated between two cycles, the contact to the ballast in every following cycle is achieved later than in the preceding one, indicating a residual plastic deformation [36]. The contact points alone, however, are not sufficient for a calculation of the proportion of plastic in the total ballast matrix deformation for several reasons:

- The deviation between two consecutive cycles regarding the contact points does not only depict the residual ballast matrix deformation but also the influence of the single ballast grains behavior during the withdraw phase (a_{gc}). Given that the area of the tamping tine plate or the contact area (0.017 m^2 for the tine No.64) is only negligibly bigger than the ballast grains, meaning that the intrusion of one single grain would influence the contact points considerably, without depicting the ballast matrix plastic deformation.

- As stated before, motion of the ballast grains during compaction is not only limited to the direction of the tamping tine motion. Quite the contrary, the motion on the tamping tine does not only compact the ballast matrix under the sleeper but pushes the ballast grains aside the tines instead. Motion of the ballast grain away from the tine increases the gap between the contact points of two consecutive cycles but neither indicates an increase of the ballast matrix plastic deformation nor changes of the ballast bulk density. This phenomenon is especially noticeable at higher frequency levels ([59]), as well as in clean ballast conditions, where after a certain number of cycles ballast floating takes place (Chapter 7.2).

- With increasing squeezing velocity the withdraw phase shortens, simultaneously decreasing the appearance of ballast creep behavior and gap closing acceleration, both constitutive parts of the reversible ballast matrix deformation. Higher squeezing velocity increases the difference between the contact points of the two consecutive cycles, but also does not indicate higher values of the plastic deformation but rather a share of the elastic deformation that is released after the last cycle is completed and the tamping tines are opened and pulled out of the ballast simultaneously.

Die approbierte gedruckte Originalversion dieser Dissertation ist an der TU Wien Bibliothek verfügbar.
The approved original version of this doctoral thesis is available in print at TU Wien Bibliothek.
TU Bibliothek Your knowledge hub WIEN

All of the reasons listed above indicate that the spring stiffness k_p that determines the behavior of the plastic spring can hardly be recalculated from the in-situ measurement. The considerations proposed by *Adam* [24] are taken into account in order to define a purposeful value of the spring stiffness needed for the mechanical model, comparing the behavior of the soil in a single cycle during compaction with vibratory rollers to the bearing capacity of shallow footings, where the ballast load bearing capacity R_k is calculated as a product of the contact area A and the stress σ_B, thereby describing the elasto-plastic material behavior in the loading phase with a linear-elastic one (in detail in [24]). This simplification is based not only on the theoretical approach, but was also confirmed by a series of conducted model and in-situ tests, proving that the plastic soil deformation during quasi-static loading and unloading can be approximated to a straight line, meaning that the value of the plastic stiffness k_p remains constant (Figure 8.10).

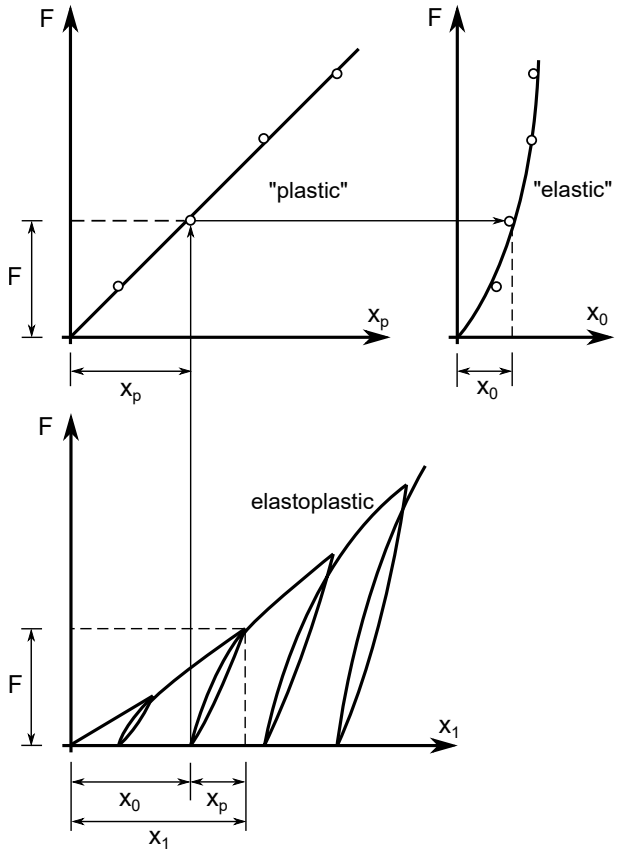

Figure 8.10: Selective determination of plastic and elastic deformation proportion based on a model test conducted with a curved contact surface (modified from [24])

Given that the purpose of the mechanical model described is the simulation of different ballast conditions, a special consideration was given to the changes of the plastic and elastic stiffness during compaction. For this purpose, three different load-displacement curves (Figure 6.3) are taken as typical representatives of the different ballast conditions and a "best-fitting" is conducted in order to conduct a back calculation for a reasoned value of k_p to be used for the mechanical model. Given that one of the most significant distinctions between the load-displacement curves that were obtained from the in-situ measurements in different

Die approbierte gedruckte Originalversion dieser Dissertation ist an der TU Wien Bibliothek verfügbar.
The approved original version of this doctoral thesis is available in print at TU Wien Bibliothek.
TU Bibliothek Your knowledge hub WIEN

ballast conditions is the shape of the curve in unloading phase of the cycle. Variation of the plastic parameter k_p alone is insufficient for the modeling due to the fact that it describes the behavior of the plastic spring that is inactive ("locked") during unloading. Nevertheless, a parameter study was conducted in order to determine the "optimum" value of k_p.

A single cycle in form of a load-displacement diagram is presented in Figure 8.11, showing the influence of k_p on the diagram shape, maximum force, energy and loading response. As stated before, no influence is expected on the unloading response where the force in the ballast model is calculated only in dependence on the elastic model parameters. Ballast properties required for the calculation of the cone model elastic parameters (Chapter 8.4.1.4) are kept constant, allowing only the influence of k_p alteration to be seen. With a constant tamping tine oscillation amplitude in the tamping direction, given an increase of k_p, an increase of the reaction force F is expected and can be seen in Figure 8.11. A higher force F required to compress the plastic spring defined by a higher value of k_p to the same extend (given that the elastic parameters are kept constant) also increases both the loading response and the energy consumption. Furthermore, Figure 8.11 shows the influence of the stiffness k_p on the first contact point (tamping tine - ballast matrix contact beginning). With the increase of k_p the proportion of the plastic spring in relation to the Cone model deformation decreases. Given that the Cone model deformation is resilient and the elastic spring expands into its original length during the unloading and withdraw phase, smaller plastic spring deformation during loading phase will indicate sooner contact establishment between the tine and the ballast matrix model.

Due to the fact that the value of k_p cannot influence the shape of the load-displacement curve in the unloading phase, it was not selected as a variable parameter to perform the "best fitting" to the different ballast responses measured in-situ. Stiffness k_p is given a constant value of 4 MN/m that is not varied throughout the simulation.

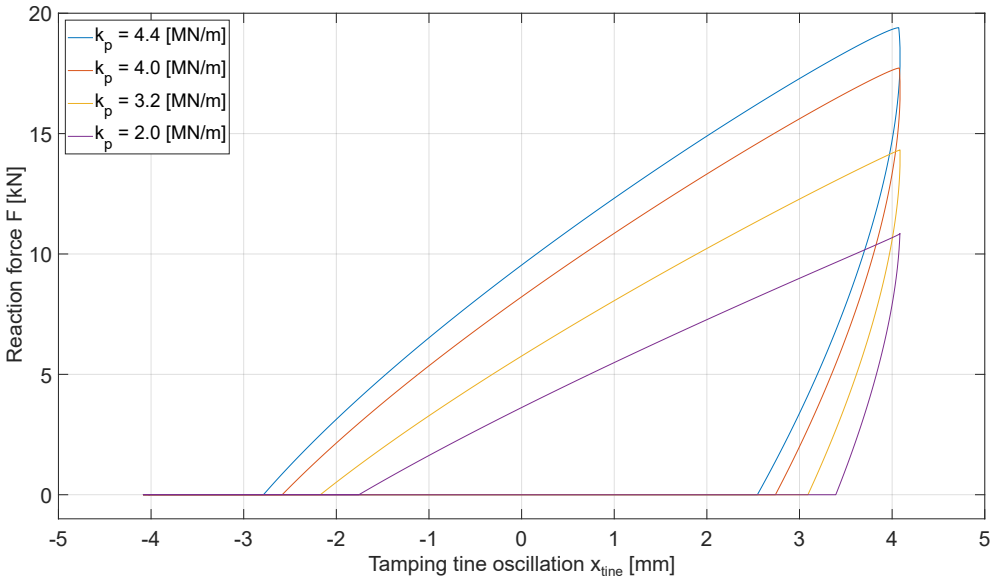

Figure 8.11: Influence of the ballast matrix model plastic stiffness k_p on the shape of load-displacement curves, G_d = 20 MN/m^2, k_e and c_e given by Equations 8.42a and 8.42b

Die approbierte gedruckte Originalversion dieser Dissertation ist an der TU Wien Bibliothek verfügbar.
The approved original version of this doctoral thesis is available in print at TU Wien Bibliothek.
TU Bibliothek Your knowledge hub WIEN

8.4.3 Gap closing acceleration

Following the loss of contact between the tamping tine and the ballast matrix model during the backwards movement of the tine, the ballast grains will form a free-standing, vertical ballast "wall" [36]. In order to enable the modeling of ballast grains motion during this phase of the cycle, acceleration a_{gc} of the grains during loss of contact, i.e. during withdraw, is calculated. Implementation of the "gap closing acceleration" enables calculation of the exact ballast matrix position $x_{ballast}$ before it is reached by the tamping tine and the next cycle begins. The acceleration of the ballast grains striving to close the gap between the tine and the ballast, i.e. to bring down the vertical ballast wall, is calculated using the sliding block theory and the *Rankine*'s earth-pressure theory, dependent on the ballast friction angle and the excitation frequency.

8.4.3.1 *Rankine*'s earth-pressure and the sliding block theory

Prior to loss of contact ballast grains behavior can be identified as behavior of backfill behind the retaining wall i.e. tamping tine. This behavior is described by the *Rankine's* earth-pressure theory for cohesionless soils against smooth vertical walls [46]. According to the *Rankine's* theory, the retaining wall always yields somewhat under the pressure of the adjoining backfill. Yielding of the retaining wall was in this case substituted with the backwards movement of the tine which precedes the loss of contact. If the ballast is stretched continuously following loss of contact, the pressure will also be gradually decreased until the failure of a soil in form of a wedge at an angle of $45° + \varphi/2$ to the horizontal (Figure 8.13) behind the tamping tine contact plate with an area $2a \cdot 2b$ takes place. On further movement of the ballast there will be no further decrease in the horizontal pressure on the vertical side of the tine but the ballast grains flow out of formation. The sliding block theory (Figure 8.12)[126] is implemented in order to calculate the acceleration of the gap closing ballast movement.

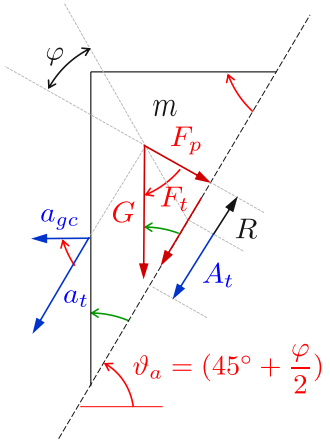

Figure 8.12: Ballast motion in form of a wedge at an angle of $45° + \varphi/2$ to the horizontal behind the tamping tine contact plate

Die approbierte gedruckte Originalversion dieser Dissertation ist an der TU Wien Bibliothek verfügbar.
The approved original version of this doctoral thesis is available in print at TU Wien Bibliothek.
TU Bibliothek Your knowledge hub WIEN

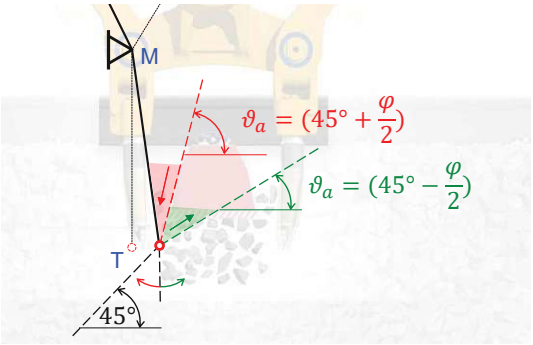

Figure 8.13: Boundaries of zone of plastic equilibrium under the sleeper

Calculation of the gap closing acceleration is applied for a wedge of ballast grains with a unit weight $G = mg$. Two forces acting at the base can be calculated in dependence on the ballast internal friction angle with the following equations for the perpendicular F_p and tangential force F_t, respectively:

$$F_p = m \cdot g \cdot \cos(\vartheta_a) \tag{8.46}$$

$$F_t = m \cdot g \cdot \sin(\vartheta_a) \tag{8.47}$$

The resisting frictional force R at the base is calculated as:

$$R = F_p \cdot \tan \varphi \tag{8.48}$$

giving the resulting driving force A_t at the base:

$$A_t = F_t - R \tag{8.49}$$

The resulting acceleration of the sliding block a_s in the direction of sliding is computed:

$$a_t = \frac{F_t}{m} \tag{8.50}$$

Horizontal component a_{gc} of the resulting acceleration a_t depicts the movement of the ballast grains striving to close the gap between the tine and the ballast. The value of a_{gc} in dependence on the ballast internal friction angle (Figure 8.14) is calculated for the excitation frequency of 35 Hz and the tine oscillation amplitude ± 4-5 mm as follows:

$$a_{gc} = a_t \cdot \cos(\vartheta_a) \tag{8.51}$$

Die approbierte gedruckte Originalversion dieser Dissertation ist an der TU Wien Bibliothek verfügbar.
The approved original version of this doctoral thesis is available in print at TU Wien Bibliothek.
TU Bibliothek Your knowledge hub WIEN

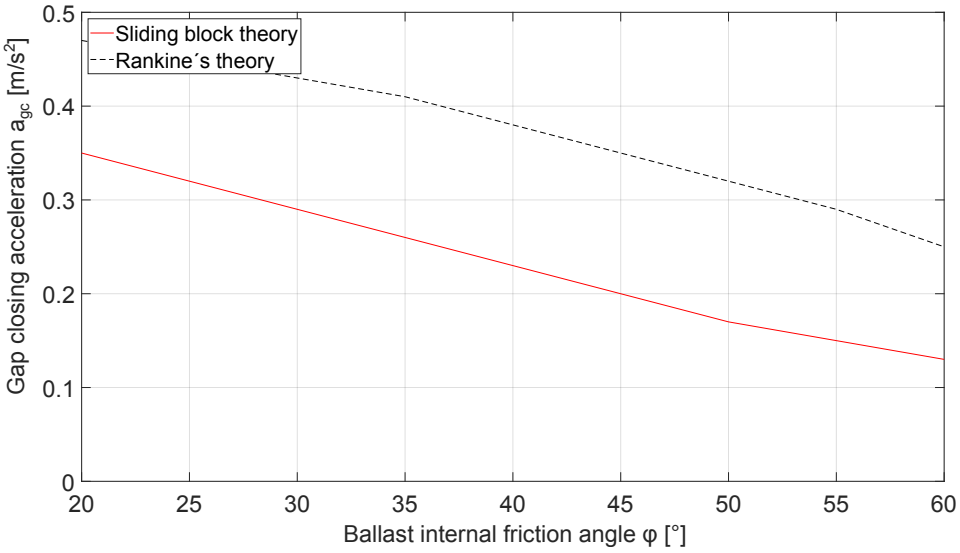

Figure 8.14: Calculation of the gap closing acceleration a_{gc}

Substituting Equations 8.47, 8.49 and 8.50 in 8.51 yields to:

$$a_{gc} = g \cdot [\sin(\vartheta_a) - \cos(\vartheta_a) \cdot \tan(\varphi)] \cdot \cos(\vartheta_a) \tag{8.52}$$

Rankine's theory describes the wedge of soil at an angle of $45° + \varphi/2$ to the horizontal acting against the retaining wall as the active zone (red wedge, Figure 8.13). As the moving mass of ballast grains stretches, the value of the coefficient of earth pressure K in the active zone decreases until it becomes equal to the active earth pressure coefficient K_a at which point the ballast is in active *Rankine* state [126]. Ballast internal friction angle needed to calculate the gap closing acceleration is dependent on the ballast parental rock as well as the condition of the ballast bed.

8.4.4 Ballast matrix operating phases

During the squeezing movement, the tamping tine displacement x_{tine} is transferred to the ballast matrix and the ballast matrix deformation as well as its reaction in form of the force F is calculated. The force is used as input for the calculation of the tine displacement in the following cycle. Depending on the current position of the tine to the ballast matrix, as well as on the calculated force F, the model modus operandi is based on one of the three operating phases:

- B1 - Loading
- B2 - Unloading
- B3 - Withdraw

Ballast matrix operating phases are described in detail in the following chapters.

Die approbierte gedruckte Originalversion dieser Dissertation ist an der TU Wien Bibliothek verfügbar.
The approved original version of this doctoral thesis is available in print at TU Wien Bibliothek.

8.4.4.1 B1 - Loading

The loading part of the squeezing process is defined by the position of the tamping tine to the ballast matrix model. As soon as the tine comes into contact with the ballast matrix model, the loading part of the process begins (Figure 8.15).

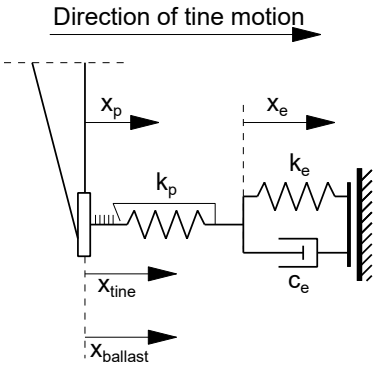

Figure 8.15: Ballast matrix model during the loading process

Apart from the tine displacement, the ballast matrix also adopts the tamping tine velocity during the loading phase:

$$x_{ballast} = x_{tine} \tag{8.53}$$

$$\dot{x}_{ballast} = \dot{x}_{tine} \tag{8.54}$$

As stated before, the ballast matrix response to the tamping tine displacement can be expressed by the force F, which is calculated using one of the two following equations and used as an input for the calculation of the force P in the tamping unit for the next cycle:

$$F = [(x_{ballast} - x_p) - x_e] \cdot k_p + F_p \tag{8.55}$$

$$F = F_{ke} + F_{ce} = x_e \cdot k_e + \dot{x}_e \cdot c_e \tag{8.56}$$

Progress of the ballast matrix model force F and both constitutive force components F_{ke} and F_{ce} (Equation 8.56) can be seen in Figure 8.16. Force in the ballast matrix model arises from the sum of the two components, where force in the elastic spring that is proportional to the deformation x_e can only take up a positive value, while the dashpot force F_{ce} changes to a negative sign as soon as the maximum elongation has been reached. Detailed description of the progress of all three forces and their characteristics is given in Chapter 8.6.

Progress of the force F in the ballast matrix model in all three operating phases and its dependence on the tamping unit model force P can be seen in Figure 8.17. Dependent on the tamping unit operating phase (T1-T2), the tamping tine motion is displacement controlled (T1) or force controlled (T2).

When the tine displacement is transferred to the soil model described in this chapter, both the *Kelvin-Voigt* model, consisting of a *Newton*ian dashpot and a *Hooke*an elastic spring and the plastic spring, modeling ballast compaction under the sleeper, will be compressed

Die approbierte gedruckte Originalversion dieser Dissertation ist an der TU Wien Bibliothek verfügbar.
The approved original version of this doctoral thesis is available in print at TU Wien Bibliothek.
TU Bibliothek Your knowledge hub WIEN

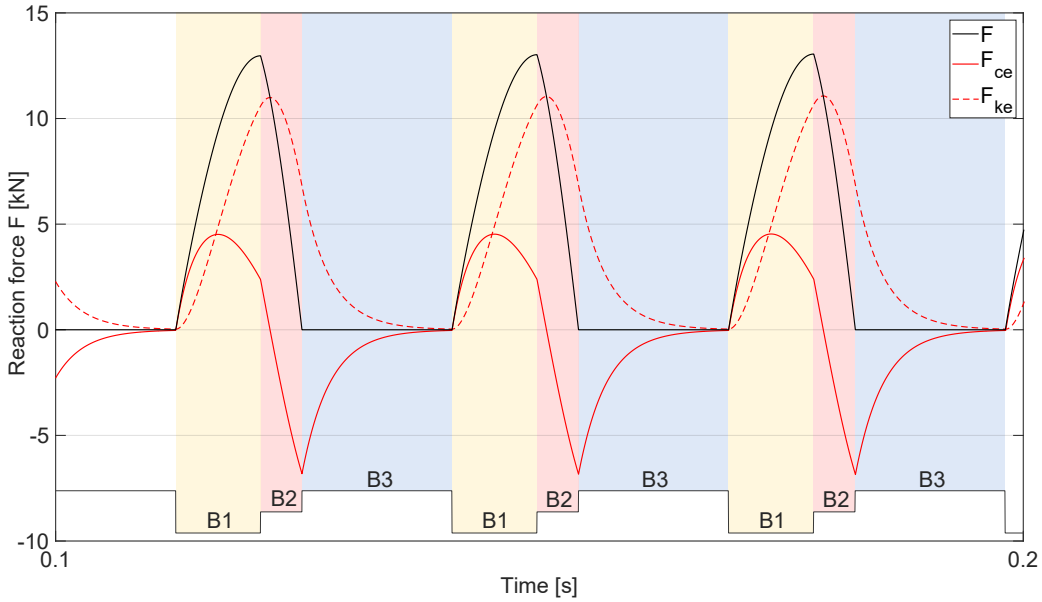

Figure 8.16: Ballast matrix model force F and both constitutive force components F_{ke} and F_{ce} (Equation 8.56) over several cycles

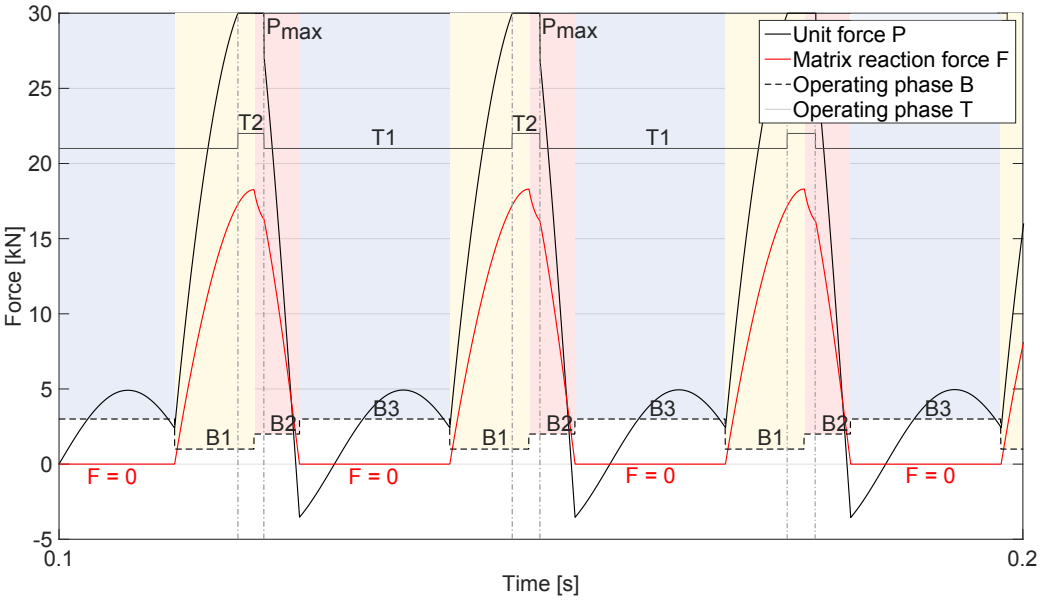

Figure 8.17: Progress of the force F in the ballast matrix model in all three operating phases as well as its dependence on the tamping unit model force P

up to a certain amount depending on the spring stiffness and dashpot coefficient. The spring stiffness k_p and k_e as well as the dashpot coefficient c_e are given constant values which do not change during one squeezing movement. The altogether displacement exerted to the matrix generates a force that can be calculated either as a force in the plastic (8.55) or in the elastic (8.56) component of the model. The force in the ballast matrix model required for the following calculations is obtained from Equation 8.55, using the deformation in the plastic spring $x_{plastic} = (x_{ballast} - x_p) - x_e$, dependent on the spring stiffness k_p and on the force F_p remaining in the spring from the preceding cycle. The deformation of the spring is obtained

Die approbierte gedruckte Originalversion dieser Dissertation ist an der TU Wien Bibliothek verfügbar.
The approved original version of this doctoral thesis is available in print at TU Wien Bibliothek.

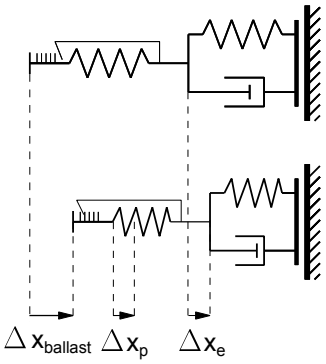

Figure 8.18: Compressed ballast matrix during the loading process

from the current tine i.e. ballast position $x_{ballast}$, reduced by the cumulative predeformation in the plastic spring resulting from preceding cycles x_p and the current deformation of the elastic spring x_e. Taking into consideration that the force in the plastic and the elastic model component has to be equal, the two Equations (8.55 and 8.56) can be set equal and transformed for a single time step:

$$\Delta x_p \cdot k_p = \Delta x_e \cdot k_e + \Delta \dot{x}_e \cdot c_e \tag{8.57}$$

The deformation of the plastic spring between two timesteps Δx_p (Figure 8.18) can be calculated as a difference between the cumulative ballast matrix deformation of the timestep given by $\Delta x_{ballast}$ and the deformation in the elastic spring Δx_e (Figure 8.18):

$$\Delta x_p = \Delta x_{ballast} - \Delta x_e \tag{8.58}$$

The cumulative ballast matrix deformation in a single time step is given by:

$$\Delta x_{ballast} = x_{ballast} - x_{ballast(i-1)} \qquad (i = 1, 2, 3, \ldots length(t)) \tag{8.59}$$

The rate of the plastic spring deformation between two timesteps can be calculated accordingly:

$$\Delta \dot{x}_e = \frac{\Delta x_e - \Delta x_{e(i-1)}}{\Delta t} \qquad (i = 1, 2, 3, \ldots length(t)) \tag{8.60}$$

Substituting (8.58) and (8.60) in (8.57) yields to:

$$\Delta x_e = \frac{\Delta x_{ballast} \cdot k_p + F_p}{k_e + k_p + \frac{c_e}{\Delta t}} \tag{8.61}$$

Deformation of the *Kelvin-Voigt* model can be calculated by substituting (8.61) in (8.55):

$$x_e = \frac{(x_{ballast} - x_p) \cdot k_p - \frac{\Delta x_e}{\Delta t} \cdot c_e + F_p}{k_p + k_e} \tag{8.62}$$

Die approbierte gedruckte Originalversion dieser Dissertation ist an der TU Wien Bibliothek verfügbar.
The approved original version of this doctoral thesis is available in print at TU Wien Bibliothek.
TU Bibliothek Your knowledge hub WIEN

As stated before, x_p denotes the cumulative predeformation in the plastic spring resulting from preceding cycles including the current one, and can be calculated as:

$$x_p = x_{p(i-1)} + (\Delta x_{ballast} - \Delta x_e) \qquad (i = 1, 2, 3, ... length(t)) \tag{8.63}$$

The last remaining unknown for the calculation of the force F is the force remaining in the spring from the preceding cycle F_p. This force differs from zero only in the case of a phase-switch directly from unloading to loading, without loss of contact. In this case, only at the switch between phases B2 and B1, the predeformation in the plastic spring has to be taken into consideration by calculating the remaining force in the spring F_p:

$$F_p = F \tag{8.64}$$

In case the following condition is fulfilled at any point during loading, a phase-switch to unloading is required:

$$F < F_{i-1} \qquad (i = 1, 2, 3, ... length(t)) \tag{8.65}$$

8.4.4.2 B2 - Unloading

Equation 8.65 states that an increase of the force in the ballast matrix is expected during loading. Should the force start to decrease at any given moment, a phase-switch from loading to unloading is necessary. As stated before, during the unloading part of the squeezing process, only the *Kelvin-Voigt* model is active, while the plastic spring remains "locked", modeling the plastic deformation of the matrix, i.e. its compaction under the sleeper (Figure 8.19).

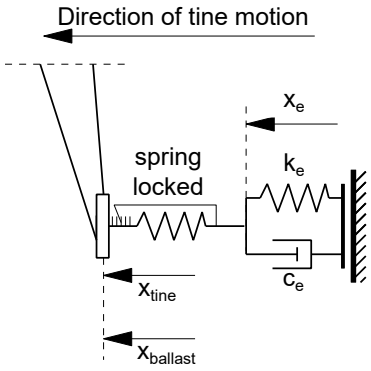

Figure 8.19: Ballast matrix during the unloading process

However, tamping tine and ballast matrix remain in contact during the unloading part of the process, and once again, apart from the tine displacement (8.53), the ballast matrix also adopts the tamping tine velocity that is – in this case – equal to the rate of increase of

Die approbierte gedruckte Originalversion dieser Dissertation ist an der TU Wien Bibliothek verfügbar.
The approved original version of this doctoral thesis is available in print at TU Wien Bibliothek.

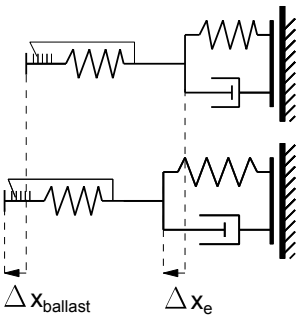

Figure 8.20: Compressed ballast matrix during the unloading process

deformation in the *Kelvin-Voigt* model:

$$\dot{x}_{ballast} = \dot{x}_{tine} = \dot{x}_e \tag{8.66}$$

Given that the plastic spring allows no deformation in the unloading phase, the force in the matrix is solely dependent on the *Kelvin-Voigt* model and can be calculated with the following equation:

$$F = x_e \cdot k_e + \dot{x}_e \cdot c_e \tag{8.67}$$

The rate of increase of deformation in the *Kelvin-Voigt* model $\dot{x}_e$ can be taken from (8.66), and the deformation x_e is now only dependent on the tamping tine movement and the cumulative predeformation in the plastic spring resulting from preceding cycles (Figure 8.21):

$$x_e = x_{tine} - x_p = x_{ballast} - x_p \tag{8.68}$$

An increase of the plastic spring deformation is only possible during loading and the cumulative predeformation is calculated at the transition from B1 to B2 using the following term:

$$x_p = x_{p(i-1)} + \frac{F - F_p}{k_p} \qquad (i = 1, 2, 3, \ldots length(t)) \tag{8.69}$$

During unloading, the cumulative predeformation of the plastic spring remains a constant value (Figure 8.21). Once the force F in the matrix is obtained, the calculation of the state variables can be proceeded for the succeeding cycle, if the force continues to decrease. Should an increase in force be noted, a phase-switch back to loading is necessary. Depending on the ballast characteristics, at a certain point during the tamping tine motion, the force in the matrix is going to reach the value of zero, i.e. take up a negative value. Given that the ballast cannot transfer any tensile stresses, a negative value of the force in the matrix is not allowed, and a phase-switch to withdraw, i.e. modeling the loss of contact is required.

Die approbierte gedruckte Originalversion dieser Dissertation ist an der TU Wien Bibliothek verfügbar.
The approved original version of this doctoral thesis is available in print at TU Wien Bibliothek.

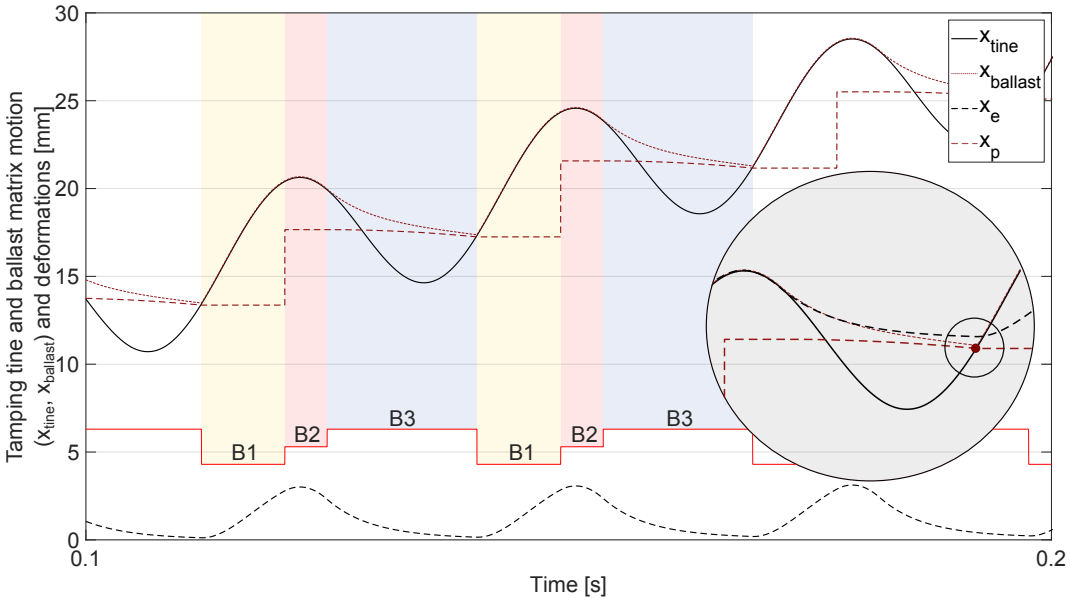

Figure 8.21: Ballast matrix model deformations in all three operating phases and the influence of the gap closing acceleration

8.4.4.3 B3 - Withdraw / Loss of contact

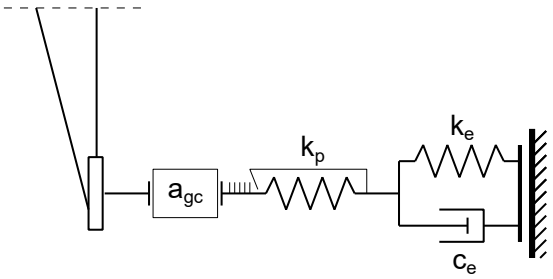

Figure 8.22: Ballast matrix during the withdraw phase

During the unloading phase the force F in the ballast matrix model will eventually take a negative value, indicating a tensile force in the soil. Since the soil matrix is unable to transmit tensile forces, the force in the ballast matrix is set to zero ($F = 0$) as soon as this occurs, indicating the beginning of the withdraw phase. Nonetheless, this does not mean that no movement in the matrix is to be expected. The *Kelvin-Voigt* model represents the elastic component of the system, and is as such unable to model any residual deformation. While the tine reaches back before starting a new cycle, the *Kelvin-Voigt* model is going to expand until it reaches its original position, modeling soil creep motion. Current deformation of the *Kelvin-Voigt* model, as well as the velocity of the creep motion can be calculated using the two following equations:

$$\dot{x}_e = -\frac{x_e \cdot k_e}{c_e} \tag{8.70}$$

$$x_e = x_{e(i-1)} + \dot{x}_e \cdot \Delta t \qquad (i = 1,2,3,...length(t)) \tag{8.71}$$

Die approbierte gedruckte Originalversion dieser Dissertation ist an der TU Wien Bibliothek verfügbar.
The approved original version of this doctoral thesis is available in print at TU Wien Bibliothek.
TU Bibliothek Your knowledge hub WIEN

As mentioned before, during the withdraw phase, when the tine is no longer in contact with the ballast, the gap closing acceleration is activated. The velocity of the ballast grains is obtained dependent on the frequency and the internal friction angle of the ballast, and is calculated as:

$$v_{gc} = v_{gc(i-1)} + a_{gc} \cdot \Delta t \qquad (i = 1, 2, 3, \ldots length(t)) \tag{8.72}$$

The gap closing motion of the ballast grains occurs in the exact opposite direction from the tamping tine, causing a reduction of the cumulative predeformation of the plastic spring (Figure 8.21). A new value of x_p is calculated as:

$$x_p = x_{p(i-1)} - v_{gc} \cdot \Delta t \qquad (i = 1, 2, 3, \ldots length(t)) \tag{8.73}$$

The calculation of the correct ballast matrix position is still necessary for every time step:

$$x_{ballast} = x_e + x_p \tag{8.74}$$

As soon as the tine comes in contact with the ballast matrix again (8.53), a new loading phase begins. Tamping tine and ballast matrix motion at the contact to the tine in all three operating phases (loading-unloading-withdraw) can be seen in Figure 8.23.

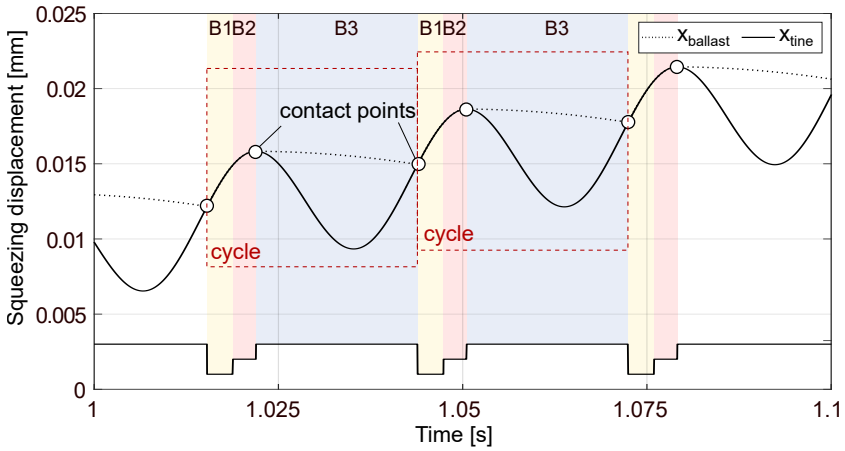

Figure 8.23: Tamping tine and ballast matrix model movement during all three phases over several cycles (detail)

An overview of operating phases and phase transition conditions for both tamping unit and the ballast matrix model is presented as a flowchart in Figure 8.24.

8.5 Energy consumption balance

Energy consumption comparison between different operating phases is necessary in order to verify calculations conducted during mechanical modeling. Energy consumption calculation is conduced for both tamping unit operating phases T1 and T2, as well as for the ballast matrix model. Work W conducted during one cycle is calculated as a sum of work carried out per time-step ΔW ($\alpha = \omega t$, Equation 8.2):

Die approbierte gedruckte Originalversion dieser Dissertation ist an der TU Wien Bibliothek verfügbar.
The approved original version of this doctoral thesis is available in print at TU Wien Bibliothek.
TU Bibliothek Your knowledge hub WIEN

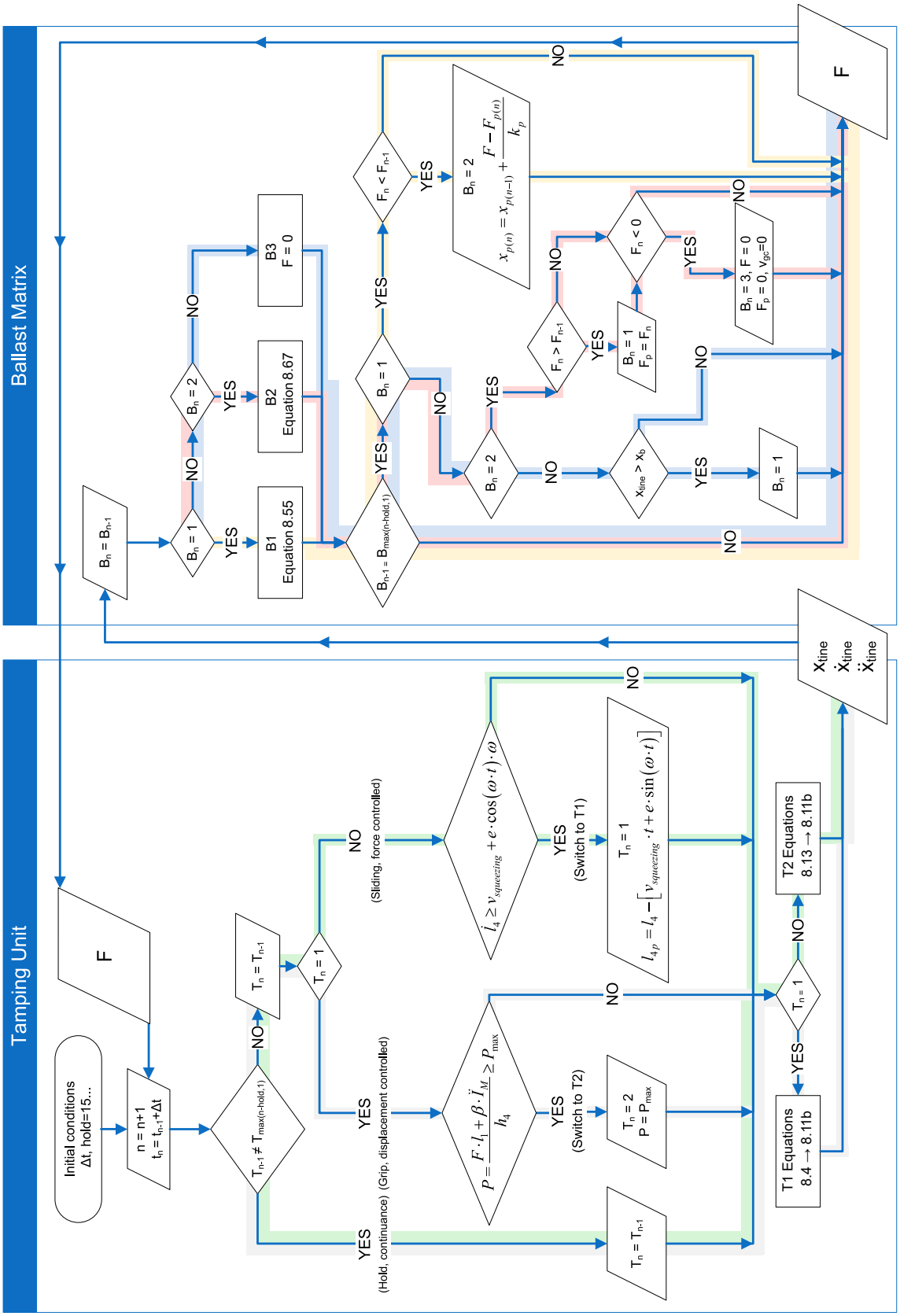

Figure 8.24: An overview (flowchart) of operating phases an phase transition conditions

TU Bibliothek Your knowledge hub
Die approbierte gedruckte Originalversion dieser Dissertation ist an der TU Wien Bibliothek verfügbar.
The approved original version of this doctoral thesis is available in print at TU Wien Bibliothek.

$$W = \sum_{\alpha=0}^{2\pi} \Delta W \tag{8.75}$$

Work carried out during one time-step Δt is calculated for the tamping unit model, consisting of a dynamic part (drive shaft) and a quasi static part (squeezing cylinder):

$$\Delta W = P \cdot (e \cdot \cos(\omega t)) \cdot \omega \cdot \Delta t + P \cdot v_{sqeezing} \cdot \Delta t \tag{8.76}$$

During the inactive phase of the friction element T1, the work transmitted to the tamping tine will be equal to the one calculated by the Equation 8.76 and can be expressed as:

$$\Delta W = P \cdot \dot{l}_4 \cdot \Delta t \tag{8.77}$$

Is the maximum permissible force P_{max} in the tamping unit model reached, the friction element is activated and the elongation of the rod l_4 is decelerated. Opening and sliding motion in the friction element causes an energy loss between the tamping unit model drive (static and dynamic) and the tamping tine (Figure 8.25).

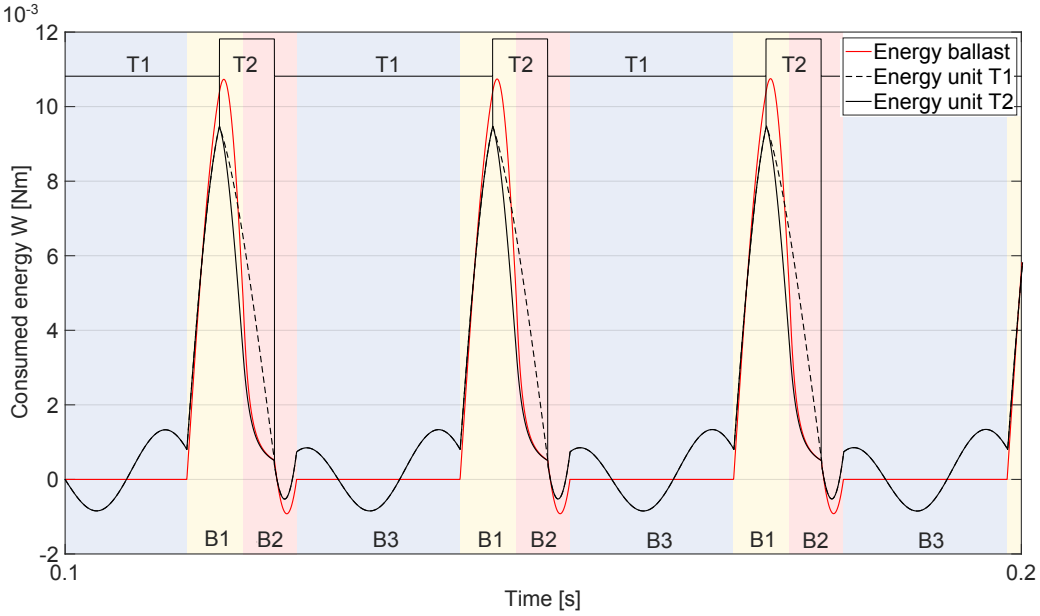

Figure 8.25: Energy consumption calculation over three cycles in both tamping unit model operating phases

Energy consumption in the ballast matrix model is also calculated and compared to the tamping unit in order to validate the model. As a product of force and displacement in the same direction, work carried out in the ballast matrix model can be obtained by a general expression given for the force F in the ballast matrix model and the displacement $x_{ballast}$ for a single time-step, it yields:

$$\Delta W = F \cdot \dot{x}_{ballast} \cdot \Delta t \tag{8.78}$$

Displacement in the ballast matrix model is subdivided between the elastic part in the

Die approbierte gedruckte Originalversion dieser Dissertation ist an der TU Wien Bibliothek verfügbar.
The approved original version of this doctoral thesis is available in print at TU Wien Bibliothek.
TU Bibliothek Your knowledge hub WIEN

Cone model and the deformation of the plastic spring during the loading phase of every cycle and can therefore be calculated as a sum of the following three equations:

$$\Delta W = F \cdot (\Delta x_{ballast} - \Delta x_e) \tag{8.79a}$$

$$\Delta W = (\frac{x_e}{\Delta t} \cdot c_e) \cdot \Delta x_e \tag{8.79b}$$

$$\Delta W = (F - \frac{\Delta x_e}{\Delta t} \cdot c_e) \cdot \Delta x_e \tag{8.79c}$$

Equation 8.79a takes into consideration the deformation of the plastic spring during the loading phase. Equation 8.79b is used to calculate the energy consumed by the dashpot in which the force is expressed as a product of the rate of increase of the elastic spring deformation $x_e/\Delta t$ and the dashpot coefficient c_e and the elastic spring deformation in a single time-step. Given that the elastic spring is compressed during the loading phase and extended back to its original position during unloading and withdraw phase leaving no residual deformation the work carried out by the elastic spring equalizes over one cycle and is expressed by the Equation 8.79c.

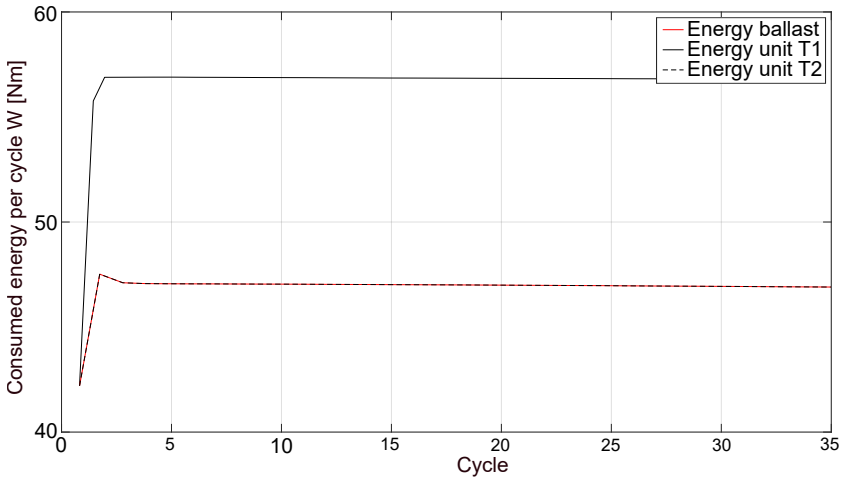

Figure 8.26: Energy consumption per cycle over 35 cycles (simulation time)

Model validation is conducted by summarizing and comparing the energy consumption for each cycle over the whole simulation time. As can be seen in Figure 8.26, as soon as the maximum force in the tamping unit P_{max} has been reached (2nd cycle), a sudden drop in energy occurs in the operating phase T2, modeling the energy consumption due to friction in the activated friction element. However, once the steady state is reached, the energy transferred by the tamping tine coincides to the one calculated for the ballast matrix model.

Die approbierte gedruckte Originalversion dieser Dissertation ist an der TU Wien Bibliothek verfügbar.
The approved original version of this doctoral thesis is available in print at TU Wien Bibliothek.
TU Bibliothek Your knowledge hub WIEN

8.6 Load-displacement curve

Motivation behind the development of the mechanical model was in the first place to simulate the tamping tine - ballast matrix interaction that was measured in-situ, followed by a parameter study in order to determine the optimum combination of tamping parameters for different ballast conditions. Lead by experience gathered during analysis of the in-situ measurements, the first focus was to simulate different ballast conditions and present them in form of load-displacement curves that can, with their shape and selected parameters, be compared to the ones obtained from the measurements. For this purpose the force in the ballast matrix model F is plotted against the tamping tine oscillation x_{tine} showing all three phases of a single cycle, loading, unloading and withdraw. The tamping tine oscillation x_{tine} plotted on the ordinate does not represent the total tamping tine displacement but a relative one, folded back to the starting position of x_{tine} by taking the squeezing velocity into consideration and ensuring the comparability of the simulated and in-situ measured load-displacement diagrams.

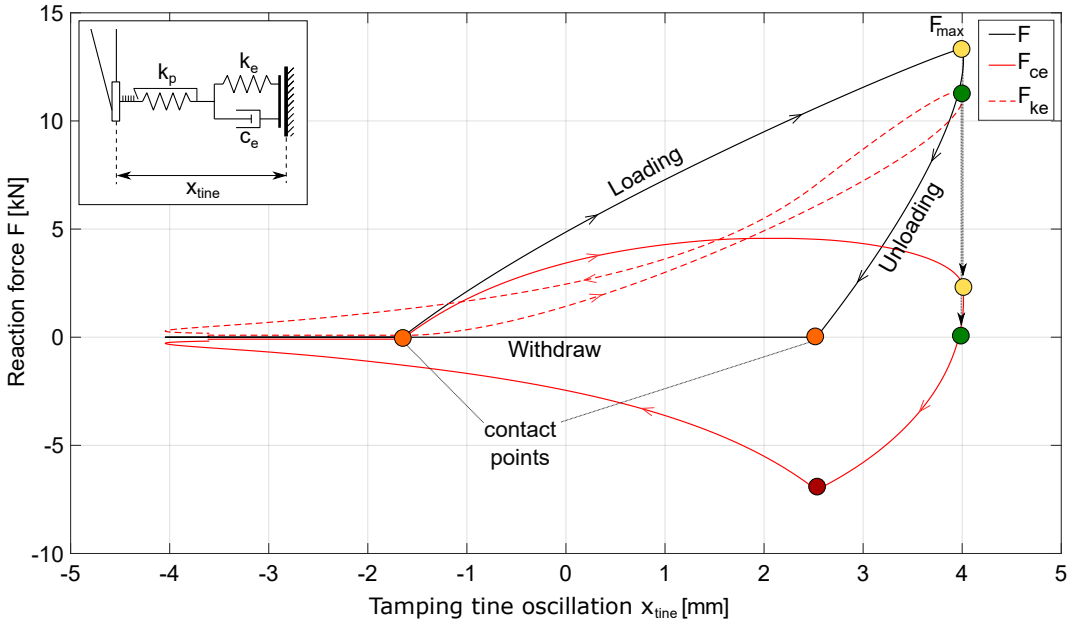

Figure 8.27: Load-displacement curve obtained from the simulation presented together with both force components F_{ke} and F_{ce}

A typical load-displacement curve obtained from the simulation is presented in Figure 8.27 together with both constitutive force components (Equation 8.56):

- force in the elastic spring that scales with respect to the spring deformation F_{ke}
- damping force proportional to the velocity of deformation F_{ce}

Figure 8.28 shows the *Kelvin-Voigt* model force components F_{ke} and F_{ce} plotted against the deformation x_e. Spring with a stiffness k_e shows a linear increase of force F_{ke} and decrease during one cycle as a purely elastic response with no energy dissipation. Conversely, the viscous dashpot c_e, modeling the geometrical damping of the ballast matrix, causes a

Die approbierte gedruckte Originalversion dieser Dissertation ist an der TU Wien Bibliothek verfügbar.
The approved original version of this doctoral thesis is available in print at TU Wien Bibliothek.
TU Bibliothek Your knowledge hub WIEN

significant energy dissipation that can be calculated as the area enclosed by the curve presented in Figure 8.28.

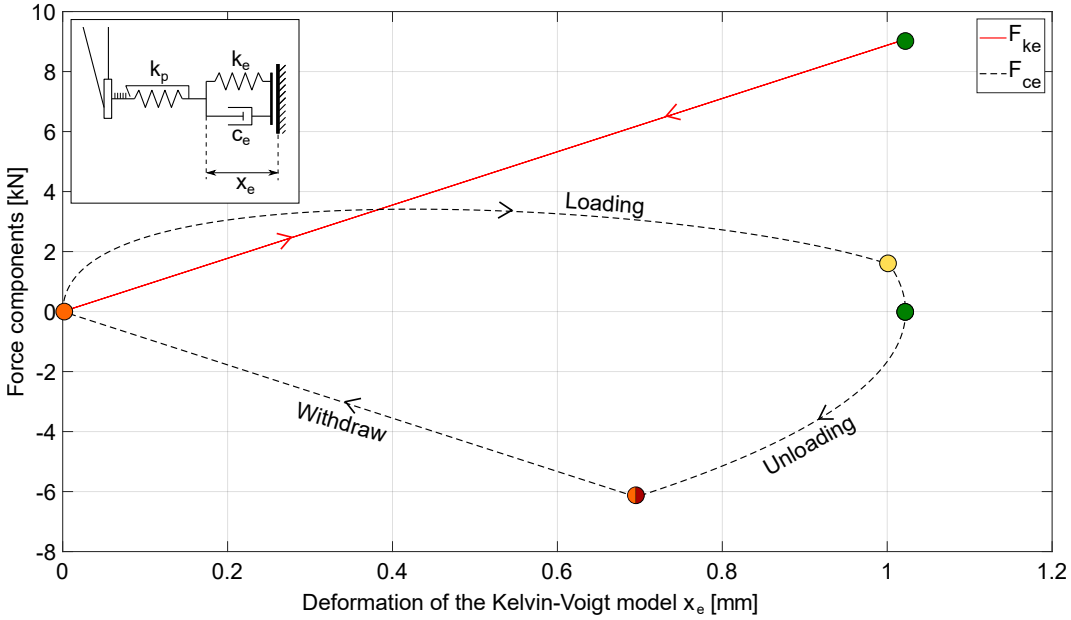

Figure 8.28: Force components F_{ke} and F_{ce} plotted against the *Kelvin-Voigt* model deformation

Constitutive components of the ballast matrix model force F are additionally plotted over time for several cycles in Figure 8.30. The progress of both elastic deformation x_e and the rate of increase of deformation in the *Kelvin-Voigt* model $\dot{x}_e$ are presented in Figure 8.31.

The load-displacement curve presented in Figure 8.27 provides and insight into all three soil model operating phases as well as into the influence of the plastic spring on the force F and its constitutive components. During the loading phase the inclination of the load-displacement curve is defined by all three active model components, elastic spring with the stiffness k_e, dashpot with a coefficient c_e and the plastic spring k_p, whereas the unloading segment is only influenced by the extension of the *Kelvin-Voigt* model given that the plastic spring remains "locked" ($k_p = \infty$). The shape of the load-displacement curve has been proven to be a reliable indicator of the ballast condition and response to compaction and can be analyzed in detail based on several characteristic points whose interdependence can be seen in Figures 8.27, 8.30 and 8.31:

- Points marking beginning (= switch from withdraw to the loading phase) and loss of contact (= switch from unloading to withdraw phase) between the tamping tine and the ballast (Figure 5.19). Exact position of the two contact points is influenced by the stiffness of the ballast matrix model defined by k_e and k_p, ballast movement in the withdraw phase defined by the gap closing acceleration and creep behavior and finally, mainly by the squeezing velocity $v_{squeezing}$ (Figure 8.29). As explained in Chapter 5.5, increasing the squeezing velocity while keeping the amplitude and frequency constant, leads to an increase of tamping tine - ballast loading contact duration and length by sooner contact initiation.

Die approbierte gedruckte Originalversion dieser Dissertation ist an der TU Wien Bibliothek verfügbar.
The approved original version of this doctoral thesis is available in print at TU Wien Bibliothek.

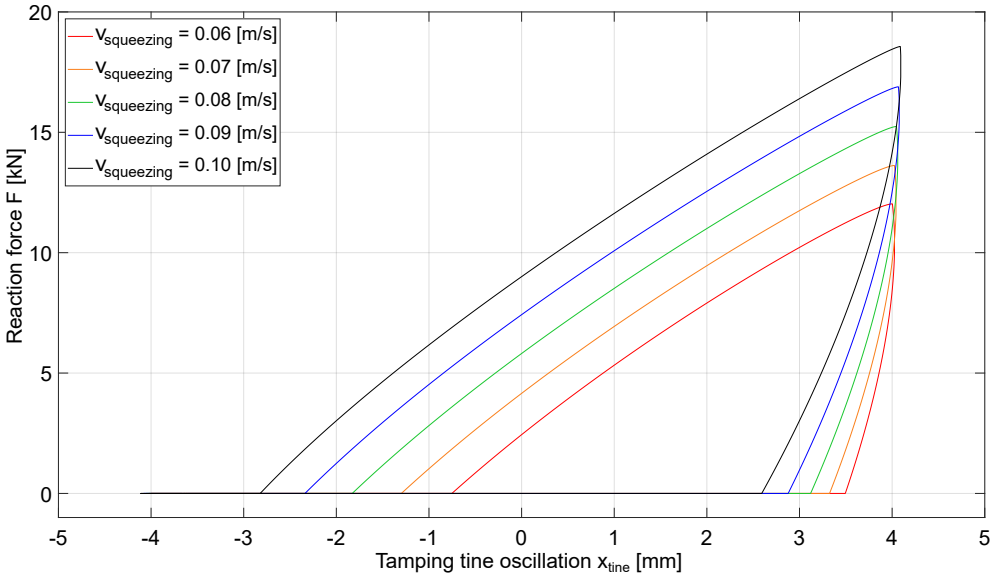

Figure 8.29: Influence of the squeezing velocity on the form of the load-displacement curves and the contact points

- Switch between loading and unloading operating phase of the ballast matrix model is defined by the maximum force F_{max} (Figures 8.27 and 8.30). A bend in the curve progression indicates the changing ballast matrix model stiffness between the two contact phases (loading and unloading), concurrently indicating the existing plastic deformation during the loading phase. Further indications of change in the model stiffness can be seen in both curve progressions presenting the damping force F_{ce} and the force in the elastic spring F_{ke} (Figure 8.27).

- Based on the in-situ observations it is clear that, dependent on the ballast condition, the maximum force measured on the tamping tine during the squeezing movement does not always coincide with the maximum tine elongation (clean ballast conditions, Figures 8.30 and 6.4a). In the context of the mechanical model, this effect can be observed in the progress of elastic spring force F_{ke} and the spring deformation x_e (Figure 8.31). Given a constant spring stiffness k_e, the maximum force F_{ke} indicates a maximum elastic deformation x_e that takes place in the unloading phase, after the maximum force F in the ballast matrix model has been reached. At the same time the maximum elastic deformation has to coincide with the minimum velocity of deformation $\dot{x}_e$, which is confirmed by the value of the damping force (F_{ce} = 0 m/s) in Figures 8.27, 8.28, 8.30 and 8.31.

- Last characteristic point can be seen at the switch between unloading and withdraw phase in the progress of the damping force F_{ce} (Figures 8.27, 8.28 and 8.30) and in the velocity of deformation $\dot{x}_e$ (Figure 8.31). As the tine looses contact to the ballast matrix model, a noticeable cusp[1] can be seen in the damping force F_{ce} (Figures 8.27 and 8.28). At the moment when the loss of contact occurs, the tine continues its motion

[1] type of singular point of a curve where a moving point must change direction

Die approbierte gedruckte Originalversion dieser Dissertation ist an der TU Wien Bibliothek verfügbar.
The approved original version of this doctoral thesis is available in print at TU Wien Bibliothek.
TU Bibliothek Your knowledge hub WIEN

with the same velocity $\dot{x}_{tine}$, while the elastic component of the ballast matrix model continues its creep motion with the velocity given by the Equation 8.70. During the withdraw phase the influence of the gap closing acceleration is activated, reducing the cumulative predeformation of the plastic spring (Equation 8.73).

During the loading part of the process, the shape of the load-displacement diagram is dependent on all three model constitutive parts, and the loading response of the ballast matrix model as defined in Chapter 5.4.2 can once again be calculated from the curve inclination that changes in dependence on the selected model parameters. The curve shape and area enclosed by the loading and unloading paths is not only defined by the spring stiffness k_e and k_p, but is highly dependent on the time or the rate at which the deformations are developed in the ballast matrix model $\dot{x}_e$. Given that the presented model only allows for plastic deformations in the loading phase and during loss of contact by considering the gap closing acceleration, the unloading phase represents a purely linear elastic process. In the withdraw phase the contact force F is per definition equal to zero, which not only arises from the predefined contact conditions, but also from the sum of the two force components F_{ce} and F_{ke} (Figure 8.28). The both force components result from the creep motion of the elastic, i.e. *Kelvin-Voigt* model components that is activated as soon as the tine loses contact to the ballast matrix model.

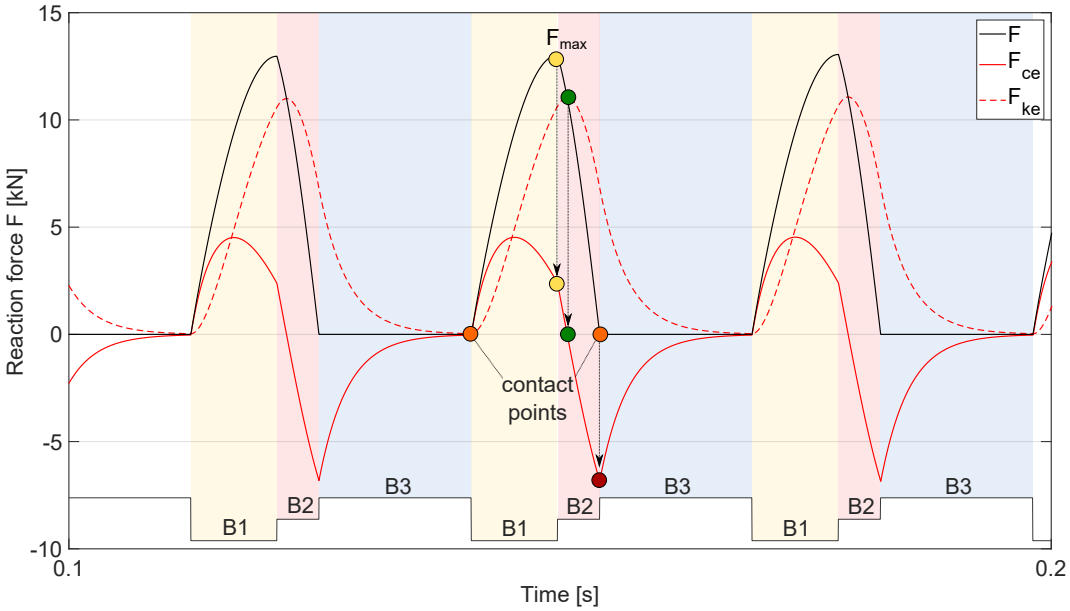

Figure 8.30: Constitutive components of the force F

Die approbierte gedruckte Originalversion dieser Dissertation ist an der TU Wien Bibliothek verfügbar.
The approved original version of this doctoral thesis is available in print at TU Wien Bibliothek.

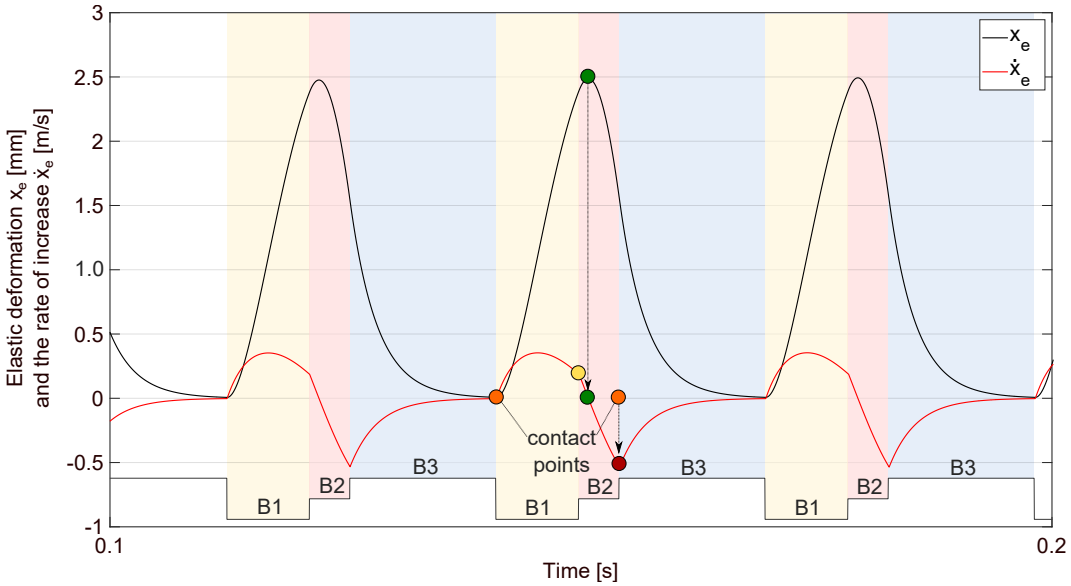

Figure 8.31: Elastic deformation x_e and the rate of increase of deformation in the *Kelvin-Voigt* model $\dot{x}_e$

8.6.1 Influence of shear modulus and elastic spring stiffness on the load-displacement curve

A study had to be conducted on various decisive parameters in order to be able to utilize the mechanical model described to simulate different ballast responses to compaction dependent on ballast condition. Expected goal of the conducted study was to find the satisfactory parameter combination that depicts the process of ballast fouling.

Apart from the plastic spring stiffness (Figure 8.11) and the squeezing velocity (Figure 8.29), the influence of the shear modulus G_d and the elastic spring stiffness k_e is taken into consideration as a possible indication of ballast fouling results results presented in the following.

Influence of the shear modulus G_d

As stated before, the increase of the shear modulus indicates the progress of ballast fouling only up to a certain limit after which the shear modulus decreases again until it reaches a value lower that the initial one (for clean ballast). Nevertheless, a parametric study is conducted in order to investigate the influence of the shear modulus on the shape of the curve and the selected parameters. Results can be seen in Figure 8.32.

Die approbierte gedruckte Originalversion dieser Dissertation ist an der TU Wien Bibliothek verfügbar.
The approved original version of this doctoral thesis is available in print at TU Wien Bibliothek.

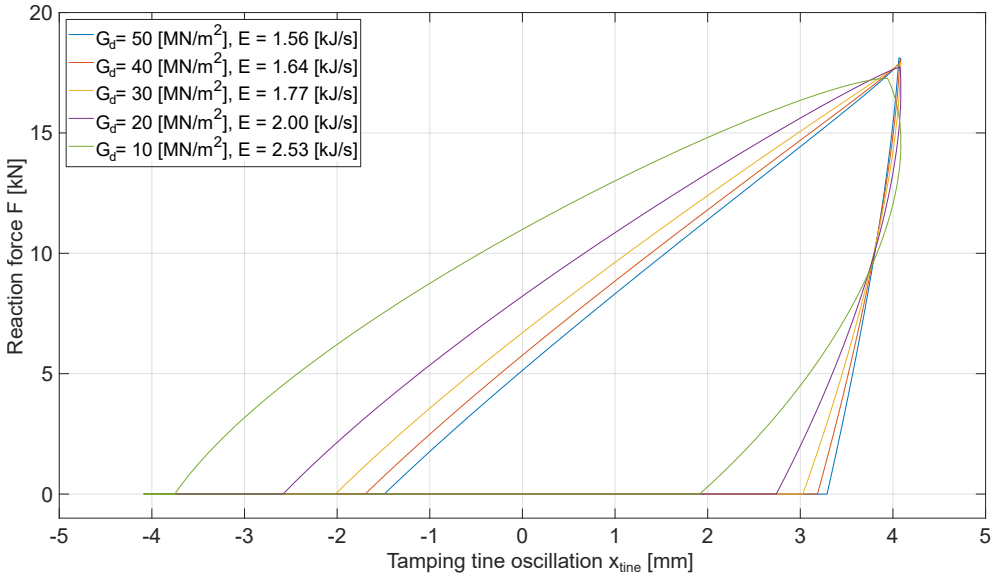

Figure 8.32: Influence of the shear modulus G_d on the shape of the load-displacement curves and the compaction energy (k_p = 3 MN/m, k_e and c_e given by Equations 8.42a and 8.42b)

At lower shear modulus values the influence of the dashpot part of the elastic model component becomes more prominent, increasing the energy needed for the tine to conduct one cycle during the squeezing movement without causing any significant changes in the maximum force F (the curve is more "belly-shaped"). Increasing the shear modulus causes a linear increase of the elastic spring stiffness (Equation 8.42a) and a significantly smaller increase of the dashpot coefficient c_e (to the power of 0.5 - Equation 8.42b, Figure 8.9). With an increase of the shear modulus both the loading and the unloading response of the ballast matrix model increase due to the increase in the elastic stiffness. Given that several researches [76] have proven that the shear modulus does not increase constantly during the process of ballast fouling, but rather starts to decrease after the optimum fouling point is reached, due to changes in the particle size distribution and the internal friction angle, this parameter is not selected for the variation simulating the ballast fouling.

Influence of the ballast matrix model elastic spring stiffness k_e

Stiffness of the elastic component of the described model influences the response of the ballast matrix model to compaction during both loading and unloading part of every cycle. The higher the stiffness k_e the lower the energy consumption during compaction (Figure 8.33). With a decrease of elastic stiffness, apart for the energy, the maximum force in the ballast matrix model F also decreases. The remaining two parameters that have been proven to implicate the differences between ballast conditions are the loading and unloading response of the ballast matrix. As can be seen in Figure 8.33, the loading response is higher at lower k_e stiffness values. Unloading response that influences the shape of the load-displacement curves at most starts to take up a negative sign as the stiffness decreases. All of the described phenomena have also been observed in-situ and have been proved to indicate the differences in ballast matrix condition, i.e. the ballast fouling process. A decrease of stiff-

Die approbierte gedruckte Originalversion dieser Dissertation ist an der TU Wien Bibliothek verfügbar.
The approved original version of this doctoral thesis is available in print at TU Wien Bibliothek.
TU Bibliothek Your knowledge hub WIEN

ness k_e by a factor of 10^3 allows much higher elastic deformations which corresponds with characteristics that were observed during clean ballast compaction.

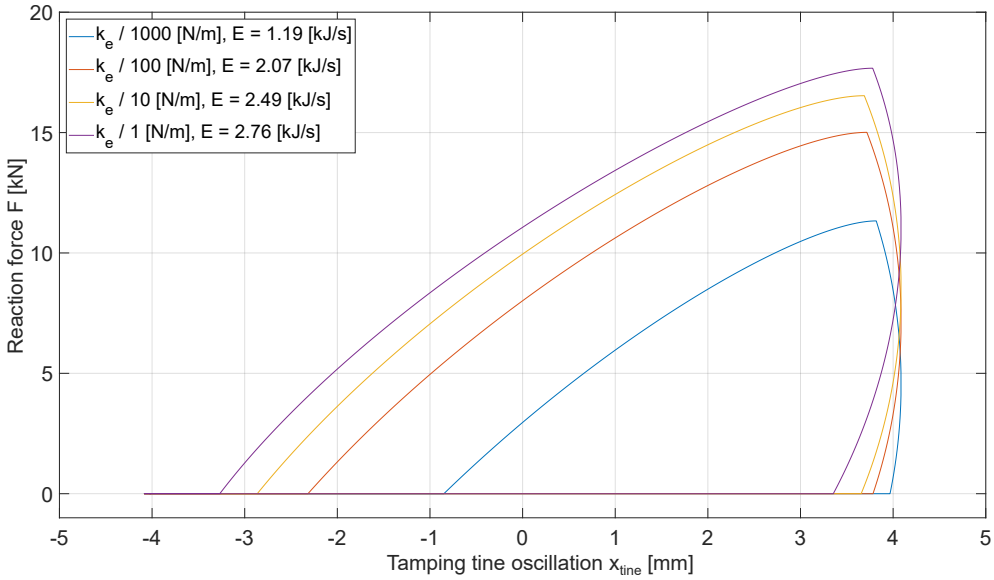

Figure 8.33: Influence of the ballast matrix model elastic stiffness k_e on the shape of the load-displacement curves and the compaction energy (G_d = 20 MN/m^2, k_p = 3 MN/m, c_e given by Equation 8.42b)

Due to the fact that variation of the elastic spring stiffness k_e has been proven to be the most important parameter that influences the shape of the load-displacement curve in the unloading phase and is able to reproduce all of the phenomena observed during the in-situ measurements, it has been selected to simulate the ballast fouling process within the presented mechanical model.

8.6.2 Modeling different ballast conditions

Following successful determination of the parameter that can be varied in order to simulate different ballast conditions, simulations are conducted to obtain the optimum parameter combination to present the ballast behavior observed in-situ. Load-displacement curve is selected as the most reliable indicator of the ballast matrix response to compaction. Simulation of different load-displacement curves during the squeezing movement in clean, moderately clean and fouled ballast (Figure 8.34) is based not only on the shape of the diagram and the maximum force, but also on the loading and unloading response of the matrix, compaction energy and contact points (Table 6.5). Load-displacement diagrams, however, only display the behavior of the ballast bed section in contact to the tamping tine and cannot take into consideration the ballast particles in the surrounding areas set into motion due to the dynamic excitation. Nevertheless, the most important indication of successful ballast compaction under the sleeper is the increase of the ballast matrix stiffness i.e. its resistance to compaction that can indeed be measured during the tamping tine - ballast matrix contact.

Aforementioned ballast conditions have been reproduced by the mechanical model not only based on the load-displacement diagrams and their shape, but also on several other

Die approbierte gedruckte Originalversion dieser Dissertation ist an der TU Wien Bibliothek verfügbar.
The approved original version of this doctoral thesis is available in print at TU Wien Bibliothek.
TU Bibliothek Your knowledge hub WIEN

tamping parameters discussed in Chapter 9.4. An approach that is as simple as possible but at the same time as complex as it needs to be to consider the characteristic phenomena observed during the analysis of the in-situ conducted track tamping is selected. It is based on a parameter variation that is reduced to the stiffness of the elastic spring k_e in the Cone model. The conducted parameter analysis proves that the stiffness k_e as defined by *Wolf* [139] and used for the calculation of the Cone model properties best suits fouled ballast conditions, with the ballast matrix characterized by following properties:

- smaller particle sizes, excessive amount of fine particles filling the voids,
- lower angularity, higher bulk density and degree of compaction.

Significantly higher reaction force F (in comparison to clean ballast condition) is needed during the squeezing movement to "set in motion" this already well compacted fouled ballast matrix in order to accomplish the elevation necessary to minimize the deterioration of track geometry and improve track stability.

Constant amplitude of excitation (Point E, Figure 8.1) results in a tamping tine plate oscillation with the amplitude of $\pm$4-5 mm exerted on the ballast matrix. Tine motion in the squeezing direction induces a ballast matrix deformation that is, depending on the ballast matrix model stiffness, subdivided between the elastic deformation x_e and the plastic one $x_{plastic}$. As can be seen from the statistical analysis of the in-situ conducted measurements, with the process of ballast fouling, the stiffness of the ballast bed increases, and, given a constant squeezing pressure, the maximum tamping tine elongation in fouled ballast conditions will be significantly than the amplitude in clean ballast conditions (Figures 6.4a and 6.4c). A similar effect can be simulated with the developed mechanical model by varying the stiffness of the elastic spring k_e, resulting in different shapes of the load-displacement diagrams presented in Figure 8.34.

Die approbierte gedruckte Originalversion dieser Dissertation ist an der TU Wien Bibliothek verfügbar.
The approved original version of this doctoral thesis is available in print at TU Wien Bibliothek.
TU Bibliothek Your knowledge hub WIEN

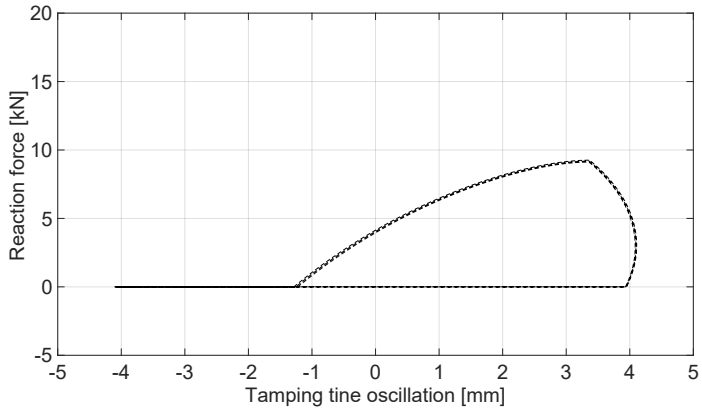

(a) Three consecutive load-displacement curves during the simulation of clean ballast compaction, $k_e = k_e/10^3$

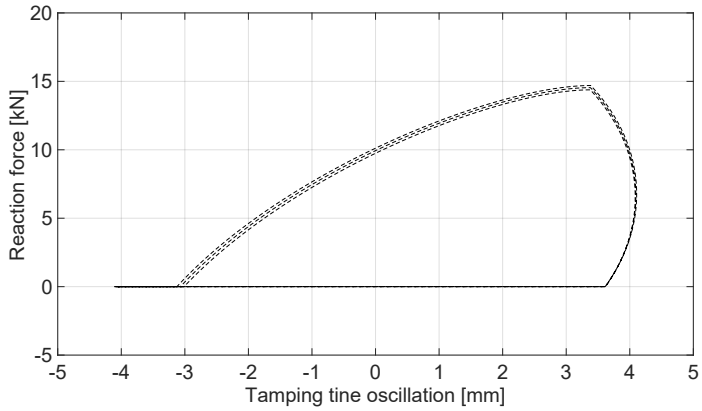

(b) Three consecutive load-displacement curves during the simulation of moderately clean ballast compaction, $k_e = k_e/10^2$

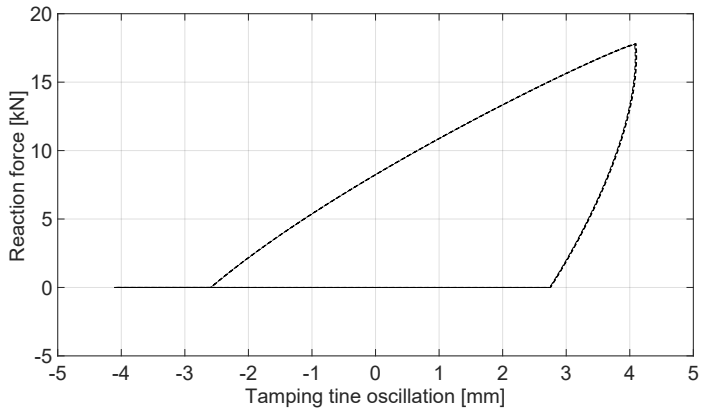

(c) Three consecutive load-displacement curves during the simulation of fouled ballast compaction, $k_e = k_e$

Figure 8.34: Characteristic load-displacement curves for different ballast conditions as a result of mechanical modeling. $G_d = 20\ \mathrm{MN/m^2}$, $v_{squeezing} = 0.1\ \mathrm{m/s}$, $k_p = 3\ \mathrm{MN/m}$

Die approbierte gedruckte Originalversion dieser Dissertation ist an der TU Wien Bibliothek verfügbar.
The approved original version of this doctoral thesis is available in print at TU Wien Bibliothek.

8.6.3 Derivation of the *system response* stiffness from the load-displacement curve

Following a successful parameter determination that can depict behavior of the ballast matrix in different conditions when subjected to dynamic loads during track tamping, an attempt was made to define a *system response* stiffness In the context of the mechanical model, the high force F values correlate with the high stiffness of the fouled ballast matrix model k_T that is dependent on the tamping tine plate area, Cone model parameters, stiffness k_p and the velocity proportional dashpot:

$$k_T = f(G, \nu, \rho, a, b, k_p, c_e, t) \tag{8.80}$$

This "system response" stiffness k_T as an equivalent spring constant for the two model components connected in series can, for the loading phase be expressed as:

$$\frac{1}{k_T(t)} = \frac{1}{k_e + c_e \frac{d}{dt}} + \frac{1}{k_p} \tag{8.81}$$

which yields to:

$$k_T(t) = \frac{k_p(k_e + c_e \frac{d}{dt})}{k_p + k_e + c_e \frac{d}{dt}} \tag{8.82}$$

Since the elastic and the plastic model component are connected in a series, following terms apply in the simplified form without considering the preload force F_p:

$$F = F_{elastic} = F_{plastic} \tag{8.83a}$$

$$F = x_e \cdot k_e + \dot{x}_e \cdot c_e = x_{plastic} \cdot k_p \tag{8.83b}$$

where $F_{elastic}$ and $F_{plastic}$ represent forces in the elastic and the plastic model components, respectively. The total ballast matrix model deformation x_T can be expressed as:

$$x_T = x_e + x_{plastic} \tag{8.84}$$

where the total deformation at any given moment can also be calculated by subtracting the position of the first contact point (beginning of contact, Figure 5.19) from the current position of the tamping tine x_{tine} that is equal to $x_{ballast}$ during the loading and unloading phase.

In terms of ballast matrix model deformations, the Equation 8.84 can be expressed for the both constituent model parts:

Die approbierte gedruckte Originalversion dieser Dissertation ist an der TU Wien Bibliothek verfügbar.
The approved original version of this doctoral thesis is available in print at TU Wien Bibliothek.

$$x_e = \frac{F}{k_e + c_e \frac{d}{dt}} \tag{8.85a}$$

$$x_{plastic} = \frac{F}{k_p} \tag{8.85b}$$

During the unloading phase the plastic spring remains locked ($k_p = \infty$) and the system response stiffness yields to:

$$k_T(t) = k_e + c_e \frac{d}{dt} \tag{8.86}$$

The system response stiffness of the ballast matrix expressed by Equations 8.82 and 8.86 is therefore dependent not only on the plastic and elastic spring stiffness k_e and k_p but also on the time component taken into consideration by the speed proportional dashpot. As can be seen in Figure 8.4, the velocity of the tine oscillation x_{tine} (=$x_{ballast}$ in the both contact phases) is not constant, meaning that the ballast matrix model stiffness also varies in a context of a single tine oscillation, i.e. cycle (Figures 8.35 and 8.36).

The influence of the speed proportional dashpot on the stiffness of the ballast matrix model expressed by the term d/dt can be taken into consideration by comparing the rate of increase of deformation in the *Kelvin-Voigt* model $\dot{x}_e$ to its deformation x_e for every time-step, yielding the Equations 8.82 and 8.86 to:

$$k_T(t) = \frac{k_p(k_e + c_e \frac{\Delta \dot{x}_e(t)}{\Delta x_e(t)})}{k_p + k_e + c_e \frac{\Delta \dot{x}_e(t)}{\Delta x_e(t)}} \tag{8.87}$$

$$k_T(t) = k_e + c_e \frac{\Delta \dot{x}_e(t)}{\Delta x_e(t)} \tag{8.88}$$

Ballast matrix model system response progress for every time-step can also by obtained by time-step calculation from the load-displacement diagram (Figure 8.35).

Die approbierte gedruckte Originalversion dieser Dissertation ist an der TU Wien Bibliothek verfügbar.
The approved original version of this doctoral thesis is available in print at TU Wien Bibliothek.

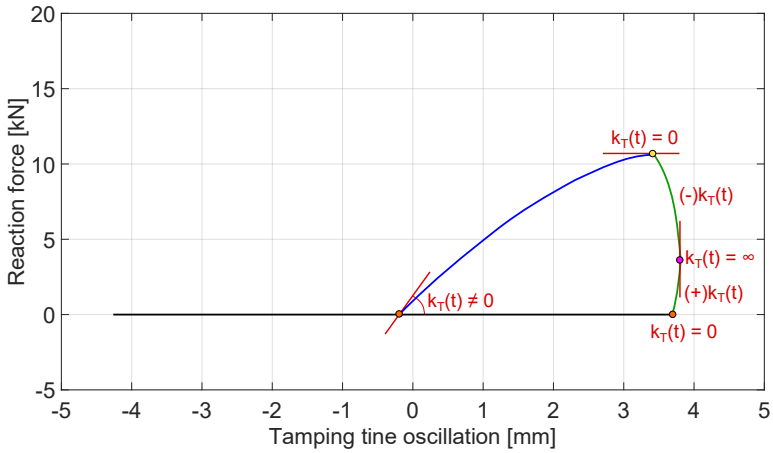

Figure 8.35: Ballast matrix model system response progress plotted over a load-displacement diagram for clean ballast conditions

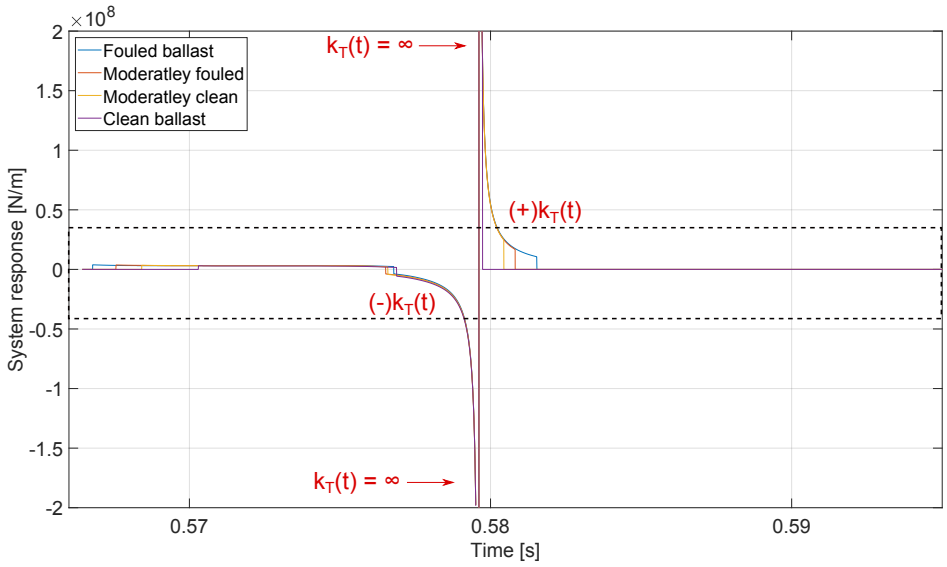

Figure 8.36: Ballast matrix model system response of one cycle for different ballast conditions

Die approbierte gedruckte Originalversion dieser Dissertation ist an der TU Wien Bibliothek verfügbar.
The approved original version of this doctoral thesis is available in print at TU Wien Bibliothek.

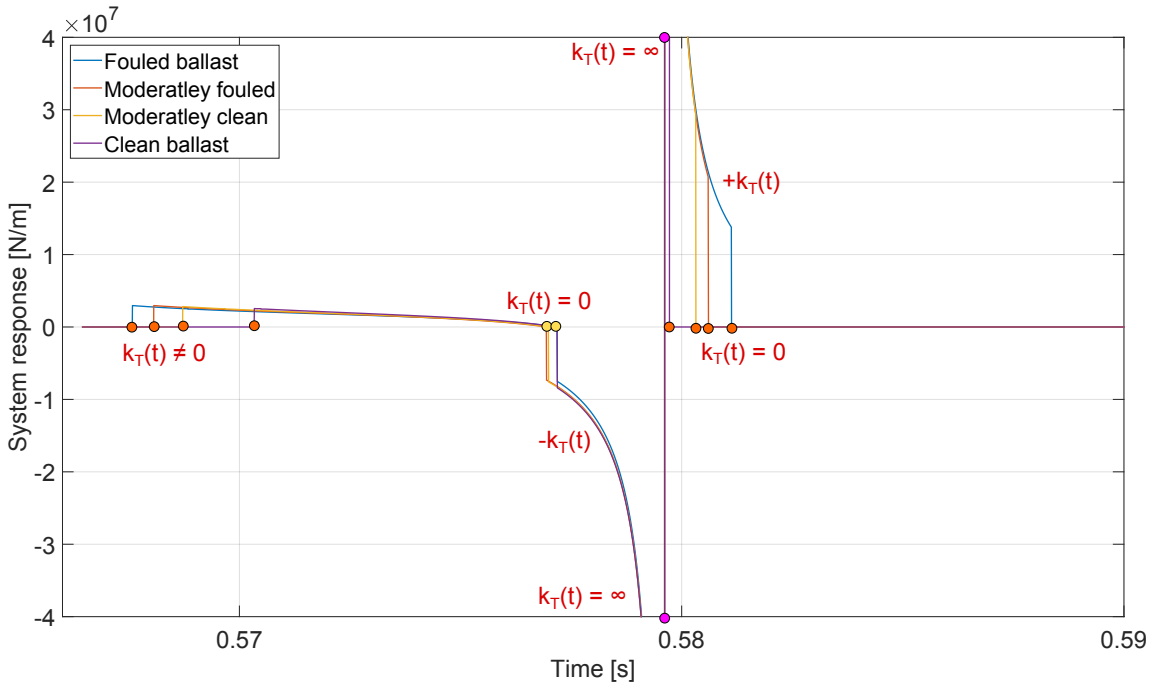

Figure 8.37: Detail of the ballast matrix model system response of one cycle for different ballast conditions with characteristic points

8.6.4 Mechanical model for ballast penetration

Additional to the squeezing movement, a mechanical model for ballast penetration can be developed using the same approach. During ballast penetration, the tamping tine is lowered vertically into the ballast bed, overcoming ballast resistance to penetration on both sides of the tamping tine. Contact forces are measured on the front and back side of the tine and result in characteristic load-displacement diagrams (one of which, measured in-situ, can be seen in Figure 5.20a). A model that can be used for this simulation is presented in Figure 8.38.

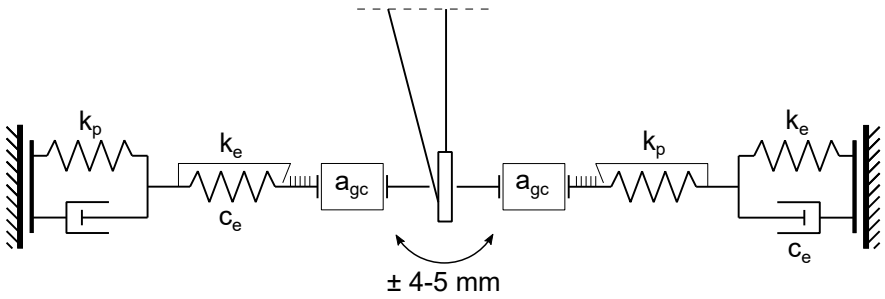

Figure 8.38: Mechanical model for ballast penetration

Die approbierte gedruckte Originalversion dieser Dissertation ist an der TU Wien Bibliothek verfügbar.
The approved original version of this doctoral thesis is available in print at TU Wien Bibliothek.

Chapter 9

Result verification and study of tamping parameters

9.1 Introduction

Observing and understanding ballast response to tamping in-situ serves as a basis for further development of the track tamping process. Locations where track tamping has been conducted and evaluated are listed and described in Chapter 6. Prior to track tamping, no additional information about the ballast condition on the selected locations was available, except for a general statement if the track was reconstructed (replacing the ballast bed prior to compaction) or maintained (compaction of the existing ballast bed). Even though the ballast reaction is also influenced and dependent on several other factors described in Chapter 2 such as ballast parent rock, chemical and physical characteristics, fracture, compressive and tensile strength, the most important factor to define ballast response to and behavior during compaction is the progress of ballast fouling. Other than the ballast dependent factors, the progress of ballast compaction is highly influenced by the variable tamping parameters (Chapter 5.3.4), that are selected based on experience for every location. The focus was set on the interaction between the tamping tine and ballast matrix during ballast compaction under the sleeper in order to simplify this complex structure of possible parameter variations that cannot all be defined beforehand without conducting time consuming and costly ballast sampling. It has been proven that this interaction can be described by several ballast response parameters listed in Chapter 9.4 that vary in dependence on the ballast bed condition, i.e. on the progress of ballast fouling. Ballast fouling quantification in correlation with the Fouling Index is conducted based on the available information about the ballast bed condition provided either by *ÖBB* and *Plasser & Theurer* (track reconstruction, track tamping six weeks after reconstruction, track maintenance) or by ballast sampling conducted at one location (*Eisenstadt*, fouled ballast, Appendix A). In addition to the in-situ conducted measurements a mechanical model of the same interaction is developed. Result comparison of the two approaches, as well as a proposal for a system of identification of ballast condition and parameter combination needed to accomplish it are given in the following chapters.

Die approbierte gedruckte Originalversion dieser Dissertation ist an der TU Wien Bibliothek verfügbar.
The approved original version of this doctoral thesis is available in print at TU Wien Bibliothek.
TU Bibliothek Your knowledge hub WIEN

9.2 Results comparison

Mechanical model presented and described in Chapter 8 is used to simulate the tamping tine-ballast matrix interaction measured in-situ. Simulation results are compared to the in-situ collected data and plotted together in Figure 9.1. Comparison of the load-displacement diagrams is taken as a verification of the model. A high level of correlation confirms that the approximations made in the mechanical model lead to a correct interpretation of the ballast behavior during compaction. As presented in Figure 9.1, a shift of the modeled diagrams in comparison to the in-situ measured ones, is obvious. It results from the difference between the actual maximum tine elongation measured in in-situ and theoretical one simulated by the model. Influence of this shift cannot, however, be noticed in the maximum reaction force per cycle, energy, loading or the unloading response, since they all provide information that is not related to the exact tine position at a given moment. During movement in the squeezing direction the amplitude reduces in the dependence on the ballast condition which can be attributed to the ballast resistance to compaction that increases with the progress of ballast fouling.

As an input for model calculations producing the results displayed in Figure 9.1, following parameter set is used:

Table 9.1: Tamping unit geometry and constant input parameters

Parameter	**Value**
excitation frequency	$f = 35\text{Hz}$
excitation amplitude	$e = 0.002\text{m}$
shear modulus	$G = 20\text{MN/m}^2$
squeezing velocity	$v_{squeezing} = 0.1\text{m/s}$
plastic spring rate	$k_p = 3\text{MN/m}^2$
elastic spring rate	k_e dependent on the ballast condition

An important aspect to state is that the gradual process of ballast fouling is simulated with the model by varying only one single parameter, the stiffness of the elastic spring k_e. Figure 9.1 clearly displays ballast matrix properties as were observed in-situ, recreated by the model. Apart from the clear correlations between the load-displacement diagrams, a study i.e. comparison of decisive tamping characteristics, is conducted. Value ranges of the four characteristics from all the analyzed in-situ locations are compared to those that are calculated by the mechanical model (Tables 9.2, 9.3, 9.4) and result in the diagrams presented in Figure 9.1.

Die approbierte gedruckte Originalversion dieser Dissertation ist an der TU Wien Bibliothek verfügbar.
The approved original version of this doctoral thesis is available in print at TU Wien Bibliothek.
TU Bibliothek Your knowledge hub WIEN

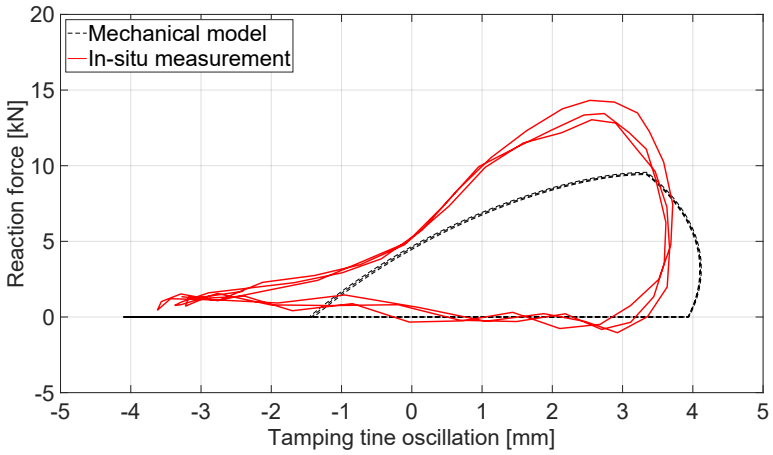

(a) Comparison of three consecutive load-displacement curves during both in-situ track tamping and the mechanical modeling of *clean* ballast compaction ($k_e = k_e/10^3$)

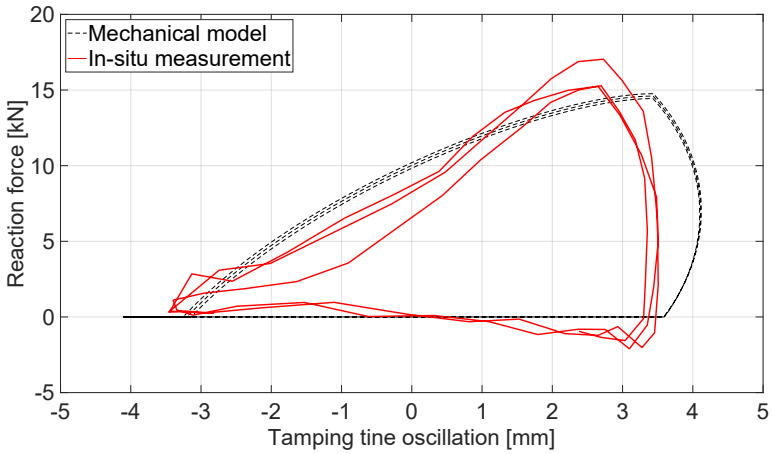

(b) Comparison of three consecutive load-displacement curves during both in-situ track tamping and the mechanical modeling of *moderately clean* ballast compaction ($k_e = k_e/10^2$)

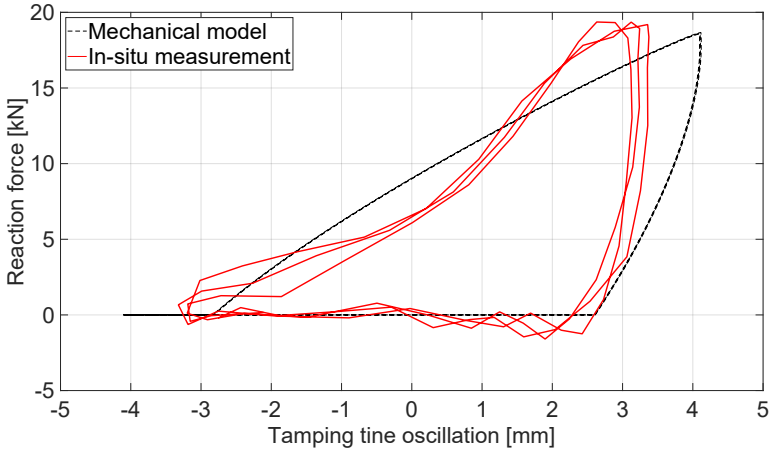

(c) Comparison of three consecutive load-displacement curves during both in-situ track tamping and the mechanical modeling of *fouled* ballast compaction ($k_e = k_e$)

Figure 9.1: Comparison of characteristic load-displacement curves for different ballast conditions

Die approbierte gedruckte Originalversion dieser Dissertation ist an der TU Wien Bibliothek verfügbar.
The approved original version of this doctoral thesis is available in print at TU Wien Bibliothek.

Table 9.2: Comparison of the values for the four tamping characteristics between the in-situ and mechanical modeling results for *clean* ballast conditions. Values for the in-situ measurements in clean ballast conditions are presented as range for both first and second squeezing movement

Tamping parameter	Unit	Value	
		In-situ measurement	Mechanical model
Maximum reaction force per cycle	[kN]	9.0 – 13.0	9.6
Energy per squeezing movement	[kJ/s]	0.85 – 1.2	1.22
Loading response	[MN/m]	0.85 – 1.9	2.20
Unloading response	[MN/m]	-16.0 – -10.0	-11.31

Table 9.3: Comparison of the values for the four tamping characteristics between the in-situ and mechanical modeling results for *moderately clean* ballast conditions

Tamping parameter	Unit	Value	
		In-situ measurement	Mechanical model
Maximum reaction force per cycle	[kN]	14.95	14.77
Energy per squeezing movement	[kJ/s]	1.36	2.41
Loading response	[MN/m]	1.84	2.36
Unloading response	[MN/m]	-18.50	-23.78

Table 9.4: Comparison of the values for the four tamping characteristics between the in-situ (range) and mechanical modeling results for *fouled* ballast conditions

Tamping parameter	Unit	Value	
		In-situ measurement	Mechanical model
Maximum reaction force per cycle	[kN]	15.0 – 20.0	18.66
Energy per squeezing movement	[kJ/s]	1.6 – 2.1	2.15
Loading response	[MN/m]	2.0 – 2.8	2.58
Unloading response	[MN/m]	11.0 – 18.0	13.07

A significantly lower reaction force is needed to set the grains forming a clean ballast matrix into motion, rearranging them into a denser packing. This visco-fluidization of the matrix causes a severe (but temporary) reduction of the shear strength during which a significantly lower energy level is needed to continue the tine motion during the squeezing movement. Furthermore, a reduction of the mobilized friction angle due to continuous grain motion is evident in the clean ballast matrix loading response, showing considerably lower values (Table 9.2) in comparison to the progressed ballast fouling cases (Tables 9.3 and 9.4). Last but not least, the shape of the load-displacement curve in the unloading phase displays a significant modification, changing from a negative to a positive value as the process of ballast fouling progresses. As the ballast particles start to change their shape and the voids

Die approbierte gedruckte Originalversion dieser Dissertation ist an der TU Wien Bibliothek verfügbar.
The approved original version of this doctoral thesis is available in print at TU Wien Bibliothek.
TU Bibliothek Your knowledge hub WIEN

of matrix are filled with finer particles, a higher force is necessary to trigger this convection flow in the granular (ballast) matrix. In moderately clean ballast this is still possible but requires an increase of reaction force of about 20% in comparison to the highest value in clean ballast condition. Energy per squeezing movement as well as the loading response increase accordingly.

9.3 Impulse of force analysis as an indicator of ballast condition

Stiffness of the elastic spring has been recognized as the key factor in modeling different ballast conditions (Figure 9.1). In addition to the two borderline examples (clean and fouled) the remaining ballast bed conditions (moderately clean, moderately fouled and highly fouled) according to Fouling index definition (Chapter 3.2.2) are defined by further elastic spring stiffness variation and listed in Table 9.5.

Table 9.5: Ballast bed condition classification

Elastic spring stiffness	Classification
k_e / 10^3	clean
k_e / 10^2	moderately clean
k_e / 10	moderately fouled
k_e	fouled
k_e / 10^{-1}	highly fouled

Monitoring of tamping process during regular track maintenance has shown a significant difference in ballast bed reaction to compaction dependent on its condition. Following a successful result verification (Chapter 9.2) the mechanical model developed is used to present different ballast matrix conditions by comparing the impulse of force between the elastic and the plastic component of the ballast matrix model using the impulse-momentum theorem. The impulse of force can be defined as the change of momentum of the body to which a resultant force is applied or as the integral of a force over the time interval for which it acts. The impulse vector is denoted by the symbol J [Ns]. For a constant acting force it can be expressed as:

$$J = \Delta p = F \cdot \Delta t \tag{9.1}$$

where p stands for the linear momentum, the product of mass and velocity (vector with the same direction as the velocity):

$$p = m \cdot v \tag{9.2}$$

If the force is not constant, the impulse of force from time t_1 to t_2 can be calculated as:

$$J = \int_{t_1}^{t_2} F(t)\, dt \tag{9.3}$$

Die approbierte gedruckte Originalversion dieser Dissertation ist an der TU Wien Bibliothek verfügbar.
The approved original version of this doctoral thesis is available in print at TU Wien Bibliothek.
TU Bibliothek Your knowledge hub WIEN

During the loading phase of one cycle (Chapter 8.4.4.1) both components of the ballast matrix model are compressed (Figure 8.18) and the both constitutive force components $F_{plastic}$ and $F_{elastic}$ are equal and equal to the ballast matrix model force F (Equation 8.83a). For the calculation of the impulse of force in the loading phase, the integration with respect to time (Equation 9.3) is conducted between the first contact point (Equation 9.4) and the corresponding time where the force F reaches its maximum (Equation 9.5), triggering the switch between phases to unloading.

$$t_1 = t_{contact\ beginning} \tag{9.4}$$

$$t_2 = t_{F_{max}} \tag{9.5}$$

$$\Delta t = t_2 - t_1 \tag{9.6}$$

Given that the both constitutive force components $F_{plastic}$ and $F_{elastic}$ are equal and the time interval Δt (Equation 9.6) remains the same, calculation of the impulse of force for the ballast matrix model as well as for both constitutive ballast matrix model components can be conducted as follows:

$$J = J_{plastic} = J_{elastic} = \int_{t_1}^{t_2} F(t)\, dt \tag{9.7}$$

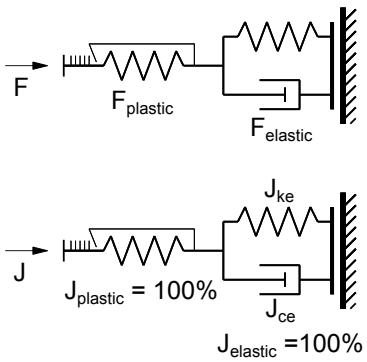

Figure 9.2: Ballast matrix model components - forces and impulse of force per component

Expressed in percentage, the impulse of force in the plastic model component amounts to 100% and the 100% of the impulse in the elastic model component will, similar to the force $F_{elastic}$ be subdivided between the elastic spring and the viscous dashpot (Figures 9.2 and 9.3):

$$F_{elastic} = F_{ke} + F_{ce} \tag{9.8}$$

$$J_{elastic} = J_{ke} + J_{ce} \tag{9.9}$$

Die approbierte gedruckte Originalversion dieser Dissertation ist an der TU Wien Bibliothek verfügbar.
The approved original version of this doctoral thesis is available in print at TU Wien Bibliothek.

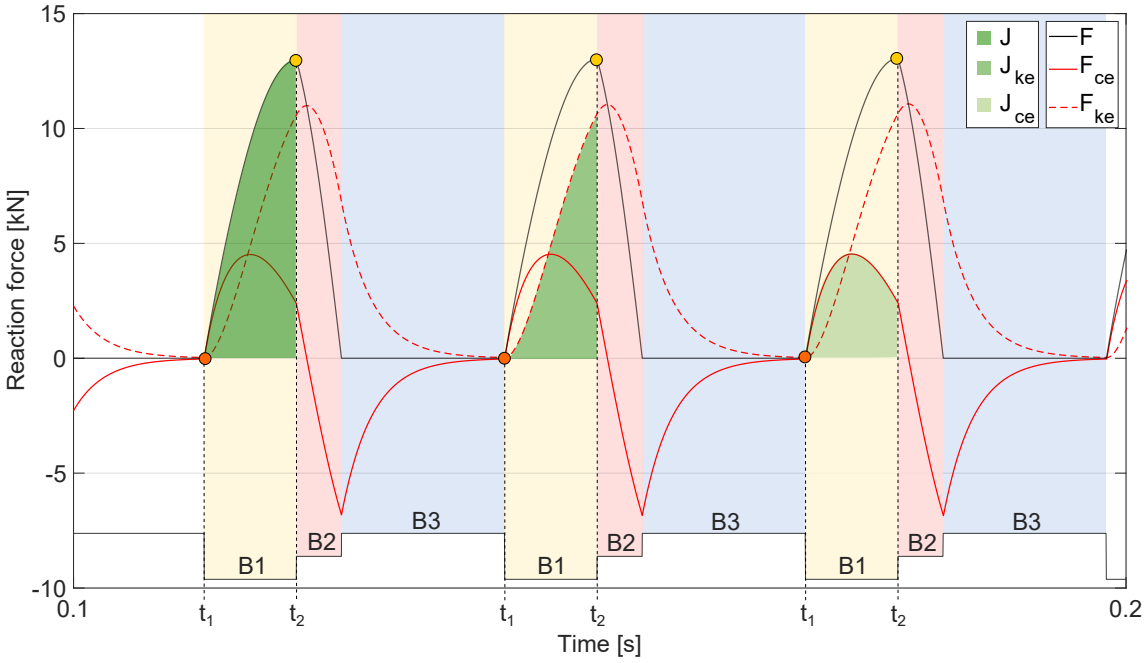

Figure 9.3: Impulse of force components in the loading phase displayed over three cycles

Variation of the plastic spring stiffness influences the subdivision of the force between the two components of the elastic part of the ballast matrix model (Equation 8.56). Calculation of the impulse of force percentage per component in the elastic part (Figure 9.4) provides valuable information about the changes in the ratio of impulse per component with the progress of ballast fouling.

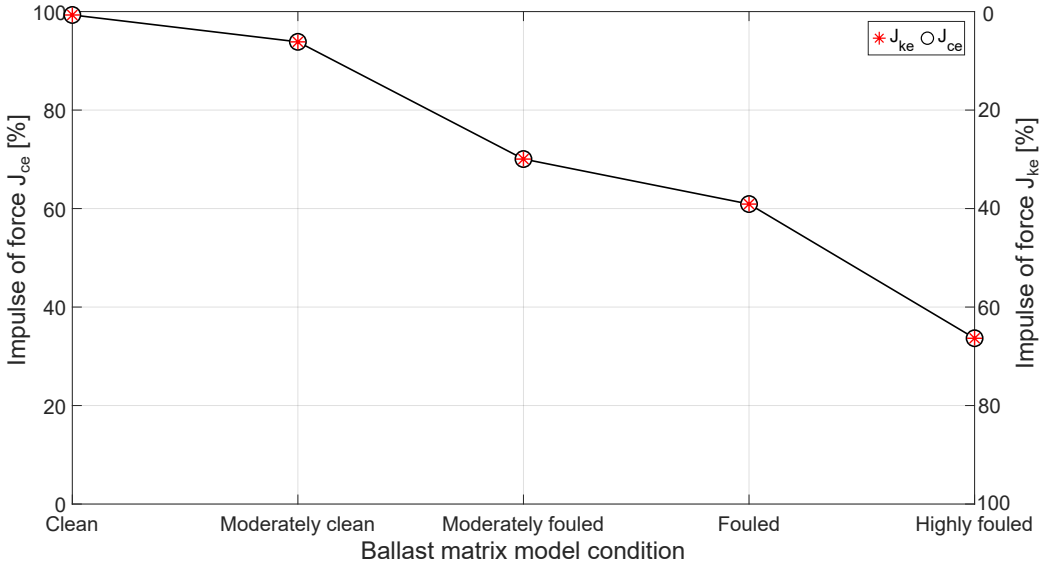

Figure 9.4: Impulse of force in the elastic part of the ballast matrix model for different ballast conditions

Die approbierte gedruckte Originalversion dieser Dissertation ist an der TU Wien Bibliothek verfügbar.
The approved original version of this doctoral thesis is available in print at TU Wien Bibliothek.

9.4 Study of tamping parameters

Following a successful verification of the results obtained from the mechanical model, a parameter study is conducted using the model in order to investigate the influence of the following tamping parameters on the tamping characteristics that are interpreted from the load-displacement diagrams:

- amplitude of excitation - standard set value of the amplitude of excitation for all the in-situ measurements analyzed and presented in Chapter 6 is 2 mm, ideally resulting in a 4-5 mm tamping tine amplitude. The standard value was decreased by 25% to 1.5 mm and increased by 25% to 2.5 mm in order to investigate the influence of possible variation of the amplitude of excitation
- squeezing velocity - as a second possible variable tamping parameter, the influence of squeezing velocity is investigated. Quasi-static squeezing displacement measured by the laser range finder is used to calculate the squeezing velocity (Chapter 6.7). Based on the values measured in-situ (Table 6.3), the velocity was reduced from 0.1 m/s used for the mechanical model down to 0.06 m/s
- excitation frequency - state of the art *Plasser & Theurer* tamping machines operate with the frequency modulation described in Chapter 4. The squeezing movement is preformed by a frequency of 35 Hz. Variation of the excitation frequency is conducted in the scope of the tamping parameter study in order to determine its influence on the tamping characteristics. Excitation frequency during squeezing is reduced to 30 Hz (approximately the excitation frequency during tamping unit relocation) and increased up to 50 Hz (approximately the excitation frequency during ballast penetration)
- ballast bed condition - in addition to the two borderline examples (clean and fouled), remaining ballast bed conditions (moderately clean, moderately fouled and highly fouled) according to Fouling Index definition (Chapter 3.2.2) are investigated

Given that it would not be possible to single out the influence of only one tamping parameter if all parameters are altered at the same time, following parameter combination is selected:

- amplitude of excitation and squeezing velocity for clean and fouled ballast bed conditions (Chapters 9.4.3 and 9.4.1); excitation frequency is kept constant at 35 Hz
- amplitude of excitation and excitation frequency for clean and fouled ballast bed conditions (Chapters 9.4.4 and 9.4.2); squeezing velocity is kept constant at 0.1 m/s
- squeezing velocity and ballast bed condition (Chapter 9.5.1)
- excitation frequency and ballast bed condition (Chapter 9.5.2)

Die approbierte gedruckte Originalversion dieser Dissertation ist an der TU Wien Bibliothek verfügbar.
The approved original version of this doctoral thesis is available in print at TU Wien Bibliothek.
TU Bibliothek Your knowledge hub WIEN

9.4.1 Influence of squeezing velocity on tamping characteristics - Clean ballast

Depending on the the tamping unit geometry and the exact position of the tine observed, changes of the excitation amplitude influence the tamping tine plate oscillation amplitude. Excitation amplitude of 2 mm during the in-situ measurements generates a tine oscillation amplitude of approximately 4 mm. Same effect can be seen in Figure 9.5, presented by the red lines. Accordingly, if the excitation amplitude is increased by 25%, the tine oscillation amplitude will increase by the same amount. In addition to excitation amplitude, the squeezing velocity is varied. Values are selected based on the in-situ measurements and range from 0.1 m/s to 0.06 m/s. Figure 9.5 portrays load-displacement curves resulting from all three excitation amplitudes over five selected squeezing velocity levels. Points plotted on the x axis display maximum tine elongation in both moving directions. Changes of the eight tamping characteristics that are calculated from the load-displacement diagrams are presented in Figures 9.6 to Figure 9.13. Clean ballast conditions are simulated by the model using the parameter set given in Table 9.1 and ballast condition determining factor from Table 9.5. Excitation frequency is kept constant at 35 Hz.

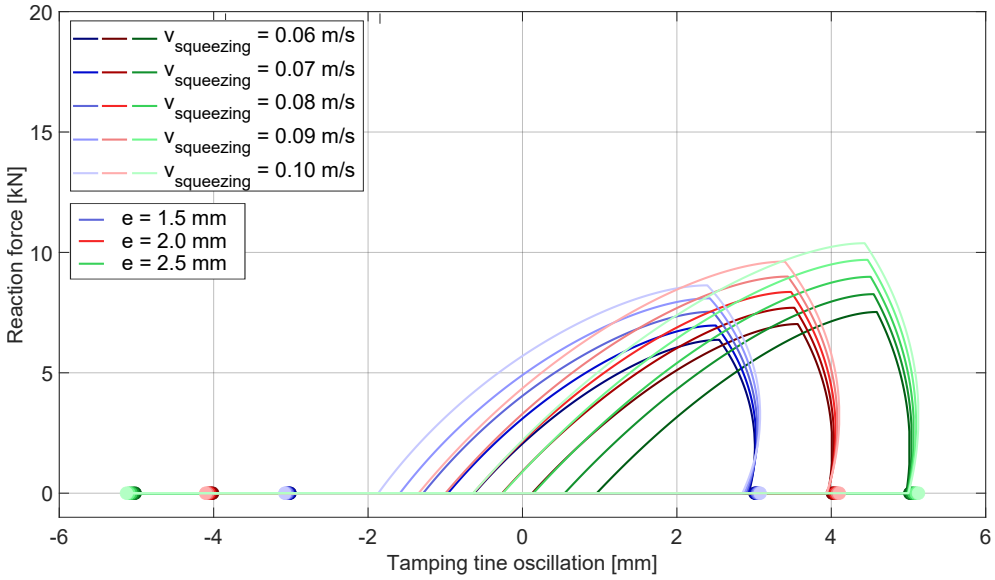

Figure 9.5: Clean ballast - variation of the squeezing velocity and excitation amplitude and their influence on tamping characteristics. Points plotted on the x axis display maximum tine elongation in both moving directions

Maximum reaction force per cycle is the first tamping characteristic to be considered. Measurements conducted and analyzed in Chapter 6 have shown a distinctive difference when comparing the maximum reaction force between ballast conditions. An overview of the values for clean ballast is given in Table 9.2. Figure 9.5 is used to highlight the changes of the reaction force induced by a reduction or increase of both excitation amplitude and squeezing velocity.

An increase of force with the increase of both varied tamping parameters is evident. A 25% change of amplitude leads to variation of reaction force of about 1.5 kN. If the squeezing velocity is increased from 0.06 m/s to 0.1 m/s, the reaction force increases by 45% in average,

Die approbierte gedruckte Originalversion dieser Dissertation ist an der TU Wien Bibliothek verfügbar.
The approved original version of this doctoral thesis is available in print at TU Wien Bibliothek.
TU Bibliothek Your knowledge hub WIEN

and the growth is amplified at higher amplitude levels. Calculated values correlate to those given in Table 9.2.

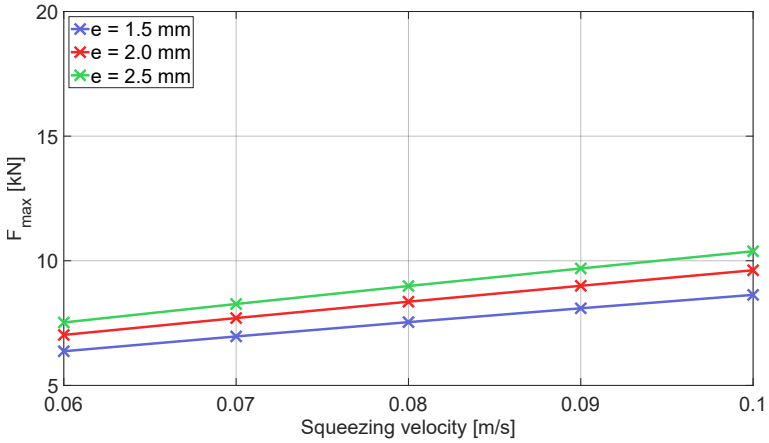

Figure 9.6: Maximum reaction force per cycle - study of tamping characteristics

Figure 9.7 gives an insight into the changes of the energy transferred during one cycle, calculated as the area within the load-displacement curves. The value variations follow the tendency that is presented in Figure 9.6. Higher velocity levels result in higher energy levels - an increase of almost 50% between both extreme values of squeezing velocity is noticeable, only slightly enhanced by the increase of excitation amplitude, which leads to an increase of 0.1 kJ/s in average between two adjacent values. All values correlate to those given in Table 9.2.

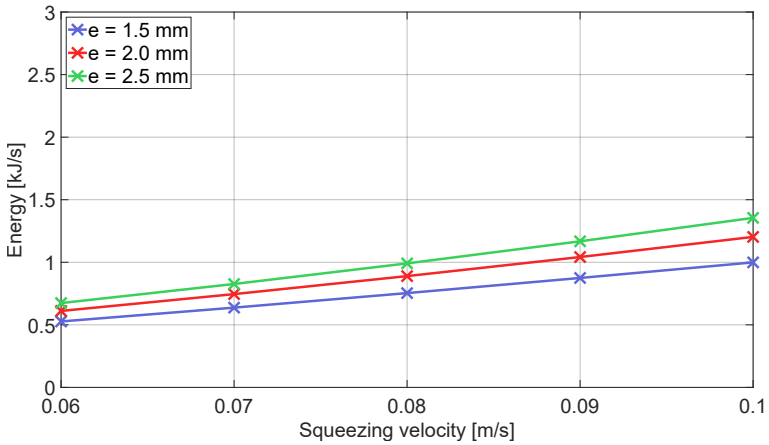

Figure 9.7: Energy per squeezing movement - study of tamping characteristics

Inclination of the load-displacement diagram in the loading phase is used to calculate the ballast response to the interaction with the tamping tine. Figure 9.8 shows that, independent of the excitation amplitude or squeezing velocity, all load-displacement diagrams that are plotted in Figure 9.5 are nearly parallel to one another in the loading phase, as the value of the loading response between different amplitude and velocity levels only changes insignificantly. A minor increase of the loading response with the increase of excitation amplitude is present. All values are slightly higher than those given in Table 9.2.

Die approbierte gedruckte Originalversion dieser Dissertation ist an der TU Wien Bibliothek verfügbar.
The approved original version of this doctoral thesis is available in print at TU Wien Bibliothek.
TU Bibliothek Your knowledge hub WIEN

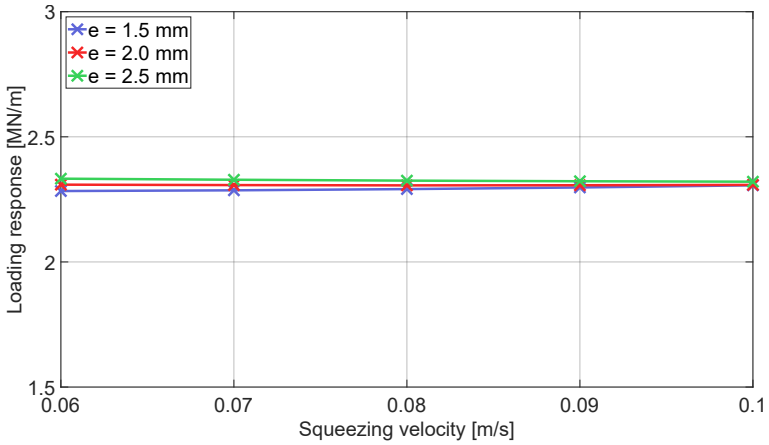

Figure 9.8: Ballast loading response - study of tamping characteristics

Similar to Figure 9.8, Figure 9.9 does not show a significant variation of the unloading response. An insignificant difference is noticeable at lower velocity levels, but it decreases with the increase of squeezing velocity. One meaningful observation can be made - the unloading response of clean ballast simulation always comes with a negative sign, and decreases (further in the negative share) with the increase of excitation amplitude. All values correlate to those given in Table 9.2.

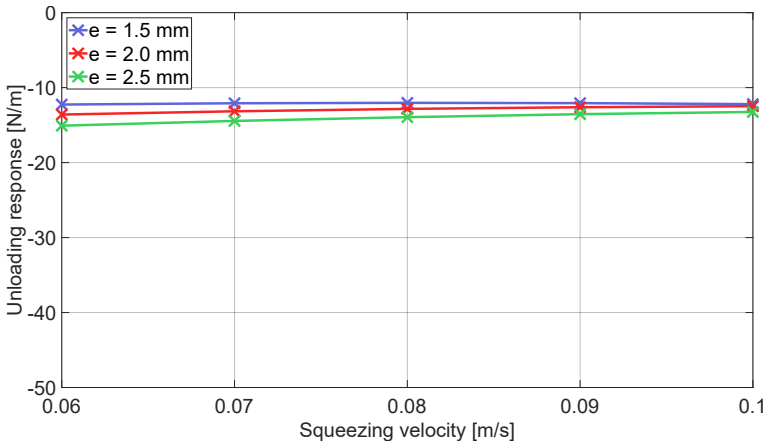

Figure 9.9: Ballast unloading response - study of tamping characteristics

Intersection point of the load-displacement diagram with the x axis provides information about the beginning and loss of contact between the tine and the ballast matrix. These two values are used to calculate the duration and length of tamping tine contact with the ballast matrix. Increase of squeezing velocity shifts of the first (left) contact point approximately 0.3 mm to the left when comparing two adjacent velocity values ($\Delta = 0.1$ m/s), independent of the amplitude. Figure 9.10 displays this behavior clearly; beginning of contact points shift for approximately 1.2 mm when comparing the lowest and highest velocity levels.

Study on the changes of position of the second contact point (loss of contact) is plotted in Figure 9.11, and the intersection points can be seen in Figure 9.5. Squeezing velocity does not have a noticeable influence on the second contact point. A 25% increase of the excitation

Die approbierte gedruckte Originalversion dieser Dissertation ist an der TU Wien Bibliothek verfügbar.
The approved original version of this doctoral thesis is available in print at TU Wien Bibliothek.
TU Bibliothek Your knowledge hub WIEN

amplitude results in a 1 mm shift of the in-contact part of the load-displacement curve to the right, which is observable in the second contact point (Figure 9.11).

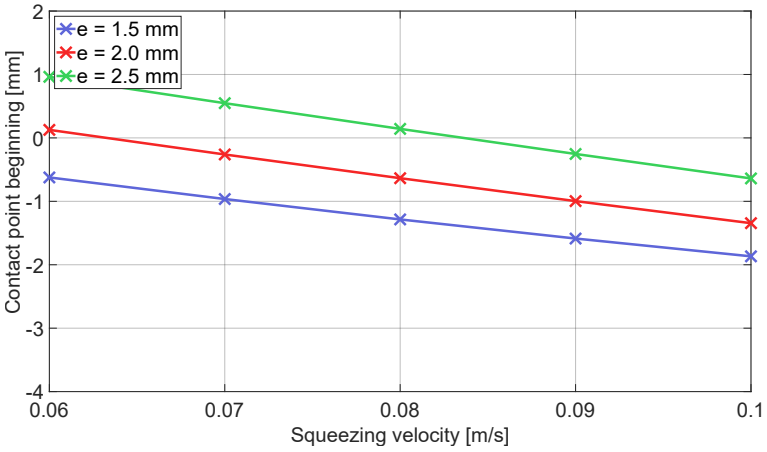

Figure 9.10: Contact point beginning - study of tamping characteristics

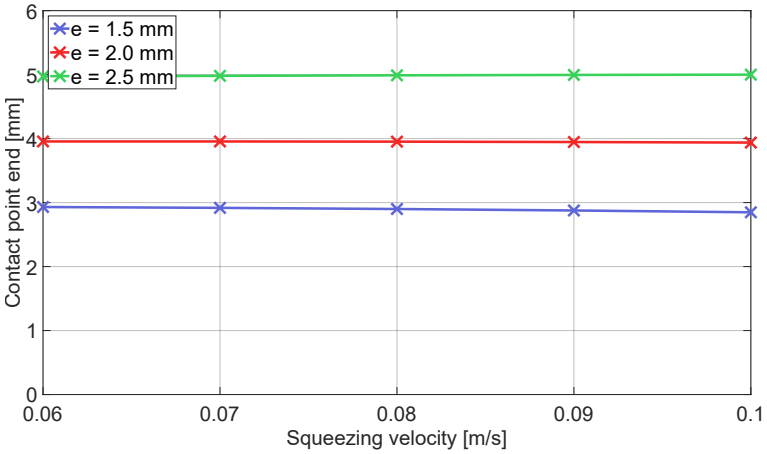

Figure 9.11: Contact point end - study of tamping characteristics

Figures 9.12 and 9.13 depict the dependence of contact duration and contact length on the excitation amplitude and squeezing velocity. Contact duration provides information about the percentage of the entire tamping tine displacement (two time the tine amplitude) in which contact to the ballast matrix is established. Figure 9.13 gives the same information in the context of contact duration in [mm], calculated against the whole tamping tine displacement.

Given that the point of loss of contact is not influenced by the squeezing velocity and only the point of contact beginning shifts to the left, contact duration increases with the increase of velocity (Figure 9.12). Contact duration is reduced significantly at higher amplitude levels, ranging between 40% and 55% for a 2.5 mm and up to 80% for a 1.5 mm amplitude. This indicates that a higher excitation frequency prolongs the contactless phase. Figure 9.13, shows similar course of values. Even if a higher amplitude results in a shorter contact duration in percentage, the tine still crosses a somewhat longer path in contact with the ballast matrix.

Die approbierte gedruckte Originalversion dieser Dissertation ist an der TU Wien Bibliothek verfügbar.
The approved original version of this doctoral thesis is available in print at TU Wien Bibliothek.
TU Bibliothek Your knowledge hub WIEN

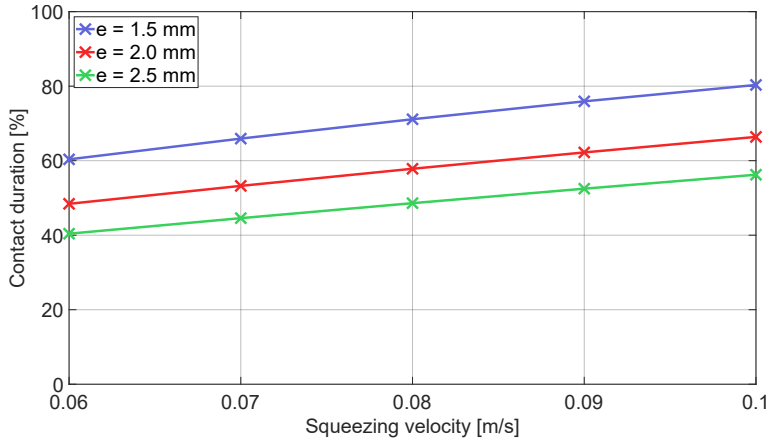

Figure 9.12: Contact duration per cycle - study of tamping characteristics

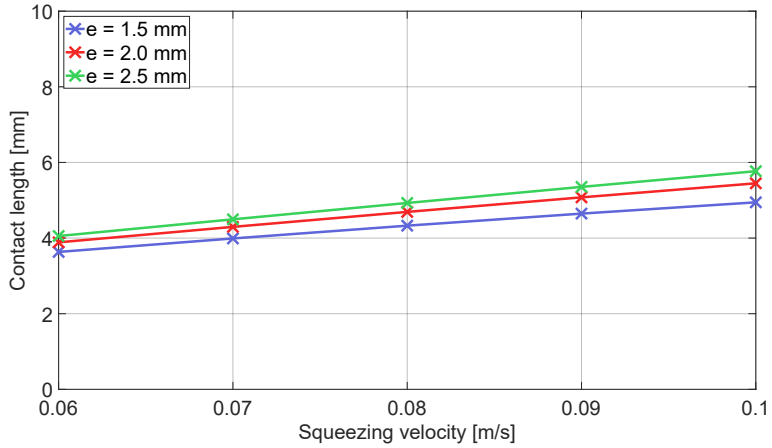

Figure 9.13: Contact length per cycle - study of tamping characteristics

Even if the squeezing velocity does not influence the tine relative movement within the cycle, it significantly influences the absolute tine position between the cycles, increasing the absolute traversed distance. Most significant influence of the higher squeezing velocity can therefore be seen in the first contact point that shifts to the left, meaning that the tine establishes contact with the ballast sooner. Higher squeezing velocity does not, however, have an influence on the second contact point in clean ballast conditions. As an immediate consequence, the duration of contact increases. If expressed in [%] of the entire tamping tine displacement, the highest value can be reached with the lowest amplitude. However, given that the length of the tamping tine displacement shortens with the reduction of amplitude, the contact length also reduces. Increasing the amplitude in clean ballast prolongs the contactless phase but increases the contact length, giving more time for the increase of force and thereat an increase of energy. Neither the excitation amplitude not the squeezing velocity have an influence on the loading and unloading response of the ballast matrix.

Die approbierte gedruckte Originalversion dieser Dissertation ist an der TU Wien Bibliothek verfügbar.
The approved original version of this doctoral thesis is available in print at TU Wien Bibliothek.
TU Bibliothek Your knowledge hub WIEN

9.4.2 Influence of frequency on tamping characteristics - Clean ballast

Influence of the excitation frequency on the eight selected tamping characteristics is investigated in combination with different excitation amplitude values and the result in form of load-displacement diagrams is presented in Figure 9.14. Points plotted on the x axis display maximum tine elongation in both moving directions. Eight tamping characteristics calculated from the load-displacement diagrams are presented in Figures 9.15 to 9.22.

As stated before, the squeezing movement is performed with a 35 Hz frequency. This reference value is altered up to 50 Hz (approximately the excitation frequency during ballast penetration) and down to 30 Hz (approximately the excitation frequency during tamping unit relocation). Clean ballast conditions are simulated using the parameter set given in Table 9.1 and ballast condition determining factor from Table 9.5. Squeezing velocity is kept constant at 0.1 m/s. Values calculated for the excitation frequency of 35 Hz correlate to those given in Table 9.2 .

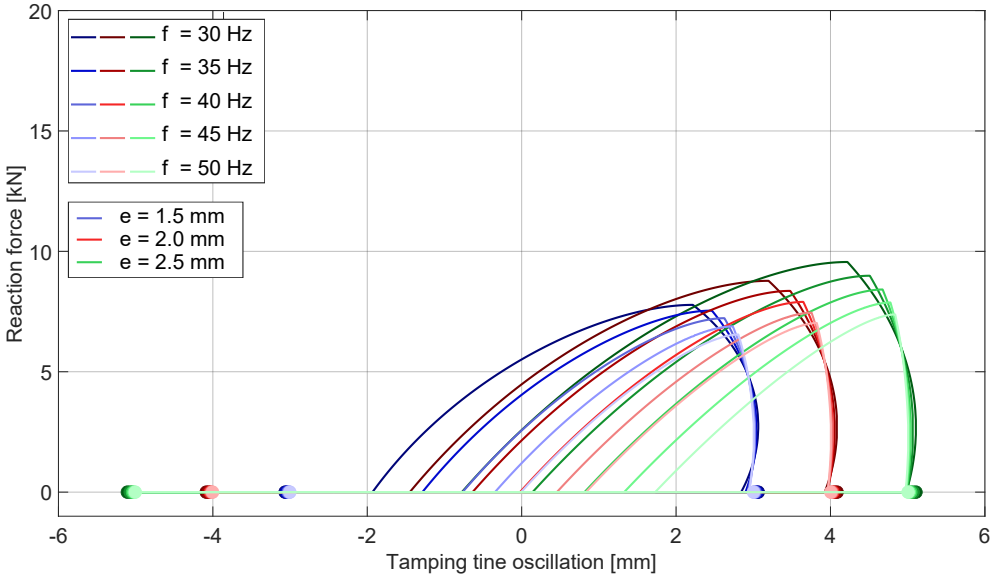

Figure 9.14: Clean ballast - variation of the excitation frequency and amplitude and their influence on tamping characteristics. Points plotted on the x axis display maximum tine elongation in both moving directions

If the frequency is increased, the duration of a single cycle decreases. Maximum reaction force per cycle is dependent on the cycle duration (Figure 9.15), given a constant squeezing velocity. If insufficiency time for the force build-up is given, the force level that was obtained from in-situ measurement analysis (Table 9.2) cannot be reached. As the frequency increases the maximum reaction force decreases and vice versa (Figure 9.15). Higher amplitude levels somewhat increase the contact length and time, thus increasing the force. At 30 Hz an increase of approximately 1 kN is noticeable when comparing adjacent amplitude levels.

Die approbierte gedruckte Originalversion dieser Dissertation ist an der TU Wien Bibliothek verfügbar.
The approved original version of this doctoral thesis is available in print at TU Wien Bibliothek.

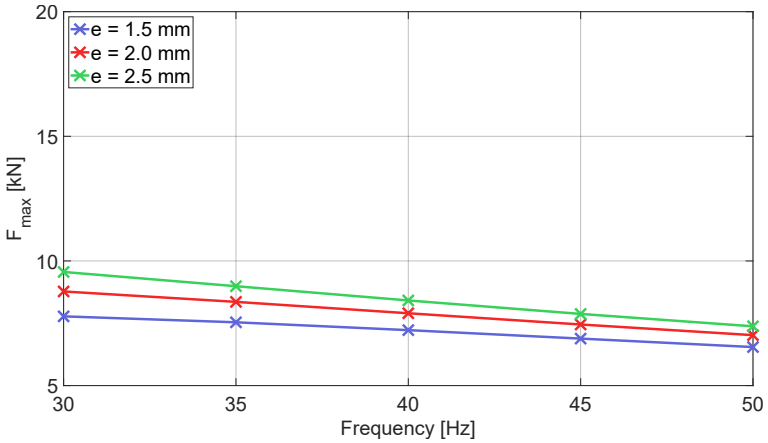

Figure 9.15: maximum reaction force per cycle - study of tamping characteristics

Similar to the maximum reaction force per cycle, the transferred energy is also dependent on the cycle duration and decreases with the increase of frequency (Figure 9.16). At lower frequency levels the influence of excitation amplitude is noticeable and it decreases with the increase of frequency. Calculated values correlate to those given in Table 9.2.

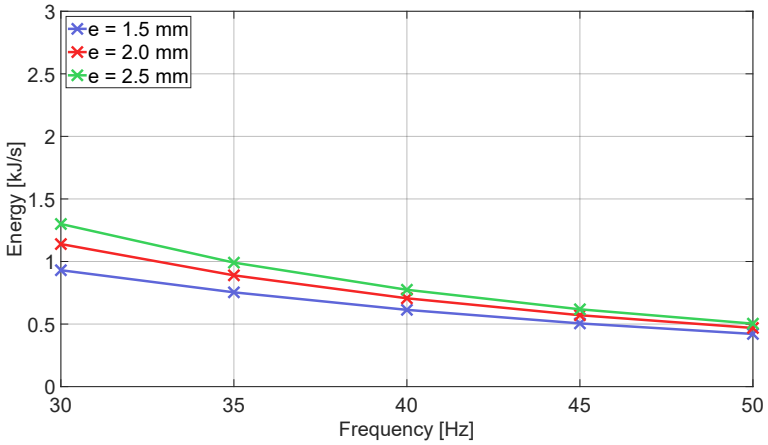

Figure 9.16: Energy per squeezing movement - study of tamping characteristics

The excitation amplitude has been proven influence the loading response values. Figure 9.17 shows that, independent of the excitation amplitude, all load-displacement diagrams plotted in Figure 9.14 at one frequency level are parallel to each other in the loading phase, given that the loading response values remain constant. An increase of about 20% is observable between the lowest and highest frequency. Calculated values are higher than those given in Table 9.2.

Die approbierte gedruckte Originalversion dieser Dissertation ist an der TU Wien Bibliothek verfügbar.
The approved original version of this doctoral thesis is available in print at TU Wien Bibliothek.
TU Bibliothek Your knowledge hub WIEN

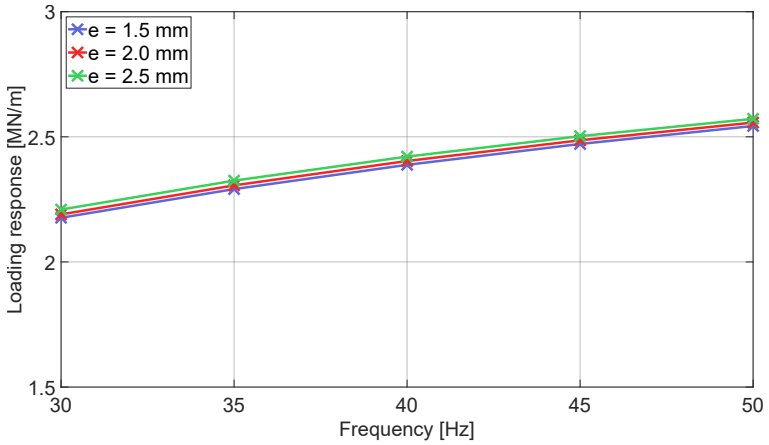

Figure 9.17: Ballast loading response - study of tamping characteristics

Even if the differences in the load-displacement diagram inclination in the unloading phase are not so easily noticeable in Figure 9.14, the calculation has shown that the unloading response values have a high level dependency on the excitation frequency. The higher the frequency, the less "belly-shaped" the load-displacement, i.e. the lower (further in the negative spectrum) the unloading response value (Figure 9.18). At a frequency level of 35 Hz, the curve inclination values match the ones given in Table 9.2, independent of the excitation frequency. It can be stated that the amplitude of excitation only (significantly) influences the unloading response values at higher frequency levels. At 50 Hz the unloading response value decreases by approximately 10% when comparing two adjacent values.

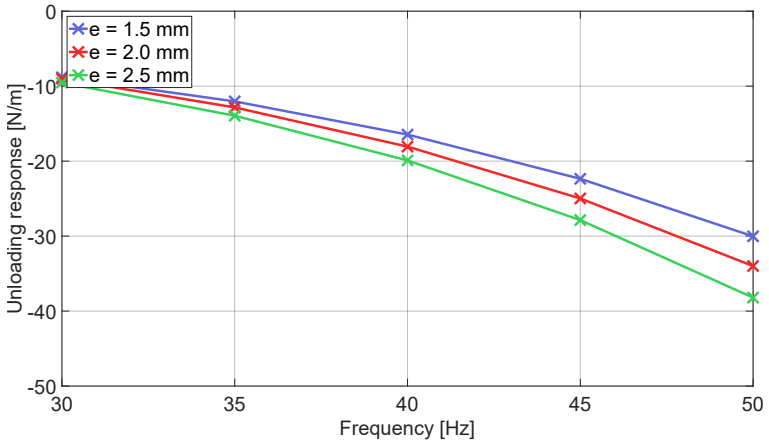

Figure 9.18: Ballast unloading response - study of tamping characteristics

Position of the first contact point dependent on the excitation frequency and amplitude is presented in Figure 9.14. The lower the frequency, the longer two model components stay in contact. This can be recognized in Figure 9.19 - lower values indicate a shift of the contact point further to the left. For one excitation amplitude level, the beginning of contact point shifts for approximately 2 mm between the lowest and highest frequency level. Amplitude of excitation also influences the point position significantly, causing a shift of close to 1 mm when comparing two adjective amplitudes at the highest frequency.

Die approbierte gedruckte Originalversion dieser Dissertation ist an der TU Wien Bibliothek verfügbar.
The approved original version of this doctoral thesis is available in print at TU Wien Bibliothek.
TU Bibliothek Your knowledge hub WIEN

Changes of position of the second contact point (loss of contact) in dependence on the excitation frequency and amplitude is plotted in Figure 9.20, with intersection points presented in Figure 9.14. Squeezing velocity does not influence the position of the second contact. Once again, a 25% increase of excitation amplitude results in an approximately 1 mm shift of the in-contact part of the load-displacement curve to the right, which is observable in the second contact point (Figure 9.20).

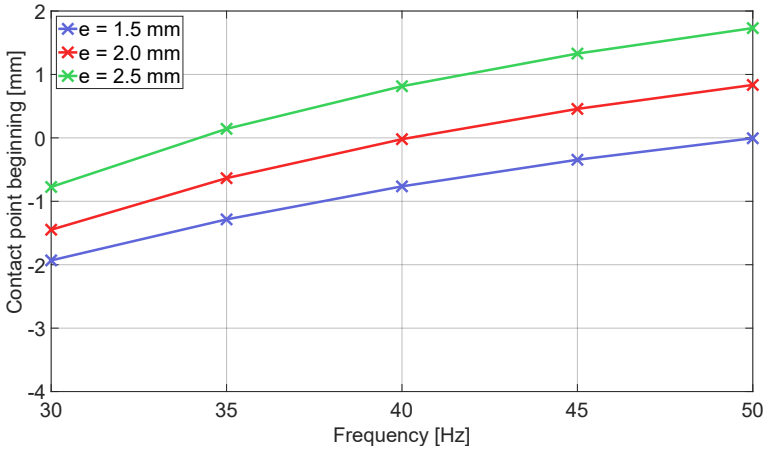

Figure 9.19: Contact point beginning - study of tamping characteristics

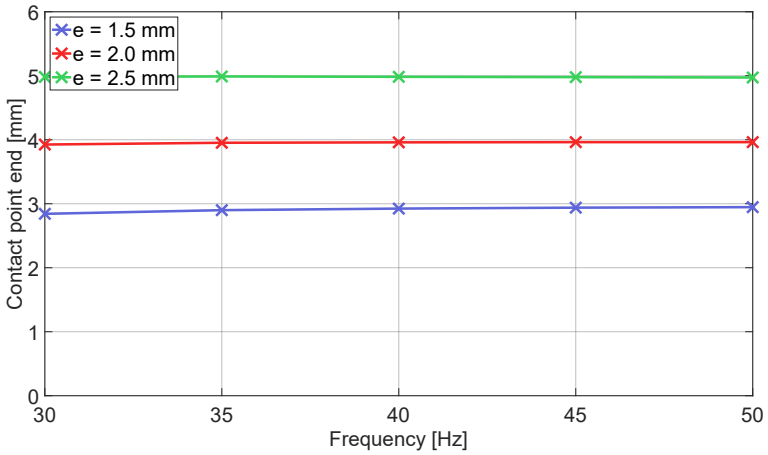

Figure 9.20: Contact point end - study of tamping characteristics

Figure 9.21 shows a 20% decrease of contact duration between the two extreme frequency levels. At lower amplitude levels the contact duration extends significantly - approximately 10% at lower frequency for two adjacent amplitudes.

Contact length is also influenced by the changes in frequency, somewhat less by the variation of excitation amplitude (Figure 9.22). The length obviously increases with the increase of amplitude simply because the tamping tine crosses a longer path altogether, but this influence is only limited to lower frequency levels. Influence of excitation frequency is noticeable as a contact prolongation of about 2 mm between the highest and lowest frequency.

Die approbierte gedruckte Originalversion dieser Dissertation ist an der TU Wien Bibliothek verfügbar.
The approved original version of this doctoral thesis is available in print at TU Wien Bibliothek.
TU Bibliothek Your knowledge hub WIEN

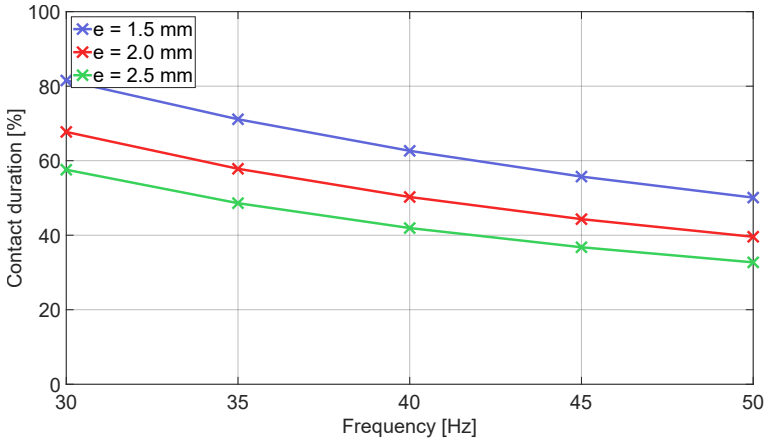

Figure 9.21: Contact duration per cycle - study of tamping characteristics

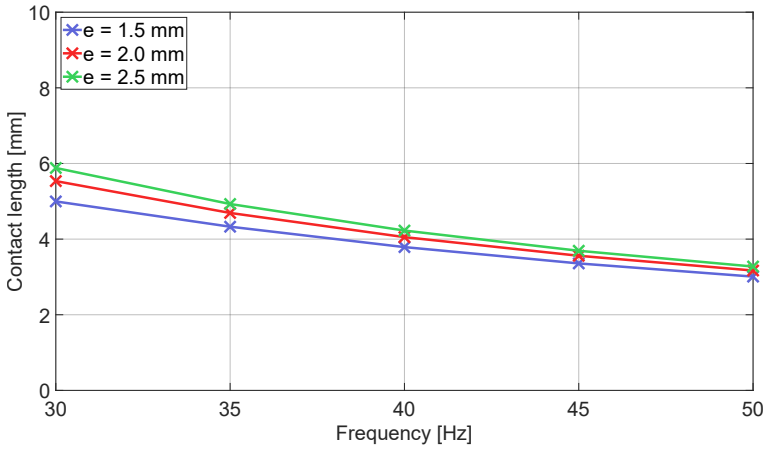

Figure 9.22: Contact length per cycle - study of tamping characteristics

Higher excitation frequency increases the number of cycles per squeezing movement and decreases the cycle duration. With high frequency in combination with a high amplitude, velocity of the relative tine movement within the cycle is significantly increased. Several tamping characteristics are affected by the high relative tine velocity:

- first contact point shifts to the right, second one is not effected
- both contact duration and length decrease
- due to the decrease of the contact phase duration and length, the force decreases together with the energy
- loading response is independent on the amplitude but increases with the frequency. The opposite effect can be seen in the unloading response

Die approbierte gedruckte Originalversion dieser Dissertation ist an der TU Wien Bibliothek verfügbar.
The approved original version of this doctoral thesis is available in print at TU Wien Bibliothek.
TU Bibliothek Your knowledge hub WIEN

9.4.3 Influence of squeezing velocity on tamping characteristics - Fouled ballast

Influence of different squeezing velocity and excitation amplitude levels on fouled ballast response to tamping is investigated using the parameter set from Table 9.1 and the ballast condition determining factor from Table 9.5. Load-displacement diagrams are plotted once again for three amplitudes and five velocities (Figure 9.23), as described in Chapter 9.4. Points plotted on the x axis display maximum tine elongation in both moving directions. Influence of the two tamping parameters on the tamping characteristics is calculated and the results are presented in Figures 9.24 to 9.31. Table 9.4 gives reference values of the four decisive tamping characteristics for fouled ballast conditions and is used for comparison and correlation with the results of this parameter study. Excitation frequency is kept constant at 35 Hz.

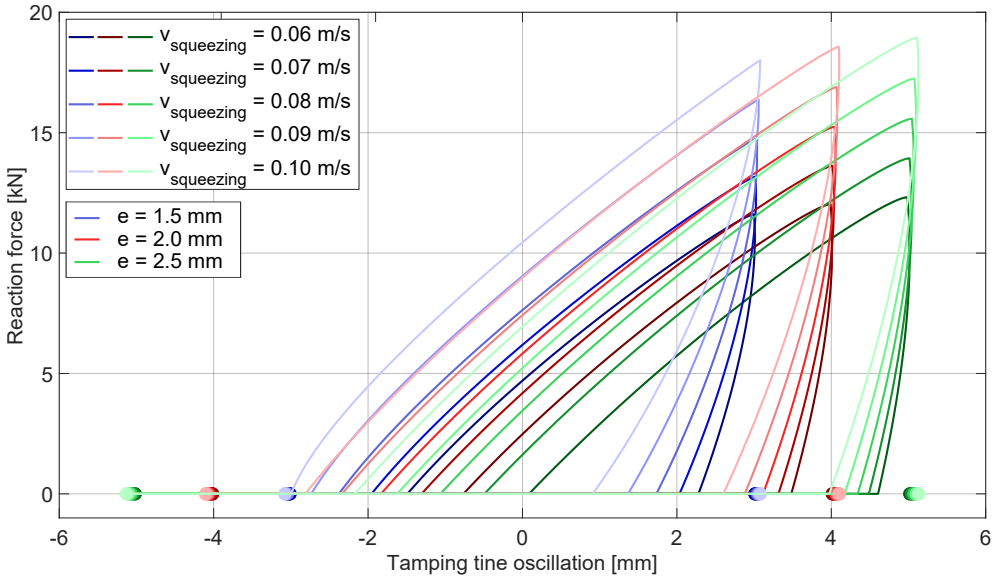

Figure 9.23: Fouled ballast - variation of the squeezing velocity and excitation amplitude and their influence on tamping characteristics. Points plotted on the x axis display maximum tine elongation in both moving directions

An increase of the squeezing velocity results in an increase of the maximum reaction force per cycle. An 5 kN increase can be seen for all amplitudes between the lowest and the highest velocity. Maximum reaction force per cycle values at higher squeezing velocity levels match the values given in Table 9.4. Figure 9.24 shows that the increase/decrease of maximum reaction force per cycle induced by the 25% increase/decrease of the excitation amplitude is insignificant (less than 0.5 kN) and independent of the squeezing velocity.

Die approbierte gedruckte Originalversion dieser Dissertation ist an der TU Wien Bibliothek verfügbar.
The approved original version of this doctoral thesis is available in print at TU Wien Bibliothek.

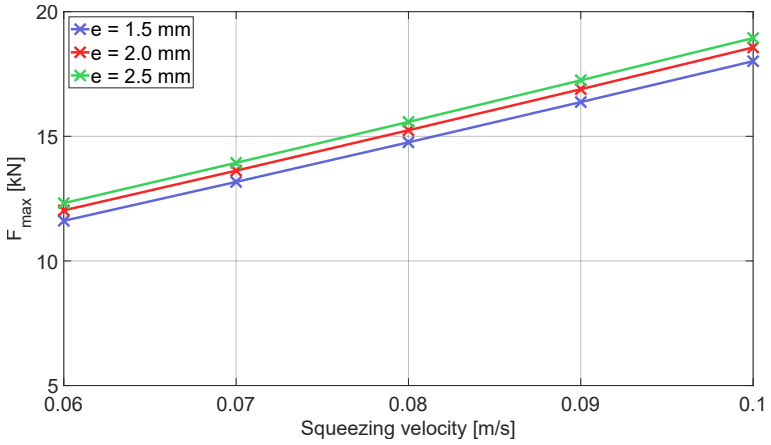

Figure 9.24: Maximum reaction force per cycle - study of tamping characteristics

As the squeezing velocity decreases, the contact duration between two model components is shortened (Figure 9.30), allowing less time for the transfer of energy within the cycle (Figure 9.25), as well as for force build-up (Figure 9.24). As already observed by *Fischer* [59], an increase of squeezing velocity at given constant frequency extends the contact duration, increases transferred energy and reaction force, thus aiding the desired rearrangement of the ballast grains. However, an increase beyond the upper limit could potentially accelerate the process of ballast fouling. Unlike the maximum reaction force, the energy values are influenced by the changes of the excitation frequency to a slightly higher extent, as can be seen in Figure 9.25. At the highest observed velocity level, energy increases approximately 30% between 1.5 mm and 2.0 mm excitation amplitude.

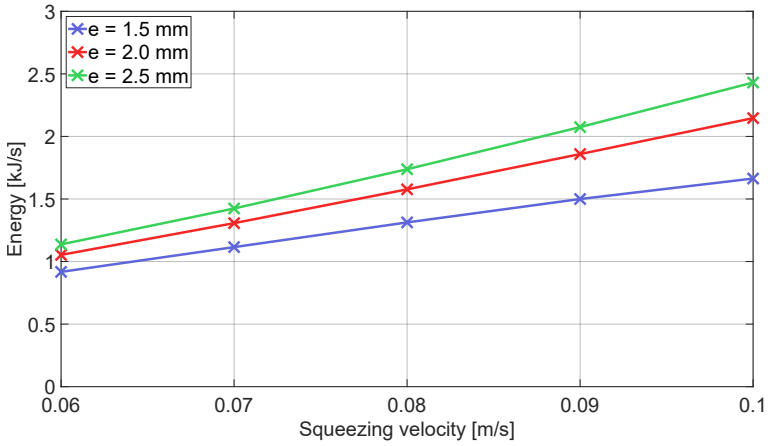

Figure 9.25: Energy per squeezing movement - study of tamping characteristics

The loading parts (prior to the maximum force reach point) of all load-displacement diagrams are almost parallel to each other, independent of the amplitude of excitation and squeezing velocity (see Figure 9.23). This is proven in Figure 9.26, showing that the loading response to a minor degree depends on the excitation amplitude only at the highest observed velocity level.

Die approbierte gedruckte Originalversion dieser Dissertation ist an der TU Wien Bibliothek verfügbar.
The approved original version of this doctoral thesis is available in print at TU Wien Bibliothek.
TU Bibliothek Your knowledge hub WIEN

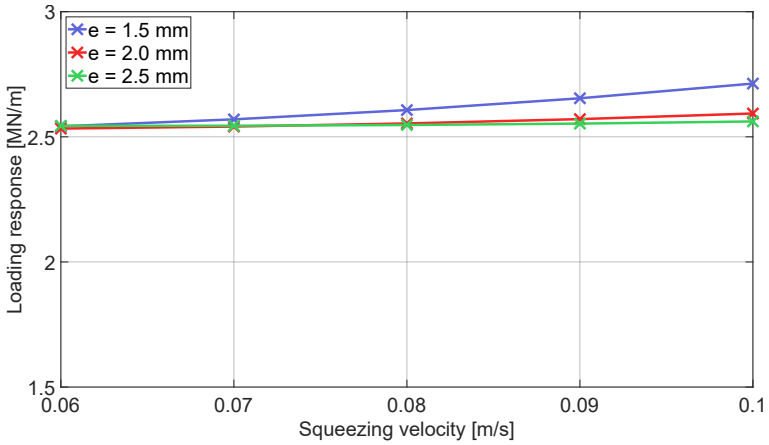

Figure 9.26: Ballast loading response - study of tamping characteristics

Correlation to the unloading response values given in the Table 9.4 can be seen at higher velocity levels in Figure 9.27. At lower levels the values increase. The values almost double between the highest and the lowest observed velocity level, and decrease significantly (up to 25%) with the decrease of excitation amplitude.

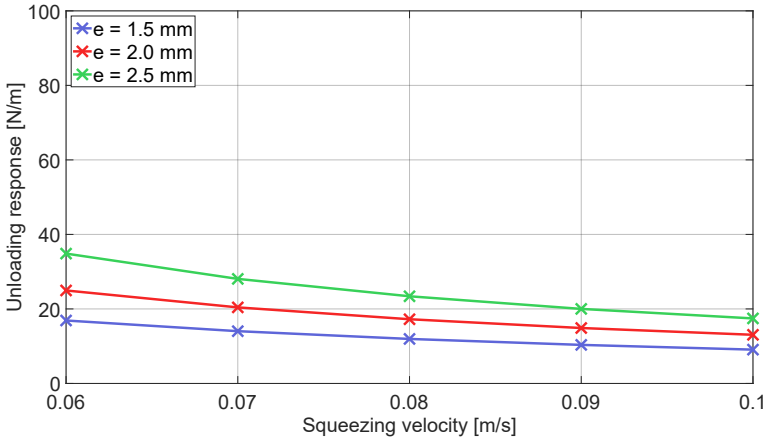

Figure 9.27: Ballast unloading response - study of tamping characteristics

Points indicating the beginning of contact between the tine and the ballast are marked in Figure 9.23 as the left intersection point of each load-displacement diagram with the x axis. It can be inferred from Figure 9.28 that the contact points shift to the left with the decrease of amplitude, further in the negative spectrum (approximately by 0.5 mm, comparing two adjacent amplitudes). Following a similar principle, the higher the squeezing velocity, the further the point of contact beginning lays in the negative spectrum. Inclination change of the line presenting the beginning of contact for a 1.5 mm amplitude (between 0.9 m/s and 1.0 m/s, Figure 9.28) indicates model limitations.

Especially observable is the fact that, with the increase of velocity the tine comes into contact with the ballast matrix significantly sooner. When comparing the two extreme values of squeezing velocity, the beginning of contact for the smallest amplitude shifts for 1.5 mm, whereas the shift for the biggest amplitude increases to 2.2 mm. This observation correlates with the study of transferred energy per cycle - at higher velocity levels the energy level is

Die approbierte gedruckte Originalversion dieser Dissertation ist an der TU Wien Bibliothek verfügbar.
The approved original version of this doctoral thesis is available in print at TU Wien Bibliothek.
TU Bibliothek Your knowledge hub WIEN

higher which is unambiguously linked to longer duration of contact (Figure 9.30) between the two model components that extends if the contact is achieved further in the negative spectrum.

As evident in Figure 9.29, even if the increase of amplitude shifts the load-displacement curves to the left, the right intersection point of each load-displacement diagram with the x axis indicating the loss of contact shifts further into the positive spectrum. Variation of the squeezing velocity induces similar results as presented in Figure 9.28. An increase leads to a shift of contact loss point in the negative direction, following the shift of contact beginning points. Figure 9.29 provides another interesting insight. The smaller the excitation amplitude the more impact an increase of squeezing velocity induces. When comparing the two extreme values of the squeezing velocity, the loss of contact for the smallest amplitude shifts for 1.3 mm, whereas the shift for the biggest amplitude reduces to 0.7 mm.

It can be concluded that an increase of velocity has a stronger impact on the the first contact point, and the influence on the second one increases with the progress of ballast fouling. Both are influenced by the excitation amplitude, its increase shifts both contact points to the left.

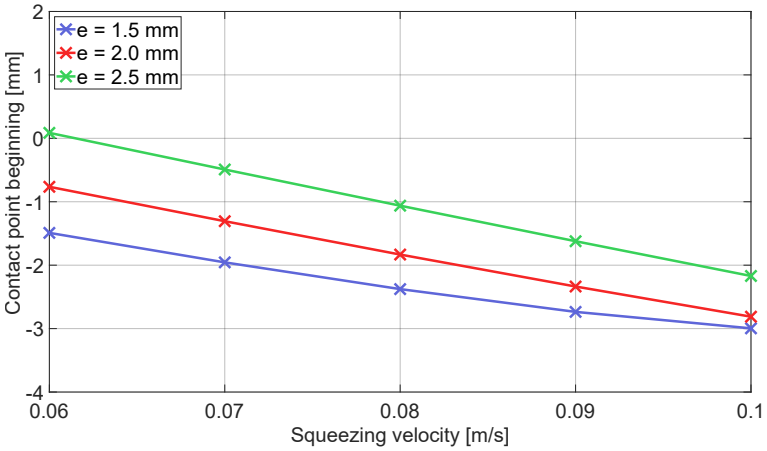

Figure 9.28: Contact point beginning - study of tamping characteristics

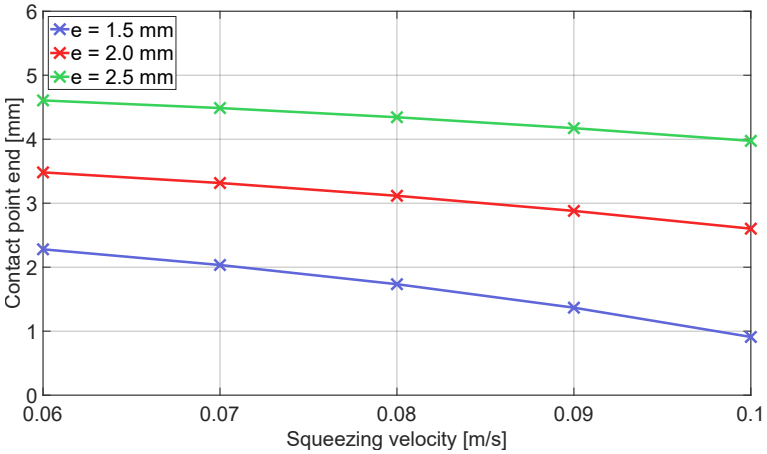

Figure 9.29: Contact point end - study of tamping characteristics

Die approbierte gedruckte Originalversion dieser Dissertation ist an der TU Wien Bibliothek verfügbar.
The approved original version of this doctoral thesis is available in print at TU Wien Bibliothek.
TU Bibliothek Your knowledge hub WIEN

Study of several other tamping characteristics such as maximum reaction force and transferred energy per cycle have already shown that faster squeezing motion of the tine causes an increase of contact length and duration, providing the necessary time for force and energy build-up and rearrangement of ballast particles. Both Figures 9.30 and 9.31 confirm this observation. A significant prolongation of contact duration and contact length is noticeable with the increase of velocity. An increase of amplitude, however, extends the contactless phase, as the contact duration and length are reduced.

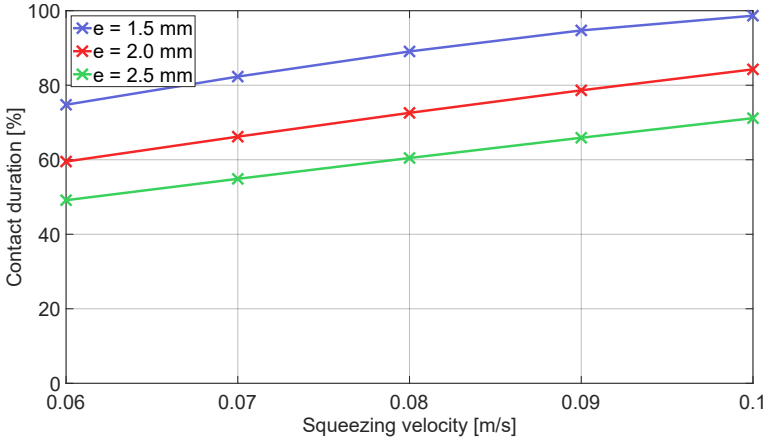

Figure 9.30: Contact duration per cycle - study of tamping characteristics

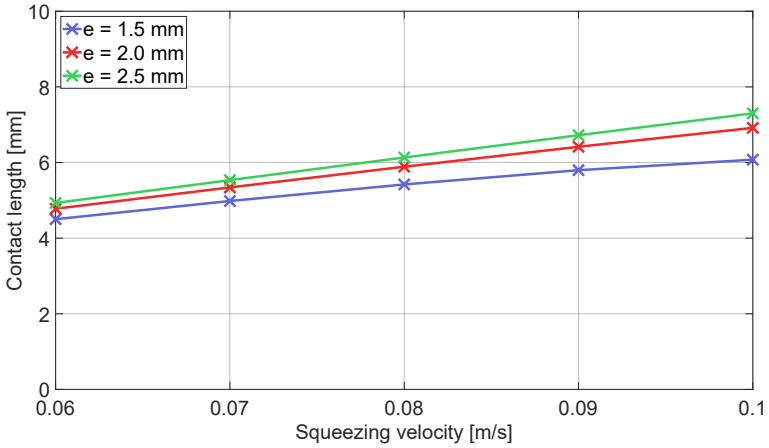

Figure 9.31: Contact length per cycle - study of tamping characteristics

Very similar to the clean, simulating tamping in fouled ballast conditions shows that an increase of energy extends the contact duration and length, concurrently increasing the maximum force and transferred energy. Both loading and unloading response are only to a minor extend influenced by the changes.

Die approbierte gedruckte Originalversion dieser Dissertation ist an der TU Wien Bibliothek verfügbar.
The approved original version of this doctoral thesis is available in print at TU Wien Bibliothek.

9.4.4 Influence of frequency on tamping characteristics - Fouled ballast

Influence of the excitation frequency on the eight selected tamping characteristics is investigated in combination with the different excitation amplitude values and the results in form of load-displacement diagrams can be seen in Figure 9.32. Points plotted on the x axis display maximum tine elongation in both moving directions. Eight tamping characteristics calculated from the load-displacement diagrams are presented in Figures 9.33 to 9.40. Fouled ballast conditions are once again simulated by the model using the parameter set given in Table 9.1 and ballast condition determining factor from Table 9.5. Squeezing velocity is kept constant at 0.1 m/s. Calculated values are correlated to those given in Table 9.4.

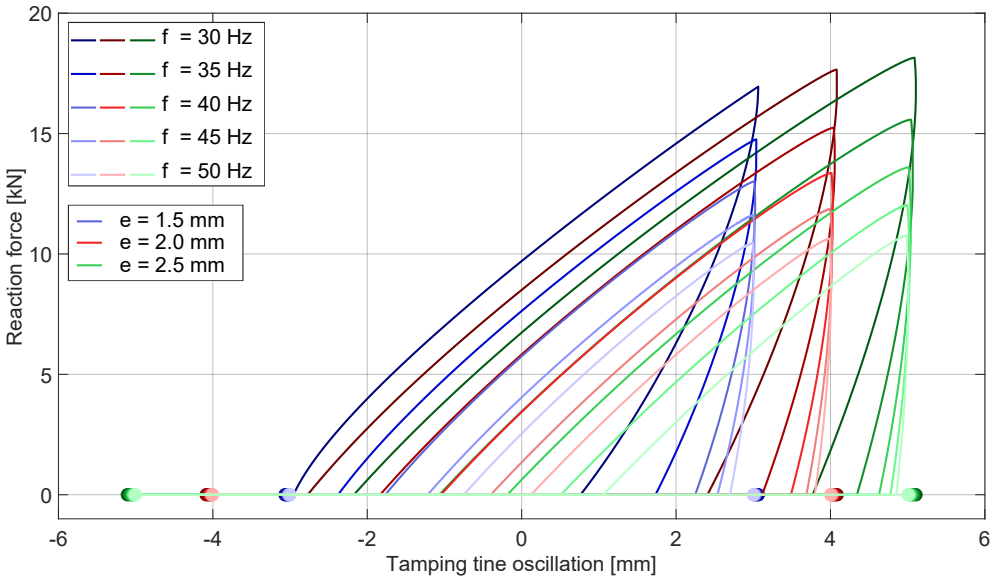

Figure 9.32: Fouled ballast - Variation of the excitation frequency and amplitude and the influence on the taming characteristics. Points plotted on the x axis display maximum tine elongation in both moving directions

Increase of frequency decreases the maximum reaction force per cycle significantly, by approximately 8 kN between lowest and highest frequency for one amplitude level. This is again related to the contact duration, given that at higher frequencies the cycle and contact duration decrease, reducing the available time for the increase of force. The excitation amplitude does influence the force substantially. An increase of 0.5 kN between two defined amplitude values results at the lowest frequency but the influence reduces as the frequency increases. Values at lower frequencies correlate to those given in the Table 9.4.

Die approbierte gedruckte Originalversion dieser Dissertation ist an der TU Wien Bibliothek verfügbar.
The approved original version of this doctoral thesis is available in print at TU Wien Bibliothek.
TU Bibliothek Your knowledge hub WIEN

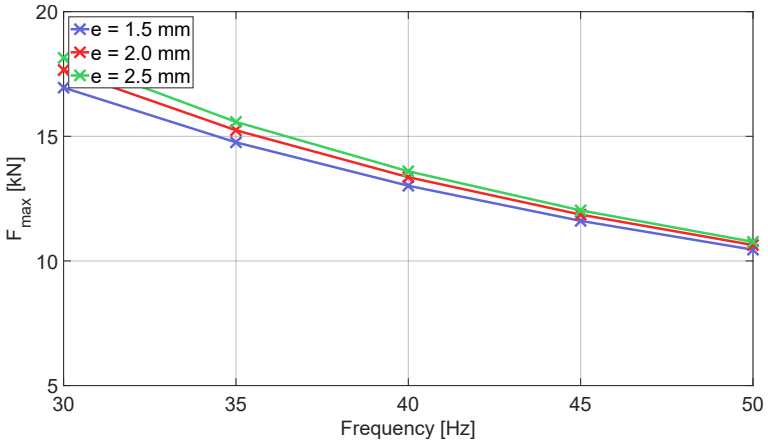

Figure 9.33: Maximum reaction force per cycle - study of tamping characteristics

Similar to the force, the transferred energy is also influenced by the reduction of cycle duration, i.e. by the increase of frequency. The area within the load-displacement curve decreases considerably at higher frequency levels (see Figure 9.32). Figure 9.34 shows a significant decrease of energy from 2 kJ/s to 0.8 kJ/s within the frequency range for the 2 mm excitation amplitude. The amplitude itself only shows a relevant influence at lower frequencies, and the differences between different amplitudes decrease as the frequency increases. Values at lower frequencies correlate to those given in the Table 9.4.

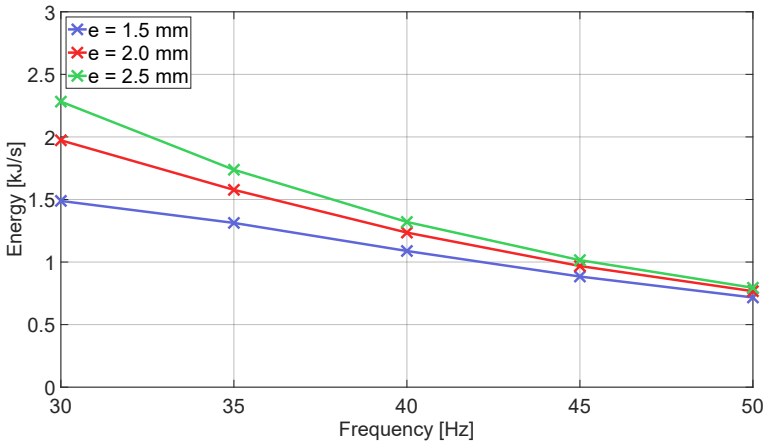

Figure 9.34: Energy per squeezing movement - study of tamping characteristics

Similar to the Figure 9.17, Figure 9.35 also shows a stable but less significant increase of the loading response with the increase of frequency. An increase of about 15% is noticeable for one amplitude between 30 Hz and 50 Hz. This behavior is also explainable by the shortening of cycle duration which is not proportional to the force decrease with the increase of frequency, meaning that the tamping tine at high frequency levels has less time to achieve the same force increase. The non-linear course of the upper (blue) line in Figure 9.35 showing the values for the smallest excitation amplitude does not indicate a different ballast behavior but rather the limitations of the model. Loading response values correlate to those given in the Table 9.4.

Die approbierte gedruckte Originalversion dieser Dissertation ist an der TU Wien Bibliothek verfügbar.
The approved original version of this doctoral thesis is available in print at TU Wien Bibliothek.
TU Bibliothek Your knowledge hub WIEN

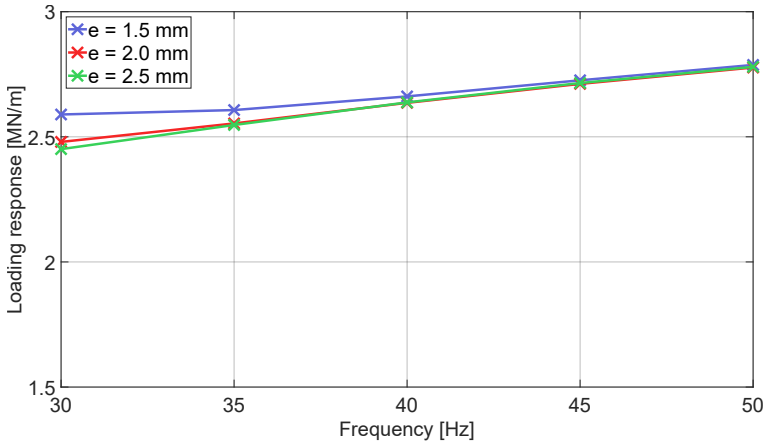

Figure 9.35: Ballast loading response - study of tamping characteristics

Figure 9.36 displays the changes of the unloading response generated by variations of frequency and amplitude. Different inclinations of the load-displacement curves in the unloading phase can be recognized in Figure 9.32. Low frequencies produce a more gradual incline of the unloading line when compared to higher frequencies. This results in lower unloading response values that increase when the curve steepens i.e. frequency increases. An important fact to state once again is that the point of maximum tine elongation in the squeezing direction correlates with the maximum reaction force per cycle while the loss of contact point is positioned further to the left, resulting in positive unloading response values. The excitation amplitude also plays a significant role - the higher the amplitude the steeper the unloading section of the load-displacement diagram. Values at lower frequency levels correlate to those given in the Table 9.4.

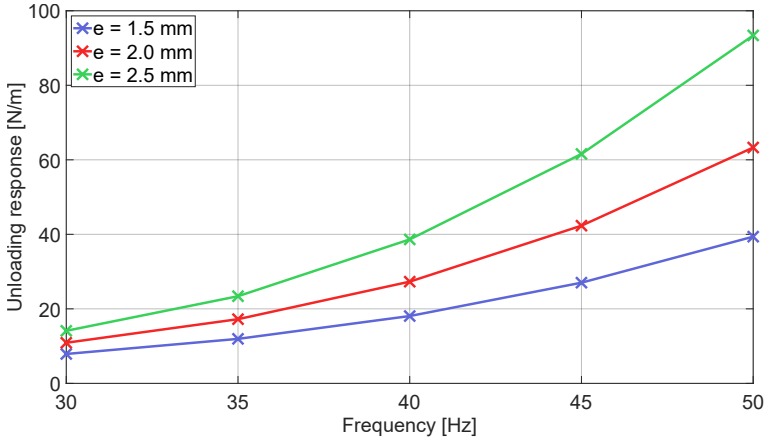

Figure 9.36: Ballast unloading response - study of tamping characteristics

Changes of position of contact points plotted in Figure 9.32 as intersection points of each diagram with the x axis are displayed in Figures 9.37 and 9.38. Increase of frequency in fouled ballast conditions results in a shift of both contact points to the right. The magnitude of the shift for the first contact point is 2.2 mm between 30 Hz and 50 Hz for the smallest amplitude of 1.5 mm and it increases with the increase of amplitude (3.2 mm for a 2.5 mm amplitude).

Die approbierte gedruckte Originalversion dieser Dissertation ist an der TU Wien Bibliothek verfügbar.
The approved original version of this doctoral thesis is available in print at TU Wien Bibliothek.
TU Bibliothek Your knowledge hub WIEN

The second contact point is also influenced by the excitation frequency. However, an important observation can be made based on the results presented in Figure 9.38. The higher the frequency the shorter the shift of the contact point on x axis to the right.

Increasing the excitation amplitude causes a general shift of the load-displacement diagrams to the right and a prolongation of the contactless phase. As stated before, a certain minimum duration of the continuous contact (loading + unloading) phase is necessary for the tamping tine to transfer the desired energy to the ballast matrix - the further the contact points are from one another, the higher the energy per cycle transferred to the ballast matrix (given constant frequency).

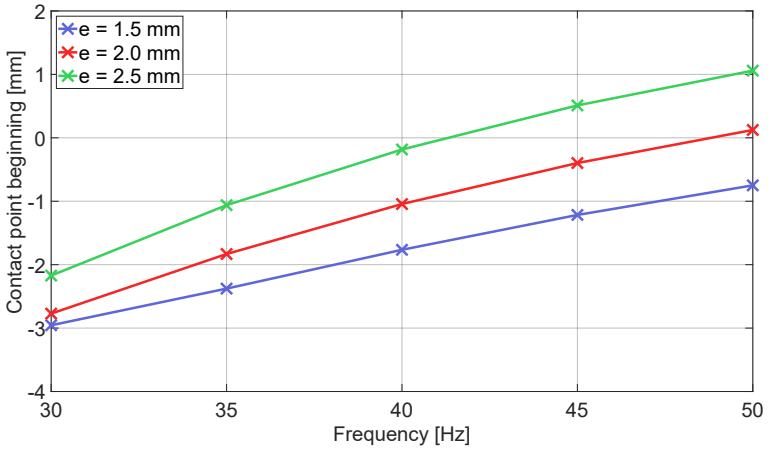

Figure 9.37: Contact point beginning - study of tamping characteristics

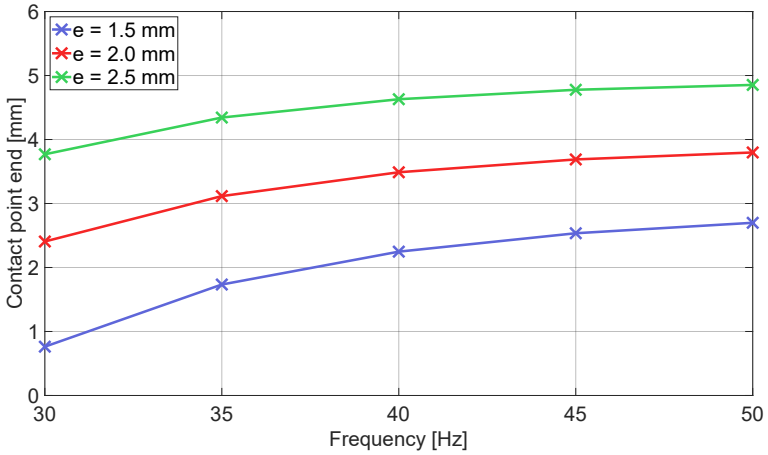

Figure 9.38: Contact point end - study of tamping characteristics

Shortening the cycle duration by increasing frequency leads to a shortening of contact duration and length (Figures 9.39 and 9.40). The decrease of contact duration is most strongly expressed for the smallest selected excitation amplitude (1.5 mm) where the contact duration decreases from 98% at 30 Hz to 62% at 50 Hz. As stated before, the reduction in the contact duration does not necessarily mean that the length of contact is reduced following the same principle. Quite the contrary, Figure 9.40 shows that the most significant decrease of contact length is expected for the highest amplitude - from 7.4 mm at 30 Hz to 4.0 mm at

Die approbierte gedruckte Originalversion dieser Dissertation ist an der TU Wien Bibliothek verfügbar.
The approved original version of this doctoral thesis is available in print at TU Wien Bibliothek.
TU Bibliothek Your knowledge hub WIEN

50 Hz. General statement following this analysis is that the increase of frequency reduces cycle duration and by doing so influences all of the remaining tamping characteristics.

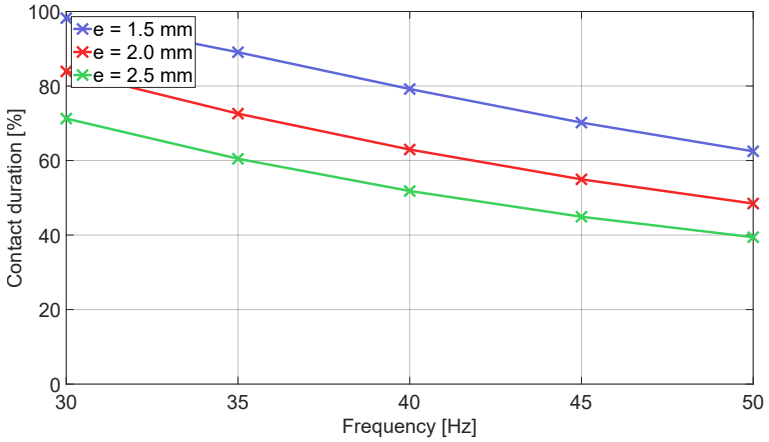

Figure 9.39: Contact duration per cycle - study of tamping characteristics

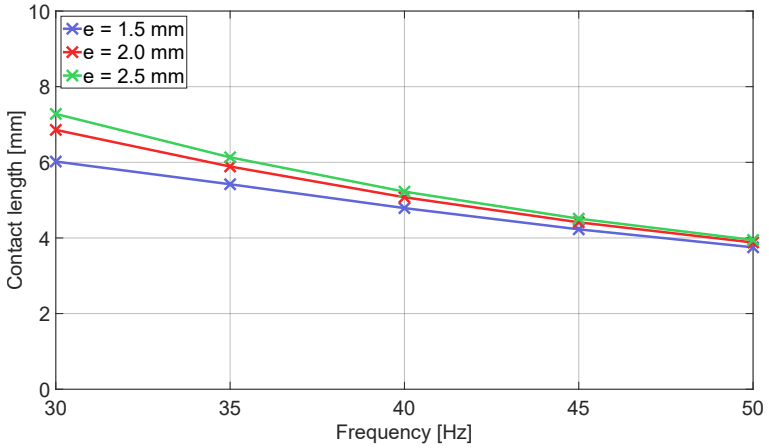

Figure 9.40: Contact length per cycle - study of tamping characteristics

As a general conclusion it can be state that the goal of a successful tamping process is to fill the void under the sleeper and at the same time increase the bulk density of the ballast by compaction it into a more stable bedding. In order to do so, a certain amount of energy need to be transferred to the ballast matrix. In order to improve and optimize this process, an aspiration to reduce the duration of the tamping process is present, given that that would also reduce the whole maintenance process and the track closure window.

Transferring the same amount of energy in a shorter time frame requires a high force build-up rate. This can be achieved by either increasing the excitation amplitude, i.e. the contact length, thus preserving the cycle duration but decreasing the required number of cycles needed *and/or* by increasing the squeezing velocity which also results in a longer contact duration. Frequency variation has shown that higher frequency levels are not beneficial for a successful energy transfer and force build-up, which is confirmed by comparison with the existing research [59].

Die approbierte gedruckte Originalversion dieser Dissertation ist an der TU Wien Bibliothek verfügbar.
The approved original version of this doctoral thesis is available in print at TU Wien Bibliothek.

9.5 Study of different ballast bed conditions

As stated before, following a successful calibration and verification, the mechanical model can now be used to conduct a study on the influence of tamping parameters on the tamping characteristics (Chapter 9.4). Tamping characteristics however, are not the only variable factor of influence that is encountered in-situ. The ballast bed condition significantly influences the tamping characteristics. Unlike other tamping parameters such as the squeezing velocity or the number of insertions that could easily be altered during, for example, a measurement on a secondary track, the influence of ballast bed condition can hardly be investigated in-situ during a single measurement. This "parameter" variation was one of the main motivations behind the development of the mechanical model. This tool allows the variation of ballast bed condition and provides the possibility to investigate and analyze changes of the tamping characteristics through all five ballast fouling stages.

Interpretations displayed in the following chapters result from a calculation using the parameters listed in Table 9.1, with following variations:

- squeezing velocity - reduced from 0.1 m/s down to 0.06 m/s. By choosing the same velocities as those investigated in Chapter 9.4 a comparison between the parameter studies is possible. For different squeezing velocities the excitation frequency is kept constant at 35 Hz
- excitation frequency - reduced to 30 Hz (approximately the excitation frequency during tamping unit relocation) and increased up to 50 Hz (approximately the excitation frequency during ballast penetration); for different excitation frequencies the squeezing velocity is kept constant at 0.08 m/s
- ballast bed condition - the progress of ballast fouling is simulated by increasing the stiffness of the elastic spring k_e, following the principle given in Table 9.5.

For each parameter combination, all tamping characteristics are again plotted in the following order:

1. Maximum reaction force per cycle [kN]
2. Energy per squeezing movement [kJ/s]
3. Loading response [MN/m]
4. Unloading response [MN/m]
5. Contact point beginning [mm]
6. Contact point end [mm]
7. Contact duration [%]
8. Contact length [mm]

Die approbierte gedruckte Originalversion dieser Dissertation ist an der TU Wien Bibliothek verfügbar.
The approved original version of this doctoral thesis is available in print at TU Wien Bibliothek.

Each of the following diagrams is a result of an analysis conducted on 25 load-displacement curves altogether. Load-displacement curves for the values that do not follow the expected pattern are plotted additionally and denoted on every diagram in order to gain insight into presented results. Ranges of all characteristics are kept constant in all variations in order to facilitate a more straightforward comparison.

9.5.1 Influence of squeezing velocity on tamping characteristics

Five colors present the five stages of ballast fouling starting from clean ballast bed presented by a green color, to the highly fouled presented in red. The five load-displacement diagrams are presented additionally in Figure 9.43, for the squeezing velocity of 0.08 m/s. Values that are plotted in Figure 9.43 are highlighted in every diagram by a dashed rectangular shape. The ballast condition, i.e. fouling phase order, is marked by black arrows.

An increase of squeezing velocity of the tamping tine should result in an increase of duration and length of tine contact to the ballast matrix (Figure 5.21). If the contact time is prolonged, the contact force as well as the transferred energy are expected to increase. In the context of ballast bed condition, the maximum reaction force per cycle increases, as expected, with the progress of ballast fouling, reaching its maximum of 19 kN for highly fouled ballast and the highest squeezing velocity (Figure 9.41). The increase of force can be observed between each two adjacent ballast condition phases, but the rate of increase decreases as the ballast fouling process progresses.

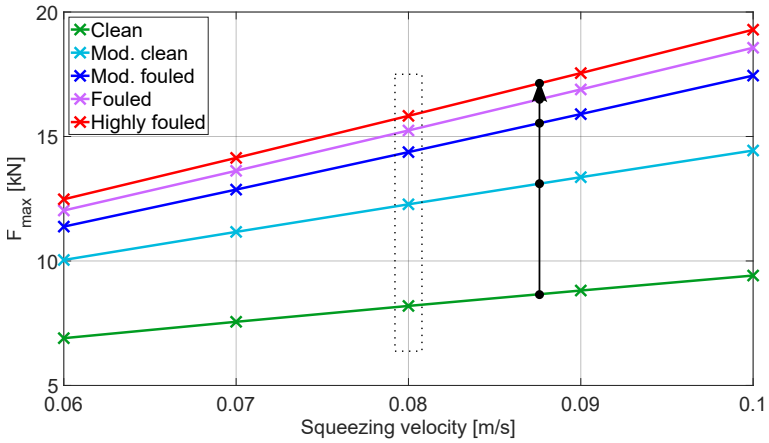

Figure 9.41: Maximum reaction force per cycle - parameter study

Similar to the maximum reaction force per cycle, energy per squeezing movement, obtained as the area within the load-displacement curve, is expected to increase with squeezing velocity and with ballast fouling progress. This, however, is not the case for all the ballast condition phases. The values seem to increase up to a certain level (moderately fouled ballast condition), and continue to decrease as the fouling of the ballast bed progresses (Figure 9.42). This behavior can either be explained by model limitations, meaning that a certain tamping parameter combination does not produce plausible results, or by the fact that this tamping characteristic cannot be taken into consideration as a reliable indicator of ballast

Die approbierte gedruckte Originalversion dieser Dissertation ist an der TU Wien Bibliothek verfügbar.
The approved original version of this doctoral thesis is available in print at TU Wien Bibliothek.
TU Bibliothek Your knowledge hub WIEN

condition. Load-displacement curves for all five ballast conditions and a squeezing velocity of 0.08 m/s are plotted in order to determine the cause of this atypical variation of values (Figure 9.43). As can be seen, the model does not provide credible results for the last stage of ballast fouling. A loop that can be seen in the upper part of the diagram would indicate that the tamping tine starts its motion in the direction opposite to squeezing before the maximum force has been reached, which is not plausible. The load-displacement curves depicting fouled ballast behavior, however, show plausible values and comprise the expected shape but does not meet the expected energy value. This leads to the conclusion that the energy per squeezing movement cannot be taken into consideration as a reliable indication for higher levels of ballast bed fouling.

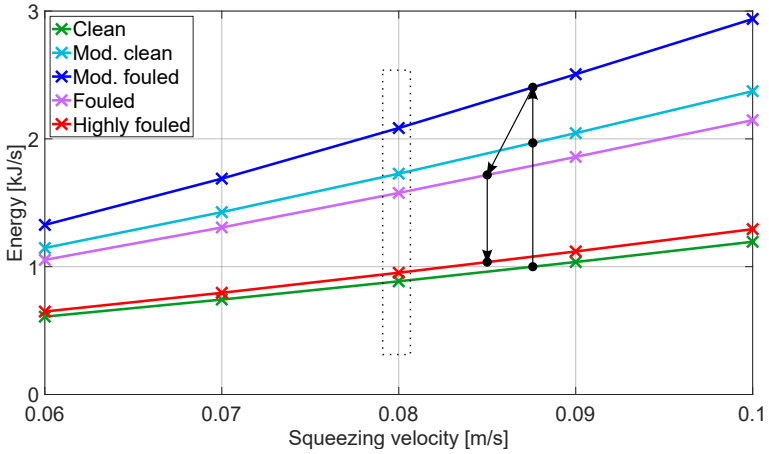

Figure 9.42: Energy per squeezing movement - parameter study

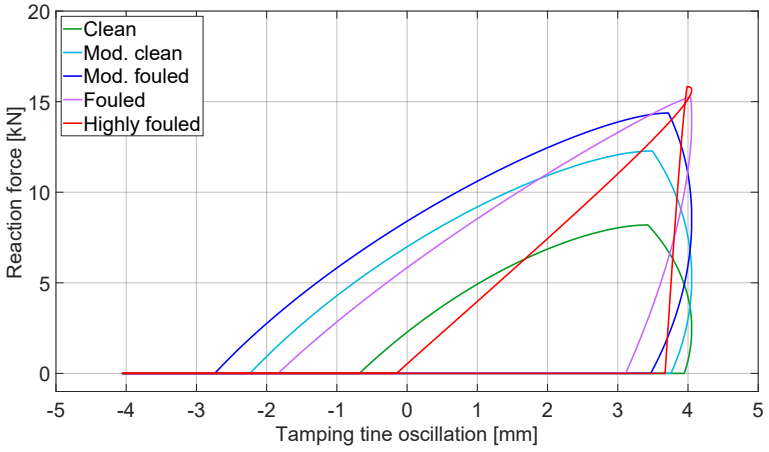

Figure 9.43: Load-displacement curves evaluated in the Figure 9.42, $v_{squeezing}$ = 0.08 m/s, f = 35 Hz

Loading response of the ballast matrix is also expected to increase with the progression of ballast fouling, which is confirmed in Figure 9.44. Loading response values for highly fouled ballast are far beyond the expected values, which can be easily observed in the steepness of the load-displacement diagram in Figure 9.43. Furthermore, the velocity of the tamping tine movement should not influence the loading response of the ballast matrix - this is also

Die approbierte gedruckte Originalversion dieser Dissertation ist an der TU Wien Bibliothek verfügbar.
The approved original version of this doctoral thesis is available in print at TU Wien Bibliothek.

depicted in Figure 9.44 for all the ballast condition stages, except for the highly fouled one which additionally confirms that this stage does not provide reliable results.

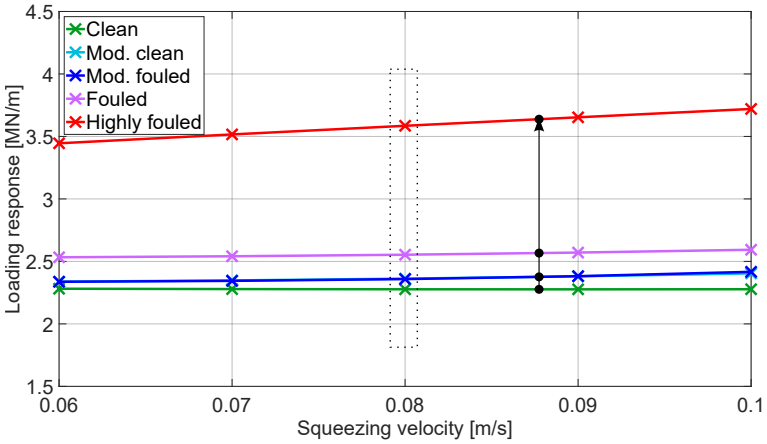

Figure 9.44: Ballast loading response - parameter study

The unloading response is defined by the shape of the load-displacement curve in the unloading phase. This is the only tamping characteristic that changes from a negative to a positive value between clean and fouled ballast (as was observed in-situ), thus, it is a difficult parameter to consider as a reliable indicator. As the progress of ballast fouling progresses, the inclination of the curve in the unloading phase starts to increase striving to a vertical line. This leads to an increase of unloading response absolute value, as can be seen for clean and moderately clean ballast in Figure 9.45. Once the imaginary vertical line has been crossed, the values in the positive spectrum are expected to decrease as the line steepness decreases. This is, however, not valid for the change between fouled and highly fouled ballast conditions, given that the unloading response values continue to increase. The load-displacement curves showing moderately fouled ballast behavior are the border ones, crossing from a negative to a positive number spectrum (darkblue line, Figure 9.45).

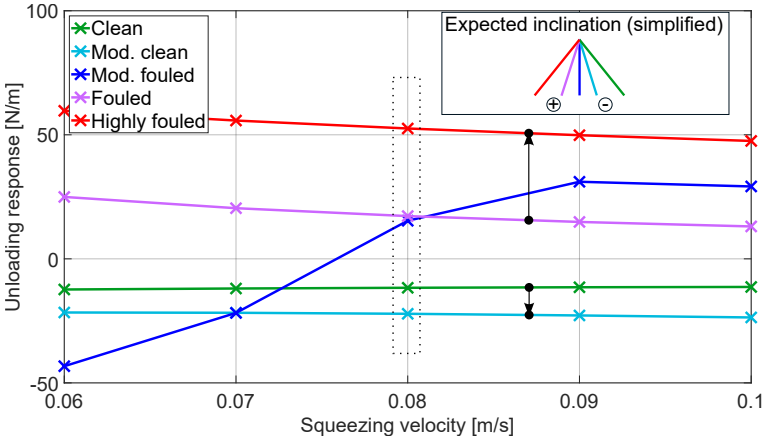

Figure 9.45: Ballast unloading response - parameter study

Since the increase of squeezing velocity is expected to increase the contact duration, this should also be visible on the contact points. Figure 9.46 shows the dependence of the first

Die approbierte gedruckte Originalversion dieser Dissertation ist an der TU Wien Bibliothek verfügbar.
The approved original version of this doctoral thesis is available in print at TU Wien Bibliothek.
TU Bibliothek Your knowledge hub WIEN

contact point on the squeezing velocity and ballast condition. A shift to the left (further in the negative segment) is expected with both the increase of velocity and progress of ballast fouling. This is proven for the first three stages of the process, showing a linear shift with the increase of velocity. Moreover, Figure 9.43 revelas that the start of contact of the load-displacement curve displaying fouled ballast behavior is well beyond the expected position.

It has already been proven in Chapter 9.4 that the location of the second contact point (loss of contact) is only influenced at higher stages of ballast fouling. The same behavior can be read in Figure 9.47 - the position of the loss of contact does not change with increase of squeezing velocity in clean ballast condition, and the change in moderately clean ballast is of minor relevance. The following two stages (moderately fouled and fouled) show a moderate dependence on the contact point location on the squeezing velocity, whereas the maximum deviation between two defined adjacent velocity values is about 0.3 mm.

Once again, the positions of both contact points resulting from the highly fouled ballast simulation do not match the expected values, showing that this level of ballast fouling cannot be simulated with the selected parameter set (Table 9.1 and ballast condition determining factor from Table 9.5.

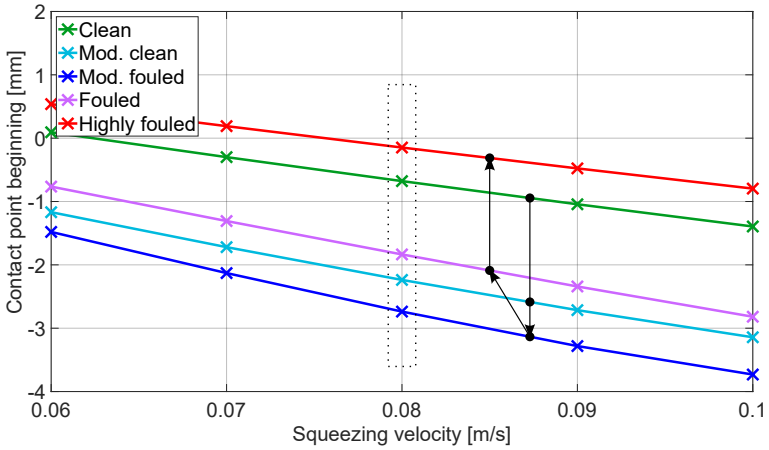

Figure 9.46: Contact point beginning - parameter study

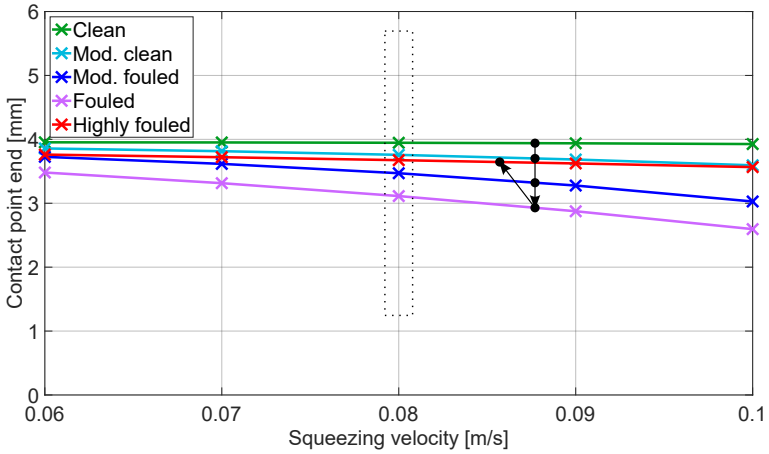

Figure 9.47: Contact point end - parameter study

Die approbierte gedruckte Originalversion dieser Dissertation ist an der TU Wien Bibliothek verfügbar.
The approved original version of this doctoral thesis is available in print at TU Wien Bibliothek.
TU Bibliothek Your knowledge hub WIEN

Increase of squeezing velocity increases the contact duration increases as well as the contact length. The contact duration expressed in percentage can theoretically increase until the loss of contact is no longer observable, i.e. the contact duration reaches 100%. This is not the case for any of the simulated ballast conditions. Study conducted in Chapter 9.4 states that the contact duration between the tamping tine and the ballast matrix is significantly longer in fouled than in clean ballast. The same results can be seen in Figure 9.48. The rest of the values, however, do not follow as expected, given that the contact duration increases at first from clean to moderately clean and moderately fouled only to decrease back again for the remaining two ballast conditions, following the same trend in both contact duration (Figure 9.48) and contact length (Figure 9.49). This trend is considered not reliable for the ballast condition interpretation.

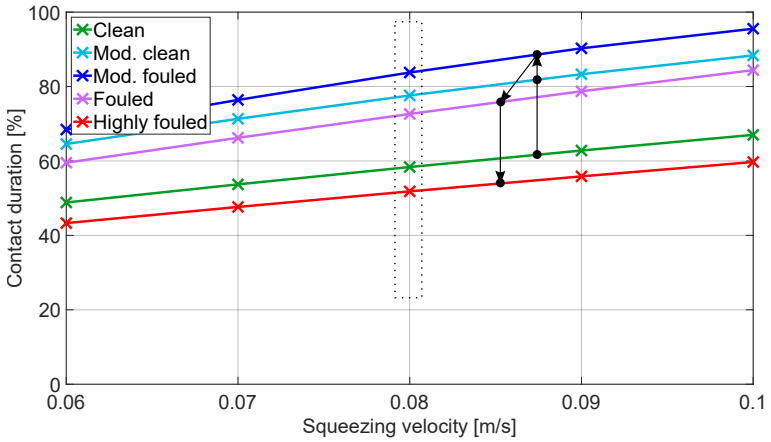

Figure 9.48: Contact duration per cycle - parameter study

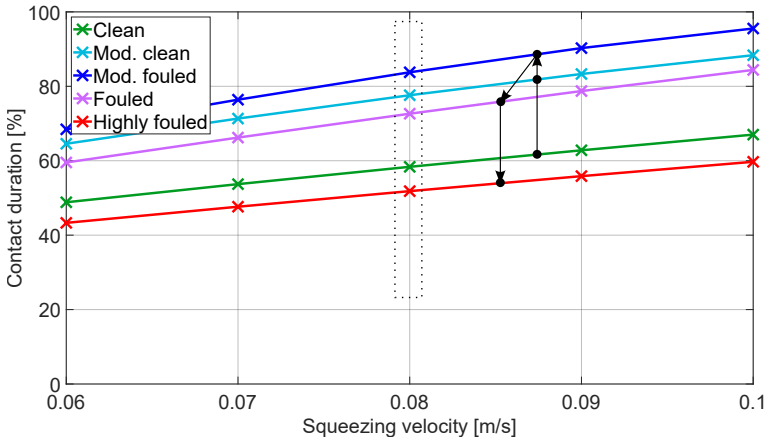

Figure 9.49: Contact length per cycle - parameter study

9.5.2 Influence of frequency on tamping characteristics

Following the same principle presented in Chapter 9.5.1, five colors present the five stages of ballast fouling. Five load-displacement diagrams are presented additionally in Figure 9.52 for an excitation frequency of 40 Hz. Values that are plotted in Figure 9.52 are again high-

Die approbierte gedruckte Originalversion dieser Dissertation ist an der TU Wien Bibliothek verfügbar.
The approved original version of this doctoral thesis is available in print at TU Wien Bibliothek.
TU Bibliothek Your knowledge hub WIEN

lighted in every diagram by a dashed rectangular shape. The ballast condition, i.e. fouling phase order, is marked by black arrows.

An increase of excitation frequency reduces the cycle duration and the tamping tine - ballast matrix contact duration and length. As the contact duration decreases, the available time for the force increase within a cycle decreases, which leads to a general, stable decrease of the maximum reaction force per cycle, as can be seen in Figure 9.50. There are several aspects to consider when looking into possible different frequencies to be set during the squeezing movement:

- Increase of frequency beyond a certain level results in a higher ballast bed load-bearing capacity, but does not provide the possibility to elevate the ballast to the desired level, given that higher frequency levels emphasize the ballast fluidization, and would lead to ballast grains movement away from the tines.
- According to research conducted by *Fischer* [59], the ideal impulse duration[1] in clean ballast condition is between 2 and 4 ms, for a squeezing velocity of 0.018 m/s. Shorter impulse duration does not allow the energy to be transferred to the ballast matrix during the loading contact. Longer duration would lead to higher reaction forces that would accelerate the process of ballast fouling. In the scope of this research it has been proven that the contact between the tamping tine and the ballast matrix extends over the point where the maximum reaction force has been reached. In addition, the squeezing velocities used within the framework of this parameter study are correlated to the measured in-situ values and are significantly higher than the one proposed by *Fischer* [59]. Nevertheless, an effort is made to compare the simulation values to the ones existing in the literature.

Maximum reaction force per cycle decreases with the increase of frequency and increases with the progress of ballast fouling. Figure 9.50 confirms that the expected results match the simulated values. A significant increase is noticeable between the clean and moderately clean ballast bed, and the rate of increase decreases between the following ballast fouling phases.

Once more, the energy per squeezing movement is expected to follow the same trend as the maximum reaction force per cycle. Increase of reaction force corresponds with the increase of the area within the load-displacement curve, which leads to an increase of energy transferred (Tables 9.2, 9.3 and 9.4). Since this premise is only confirmed in the first three steps of ballast fouling (Figure 9.51), an additional insight into the load-displacement curves is plotted in Figure 9.52. Curve depicting highly fouled ballast is again considered to be outside of the model limits. Energy consumed during fouled ballast compaction is indeed higher than the energy transferred for clean ballast compaction, but this trend cannot be applied when comparing moderately fouled and fouled ballast bed. This again leads to a conclusion that energy per squeezing movement cannot be taken into consideration from the applied simulation model as a reliable indication for higher levels of ballast bed fouling.

[1] pulse duration is defined as duration of the loading phase

Die approbierte gedruckte Originalversion dieser Dissertation ist an der TU Wien Bibliothek verfügbar.
The approved original version of this doctoral thesis is available in print at TU Wien Bibliothek.
TU Bibliothek Your knowledge hub WIEN

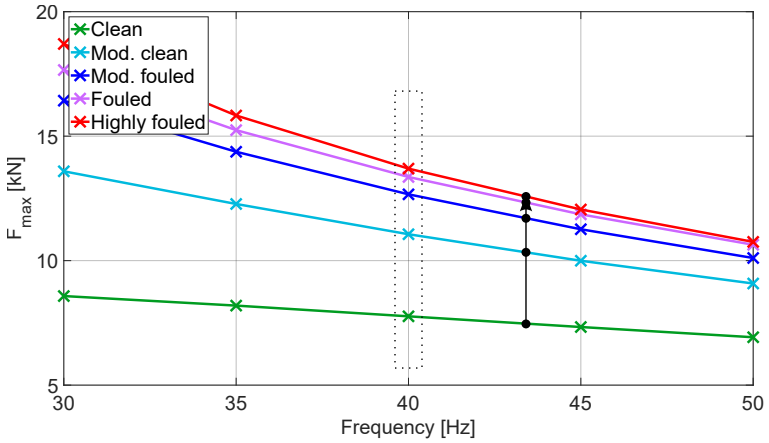

Figure 9.50: Maximum reaction force per cycle - parameter study

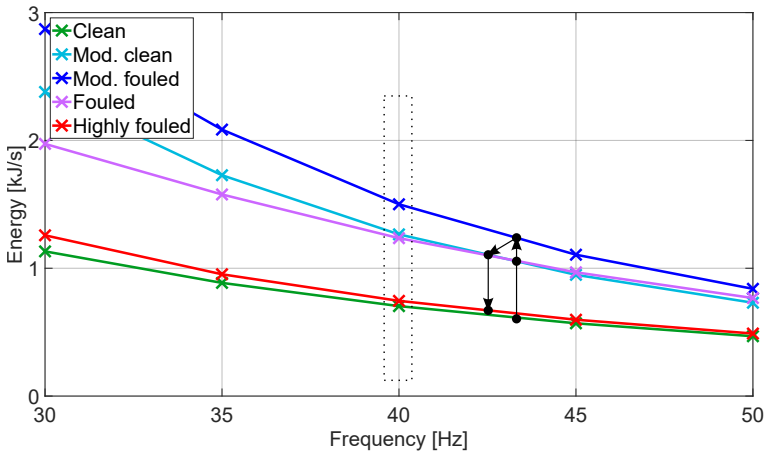

Figure 9.51: Energy per squeezing movement - parameter study

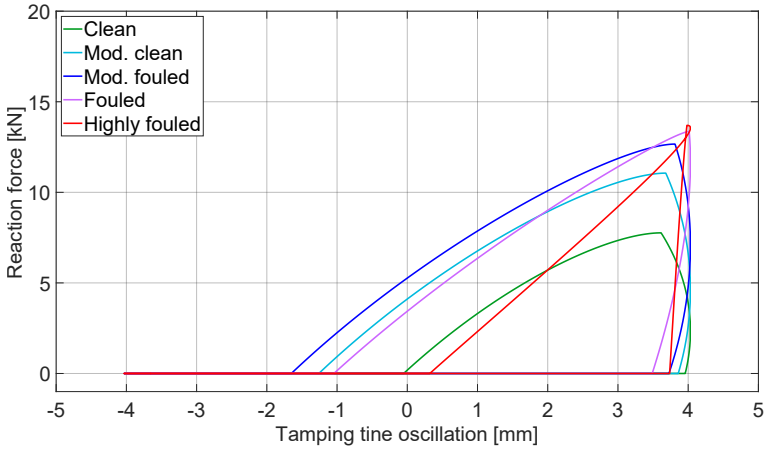

Figure 9.52: Load-displacement curves evaluated in the Figure 9.51, $v_{squeezing}$ = 0.08 m/s, f = 40 Hz

Loading response (Figure 9.53) increases with the progress of ballast fouling and is affected by the excitation frequency, as it increases with the increase of frequency. Loading response values for highly fouled ballast reach far beyond the expected values, which can

Die approbierte gedruckte Originalversion dieser Dissertation ist an der TU Wien Bibliothek verfügbar.
The approved original version of this doctoral thesis is available in print at TU Wien Bibliothek.

be easily observed in the steepness of the load-displacement diagram in Figure 9.52. A slight increase of the loading response with the increase of frequency is expected in each ballast condition, as was proven in Chapter 9.4. This is only true for the first four stages of the fouling process whereas the highly fouled values again do not follow the expected course. Nevertheless, the loading response has once more been confirmed to provide reliable information about the ballast bed condition simulated by the mechanical model, with the exception of highly fouled ballast.

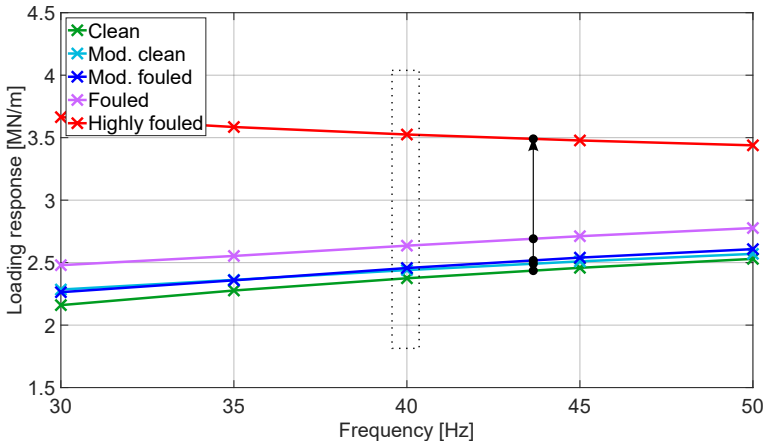

Figure 9.53: Ballast loading response - parameter study

As mentioned before, the unloading response is defined by the shape of the load-displacement curve in the unloading phase and it is the only tamping characteristic that changes from a negative to a positive value between clean and fouled ballast. As can be seen in Figure 9.54, once again the loading response shows expected values for the first two stages of the ballast fouling process. Values in the positive spectrum are again expected to decrease as the line steepness decreases. This is, however, not valid for the change between fouled and highly fouled ballast condition, given that the unloading response values continue to increase. The load-displacement curves showing moderately fouled ballast behavior are the border ones, crossing from a negative to a positive number spectrum (darkblue line, Figure 9.54).

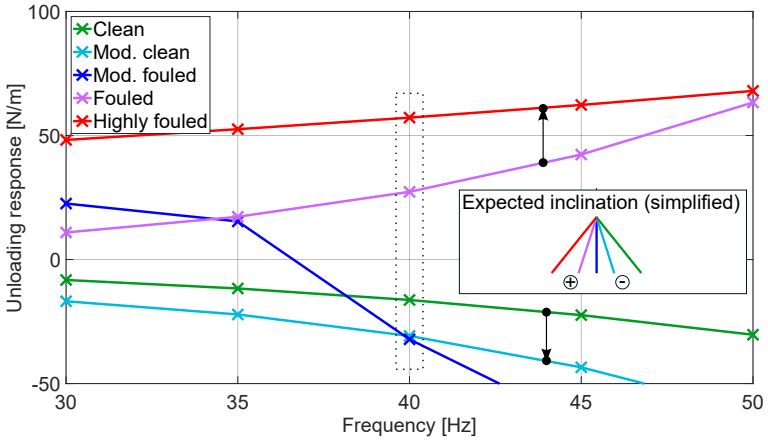

Figure 9.54: Ballast unloading response - parameter study

Die approbierte gedruckte Originalversion dieser Dissertation ist an der TU Wien Bibliothek verfügbar.
The approved original version of this doctoral thesis is available in print at TU Wien Bibliothek.
TU Bibliothek Your knowledge hub WIEN

Increasing frequency leads to a shorter cycle and a shorter contact duration which should cause a shift of the first contact point to the right, further in the positive segment. This exact behavior can be seen in Figure 9.55 for the first three stages of the fouling process.

Similar to the analysis conducted in Chapter 9.4, Figure 9.56 proves that the dependence of the second contact point location on the excitation frequency is also only noticeable at higher stages of ballast fouling. Only a moderate dependence can be observed in moderately clean ballast, and somewhat higher at lower frequency levels of the last two ballast fouling stages, with a maximum deviation between two adjacent velocity values of 0.5 mm.

Once again, the position of both contact points resulting from the highly fouled ballast simulation does not match the expected values, showing that this level of ballast fouling cannot be simulated with the selected parameter set (Table 9.1 and ballast condition determining factor from Table 9.5.

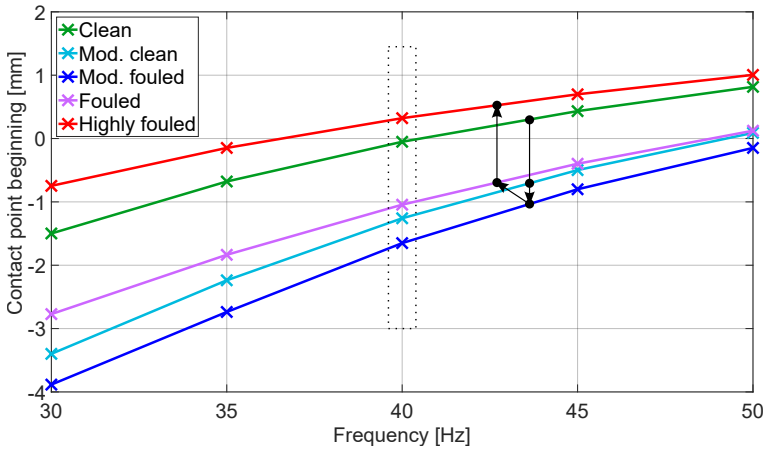

Figure 9.55: Contact point beginning - parameter study

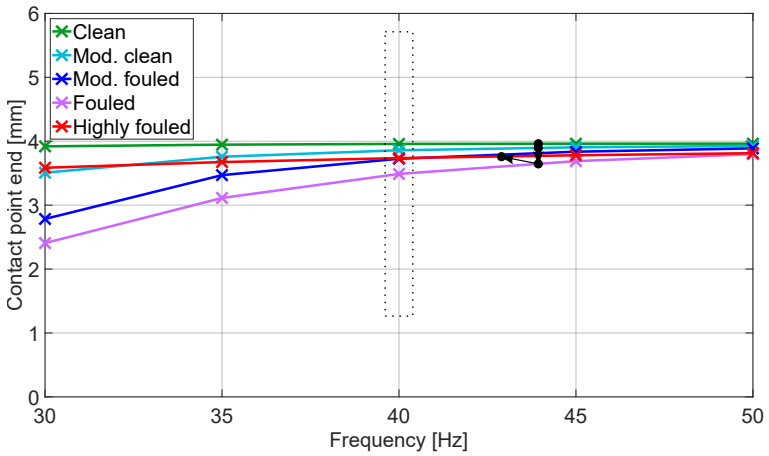

Figure 9.56: Contact point end - parameter study

An increase of frequency decreases the contact duration as well as the contact length. Similar to the results of squeezing velocity variation, Figures 9.57 and 9.58 show that the contact duration between the tamping tine and the ballast matrix is significantly longer in fouled than in clean ballast, for all frequency levels. The rest of the values, however, do not

Die approbierte gedruckte Originalversion dieser Dissertation ist an der TU Wien Bibliothek verfügbar.
The approved original version of this doctoral thesis is available in print at TU Wien Bibliothek.
TU Bibliothek Your knowledge hub WIEN

follow as expected, given that the contact duration increases at first from clean to moderately clean and moderately fouled only to decrease back again for the remaining two ballast conditions, following the same trend in both contact duration (Figure 9.57) and contact length (Figure 9.58). This course of values is considered not reliable for the ballast condition interpretation.

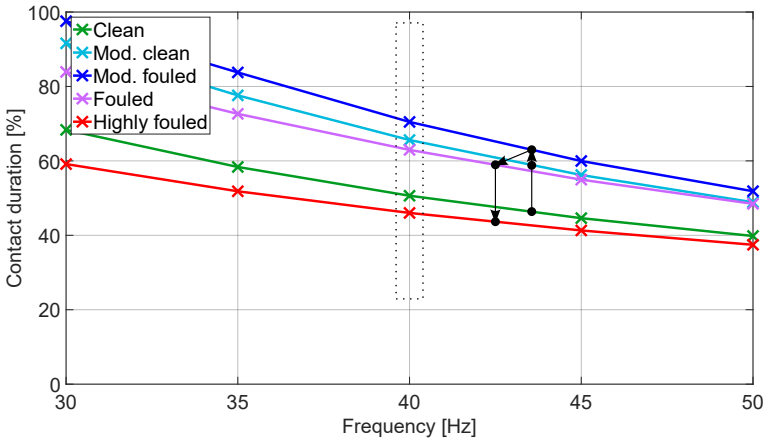

Figure 9.57: Contact duration per cycle - parameter study

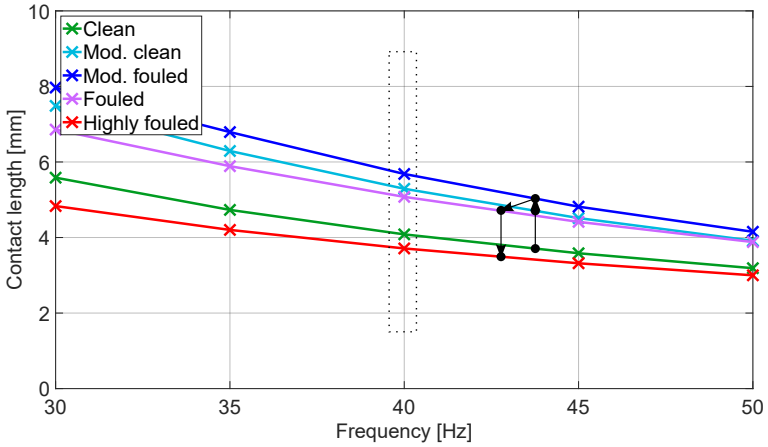

Figure 9.58: Contact length per cycle - parameter study

Validation of the finding regarding the optimal impulse duration of 2 - 4 ms (*Fischer* [59]) can be made by reference to Figure 9.57. If the simulation time is set to 1 s and the excitation frequency to 35 Hz, the duration of a single cycle is 29 ms. Contact duration in clean ballast conditions (at 35 Hz) is approximately 60%, which yields to an contact duration of 17 ms (Figure 9.57). However, results plotted in Figure 9.57 are based on a squeezing velocity of 0.08 m/s, whereas *Fischer* considered a significantly lower velocity of 0.018 m/s. In order to compare results between the mechanical model and conducted research a linear dependence of the contact duration and the squeezing velocity (Figure 9.48) is assumed, resulting in a theoretical contact duration of 3.8 ms (clean ballast, squeezing velocity 0.018 m/s). Even if this values is reduced due to the fact that impulse duration as defined by *Fischer* [59] consist only of the loading phase, the resulting value is still between the proposed limits of 2 - 4 ms.

Die approbierte gedruckte Originalversion dieser Dissertation ist an der TU Wien Bibliothek verfügbar.
The approved original version of this doctoral thesis is available in print at TU Wien Bibliothek.
TU Bibliothek Your knowledge hub WIEN

9.6 Identification of ballast condition

Steps in the research conducted in the scope of this thesis were defined pursuing the following guiding principle:

1. Development of a measuring system, i.e. of a method to measure primarily the force-displacement relationship of the tamping tine and the track ballast matrix.
2. Conducting basic experimental research using the proposed measuring system. Instrumentation of the Dynamic Tamping Express 09-4X E^3 tamping machine and performing several in-situ measurements in order to gain an insight into ballast behavior during track tamping and its response to compaction. Analysis of the data collected by the measuring system and interpretation of fundamental dynamic track ballast processing phenomena. Development of a data processing and analysis algorithm. Deriving the tamping characteristics.
3. Monitoring of tamping process during regular track maintenance. Development of ballast condition determination method based on the measured tamping characteristics.
4. Development of the mechanical model. Calibration of the mechanical model in order to simulate the ballast behavior observed in-situ. Recognizing the elastic spring constant as a parameter that can be varied in order to model all stages of ballast fouling.
5. Conducting result verification and a study of tamping parameters and characteristics.

Every step of the process leads to a common goal: further development of tamping process in railway engineering. The way to a breakthrough in this field leads to the development of condition-based tamping. The cornerstone of doing so is the identification of ballast condition to which the tamping parameters could possibly be adapted. After the measurement data was analyzed, several irrefutable differences were recognized among the derived tamping characteristics of different measurement locations. Most of them can be attributed to the condition of the ballast bed, i.e. to the differences in ballast matrix reaction to the interaction with the tamping tine. Relying on the existing definitions (Chapter 3.2.2) the process of ballast fouling is subdivided into five phases (Table 3.1). Three of these phases were encountered in-situ and "recognized" by the developed ballast condition identification method.

Mechanical model of the tamping tine - ballast matrix interaction was developed in order to provide a possibility to extrapolate from the existing analysis results to the remaining ballast fouling phases. It is also used to provide a theoretical background and a clear definition of ballast physical, soil mechanics properties that change during the process of ballast fouling. Calibration of the model and result verification is conducted based on the analysis results described and discussed in Chapter 6. Given that a high correlation ratio between

Die approbierte gedruckte Originalversion dieser Dissertation ist an der TU Wien Bibliothek verfügbar.
The approved original version of this doctoral thesis is available in print at TU Wien Bibliothek.
TU Bibliothek Your knowledge hub WIEN

the measured and simulated values was established, the model was then utilized to conduct a study on possibly variable tamping parameters and their influence on the tamping characteristics.

Influence of the squeezing velocity, excitation frequency and amplitude on the eight tamping characteristics was investigated. Parameter variation mostly resulted in expected effects on the tamping characteristics. Results presented in Chapter 9.4 confirm that, if ballast parameters remain unchanged and only the tamping parameters are altered, the simulation delivers expected and stable results. Increasing the squeezing velocity prolongs the contact duration and by doing so increases the force and energy levels and has the desired influence on the ballast matrix loading and to a certain extend on the unloading response. Same effect is observed as the excitation amplitude is increased. This is true for the both borderline ballast conditions. All of the observations stated above lead, in adaptation to the parameter study, to a second successful model verification.

Table 9.6: Overview of the decisive tamping characteristics based on variation of both the squeezing velocity and excitation frequency

Condition / Characteristic	Clean	Moderately clean	Moderately fouled	Fouled	Highly fouled
Max. reaction force per cycle	✓	✓	✓	✓	✓
Energy per SM	✓	✓	✓	×	×
Loading response	✓	✓	✓	✓	✓
Unloading response	✓	✓	✓	✓	×
Contact point beginning	✓	✓	✓	×	×
Contact point end	✓	✓	✓	✓	×
Contact duration	✓	✓	✓	×	×
Contact length	✓	✓	✓	×	×

A step further in the parameter study is made in Chapter 9.5, where the condition of the ballast bed is altered in addition to the tamping parameter alteration. The goal of this study is to single out those tamping characteristics that can be defined as decisive in determining the ballast bed condition. An overview of the decisive tamping characteristics based on the variation of both the squeezing velocity and excitation frequency, is given in Table 9.6. The second expected result was to recognize and establish simulation limits. It has been proven that the model can be used to successfully simulate the first three phases of the ballast fouling process defined according to Table 9.5. For the simulations of the clean, moderately clean and moderately fouled ballast bed *all* observed tamping characteristics show expected behavior during variation of both the squeezing velocity and excitation amplitude. In-situ measured values of the tamping characteristics for fouled ballast condition correlate to those simulated by the model in the sense that they are in the "right relationship" to the clean ballast values, but some of the tamping characteristics do not follow as expected when compared to the other three ballast fouling stages. Shape of the load-displacement diagram as well as the maximum reaction force per cycle, loading and unloading response

Die approbierte gedruckte Originalversion dieser Dissertation ist an der TU Wien Bibliothek verfügbar.
The approved original version of this doctoral thesis is available in print at TU Wien Bibliothek.
TU Bibliothek Your knowledge hub WIEN

and the position of the second contact point can be taken as decisive tamping characteristics to indicate fouled ballast condition. Simulation of the highly fouled ballast using the same parameter set and ballast condition determining factor from Table 9.5 is on the border of simulation limits. Only two tamping characteristics, maximum reaction force per cycle and the loading response show the expected values for the last stage of the ballast fouling process. Better adjustment of the parameter set used for the simulation of fouled and highly fouled ballast could provide results that more realistically model the in-situ behavior of these two phases of the ballast fouling process.

Die approbierte gedruckte Originalversion dieser Dissertation ist an der TU Wien Bibliothek verfügbar.
The approved original version of this doctoral thesis is available in print at TU Wien Bibliothek.
TU Bibliothek Your knowledge hub WIEN

Chapter 10

Summary, conclusions and outlook

Within the framework of this research an "in-depth look" at the interaction between the tamping tine and ballast matrix during compaction under the sleeper was made. For the very first time, these two components were investigated on a cycle scale and every single tamping tine oscillation and contact to the ballast matrix was recorded and analyzed. A short summary of the conducted work, as well as of all important results and conclusions is outlined in this chapter. At the very end, the immense potential of the findings is discussed, together with the possibility to implement the gained knowledge towards development of a *Smart tamping tool*.

An overview of track ballast functions and geomechanical properties such as grain distribution, geometry and petrography, followed by the technical requirements and mechanical resistance of both the single grain and grain structure, i.e. ballast matrix, are discussed in the second chapter of the thesis.

The process of ballast aging, i.e. *fouling* (wear and contamination) together with the fouling sources and existing ballast fouling quantification methods are addressed in the third chapter. Well established ballast condition classifications and grading extend from clean, sharp-edged to highly contaminated, refined and worn track ballast at the end of its serviceability. Described methods are subsequently used as a reference for the ballast assessment developed in the thesis. Furthermore, ballast response and degradation assessment by laboratory testing as well as changes of the ballast soil mechanical properties are outlined.

Common practice of restoring initial track geometry with lifting and leveling units, tamping and subsequent compaction and stabilization by means of dynamic track stabilizer is discussed in Chapter 4. An overview of state-of-the-art techniques used in track maintenance is provided in order to grant a theoretical background for the measurements and analysis described in the following chapters. Tamping process is described in detail, the development, methodology and decisive tamping parameters.

Original experimental research carried out within the framework of this thesis is described beginning with Chapter 5. Scientific guiding principle followed states that a reliable method of measuring the force-deformation relationship of the tamping tine - track ballast interaction has to be determined. In order to curtail possible errors and misinterpretations of the data collected, measurements should be conducted as close to the contact point (tamp-

Die approbierte gedruckte Originalversion dieser Dissertation ist an der TU Wien Bibliothek verfügbar.
The approved original version of this doctoral thesis is available in print at TU Wien Bibliothek.
TU Bibliothek Your knowledge hub WIEN

ing tine plate) and as directly as possible. A measurement system implemented directly to the tamping unit is developed especially for this purpose. Once the fundamental phenomena appearing in the course of dynamic track ballast processing have been apprehended, recorded and interpreted, correlations of the recognized regularities are established. This allows for a "step backwards" in the sense of limiting the measurement of machine parameters to signals that are suitable for practical use (e.g. hydraulic squeezing pressure).

Specially developed monitoring system installed to the tamping unit consists primarily of strain gauges that measure the acting forces (reaction and penetration resistance forces) at the tine plate and of tine movement measurement. The latter is accomplished dynamically by accelerometers and "stationary" by a laser range finder that was replaced by angle encoders in later measurement campaigns. This measurement system provides the possibility to conduct a precise observation of the force-deformation relation in-situ. Results are expressed in form of load-displacement diagrams. Load-displacement curves are remarkably suited for the tamping tine - track ballast interaction evaluation. Since neither the reaction force nor the tine displacement can be determined (measured) directly at the contact point, associated sensors are located somewhat further away on the tine shaft and on the upper part of the tamping arm.

It would have also been possible to compensate for the mass inertia forces that are detected during data analysis and that lead to a slight distortion of the load-displacement diagram as well as for the tine bending (elasticity) that leads to a slight overestimation of the tine displacement. Due to sub-optimal quality of the transmitted measurement data (inadequate recording of the "stationary" squeezing displacement), this compensation was omitted in order not to falsify the results by speculative assumptions.

A crucial observation is made based on the shape of load-displacement diagrams. It was for the first time possible to clearly demonstrate that the track ballast is not able to completely follow the retreating tamping tine during dynamic unloading. In other words, the load-displacement diagram provided irrefutable evidence of a periodic loss of contact between the tamping tine and the ballast matrix. A speculative reference to this phenomenon was given by *Fischer* [59] with the term pulse duration, but was never proven by measurement. This contactless condition has a significant influence on ballast processing and compaction given that the load transmitted to the ballast matrix cannot be described as approximately harmonic, but rather as a periodic pulsating load with subsequent loss of contact.

Decisive tamping characteristics that describe the tamping tine - ballast matrix interaction are derived from the load-displacement diagram during the squeezing movement (Figure 5.19): maximum reaction force per cycle, dynamic energy input per cycle (corresponding to the area within the diagram), curve inclination during loading and unloading (could be interpreted as "reaction stiffness") as well as the position of contact points. Analyzed tamping characteristics have been proven as reliable indicators that can be used not only to determine the condition of the ballast bed on-the-spot, but also as an interface for practical modeling of ballast compaction.

Further experiments that usually take place at this point of the research on test tracks under defined boundary conditions with parameter variation far beyond reasonable val-

Die approbierte gedruckte Originalversion dieser Dissertation ist an der TU Wien Bibliothek verfügbar.
The approved original version of this doctoral thesis is available in print at TU Wien Bibliothek.
TU Bibliothek Your knowledge hub WIEN

ues could not take place due to the fact that the test machine had to be used for regular track maintenance. The implemented measuring system was, however, used to monitor and record the tamping process during regular track maintenance (Chapter 6). Collected and analyzed data is compared with the adopted ballast condition determination. Results unmistakably indicate that it is possible to clearly identify the condition of track ballast based on the selected tamping characteristics. Track ballast condition is determined with a form of "blind tasting" in subsequent analysis of measurement data of initially unknown origin. The hit rate is 100%, and it is not only possible to distinguish between fouled and clean ballast, but also to clearly identify intermediate grades. Additional investigation conducted at Graz University of Technology [99] dealt with a statistical comparison of tamping characteristics evaluated from load-displacement diagrams and track condition information collected during routine surveys of the track measurement vehicle and available ground-penetrating radar ballast condition information. An unambiguous correlation was established, which additionally confirmed the technical relevance of the methodology developed within this research.

In Chapter 7, various accompanying experiments conducted as plausibility checks are described. A qualitative description of track ballast dynamic fluidization is carried out in form of in-situ conducted tests (Chapter 7.2). This phenomenon plays a decisive role in clean ballast compaction by both the tamping unit and dynamic track stabilizer. This experimental approach is quite illustrative and valuable in terms of differences verification between the dynamic behavior of clean and fouled track ballast. The second concomitant test (Chapter 7.3) clearly shows the soil mechanical consequences of the proven loss of contact between the tamping tine and ballast matrix. A Fast Fourier Transformation (FFT) analysis conducted on data recorded on a test cross section shows an anti-cyclical synchronized movement of the tamping tines on both sides of the sleeper, resulting in a twice the excitation frequency acting under the sleeper. Single grain crushing strength was investigated in another accompanying test in order to interpret occasionally measured negative peak values of the reaction force detected during the lifting phase of the squeezing process. This allowed the observed phenomenon to be explained by single ballast grains getting "trapped" against the back of the tamping tines. In addition, compression and Ultrasonic Pulse Velocity test are conducted in order to determine if the "entrapment" could trigger particle chipping or attrition.

A numerical simulation of the tamping tine - ballast matrix interaction during the squeezing movement is outlined in Chapter 8. Developed mechanical model is used to conduct detailed parameter studies outlined in Chapter 9. Following the idea that the simulation model should be as simple as possible and yet as complicated as necessary to describe all of the effects measured in-situ, the model was composed of physically plausible elements based on the measurement findings. Tamping unit model depicts both the relative, governed by the dynamic excitation, and absolute motion of the tamping tine governed by the squeezing velocity. It is modeled to the exact geometry of the tine 64 used for the measurements. The dynamic excitation creates a displacement-controlled motion that is presented as the tamping tine oscillation. This motion is superimposed by the "stationary" squeezing motion, i.e. opening and closing of the hydraulic cylinder. In addition, a throttle incorporated into the

Die approbierte gedruckte Originalversion dieser Dissertation ist an der TU Wien Bibliothek verfügbar.
The approved original version of this doctoral thesis is available in print at TU Wien Bibliothek.
TU Bibliothek Your knowledge hub WIEN

squeezing cylinder modeled by a force constraint can be used to simulate force controlled tamping tine motion. Contact conditions are defined by preventing the transfer of tensile forces into the track ballast, resulting in a gap between the tamping tine and the ballast matrix front when loss of contact occurs. Given that the ballast matrix front cannot keep its vertical positions in the contactless phase, ballast grains begin their movement following the tine and filling the void left behind. This movement of the collapsing front was considered as a "gap closing acceleration". Plastic deformation of the ballast matrix in the vicinity of the tamping tine is presented by a "plastic spring" that is compressed in the loading phase but does not expand during unloading, thus modeling the residual plastic deformation. The range of elastic ballast matrix reaction was described using a *Kelvin-Voigt* model that consist of a purely elastic spring and a purely viscous dashpot connected in parallel. Parameters used to calculate the spring stiffness and dashpot coefficient are derived from soil properties (shear modulus, *Poisson's* ratio and ballast density). The two systems (tamping tine and track ballast) are coupled by compatibility conditions (force and displacement) during the contact phase and allowed to move independently when loss of contact occurs until contact is geometrically re-established. Given the predefined tamping parameters (amplitude, frequency, squeezing pressure etc.) and assumed parameters for the ballast matrix description ("gap closing acceleration", plastic and elastic spring constant and dashpot coefficient), simulated load-displacement diagrams can be calculated.

By means of model updating, ballast parameters are adjusted in such a way that the tamping characteristics derived from the load-displacement diagrams calculated in the simulation largely corresponded to those measured in-situ. One of the most important steps forward in the model development was recognizing the elastic spring constant as a parameter that can be varied in order to model all stages of ballast fouling with this simple approach.

Finding that fouled ballast matrix plastic deformation under dynamic loading is lower in comparison to clean ballast in which ballast fluidization can occur also reflects in impressive progress in enhancement of the numerical simulation.

While the parameter set for fouled ballast simulation implied a notable influence of the elastic spring, the same parameter is of significantly less importance for clean ballast, meaning that ballast fluidization is simulated primarily by the viscous dashpot. The aging, i.e. fouling of the ballast, was thus continuously adjustable in the model by adapting the elastic spring constant to the condition of the track ballast. It would not have been difficult to reproduce the load-displacement diagrams observed in-situ more accurately by additional, complex parameter variations, but this was not the desired goal. Quite the contrary, the appeal of simple modeling lies in the physically comprehensible and clearly assignable individual parameters and in the resulting possibility of simple adjustment of ballast condition by alternating only one parameter. By doing so, continuous fouling of the track ballast is simulated, providing significantly higher acquired knowledge resulting from this simple method in comparison to that expected from more complicated procedures.

Finally, in Chapter 9, a parameter study is carried out using the developed mechanical model. One parameter at a time is varied around a standard set of tamping parameters obtained from the measurements, and the effects on the load-displacement curve and its

Die approbierte gedruckte Originalversion dieser Dissertation ist an der TU Wien Bibliothek verfügbar.
The approved original version of this doctoral thesis is available in print at TU Wien Bibliothek.
TU Bibliothek Your knowledge hub WIEN

characteristics are investigated. The excitation amplitude is varied in combination with either the squeezing velocity or the excitation frequency. These three tamping parameters are selected as possible key variables in the future optimization of the tamping process. It can, for example, be observed that the maximum reaction force increases with the increase of amplitude and squeezing velocity (Figure 9.23). The higher the squeezing velocity, the earlier (further in the negative range) the contact point is reached (Figure 9.28).

Regarding the ballast condition, five phases of the fouling process are defined according to the *fouling index* definition and simulated by elastic stiffness variation (Table 9.5), as was defined by model updating. As the progress of ballast fouling advances, it can unmistakably be concluded that the reaction force will increase with both the increase of squeezing velocity (Figure 9.41) and the decrease of frequency (Figure 9.50). Another factor to be considered as a stable and reliable indicator of ballast condition is the loading response - it increases significantly with the progress of ballast fouling (Figure 9.44) and with the increase of frequency (Figure 9.53).

Methodology developed in the scope of this thesis (set-up and evaluation of the load - displacement diagrams) shall be considered as basic research and provide proof of the occurrences that arise during track tamping, such as the loss of contact between the tamping tine and ballast matrix or the measured double excitation frequency under the sleeper (Figure 7.21). On the other hand, same methodology should be used to lead the way to the development of a *Smart tamping tool*, a tamping unit capable of determining the ballast bed condition on-the-spot. Potential for this development has been conclusively proven by measurements conducted during regular track maintenance and by the numerical simulations.

Optimization of the track ballast compaction can hardly be carried out solely based on the methodology developed in the scope of this research. Given that the ballast bed compaction and sleeper settling into the ballast grain structure are not completed after tamping, a final statement on the compaction success immediately after tamping is either not possible or not relevant.

Only after the employment of dynamic track stabilizer that induces dynamic excitation transverse to the track direction the compaction of the track ballast is completed. Otherwise the final ballast compaction is left to be defined by future traffic loads. Accordingly, in the near future the dynamic track stabilizer will also be converted from a compaction device to a measuring device that evaluates the compaction process. Operating principle of track maintenance machines dictates that the optimum final compaction has to be achieved after a single machine employment. This is the reason why often, depending on the working speed of the machine, two dynamic track stabilizers are often arranged one after the other. Given that they influence each other, this does not lead to two completely independent measurements. No conventional tests to determine the compaction success during track tamping exist, except for the indirect measurement of sleeper resistance to lateral displacement. The latter, however, only allows for the compaction success to be established by long-term observation of the track position (defined by deterioration rates) with all associated uncertainties.

Die approbierte gedruckte Originalversion dieser Dissertation ist an der TU Wien Bibliothek verfügbar.
The approved original version of this doctoral thesis is available in print at TU Wien Bibliothek.
TU Bibliothek Your knowledge hub WIEN

This approach does not provide a sufficient basis for short-term in-situ decision making in a sense of condition-based track tamping.

Future development plans lead to a dynamic track stabilizer that also acts as a measuring device during separate employment. Furthermore, in addition to the results from the monitoring system presented in the scope of this thesis, tamping units of several other switch and line tamping machines worldwide have been equipped with similar measuring systems in order to obtain a better data base for measurement analysis according to the principles developed here. This will additionally sharpen the ballast condition definition and condition determination possibilities. Other aspects, such as penetration resistance force, squeezing displacement and lifting values that define the size of the void under the sleeper which is filled with ballast during tamping, will also still be investigated. Described measurements will form a detailed fundamental research on both secondary track and during tamping machine deployment for regular track maintenance.

Measurement system and analysis algorithm presented in this thesis provide the possibility to transform and upgrade the tamping unit from a track maintenance tool into a measuring device. Using this new technology, condition of the ballast bed can be determined in-situ, during track tamping by the tamping unit itself, eliminating the need for additional measurements. Ballast compaction method of both the tamping unit and dynamic track stabilizer can be adapted to the product of ballast condition determination, resulting in an optimization of the ballast life-cycle while increasing the quality of the whole track system and reducing costs by extending maintenance cycles.

For all of the reasons stated above, this thesis fits into the framework of the much more comprehensive project of further development of condition-based optimization of track ballast processing in the course of track maintenance.

Die approbierte gedruckte Originalversion dieser Dissertation ist an der TU Wien Bibliothek verfügbar.
The approved original version of this doctoral thesis is available in print at TU Wien Bibliothek.
TU Bibliothek Your knowledge hub WIEN

Glossary

cycle (German *Vibrationszyklus*) a single oscillation of the tamping tine forward and backwards. Number of cycles per squeezing movement is dependent on the frequency and the duration of the process i.e. squeezing time.

squeezing movement (German *Beistellen*) consists of a certain number of cycles, defined as a closing movement of the tines around the sleeper with the objective of ballast compaction. The movement is initiated when all tamping tines have reached the level 30 mm above nominal squeezing level.

squeezing process (German *Beistellvorgang*) a single tamping process performed on one sleeper, consisting of ballast penetration, squeezing movement, lifting, tamping unit relocation and the section between two squeezing processes.

tamping process (German *Stopfvorgang*) consisting of 1 to 3 squeezing processes, comprises the collective tamping work executed on one sleeper.

tamping process start end the lowering pedal is taken as a dependable signal indicating the start of the tamping process. With a step on the pedal, the machine operator starts the procedure of lowering the tamping unit, thus starting the tamping process. Accordingly, the next pedal signal marks the end of the current process and the start of the following one.

tamping parameters machine parameters such as excitation frequency, amplitude, squeezing velocity, number of insertions etc. that could possibly be altered to match the ballast bed condition encountered in-situ.

tamping characteristics values derived from the load-displacement curves; they result from a chosen set of tamping parameters.

Die approbierte gedruckte Originalversion dieser Dissertation ist an der TU Wien Bibliothek verfügbar.
The approved original version of this doctoral thesis is available in print at TU Wien Bibliothek.
TU Bibliothek Your knowledge hub WIEN

Die approbierte gedruckte Originalversion dieser Dissertation ist an der TU Wien Bibliothek verfügbar.
The approved original version of this doctoral thesis is available in print at TU Wien Bibliothek.

References

[1] ÖNORM EN 1097-1:2011. *Tests for mechanical and physical properties of aggregates - Part 1: Determination of the resistance to wear (micro-Deval)*. 2011.

[2] ÖNORM EN 1097-2:2018. *Tests for mechanical and physical properties of aggregates - Part 2: Methods for the determination of resistance to fragmentation*. 2018.

[3] ÖNORM EN 1097-6:2013. *Tests for mechanical and physical properties of aggregates - Part 6: Determination of particle density and water absorption*. 2013.

[4] EN 12407:2019. *Natural stone test methods - Petrographic examination*. 2019.

[5] ÖNORM EN 12880:2001. *Characterization of sludges - Determination of dry residue and water content*. 2001.

[6] ÖNORM EN 13231-1:2013. *Railway applications - Track - Acceptance of works - Part 1: Works on ballasted track - Plain line, switches and crossings*. 2013.

[7] ÖNORM EN 13346:2001. *Characterization of sludges - Determination of trace elements and phosphorus - Aqua regia extraction methods*. 2000.

[8] ÖNORM EN 13450:2015. *Aggregates for railway ballast*. 2015.

[9] ÖNORM EN 1367-1:2007. *Tests For Thermal And Weathering Properties Of Aggregates - Part 1: Determination Of Resistance To Freezing And Thawing*. 2007.

[10] ÖNORM EN 1367-2:2009. *Tests For Thermal And Weathering Properties Of Aggregates - Part 2: Magnesium sulfate test*. 2009.

[11] ÖNORM EN 1367-3:2005. *Tests For Thermal And Weathering Properties Of Aggregates - Part 3: Boiling test for "Sonnenbrand basalt"*. 2005.

[12] ÖNORM EN 1367-6:2008. *Tests For Thermal And Weathering Properties Of Aggregates - Part 6: Determination of resistance to freezing and thawing in the presence of salt (NaCI)*. 2008.

[13] ÖNORM EN 13848-1:2019. *Railway applications - Track - Track geometry quality - Part 1: Characterisation of track geometry*. 2019.

[14] ÖNORM B 3123-1:1990. *Testing Of Natural Stone; Resistance To Weathering; Principles For Assessment*. 1990.

[15] ÖNORM B 3133:2003. *Rules for the implementation of the ÖNORM EN 13450*. 2003.

[16] British Standard Institution 812:1983. *Methods for sampling and testing of mineral aggregates sands and filters*. 1983.

Die approbierte gedruckte Originalversion dieser Dissertation ist an der TU Wien Bibliothek verfügbar.
The approved original version of this doctoral thesis is available in print at TU Wien Bibliothek.
TU Bibliothek Your knowledge hub WIEN

[17] EN 923-1:1996. *Tests for general properties of aggregates Part 1: Part 1: Methods for sampling*. 1996.

[18] EN 923-3:2004. *Tests for general properties of aggregates Part 3: Procedure and terminology for simplified petrographic description (EN 932-3:1996 + A1:2003)*. 2004.

[19] ÖNORM EN 933-1:2013. *Tests for geometrical properties of aggregates - Part 1: Determination of particle size distribution - Sieving method*. 2013.

[20] ÖNORM EN 933-2:2020. *Tests for geometrical properties of aggregates - Part 2: Determination of particle size distribution - Test sieves, nominal size of apertures*. 2020.

[21] ÖNORM EN 933-3:2012. *Tests for geometrical properties of aggregates - Part 3: Determination of particle shape - Flakiness index*. 2012.

[22] ÖNORM EN 933-4:2008. *Tests for geometrical properties of aggregates - Part 4: Determination of particle shape - Shape index*. 2008.

[23] ÖNORM EN 933-5:2020. *Tests for geometrical properties of aggregates - Part 5: Determination of percentage of crushed particles in coarse and all-in natural aggregates*. 2020.

[24] D. Adam. "Continuous Compaction Control (CCC) with Vibrating Rollers". Doctoral thesis. TU Wien, Faculty of Civil Engineering, Institute of Geotechnics, 1996.

[25] D. Adam. *Grundbau und Bodenmechanik; Studienunterlagen zur Vorlesung*. Institut für Geotechnik, TU Wien, 2019.

[26] B. Antony. "Messung und Beurteilung von Erschütterungen der dynamischen Gleisstabilisation". Master's Thesis. University of Natural Resources and Life Sciences, Vienna, 2015.

[27] F. Auer. *Infrastrukturmanagement*. Vol. 1. Auflage. Hamburg: DVV Media Group GmbH Eurailpress, 2017.

[28] F. Auer. *Kurzbericht: Versuch Design-Stopfen*. Tech. rep. ÖBB, 2003, p. 7.

[29] F. Auer. "Zur Verschleißreduktion von Gleisen in engen Bögen". Doctoral thesis. Graz University of Technology, Institute for Railway Engineering and Transport Economy, 2010.

[30] F. Auer and B. Antony. "Tracking the Dynamic Track Stabiliser - results of large-scale investigations provide a better understanding of its effectiveness". *Rail Engineering International Edition* 3 (2019), p. 3.

[31] F. Auer, R. Hauke, and R. Wenty. "High-Tech-Stopfaggregate: Gleislageverbesserung, Prozesssicherheit und Zuverlässigkeit im Fokus der Weiterentwicklung". *Der Eisenbahningenieur EI* 11 (2015).

[32] H. Bach. "Evaluation of attrition tests for railway ballast". Doctoral thesis. Graz University of Technology, Institute for Railway Engineering and Transport Economy, 2013.

Die approbierte gedruckte Originalversion dieser Dissertation ist an der TU Wien Bibliothek verfügbar.
The approved original version of this doctoral thesis is available in print at TU Wien Bibliothek.
TU Bibliothek Your knowledge hub WIEN

[33] O. Barbir, D. Adam, F. Kopf, J. Pistrol, and F. Auer. "Development of condition-based tamping process in railway engineering". In: *Proceedings of the XVI Danube - European Conference on Geotechnical Engineering, Skopje, R. Macedonia*. 2018, p. 6.

[34] O. Barbir, D. Adam, F. Kopf, J. Pistrol, and F. Auer. "In-situ measurements and a semi-analytical approach to ballast bed modelling during compaction". In: *Geotechnical Challenges in Karst, ISRM Specialised Conference / Međunarodna konferencija 8. Savjetovanje Hrvatskog geotehničkog društva, Omiš – Split, Croatia*. 2019.

[35] O. Barbir, B. Antony, C. Koczwara, F. Auer, D. Adam, F. Kopf, and J. Pistrol. "Automation of the tamping process". In: *VÖBU Fair & 13. Österreichische Geotechniktagung, Wien*. 2022.

[36] O. Barbir, J. Pistrol, F. Kopf, D. Adam, F. Auer, and B. Antony. "Gleisstopfen: Modellierung der Stopfpickel-Schotterbett-Interaktion". *Geotechnik* 42.4 (2019), pp. 219–228. DOI: https://doi.org/10.1002/gete.201900019.

[37] O. Barbir and B. Štimac. "Influence of gravity on granular flow in silo centrifuge models in comparison with Beverloo equation". Master's Thesis. University of Natural Resources and Life Sciences, Vienna, Institute of Geotechnics, 2013, p. 153.

[38] R. Bayerhofer. "Gleisstopfverfahren im Eisenbahnwesen - Stand der Technik". Master's Thesis. TU Wien, Faculty of Civil Engineering, Institute of Geotechnics, 2018.

[39] N. J. F. Bostanudin. "Computational Methods for Processing Ground Penetrating Radar Data". Doctoral thesis. University of Portsmouth, School of Engineering, 2013.

[40] S. F. Brown and E. T. Selig. "The Design of Pavement and Rail Track Foundations". *Cyclic Loading of Soils: from Theory to Design* (1991), pp. 249–305.

[41] Y. S. Chae, W. C. Au, and Y. C. Chiang. "Determination of Dynamic Shear Modulus of Soils from Static Strength". *International Conferences on Recent Advances in Geotechnical Earthquake Engineering and Soil Dynamics* 7 (1981).

[42] K. B. Chary, L. P. Sarma, K. J. Prasanna Lakshmi, N. A. Vijaya Kumar, V. Naga Lakshmi, and M. V. M. S. Rao. "Evaluation of Engineering Properties of Rock Using Ultrasonic Pulse Velocity and Uniaxial Compressive Strength". In: *Proceedings of the National Seminar on Non-Destructive Evaluation, Dec. 7 - 9, 2006, Hyderabad*. National Geophysical Research Institute, Hyderabad, 2006.

[43] L. Chin-Diew, D. Murthy, and M. Xie. "Weibull Distributions and Their Applications". *Springer Handbook of Engineering Statistics* (Feb. 2006), pp. 63–78. DOI: 10.1007/978-1-84628-288-1_3.

[44] S. M. Chrismer. "Considerations of factors affecting ballast performance". *American Railway Engineering Association (AREA) Bulletin 704, AAR Research and Test Department* WP-110 (1985), pp. 118–150.

[45] E. Coenraad. *Modern Railway Track*. MRT Productions, 2001, p. 654. ISBN: 90-800324-3-3.

Die approbierte gedruckte Originalversion dieser Dissertation ist an der TU Wien Bibliothek verfügbar.
The approved original version of this doctoral thesis is available in print at TU Wien Bibliothek.
TU Bibliothek Your knowledge hub WIEN

[46] G. Cook. "Rankine and the theory of earth pressure". *Geotechnique* (1951). ISSN: 17517656. DOI: 10.1680/geot.1951.2.4.271.

[47] M. Dafert. "Erkenntnisse aus Messungen am dynamischen Gleisstabilisator". Master's Thesis. TU Wien, Faculty of Civil Engineering, Institute of Geotechnics, 2019.

[48] M. Dafert, F. Kopf, J. Pistrol, and D. Adam. *On site measurements at Retz/Unternalb; DGS-F 2.0*. Tech. rep. DGS Research Project. 2021.

[49] O. Danquah, G. S. Ghataora, and M. P. N. Burrow. "The effect of ballast fouling on the hydraulic conductivity of the rail track". In: *Proceedings of the XV Danube - European Conference on Geotechnical Engineering, Vienna, Austria*. September. 2014, pp. 9–11. DOI: 10.13140/2.1.4515.4242.

[50] V. A. Diyaljee. "Effects of stress history on ballast deformation". *Journal of Geotechnical Engineering, ASCE* 113.8 (1987), pp. 909–914.

[51] *Dynamic track stabilisation: Principle and effect*. [Online; accessed 30-August-2021]. 2021. URL: https://www.plassertheurer.com/en/machines-systems/stabilisation-consolidation/perfecting-track-maintenance.

[52] A. Ebrahimi, J. M. Tinjum, and T. B. Edil. "Deformational behavior of fouled railway ballast". *Canadian Geotechnical Journal* 52.3 (2015), pp. 344–355. ISSN: 12086010. DOI: 10.1139/cgj-2013-0271.

[53] J. Eisenmann. "Schienenkopfbeanspruchung - Vergleich zwischen Theorie und Praxis". *Eisenbahntechnische Rundschau (ETR)* (1967), pp. 355–361.

[54] American Railway Engineering and Maintenance-of-Way Association. *Manual for Railway Engineering*. 2011.

[55] E. O. Eze. "Variability in Rock Strength Prediction using Ultrasonic Pulse Velocity". *Advanced Materials Research, Trans Tech Publications, Switzerland* 367 (2011), pp. 581–587. ISSN: 1662-8985. DOI: 10.4028/www.scientific.net/AMR.367.581.

[56] F. Feldman and D. Nissen. "Alternative testing method for the measurement of ballast fouling: percentage void contamination". In: *Cost efficient railways through engineering: CORE 2002: Conference on railway engineering, Wollongong, New South Wales, Australia*. 2002, p. 11.

[57] J. F. Ferellec, R. Perales, V. H. Nhu, M. Wone, and G. Saussine. "Analysis of compaction of railway ballast by different maintenance methods using DEM". *EPJ Web of Conferences* 140 (Jan. 2017), p. 15032. DOI: 10.1051/epjconf/201714015032.

[58] J. E. Vidueira Ferreira, M. T. Silva Pinheiro, W. R. Santos dos Santos, and R. da Silva Maia. "Graphical representation of chemical periodicity of main elements through boxplot". *Educación química* 27.3 (2016).

[59] J. Fischer. "Einfluss von Frequenz und Amplitude auf die Stabilisierung von Oberbauschotter". Doctoral thesis. Graz University of Technology, Institute for Railway Engineering and Transport Economy, 1983.

Die approbierte gedruckte Originalversion dieser Dissertation ist an der TU Wien Bibliothek verfügbar.
The approved original version of this doctoral thesis is available in print at TU Wien Bibliothek.
TU Bibliothek Your knowledge hub WIEN

[60] J. Fischer. *Untersuchungen zur Schotterqualität - Seminar über Gleishaltung*. Borlänge, Schweden. 1989.

[61] S. Fontul, A. Paixão, M. Soll, and L. Pajewski. "Railway Track Condition Assessment at Network Level by Frequency Domain Analysis of GPR Data". *Remote Sensing* 10.4 (2003), pp. 157–167. DOI: 10.3390/rs10040559.

[62] H. Gräbe and J. S. Maree. "The use of a dynamic track stabiliser to improve track maintenance and the optimisation of track tamping". In: *Proceedings of the 6th International Heavy Haul Association Conference at Cape Town, South Africa*. 1997.

[63] A. H. Hammam and M. Eliwa. "Comparison between results of dynamic & static moduliof soil determined by different methods". *Housing and Building National Research Center, HBRC Journal* 9 (2012), pp. 144–149.

[64] F. Hansmann, B. Antony, S. Offenbacher, O. Barbir, and M. Landgraf. "Smart tamping - The fundamentals of tamping". In: *Proceedings of the AREMA 2020 virtual conference & expo*. 2020.

[65] F. Hansmann and O. Barbir. "Schotterzustandsbeschreibung 2.0". *IGU Webinar* online (2020).

[66] H. Hertz. *Über die Berührung fester elastischer Körper*. Vol. 1. Leipzig: Gesammelte Werke, 1895.

[67] W. G. Holtz and H. J. Gibbs. "Triaxial shear tests on pervious gravelly soils". *Journal of the Soil Mechanics and Foundations Division, ASCE* 12 (2012), pp. 867.1–867.22.

[68] E. Y. Huang. *An improved particle index test for the evaluation of geometric characteristics of aggregates*. Tech. rep. Michigan Highway Research Project No. 86546. 1965.

[69] H. Huang, E. Tutumluer, and W. Dombrow. "Laboratory Characterization of Fouled Railroad Ballast Behavior". *Transportation Research Record Journal of the Transportation Research Board* 2117 (2009), pp. 93–101. DOI: 10.3141/2117-12.

[70] Q. Huang, W. Zhou, G. Ma, T.T. Ng, and K. Xu. "Experimental and numerical investigation of Weibullian behavior of grain crushing strength". *Geoscience Frontiers* 11.2 (2020), pp. 401–411. ISSN: 1674-9871. DOI: https://doi.org/10.1016/j.gsf.2019.07.007.

[71] B. Indraratna, D. Ionescu, and D. Christie. "Shear Behavior of Railway Ballast Based on Large-Scale Triaxial Tests". *Journal of Geotechnical and Geoenvironmental Engineering* 124.5 (1998), pp. 439–449.

[72] B. Indraratna, J. Lackenby, and D. Christie. "Effect of confining pressure on the degradation of ballast under cyclic loading". *Géotechnique* 55.4 (2005), pp. 325–328. DOI: DOI:10.1680/geot.55.4.325.65490.

[73] B. Indraratna, N. T. Ngo, S. Nimbalkar, and C. Rujikiatkamjorn. "Two Decades of Advancement in Process Simulation Testing of Ballast Strength, Deformation and Degradation" (2018). DOI: 10.1520/STP160520170029.

Die approbierte gedruckte Originalversion dieser Dissertation ist an der TU Wien Bibliothek verfügbar.
The approved original version of this doctoral thesis is available in print at TU Wien Bibliothek.
TU Bibliothek Your knowledge hub WIEN

[74] B. Indraratna, S. S. Nimbalkar, and C. Rujikiatkamjorn. "Stabilisation of ballast and subgrade with geosynthetic grids and drains for rail infrastructure". In: 2011.

[75] B. Indraratna and W. Salim. "Deformation and degradation mechanics of recycled ballast stabilised with geosynthetics". *Soils and fundations, Japanese Geotechnical Society* 43.4 (2003), pp. 35–46.

[76] B. Indraratna, W. Salim, and C. Rujikiatkamjorn. *Advanced Rail Geotechnology - Ballasted Track*. CRC Press, 2011. ISBN: 9780429212918. DOI: 10.1201/b10861.

[77] B. Indraratna, L. Su, and C. Rujikiatkamjorn. "A new parameter for classification and evaluation of railway ballast fouling". 326 (2011), pp. 322–326. DOI: 10.1139/T10-066.

[78] B. Indraratna, Q. Sun, and S. S. Nimbalkar. "Observed and predicted behaviour of rail ballast under monotonic loading capturing particle breakage". *Canadian Geotechnical Journal* 52 (2015), pp. 73–86.

[79] B. Indraratna, J. S. Vinod, and J. Lackenby. "Influence of particle breakage on the resilient modulus of railway ballast". *Geotechnique* 59.7 (2008), pp. 643–646. DOI: 10.1680/geot.2008.T.005.

[80] D. Ionescu. "Ballast Degradation and Measurement of Ballast Fouling". *7th Railway Engineering Proceedings* 2 (2005), pp. 12–18.

[81] R. Janardhanam and C. S. Desai. "Three-dimensional testing and modeling of ballast". *Journal of Geotechnical Engineering, ASCE* 109.6 (1983), pp. 783–796.

[82] T. G. Johns, S. G. Sampath, J. C. Bell, and K. B. Davies. *Engineering Analysis of Stresses in Railroad Rails - Final report*. Tech. rep. Office of Research and Development Washington, D.C. 20590. 1981.

[83] E. Kapogianni and M. Sakellariou. "Application of Particle Image Velocimetry (PIV) and Digital Image Correlation (DIC) techniques on scaled slope models". In: *International Research Journal of Engineering and Technology (IRJET)*. 2017.

[84] R. Katzenbach and G. Festag. "Material behaviour of dry sand under cyclic loading". *Cyclic Behaviour of Soils and Liquefaction Phenomena, Proc. Of CBS 2004* (July 2004), pp. 153–158. DOI: 10.1201/9781439833452.ch19.

[85] H. G. Kempfert and Y. Hu. "Measured dynamic loading of railway underground". In: *Proceedings of the 11th Pan-American Conference on Soil Mechanics and Geotechnical Engineering, Brazil*. 1999, pp. 843–847.

[86] E. Klotzinger. "Der Oberbauschotter Teil 1: Anforderungen und Beanspruchung". *ETR. Eisenbahntechnische Rundschau* 01 (2008), pp. 34–41.

[87] J. Kolbuszewski and M. Frederick. "The significance of particle shape and size on the mechanical behaviour of granular materials". In: *Proceedings of the European Conference on the Soil Mechanics and Foundation Engineering*. 1963, pp. 253–263.

[88] C. Kuttelwascher and M. Zuzic. "Track ballast in Austria : Parts 1. - 3." *Rail Infrastructure* (), pp. 63–66.

Die approbierte gedruckte Originalversion dieser Dissertation ist an der TU Wien Bibliothek verfügbar.
The approved original version of this doctoral thesis is available in print at TU Wien Bibliothek.
TU Bibliothek Your knowledge hub WIEN

[89] D. Li, D. Read, H. Thompson, T. Sussmann, and R. McDaniel. "Evaluation of Ground Penetrating Radar Technologies for Assessing Track Substructure Conditions". In: *Proceedings of the American Railway Engineering and Maintenance of Way Association Annual Conference, Orlando, Florida*. Sept. 2010.

[90] D. Li and L. Wong. "The Brazilian Disc Test for Rock Mechanics Applications: Review and New Insights". *Rock Mechanics and Rock Engineering* 46 (2012). DOI: 10.1007/s00603-012-0257-7.

[91] N. D. Marachi, C. K. Chan, and H. B. Seed. "Evaluation of Properties of Rockfill Materials". *Journal of the Soil Mechanics and Foundations Division* 98 (1972), pp. 95–114.

[92] R. J. Marsal. "Large Scale Testing of Rockfill Materials". *Journal of the Soil Mechanics and Foundations Division* 93 (1967), pp. 7–43.

[93] J. Mathews. "Investigation of granular flow using silo centrifugemodels". Doctoral thesis. University of Natural Resources and Life Sciences, Vienna, Institute of Geotechnics, 2013.

[94] M. Moaveni, Y. Qian, H. Boler, D. Mishra, and E. Tutumluer. "Investigation of Ballast Degradation and Fouling Trends using Image Analysis". *Civil-Comp Proceedings* 104 (2014), pp. 1–15. ISSN: 17593433.

[95] P. Nagy. "Deep vibro compaction". Doctoral thesis. TU Wien, Faculty of Civil Engineering, Institute of Geotechnics, 2018.

[96] Y. Nakata, Y. Kato, M. Hyodo, A.F.L. Hyde, and H. Murata. "One-Dimensional Compression Behaviour of Uniformly Graded Sand Related to Single Particle Crushing Strength". *Soils and Foundations* 41.2 (2001), pp. 39–51. ISSN: 0038-0806. DOI: https://doi.org/10.3208/sandf.41.2_39.

[97] ÖBB. *Optimierung der Schotterqualität, Sondersitzung, Ergänzung zur 10. Sitzung Erhaltungsstrategie*. Tech. rep. 2009.

[98] ÖBB. *Technical conditions of delivery for track ballast BH70*. 2007.

[99] S. Offenbacher. "Ballast Evaluation as Part of Tamping Measures". Master's Thesis. Graz University of Technology, Institute for Railway Engineering and Transport Economy, 2019.

[100] *On Track at the Strathspey Railway - Stone Blowing*. [Online; accessed 16-August-2021]. 2017. URL: http://ontrackatstrathspey.blogspot.com/2017/11/stone-blowing-kinchurdy-18th-19th.html.

[101] N. Özkaya, D. Leger, D. Goldsheyder, and M. Nordin. *Fundamentals of Biomechanics: Equilibrium, Motion, and Deformation - Mechanical Properties of Biological Tissues*. Springer International Publishing, 2017, pp. 361–387. ISBN: 978-3-319-44738-4. DOI: 10.1007/978-3-319-44738-4_15.

[102] A. Pais and E. Kausel. "Approximate formulas for dynamic stiffnesses of rigid foundations". *Soil Dynamics and Earthquake Engineering* 7.4 (1988).

Die approbierte gedruckte Originalversion dieser Dissertation ist an der TU Wien Bibliothek verfügbar.
The approved original version of this doctoral thesis is available in print at TU Wien Bibliothek.
TU Bibliothek Your knowledge hub WIEN

[103] A. Panjamani. "Study of Ballast Fouling in Railway Track Formations" (2014). DOI: 10.1007/s40098-012-0006-6.

[104] X. Perpinya. *Reliability and Safety in Railway*. 2012. ISBN: 9535104519.

[105] J. Pistrol. "Compaction with oscillating rollers". Doctoral thesis. TU Wien, Faculty of Civil Engineering, Institute of Geotechnics, 2016.

[106] R. du Plooy and H. Gräbe. "Characterisation of rigid polyurethane foam-reinforced ballast through cyclic loading box tests". *Journal of the South African Institution of Civil Engineers* 59.2 (2017), pp. 2–10. DOI: 10.17159/2309-8775/2017/v59n2a1.

[107] H. B. Poorooshasb, I. Holubec, and A. N. Sherbourne. "Yielding and flow of sand in triaxial compression: Part I." *Canadian Geotechnical Journal* 3.4 (2014), pp. 179–190.

[108] V. J. Popov. *Kontaktmechanik und Reibung*. 2nd ed. Springer, 2010.

[109] Y. Qian, H. Boler, M. Moaveni, E. Tutumluer, Y. M. A. Hashash, and J. Ghaboussi. "Characterizing ballast degradation through Los Angeles abrasion test and image analysis". *Transportation Research Record* 2448 (2014), pp. 142–151. ISSN: 21694052. DOI: 10.3141/2448-17.

[110] Y. Qian, E. Tutumluer, Y. M. A., H., and J. Ghaboussii. "Effects of ballast degradation on permanent deformation behaviour from large-scale triaxial tests" (2014), pp. 1–5.

[111] G. P. Raymond. *Stresses and deformation in railway track*. Tech. rep. Ontario, Canada: Canadian Institute of Guided Ground Transport Report, Queen's University at Kingston, 1976, p171.

[112] G.P. Raymond. "Research of Railroad Ballast Specification and Evaluation". *Transportation Research Record 1006* (1985), p. 27.

[113] The Office for Research and International Union of Railways Experiments. *Stresses in the rails, the ballast and the formation resulating from traffic loads*. Question D71, Ultrecht, Holland. 1970.

[114] K. Rießberger and R. Wenty. "40 Years of "Dynamic Track Stabilisation". *Eisenbahn-Ingenieur-Kalender – EIK; Jahrbuch für Schienenverkehr & Technik* (2015), pp. 55–76.

[115] R. Roberts and J. Rudy. "Railroad Ballast Fouling Detection Using Ground Penetrating Radar – A New Approach Based on Scattering from Voids" (2006), pp. 1–8.

[116] M. A. Roenfeldt. "A study of mechanical degradation of a coarse aggregate subject to repeated loading". Master's Thesis. University of Missouri-Rolla, Civil, Architectural and Environmental Engineering, 1980, p. 77.

[117] E. T. Selig and J. M. Waters. *Track geotechnology and substructure management*. Thomas Telford, 1994. ISBN: 0727720139.

[118] E. T. Selig, T. S. Yoo, and C. M. Panuccio. *Mechanics of Ballast Compaction Volume 1: Technical Review of Ballast Compaction and Related Topics*. Tech. rep. U.S. Department of Transportatio, Federal Railroad Administration, Washington DC, 1982.

Die approbierte gedruckte Originalversion dieser Dissertation ist an der TU Wien Bibliothek verfügbar.
The approved original version of this doctoral thesis is available in print at TU Wien Bibliothek.
TU Bibliothek Your knowledge hub WIEN

[119] N. C. Sharda and A. Choudhary. *Mechanised Tamping and Stabilisation*. Tech. rep. Pune, India: Indian Railways Institute of Civil Engineering, 2016.

[120] M. J. Shenton. "Deformation of railway ballast under repeated loading conditions". In: *Railroad Track Mechanics and Technology - Proceedings of a symposium held at Princeton University*. 1975, pp. 387–404.

[121] T. D. Stark, S. Wilk, R. Bruzek, B. Hugh, and T. R. Sussman. "Fouled Ballast Definitions and Parameters". In: 2016, pp. 1–7. ISBN: 9780791849675. DOI: 10.1115/JRC2016-5725.

[122] H. E. Stewart. "The prediction of track performance under dynamic traffic loading". PhD thesis. Department of civil engineering, University of Massachusetts Amherst, 1982.

[123] Y. Sun. "Effect of particle angularity and size distribution on the deformation and degradation of ballast under cyclic loading". Doctoral thesis. University of Wollongong, Faculty of engineering and informational sciences, 2017.

[124] T. R. Theodore Sussmanna, E. T. Selig, and J. P. Hyslip. "Railway track condition indicators from ground penetrating radar". *NDT&E International* 36 (2003), pp. 157–167.

[125] N. Tennakoon, B. Indraratna, and S.S. Nimbalkar. "Impact of Ballast Fouling on Rail Tracks Quantification of fouling". *Second International Conference on Railway Technology: Research, Development and Maintenance* March 2015 (2014), pp. 1–11. ISSN: 17593433. DOI: 10.4203/ccp.104.122.

[126] K. Terzaghi. *Theoretical Soil Mechanics*. 1943. DOI: 10.1002/9780470172766.

[127] *The L.A. Abrasion Test Method*. [Online; accessed 04-August-2021]. 2021. URL: https://www.globalgilson.com/blog/aggregate-abrasion-testing-part-2-the-la-abrasion-test.

[128] Plasser & Theurer. *Die Technologie des dynamischen Gleisstabilisierens. Allgemeine Einführung - Funktionsprinzip - Arbeitsanleitung*. Tech. rep. 2010.

[129] W. Thielicke and R. Sonntag. "Particle Image Velocimetry for MATLAB: Accuracy and enhanced algorithms in PIVlab". *Journal of Open Research Software 9* 1.334 (2021), p. 12. DOI: http://doi.org/10.5334/jors.334.

[130] N. H. Thom and S. F. Brown. "The significance of particle shape and size on the mechanical behaviour of granular materials". In: *Proceedings of the 14th Australian Road Research Board Conference*. Vol. 14. 1988, pp. 94–100.

[131] *Trackopedia - Working aggregates*. [Online; accessed 03-September-2021]. 2017. URL: https://www.trackopedia.info/encyclopedia/railway-vehicles/working-aggregates.

[132] Test Standard CRD-C119-53 U.S. Army Corps of Engineers. *Method of test for flat and elongated particles in coarse aggregate*. 1953.

Die approbierte gedruckte Originalversion dieser Dissertation ist an der TU Wien Bibliothek verfügbar.
The approved original version of this doctoral thesis is available in print at TU Wien Bibliothek.
TU Bibliothek Your knowledge hub WIEN

[133] B. A. Vallerga, H. B. Seed, C. L. Monismith, and R. S. Cooper. "Effect of shape, size and surface roughness of aggregate particles on the strength of granular materials". *ASTM STP* 212 (1957), pp. 63–76.

[134] G. Vasconcelos, P. B. Lourenco, C.S.A. Alves, and J. Pamplona. "Prediction of the mechanical properties of granites by Ultrasonic Pulse Velocity and Schmidt hammer hardness" (2007).

[135] H. Wadell. "Sphericity and roundness of rock particles". *The Journal of Geology* 41.3 (1933), pp. 310–331.

[136] S. Wadud. "Deformation and degradation aspects of ballast and constitutive modelling under cyclic loading". PhD thesis. Department of civil engineering, University of Wollongong, 2004.

[137] *Wikipedia - Railroad tie*. [Online; accessed 24-March-2020]. 2020. URL: https://en.wikipedia.org/w/index.php?title=Railroad_tie&oldid=945041735.

[138] *Wikipedia - Track (rail transport)*. [Online; accessed 23-March-2020]. 2020. URL: https://en.wikipedia.org/w/index.php?title=Track_(rail_transport)&oldid=946222379.

[139] J. P. Wolf. "Simple physical models for foundation dynamics". *Developments in Geotechnical Engineering* (1998). ISSN: 01651250. DOI: 10.1016/S0165-1250(98)80004-7.

[140] L. Zaayman. *The basic principles of mechanised track maintenance*. 2016. ISBN: 978-3-200-05145-4.

[141] S. Zaidan and A. Al Ani. "Determination of The Weibull Modulus by Electrical Breakdown and Mechanical Strength for Soda Lime Glass". *IOP Conference Series: Materials Science and Engineering* 757 (Apr. 2020), p. 012061. DOI: 10.1088/1757-899X/757/1/012061.

[142] H. Zimmermann. *Die Berechnung des Eisenbahnoberbaues*. W. Ernst & Sohn, Berlin, 1941.

Die approbierte gedruckte Originalversion dieser Dissertation ist an der TU Wien Bibliothek verfügbar.
The approved original version of this doctoral thesis is available in print at TU Wien Bibliothek.
TU Bibliothek Your knowledge hub WIEN

List of Tables

2.1 Categories for maximum values of LA_{RB} as a result of the LAA Test defined by EN 13450 [8] . . . 22
2.2 Categories for maximum values of resistance to impact SZ_{RB} as a result of impact test method defined by EN 13450 [8] . . . 23
2.3 Categories for maximum values of resistance to wear M_{DERB} as a result of Micro-Deval test defined by EN 13450 [8] . . . 24
2.4 Ballast bed modulus for different subsoils [86] . . . 41

3.1 Fouled ballast classification based on the Fouling Index FI [80] . . . 49
3.2 Fouled ballast classification based on the Percentage of Fouling (Percentage Passing), adapted from [76] . . . 50
3.3 Fouled ballast classification based on the Percentage Void Contamination, adapted from [76] . . . 51
3.4 Fouled ballast classification based on the Relative Ballast Fouling Ratio (adapted from [76]) . . . 53
3.5 Comparison between PVC, Percentage of Fouling and Relative Ballast Fouling Ratio $R_{b\text{-}f}$ [77]. For example, a value of 10 would characterize a clean ballast according to PVC, moderately fouled according to Percentage of Fouling and moderately clean according to $R_{b\text{-}f}$ . . . 56

6.1 Ballast bed condition and locations of conducted measurements . . . 120
6.2 Calculated and analyzed tamping characteristics . . . 129
6.3 Tamping characteristics measured in different ballast conditions . . . 130
6.4 Characteristic values for the four tamping characteristics in both reference ballast conditions. Values for the *clean* ballast are presented for the first and second squeezing movement respectively . . . 131
6.5 Ranges of characteristic values for the four tamping characteristics in both ballast conditions for all analyzed locations . . . 131
6.6 Characteristic values of the selected tamping characteristics. Track tamping conducted 6 weeks after track reconstruction . . . 132

7.1 Approximate pile dimensions prior to and after the test . . . 160
7.2 Results of tensile strength tests conducted on eight ballast grains . . . 180

Die approbierte gedruckte Originalversion dieser Dissertation ist an der TU Wien Bibliothek verfügbar.
The approved original version of this doctoral thesis is available in print at TU Wien Bibliothek.
TU Bibliothek Your knowledge hub WIEN

7.3 Results of UPV tests conducted on eight ballast grains 184

8.1 Mechanical model parameters, notations and symbols 188
8.2 Tamping unit geometry and constant input parameters 192

9.1 Tamping unit geometry and constant input parameters 236
9.2 Comparison of the values for the four tamping characteristics between the in-situ and mechanical modeling results for *clean* ballast conditions. Values for the in-situ measurements in clean ballast conditions are presented as range for both first and second squeezing movement 238
9.3 Comparison of the values for the four tamping characteristics between the in-situ and mechanical modeling results for *moderately clean* ballast conditions 238
9.4 Comparison of the values for the four tamping characteristics between the in-situ (range) and mechanical modeling results for *fouled* ballast conditions . 238
9.5 Ballast bed condition classification 239
9.6 Overview of the decisive tamping characteristics based on variation of both the squeezing velocity and excitation frequency 275

Die approbierte gedruckte Originalversion dieser Dissertation ist an der TU Wien Bibliothek verfügbar.
The approved original version of this doctoral thesis is available in print at TU Wien Bibliothek.
TU Bibliothek Your knowledge hub WIEN

List of Figures

2.1 Principle of track structure: cross section (adapted from *Selig and Waters* [117]) 6
2.2 Principle of track structure: longitudinal section (adapted from *Selig and Waters* [117]) 6
2.3 Definition of roundness, adapted from *Sun* [123] 9
2.4 Influence of particle shape on the ballast mechanical properties [117] 11
2.5 Particle size distribution of crushed dolomite ballast samples with different gradation parameter n (a), and the influence of sample gradation on: friction angle (b), density (c), elastic shear stiffness (d) and permeability (e) (*Thom and Brown* [130] and *Indraratna et al.* [76]) 14
2.6 Track settlement after tamping: a) in plain scale, b) in semi-logarithmic scale (adapted from *Shenton* [120] and *Indraratna et al.* [76]) 15
2.7 Parent rock classification for ballast aggregate selection 17
2.8 Delivery quantities of different railway ballast rock types during the year 2008 according to the Austrian Federal Railways (ÖBB) [97] 19
2.9 Grain size distribution curves of railway ballast. Solid lines indicate the lower and upper limits; the dashed line delineates the tolerance limit [97] . 20
2.10 Los Angeles testing drum - test kinematics and impact [127] 21
2.11 Overview and comparison of mean values and scattering of coefficients for different ballast rock types (adapted from [88]) 24
2.12 Ballast behavior under cyclic loading: a) showing the maximum and minimum deviator stress; b) representation of strains under cyclic load application (ε_p - plastic strain, ε_r - resilient or recoverable strain); c) decrease of volume representing ballast compaction (adapted from [117] and [79]) . . . 27
2.13 Resilient modulus under partial unloading and stress reversal conditions (adapted from [117]) 28
2.14 Effect of grain size on ballast resilient modulus (ksi = 6.894 MPa, psi = 6.894 kPa) (adapted from [81]) 28
2.15 Schematic presentation of ballast grain fracture test (adapted from [76]) . . . 30
2.16 Characteristic tensile strength determined by single particle crushing tests (modified from [75]) 31
2.17 Ultrasonic Pulse Velocity test on a single ballast grain 32
2.18 Rail profile types 33

Die approbierte gedruckte Originalversion dieser Dissertation ist an der TU Wien Bibliothek verfügbar.
The approved original version of this doctoral thesis is available in print at TU Wien Bibliothek.

2.19 Implemented rail joints [138] . . . 34
2.20 Different sleeper materials [137] . . . 35
2.21 Wheel-rail contact according to the *Hertzian* theory (modified from [82]) . . 38
2.22 Contact distribution between wheel and rail according to *Eisenmann* (modified from [45]) . . . 39
2.23 Conversion of the cross-sleeper track in a theoretical longitudinal sleeper track (s - track gauge) [86] . . . 42
2.24 Individual force paths in the ballast bed (modified from [26]) . . . 43

3.1 Critical ballast fouling phases (adapted from [69] and [86]) . . . 46
3.2 Hydraulic action on ballast and sleepers [117] . . . 47
3.3 Size distribution curves showing ballast conditions with Fouling Index FI from clean to highly fouled given by Equation 3.3a, adapted from [117] . . . 49
3.4 Ballast fouling phases, classification by Relative Ballast Fouling Index (adapted from [49]) . . . 52
3.5 Ballast Breakage Index determination [77] . . . 53
3.6 Comparison of Percentage of Fouling and Relative Ballast Fouling Ratio to the Fouling Index, adapted from [77] . . . 55
3.7 Stress-strain and volumetric behavior of fresh and recycled ballast under monotonic loading (adapted from [76]) . . . 57
3.8 Particle breakage, comparison of fresh and recycled ballast (adapted from [76]) 58
3.9 Gradation properties of granite ballast material (adapted from [109]) . . . 58
3.10 Gradations of granite ballast changing with LA abrasion drum turns (adapted from [109]) . . . 59
3.11 Repeated load triaxial test results for permanent deformation accumulation [110] . . . 60
3.12 Settlement of fresh and recycled ballast under cyclic loading (25 ton/axle, 15 Hz), modified from [76] . . . 61
3.13 Zones of effect of confining pressure on ballast particle breakage [76] . . . 62

4.1 Schematic survey of maintenance and renewal methods [45] . . . 66
4.2 Definition of principal track geometry parameters according to the EN 13848-1:20191 [13] (adapted from [47]). Coordinate system: x - track direction, y - sleeper direction, z - vertical . . . 68
4.3 Theoretical track condition deterioration curve (adapted from [140]) . . . 69
4.4 Tamping machine *Dynamic 09-3X* (©*Plasser & Theurer*) . . . 72
4.5 Tamping unit lowered into work position (©*Plasser & Theurer*) . . . 72
4.6 Tamping units [131] . . . 73
4.7 Low-wear tamping tine in optimized shape (©*Plasser & Theurer*) . . . 73
4.8 Lifting and levelling units [131] . . . 74
4.9 Ballast compaction and elevation in dependence on excitation frequency (adapted from [59]) . . . 75

Die approbierte gedruckte Originalversion dieser Dissertation ist an der TU Wien Bibliothek verfügbar.
The approved original version of this doctoral thesis is available in print at TU Wien Bibliothek.
TU Bibliothek Your knowledge hub WIEN

4.10 Track settlement in dependence on vibration amplitude [31] 76
4.11 Tamping machines (©*Plasser & Theurer*) 78
4.12 Comparison of conventional and design overlift tamping methods and the influence of "track memory" (modified from [28]) 79
4.13 Different stoneblowing principles 80
4.14 Schematic presentation of the stoneblowing principle [76] 80
4.15 First production version - DTS 42 N [114] 81
4.16 The principle of Dynamic Track Stabilization: (1) variable unbalance, (2) induced horizontal vibrations, (3) hydraulic cylinder, (4) vertical load [51] . 82
4.17 Ballast bed compaction - effect of tamping and dynamic track stabilization [51] 82

5.1 Tamping machine *Dynamic Tamping Express 09-4X* E^3 (©*Plasser & Theurer*) . 86
5.2 Tamping unit and the proposed sensor positions 87
5.3 Expected simplified load – displacement curve showing a single tamping tine oscillation 88
5.4 Expected simplified load – displacement curve showing a single tamping tine oscillation and the simplified approach to ballast matrix response calculation during the both contact phases 90
5.5 Tamping unit and tine array of the *Dynamic Tamping Express 09-4X* E^3 track tamping machine 92
5.6 Exact position of the applied sensors on the tamping unit of *Dynamic Tamping Express 09-4X* E^3: strain gauges (red), accelerometers (blue), squeezing distance measurement (green), pressure measurement (yellow) (©*Plasser & Theurer*) 93
5.7 Tamping unit 3 - applied sensors 93
5.8 Total tamping tine motion and the influence of squeezing velocity 94
5.9 Result of integration of oscillation velocity (black) to oscillation displacement (green) and the calculated moving mean value function (red) for offset removal. Data set segment shows the tamping tine oscillation in the air prior to ballast penetration 95
5.10 Tine oscillation velocity and displacement as a result of the double integration of the measured accelerometers. Data set segment shows the tamping tine oscillation in the air prior to ballast penetration 96
5.11 Tine oscillation velocity and displacement as a result of the double integration of the measured accelerometers over 0.1 seconds with highlighted one cycle. Data set segment shows the tamping tine oscillation in the air prior to ballast penetration 97
5.12 Validation of the laser range finder measurements 98
5.13 Plausibility check of the laser range finder measurements 99
5.14 Tamping process subdivision (©*Plasser & Theurer*) 99
5.15 Overview of the tamping and squeezing process subdivision and component parts color code 101

Die approbierte gedruckte Originalversion dieser Dissertation ist an der TU Wien Bibliothek verfügbar.
The approved original version of this doctoral thesis is available in print at TU Wien Bibliothek.
TU Bibliothek Your knowledge hub WIEN

5.16 Three consecutive tamping processes and signals used for the tamping process subdivision. Start and end time of a single process are obtained from the lowering pedal signal given by the machine operator, presented by a red line . . . 102
5.17 Subdivision of a double tamping process performed on one sleeper - ballast penetration (green), squeezing movement (red) and lifting the tamping unit (blue) . . . 103
5.18 Subdivision of a double tamping process performed on one sleeper - ballast penetration (green), squeezing movement (red) and lifting the tamping unit (blue) . . . 104
5.19 Simplified load – displacement curve showing a single tamping tine oscillation and the seven obtained tamping characteristics . . . 108
5.20 Examples of the load-displacement curves during different phases of a squeezing process. Three consecutive cycles and the total inclination (green line) of the thickest curve are displayed . . . 111
5.21 Influence of amplitude on the pulse duration [59] . . . 113
5.22 Display of the tamping tine deflection and its influence on the tine motion behavior . . . 115

6.1 Locations of recorded track maintenance conducted by the *Dynamic Tamping Express 09-4X* E^3 in Austria. Locations with *clean* ballast conditions are presented in green, *moderately clean* in blue and *fouled* conditions in red color 119
6.2 Examples of tamping process in overview. Presented are the consumed energy per cycle (subdivided into phases: ballast penetration - green, squeezing movement - red, lifting - blue) [Nm] and per tamping process [kJ], frequency (raw and smooth) [Hz], lowering position of the tamping unit [mm] (green line), pressure in the hydraulic cylinder [bar] (pink line), position of the lowering pedal (dashed line) and the reaction force [kN], respectively, for all three measured ballast bed conditions . . . 125
6.3 Comparison of characteristic load-displacement curves for three different ballast bed conditions . . . 127
6.4 Characteristic load-displacement curves for three different ballast conditions 128
6.5 Overview of all tamping characteristics presented in Table 6.3 and comparison between ballast conditions . . . 130
6.6 Ranges of values for the four tamping characteristics and comparison between ballast conditions for all analyzed locations . . . 132
6.7 Comparison of characteristic load-displacement curves for different ballast conditions, adapted from [58] . . . 134
6.8 Symmetric and asymmetric dataset distributions and the corresponding box plots, adapted from [58] . . . 135
6.9 Maximum reaction force per cycle of two consecutive squeezing movements (SM) of a double tamping process conducted in *clean* ballast bed conditions 137

Die approbierte gedruckte Originalversion dieser Dissertation ist an der TU Wien Bibliothek verfügbar.
The approved original version of this doctoral thesis is available in print at TU Wien Bibliothek.
TU Bibliothek Your knowledge hub WIEN

6.10 Energy per cycle of two consecutive squeezing movements (SM) of a double tamping process conducted in *clean* ballast bed conditions 138
6.11 Loading response of the ballast matrix per cycle of two consecutive squeezing movements (SM) of a double tamping process conducted in *clean* ballast bed conditions 139
6.12 Start of contact in every cycle of two consecutive squeezing movements (SM) of a double tamping process conducted in *clean* ballast bed conditions 139
6.13 Cylinder pressure in every cycle of two consecutive squeezing movements (SM) of a double tamping process conducted in *clean* ballast bed conditions 140
6.14 Maximum reaction force per cycle during one squeezing movement of a single tamping process conducted on one sleeper in *moderately clean* ballast conditions 141
6.15 Energy per cycle during one squeezing movement of a single tamping process conducted on one sleeper in *moderately clean* ballast conditions 142
6.16 Loading response of the ballast matrix per cycle during one squeezing movement of a single tamping process conducted on one sleeper in *moderately clean* ballast conditions 142
6.17 Start of contact in every cycle during one squeezing movement of a single tamping process conducted on one sleeper in *moderately clean* ballast conditions 143
6.18 Cylinder pressure in every cycle during one squeezing movement of a single tamping process conducted on one sleeper in *moderately clean* ballast conditions 143
6.19 Maximum reaction force per cycle during one squeezing movement of a single tamping process conducted on one sleeper in *fouled* ballast conditions 144
6.20 Energy per cycle during one squeezing movement of a single tamping process conducted on one sleeper in *fouled* ballast conditions 145
6.21 Loading response of the ballast matrix per cycle during one squeezing movement of a single tamping process conducted on one sleeper in *fouled* ballast conditions 146
6.22 Start of contact in every cycle during one squeezing movement of a single tamping process conducted on one sleeper in *fouled* ballast conditions 146
6.23 Cylinder pressure in every cycle during one squeezing movement of a single tamping process conducted on one sleeper in *fouled* ballast conditions 147
6.24 Squeezing movement, waterfall diagrams – showing selected stacked consecutive load–displacement curves in different ballast conditions 149
6.25 Squeezing movement, heat maps – showing selected stacked consecutive load–displacement curves in different ballast conditions 151
6.26 Penetration resistance force during every cycle of two consecutive ballast penetrations of a double tamping process conducted on one sleeper in *clean* ballast conditions 152

Die approbierte gedruckte Originalversion dieser Dissertation ist an der TU Wien Bibliothek verfügbar.
The approved original version of this doctoral thesis is available in print at TU Wien Bibliothek.
TU Bibliothek Your knowledge hub WIEN

6.27 Penetration resistance force during every cycle of a single tamping process conducted on one sleeper in *moderately clean* ballast conditions 153
6.28 *Fouled* ballast bed depth profile 153
6.29 Penetration resistance force during every cycle of a single tamping process conducted on one sleeper in *fouled* ballast conditions 154
6.30 Calculation of squeezing velocity in a double squeezing process from the displacement measurement 155
6.31 Comparison of squeezing velocity and maximum reaction force per cycle in different ballast conditions 156

7.1 Loosely bedded ballast sample moves to a denser bedding due to ballast fluidization (contraction). Extremely dense ballast sample goes into a somewhat looser bedding when subjected to fluidization (dilatancy) 157
7.2 Excess pressure (hydrostatic pressure on the grain structure) significantly reduces or prevents ballast fluidization entirely 158
7.3 Wave transmission in ballast bed, during fluidization through a loose bedding (left) and following the fluidization through a dense bedding (right) . 158
7.4 Ballast fluidization testing in-situ 159
7.5 *Fast Fourier Transformation* of the accelerations measured by all four sensors in y direction 161
7.6 Absolute and static acceleration measured by all four accelerometers 162
7.7 Detail showing measurement results of accelerometer 2 163
7.8 Description of PIV vector calculation [37] 165
7.9 PIV analysis - Settings and parameters 166
7.10 Examples of single images extracted from the video recording used for the PIV analysis 166
7.11 Histograms showing average single grain velocities in both directions during tamping unit employment 167
7.12 Histograms showing velocity magnitudes recorded during tamping unit employment 168
7.13 Velocity field resulting from tamping unit employment 168
7.14 Heat map showing velocity magnitudes of the highlighted area recorded during the tamping process 169
7.15 Histograms showing average single grain velocities in both directions during DTS employment 170
7.16 Histograms showing velocity magnitudes recorded during during DTS employment 170
7.17 Velocity field resulting from DTS employment 171
7.18 Heat map showing velocity magnitudes of the highlighted area recorded during DTS employment 171
7.19 Exact position of the sensors on the Unimat 09-4x4/4S DTS and in the track (adapted from [48]) 173

Die approbierte gedruckte Originalversion dieser Dissertation ist an der TU Wien Bibliothek verfügbar.
The approved original version of this doctoral thesis is available in print at TU Wien Bibliothek.
TU Bibliothek Your knowledge hub WIEN

7.20 Accelerations in all three directions (x_o, y_o and z_o) and the pressure P_o, measured under the sleeper at the bottom edge of the ballast bed. Squeezing process subdivision color code: ballast penetration (green), squeezing movement (red), lifting (blue) 174
7.21 *Fast Fourier Transformation* of the accelerations plotted in Figure 7.20 for both squeezing processes 174
7.22 Tamping tine array of the Tamping machine *Dynamic Tamping Express 09-4X E*^{3}, showing the dynamic motion direction of single tamping tines in a cycle context 175
7.23 Example of a double tamping process with high reaction forces (framed in a red rectangle) measured during the lifting phase of both squeezing processes. Squeezing process component parts color code: ballast penetration (green), squeezing movement (red), lifting (blue) 177
7.24 Tamping tine array of the Tamping machine *Dynamic Tamping Express 09-4X E*^{3}, showing the position of a single "trapped" ballast grain 178
7.25 Single grain compression test on three grains of fine-grained granite 179
7.26 Effect of particle size (d is defined as the distance between two plates at failure) on single particle tensile strength 181
7.27 Ballast particle breakage as a result of conducted compression tests 181
7.28 Examples of single grain compression test on two particles 182
7.29 Determination of the *Weibull* modulus 183
7.30 Single particle crushing strength of fine-graded granite samples and the survival probability curve 183
7.31 Relation between UPV and granite tensile strength (extended from [134]) . . 185
7.32 Comparison of tensile strength values from UPV and compression tests on single ballast grains 185

8.1 Mechanical model of the tamping unit lowered into work position 191
8.2 Mechanical model of the tamping unit during squeezing movement [36] . . 192
8.3 Angle of rotation β around the bearing M, angular velocity $\dot{\beta}$ and angular acceleration $\ddot{\beta}$ during 3.5 cycles, f = 35 Hz, $v_{squeezing}$ = 0 m/s 194
8.4 Tamping tine oscillation x_{tine}, velocity $\dot{x}_{tine}$ and acceleration $\ddot{x}_{tine}$ during 3.5 cycles, f = 35 Hz, $v_{squeezing}$ = 0 m/s 194
8.5 Tamping tine oscillation x_{tine} during both tamping unit operating phases T1 and T2, f = 35 Hz, $v_{squeezing}$ = 0.05 m/s 195
8.6 Ballast matrix model with its three components 198
8.7 Disk on surface of half-space with truncated semi-infinite cone for vertical translation rotated in 90° to model the ballast matrix-tamping tine interaction in the tamping tine movement direction x (adapted from [105] and [139]) 199
8.8 Variation of shear modulus and shear wave velocity of clayey sand fouled ballast with Percentage of fouling (modified from [76]) 205

Die approbierte gedruckte Originalversion dieser Dissertation ist an der TU Wien Bibliothek verfügbar.
The approved original version of this doctoral thesis is available in print at TU Wien Bibliothek.
TU Bibliothek Your knowledge hub WIEN

8.9 Stiffness of the elastic spring k_e [MN/m] and the dashpot coefficient c_e [kNs/m] in dependence of the shear modulus . . . 205
8.10 Selective determination of plastic and elastic deformation proportion based on a model test conducted with a curved contact surface (modified from [24]) 207
8.11 Influence of the ballast matrix model plastic stiffness k_p on the shape of load-displacement curves, G_d = 20 MN/m^2, k_e and c_e given by Equations 8.42a and 8.42b . . . 208
8.12 Ballast motion in form of a wedge at an angle of $45° + \varphi/2$ to the horizontal behind the tamping tine contact plate . . . 209
8.13 Boundaries of zone of plastic equilibrium under the sleeper . . . 210
8.14 Calculation of the gap closing acceleration a_{gc} . . . 211
8.15 Ballast matrix model during the loading process . . . 212
8.16 Ballast matrix model force F and both constitutive force components F_{ke} and F_{ce} (Equation 8.56) over several cycles . . . 213
8.17 Progress of the force F in the ballast matrix model in all three operating phases as well as its dependence on the tamping unit model force P . . . 213
8.18 Compressed ballast matrix during the loading process . . . 214
8.19 Ballast matrix during the unloading process . . . 215
8.20 Compressed ballast matrix during the unloading process . . . 216
8.21 Ballast matrix model deformations in all three operating phases and the influence of the gap closing acceleration . . . 217
8.22 Ballast matrix during the withdraw phase . . . 217
8.23 Tamping tine and ballast matrix model movement during all three phases over several cycles (detail) . . . 218
8.24 An overview (flowchart) of operating phases an phase transition conditions 219
8.25 Energy consumption calculation over three cycles in both tamping unit model operating phases . . . 220
8.26 Energy consumption per cycle over 35 cycles (simulation time) . . . 221
8.27 Load-displacement curve obtained from the simulation presented together with both force components F_{ke} and F_{ce} . . . 222
8.28 Force components F_{ke} and F_{ce} plotted against the *Kelvin-Voigt* model deformation . . . 223
8.29 Influence of the squeezing velocity on the form of the load-displacement curves and the contact points . . . 224
8.30 Constitutive components of the force F . . . 225
8.31 Elastic deformation x_e and the rate of increase of deformation in the *Kelvin-Voigt* model $\dot{x}_e$ . . . 226
8.32 Influence of the shear modulus G_d on the shape of the load-displacement curves and the compaction energy (k_p = 3 MN/m, k_e and c_e given by Equations 8.42a and 8.42b) . . . 227

Die approbierte gedruckte Originalversion dieser Dissertation ist an der TU Wien Bibliothek verfügbar.
The approved original version of this doctoral thesis is available in print at TU Wien Bibliothek.
TU Bibliothek Your knowledge hub WIEN

8.33 Influence of the ballast matrix model elastic stiffness k_e on the shape of the load-displacement curves and the compaction energy (G_d = 20 MN/m^2, k_p = 3 MN/m, c_e given by Equation 8.42b) . . . 228
8.34 Characteristic load-displacement curves for different ballast conditions as a result of mechanical modeling. G_d = 20 MN/m^2, $v_{squeezing}$ = 0.1 m/s, k_p = 3 MN/m . . . 230
8.35 Ballast matrix model system response progress plotted over a load-displacement diagram for clean ballast conditions . . . 233
8.36 Ballast matrix model system response of one cycle for different ballast conditions . . . 233
8.37 Detail of the ballast matrix model system response of one cycle for different ballast conditions with characteristic points . . . 234
8.38 Mechanical model for ballast penetration . . . 234

9.1 Comparison of characteristic load-displacement curves for different ballast conditions . . . 237
9.2 Ballast matrix model components - forces and impulse of force per component 240
9.3 Impulse of force components in the loading phase displayed over three cycles 241
9.4 Impulse of force in the elastic part of the ballast matrix model for different ballast conditions . . . 241
9.5 Clean ballast - variation of the squeezing velocity and excitation amplitude and their influence on tamping characteristics. Points plotted on the x axis display maximum tine elongation in both moving directions . . . 243
9.6 Maximum reaction force per cycle - study of tamping characteristics . . . 244
9.7 Energy per squeezing movement - study of tamping characteristics . . . 244
9.8 Ballast loading response - study of tamping characteristics . . . 245
9.9 Ballast unloading response - study of tamping characteristics . . . 245
9.10 Contact point beginning - study of tamping characteristics . . . 246
9.11 Contact point end - study of tamping characteristics . . . 246
9.12 Contact duration per cycle - study of tamping characteristics . . . 247
9.13 Contact length per cycle - study of tamping characteristics . . . 247
9.14 Clean ballast - variation of the excitation frequency and amplitude and their influence on tamping characteristics. Points plotted on the x axis display maximum tine elongation in both moving directions . . . 248
9.15 maximum reaction force per cycle - study of tamping characteristics . . . 249
9.16 Energy per squeezing movement - study of tamping characteristics . . . 249
9.17 Ballast loading response - study of tamping characteristics . . . 250
9.18 Ballast unloading response - study of tamping characteristics . . . 250
9.19 Contact point beginning - study of tamping characteristics . . . 251
9.20 Contact point end - study of tamping characteristics . . . 251
9.21 Contact duration per cycle - study of tamping characteristics . . . 252
9.22 Contact length per cycle - study of tamping characteristics . . . 252

Die approbierte gedruckte Originalversion dieser Dissertation ist an der TU Wien Bibliothek verfügbar.
The approved original version of this doctoral thesis is available in print at TU Wien Bibliothek.
TU Bibliothek Your knowledge hub WIEN

9.23 Fouled ballast - variation of the squeezing velocity and excitation amplitude and their influence on tamping characteristics. Points plotted on the x axis display maximum tine elongation in both moving directions 253
9.24 Maximum reaction force per cycle - study of tamping characteristics 254
9.25 Energy per squeezing movement - study of tamping characteristics 254
9.26 Ballast loading response - study of tamping characteristics 255
9.27 Ballast unloading response - study of tamping characteristics 255
9.28 Contact point beginning - study of tamping characteristics 256
9.29 Contact point end - study of tamping characteristics 256
9.30 Contact duration per cycle - study of tamping characteristics 257
9.31 Contact length per cycle - study of tamping characteristics 257
9.32 Fouled ballast - Variation of the excitation frequency and amplitude and the influence on the taming characteristics. Points plotted on the x axis display maximum tine elongation in both moving directions 258
9.33 Maximum reaction force per cycle - study of tamping characteristics 259
9.34 Energy per squeezing movement - study of tamping characteristics 259
9.35 Ballast loading response - study of tamping characteristics 260
9.36 Ballast unloading response - study of tamping characteristics 260
9.37 Contact point beginning - study of tamping characteristics 261
9.38 Contact point end - study of tamping characteristics 261
9.39 Contact duration per cycle - study of tamping characteristics 262
9.40 Contact length per cycle - study of tamping characteristics 262
9.41 Maximum reaction force per cycle - parameter study 264
9.42 Energy per squeezing movement - parameter study 265
9.43 Load-displacement curves evaluated in the Figure 9.42, $v_{squeezing} = 0.08$ m/s, $f = 35$ Hz 265
9.44 Ballast loading response - parameter study 266
9.45 Ballast unloading response - parameter study 266
9.46 Contact point beginning - parameter study 267
9.47 Contact point end - parameter study 267
9.48 Contact duration per cycle - parameter study 268
9.49 Contact length per cycle - parameter study 268
9.50 Maximum reaction force per cycle - parameter study 270
9.51 Energy per squeezing movement - parameter study 270
9.52 Load-displacement curves evaluated in the Figure 9.51, $v_{squeezing} = 0.08$ m/s, $f = 40$ Hz 270
9.53 Ballast loading response - parameter study 271
9.54 Ballast unloading response - parameter study 271
9.55 Contact point beginning - parameter study 272
9.56 Contact point end - parameter study 272
9.57 Contact duration per cycle - parameter study 273
9.58 Contact length per cycle - parameter study 273

Die approbierte gedruckte Originalversion dieser Dissertation ist an der TU Wien Bibliothek verfügbar.
The approved original version of this doctoral thesis is available in print at TU Wien Bibliothek.
TU Bibliothek Your knowledge hub WIEN

A.1 Laboratory test results of ballast samples taken in Eisenstadt on the 30.05.2016 - general information 316
A.2 Laboratory test results of ballast samples taken in Eisenstadt on the 30.05.2016 - general information 317
A.3 Laboratory test results of ballast samples taken in Eisenstadt on the 30.05.2016 - particle size distribution, content of fines 318
A.4 Laboratory test results of ballast samples taken in Eisenstadt on the 30.05.2016 - gross density, impact-attrition strength 319

Die approbierte gedruckte Originalversion dieser Dissertation ist an der TU Wien Bibliothek verfügbar.
The approved original version of this doctoral thesis is available in print at TU Wien Bibliothek.
TU Bibliothek Your knowledge hub WIEN

Die approbierte gedruckte Originalversion dieser Dissertation ist an der TU Wien Bibliothek verfügbar.
The approved original version of this doctoral thesis is available in print at TU Wien Bibliothek.

List of abbreviations and symbols

Abbreviations and other symbols

B1, B2, B3	ballast matrix operating phases
BBI	Ballast Breakage Index [%]
CCC	Continuous compaction control
CLAHE	Contrast Limited Adaptive Histogram Equalisation
DTS	Dynamic track stabilizer
FFT	Fast Fourier transformation
FI	Fouling Index [%]
IQR	interquartile range
MDZ	Mechanized maintenance train
PIV	Particle image velocimetry
PSD	Particle Size Distribution plot
PVC	Percentage Void Contamination [%]
SM	squeezing movement
T1, T2	tamping unit operating phases
UPV	Ultrasonic Pulse Velocity
VC	Void Contaminant Index [%]
ÖBB	Austrian Federal Railways

Greek symbols

α_4	angle between l_2 and l_3 when the tamping tine is in vertical position [rad]

Die approbierte gedruckte Originalversion dieser Dissertation ist an der TU Wien Bibliothek verfügbar.
The approved original version of this doctoral thesis is available in print at TU Wien Bibliothek.
TU Bibliothek Your knowledge hub WIEN

β	angle of rotation (around M) [rad]
$\ddot{\beta}$	angular acceleration [rad/s^2]
$\dot{\beta}$	angular velocity [rad/s]
η	*Zimmermann*'s influencing factor [/]
ν	ballast *Poisson's* ratio [/]
ω	angular frequency [rad/s]
ρ	ballast density [kg/m^3]
σ	characteristic tensile stress [kN/m^2]
$\sigma'_1, \sigma'_2, \sigma'_3$	principal effective stresses [kPa]
σ_f	characteristic particle tensile strength at failure [kN/m^2]
θ'	bulk effective stress in the loaded phase calculated as the sum of the three principal effective stresses at maximum loading [MPa]
υ_W, υ_R	*Poisson*'s ratios the the wheel and rail [/]
ε_N	permanent strain after N loading cycles [%]
ε_r	recoverable (resilient) axial strain during triaxial unloading [%]

Latin symbols

$\ddot{l}_4$	acceleration or rate of change of $\dot{l}_4$ [m/s^2]
$\ddot{x}_{ballast}$	ballast matrix acceleration [rad/s^2]
$\ddot{x}_{tine}$	tamping tine acceleration [rad/s^2]
Δq	difference between q_{max} and q_{min} [kPa]
Δt	time step [s]
$\Delta x, \Delta \dot{x}$	single time step values of observed state variables [red], [rad/s]
$\dot{l}_4$	velocity or rate of change of the length l_4 [m/s]
$\dot{x}_e$	rate of increase of deformation in the *Kelvin-Voigt* model [rad/s]
$\dot{x}_{ballast}$	ballast matrix velocity [rad/s]
$\dot{x}_{tine}$	tamping tine velocity [rad/s]
A	contact area between two curved elastic bodies such as wheel and rail head [mm^2]

Die approbierte gedruckte Originalversion dieser Dissertation ist an der TU Wien Bibliothek verfügbar.
The approved original version of this doctoral thesis is available in print at TU Wien Bibliothek.
TU Bibliothek Your knowledge hub WIEN

a, b	half length and width of tamping tine-area [m]
A_0	surface area of a massless circular foundation (Cone model) [m^2]
A_1	half supporting sleeper surface [m^2]
a_e, b_e	major and minor axes of the contact ellipse A [kN]
a_i	tamping tine amplitude [m]
A_s	surface of the assumed longitudinal beam/sleeper [m^2]
a_s	length of the assumed longitudinal beam/sleeper, equal to the sleeper spacing [m]
A_x	area at depth x (Cone model) [m^2]
a_{gc}	gap closing acceleration [m/s^2]
b_1	half supporting sleeper width [m]
B_g	Index of Particle Breakage [%]
b_s	width of the assumed longitudinal beam/sleeper [m]
b_{UPV}	length/width of the sample [m]
C, K	constant coefficients for the spring and the dashpot (Cone model) [/]
C_b	ballast bed coefficient [/]
C_c	coefficient of curvature [/]
c_e	dashpot coefficient *Kelvin-Voigt* model [Ns/m]
c_p	P-wave or compressional wave
C_u	coefficient of uniformity [/]
d	particle diameter [m]
d_p	displacement due to rail-wheel contact caused by the wheel loads transferred to the rail head [mm]
d_{10}	grain diameter corresponding to 10% passing by weight [mm]
d_{30}	grain diameter corresponding to 30% passing by weight [mm]
d_{60}	grain diameter corresponding to 60% passing by weight [mm]
e	amplitude of excitation [m]
E^*	equivalent system stiffness [MPa]

Die approbierte gedruckte Originalversion dieser Dissertation ist an der TU Wien Bibliothek verfügbar.
The approved original version of this doctoral thesis is available in print at TU Wien Bibliothek.
TU Bibliothek Your knowledge hub WIEN

E_W, E_R	moduli of elasticity of the wheel and rail [MPa]
F	force in the ballast matrix [N]
f	excitation frequency [Hz]
F_c	diametral compressive force [kN]
F_f	diametral compressive force at failure [kN]
F_N	acting normal force on the contact area A [kN]
F_P	fractured particles [/]
F_p	preload force in the ballast model when switching from unloading to loading [N]
F_w	acting effective wheel force [kN]
$F_{elastic}$	force in the ballast matrix elastic [N]
$F_{plastic}$	force in the ballast matrix plastic [N]
F_{sp}	force acting on a single particle embedded in a soil matrix [kN]
G	ballast shear modulus [N/m^2]
G_d	ballast dynamic shear modulus [N/m^2]
h_4	distance l_4 – M (lever) [m]
I_M	tamping arm moment of inertia around bearing M [kgm^2]
J	Impulse of force [Ns]
$J_{elastic}$	Impulse of force, elastic [Ns]
$J_{plastic}$	Impulse of force, plastic [Ns]
K_1, K_2	soil constants determined from laboratory tests [/]
k_e	elastic spring rate/stiffness *Kelvin-Voigt* model [N/m]
k_f	coefficient of permeability [m/s]
k_p	plastic spring rate/stiffness [N/m]
K_R	static-stiffness of an embedded rectangular foundation (Cone model) [/]
k_T	system response stiffness [N/m]
L	diameter of the smallest sphere that would circumscribe the particle [m]
l_1	distance bearing-soil contact M-T [m]
l_2	distance upper-bearing M-B [m]

Die approbierte gedruckte Originalversion dieser Dissertation ist an der TU Wien Bibliothek verfügbar.
The approved original version of this doctoral thesis is available in print at TU Wien Bibliothek.
TU Bibliothek Your knowledge hub WIEN

l_3	distance excitation-bearing M-E [m]
l_4	distance excitation-bearing B-E [m]
L_i	longest dimension of the particle i [m]
l_s	length of the assumed longitudinal beam/sleeper [m]
l_{4p}	compensation of the change in length l_4 (T1 to T2) [m]
LA_{RB}	Los Angeles coefficient [/]
M	mass of the test specimen before testing [g]
M_1	mass passing the 8 mm sieve [g]
m_1	initial dry mass of the test portion [g]
m_2	dry mass retained on the 1.6 mm sieve after fragmentation [g]
m_A	original sample weight [g]
m_B	mass of material retained on the 1.6 mm sieve [g]
M_R	material resilient modulus (also denoted as E_r) [MPa]
$M_{DE,RB}$	impact fragmentation value [/]
N	number of repeated loading cycles [/]
n	porosity of the sample [/]
o_s	sleeper overhang [m]
P	force in the tamping unit [N]
p	Linear momentum [kgm/s]
p_b	surface pressure between the sleeper and ballast [MN/m^2]
P_{max}	maximum allowed force in the tamping unit (per tine) [N]
q	deviator stress equal to $\sigma_1' - \sigma_3'$ [kPa]
R	surface angularity [/]
r_0	radius of a massless circular foundation (Cone model) [m]
r_i	radius of each corner in the particle outline [m]
R_W, R_R	radii of the weal and of the rail [m]
R_{b-f}	Relative Ballast Fouling Ratio [%]
r_{max-in}	radius of the maximum inscribed circle [m]

Die approbierte gedruckte Originalversion dieser Dissertation ist an der TU Wien Bibliothek verfügbar.
The approved original version of this doctoral thesis is available in print at TU Wien Bibliothek.
TU Bibliothek Your knowledge hub WIEN

S	Ballast settlement [mm]
S_f	shape factor [/]
s_i	loading contact length [m]
S_p	sphericity [/]
SZ_{RB}	impact fragmentation value [/]
t	simulation time/squeezing time [s]
t_1	simulation time at beginning of contact [s]
t_2, $t_{F_{max}}$	simulation time as the maximum force in the ballast matrix model is reached [s]
T_i	shortest dimension of the particle i [m]
t_i	impulse duration [s]
$t_{Contactbeginning}$	simulation time at beginning of contact [s]
t_{UPV}	travel time of the P-wave through the rock sample [s]
V	particle volume [m^3]
V_s	volume of solids on a unit volume [m^3]
V_{sp}	average volume of a single particle in a matrix [m^3]
v_{UPV}	travel velocity of the P-wave through the rock sample [m/s]
W_p	weight of the fractured particles [kg]
W_T	weight of the sample [kg]
x_e	deformation of the *Kelvin-Voigt* model [rad]
x_p	cumulative predeformation in the plastic spring [rad]
$x_{ballast}$	ballast matrix position in T [rad]
$x_{plastic}$	cumulative predeformation in the plastic spring [rad]
x_{tine}	tamping tine displacement in T [rad]
z	elastic depression of the rail [m]

Die approbierte gedruckte Originalversion dieser Dissertation ist an der TU Wien Bibliothek verfügbar.
The approved original version of this doctoral thesis is available in print at TU Wien Bibliothek.
TU Bibliothek Your knowledge hub WIEN

Appendix A

Laboratory test results - fouled ballast

Die approbierte gedruckte Originalversion dieser Dissertation ist an der TU Wien Bibliothek verfügbar.
The approved original version of this doctoral thesis is available in print at TU Wien Bibliothek.

MAPAG
Baustoffuntersuchung und Umweltanalytik
Staatlich akkreditierte Prüf- und Inspektionsstelle

MAPAG Materialprüfung G.m.b.H
2352 Gumpoldskirchen, Industriestraße 7
www.mapag.at

Baustoffuntersuchung Tel.: 0 22 52 / 62 797
bau@mapag.at Fax: DW 33

Umweltanalytik Tel.: 0 22 52 / 63 563
umwelt@mapag.at Fax: DW 46

Bankverbindung: ERSTE Bank
IBAN: AT29 2011 1000 0514 8111 - BIC: GIBAATWW
LG Wiener Neustadt FN 41076 g - DVR: 0386553 - ATU 19143905

An die
ÖBB Infrastruktur AG
SAE/FWT
z.H. Herrn DI Kuttelwascher
Nordbahnstraße 50
1020 Wien

Gumpoldskirchen 16.06.2016
Labor Nr. **2941/2016**
Sachbearbeiter Schneider

P R Ü F B E R I C H T

Entnahme und Untersuchung von zwei Oberbauschotterproben I 31,5/63 aus der eingebauten Schotterschicht der Baustelle Bahnhof Eisenstadt

Prüfungen gemäß EN 13450, BH 700, Ausgabe 01.04.2012

Am 30.05.2016 wurden von der MAPAG im Beisein von Herrn DI Popp der ÖBB zwei Oberbauschotterproben aus dem bestehenden Gleiskörper zur Untersuchung entnommen.

entnommene Proben:

Entnahmestelle:	Gleis 1, Mast 56
Probe 1.1	150 kg Oberbauschotter I 31,5/63 Schwellenoberkante bis Schwellenunterkante
Probe 1.2	440 kg Oberbauschotter I 31,5/63 Schwellenoberkante bis Schwellenunterkante

Die Korngrößenverteilung, der Feinkornanteil und der Feinstkornanteil der entnommenen Proben wurden gemäß EN 933-1 durch eine Nasssiebanalyse ermittelt. Die Mindestprobenmenge für die Korngrößenverteilung beträgt abweichend von der EN 933-1 gemäß BH 700 für Oberbauschotter I 31,5/63 100 kg.

Die Untersuchungsergebnisse sind auf den Beilagen 1 bis 2 zusammengestellt.

Anhand der Gesamtgewichte der entnommenen Einzelproben wurde wunschgemäß die gewichtete Korngrößenverteilung berechnet und in der Beilage 3 dargestellt.

MAPAG Akkreditierung Austria A 0002 ISO/IEC 17025 T Staatlich akkreditierte Prüfstelle

Die Prüfergebnisse beziehen sich ausschließlich auf das untersuchte Prüfgut. Prüf- und Inspektionsberichte oder Teile davon dürfen nur mit schriftlicher Zustimmung der MAPAG veröffentlicht werden.

Akkreditiert durch das BMWFW als Prüfstelle mit der GZ: BMWFW-92.221/0109-I/12/2016 vom 11. Februar 2016 und als Typ A-Inspektionsstelle mit der GZ: BMWFW-92.251/0061-I/12/2016 vom 11. Februar 2016.

Figure A.1: Laboratory test results of ballast samples taken in Eisenstadt on the 30.05.2016 - general information

Die approbierte gedruckte Originalversion dieser Dissertation ist an der TU Wien Bibliothek verfügbar.
The approved original version of this doctoral thesis is available in print at TU Wien Bibliothek.
TU Bibliothek Your knowledge hub WIEN

MAPAG
Staatlich akkreditierte Prüf- und Inspektionsstelle

Die weiteren Untersuchungen wurden an der Probe 1.1 durchgeführt.

Die Bestimmung des Widerstandes gegen Zertrümmerung mit dem Los-Angeles-Prüfverfahren erfolgte gemäß EN 1097-2 Punkt 5, Anhang A.

Der Widerstand gegen Verschleiß mit dem Micro-Deval-Prüfverfahren wurde gemäß EN 1097-1, Anhang A ermittelt.

Aus der Oberbauschotterprobe wurden 15 kg der Kornklasse 31,5/40 mm herausgesiebt, gewaschen und bei (110 ± 5) °C getrocknet. Die so vorbereiteten Prüfkörnungen wurden an das Nievelt Labor Deutschland GmbH, D-08451 Crimmitschau zur Bestimmung des Widerstandes gegen Zertrümmerung mit dem Schlagversuch gemäß EN 1097-2 Punkt 6, Anhang A übersandt.

Die Untersuchungsergebnisse sind auf der Beilage 4 zusammengestellt.

Weiters wurden dem Ingenieurbüro GEOsolution in 5351 Aigen-Voglhub ca. 75 kg Oberbauschotter der Probe 5 aus dem Schwellenfach 2 übersandt, der zuvor gewaschen und die Kornklasse 22,4/63 mm ausgesiebt wurde.

Prüfzeitraum: 30.05.- 15.06.2016

Eine Kopie des Entnahmeprotokolls ist als Beilagen 5 beigelegt.

MAPAG Akkreditierung Austria A 0002 ISO/IEC 17025 Staatlich akkreditierte Prüfstelle

Herr Ing. Christian Giller
Zeichnungsberechtigter

Verteiler:
1 x ÖBB, z.H. Herrn DI Kuttelwascher

2941/2016
Dieser Bericht umfasst 2 Seiten und 5 Beilagen.

Figure A.2: Laboratory test results of ballast samples taken in Eisenstadt on the 30.05.2016 - general information

Die approbierte gedruckte Originalversion dieser Dissertation ist an der TU Wien Bibliothek verfügbar.
The approved original version of this doctoral thesis is available in print at TU Wien Bibliothek.
TU Bibliothek Your knowledge hub WIEN

MAPAG
Staatlich akkreditierte Prüf- und Inspektionsstelle

Beilage 3 zu 2941/2016

Oberbauschotter I 31,5/63

Baustelle: Bahnhof Eisenstadt
Entnahmestelle: Gleis 1, Mast 56
gewichtete Mischprobe

Korngrößenverteilung ÖNORM EN 933-1 (Quadratlochsiebe):

Korngröße [mm]	Siebdurchgang [M.-%]	zulässige Anteile gemäß BH 700 Soll [M.-%]	Toleranz [M.-%]
80	**100**	100	100
63	**97**	95 - 100	95 - 100
50	**67**	65 - 95	65 - 95
40	**34**	30 - 60	30 - 65
31,5	**11**	1 - 25	1 - 25
22,4	**3**	0 - 5*	0 - 5*
31,5/50	**56**	mind. 50	mind. 50

* Bei Probenahme auf der Baustelle

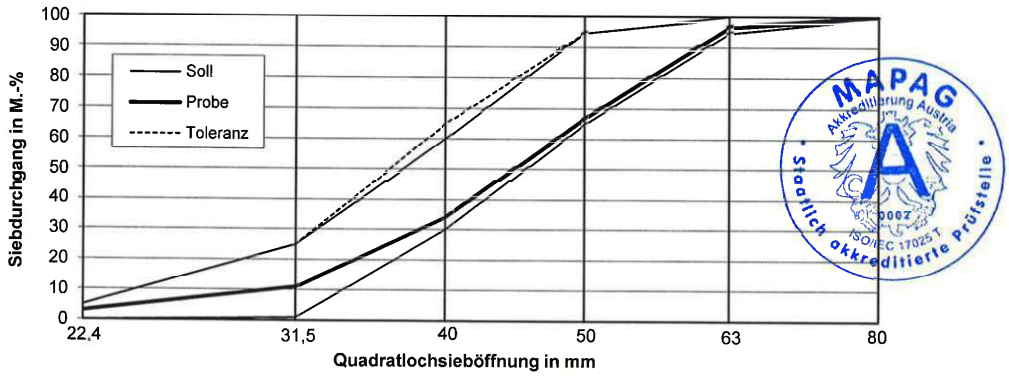

		zulässige Anteile BH 700	Kategorie EN 13450 ÖNORM B 3133
Gehalt an Feinkorn:			
Anteil < 0,5 mm in M.-%:	**0,5**	max. 1,0	B
Gehalt an Feinstkorn:			
Anteil < 0,063 mm in M.-%:	**0,3**	max. 1,0	B

Figure A.3: Laboratory test results of ballast samples taken in Eisenstadt on the 30.05.2016 - particle size distribution, content of fines

Die approbierte gedruckte Originalversion dieser Dissertation ist an der TU Wien Bibliothek verfügbar.
The approved original version of this doctoral thesis is available in print at TU Wien Bibliothek.
TU Bibliothek Your knowledge hub WIEN

MAPAG
Staatlich akkreditierte Prüf- und Inspektionsstelle

Beilage 4 zu 2941/2016

Baustelle Bahnhof Eisenstadt

Entnahmestelle: Gleis 1,Mast 56, Schwellenfach
Schwellenoberkante bis Schwellenunterkante, Probe 1.1

Rohdichte EN 1097-6 Anhang B:

Kornklasse:	Masse der Messprobe:	ρ_{cm}		zulässige Anteile BH 700	Kategorie EN 13450 ÖNORM B 3133
50/63	2479 g	**2,69**	Mg/m³	anzugeben	anzugeben

Widerstand gegen Zertrümmerung, Los-Angeles-Koeffizient EN 1097-2:

Kornklasse:		LA_{RB}:			
	31,5/50		**20**	max. 22	$LA_{RB}20$

Widerstand gegen Verschleiß, Nassprüfung, Micro-Deval-Koeffizient EN 1097-1:

Kornklasse: 31,5/50

		M.-%		
Einzelwerte:	$M_{DE}RB$:	9,8		
	$M_{DE}RB$:	10,9		
Mittelwert:	$M_{DE}RB$:	**10**	max. 16 M.-%	$M_{DE}RB$ 15

Widerstand gegen Zertrümmerung, Schlagzertrümmerung EN 1097-2:

Werte übernommen aus Prüfbericht 017/2016/62/2941 der Nievelt - Labor Deutschland GmbH

Kornklasse: 31,5/40

		M.-%		
Einzelwerte:	SZ_{RB}:	23,33		
	SZ_{RB}:	23,72		
	SZ_{RB}:	23,26		
Mittelwert:	SZ_{RB}:	**23,4**	max. 24,0 M.-%[1)]	$SZ_{RB}22$

[1)] Wenn der Los-Angeles-Koeffizient LA_{RB} max. 20 und der Micro-Deval-Koeffizient $M_{DE}RB$ max. 12 M.-% beträgt.

$$GKZ = \frac{(LA_{RB} + SZ_{RB} + M_{DE}RB * 1{,}37)}{3} = \mathbf{19{,}2}$$

MAPAG Akkreditierung Austria A 0002 ISO/IEC 17025 Staatlich akkreditierte Prüfstelle

Figure A.4: Laboratory test results of ballast samples taken in Eisenstadt on the 30.05.2016 - gross density, impact-attrition strength

Die approbierte gedruckte Originalversion dieser Dissertation ist an der TU Wien Bibliothek verfügbar.
The approved original version of this doctoral thesis is available in print at TU Wien Bibliothek.
TU Bibliothek Your knowledge hub WIEN

Die approbierte gedruckte Originalversion dieser Dissertation ist an der TU Wien Bibliothek verfügbar.
The approved original version of this doctoral thesis is available in print at TU Wien Bibliothek.

Curriculum Vitae

Personal information

Dipl.-Ing. Olja Barbir
[redacted]

Education

2008 - 2011:	Bachelor's degree Faculty of Civil Engineering, University of Rijeka, Croatia
2011 - 2013:	Master's degree Faculty of Civil Engineering, University of Rijeka, Croatia
03 - 09/2013:	Master's thesis Institute of Geotechnics, University of Natural Resources and Life Sciences, Vienna
2016 - 2022:	Doctoral programme in Engineering Sciences, Civil Engineering Institute of Geotechnics, TU Wien

Work experience

2015-2018:	Teaching and research assistant Institute of Geotechnics, Research Unit Ground Engineering, Soil and Rock Mechanics, TU Wien
2019-2020:	Project assistant Institute of Geotechnics, Research Unit Ground Engineering, Soil and Rock Mechanics, TU Wien
since 06/2022:	System Engineer Plasser & Theurer, Export von Bahnbaumaschinen, Gesellschaft m.b.H., Vienna

Distinction

2013:	Graduated "Magna cum laude" Faculty of Civil Engineering, University of Rijeka, Croatia

Vienna, September 2022

Die approbierte gedruckte Originalversion dieser Dissertation ist an der TU Wien Bibliothek verfügbar.
The approved original version of this doctoral thesis is available in print at TU Wien Bibliothek.
TU Bibliothek Your knowledge hub WIEN

Die approbierte gedruckte Originalversion dieser Dissertation ist an der TU Wien Bibliothek verfügbar.
The approved original version of this doctoral thesis is available in print at TU Wien Bibliothek.